frontiers | Research Topics

Bioactive materials for disease diagnosis and therapy

Edited by
Dan Shao, Mingqiang Li, Jie Tang and Yuce Li

Published in
Frontiers in Bioengineering and Biotechnology

FRONTIERS EBOOK COPYRIGHT STATEMENT

The copyright in the text of individual articles in this ebook is the property of their respective authors or their respective institutions or funders. The copyright in graphics and images within each article may be subject to copyright of other parties. In both cases this is subject to a license granted to Frontiers.

The compilation of articles constituting this ebook is the property of Frontiers.

Each article within this ebook, and the ebook itself, are published under the most recent version of the Creative Commons CC-BY licence. The version current at the date of publication of this ebook is CC-BY 4.0. If the CC-BY licence is updated, the licence granted by Frontiers is automatically updated to the new version.

When exercising any right under the CC-BY licence, Frontiers must be attributed as the original publisher of the article or ebook, as applicable.

Authors have the responsibility of ensuring that any graphics or other materials which are the property of others may be included in the CC-BY licence, but this should be checked before relying on the CC-BY licence to reproduce those materials. Any copyright notices relating to those materials must be complied with.

Copyright and source acknowledgement notices may not be removed and must be displayed in any copy, derivative work or partial copy which includes the elements in question.

All copyright, and all rights therein, are protected by national and international copyright laws. The above represents a summary only. For further information please read Frontiers' Conditions for Website Use and Copyright Statement, and the applicable CC-BY licence.

ISSN 1664-8714
ISBN 978-2-8325-4788-5
DOI 10.3389/978-2-8325-4788-5

About Frontiers

Frontiers is more than just an open access publisher of scholarly articles: it is a pioneering approach to the world of academia, radically improving the way scholarly research is managed. The grand vision of Frontiers is a world where all people have an equal opportunity to seek, share and generate knowledge. Frontiers provides immediate and permanent online open access to all its publications, but this alone is not enough to realize our grand goals.

Frontiers journal series

The Frontiers journal series is a multi-tier and interdisciplinary set of open-access, online journals, promising a paradigm shift from the current review, selection and dissemination processes in academic publishing. All Frontiers journals are driven by researchers for researchers; therefore, they constitute a service to the scholarly community. At the same time, the *Frontiers journal series* operates on a revolutionary invention, the tiered publishing system, initially addressing specific communities of scholars, and gradually climbing up to broader public understanding, thus serving the interests of the lay society, too.

Dedication to quality

Each Frontiers article is a landmark of the highest quality, thanks to genuinely collaborative interactions between authors and review editors, who include some of the world's best academicians. Research must be certified by peers before entering a stream of knowledge that may eventually reach the public - and shape society; therefore, Frontiers only applies the most rigorous and unbiased reviews. Frontiers revolutionizes research publishing by freely delivering the most outstanding research, evaluated with no bias from both the academic and social point of view. By applying the most advanced information technologies, Frontiers is catapulting scholarly publishing into a new generation.

What are Frontiers Research Topics?

Frontiers Research Topics are very popular trademarks of the *Frontiers journals series*: they are collections of at least ten articles, all centered on a particular subject. With their unique mix of varied contributions from Original Research to Review Articles, Frontiers Research Topics unify the most influential researchers, the latest key findings and historical advances in a hot research area.

Find out more on how to host your own Frontiers Research Topic or contribute to one as an author by contacting the Frontiers editorial office: frontiersin.org/about/contact

Bioactive materials for disease diagnosis and therapy

Topic editors

Dan Shao — South China University of Technology, China
Mingqiang Li — Third Affiliated Hospital of Sun Yat-sen University, China
Jie Tang — Monash University, Australia
Yuce Li — Sungkyunkwan University, Republic of Korea

Citation

Shao, D., Li, M., Tang, J., Li, Y., eds. (2024). *Bioactive materials for disease diagnosis and therapy*. Lausanne: Frontiers Media SA. doi: 10.3389/978-2-8325-4788-5

Table of contents

frontiers | Frontiers in Bioengineering and Biotechnology

TYPE Editorial
PUBLISHED 05 April 2024
DOI 10.3389/fbioe.2024.1403980

Check for updates

OPEN ACCESS

EDITED AND REVIEWED BY
Hasan Uludag,
University of Alberta, Canada

*CORRESPONDENCE
Yuce Li,
liyuce@wust.edu.cn
Mingqiang Li,
limq567@mail.sysu.edu.cn
Jie Tang,
Jie.Tang4@monash.edu
Dan Shao,
shaodan@scut.edu.cn

RECEIVED 20 March 2024
ACCEPTED 22 March 2024
PUBLISHED 05 April 2024

CITATION
Li Y, He J, Liu J, Li M, Tang J and Shao D (2024), Editorial: Bioactive materials for disease diagnosis and therapy.
Front. Bioeng. Biotechnol. 12:1403980.
doi: 10.3389/fbioe.2024.1403980

COPYRIGHT
© 2024 Li, He, Liu, Li, Tang and Shao. This is an open-access article distributed under the terms of the Creative Commons Attribution License (CC BY). The use, distribution or reproduction in other forums is permitted, provided the original author(s) and the copyright owner(s) are credited and that the original publication in this journal is cited, in accordance with accepted academic practice. No use, distribution or reproduction is permitted which does not comply with these terms.

Editorial: Bioactive materials for disease diagnosis and therapy

Yuce Li[1]*, Jing He[1], Jixiu Liu[1], Mingqiang Li[2]*, Jie Tang[3]* and Dan Shao[4]*

[1]College of Life Science and Health, Wuhan University of Science and Technology (WUST), Wuhan, China, [2]Laboratory of Biomaterials and Translational Medicine, Center for Nanomedicine, The Third Affiliated Hospital, Sun Yat-sen University, Guangzhou, China, [3]Monash Institute of Pharmaceutical Sciences, Monash University, Parkville, VIC, Australia, [4]School of Biomedical Sciences and Engineering, Guangzhou International Campus, South China University of Technology, Guangzhou, China

KEYWORDS

bioactive materials, drug delivery, tissue engineering, regenerative medicine, disease diagnostics

Editorial on the Research Topic
Bioactive materials for disease diagnosis and therapy

Traditional biomaterials such as drug carriers and tissue engineering scaffolds are often biologically inert to avoid unnecessary concerns regarding biocompatibility. Bioactive materials are a class of materials that possess intrinsic biological activity, allowing them to interact with organs, tissues, or cells in the microenvironment of diseases, thereby regulating biological functions or enhancing the therapeutic effect of intervention. The emergence of bioactive materials has provided a new paradigm for the treatment and diagnosis of diseases. This Research Topic focuses on bioactive materials for disease diagnosis and treatment, with a total of 16 papers published, including seven review papers and nine original research papers. These papers were authored by 118 researchers from universities, hospitals, research institutes, and companies around the world, and have attracted 25.1 thousand views, 5.5 thousand downloads, and 15 citations from researchers worldwide as of 20 March 2024. Certainly, this Research Topic has undoubtedly served as a valuable platform for researchers to exchange advancements in the field of biologically active materials.

The seven review papers provided by this Research Topic summarize the research progress of bioactive materials such as nanomaterials, nanobiosensors, and dental implants, outlining their applications in the diagnosis and treatment of diseases such as ischemic stroke, bone and cartilage repair, bacterial infections, tuberculosis, and urinary tissue engineering. Zhan et al. introduced the advancements in stimulus-responsive nanomedicines for treating ischemic stroke. Duan et al. outlined the utilization of bioactive materials and innovative technologies for urinary regeneration and tissue engineering. In the field of dental implants, Wang et al. comprehensively reviewed the progress in biomimetic structures and associated signal pathways regarding the surface modification methods and emerging biomaterials to accelerate osseointegration. Yang et al. systematically introduced the current research status of functional nanobiosensors for diagnosis of tuberculosis. In the field of combating bacterial infections, Chen et al. specifically introduced bioactive materials for targeted delivery of antibiotics from the aspects of drug delivery and endogenous biological functions. Yu et al. introduced the research progress of graphene and its derivatives in the fields of bone tissue engineering and

cartilage tissue engineering, and prospected the possible direction of graphene-based materials in orthopedics. Particularly, Fernández-Gómez et al. focused on the latest nanotechnology developed by Spanish authors for disease treatments during the period from 2017 to 2022, and outlined the future trends and directions of nanomedical research.

Since the dawn of human civilization, we have grappled with the challenge of malignant tumors, while they persisted as a significant threat to human health and life. Treatments that leverage the generation of reactive oxygen species (ROS) within tumor cells to induce tumor cell death, including photodynamic therapy, chemotherapy, and so on, represent a class of recently developed therapies with good therapeutic effects and fewer side effects. Luo et al. encapsulated the photosensitizer chlorin e6 (Ce6) within albumin nanocages to fabricate Ce6-albumin nanoparticles (CA-NPs) using a well-defined nanoprecipitation method. These nanoparticles exhibit enhanced photostability, photoreactivity, and remarkable resistance towards photobleaching compared to free Ce6. Animal experiments have demonstrated the efficient accumulation of these nanoparticles in bladder cancer, leading to significant tumor treatment efficacy upon light exposure. Moreover, these nanoparticles effectively induced apoptosis in fresh human bladder tumor tissue samples. In another study, Zhang et al. introduced a novel nanocatalyst based on non-oxidized MXene-Ti_3C_2Tx quantum dots. Within cancer cells, this nanocatalyst facilitates the Fenton reaction, converting hydrogen peroxide into highly reactive hydroxyl radicals (•OH). Consequently, it induces ferroptosis in tumor cells through lipid peroxidation and mitochondrial dysfunction. Moreover, Zhang et al. utilized cancer cell membrane (CM)-coated mesoporous silica nanoparticles (MSNs) to load a two-photon fluorescence probe (TPFP), constructing a tumor-targeted bioactive nanosensor. This sensor enables the monitoring of hydrogen peroxide levels generated within tumors using two-photon microscopy and predicts the prognosis of chemotherapy based on hydrogen peroxide content. Photothermal therapy and gas therapy are two types of non-invasive treatments that kill tumor cells by generating heat or releasing gases such as carbon monoxide/nitric oxide locally in the tumor. Zuo et al. loaded nitric oxide donors into gold nanoparticles and investigated their applications in radiotherapy sensitization, photothermal therapy and nitric oxide gas therapy. Through the combination of near-infrared light and X-ray irradiation, these nanoparticles released a large amount of heat, ROS, and nitric oxide locally in the tumor. It is noteworthy that the reaction between ROS and nitric oxide produces more toxic reactive nitrogen species (RNS). This synergistic effect leads to excellent anti-tumor therapeutic effects.

Bacterial infections pose a significant obstacle during the process of skin tissue regeneration and represent a serious threat to human health. Despite the development of numerous antibiotics to combat bacterial infections, the emergence of superbugs has rendered these antibiotics ineffective. Bioactive materials for antimicrobial purposes have been widely utilized in various aspects of daily life. Liu et al. prepared a complex of Cu^{2+} and MXene (Cu(II)@MXene) and incorporated it into hyaluronic acid hydrogel to fabricate antibacterial dressings. These dressings facilitate easy application to wounds of various shapes owing to their rapid adhesion, self-healing, and injectability properties. The Cu(II)@MXene significantly accelerated the healing of infected wounds by serving as a photothermal antibacterial barrier, eliminating ROS generated during wound healing and promoting vascular regeneration. Bao et al. synthesized a bioactive antibacterial material, Ag-TiO_2/ZIF-8, using a solvothermal method. They achieved excellent antibacterial effects against *E. coli* and *B. subtilis* by controlling the ratio of Ag-TiO_2. Moreover, the prepared material demonstrated good stability and durability, and the antibacterial activity remained effective for over 5 months.

Tissue regeneration and repair provide crucial opportunities for the treatment of various diseases and injuries. Intracranial stents serve to support blood vessels, restore cerebral blood flow, and prevent ischemia and damage to brain tissue, playing a significant role in the treatment and postoperative repair of cerebrovascular diseases. Bi et al. incorporated a bioactive compound derived from *Salvia miltiorrhiza*, salvianolic acid B (SALB), into chitosan and immobilized it onto a nickel-titanium alloy plate using dopamine, thereby creating a bioactive coating. Continuous release of SALB was observed within 28 days after application. This bioactive layer effectively inhibited the proliferation, adhesion, and migration of smooth muscle cells, thereby preventing the occurrence of neointimal hyperplasia and restenosis. Osteogenesis and the restoration of bone function are closely associated with the generation of nerves and blood vessels. Han et al. investigated the characteristics of sensory nerves and neovascularization during *in situ* osteogenesis, examining their relationship with neurovascular networks, mineralization, and their biological regulators. The findings revealed that during osteogenesis, the expression of semaphorin 3A (Sema3A) increased, initiating the appearance of sensory fibers followed by vascular and bone formation. Furthermore, the occurrence of innervation and vascularization showed temporal and spatial correlation. Thus, Sema3A emerges as a potential target for regulating bone formation.

The growing emphasis on healthy living has spurred rapid developments in beauty and anti-aging treatments over recent years. While stem cells possess excellent therapeutic potential for skin rejuvenation, their safety concerns constrain their widespread application. Extracellular vesicles derived from stem cells contain biological contents similar to those of stem cells and exhibit therapeutic efficacy comparable to stem cells in anti-aging and skin repair. Ye et al. isolated exosomes from mesenchymal stem cells (hMSC-Exo) and investigated their potential in treating sensitive skin. *In vitro* experiments revealed that hMSC-Exo significantly boosted the proliferation and migration of human fibroblasts. Importantly, the authors conducted a clinical trial, demonstrating that twice-daily application of hMSC-Exo for 28 days markedly reduced skin sensitivity to lactic acid-induced sting and decreased skin sebum production. These findings suggest that hMSC-Exo exerts a substantial alleviating effect on symptoms in individuals with sensitive skin.

In summary, this Research Topic included a series of excellent research papers regarding bioactive materials and their applications in disease diagnosis and therapy. It may help the researchers around the world to share their opinions in this field. It is foreseeable that

this field will become an important branch in biomaterials and play more important roles in disease treatment and diagnoses.

Author contributions

YL: Writing–original draft, Writing–review and editing. JH: Writing–original draft. JL: Writing–original draft. ML: Writing–review and editing. JT: Writing–review and editing. DS: Writing–review and editing.

Acknowledgments

The editors appreciate the contributions of all authors to this Research Topic, the constructive comments of all the reviewers, and the editorial support from Frontiers throughout the publication process.

Conflict of interest

The authors declare that the research was conducted in the absence of any commercial or financial relationships that could be construed as a potential conflict of interest.

The author(s) declared that they were an editorial board member of Frontiers, at the time of submission. This had no impact on the peer review process and the final decision.

Publisher's note

All claims expressed in this article are solely those of the authors and do not necessarily represent those of their affiliated organizations, or those of the publisher, the editors and the reviewers. Any product that may be evaluated in this article, or claim that may be made by its manufacturer, is not guaranteed or endorsed by the publisher.

frontiers | Frontiers in Bioengineering and Biotechnology

TYPE Original Research
PUBLISHED 06 October 2022
DOI 10.3389/fbioe.2022.1028470

Check for updates

OPEN ACCESS

EDITED BY
Dan Shao,
South China University of Technology, China

REVIEWED BY
Yingshuai Wang,
Weifang Medical University, China
Li Li,
Suzhou Institute of Biomedical Engineering and Technology, (CAS), China

*CORRESPONDENCE
Yi Qu,
yiqucn@sdu.edu.cn

SPECIALTY SECTION
This article was submitted to Biomaterials, a section of the journal Frontiers in Bioengineering and Biotechnology

RECEIVED 26 August 2022
ACCEPTED 26 September 2022
PUBLISHED 06 October 2022

CITATION
Zhang H, Li X, You P, Song X, Fan Q, Tao X and Qu Y (2022), Highly tumoricidal efficiency of non-oxidized MXene-Ti_3C_2Tx quantum dots on human uveal melanoma. *Front. Bioeng. Biotechnol.* 10:1028470. doi: 10.3389/fbioe.2022.1028470

COPYRIGHT
© 2022 Zhang, Li, You, Song, Fan, Tao and Qu. This is an open-access article distributed under the terms of the Creative Commons Attribution License (CC BY). The use, distribution or reproduction in other forums is permitted, provided the original author(s) and the copyright owner(s) are credited and that the original publication in this journal is cited, in accordance with accepted academic practice. No use, distribution or reproduction is permitted which does not comply with these terms.

Highly tumoricidal efficiency of non-oxidized MXene-Ti_3C_2Tx quantum dots on human uveal melanoma

Huankai Zhang[1], Xuesong Li[2], Pan You[3], Xian Song[1], Qian Fan[1], Xutang Tao[2] and Yi Qu[1]*

[1]Department of Ophthalmology, Shandong Provincial Qianfoshan Hospital, Shandong University, Jinan, China, [2]State Key Laboratory of Crystal Materials, Shandong University, Jinan, China, [3]Department of Cell Biology, School of Basic Medical Sciences, Shandong University, Jinan, China

Uveal melanoma (UM) is a highly malignant intraocular tumor with poor prognosis. Current topical ophthalmic therapies purpose to conserve the eye and useful vision. Due to the risks and limited clinical benefits, the topical treatments of UM remain challenging and complex. In this study, newly developed non-oxidized MXene-Ti_3C_2Tx quantum dots (NMQDs-Ti_3C_2Tx) are proposed for UM treatment. Surprisingly, NMQDs-Ti_3C_2Tx shows significant tumor-killing effects on UM cells in a dose-dependent manner and causes severe necrosis near the injection site on the xenograft UM tumor model. Moreover, NMQDs-Ti_3C_2Tx exhibits excellent biocompatibility with normal retina pigment epithelium (RPE) cells and does not cause any damage in C57BL/6 mice eyes. Mechanistically, NMQDs-Ti_3C_2Tx inhibits the proliferation, invasion, and migration of UM cells *via* its desirable reactive oxygen species (ROS) generation ability, which causes lipid peroxidation and mitophagy, triggering cell ferroptosis. Furthermore, NMQDs-Ti_3C_2Tx is detected accumulating in autolysosomes which exacerbates cell death. This work provides new light on the topical treatment of UM.

KEYWORDS

uveal melanoma, non-oxidized MXene-Ti_3C_2Tx quantum dots, reactive oxygen species, ferroptosis, mitophagy

1 Introduction

Uveal melanoma (UM) is the most common intraocular malignancy that occurs in adults (Mallone et al., 2020). Currently, the first-line topical treatments targeting UM aimed to conserve the eye and useful vision are radiotherapy, surgery, transpupillary thermotherapy (TTT) and photodynamic therapy (PDT). Radiotherapy, including plaque brachytherapy and radiation, is the most common eye-conserving therapy and has achieved certain efficacy in UM therapy (Jager et al., 2020). However, these treatments need surgeons to place plaques or place fiducial markers; the side effects of radiotherapy, such as damage to the neighboring normal tissues, neovascular

glaucoma, retinal detachment, or cataract, have plagued clinicians for years (Bianciotto et al., 2010). Surgery, including local resection, enucleation, and exenteration, is always employed when the tumor is unsuitable for radiotherapy (Jager et al., 2020). Local resection could probably maximize the removal of neoplasm while keeping the integrity of the eye as possible, but even then, vision is affected by different degrees. Enucleation and exenteration could affect the facial appearance of patients, which further impacts their quality of life. TTT and PDT were initially designed as alternatives to radiotherapy; however, these therapies show limited clinical benefit while carrying several risks (Pereira et al., 2013). Recently, AU-011, a novel kind of PDT, has been approved by Food and Drug Administration (FDA) as an orphan drug targeting UM, but the tumor-killing effect of AU-011 is limited if the tumor has an anterior location and could not be irradiated entirely (Kines et al., 2018). Hence, topical ophthalmic therapies for UM aimed to conserve the eye and useful vision are still needed.

Over the past few decades, due to the fast-growing area of nanotechnology, Chemodynamic therapy (CDT), one kind of novel tumor therapeutic strategy, has achieved breakthroughs. Iron-based nanocatalysts, which could release ferrous ions, are the most common catalysts for CDT. Other nanocatalysts, such as Cu^{1+} and $Mn^{2+,}$ also reveal the desirable catalytic ability (Nie et al., 2019; Wang et al., 2020; Lin et al., 2021). They could initiate the Fenton reaction and catalyze hydrogen peroxide (H_2O_2) into hydroxyl radical (•OH), which exerts powerful toxic effects on tumor cells (Tang et al., 2019). Thus, CDT based on nanocatalysts exhibits great potential applications in the ocular treatment of UM. However, conventional CDT has several shortcomings. Due to the weakly acidic tumor microenvironment (TME), the efficiency of the Fenton reaction is relatively low, which cannot generate enough reactive oxygen species (ROS) to kill tumor cells (Ranji-Burachaloo et al., 2018). Besides that, the potential toxicity risk of nanoparticles might be dosage-dependent (Hu et al., 2018). To avoid potential side effects, more efficacious and safer nanoparticles for CDT need to be explored.

As reported previously (Li et al., 2020), we have successfully prepared non-oxidized MXene-Ti_3C_2Tx quantum dots (NMQDs-Ti_3C_2Tx), a new kind of Ti-based nanocatalysts with excellent dispersion and stability. Surprisingly, NMQDs-Ti_3C_2Tx exhibits highly efficient tumor-killing effects on cervical and breast cancer cells and shows excellent biocompatibility. Therefore, the characteristics of NMQDs-Ti_3C_2Tx inspire us that the new Ti-based material may have great potential to be applied to UM as a kind of agent *in situ*.

In this study, we focus on evaluating the tumoricidal efficacy of NMQDs-Ti_3C_2Tx on UM cells and UM xenograft mouse models. As expected, the performance of NMQDs-Ti_3C_2Tx in UM cells is incredible. NMQDs-Ti_3C_2Tx shows a robust tumor-killing capacity in UM cells. NMQDs-Ti_3C_2Tx could significantly inhibit the activity of UM cells and show no protumor effect even below 100 μg ml^{-1}. More importantly, NMQDs-Ti_3C_2Tx only has toxicity to tumor cells near the injection site in UM xenograft mouse models, which is very suitable for ocular topical therapies. Biocompatibility of NMQDs-Ti_3C_2Tx is explored on retinal pigment epithelium (RPE) cells and in normal eyes of C57BL/6 mice. No apparent toxicity is observed. Mechanistically, NMQDs-Ti_3C_2Tx could induce a large amount of •OH in UM cells, resulting in lipid peroxidation and mitochondrial dysfunction. Meanwhile, NMQDs-Ti_3C_2Tx is detected accumulating in autolysosomes, and the ROS reaction in autolysosomes could destruct the autolysosomes and further accelerate cell death (Figure 1). As a result, a low dosage of NMQDs-Ti_3C_2Tx could have the potential for topical therapy on UM.

2 Materials and methods

2.1 The synthesis and characterization of NMQDs-Ti_3C_2Tx

NMQDs-Ti_3C_2Tx was synthesized using a micro-explosion method described previously (Li et al., 2020). The MXene-Ti_3C_2Tx and NMQDs-Ti_3C_2Tx were characterized using a Hitachi S-4800 field-emission SEM system and a JEOL JEM 2100F transmission electron microscope.

2.2 Cell lines and cell culture

Human RPE cell line, UM cell line C918, and UM cell line MUM-2B were purchased from the Chinese Academy of Sciences Cell Bank (Shanghai, China). RPE cells were cultured in Dulbecco's modified Eagle's medium (DMEM, Gibco) with 10% fetal bovine serum (FBS, Gibco). UM cells were cultured in RPMI-1640 (Gibco, United States) with or without 10% FBS. All cell lines were grown at 37°C and 5% CO_2.

2.3 Cell viability assay

Cell-counting kit-8(CCK-8) assay (Beyotime, China) was used to examine the effect of NMQDs-Ti_3C_2Tx on normal and UM cell viability. Before incubation with the indicated concentrations of NMQDs-Ti_3C_2Tx for different incubation times, cells were seeded into a 96-well plate at 3.0×10^3 cells per well and cultured for 12 h for cell attachment. Considering the absorbance of NMQDs-Ti_3C_2Tx itself, the fresh medium was replaced before adding 10 μL of CCK-8 solution per well. After 3 h of incubation at 37°C and 5% CO_2, the absorbance at 450 nm was measured.

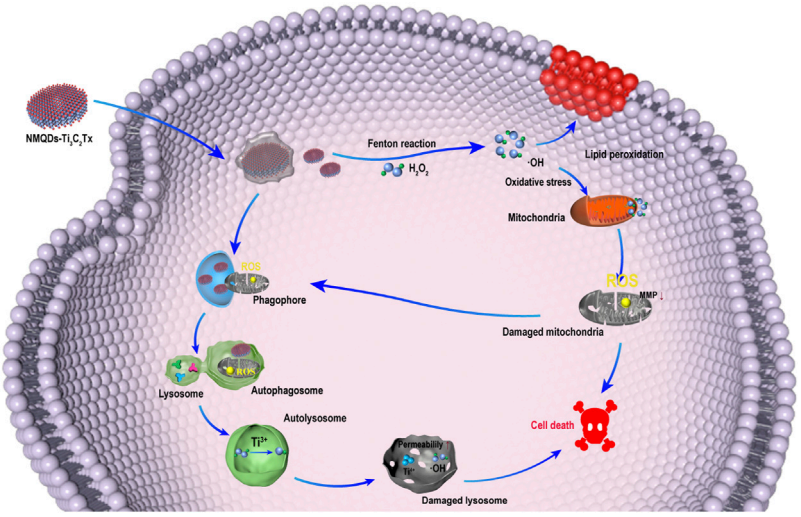

FIGURE 1
Schematic illustrating the antitumor pathway of NMQDs-Ti_3C_2Tx.

2.4 Cell live/dead staining

Cells were seeded into a 6-well plate at 7.0×10^5 cells per well and cultured for 12 h for cell attachment before incubation with the indicated concentrations NMQDs-Ti_3C_2Tx for 6 h. Then, Cells were washed gently once in phosphate-buffered saline (PBS) before Live/Dead (Abbkin, China) assay. Finally, a fluorescence microscope (Olympus IX 73 fluorescence microscope, Japan) was used to capture the images.

2.5 Colony formation assay

Cells were seeded into a 6-well plate at a density of 300 cells per well. Then, cells were incubated with different concentrations of NMQDs-Ti_3C_2Tx for approximately 2 weeks. The indicated concentrations of NMQDs-Ti_3C_2Tx were added every 3 days during this period. Once the colonies were visible to the naked eye, the cells were fixed using 4% paraformaldehyde, and then 0.1% crystal violet solution was used to stain the cells. The number of cell colonies was counted using a microscope and ImageJ in the end.

2.6 Cell invasion assay and cell wound-healing assay

The invasion assays were performed using a Transwell BD Matrigel (Corning, United States). The cells previously incubated with different concentrations of NMQDs-Ti_3C_2Tx for 6 h were seeded in upper chambers in a serum-free medium. At the same time, 800 μL cultured medium with 20% FBS was supplemented in lower chambers. Before adding UM cells, diluted Matrigel (ratio: 1:8) (Corning Costar, United States) was added to the upper chambers. After 24 h, cells were stained with 0.1% crystal violet. A microscope was used to capture the images.

The cells previously incubated with different concentrations of NMQDs-Ti_3C_2Tx for 6 h were seeded into a 6-well plate at a density of 7.0×10^5 cells per well. Cells were scratched with a sterile 200-μL pipette tip after adhering to the wall. Cells were then cultured with different concentrations of NMQDs-Ti_3C_2Tx. At 0 and 12 h, the images of wounds were captured.

2.7 Measurement of ROS generation, lipid hydroperoxide generation, mitochondrial membrane potential (MMP) alteration, Malondialdehyde (MDA), and Glutathione (GSH)

Cells were seeded into a 6-well plate at a density of 7.0×10^5 cells per well. After 12 h, cells were incubated with different concentrations of NMQDs-Ti_3C_2Tx for 6 h. The cells were then incubated with H2DCFDA (Beyotime, China), C11-BODIPY (MkBio, China), or Tetramethylrhodamine (TMRM, Sigma, United States) solution according to the instruction. According to the manufacturer's protocol, MDA content was measured using an MDA assay kit (Abbkin, China), and GSH content was measured using a GSH/GSSG assay kit (Beyotime, China).

2.8 Real-time PCR

According to the manufacturer's protocol, the total RNA from UM cells was isolated using the Fastagen (Feijie Biotech, China). RNA then underwent reverse transcription using the NeuScript II 1st strand cDNA synthesis kit (Vazyme, China). Then, the SYBR Green (CWBIO, China) real-time PCR (RT-PCR) was analyzed on Roche LightCycler 96 system. The relative RNA expression of PTGS2, SLC7A11 and LC3 were normalized using the RNA expression of GAPDH. The specific primers applied for RT-PCR reaction are shown in (Supplementary Table S1).

2.9 Electron microscopy

After 6 h stimulation of NMQDs-Ti_3C_2Tx, UM cells were harvested and fixed with the electron microscope fixation liquid at 4°C for storage. 1% osmic acid and 0.1 M phosphate buffer (PH7.4) mixture were used for 2 h post-fixation. UM cells were then dehydrated with different concentrations of alcohol and then dehydrated with 100% acetone twice. Next, cells were infiltrated with acetone/812 embedding agent and embedded in a pure 812 embedding agent. Then, UM cells were placed at 60°C for 48 h. Next step, UM cell samples were chopped into 60–80 nm sections and stained with 2% uranyl acetate saturated alcohol solution for 8 min in the dark. 2.6% Lead citrate was used to avoid CO2 staining. Finally, the copper mesh slices were dried at room temperature overnight in a copper mesh box. Images were observed under a transmission electron microscope.

2.10 Lysosomes and mitochondrion colocalization

UM cells were seeded in a 6-well plate containing slides and then cultured with NMQDs-Ti_3C_2Tx (100 g ml^{-1}) for 1 h. The Lyso-Tracker Red and Mito-Tracker Red (Beyotime, China) were used to stain the lysosomes and mitochondrion of UM cells, respectively. Finally, UM cells were observed on a fluorescence microscope (Olympus IX 73 fluorescence microscope, Japan).

2.11 Animal studies

All experimental procedures were approved by the Laboratory Animal Ethical and Welfare Committee of Shandong University Cheeloo College of Medicine (Shandong, China). The permission number of animal experiment ethical approval is 20158.

Intraocular injection mouse model: Six C57 BL/6 mice were randomly divided into two groups. Mice in the control group received unilateral intraocular injections of 1 μL saline. Mice in the experimental group received unilateral intraocular injections of 1 μL NMQDs-Ti_3C_2Tx (2 μg L^{-1}). After 3 days, all mice were sacrificed under deep anesthesia, and the eyes were excised for further characterization.

UM xenograft mouse model: Eight BALB/c nude mice (6-week-old female) were subcutaneously injected with 100 μl of 5×10^6 C918 cells to the right shoulder. The mice were randomly divided into two groups (n = 4) for antitumoral studies when the tumor volume reached 50–100 mm^3. The tumor-bearing mice were treated with 1) saline and 2) 10 mg kg^{-1} NMQDs-Ti_3C_2Tx, *via* intra-tumoral administration. Tumor volume and body weight were recorded every 2 days. The tumor volume was measured using the formula: tumor volume (mm^3) = (length × $width^2$)/2. On the eighth day after the first administration, xenograft tumors were excised for further characterization.

2.12 Statistical analysis

Data are presented as mean ± standard error of the mean (error bars). Every experiment was repeated at least three times independently. The differences between two groups were evaluated using Student's t-test, whereas the statistical analysis of multiple groups was performed using the one-way ANOVA. Statistics were calculated using GraphPad Prism 7. Significant differences are indicated as $^*p < 0.05$, $^{**}p < 0.005$, $^{***}p < 0.0005$, $^{****}p < 0.0001$.

3 Results and discussion

3.1 Synthesis of NMQDs-Ti_3C_2Tx

We first prepared MXene-Ti_3C_2Tx, the raw material of NMQDs-Ti_3C_2Tx, through etching Ti3AlC2. The MXene-Ti_3C_2Tx has a typical accordion-like microstructure (Figure 2A). Then, NMQDs-Ti_3C_2Tx was obtained by using the micro explosion method as previously reported by our group (Li et al., 2020). We inserted liquid nitrogen (L-N_2) into Ti_3C_2Tx layers and subsequently loaded with boiling deionized water. Drastic temperature changes caused micro-explosion. Finally, the pale-yellow powders of NMQDs-Ti_3C_2Tx were obtained from aqueous dispersion by freeze-drying. Moth-eaten cavities caused by micro explosion demonstrated that NMQDs-Ti_3C_2Tx was successfully prepared (Figure 2B). Through the transmission electron microscopic (TEM), we could find NMQDs-Ti_3C_2Tx exhibits a regular disc shape (Figure 2C). And the aqueous solution of NMQDs-Ti_3C_2Tx is pale yellow (Figure 2D).

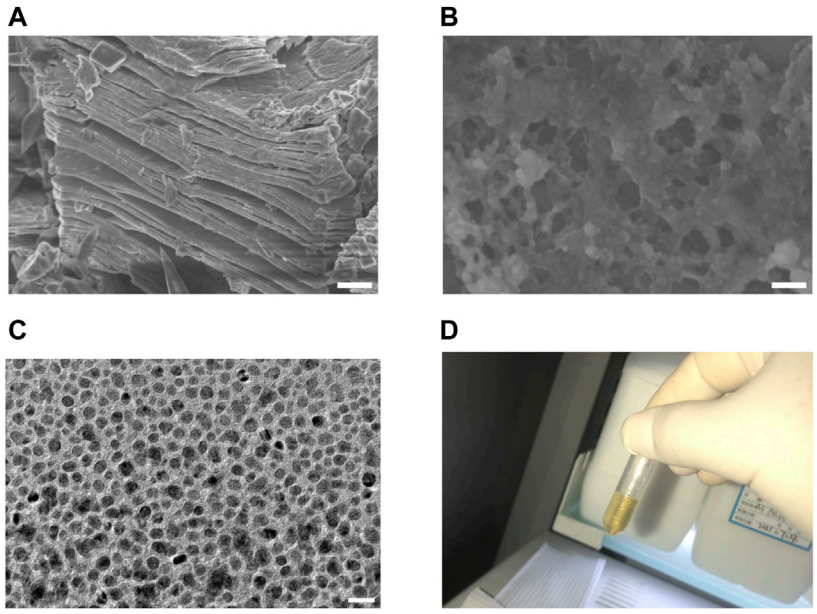

FIGURE 2
The preparation and characterization of NMQDs-Ti_3C_2Tx **(A)** SEM image of MXene-Ti_3C_2Tx. Scale bar: 2 μm. **(B)** SEM image of MXene-Ti_3C_2Tx after microexplosion. Scale bar: 200 nm **(C)** TEM image of NMQDs-Ti_3C_2Tx. Scale bar: 20 nm. **(D)** the aqueous solution of NMQDs-Ti_3C_2Tx.

3.2 NMQDs-Ti_3C_2Tx inhibits UM cell proliferation and clonogenic potential

To assess the cytotoxicity of NMQDs-Ti_3C_2Tx, Two UM cell lines C918 and Mum-2B were treated with different concentrations (0, 25, 50, 100, 150, and 200 μg ml^{-1}) of NMQDs-Ti_3C_2Tx for different times (12, 24 and 36 h). Effects of NMQDs-Ti_3C_2Tx on cell proliferation were analyzed by a CCK-8 assay. As shown in Figures 3A,B, the proliferation viability of UM cells was decreased in a dose-dependent manner. For C918 cells, the IC50 values of NMQDs-Ti_3C_2Tx at 12 h, 24 h, and 36 h were 69.80 μg ml^{-1}, 63.37 μg ml^{-1}, and 63.15 μg ml^{-1}, respectively; while for MUM-2B cells, the values were 64.36 μg ml^{-1}, 63.28 μg ml^{-1}, and 55.94 μg ml^{-1}, respectively. Low cytotoxicity for normal cells is one of the essential properties of nanocatalysts in tumor detection and therapy, especially in the human eye, a highly specialized organ of vision. Hence, normal retina pigment epithelium (RPE) cell line was used as a control. As shown in (Supplementary Figure S1), there was no significant effect on the normal RPE cell viability cultured with NMQDs-Ti_3C_2Tx after different incubation times, even at a high concentration (200 μg ml^{-1}). These results illustrated that NMQDs-Ti_3C_2Tx have high toxicity for UM cells, not for healthy ocular cells.

To further investigate the ability of NMQDs-Ti_3C_2Tx on the viability of UM cells, we also measured the reproductive viability of single cells by plate colony formation assays, another experiment reflecting the potential malignant properties of tumor cells. In C918 and MUM-2B cell lines, the number and the size of colonies were mildly decreased in the presence of 25 μg ml^{-1} NMQDs-Ti_3C_2Tx; at the concentration of 50 μg ml^{-1}, the number and the size of colonies were significantly decreased. In addition, there was no colony formation at the concentration of 100 μg ml^{-1} and 200 μg ml^{-1} (Figures 3C–F; Supplementary Figure S2). However, in the CCK-8 assay, we observed no statistically significant difference between 0 μg ml^{-1} and 25 μg ml^{-1}. We considered that the long-term stimulation of NMQDs-Ti_3C_2Tx for UM cells in plate colony formation assays led to different outcomes compared with the CCK-8 assay.

Moreover, C918 and MUM cells were subjected to live/dead staining, where viable cells were stained with Calcein-AM (green) and dead cells were stained with PI (red). After being stimulated with NMQDs-Ti_3C_2Tx for 6 h, few dead cells were observed when cultured with NMQDs-Ti_3C_2Tx at 50 μg ml^{-1}, while a small number of dead cells were observed when cultured with NMQDs-Ti_3C_2Tx at 100 μg ml^{-1} (Figures 3G,H). Hence, to avoid cell death-related effects, UM cells were cultured with indicated concentrations (50 and 100 μg ml^{-1}) of NMQDs-Ti_3C_2Tx for 6 h in subsequent experiments.

3.3 NMQDs-Ti_3C_2Tx inhibits UM cell invasion and migration

It is well known that tumor invasion and migration are the two essential features of tumor metastasis. Upon detachment

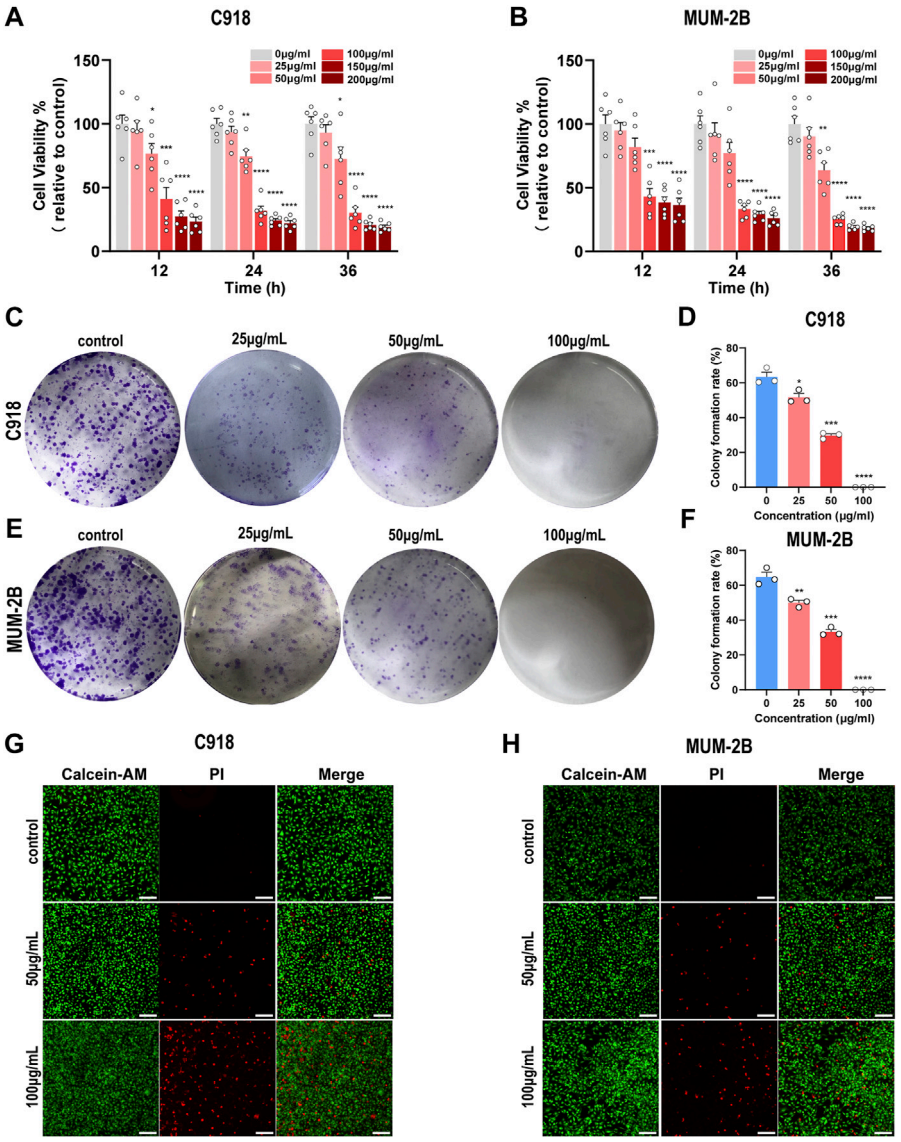

FIGURE 3
NMQDs-Ti_3C_2Tx inhibits UM cell proliferation and clone formation **(A and B)** The CCK-8 assay of C918 and Mum-2B cells cultured with different concentrations of NMQDs-Ti_3C_2Tx for 12, 24, and 36 h (n = 6; *$p < 0.05$, **$p < 0.005$, ***$p < 0.0005$, ****$p < 0.0001$) **(C and E)** Colony formation assay results. C918 and Mum-2B UM cells were cultured with different concentrations of NMQDs-Ti_3C_2Tx for 12 days **(D and F)** The clone formation rate results were counted according to the graph C and E (n = 3; *$p < 0.05$, **$p < 0.005$, ***$p < 0.0005$, ****$p < 0.0001$). **(G and H)** Live/dead staining results. The live cells were stained with Calcein- AM, and the dead cells were stained with PI. Scale bar: 200 μm. All above data are presented as the mean ± SEM.

from the primary site, invasion and migration of tumor cells into surrounding microvasculature of the lymphatic and blood vessels start, eventually resulting in tumor colonization of distant organs (Polacheck et al., 2013). Up to 50% of patients with UM will have metastases. Once metastases develop, the prognosis becomes poor. Although 5-year survival rates of UM patients have not improved, early intervention for UM could efficiently conserve the eye and useful vision with additional potential for improving long-term survival (Kines et al., 2018). Hence, we wonder whether NMQDs-Ti_3C_2Tx has the potential to suppress UM cell invasion and migration.

A transwell invasion assay was employed to explore the UM cell invasion capacity, and a wound-healing assay was used to investigate the UM cell migration capacity. In order to guarantee the correct results, UM cells were cultured with indicated concentrations of NMQDs-Ti_3C_2Tx for 6 h before the experiments. Following the increased concentration of NMQDs-Ti_3C_2Tx in UM cell lines, the results of the

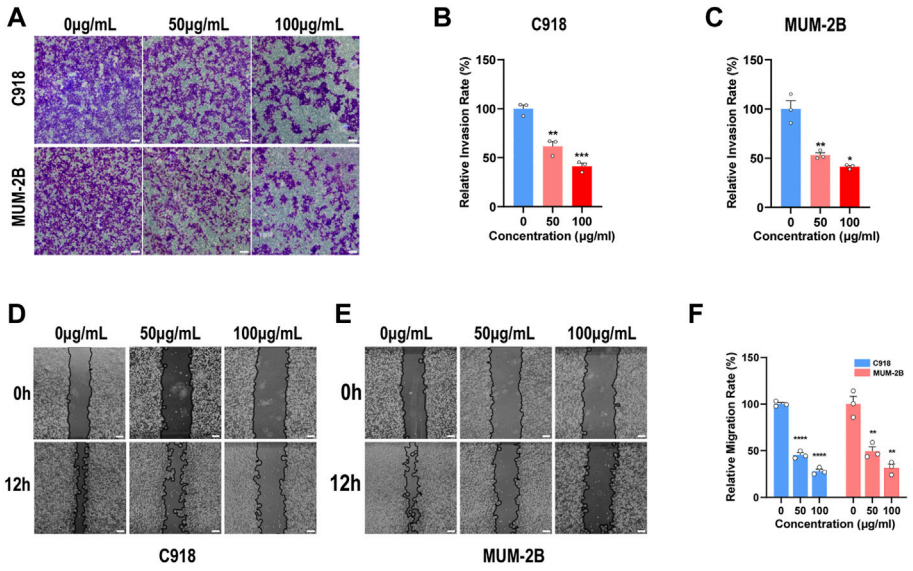

FIGURE 4
NMQDs-Ti_3C_2Tx inhibits UM cell invasion and migration **(A,B and C)** The transwell assay of the UM cells cultured with different concentrations of NMQDs-Ti_3C_2Tx. Scale bar: 200 μm. **(D,E and F)** The wound healing assay of the UM cells cultured with different concentrations of NMQDs-Ti_3C_2Tx. Scale bar: 200 μm. These assays were analyzed and calculated using ImageJ (n = 3, $*p < 0.05$, $**p < 0.005$, $***p < 0.0005$, $****p < 0.0001$). The above data are presented as the mean ± SEM.

Transwell assay revealed that the number of migratory cells was significantly decreased (Figures 4A–C). The invasion ability of UM cells decreases by 50% as the concentration of NMQDs-Ti_3C_2Tx increases to 100 μg ml^{-1}. Similarly, the wound healing assay results also illustrated that NMQDs-Ti_3C_2Tx significantly inhibited the invasive ability of UM cells (Figures 4D–F). Accordingly, the marked ability of NMQDs-Ti_3C_2Tx to suppress UM cell invasion and migration may achieve an additional benefit in the course of treatment for UM.

3.4 NMQDs-Ti_3C_2Tx causes lipid peroxidation and triggers ferroptosis in UM cells

We further investigate the molecular mechanisms of NMQDs-Ti_3C_2Tx in UM cells. Our previous study has illustrated that NMQDs-Ti_3C_2Tx is a strong reducing agent, and it can generate the highly reactive •OH by readily reacting with H_2O_2(Li et al., 2020). Within the cytoplasm, •OH is the most reactive ROS and is an initiator of lipid peroxidation (Sies and Jones, 2020). •OH could attack the polyunsaturated fatty acids (PUFAs) of lipid membranes and induce lipid peroxides generation, a well-established mechanism of cellular injury (Del Rio et al., 2005). Thus, we investigated whether ROS and lipid peroxides would be generated in UM cells cultured with NMQDs-Ti_3C_2Tx.

To demonstrate whether •OH is induced in the cytoplasm in UM cells incubated with NMQDs-Ti_3C_2Tx, we used the ROS fluorescence probe 2′,7′-dichlorofluorescein diacetate (H2DCFDA) to evaluate the intracellular •OH generation (Li et al., 2020) and analyzed through Fluorescence Activating Cell Sorter (FACS). As shown in Figures 5A–C, after 6 h of NMQDs-Ti_3C_2Tx (100 μg ml^{-1}) stimulation, the levels of intracellular ROS markedly increased in UM cells. In contrast, the ROS production was not significantly altered when the probe H2DCFDA was added to RPE cells cultured with NMQDs-Ti_3C_2Tx (Supplementary Figure S3), which indicated the presence of NMQDs-Ti_3C_2Tx did not cause a significant increase of •OH in RPE cells. These suggested that ROS production contributes to UM cell death. Carbon dots (Cdots) are another kind of nanomaterial to exert tumoricidal effects by the production of ROS. Cdots exhibit a pro-tumorigenic role for UM at concentrations below 100 μg ml^{-1} (Ding et al., 2021). For NMQDs-Ti_3C_2Tx, we do not need to be concerned about the double-edged role of ROS induced by NMQDs-Ti_3C_2Tx in UM cells.

We then investigated whether UM cells exhibited lipid peroxidation incubated with NMQDs-Ti_3C_2Tx. The probe C11-BODIPY was used to measure lipid peroxidation. After stimulation of NMQDs-Ti_3C_2Tx, very similar findings were observed. We found an apparent accumulation of lipid peroxides in UM cells, not in RPE cells (Figures 5D–F; Supplementary Figure S4). The presence of MDA, a marker of lipid peroxidation, portends the disruption of membranous structures in cells (Simon et al., 2020). We evaluated the MDA levels in UM cells using an MDA assay kit. As expected, the levels of MDA elevated as the concentration of NMQDs-Ti_3C_2Tx was increased in UM cells (Figures 5G,H).

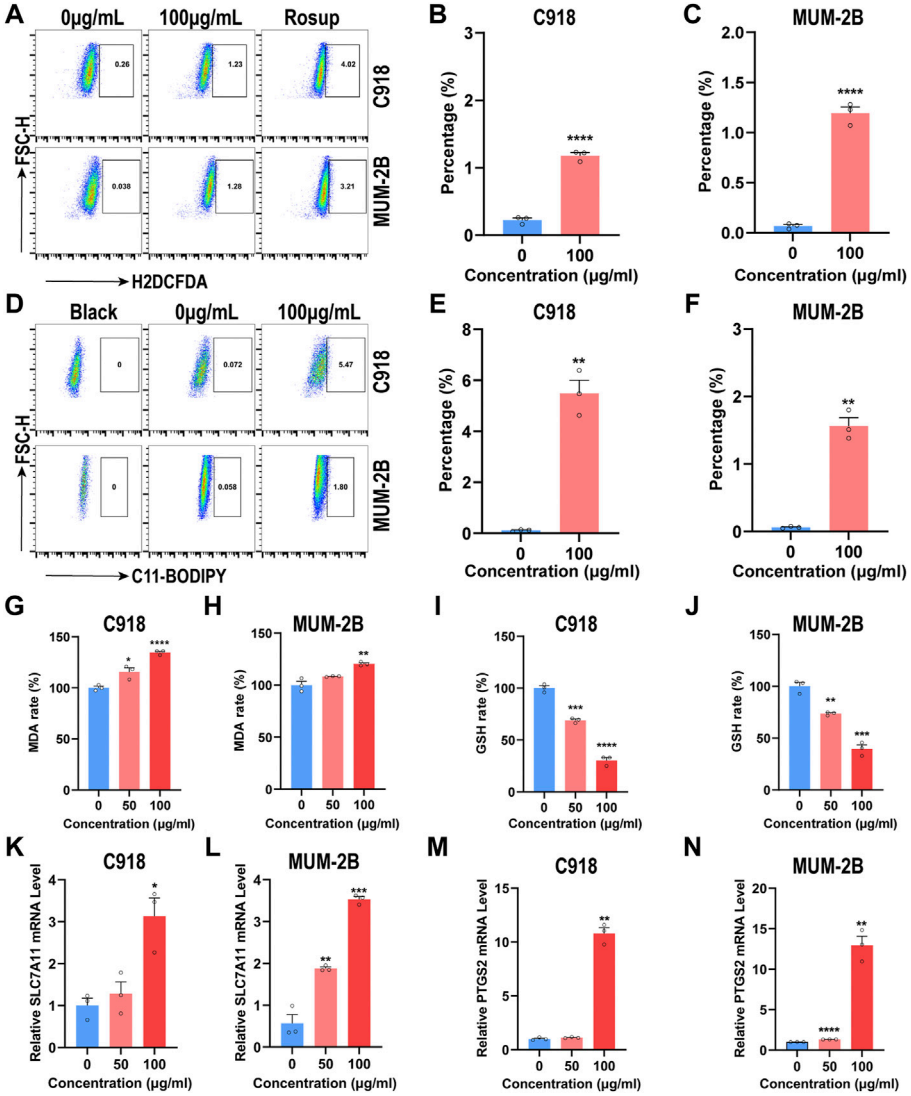

FIGURE 5
NMQDs-Ti_3C_2Tx causes ROS accumulation and induces ferroptosis in UM cells **(A,B and C)** The ROS levels in UM cells incubated with different concentrations of NMQDs-Ti_3C_2Tx were determined by flow cytometry coupled with H2DCFDA staining. Rosup, a ROS inducer, was used as the positive control (n = 3, ****$p < 0.0001$, compared with the control group) **(D,E and F)** The levels of lipid peroxides in UM cells treated with different concentrations of NMQDs-Ti_3C_2Tx were determined by flow cytometry coupled with C11-BODIPY staining (n = 3, **$p < 0.005$) **(G and H)** The MDA levels of UM cells after 6 h of incubation with 100 μg ml^{-1} of NMQDs-Ti_3C_2Tx (n = 3; *$p < 0.05$, **$p < 0.005$, ****$p < 0.0001$) **(I and J)** The GSH levels of UM cells after 6 h of incubation with 100 μg ml^{-1} of NMQDs-Ti_3C_2Tx (n = 3; **$p < 0.005$, ***$p < 0.0005$, ****$p < 0.0001$) **(K,L)** The SLC7A11 RNA levels of UM cells after 6 h of stimulation with NMQDs-Ti_3C_2Tx. GAPDH was used as a loading control (n = 3; *$p < 0.05$, **$p < 0.005$, ***$p < 0.0005$, ****$p < 0.0001$) **(M,N)** The PTGS2 RNA levels of UM cells after 6 h of stimulation with NMQDs-Ti_3C_2Tx. GAPDH was used as a loading control (n = 3; *$p < 0.05$, **$p < 0.005$, ***$p < 0.0005$, ****$p < 0.0001$). The above data are presented as the mean ± SEM.

Ferroptosis is a unique cell death program driven by lipid peroxidation (Dixon et al., 2012; Verma et al., 2020). The accumulation of Lipid peroxides and MDA indicated that NMQDs-Ti_3C_2Tx triggered ferroptosis in UM cells.

In tumor cells, the unusually high concentrations of ROS result in metabolic dysregulation. Naturally, adaptive antioxidant mechanisms would be subsequently developed (Yang et al., 2019). GSH is a substrate for GSH peroxidase 4 (GPX4) that protects cells against ROS, and it can combine with lipid peroxides to form oxidized GSH (GSSG). Usually, the intracellular GSH concentration in a cancer cell is higher than in a normal cell (Jung et al., 2013). But excess ROS would decrease the GSH level, triggering cell death. For this reason, we assessed the GSH levels in UM cells. After incubation with NMQDs-Ti_3C_2Tx, the intracellular GSH concentrations in UM cells are lower than that in control groups (Figures 5I,J). Cystine is the essential precursor of

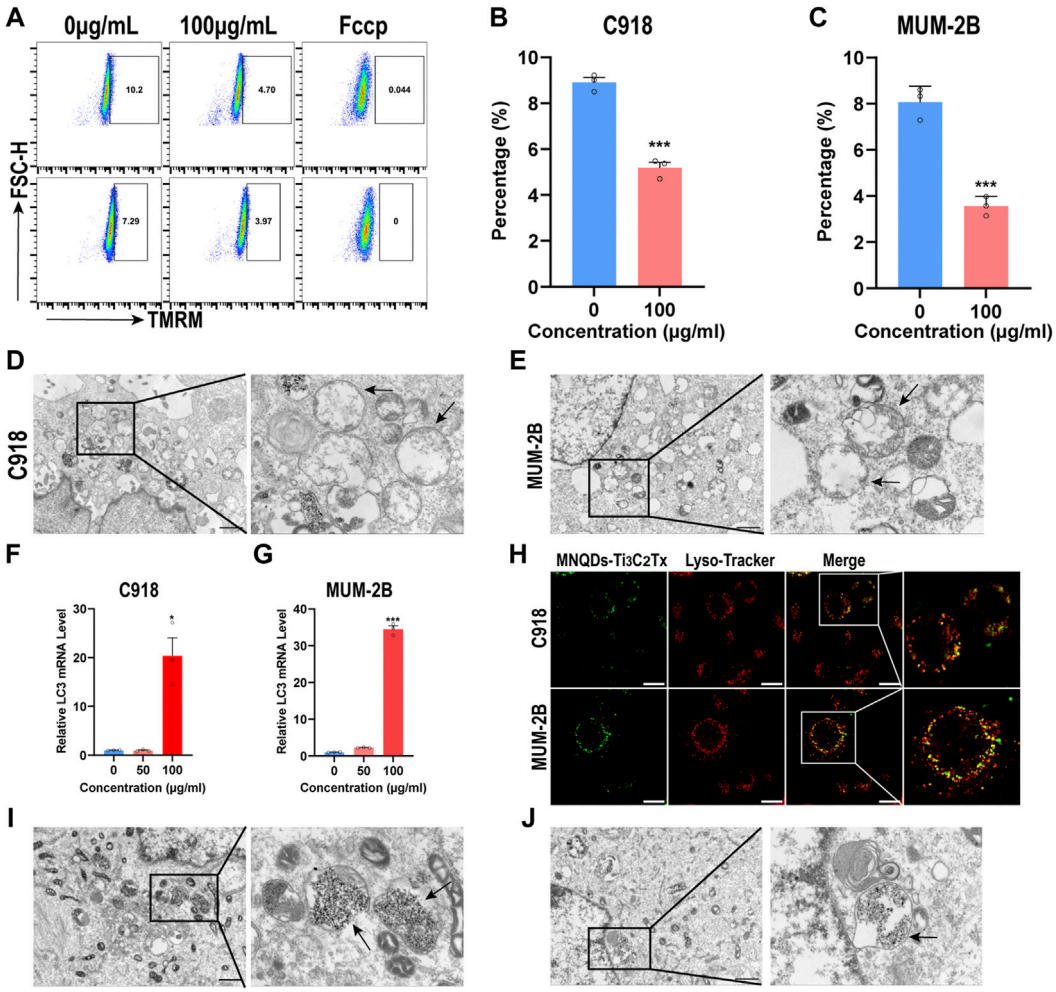

FIGURE 6
NMQDs-Ti_3C_2Tx induces mitophagy and lysosome destruction in UM cells **(A,B and C)** The levels of MMP in UM cells treated with different concentrations of NMQDs-Ti_3C_2Tx were determined using flow cytometry coupled with TMRM staining. Fccp was used as the negative control with low MMP (n = 3, ***$p < 0.0005$) **(D and E)** Bio-TEM image and partial enlarged images of UM cells after treated with 100 μg ml^{-1} of NMQDs-Ti_3C_2Tx. The black arrows point to mitochondrial edema. Scale bar: 10 μm. **(F and G)** The LC3 RNA levels of UM cells after 6 h of stimulation with 100 μg ml^{-1} of NMQDs-Ti_3C_2Tx. GAPDH was used as a loading control (n = 3; *$p < 0.05$, ***$p < 0.0005$) **(H)** Colocalization of NMQDs-Ti_3C_2Tx and lysosomes in UM cell lines. Scale bar: 20 μm. **(I and J)** Bio-TEM and partial enlarged images of UM cells after treated with NMQDs-Ti_3C_2Tx. The black arrows indicated autolysosomes. Scale bar: 10 μm.

GSH synthesis, and System xc−, a cystine/glutamate exchange transporter, leads to the uptake of cystine into the cell cytosol (Sato et al., 1999). When the intracellular GSH shortage is present, the transporter can be upregulated (Sasaki et al., 2002). Subunit solute carrier family seven member 11(SLC7A11) is the catalytic subunit of System xc−. Thus, we appraised the System xc− activity through measurement of SLC7A11. Incubated with NMQDs-Ti_3C_2Tx, the RNA levels of SLC7A11 were upregulated (Figures 5K,L). This result showed negative feedback on GSH. We also investigated the mRNA level of PTGS2 which is one of the recognized ferroptosis-related genes. After stimulation of NMQDs-Ti_3C_2Tx, the mRNA levels of PTGS2 were upregulated (Figures 5M, N). These results demonstrate that NMQDs-Ti_3C_2Tx induces excessive production of •OH and consequently causes lipid peroxidation. Finally, Overwhelming lipid peroxidation triggers ferroptosis in UM cells.

3.5 NMQDs-Ti_3C_2Tx induces mitophagy and autolysosome destruction in UM cells

Although •OH is the most reactive ROS, it reacts with biomolecules directly at the site of its generation (Galaris et al., 2019). Excessive ROS would destroy mitochondria, causing a decrease in MMP, consequently leading to cell death (Cheng et al., 2019). The mitochondrion is one crucial source of

endogenously produced H_2O_2(Dickinson et al., 2010). We wonder whether mitochondrion is affected by the •OH induced by the NMQDs-Ti_3C_2Tx.

We used a plasmid to track mitochondrion to prove this, and we found that NMQDs-Ti_3C_2Tx is colocalized with mitochondrion in UM cells (Supplementary Figure S5). Mitochondrial fluorescence dye TMRM was used to determine the MMP in a flow cytometer. As expected, MMP decreased significantly after NMQDs-Ti_3C_2Tx addition (Figures 6A–C). In contrast, MMP in RPE cells showed no significant change (Supplementary Figure S6). We also investigated the ultrastructure of mitochondria by electron microscopy. Through the view of the electron microscope, we observed many mitochondrial edemata in the UM cells incubated with NMQDs-Ti_3C_2Tx, not in normal UM cells, and the structures of mitochondria were severely damaged (Figures 6D,E; and Supplementary Figures S7,S8). These results indicate that accumulated NMQDs-Ti_3C_2Tx in UM cells leads to mitochondrial dysfunction, resulting in cell death.

Lysosomes are acidic organelles specialized in the degradation and recycling of macromolecules (Tai et al., 2020). Mitochondrial autophagy, a specialized type of autophagy, is a conserved lysosome-dependent process that plays a vital role in mitochondrial quality control and removing fragmented mitochondria (Ashrafi and Schwarz, 2013). Multiple causes cause mitochondrial dysfunction, and damaged mitochondria are specifically recognized and sequestered into autophagosomes that fuse with lysosomes to degrade mitochondria. In UM cells, NMQDs-Ti_3C_2Tx attacks mitochondria, resulting in mitochondria dysfunction. We hypothesized that mitophagy might occur in UM cells incubated with NMQDs-Ti_3C_2Tx. The LC3 subfamily is considered an autophagy marker (Weidberg et al., 2010). The RNA levels of LC3 were upregulated cultured with NMQDs-Ti_3C_2Tx in UM cells (Figures 6F,G), which proved the induction of autophagy. We also observed the ultrastructure of UM cells using electron microscopy. Under the electron microscope, we observed autolysosome formation. But we only found damaged mitochondria and black granules in autolysosomes in the therapeutic groups (Figures 6I,J and Supplementary Figures S9,S10). Extracellular macromolecules enter the cell by endocytosis and eventually terminate with lysosomal degradation. We further investigated whether NMQDs-Ti_3C_2Tx could accumulate in lysosomes. We used fluorescent probes to track lysosomes to prove this, and we found that NMQDs-Ti_3C_2Tx is colocalized with lysosomes (Figure 6H). In this way, the black granules are the result of NMQDs-Ti_3C_2Tx accumulation in autolysosomes. The lysosome is an acidic organelle, which provides the opportunity for NMQDs-Ti_3C_2Tx to induce Fenton reaction, thus leading to plasma membrane integrity disruption of the autolysosomes (Figures 6I,J). As a result of the disruption, lysosomal hydrolases are released into the cytosol, resulting in lysosomal cell death with necrotic features (Aits and Jaattela, 2013).

3.6 Activity and biocompatibility of NMQDs-Ti_3C_2Tx *In vivo*

Given the excellent tumor-killing efficacy of NMQDs-Ti_3C_2Tx *in vitro*, we continued to test its therapeutic efficacy *in vivo*. C918 cells were injected into the right axilla of the mice to create the UM subcutaneous tumor model. When the tumor grew to 50–100 mm^3 in volume, NMQDs-Ti_3C_2Tx (10 mg kg^{-1}, the therapeutic group) and the same volume of saline (the control group) were injected intratumorally every 2 days. A total of five injections were performed (Figure 7A). During the period, the sizes of the tumors and the weights of the mice were measured and compared. The tumor size in the control group obviously increased from ≈50 to ≈1015 mm^3; comparably, the tumor growth in the therapeutic group was significantly repressed. The tumor size in the therapeutic group only increased to ≈310 mm^3 (Figure 7B). Similarly, the average tumor weight in the therapeutic group is relatively lighter than that in the control group (Figure 7C). The weight of the nude mice in the control group had a mild reduction during the later phase of the experiment, which indicated that tumors had already impacted the growth of the nude mice (Figure 7D). These illustrate that NMQDs-Ti_3C_2Tx prevents xenograft tumor growth in mice.

At the end of the experiment, tumors were removed from the nude mice. We could intuitively observe black alteration on the tumor xenograft mouse models after NMQDs-Ti_3C_2Tx injection, and black regions could be found on the tumor masses (Figure 7E). Through Hematoxylin and eosin (H&E) staining of the tumor tissues, we could clarify that the black region on the tumor masses is a large area of necrosis (Figures 7F,G), which is in agreement with *in vitro* experiments. Necrosis would induce the release of new antigens and activate the immune system, thereby exerting a long-term antitumor effect (Bomze et al., 2019). We also observed a boundary line between necrosis and normal tumor tissue from the therapeutic group (Figure 7H). These illustrate that NMQDs-Ti_3C_2Tx shows no toxicity to the tumor cells far away from the injection site. These features of NMQDs-Ti_3C_2Tx make it very possible for topical intraocular treatment. However, further study is required to explore the possibility. This is the limitation of the study.

The intraocular biocompatibility of NMQDs-Ti_3C_2Tx determines the possibility of future local clinical application. Hence, the *in vivo* intraocular biosafety was investigated on C57BL/6 mice injected with NMQDs-Ti_3C_2Tx at 200 μg ml^{-1} intravitreally. After 3 days, optical coherence tomography (OCT) and histochemistry were used to evaluate the morphologic characteristics of the retina. We observed no significant changes through fundus images (Figure 7I). Similarly, the

10.3389/fbioe.2022.1028470

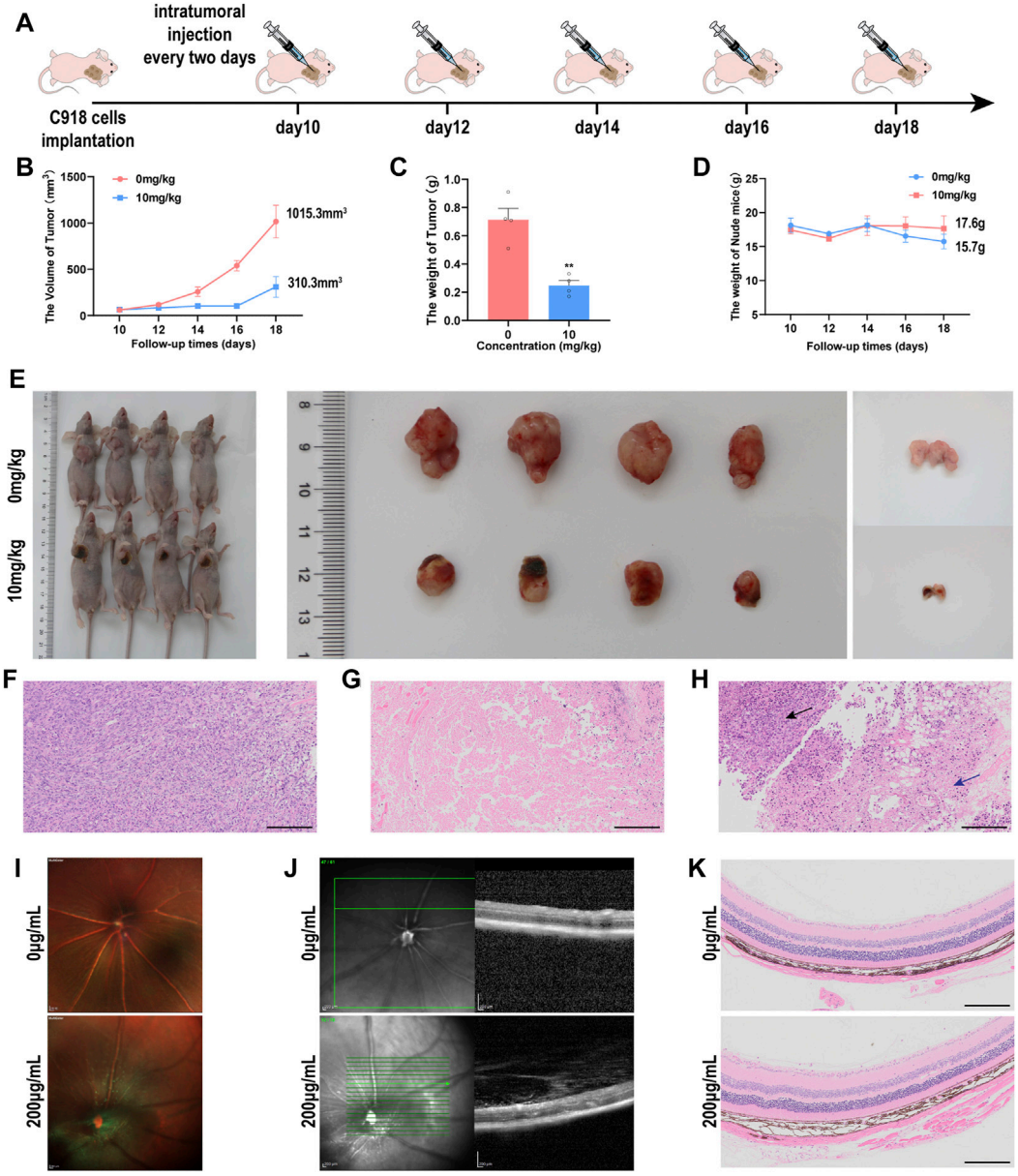

FIGURE 7
The multi-mode imaging *in vivo* **(A)** Timeline of the tumor-bearing nude mice experiment. **(B)** the tumor sizes of the UM tumor-bearing mice during the treatment **(C)** Tumor weights of the UM tumor-bearing mice at the end of the treatment (n = 4, $^{**}p < 0.005$) **(D)** The body weights of nude mice bearing UM tumor xenografts during the treatment. **(E)** Images of the sizes of xenograft UM tumors during NMQDs-Ti_3C_2Tx treatment **(F)** H&E staining of the tumors from control group. Scale bar, 200 μm. **(G)** H&E staining of the tumors from the therapeutic group. Scale bar, 200 μm **(H)** H&E staining of the tumors from the demarcation of therapeutic group. The black arrow points to the normal tumor tissue, and the blue arrow points to necrosis. Scale bar, 200 μm. **(I)** Ocular fundus images of experimental mice. Scale bar: 200 μm **(J)** OCT images of the mice retina. Scale bar: 200 μm. **(K)** H&E staining of the retina from the mice. Scale bar: 200 μm.

structure of the retina did not reveal noticeable changes compared with the control group (Figure 7J). Additionally, H&E staining disclosed that intraocular treatment with NMQDs-Ti_3C_2Tx did not significantly affect the whole retina (Figure 7K). All of these illuminate that NMQDs-Ti_3C_2Tx has excellent intraocular biocompatibility.

4 Conclusion

In summary, we illustrate that NMQDs-Ti_3C_2Tx efficiently inhibits the proliferation, invasion, and migration of UM cells and exerts robust antitumor activity *in vivo*. Furthermore, NMQDs-Ti_3C_2Tx exhibits excellent ocular biocompatibility

and has no noticeable side effects, providing the possibility for further clinical application of NMQDs-Ti_3C_2Tx. Naturally, we hope our work will provide the probability of new clinical development for the topical treatment of UM and expand the prospects of nanoparticles to treat more ocular malignant tumors in the future.

Data availability statement

The raw data supporting the conclusions of this article will be made available by the authors, without undue reservation.

Ethics statement

The animal study was reviewed and approved by the Laboratory Animal Ethical and Welfare Committee of Shandong University Cheeloo College of Medicine.

Author contributions

HZ and YQ conceived and conducted the experiments, performed the analyses, and wrote the manuscript. XT and XL involved in the preparation of materials. XS and QF were involved in the vitro experiments. PY contributed to the animal experiments. YQ contributed to the conceptualization and resources, supervised the research, and revised the manuscript.

Funding

This work was supported by grants from the National Natural Science Foundation of China (No. 31570789).

Conflict of interest

The authors declare that the research was conducted in the absence of any commercial or financial relationships that could be construed as a potential conflict of interest.

Publisher's note

All claims expressed in this article are solely those of the authors and do not necessarily represent those of their affiliated organizations, or those of the publisher, the editors and the reviewers. Any product that may be evaluated in this article, or claim that may be made by its manufacturer, is not guaranteed or endorsed by the publisher.

Supplementary material

The Supplementary Material for this article can be found online at: https://www.frontiersin.org/articles/10.3389/fbioe.2022.1028470/full#supplementary-material

References

Aits, S., and Jaattela, M. (2013). Lysosomal cell death at a glance. *J. Cell Sci.* 126, 1905–1912. doi:10.1242/jcs.091181

Ashrafi, G., and Schwarz, T. L. (2013). The pathways of mitophagy for quality control and clearance of mitochondria. *Cell Death Differ.* 20, 31–42. doi:10.1038/cdd.2012.81

Bianciotto, C., Shields, C. L., Pirondini, C., Mashayekhi, A., Furuta, M., and Shields, J. A. (2010). Proliferative radiation retinopathy after plaque radiotherapy for uveal melanoma. *Ophthalmology* 117, 1005–1012. doi:10.1016/j.ophtha.2009.10.015

Bomze, D., Hasan Ali, O., Bate, A., and Flatz, L. (2019). Association between immune-related adverse events during anti-PD-1 therapy and tumor mutational burden. *JAMA Oncol.* 5, 1633–1635. doi:10.1001/jamaoncol.2019.3221

Cheng, M. H., Huang, H. L., Lin, Y. Y., Tsui, K. H., Chen, P. C., Cheng, S. Y., et al. (2019). BA6 induces apoptosis via stimulation of reactive oxygen species and inhibition of oxidative phosphorylation in human lung cancer cells. *Oxid. Med. Cell. Longev.* 2019, 1–21. doi:10.1155/2019/6342104

Del Rio, D., Stewart, A. J., and Pellegrini, N. (2005). A review of recent studies on malondialdehyde as toxic molecule and biological marker of oxidative stress. *Nutr. Metab. Cardiovasc. Dis.* 15, 316–328. doi:10.1016/j.numecd.2005.05.003

Dickinson, B. C., Srikun, D., and Chang, C. J. (2010). Mitochondrial-targeted fluorescent probes for reactive oxygen species. *Curr. Opin. Chem. Biol.* 14, 50–56. doi:10.1016/j.cbpa.2009.10.014

Ding, Y., Yu, J., Chen, X., Wang, S., Tu, Z., Shen, G., et al. (2021). Dose-dependent carbon-dot-induced ROS promote uveal melanoma cell tumorigenicity via activation of mTOR signaling and glutamine metabolism. *Adv. Sci. (Weinh).* 8, 2002404. doi:10.1002/advs.202002404

Dixon, S. J., Lemberg, K. M., Lamprecht, M. R., Skouta, R., Zaitsev, E. M., Gleason, C. E., et al. (2012). Ferroptosis: An iron-dependent form of nonapoptotic cell death. *Cell* 149, 1060–1072. doi:10.1016/j.cell.2012.03.042

Galaris, D., Barbouti, A., and Pantopoulos, K. (2019). Iron homeostasis and oxidative stress: An intimate relationship. *Biochimica Biophysica Acta - Mol. Cell Res.* 1866, 118535. doi:10.1016/j.bbamcr.2019.118535

Hu, Y., Mignani, S., Majoral, J. P., Shen, M., and Shi, X. (2018). Construction of iron oxide nanoparticle-based hybrid platforms for tumor imaging and therapy. *Chem. Soc. Rev.* 47, 1874–1900. doi:10.1039/c7cs00657h

Jager, M. J., Shields, C. L., Cebulla, C. M., Abdel-Rahman, M. H., Grossniklaus, H. E., Stern, M. H., et al. (2020). Uveal melanoma. *Nat. Rev. Dis. Prim.* 6, 24. doi:10.1038/s41572-020-0158-0

Jung, H. S., Chen, X., Kim, J. S., and Yoon, J. (2013). Recent progress in luminescent and colorimetric chemosensors for detection of thiols. *Chem. Soc. Rev.* 42, 6019–6031. doi:10.1039/c3cs60024f

Kines, R. C., Varsavsky, I., Choudhary, S., Bhattacharya, D., Spring, S., Mclaughlin, R., et al. (2018). An infrared dye-conjugated virus-like particle for the treatment of primary uveal melanoma. *Mol. Cancer Ther.* 17, 565–574. doi:10.1158/1535-7163.MCT-17-0953

Li, X. S., Liu, F., Huang, D. P., Xue, N., Dang, Y. Y., Zhang, M. Q., et al. (2020). Nonoxidized MXene quantum dots prepared by microexplosion method for cancer catalytic therapy. *Adv. Funct. Mat.* 30, 2000308. doi:10.1002/adfm.202000308

Lin, L., Yu, J., Lu, H., Wei, Z., Chao, Z., Wang, Z., et al. (2021). Mn-DNA coordination of nanoparticles for efficient chemodynamic therapy. *Chem. Commun.* 57, 1734–1737. doi:10.1039/d0cc08191d

Mallone, F., Sacchetti, M., Lambiase, A., and Moramarco, A. (2020). Molecular insights and emerging strategies for treatment of metastatic uveal melanoma. *Cancers (Basel)* 12, 2761. doi:10.3390/cancers12102761

Nie, X., Xia, L., Wang, H. L., Chen, G., Wu, B., Zeng, T. Y., et al. (2019). Photothermal therapy nanomaterials boosting transformation of Fe (III) into Fe (II) in tumor cells for highly improving chemodynamic therapy. *ACS Appl. Mat. Interfaces* 11, 31735–31742. doi:10.1021/acsami.9b11291

Pereira, P. R., Odashiro, A. N., Lim, L. A., Miyamoto, C., Blanco, P. L., Odashiro, M., et al. (2013). Current and emerging treatment options for uveal melanoma. *Clin. Ophthalmol.* 7, 1669–1682. doi:10.2147/OPTH.S28863

Polacheck, W. J., Zervantonakis, I. K., and Kamm, R. D. (2013). Tumor cell migration in complex microenvironments. *Cell. Mol. Life Sci.* 70, 1335–1356. doi:10.1007/s00018-012-1115-1

Ranji-Burachaloo, H., Gurr, P. A., Dunstan, D. E., and Qiao, G. G. (2018). Cancer treatment through nanoparticle-facilitated Fenton reaction. *ACS Nano* 12, 11819–11837. doi:10.1021/acsnano.8b07635

Sasaki, H., Sato, H., Kuriyama-Matsumura, K., Sato, K., Maebara, K., Wang, H., et al. (2002). Electrophile response element-mediated induction of the cystine/glutamate exchange transporter gene expression. *J. Biol. Chem.* 277, 44765–44771. doi:10.1074/jbc.M208704200

Sato, H., Tamba, M., Ishii, T., and Bannai, S. (1999). Cloning and expression of a plasma membrane cystine/glutamate exchange transporter composed of two distinct proteins. *J. Biol. Chem.* 274, 11455–11458. doi:10.1074/jbc.274.17.11455

Sies, H., and Jones, D. P. (2020). Reactive oxygen species (ROS) as pleiotropic physiological signalling agents. *Nat. Rev. Mol. Cell Biol.* 21, 363–383. doi:10.1038/s41580-020-0230-3

Simon, J., Nunez-Garcia, M., Fernandez-Tussy, P., Barbier-Torres, L., Fernandez-Ramos, D., Gomez-Santos, B., et al. (2020). Targeting hepatic glutaminase 1 ameliorates non-alcoholic steatohepatitis by restoring very-low-density lipoprotein triglyceride assembly. *Cell Metab.* 31, 605–622.e10. doi:10.1016/j.cmet.2020.01.013

Tai, W., Zhao, P., and Gao, X. (2020). Cytosolic delivery of proteins by cholesterol tagging. *Sci. Adv.* 6, eabb0310. doi:10.1126/sciadv.abb0310

Tang, Z., Liu, Y., He, M., and Bu, W. (2019). Chemodynamic therapy: Tumour microenvironment-mediated Fenton and fenton-like reactions. *Angew. Chem. Int. Ed.* 58, 946–956. doi:10.1002/anie.201805664

Verma, N., Vinik, Y., Saroha, A., Nair, N. U., Ruppin, E., Mills, G., et al. (2020). Synthetic lethal combination targeting BET uncovered intrinsic susceptibility of TNBC to ferroptosis. *Sci. Adv.* 6, eaba8968. doi:10.1126/sciadv.aba8968

Wang, L., Zhang, Z., Ding, Y., Wu, J., Hu, Y., and Yuan, A. (2020). Novel copper-based and pH-sensitive nanomedicine for enhanced chemodynamic therapy. *Chem. Commun.* 56, 7753–7756. doi:10.1039/d0cc00165a

Weidberg, H., Shvets, E., Shpilka, T., Shimron, F., Shinder, V., and Elazar, Z. (2010). LC3 and GATE-16/GABARAP subfamilies are both essential yet act differently in autophagosome biogenesis. *EMBO J.* 29, 1792–1802. doi:10.1038/emboj.2010.74

Yang, B., Chen, Y., and Shi, J. (2019). Reactive oxygen species (ROS)-Based nanomedicine. *Chem. Rev.* 119, 4881–4985. doi:10.1021/acs.chemrev.8b00626

frontiers | Frontiers in Bioengineering and Biotechnology

TYPE Original Research
PUBLISHED 21 October 2022
DOI 10.3389/fbioe.2022.1053679

Check for updates

OPEN ACCESS

EDITED BY
Dan Shao,
South China University of Technology, China

REVIEWED BY
Erle Dang,
Fourth Military Medical University, China
Yang Xu,
Nanjing Medical University, China

*CORRESPONDENCE
Wei Lai,
drlaiwei@163.com
Jian Chen,
chj75_0@163.com
Yue Zheng,
benbenzhu-11@163.com

†These authors have contributed equally to this work

SPECIALTY SECTION
This article was submitted to Biomaterials, a section of the journal Frontiers in Bioengineering and Biotechnology

RECEIVED 26 September 2022
ACCEPTED 13 October 2022
PUBLISHED 21 October 2022

CITATION
Ye C, Zhang Y, Su Z, Wu S, Li Y, Yi J, Lai W, Chen J and Zheng Y (2022), hMSC exosomes as a novel treatment for female sensitive skin: An in vivo study. *Front. Bioeng. Biotechnol.* 10:1053679. doi: 10.3389/fbioe.2022.1053679

COPYRIGHT
© 2022 Ye, Zhang, Su, Wu, Li, Yi, Lai, Chen and Zheng. This is an open-access article distributed under the terms of the Creative Commons Attribution License (CC BY). The use, distribution or reproduction in other forums is permitted, provided the original author(s) and the copyright owner(s) are credited and that the original publication in this journal is cited, in accordance with accepted academic practice. No use, distribution or reproduction is permitted which does not comply with these terms.

hMSC exosomes as a novel treatment for female sensitive skin: An *in vivo* study

Congxiu Ye[1†], Yunqing Zhang[1†], Zhen Su[1†], Shuxia Wu[2†], Yuxia Li[2], Jinling Yi[1], Wei Lai[1*], Jian Chen[1*] and Yue Zheng[1*]

[1]Department of Dermato-venereology, The Third Affiliated Hospital of Sun Yat-sen University, Guangzhou, Guangdong, China, [2]AIE Bioscience (Guangdong) Co., LTD., Torch Development Zone, Zhongshan, Guangdong, China

Background: Recent studies have reported that the incidence of sensitive skin is increasing. Skin sensitivity and skin barrier functions were related to many skin diseases including atopic dermatitis, psoriasis, rosacea, and so on. Mesenchymal stem cell (MSC)-derived exosomes (hMSC) might be considered as a new effective therapeutic scheme.

Aims: This study aims to investigate the safety and efficacy of hMSC exosomes as a novel topical treatment for sensitive skin.

Patients/Methods: Exosomes were extracted from primary hMSC *via* ultracentrifugation method. The morphology of hMSC exosomes was studied *via* transmission electron microscope. Expression of exosome specific surface marker was detected *via* Western blot. 22 subjects (female, aged 18–55) diagnosed with sensitive skin were enrolled. Follow-up was conducted before, 7-day, 14-day, and 28-day after hMSC exosomes use. Transepidermal water loss (TEWL), surface hydration, sebum secretion, and L*a*b* value were simultaneously tested at the same time point in an environment-controlled room.

Results: Under transmission electron microscopy, the extracted hMSC exosomes were circular or elliptical with intact membrane structure, and their diameters ranged mainly from 40 to 80 nm. Western blot showed that the expression of markers CD63, CD9, and Tsg101 was positive. Brownian motion based nanoparticle trajectory analysis (NTA) showed that the main peak of particle size distribution occurred around 96 nm, the average particle size was 122 nm, and the main peak accounted for 96.7%. All this conformed to the biological characteristics of exosomes standardized by the International Society for Extracellular Vesicles. In the clinical trial, scores of objective symptoms including roughness, scales, erythema, and subjective symptoms including tension, burning, or itching, were improved after 7-, 14-, and 28- day using hMSC-exosomes. TEWL, hydration, sebum, pH, and a* values were tended to return to the level of healthy skin.

Conclusion: The hMSC-exosomes, with the advantages of biocompatibility and biodegradability, could improve clinical symptoms and eruptions in sensitive

skin patients, and might be as an MSC cell-free novel therapy in sensitive skin-related disease treatment.

KEYWORDS

hMSC exosomes, sensitive skin, regulating dermic immunity, suppressing neurovascular hyperreactivity, repairing skin barriers, biocompatibility, biodegradability

Introduction

Skin sensitivity was related to many skin diseases including atopic dermatitis, psoriasis, rosacea, and so on. Sensitive skin is a condition of subjective cutaneous hyper-reactivity to environmental factors such as cold, heat, and wind, and/or frequent or prolonged applications of some topical products, such as cosmetics (Berardesca, Farage, & Maibach, 2013). Recently, epidemiological studies found that sensitive skin was present in 56.8% of Koreans (Kim, Cheon, Misery, Taieb, & Lee, 2018). In China, the mean prevalence of sensitive skin was 13% (Yu et al., 2022). The condition was disturbing and detrimentally influenced the quality of life.

Extracellular vesicles (EVs), such as exosomes have been identified as mediators of an intercellular communication system. Exosomes contain a wide variety of proteins and nucleic acids that enable multifactorial signaling (Kalluri & LeBleu, 2020). Although MSCs have been used for a long time in tissue and organ repair (Akyurekli et al., 2015), EVs of mesenchymal stem/stromal cells (MSCs) have been found to promote comparable therapeutic activities as MSCs themselves. MSC-derived extracellular vesicles (EVs), which include exosomes and microvesicles (MV), are being replaced for MSC role in MSC cell-free therapies, owing to their biocompatibility, biodegradability, non-toxicity, and some specific therapeutic activities.

The therapeutic efficacy of MSC-EVs in various diseases, in diabetes mellitus, myocardial infarction, transplantation, cancer, macular degeneration, bone repairing, osteoarthritis, Alzheimer's disease (AD), ischemic stroke, multiple sclerosis, as well as COVID-19 has been reported in clinical trials (Birtwistle, Chen, & Pollock, 2021). HMSC-exosomes (hMSC-exosomes) exhibit cardio and renal-protective activity, and are efficacious in animal models of myocardial infarction, stroke, brain injury (Ahn et al., 2021), and ischemia-reperfusion injury (Alzahrani, 2019). MSC-derived exosomes could be a novel therapeutic strategy for diabetic complications involving salivary glands. (AbuBakr, Haggag, Sabry, & Salem, 2020), ulcer foot (An, Chen, Tu, & Lin, 2021), Preclinical meta-analysis (Bailey et al., 2021), Kidney repair (Aghajani Nargesi, Lerman, & Eirin, 2017; Nargesi, Lerman, & Eirin, 2017), (Bai et al., 2018), acute renal injury (Birtwistle et al., 2021), also Inflammatory disease (Baharlooi, Azimi, Salehi, & Izad, 2020), such as Autoimmune Uveitis (Bai et al., 2017; Harrell et al., 2018; Shen et al., 2021) optic neuritis (Aneesh et al., 2021), and osteoarthritis (Bao & He, 2021). These suggested that hMSC-exosomes might be a compelling alternative to hMSCs in regenerative and aesthetic medicine, as they would avoid most of the problems associated with live MSC-based therapy (Golan et al., 2018; Pelizzo et al., 2018; Kalluri & LeBleu, 2020).

Zhang et al. (2015) found that wnt4 contained in umbilical cord mesenchymal stem cell-derived exosomes (HucMSC-Exo) may enhance the translocation and activity of β-catenin, thereby promoting the proliferation and migration of skin cells and angiogenesis. Fang et al. (2016) found that HucMSC-Exo could reduce scar formation and accumulation of myofibroblasts in a mouse model of skin defect. These functions are mainly dependent on the microRNAs contained in HucMSC-Exo. This revealed the potential effect of hMSC-exosomes in skin regional usage, but its safety and efficacy on sensitive skin has not been clarified until now.

In this study, we investigate the safety and efficacy of hMSC-exosomes as a novel topical treatment for sensitive skin, and preliminarily explore the possible biological mechanisms.

Materials and methods

Preparation of the formula

HFF-1 cells were purchased from Echo Biotech Co., Ltd., Beijing, China. CO_2 incubator (Thermo Fisher, United States); refrigerated centrifuge (Sigma, United States); ultracentrifuge (Beckman, United States); transmission electron microscope (Hitachi, Japan); inverted phase contrast microscope (Olympus, Japan); flow cytometer (BD, United States); microplate reader (Molecular Devices, United States).

The umbilical cord was collected in a sterile bag and transported in a low-temperature transport box; Wharton's jelly was separated from the umbilical cord within 48 h. The umbilical cord was placed in a 50 ml centrifuge tube, washed 3 times with gentamicin-containing PBS (final concentration of gentamicin: 25 ug/ml), and then washed 3–5 times with gentamicin-free PBS. About 0.5 cm was removed from each end of the umbilical cord and the blood was rinsed off. The umbilical cord was cut into 2–3 cm long sections that were then transferred to a 50 ml centrifuge tube. The umbilical cord pieces were cleaned and cut longitudinally along the intravenous cavity. The venous intima was peeled off and the two arteries were removed. The umbilical cord lining was fully removed and

Wharton's jelly was cut into small pieces about 3–5 mm long. They were then transferred into 150 mm dishes with each dish containing about 20 pieces and 10 ml of the medium. For storage, pieces can be placed in cryotubes and stored in a liquid nitrogen tank after programmed cooling. At 48 h, the dishes were supplemented with the medium (10 ml/dish). The medium was fully changed on the 7th and the 10th days. Mesenchymal stem cells crawled out from the 12th to the 14th days (or 15 to 18th days).

Third-generation hMSCs were tested using the human umbilical cord mesenchymal stem cell osteogenic differentiation medium kit according to the instructions for induction and differentiation. After 3 weeks of induction, the formation of mineralized nodules was examined under an optical microscope after Alizarin Red S staining. Third-generation hMSCs were tested with the human umbilical cord mesenchymal stem cell adipogenic differentiation medium kit according to the instructions to induce differentiation. When the lipid droplets became large enough and round, adipogenesis was examined under an optical microscope using Oil Red O staining. hMSCs were cultured for 48 h in serum-free mediums containing no exosomes. The cell supernatant was collected and centrifuged at 300 g for 10 min. The supernatant was then collected and centrifuged at 2000 g for 10 min. The supernatant was collected again, filtered with a 0.22 μm filter, transferred to an ultrafiltration centrifuge tube with 100 kDa MWCO, and centrifuged at 4,000 g for 30–50 min. The concentrated retentate was collected and centrifuged at 10,000 g for 30 min. The supernatant was transferred to an ultracentrifuge tube and centrifuged at 100,000 g for 70 min. The last step was repeated. All above centrifugation steps were conducted at 4°C. The obtained pellet consisted of exosomes, which was resuspended in PBS and stored at −80°C for later use. BCA kit was used to determine exosomal protein concentration.

The morphology of exosomes was studied using a transmission electron microscope. The sample-loading copper mesh was placed on filter paper, 20 μl of the exosomal extract was added dropwise, and the loaded mesh was let to stand at room temperature for 3 min 30 μl of 3% phosphotungstic acid solution was added for the negative staining that took 5 min at room temperature. Western blot was used to detect the expression of exosome specific surface markers CD63, CD81, and Tsg101. Exosomes were extracted and lysed in RIPA buffer and protein concentration was determined using the BCA method. SDS-PAGE electrophoresis was performed with 50 μg of sample per well and the proteins were transferred to a PVDF membrane by wet transfer method. Then the PVDF membrane was blocked with 5% skimmed milk powder for 1 h at room temperature, and anti-CD63, anti-CD9, anti-Tsg101, and anti-β-actin antibodies were added to the solution, which was incubated overnight at 4°C. HRP-labeled secondary antibody was added and the solution was incubated at room temperature for 30 min. ECL luminescent detection was conducted and recorded on a film. The cell culture medium (hMSC-Ed-CM) without exosomes was used as a control.

Human fibroblasts scratch assay and cck-8

The scratch assay measures the migration ability of human fibroblasts. Straight lines were drawn on the back of a 6-well plate and human fibroblasts were inoculated. The appropriate density was for the cells to grow to full confluency overnight. After the cells reached full confluency, the cell monolayer was scratched with a 200 μl sterile pipette tip in lines perpendicular to the drawn lines. The plate was washed with PBS and replenished with the desired cell culture medium: containing 1% FBS for the CM group (cell culture control group) and final concentrations of 5, 10, 15, and 20 μg of exosome/ml for the Exo group to simulate the pathological environment of OA. Control groups were set up at the same time. Micrographs were taken at 0 and 12 h for each group. ImageJ software was used to analyze the scratch healing rates. CCK-8 kit detects the proliferation of human fibroblasts. Human fibroblasts were seeded into 96-well plates at a density of 2×10^3 cells/well. The next day, each group was added with the desired complete medium (the experiment grouping was the same as before), and the culture was continued for 1, 3, 5, and 7 days. After that, 10 μl of CCK-8 solution was added to each well, incubation continued for 2 h, and the absorbance at 450 nm was measured with a microplate reader.

Lactic acid

Lactic acid (Sigma Chemicals Co.) was prepared at a 5% concentration (w/v) in distilled water (DW).

Subjects

22 healthy volunteers aged from 18 to 55, whose 5% lactic acid stinging test scores were ≥3 and had repeatedly dry, tingling, burning, itching, or other discomfort symptoms participated in this study after informed consent. Subjects who were pregnant, lactating, or planning to pregnant during the trial; who had pre-existing skin disease (e.g., acne, eczema, psoriasis) or were taking the anti-inflammatory drugs; who had undergone facial cosmetic surgery, facial lifting, wrinkle removal, or scar smoothing, or planned to reshape their face within 6 months before or during the trial were excluded from the study. The study was conducted in accordance with the tenets of the Declaration of Helsinki. The study protocol was approved by the Ethics Committee Board of the hospital (2020-008-01).

Clinic study schedule

Before participation, volunteers received vital signs detection. Each volunteer visited the research center four times in total: prior to intake at baseline (0 D), 7, 14, and 28 days after the use of the product. Volunteers were given a two-week washout period

prior to the formal trial, during which they stopped using their own facial moisturizers to exclude the effects of products used prior to participation in the trial. During the study, all volunteers applied 1 ml to the face twice a day (morning and evening), after thawing the product into a liquid state and stopped using their own facial moisturizers. After thawing or unsealing, the product should be stored at 2–8°C and used up within 24 h. Adverse events caused by the formula were monitored throughout the study *via* regular consulting and questionnaires.

Subjective assessment was conducted by the same dermatologist before, 7, 14, and 28 days after the use of the product, including the objective and subjective symptoms and the improvement index. The scoring criteria were as follows. Calculation of improvement index: improvement index = (pre-treatment score—post-treatment score)/pre-treatment score × 100%. According to the improvement index, it was divided into complete improvement (improvement index >90%), significant improvement (improvement index 60%–89%), improvement (improvement index 20%–59%) and ineffective (improvement index <20%).

0 points: not dry, scales, erythema, papules, and no subjective symptoms;
1 points: slightly dry and rough, slight scales and erythema, slight tension, burning, or pruritus;
2 points: moderately dry and rough, moderate scales and erythema with a small amount of papules, moderate tension, burning, or pruritus;
3 points: severely dry and rough, severe scales and erythema with obvious papules or pustules, severe tension, burning, or itching.

The lactic acid stinging tests were conducted before, 14, and 28 days after the use of the product according to the method described previously (Misery, 2017; Ye et al., 2020).

All subjects and environments were prepared according to the method described previously (Misery, 2017; Ye et al., 2020). The cheek, the main paroxysm site of sensitive skin, was selected as the instrumental test region. The TEWL, the skin surface hydration, the skin sebum, the skin surface pH value, and the skin a* value which indicates the color direction, and the increase of a* value indicates red, a decrease of a* value indicates the color direction toward green, were measured with the Tewameter® TM 300, Corneometer®Derma, Sebumeter® Derma, Skin-pH-meter® Derma of Unit SSC3, and colorimetry CM-700d (KONICA MINOLTA), described with the L*a*b* system (Chardon, Cretois, & Hourseau, 1991)respectively, according to manufacturer's instructions. The clinical photographs taken with a VISIA™ system (Canfield Inc.), were conducted before, 7, 14, and 28 days after the use of the product.

Volunteers filled out questionnaires at 7, 14, and 28 days after the use of the product to provide their subjective satisfaction with the product. The evaluation standard was divided into A-E levels: level A, dissatisfied; level B, somewhat satisfactory; level C, satisfactory; level D, very satisfactory; level E, extremely satisfactory.

Statistical methods

Statistical analysis was conducted using SPSS® 20.0 software (IBM International Business Machines Corporation). The data were compared using the paired comparison Student's t-test. $p < 0.05$ was regarded as statistically significant.

Results

Cell isolation and characterization

The isolated primary human fibroblasts were stellate or short spindle-shaped (Figure 1A), had a high refractive index and looked like "pavement stones" when the density was high. They could be stained with toluidine blue. After adherence, hMSCs took a fusiform shape and grew in a whirlpool pattern.

Characterization of exosomes

The isolated hMSCs were characterized by stem cell multi-differentiation experiments, and the results are shown in Figure 1. After osteogenic induction, calcium deposits gradually appeared in hMSCs, After adipogenic induction, hMSCs gradually changed from a spindle shape to a round shape, small lipid droplets appeared in the cells, and the lipid droplets gradually merged into larger ones. On the 14th day, the Oil Red O stained lipid droplets appeared red (Figures 1B,C). Under transmission electron microscopy, the extracted hMSC exosomes were circular or elliptical with intact membrane structure, and their diameters ranged mainly from 40 to 80 nm (Figure 2A). Western blot showed that the expression of markers CD63, CD9, and Tsg101 was positive (Figure 2C).

Brownian motion based nanoparticle trajectory analysis

The main peak of particle size distribution occurred around 96 nm, the average particle size was 122 nm, and the main peak accounted for 96.7% (Figure 2B). All this conformed to the biological characteristics of exosomes standardized by the International Society for Extracellular Vesicles.

Human fibroblasts migration and proliferation

The scratch assay showed that hMSC–Exo significantly promoted the healing of human fibroblast scratches, and the healing speed was significantly accelerated with the increase of hMSC–Exo concentration and prolonged action time (Figure 3A).

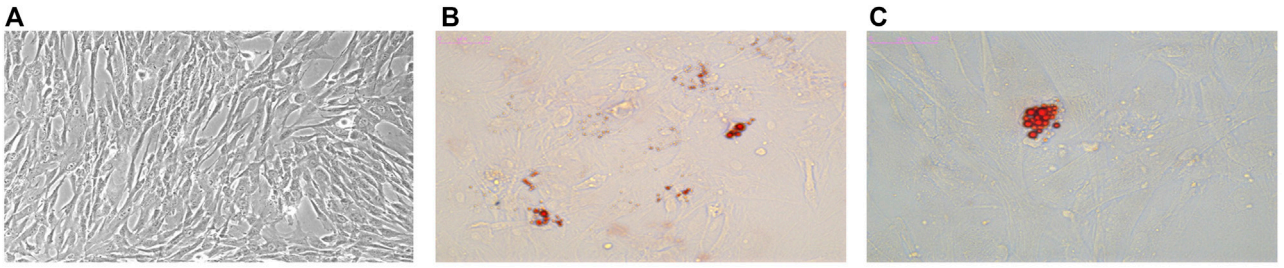

FIGURE 1
Characterization of hMSCs. Osteogenesis and adipogenesis induced differentiation of hMSCs. **(A)** Morphology of hMSCs. **(B)** Adipogenic differentiation observed with Oil Red 0 staining (× 200). **(C)** Adipogenic differentiation observed with Oil Red 0 staining (× 400).

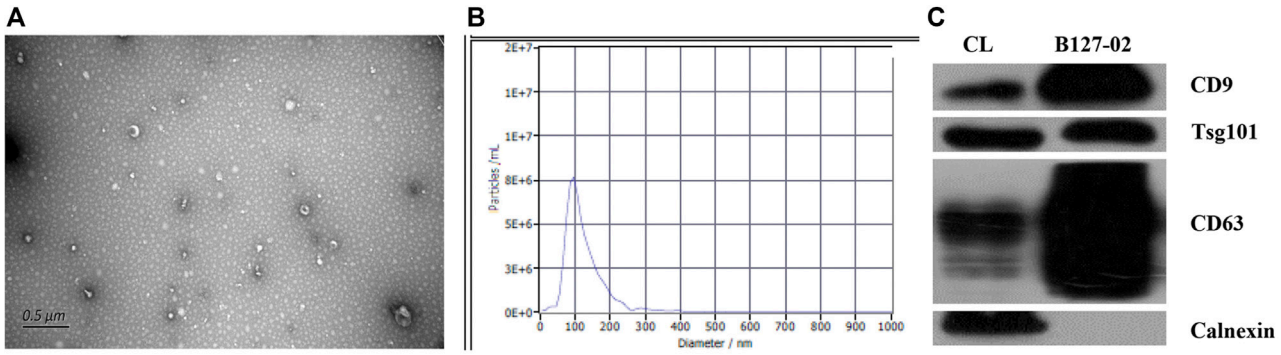

FIGURE 2
Characterization of hMSCs-exosomes. **(A)** Exosomes under transmission electron microscope **(B)** Brownian motion based nanoparticle trajectory analysis (NTA). **(C)** Western blot detection of the expression of exosomal surface marker proteins.

It had almost completely healed when treated with hMSC–Exo (20 μg/ml) for 12 h. The scratch test showed that the proliferative ability of cells of exosome-treated group was enhanced compared with the NC group. The effect was dose-dependent (Figure 3B).

The CCK-8 results showed that hMSC-Exo significantly promoted the proliferation of human fibroblasts in a time- and dose-dependent manner ($p < 0.01$) (Figure 4).

Clinical trial result

A total of 22 healthy female subjects were included in the trial, ranging from 24 to 55, and the average age was 40 ± 8.07. Two of the subjects were lost to follow-up due to the epidemic situation. The other 20 subjects completed the clinical trial as required. At the end of the clinical trial, no adverse event was found in the volunteers.

In order to assess the efficacy of the product for sensitive skin, the objective and subjective symptoms assessment was conducted by the same dermatologist firstly. As shown in Figure 5, scores of objective symptoms including roughness, scales, erythema, and subjective symptoms including tension, burning, or itching, both decreased significantly on 7, 14, and 28 days after the use of the product compared to the baseline ($p < 0.05$); scores of dryness decreased significantly on 7, 14 and 28 days after the use of the product compared to the baseline ($p < 0.05$). Then the improvement index was calculated. On 7, 14, and 28 days after the use of the product, the objective and subjective symptoms were all improved (33.3%, 29.6%, and 44.4% separately). The dryness symptoms showed improvement on day 7 (45.8%), and significant improvement both on day 14 and day 28 (75.0%, 83.3% separately).

Secondly, the skin indexes of TEWL, hydration, sebum, pH value, and the skin a* value were measured, and data were shown in Table 1. The skin a* value, which is an important index of the efficacy of the product for sensitive skin, decreased significantly on 14 and 28 days after the use of the product compared to that at the baseline ($p < 0.05$). The lactic acid

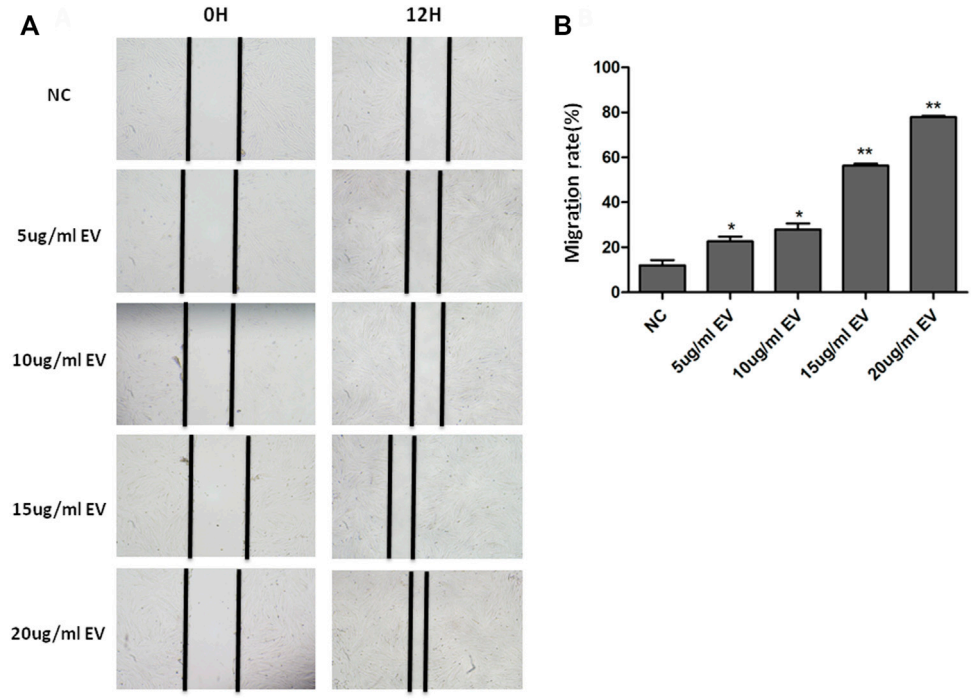

FIGURE 3
The effect of hMSC-Exo to human fibroblasts migration. **(A)** The microscopic features of human fibroblast with different concentrations of hMSC-Exo (5, 10, 15, and 20 μg/ml). **(B)** The migration rate of human fibroblast scratch assay. *$p < 0.05$, * *$p < 0.01$, compared to NC group.

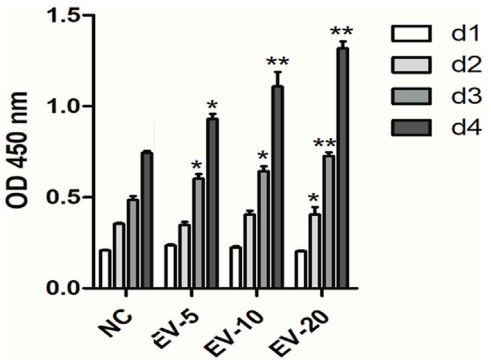

FIGURE 4
The effect of hMSC-Exo to human fibroblasts proliferation. *$p < 0.05$, **$p < 0.01$, compared to NC group.

stinging test scores decreased significantly on 7, 14, and 28 days after the use of the product compared to the baseline ($p < 0.05$). The skin sebum decreased significantly on 14 days after the use of the product compared to that at the baseline ($p = 0.026$). The skin surface pH value increased significantly on 28 days after the use of the product compared to that at the baseline ($p = 0.026$). Although there was no significant difference between the skin TEWL and hydration at each time point after the use of the product compared to the baseline ($p > 0.05$), the skin TEWL and hydration decreased or increased gradually with the extension of the use time of the product. Figure 6 showed the clinical photographs of one volunteer (sub-22) using the VISIA™ system. At 28 days, when compared to baseline (0 days), the apparent alleviation of red areas was observed in the photographs.

Thirdly, the proportions of subjects who are very satisfied with the product use experience *via* questionnaires were 75% on 7 days, 75% on 14 days, and 80% on 28 days.

Discussion

Although the pathogenesis of sensitive skin is not fully understood, skin barrier damage, inflammation, blood vessels, nerve hyperresponsiveness, and vascular proliferation/dilation were identified as key mechanisms of sensitive skin by many studies. Soluble components of MSC exosomes were capable to promote tissue regeneration, and suppress detrimental immune responses and neuron regeneration in ischemic tissues. MSC-derived secretomes showed immunoregulatory, neuron-protection, and anti-apoptotic effects that resulted in

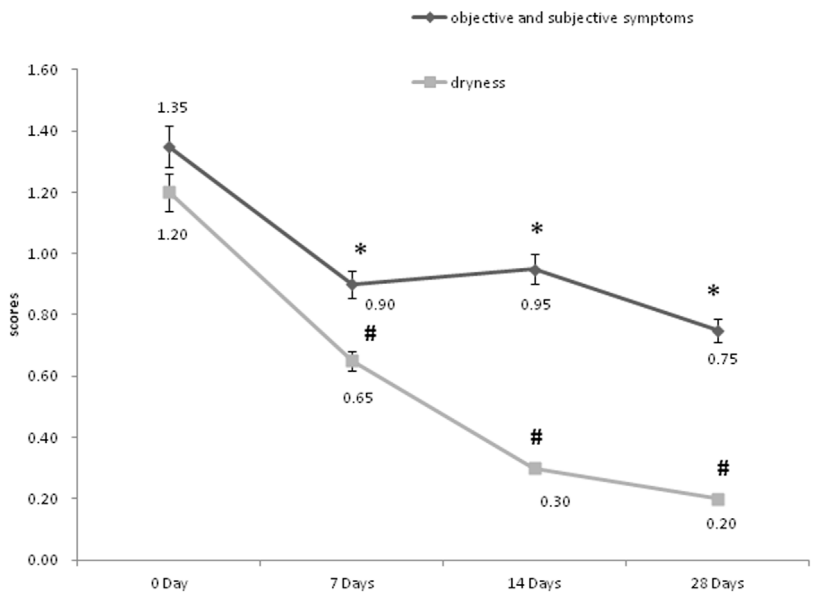

FIGURE 5
The objective, subjective symptoms and dryness assessment of the dermatologist. *$p < 0.05$, scores of objective and subjective symptoms, compared to the baseline (0 Day). #$p < 0.05$, scores of dryness, compared to the baseline (0 Day).

TABLE 1 TEWL, hydration, sebum, pH, a* value, and lactic acid stinging test scores on 0,7, 14, and 28 days after the use of the product (mean ± SD).

Parameter	0 Day	7 Days	14 Days	28 Days
Hydration (AU)	76.34 ± 8.24	74.58 ± 9.13	73.11 ± 11.43	77.29 ± 9.56
TEWL (g/m2h)	12.62 ± 4.60	12.57 ± 4.87	12.26 ± 3.19	11.96 ± 3.17
Sebum (AU)	51.00 ± 29.68	46.35 ± 29.54	43.20 ± 30.72*	50.35 ± 32.41
pH value (AU)	6.05 ± 0.55	6.29 ± 0.51	6.06 ± 0.67	6.28 ± 0.53*
a* value (AU)	12.17 ± 2.23	9.94 ± 3.73*	9.15 ± 3.50*	11.56 ± 1.96*
lactic acid stinging test scores	8.83 ± 6.10	—	4.70 ± 4.17*	4.85 ± 4.75*

*$p < 0.05$, compared to the baseline (0 Day).

enhanced tissue repair and regeneration (Ha et al., 2020). In previous experimental and preclinical settings, exosome-based therapies are widely investigated in various disease models. In this study, we found that the hMSC exosomes could improve clinical symptoms, skin eruptions, and skin indexes including TEWL, hydration, sebum, pH, and the L* a* value of sensitive skin patients. Therefore, we suggested that hMSC-exosomes could improve skin sensitive conditions by repairing skin barriers, regulating dermic immunity, and suppressing neurovascular hyperreactivity.

Sensitive skin is related to skin barrier dysfunction, which can lead to discomfort in various skin diseases (Roussaki-Schulze et al., 2005; Saint-Martory et al., 2008). Pinto et al. (2011) found that the TEWL (transepidermal water loss) of sensitive skin patients was significantly different from the normal control group by using the curve mathematical model analysis (Pinto, Rosado, Parreirão, & Rodrigues, 2011). Decreased neutral lipid levels and sheath phosphorus and the increase of lipid level in the skin of patients with sensitive skin reduces the stability of skin barrier function (Cua, Wilhelm, & Maibach, 1990; Pinto et al., 2011). The decline of barrier function is not only conducive to the entry of external irritants into the skin surface, make nerve endings more vulnerable to stimulation, and increase TEWL value (Saint-Martory et al., 2008) (Warren et al., 2005). In this study, we found that the skin index as TEWL and skin hydration which reflected the skin barrier function were improved after using hMSC-exosomes. For Hu et al. (2016) found that adipose-derived mesenchymal stem cell-derived exosomes (ASCs-Exo)

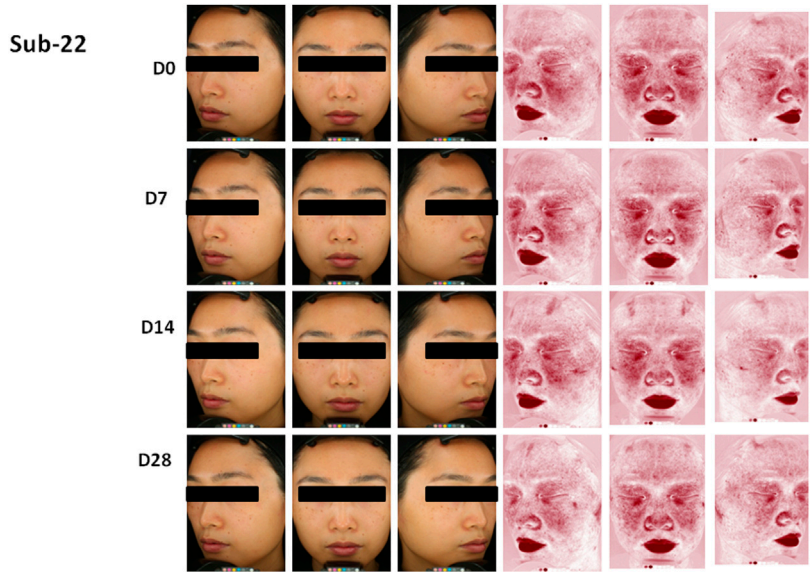

FIGURE 6
Photographs of volunteer #22 with VISTA" system at 0 day (DO), 7 days (D7), 14 days (D14) and 28 days (D28), Improvement of red areas could be seen at 28 days.

could stimulate the proliferation, migration, and collagen synthesis of fibroblasts in a dose-dependent manner, and promote cyclin 1, N-calcium. The expression of mucin, collagen type I, collagen type III and proliferating cell nuclear antigen, thereby promoting the healing of skin wounds. This may partly explain the mechanisms of dermal and epidermal repairing effects of hMSC-exosomes on sensitive skin. We suggested that the regulatory roles of hMSC exosomes in recovering skin barrier functions might be by stimulating the skin cell activity and proliferation, and promoting the secretion of sebum which is one of the important components of normal skin barrier.

Our dates showed that the skin a* value was decreased after 7-day of treatment and the skin inflammatory red area was improved under VISIA which revealed that hMSC-exosomes had anti-inflammatory and therapeutic effects. The immune pathogenesis of sensitive skin is quite complicated, while the immune regulation functions of exosomes derived from different cell sources has been reported. Li et al. (2016) studied the effect of human umbilical cord mesenchymal stem cells (hUMSCs) on the inflammatory response in a diabetic rat burn model, and found that the endogenous miR-181c of hUMSCs exosomes can pass Inhibit Toll-like receptor 4 (TLR4) signaling pathway, attenuate lipopolysaccharide-mediated inflammatory response, reduce the number of inflammatory cells such as neutrophils and macrophages, and the expression of inflammatory factors such as TNF-α and IL-1β, and promote anti-inflammatory factors IL-10 expression, thereby inhibiting the inflammatory response. In addition, miR-155 encapsulated in exosomes of bone marrow MSCs can promote endotoxin-induced inflammatory response, while miR-146a inhibits inflammatory response, and the two synergistically regulate the expression of inflammatory genes (Alexander et al., 2015). Cha et al. showed tonsil-derived mesenchymal stem cells (T-MSCs) were able to effectively attenuate TLR7-mediated skin inflammation in mice, which was accompanied by an increase in mast cell number. The present study investigated whether T-MSC extracellular vesicles, such as exosomes, are able to regulate mast cell activation in response to TLR7 stimulation. (Cho et al., 2021). We suggested that hMSC might take part in adjusting multiple inflammatory immune factors, signaling pathways and non-coding RNAs in sensitive skin. And the characteristic immune mechanisms still need further investigation.

Cutaneous vascular hyperreactivity and neurosensory dysfunction can be present in sensitive skin patients both with or without erythema. Sustained chronic inflammation characterized by a mainly Th1 macrophage and mast cell-driven infiltrate further leads to the release of incompletely understood mediators involved in vasoregulation, immunity, and fibrosis (Mascarenhas, Wang, Chang, & Di Nardo, 2017). TRP channels hyper-activation, such as TRPA1, TRPV1, TRPV3, and PAR2, can crosstalk with neuropeptide receptors or at least trigger neuropeptide release (Aubdool & Brain, 2011; Steinhoff, Schauber, & Leyden, 2013; Mascarenhas et al., 2017). TRPV3 mediates reactions to warm temperatures and camphor. TRPV4 can be activated by heat, mechanical and hypo-osmotic stress as well as UV. This hyper-reactivity can be modulated by multiple environmental factors. The link between the therapeutic mechanism of exosome and TRPV inhibition has not

been fully established. However, Li et al. (2020), showed that BMSCs-exosomes could relieve chronic pain *via* inhibition of the CGRP-positive nerve, a key effector of TRPV activation (Park et al., 2018). A study by Yu et al. (2020), found adipose-derived exosomes play a protective role in lung injury by alleviating the pulmonary endothelial barrier injury and inflammatory response, through inhibiting the TRPV4/Ca2+ pathway. Further *in vivo* data verified that TRPV4 and ROCK1 played a centric role in the neuropathic process (Yu et al., 2022). These suggested that hMSC-exosomes might improve clinical symptoms and eruptions by regulating dermic immunity and suppressing neurovascular hyperreactivity in sensitive skin patients. But its mechanisms still need further investigation.

Conclusion

The hMSC-exosomes, with the advantages of biocompatibility and biodegradability, could improve clinical symptoms and eruptions in sensitive skin patients, and might be as an MSC cell-free novel therapy in sensitive skin-related diseases treatment.

Data availability statement

The raw data supporting the conclusion of this article will be made available by the authors, without undue reservation.

Ethics statement

The studies involving human participants were reviewed and approved by Use Committee (IACUC) of the Third Affiliated Hospital of Sun Yat-sen University. The patients/participants provided their written informed consent to participate in this study. The animal study was reviewed and approved by the Clinical Research Ethics Committee and Animal Care of the Third Affiliated Hospital of Sun Yat-sen University. Written informed consent was obtained from the individual(s) for the publication of any potentially identifiable images or data included in this article.

Author contributions

CY was responsible for designing the experimental protocol, completing some of the experiments, and writing the first draft of the article. YZ and ZS participated in completing most of the experiments and analyzing the data. SW participated in designing the experiments and providing materials. WL was responsible for experimental guidance and grant support. YL and JY assisted in completing the experiments. JC and YZ edited and reviewed the article.

Funding

This research was supported by: Guangdong Basic and Apply Basic Research Foundation, (Grant/Award Number: 2022A1515012253); Science and Technology Program of Guangzhou, China (Grant/Award Number: 202102010284).

Conflict of interest

Authors SW and YL are employed by AIE Bioscience (Guangdong) Co., LTD. The remaining authors declare that the research was conducted in the absence of any commercial or financial relationships that could be construed as a potential conflict of interest.

The remaining authors declare that the research was conducted in the absence of any commercial or financial relationships that could be construed as a potential conflict of interest.

Publisher's note

All claims expressed in this article are solely those of the authors and do not necessarily represent those of their affiliated organizations, or those of the publisher, the editors and the reviewers. Any product that may be evaluated in this article, or claim that may be made by its manufacturer, is not guaranteed or endorsed by the publisher.

References

AbuBakr, N., Haggag, T., Sabry, D., and Salem, Z. A. (2020). Functional and histological evaluation of bone marrow stem cell-derived exosomes therapy on the submandibular salivary gland of diabetic Albino rats through TGFβ/Smad3 signaling pathway. *Heliyon* 6 (4), e03789. doi:10.1016/j.heliyon.2020.e03789

Aghajani Nargesi, A., Lerman, L. O., and Eirin, A. (2017). Mesenchymal stem cell-derived extracellular vesicles for kidney repair: Current status and looming challenges. *Stem Cell. Res. Ther.* 8 (1), 273. doi:10.1186/s13287-017-0727-7

Ahn, S. Y., Sung, D. K., Kim, Y. E., Sung, S., Chang, Y. S., and Park, W. S. (2021). Brain-derived neurotropic factor mediates neuroprotection of mesenchymal stem cell-derived extracellular vesicles against severe intraventricular hemorrhage in newborn rats. *Stem Cells Transl. Med.* 10 (3), 374–384. doi:10.1002/sctm.20-0301

Akyurekli, C., Le, Y., Richardson, R. B., Fergusson, D., Tay, J., and Allan, D. S. (2015). A systematic review of preclinical studies on the therapeutic potential of mesenchymal stromal cell-derived microvesicles. *Stem Cell. Rev. Rep.* 11 (1), 150–160. doi:10.1007/s12015-014-9545-9

Alexander, M., Hu, R., Runtsch, M. C., Kagele, D. A., Mosbruger, T. L., Tolmachova, T., et al. (2015). Exosome-delivered microRNAs modulate the inflammatory response to endotoxin. *Nat. Commun.* 6, 7321. doi:10.1038/ncomms8321

Alzahrani, F. A. (2019). Melatonin improves therapeutic potential of mesenchymal stem cells-derived exosomes against renal ischemia-reperfusion injury in rats. *Am. J. Transl. Res.* 11 (5), 2887–2907.

An, T., Chen, Y., Tu, Y., and Lin, P. (2021). Mesenchymal stromal cell-derived extracellular vesicles in the treatment of diabetic foot ulcers: Application and challenges. *Stem Cell. Rev. Rep.* 17 (2), 369–378. doi:10.1007/s12015-020-10014-9

Aneesh, A., Liu, A., Moss, H. E., Feinstein, D., Ravindran, S., Mathew, B., et al. (2021). Emerging concepts in the treatment of optic neuritis: Mesenchymal stem cell-derived extracellular vesicles. *Stem Cell. Res. Ther.* 12 (1), 594. doi:10.1186/s13287-021-02645-7

Aubdool, A. A., and Brain, S. D. (2011). Neurovascular aspects of skin neurogenic inflammation. *J. Investig. Dermatol. Symp. Proc.* 15 (1), 33–39. doi:10.1038/jidsymp.2011.8

Baharlooi, H., Azimi, M., Salehi, Z., and Izad, M. (2020). Mesenchymal stem cell-derived exosomes: A promising therapeutic ace card to address Autoimmune diseases. *Int. J. Stem Cells* 13 (1), 13–23. doi:10.15283/ijsc19108

Bai, L., Shao, H., Wang, H., Zhang, Z., Su, C., Dong, L., et al. (2017). Effects of mesenchymal stem cell-derived exosomes on experimental Autoimmune uveitis. *Sci. Rep.* 7 (1), 4323. doi:10.1038/s41598-017-04559-y

Bai, Y., Han, Y. D., Yan, X. L., Ren, J., Zeng, Q., Li, X. D., et al. (2018). Adipose mesenchymal stem cell-derived exosomes stimulated by hydrogen peroxide enhanced skin flap recovery in ischemia-reperfusion injury. *Biochem. Biophys. Res. Commun.* 500 (2), 310–317. doi:10.1016/j.bbrc.2018.04.065

Bailey, A. J. M., Li, H., Kirkham, A. M., Tieu, A., Maganti, H. B., Shorr, R., et al. (2021). MSC-derived extracellular vesicles to heal diabetic wounds: A systematic review and meta-analysis of preclinical animal studies. *Stem Cell. Rev. Rep.* 18, 968–979. doi:10.1007/s12015-021-10164-4

Bao, C., and He, C. (2021). The role and therapeutic potential of MSC-derived exosomes in osteoarthritis. *Arch. Biochem. Biophys.* 710, 109002. doi:10.1016/j.abb.2021.109002

Berardesca, E., Farage, M., and Maibach, H. (2013). Sensitive skin: An overview. *Int. J. Cosmet. Sci.* 35 (1), 2–8. doi:10.1111/j.1468-2494.2012.00754.x

Birtwistle, L., Chen, X. M., and Pollock, C. (2021). Mesenchymal stem cell-derived extracellular vesicles to the rescue of renal injury. *Int. J. Mol. Sci.* 22 (12), 6596. doi:10.3390/ijms22126596

Chardon, A., Cretois, I., and Hourseau, C. (1991). Skin colour typology and suntanning pathways. *Int. J. Cosmet. Sci.* 13 (4), 191–208. doi:10.1111/j.1467-2494.1991.tb00561.x

Cho, K. A., Cha, J. E., Kim, J., Kim, Y. H., Ryu, K. H., and Woo, S. Y. (2021). Mesenchymal stem cell-derived exosomes attenuate TLR7-mediated mast cell activation. *Tissue Eng. Regen. Med.* 19, 117–129. doi:10.1007/s13770-021-00395-4

Cua, A. B., Wilhelm, K. P., and Maibach, H. I. (1990). Cutaneous sodium lauryl sulphate irritation potential: Age and regional variability. *Br. J. Dermatol.* 123 (5), 607–613. doi:10.1111/j.1365-2133.1990.tb01477.x

Fang, S., Xu, C., Zhang, Y., Xue, C., Yang, C., Bi, H., et al. (2016). Umbilical cord-derived mesenchymal stem cell-derived exosomal MicroRNAs suppress myofibroblast differentiation by inhibiting the transforming growth factor-β/SMAD2 pathway during wound healing. *Stem Cells Transl. Med.* 5 (10), 1425–1439. doi:10.5966/sctm.2015-0367

Golan, K., Kumari, A., Kollet, O., Khatib-Massalha, E., Subramaniam, M. D., Ferreira, Z. S., et al. (2018). Daily onset of light and darkness differentially controls hematopoietic stem cell differentiation and maintenance. *Cell. Stem Cell.* 23 (4), 572–585.e7. e577. doi:10.1016/j.stem.2018.08.002

Ha, D. H., Kim, H. K., Lee, J., Kwon, H. H., Park, G. H., Yang, S. H., et al. (2020). Mesenchymal stem/stromal cell-derived exosomes for immunomodulatory therapeutics and skin regeneration. *Cells* 9 (5), 1157. doi:10.3390/cells9051157

Harrell, C. R., Simovic Markovic, B., Fellabaum, C., Arsenijevic, A., Djonov, V., Arsenijevic, N., et al. (2018). Therapeutic potential of mesenchymal stem cell-derived exosomes in the treatment of eye diseases. *Adv. Exp. Med. Biol.* 1089, 47–57. doi:10.1007/5584_2018_219

Hu, L., Wang, J., Zhou, X., Xiong, Z., Zhao, J., Yu, R., et al. (2016). Exosomes derived from human adipose mensenchymal stem cells accelerates cutaneous wound healing via optimizing the characteristics of fibroblasts. *Sci. Rep.* 6, 32993. doi:10.1038/srep32993

Kalluri, R., and LeBleu, V. S. (2020). The biology, function, and biomedical applications of exosomes. *Science* 367 (6478), eaau6977. doi:10.1126/science.aau6977

Kim, Y. R., Cheon, H. I., Misery, L., Taieb, C., and Lee, Y. W. (2018). Sensitive skin in Korean population: An epidemiological approach. *Skin. Res. Technol.* 24 (2), 229–234. doi:10.1111/srt.12418

Li, J., Ding, Z., Li, Y., Wang, W., Wang, J., Yu, H., et al. (2020). BMSCs-derived exosomes ameliorate pain via abrogation of aberrant nerve invasion in subchondral bone in lumbar facet joint osteoarthritis. *J. Orthop. Res.* 38 (3), 670–679. doi:10.1002/jor.24497

Li, X., Liu, L., Yang, J., Yu, Y., Chai, J., Wang, L., et al. (2016). Exosome derived from human umbilical cord mesenchymal stem cell mediates MiR-181c attenuating burn-induced excessive inflammation. *EBioMedicine* 8, 72–82. doi:10.1016/j.ebiom.2016.04.030

Mascarenhas, N. L., Wang, Z., Chang, Y. L., and Di Nardo, A. (2017). TRPV4 mediates mast cell activation in cathelicidin-induced rosacea inflammation. *J. Investig.. Dermatol.* 137 (4), 972–975. doi:10.1016/j.jid.2016.10.046

Misery, L. (2017). Neuropsychiatric factors in sensitive skin. *Clin. Dermatol.* 35 (3), 281–284. doi:10.1016/j.clindermatol.2017.01.011

Nargesi, A. A., Lerman, L. O., and Eirin, A. (2017). Mesenchymal stem cell-derived extracellular vesicles for renal repair. *Curr. Gene Ther.* 17 (1), 29–42. doi:10.2174/1566523217666170412110724

Park, K. Y., Kwon, H. J., Kim, J. M., Jeong, G. J., Kim, B. J., Seo, S. J., et al. (2018). A pilot study to evaluate the efficacy and safety of treatment with botulinum toxin in patients with recalcitrant and persistent erythematotelangiectatic rosacea. *Ann. Dermatol.* 30 (6), 688–693. doi:10.5021/ad.2018.30.6.688

Pelizzo, G., Avanzini, M. A., Icaro Cornaglia, A., De Silvestri, A., Mantelli, M., Travaglino, P., et al. (2018). Extracellular vesicles derived from mesenchymal cells: Perspective treatment for cutaneous wound healing in pediatrics. *Regen. Med.* 13 (4), 385–394. doi:10.2217/rme-2018-0001

Pinto, P., Rosado, C., Parreirão, C., and Rodrigues, L. M. (2011). Is there any barrier impairment in sensitive skin?: A quantitative analysis of sensitive skin by mathematical modeling of transepidermal water loss desorption curves. *Skin. Res. Technol.* 17 (2), 181–185. doi:10.1111/j.1600-0846.2010.00478.x

Roussaki-Schulze, A. V., Zafiriou, E., Nikoulis, D., Klimi, E., Rallis, E., and Zintzaras, E. (2005). Objective biophysical findings in patients with sensitive skin. *Drugs Exp. Clin. Res.* 31, 17–24.

Saint-Martory, C., Roguedas-Contios, A. M., Sibaud, V., Degouy, A., Schmitt, A. M., and Misery, L. (2008). Sensitive skin is not limited to the face. *Br. J. Dermatol.* 158 (1), 130–133. doi:10.1111/j.1365-2133.2007.08280.x

Shen, Z., Huang, W., Liu, J., Tian, J., Wang, S., and Rui, K. (2021). Effects of mesenchymal stem cell-derived exosomes on Autoimmune diseases. *Front. Immunol.* 12, 749192. doi:10.3389/fimmu.2021.749192

Steinhoff, M., Schauber, J., and Leyden, J. J. (2013). New insights into rosacea pathophysiology: A review of recent findings. *J. Am. Acad. Dermatol.* 69 (1), S15–S26. doi:10.1016/j.jaad.2013.04.045

Warren, R., Bauer, A., Greif, C., Wigger-Alberti, W., Jones, M. B., Roddy, M. T., et al. (2005). Transepidermal water loss dynamics of human vulvar and thigh skin. *Skin. Pharmacol. Physiol.* 18 (3), 139–143. doi:10.1159/000084911

Ye, C., Chen, J., Yang, S., Yi, J., Chen, H., Li, M., et al. (2020). Skin sensitivity evaluation: What could impact the assessment results? *J. Cosmet. Dermatol.* 19 (5), 1231–1238. doi:10.1111/jocd.13128

Yu, Q., Wang, D., Fan, S., Tang, X., He, J., Peng, J., et al. (2022). Protective effects of adipose-derived biogenic nanoparticles on the pulmonary microvascular endothelial barrier in mice with ventilator-induced lung injury via the TRPV4/ROCK1 signalling pathway. *Pulm. Pharmacol. Ther.* 73-74, 102123. doi:10.1016/j.pupt.2022.102123

Yu, Q., Wang, D., Wen, X., Tang, X., Qi, D., He, J., et al. (2020). Adipose-derived exosomes protect the pulmonary endothelial barrier in ventilator-induced lung injury by inhibiting the TRPV4/Ca(2+) signaling pathway. *Am. J. Physiology-Lung Cell. Mol. Physiology* 318 (4), L723–l741. doi:10.1152/ajplung.00255.2019

Zhang, B., Wang, M., Gong, A., Zhang, X., Wu, X., Zhu, Y., et al. (2015). HucMSC-exosome mediated-wnt4 signaling is required for cutaneous wound healing. *Stem Cells* 33 (7), 2158–2168. doi:10.1002/stem.1771

frontiers | Frontiers in Bioengineering and Biotechnology

TYPE Systematic Review
PUBLISHED 15 December 2022
DOI 10.3389/fbioe.2022.1036678

Check for updates

OPEN ACCESS

EDITED BY
Mingqiang Li,
Third Affiliated Hospital of Sun Yat-sen University, China

REVIEWED BY
Nan-Fu Chiu,
National Taiwan Normal University, Taiwan
Qing Huang,
Army Medical University, China

*CORRESPONDENCE
Jiang Pi,
jiangpi@gdmu.edu.cn
Wandang Wang,
wangwandang@126.com
Guanghui Chen,
chenguanghui416@sina.com

†These authors have contributed equally to this work and share first authorship

SPECIALTY SECTION
This article was submitted to Biomaterials, a section of the journal Frontiers in Bioengineering and Biotechnology

RECEIVED 05 September 2022
ACCEPTED 02 December 2022
PUBLISHED 15 December 2022

CITATION
Yang X, Fan S, Ma Y, Chen H, Xu J-F, Pi J, Wang W and Chen G (2022), Current progress of functional nanobiosensors for potential tuberculosis diagnosis: The novel way for TB control?
Front. Bioeng. Biotechnol. 10:1036678. doi: 10.3389/fbioe.2022.1036678

COPYRIGHT
© 2022 Yang, Fan, Ma, Chen, Xu, Pi, Wang and Chen. This is an open-access article distributed under the terms of the Creative Commons Attribution License (CC BY). The use, distribution or reproduction in other forums is permitted, provided the original author(s) and the copyright owner(s) are credited and that the original publication in this journal is cited, in accordance with accepted academic practice. No use, distribution or reproduction is permitted which does not comply with these terms.

Current progress of functional nanobiosensors for potential tuberculosis diagnosis: The novel way for TB control?

Xuran Yang[1†], Shuhao Fan[2,3†], Yuhe Ma[2,3†], Hui Chen[1], Jun-Fa Xu[2,3], Jiang Pi[2,3*], Wandang Wang[1*] and Guanghui Chen[1*]

[1]Department of Clinical Medicine Laboratory, Affiliated Xiaolan Hospital, Southern Medical University, Zhongshan, China, [2]Guangdong Provincial Key Laboratory of Medical Molecular Diagnostics, The First Dongguan Affiliated Hospital, Guangdong Medical University, Dongguan, China, [3]Institute of Laboratory Medicine, School of Medical Technology, Guangdong Medical University, Dongguan, China

Tuberculosis (TB), induced by the foxy *Mycobacterium tuberculosis* (Mtb), is still one of the top killers worldwide among infectious diseases. Although several antibiotics have been developed to significantly relieve the tuberculosis epidemics worldwide, there are still several important scientific challenges for tuberculosis. As one of the most critical issues for tuberculosis control, the accurate and timely diagnosis of tuberculosis is critical for the following therapy of tuberculosis and thus responsible for the effective control of drug-resistant tuberculosis. Current tuberculosis diagnostic methods in clinic are still facing the difficulties that they can't provide the rapid diagnostic results with high sensitivity and accuracy, which therefore requires the development of more effective novel diagnostic strategies. In recent decades, nanomaterials have been proved to show promising potentials for novel nanobiosensor construction based on their outstanding physical, chemical and biological properties. Taking these promising advantages, nanomaterial-based biosensors show the potential to allow the rapid, sensitive and accurate tuberculosis diagnosis. Here, aiming to increase the development of more effective tuberculosis diagnostic strategy, we summarized the current progress of nanobiosensors for potential tuberculosis diagnosis application. We discussed the different kind diagnostic targets for tuberculosis diagnosis based on nanobiosensors, ranging from the detection of bacterial components from *M. tuberculosis*, such as DNA and proteins, to the host immunological responses, such as specific cytokine production, and to the direct whole cell detection of *M. tuberculosis*. We believe that this review would enhance our understandings of nanobiosensors for potential tuberculosis diagnosis, and further promote the future research on nanobiosensor-based tuberculosis diagnosis to benefit the more effective control of tuberculosis epidemic.

KEYWORDS

nanomaterials, nanobiosensor, tuberculosis, diagnosis, recent progress

Introduction

Tuberculosis (TB), caused by the foxy *Mycobacterium tuberculosis* (Mtb), remains to be one of the most catastrophic diseases since human history. According to the global TB report in 2021, the newly diagnosed cases of TB were up to 10 million with an estimated 1.4 million deaths in 2020 (World Health, 2021). Although numerous advances have been made in understanding of the epidemiology, risk factors, pathophysiology, diagnosis and treatment, TB is still one of the top 10 causes of death among diseases worldwide, ranking above HIV/AIDS. Although several antibiotics have been developed to significantly relieve the TB epidemics, there are still several important scientific issues for TB. As one of the most critical issues for the control of TB and drug-resistant TB epidemics, the diagnosis of TB is critical for the timely therapy of TB.

Currently, there are several conventional methods that are widely used for *Mtb* detection or TB diagnosis, which have made plenty of contributions in the control of TB epidemic. However, these current TB diagnostic methods are still facing some difficulties that they can't provide the rapid diagnostic results with high sensitivity and accuracy simultaneously. Ziehl-Neelsen (ZN) smear microscopy is the most common used method for clinical TB diagnosis, which is inexpensive with low bio-safety standards, but it shows restricted sensitivity when the bacterial load of Mtb is lower than 10,000 organisms/ml in sputum samples (Steingart et al., 2006; Desikan, 2013). Mycobacterial cultures is a very accurate TB diagnotic strategy that offers improved sensitivity up to 60%, but it is time consuming and needs a bio-safety level-3 laboratory theoretically, which introduces severe constrains on the prompt TB diagnosis (Dolin et al., 1994; Smith, 2003; Onyango, 2011; Wang et al., 2014; World Health, 2015a; World Health, 2015b). The reactive tuberculin skin testing (TST) and interferon gamma release assays (IGRAs) provide methods for the detection of latent TB (LTB) through targeting memory T-cell receptor previously-sensitized by prior TB infection. TST is inexpensive and widely used, but it requires 48–72 h to obtain the results based on two patient visits and the results are very easily to be disturbed by some non-Mycobacterial (NTM). IGRAs based detection method possesses high sensitivity and specificity, but it might introduce false positive diagnosis in subjects with high concentration of IFN-γ. The high cost and the requirement of special laboratory settings and well-trained staffs also partially restrict the application of IGRAs. The Xpert Mtb/RIF assay, a new rapid diagnostic test based on nucleic acid amplification, works very well in diagnostic of *Mtb* and rifampicin resistance in 2 h (El-Samadony et al., 2017), but it is not only restricted by its relatively low sensitivity and high false positivity rates in same specific conditions (Arend and van Soolingen, 2018), but also show limitations for the diagnosis and management of polyresistant pulmonary tuberculosis (Hopmeier et al., 2020).

In recent decades, nanomaterials are widely used in biomedical fields and have been developed for tissue regeneration (Xue et al., 2022), anti-infection (Alotaibi et al., 2022) (Lin et al., 2022), antitumor (Wang et al., 2022). Based on their excellent physical, chemical and biological properties, nanomaterials have also been proved to show great potential in the development of new detection technologies. For example, Guthula et al. (2022) designed a method for the determination of fiber-optic gold nanolinked adsorbents based on PCR-free DNA from human gastric tumor tissues and cell lines, which has shown good sensitivity, accuracy and short detection, and can be used as an alternative to PCR with great potential for diagnostic biosensor fabrication.

In addition to the relevant detection of viral and cancer factors, more and more nanomaterials with attractive functions have been developed as promising tools for sensitive, rapid and accurate detection for TB related-samples as the unique properties of nanomaterials. Such manipulations enable nanomaterials to operate specific analytical functions and hence their applications as biosensors (Rai et al., 2016), which might benefit the development of novel TB diagnostic strategies. In this review, we systemically summarized the current progress of nanobiosensors for potential TB diagnosis application. Firstly, we introduced the basic principles of how nanobiosensor works for potential diagnosis. In the second part, we seperately discussed the current progress of nanobiosensors targeting DNA and protein of Mtb for TB diagnosis. Thirdly, we also introduced the development of nanobiosensors for Mtb infection associated cytokins production, followed the current progress of nanobiosensors for whole cell of Mtb analysis. At last, we discussed the perspectives of the functional nanobiosensors for potential tuberculosis diagnosis, which might promote the following research on nanobiosensor-based TB diagnosis and further benefit the development of diagnostic strategy for more effective control of TB epidemic.

How nanobiosensor works for potential diagnosis

The landscape of TB diagnostic strategy is still restricted by the lack of ideal strategy with low cost, high sensitivity, accurate and rapid diagnosis. The development of nanotechnology allows the possible development of nanobiosensors, which allow the detection of biological molecules or components. A nanomaterial based biosensor is actually a kind of integrated device that basically consists of a biological recognition element, transducer, and processor, which can specifically recognize the target bio-analytes we prefer to be detected.

As shown in Figure 1, the target bio-analytes include nucleic acids (DNA, RNA), proteins such as enzymes, antibodies and antigens, immune cell cytokines, and whole cells (bacterial or virus), which can be captured by complementary bio-recognition

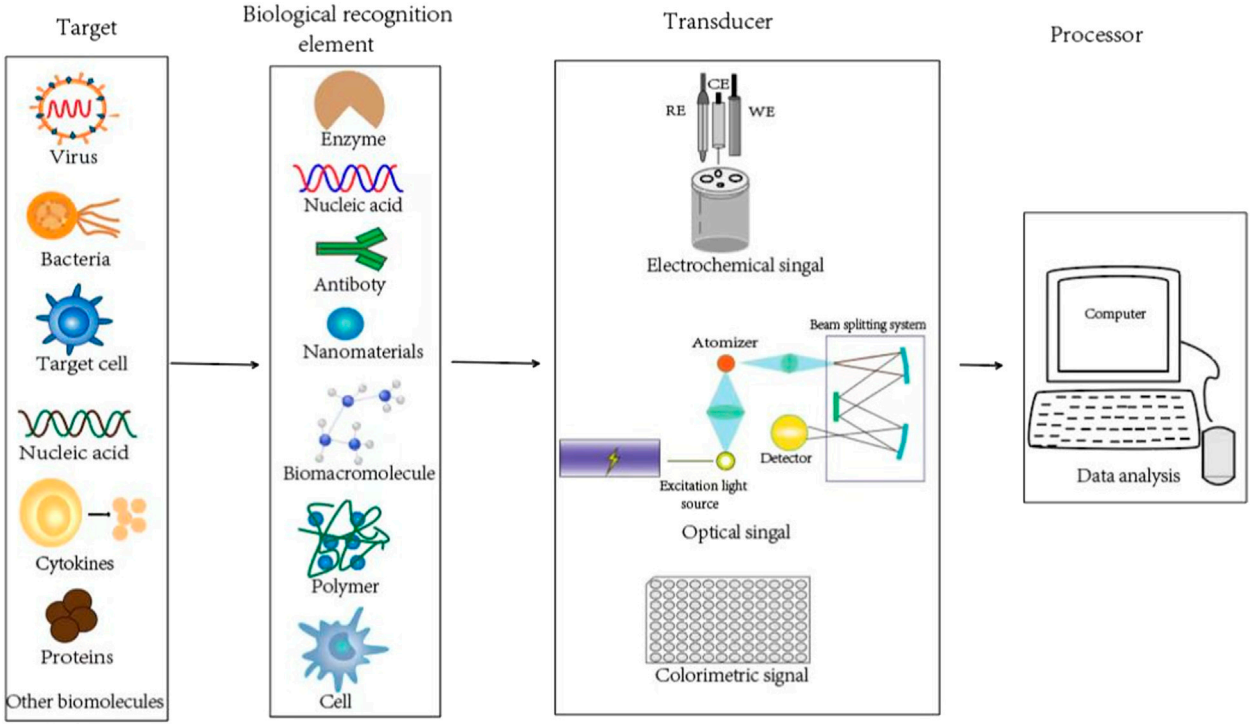

FIGURE 1
Schematics of the biological recognition element, transducer, and processor for typical nanobiosensors to detect the target bio-analytes.

probes. The typical biological recognition element for nanobiosensors is always formed by some nanomaterials, biomacromolecules (such as nucleic acid and proteins), polymers and even cells, which can be applied to specifically recognize the target bio-analytes. By establishing the linkage between specific and efficient bio-interaction with corresponding signals (such as electrical, fluorometric, luminometric or colorimetric signals), the levels or activities of elements involved in the biological recognition can be converted into specific signals by the transducers, which can be further amplified, quantified, displayed and analyzed (Abu-Salah et al., 2015; Gupta and Kakkar, 2018). Depending on the different detection parameter and theory, transducers could be classified into different strategies, such as optical (like SPR), piezoelectric (such as quartz crystal microbalance), electrochemical, thermometric, magnetic or micromechanical signal (Gupta and Kakkar, 2018). At last, the processor could translate the transducer signals into qualitative or quantitative data that could reflect the levels or activities of the targeted bio-analytes.

Taking the advantages of various unique properties like large loading volume, better electrical communication ability, stability and heat conductivity, combining nanomaterials with transducers could significantly enhance the diagnostics sensitivity, which makes nano-biosensing detection method a promising strategy for TB diagnosis. Up to now, two widely known approaches are always applied to design nanobiosensors: i.e., the modification of electrode surfaces by nanomaterials (Approach 1, example is presented as Figure 2A), or the fabrication of signal nanoprobes by nanomaterials to enhance generated signal (Approach 2, example is presented as Figure 2B). There are also some nanobiosensors constructed using both amplification approaches (hybrid biosensing, i.e., Approach 3, example is presented as Figure 2C). We also introduced the examples for the specific principles for these basic approaches as shown as in Figure 2. Nano-biosensing diagnostics about TB detection contain different kinds of bio-analytes, such as DNA, protein, cytokines and even whole bacteria. In this review, the most recent research advances in the field of nano-based biosensors developed for TB detection were summarized.

Nanobiosensors targeting DNA of Mtb for TB diagnosis

In recent decades, the methods for DNA detection has attracted increasing attentions for early diagnosis of diseases. The DNA contents of Mtb can be detected by some techniques, and some most widely used techniques are polymerase chain reaction (Sanjuan-Jimenez et al., 2013; Vinuesa et al., 2018),

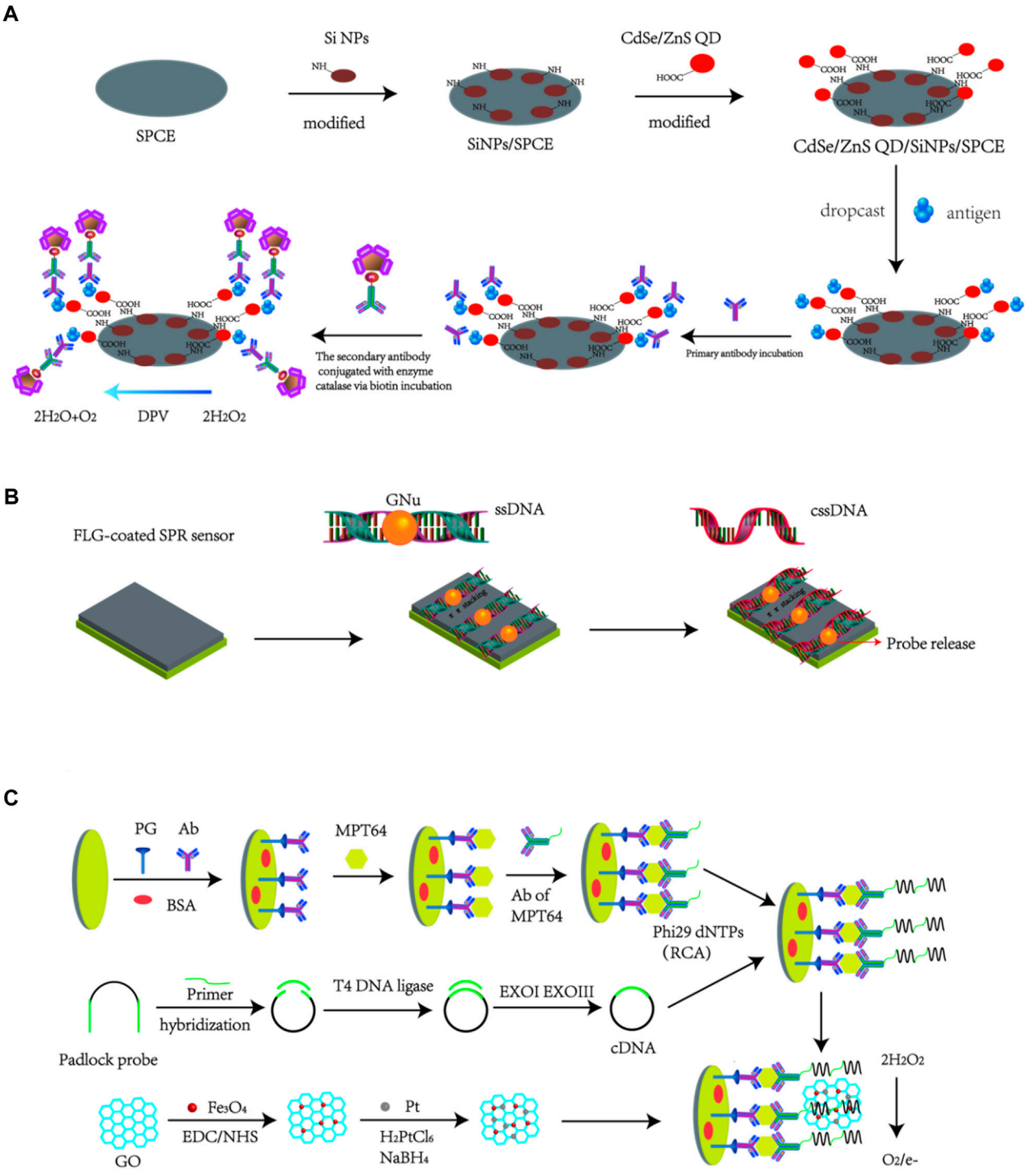

FIGURE 2
Basic approaches to design nanobiosensors: **(A)** Modification of nanoparticles onto electrode surfaces to construct functional electrode-based biosensors (Mohd Bakhori et al., 2019). **(B)** Design of nanosystems to construct nanoprobes that can be used for nanobiosensor application (Prabowo et al., 2021). **(C)** Hybrid method to construct Nanobiosensors using both approaches **(A,B)** (Gou et al., 2018).

microarray assay (Fukushima et al., 2003) and cycling probe technique (Pahwa et al., 2005) in the research laboratory. However, the existing methods were still not widely used in clinical laboratory diagnosis due to some limitations, such as complexity, time-consuming analysis duration and high cost. The rapid development of nanomaterials allows researchers a

new way to design more effective detection methods for TB infection.

As mentioned before, researchers usually develop nanobiosensors detection methods for TB detection based on the Approach 1–3 alone or together. Prabowo et al. (2021) introduced two distinct gold nanoparticle (AuNPs) structures, including gold nano-urchins (AuNu) and gold nanorods (AuNr), to bind the specifically designed single-stranded DNA probe (ssDNA) against the complex DNA of Mtb. These two kinds of AuNPs-ssDNA probes were adsorbed onto the few-layer graphene (FLG) through the π-π stacking force for SPR sensor coating, which allowed the hybridization interactions with their complementary single-stranded DNA (cssDNA). During the hybridization interactions, the strong hydrogen bond force between cssDNA and ssDNA could gradually remove the AuNPs-ssDNA from the graphene surface, which could result in a negative ΔSPR signal that could be detected by the SPR sensor. This method shows an estimated limit of detection (LOD) of ~24.5 fM cssDNA for GNus SPR signal (sensitivity), and a lower LOD of 8.2 pM cssDNA for GNrs SPR signal (sensitivity). The overall integrated approach of the graphene-based SPR sensor and AuNPs-assisted DNA detection method provided the proof-of-concept results for the further development of potential TB screening strategy. The DNA hybridization study based on the SPR sensor indicated that rough and spikey GNu could significantly reinforce the DNA hybridization signal than the smooth GNr. The DNA hybridization detection strategy was assisted by GNu to reach a outstanding limit of detection (LoD) at femtomolar level. But it is worth to note that the obtained results were all based on pure DNA samples, without any evidences to prove its applicability for the complicated clinical sample analysis. More works are still needed to test the ability of this nanobiosensor for samples isolated from patients.

To increase the sensitivity of TB diagnostic method, Hatami et al. (2020) firstly decorated the glassy carbon electrode (GCE) using zinc oxide (ZnO) before AuNPs deposition. The combination of ZnO with AuNPs could increase the surface area of the obtained electrode for better electrical communication compared to GCE, which bring higher sensitivity for DNA analysis. Later, the platform was modified with thiolated probe DNA by covalently conjugation, and then, the GCE/ZnO/AuNPs/ssDNA nanobiosensor was used to capture the targeted TB DNA. After incubated with sample solution for 45 min, the DNA nanobiosensor was analyzed by electrochemical impedance spectroscopy (EIS) with a LOD of 1.8 pM. Compared with an equimolar concentration for completely matched DNA (target), the corresponding ΔI_p values for double-base mismatched, three-base mismatched and non-complementary strands were only 48.8%, 27.0%, and 4.93%, indicating the high recognition ability of the proposed nanobiosensor towards TB DNA. In addition, the DNA nanobiosensor showed high stability as the measuredΔI_p decreased only 4.25% after storing at 4°C for 10 days. This work proposed label-free DNA nanobiosensor displayed high selectivity and sensitivity with wide linear range and picomolar LOD for TB DNA analysis. However, this work just tested the performance of the nanobiosensor for pure TB DNA sample analysis, no further attempts to detect the more complicated clinical samples.

Bai et al. (2019) also used the GCE electrode decorated with a biotin-avidin system that immobilizing with abundant capture probes (CPs) as platform to detect TB DNA. The AuNPs were immobilized into a fullerene nanoparticles and nitrogen-doped graphene nanosheet (G-nano-C_{60}/NGS), which was subsequently labeled by signal probes (SPs) for signal amplification. Later, a typical sandwich hybridization was produced in the presence of target DNA of Mtb, which was further incubated with tetraoctylammonium bromide (TOAB) to get discriminating responses. This electrochemical DNA-based nanobiosensor showed a broad linear range for the determination of Mtb DNA at a range of 10 fM-10 nM with a low LOD of 3 fM. Additionally, this prepared nanobiosensor can not only distinguish mismatched DNA sequence, but can also differentiate Mtb from other pathogens like *Staphylococcus aureus* and *Candida albicans*, indicating its strong Mtb DNA selectivity and specificity. Additionally, SPs labeled G-nanoC_{60} showed a weak peak compared to SPs labeled G-nano-C_{60}/NGS, indicating that this G-nano-C_{60}/NGS nanosystem could enhance the sensitivity of the electrochemical biosensor probably due to the presence of NGS to provide larger surface and facilitate electron transfer. Moreover, the steps for biosensor preparing was simplified as this nanohybrid was directly used to generate and enhance signals. With these merits, this electrochemical biosensor for DNA analysis is able to detect IS6110 fragments with fmol sensitivity, high specificity, reproducibility and stability, which therefore might be of great use in clinical practice. However, more works that directly analyzing the clinical samples should be further conducted to expand this nanobiosensor for clinical uses.

In comparison with other DNA-templated metal NPs, the synthesis of DNA-templated CuNPs is more convenient and significantly faster (Liu et al., 2018). DNA-templated Cu nanoparticles (NPs) exhibit great potential for instantaneous reaction, and facile integration with nucleic acid-based signal amplification and target-recognition strategies. This formation is associated with the clustering of Cu(0), which is produced by the chemical reduction of Cu(II) on the DNA backbones. Based on the quantum-confinement effects, CuNPs can be excitable by a λex at 340 nm to emit fluorescence signals with max λem at 600 nm for the *in-situ* production of fluorescent DNA-templated CuNPs in minutes. In addition, DNA-templated CuNPs are found to show large stokes shift that can help to reduce the background interference from the complicated biological matrixes. Hence, researchers investigated a dsDNA CuNPs-PCR method to rapidly detect the IS6110 DNA sequence of Mtb by *in situ* formation of a DNA-templated fluorescent CuNPs

system (Tsai et al., 2019). With combination of smartphone-assisted image analysis to quantify target DNA, the detection instrument size/cost could be reduced and the portability was enhanced when compared with electrochemical nanobiosensor. More importantly, their results showed that this proposed method achieved a LOD of 5 fg/μl in analyzing clinical TB nucleic acid samples with a linear of 10–100 fg/μl. And using this nanobiosensing method, authors successfully distinguished nine TB-negative patients from three positive TB patients. In this manner, it becomes necessary to use this method for more large-scale clinical sample investigations. And in the future, it is possible to further avoid systemic variations induced by different smartphones as detectors through using a dongle/cartridge containing LED light source and photodetector with wireless transmission function. There is also another option, which can develop a cell phone app to perform control tests for results calibration. More interestingly, DNA target molecules from drug-resistant TB and multidrug-resistant TB can also be detected with this approach by simply using different DNA probes for diagnosis.

In addition to using varies kinds of nanoparticles, nanowires can also be introduced to develop TB nanobiosensors. A nanostructure platform was constructed by combining the gold electrode, nanowires of polypyrrole (nw-PPy), dendrimers PAMAM and ferrocene as well as DNA probe (Khoder and Korri-Youssoufi, 2020). The properties of nw-PPy (such as hydrophilic character and large surface area) significantly increased the electrochemical signals based on the outstanding electron transfer rate of 18 s^{-1}, which allowed the enhancement of DNA sensing with a detection limit of about 0.36 atomolar without the use of amplification step. This biosensor was applied for the detection of genomic DNA of Mtb and mutated rifampicin resistant Mtb with high selectivity, which therefore show strong potentials for clinical sample detection. However, no direct evidences for the clinical sample analysis were presented in this work, which therefore still need further clinical sample validations of this nanobiosensor.

And to improve the detection efficacy, researchers developed many kinds of nano-biosensors based on the detection of TB DNA through electrode modification by functional nanomaterials (see Table 1). However, those diagnostic methods still need to be validated with clinical samples. To evaluate the sensitivity and specificity of this AuNPs-assisted colorimetric detection method, El-Samadony et al. (2019) designed a-case control study by analyzing the collected clinical sputum samples. DNA extracted from sputum samples were used for PCR analysis targeting IS6110 TB DNA. The results obtained by this TB nanogold assay could be observed by the naked eye just after 2 min of the addition of AuNPs to the test solution. Positive result could be defined as red color and negative result could be defined as red-to-violet color shift of the tested solution, which therefore allows very rapid and direct results for the tests. Their estimated TB nanogold assay showed higher performance than the combining of sputum smear microscopy (SSM) with chest X-ray (CXR), which indicated accurate and rapid detection for potential uses in clinic to improve accuracy of SSM and CXR. However, their verification experiment just involved a small sample size which therefore need more larger bacthes of clinical sample analysis. Some other developed new nanobisosensor based detection methods also did verification experiments by some TB clinical samples or even by adding the target markers into healthy patients' serum, however, these strategies also need larger sizes of clinical sample analysis (Chen et al., 2017; Bai et al., 2019; Tsai et al., 2019).

In recent years, nucleic acid testing strategies have been widely developed and used worldwide under the COVID-19 epemdics, which also remind the potentials of nucleic acid testing strategies for other disease diagnosis. For the DNA analysis of Mtb, samples are very important issues as most clinical samples might didn't have Mtb DNA contents. The most available and non-invasive samples for pulmonary TB analysis based on the DNA is the sputum sample, which requires DNA extraction procedures for further DNA analysis. Unlike the typical polymerase chain reaction (PCR) methods, most nanobiosensors don't need amplification precodures and allow the direct analysis of DNA samples with shorten analysis time after the successful fabrication of nanobiosensors. But the times and costs used for the complicated nanobiosensor preparation should be a disadvantages compared with the PCR strategy. Moreover, the DNA from dead Mtb could also be detected by the DNA analysis methods, which therefore remind that the DNA detection method should act as auxiliary strategies for the current clinical diagnostic strategies.

Detection of Mtb proteins by functional nanobiosensors

Nanobiosensors targeting CFP10/ESAT6

Although DNA detection possesses the advantage of high sensitivity as well as high specificity, it requires preparation of DNA samples that needs special instruments, which cannot meet rapid diagnostic needs. Moreover, DNA detection could not effectively distinguish TB patients from latent TB patients. Therefore, some researchers pay more attentions to the protein detection that naturally secreted by Mtb, which allows the rapid diagnosis for the timely treatment of TB. To date, various kinds of proteins has involved in for target biomarkers of *Mtb*, such as the 6-kDa early secreted antigenic target (ESAT6) (Diouani et al., 2017), 10-kDa culture-filtered protein (CFP10) (Welin et al., 2015), *Mtb* protein 64 (MPT64) (Arora et al., 2015), the secreted protein antigen 85 complex B (Ag85B) (Saengdee et al., 2016), proline-proline-glutamic acid (PPE68) (Xu et al., 2012; Wang et al., 2020).

TABLE 1 Comparison of the performance of different kinds of DNA nanobiosensors.

Modified electrode	Probe	Signal detection method	Linear range	LOD/ Sensitivity	Reaction time	References (publication years)
FLG/GNus	ssDNA	SPR	—	24.5 fM	—	Prabowo et al. (2021)
FLG/GNrs	ssDNA	SPR	—	8.2 pM	—	Prabowo et al. (2021)
GCE-ZnO-AuNPs	ssDNA	DPV	2.5–250 pM	1.8 pM	45 min	Hatami et al. (2020)
Gold electrode/nw-PPy	(Mutated) *rpoB* gene	SWV	1 aM–100 fM	0.36 aM	30 min	Khoder and Korri-Youssoufi, (2020)
SPs-G-nano-C_{60}/NG + CPs-bitoin-adivin-AuNPs/GCE + TOAB	*IS6110*	DPV	10 fM–10 nM	3 fM	4 h	Bai et al. (2019)
CuNPs	*IS6110*	Fluorescence stokes shift	10–100 fg/μl	5 fg/μl		Tsai et al. (2019)
3D graphene-GNrs	*IS6110*	EIS	10 fM–100 nM	—	—	Perumal et al. (2018)
Gold electrode/CPs + SPs/AuNPs/ PAn-rGO	*IS6110*	DPV	0.1 pM-10 nM	50 fM	2.5 h	Chen et al. (2017)
SPCE/NH2-GO/CdSe QDs	PNA-DNA	DPV	10 pM-100 nM	0.895 pM	50 min	Mat Zaid et al. (2017)
Gold nanotubes array electrode platform	ssDNA	DPV	10–10^5 pg/μl	10 pg/μl	50 min	Torati et al. (2016)
CdSe QDs-SA/MCH/probe DNA/ AuNPs/GCEs + *msp I*	DNA	SWV	10 fM–1 nM	8.7 fM	6 h	Zhang et al. (2015)
MWCNTs-PPy-PAMAM-Fc	*rpoB* gene	SWV	1 pM–100 nM	0.3 fM	60 min	Miodek et al. (2015)
Ru-GO/Fc-ssDNA	Mutated *rpoB* gene	ECL	0.1–100 nM	0.04 nM	50 min	Li et al. (2014)
GCE/rGO–AuNPs-PANI nano-composite	DNA	DPV	1 fM–1 nM	1.0 fM	4 h	Liu et al. (2014)

Note: PAn, means polyaniline; rGO, means reduced graphene oxide; SPCE, means screen-printed carbon electrode; NH2-GO, means amino group functionalized graphene oxide; QDs, means quantum dots; MCH, means 6-mercapto-1-hexanol; MWCNTs, means multiwalled carbon nanotubes; PAMAM, means poly (amidoamine) dendrimers; Fc means ferrocene; Ru-GO, means ruthenium (II) complex functionalized graphene oxide; DPV, means Differential pulse Voltammetry; SWV, means Square Wave Voltammetry; EIS, means Electrochemical Impedance Spectroscopy; ECL, means electrochemiluminescence.

Comparative genomics analysis has revealed that the CFP10 and ESAT6 are encoded by the Rv3874 and Rv3875 genes, respectively. These genes are located in the region of difference-1 (RD-1) of the virulent Mtb genome but are absent in all strains of vaccine-BCG strains (Mahairas et al., 1996; Behr et al., 1999; Gordon et al., 1999; Aagaard et al., 2006). These two low molecular weight secretary proteins can bind with each other through the Van der Waals and hydrophobic interactions. Therefore, the formed ESAT6-CFP10 complex is a specific antigen for the virulent Mtb that can no be found in BCG (Vordermeier et al., 2001), in another words, prior BCG vaccinations in the patients would not induce false-positive results using CFP10 and ESAT6 as detection targets. In addition, both CFP10 and ESAT6 are secreted by Mtb at an early stage of infection (Renshaw et al., 2002). Hence, these two proteins can be used as early diagnostic markers of TB with the potent to distinguish between Mtb-infected and BCG-vaccinated groups (Weldingh and Andersen, 2008).

Similar to DNA detection, the pivotal part of nano-biosensor development for protein detection is biosensor modification. As early as in 2016, Noremylia's laboratory has developed a G-interdigital electrode (IDE)/CFP10-ESAT6 aptamer/DNA-AuNPs based system as multi-channel piezoelectric quartz crystal (MSPQC) sensor to detect the combination protein of CFP10-ESAT6 (He et al., 2016). Here, the complementary DNA-AuNPs were modified onto the microelectrode with CFP10-ESAT6 aptamer functionalization to obtain the G-IDE/CFP10-ESAT6 aptamer/DNA-AuNPs probe. CFP10-ESAT6 aptamer could interact with the CFP10-ESAT6 protein specifically to form complex on the surface of electrode, which would result in the fell away of the DNA-AuNPs fragments from the electrode surface. These changes can be captured by the IDE-MSPQC sensor with high sensitivity. Other kinds of bacterial like *M.smegmatis*, *S.aureus*, *E.coli*, and *E.faecaliss* were also used for analysis by the above sensor to show frequency shift lower than exceed 15 Hz, whereas it reached 73–121 Hz in Mtb detection, indicating the high selectivity of the proposed sensor. This approach was specific, more sensitive, and expected to become a valuable analysis tool for the early detection of M. tuberculosis in clinical sample. However, the

detection times of this method need up to 96.3 h, which couldn't achieve the need of rapid detection. Moreover, this nanobiosensor was also not used for clinical sample analysis, which requires further validations of this strategy in clinical samples.

Additionally, Noremylia and co-workers developed a (CdSe-ZnS QD/silica NPs (SiNPs)/SPCE)-modified electrode as nanobiosensors to detect CFP10-ESAT6 fusion protein (Mohd Bakhori et al., 2019). The obtained electrode could be linked to the biocatalytic interactions for the enzyme catalase through specific antigen-antibody binding by means of producing a DPV current. The developed method indicated a linear range of signals towards CFP10-ESAT6 in different concentrations with a R^2 value of 0.9937, yielding a LOD of 0.15 ng/ml and good reproducibility for the targeted analyte. However, this nanobiosensor is also not applied for the more complicated clinical sample analysis. And they further found that DPV responses for both BSA and MPT64 were more than half of that for CFP10-ESAT6 detection, which might be attributed to that the modification of the electrode by CdSe-ZnS QD/SiNPs/SPCE could increase the effective surface area of the electrode to lead the peak current. These results showed that the selectivity and specificity of their obtained nanobiosensor are not strong enough as other kind of proteins in the complicated clinical samples might affect the accuracy of the results. Thus, the selectivity and specificity of the proposed nanobiosensor remain to be further improved, which would be the most critical issue for their following clinical sample researches.

Researchers also designed a CFP10-ESAT6 targeted aptamer-graphene (GP)-PAn-screen-printed gold electrode to detect the CFP10-ESAT6 fusion protein (Azmi et al., 2021). By interacting with the CFP10-ESAT6 antigen complex, the specific aptamer could capture the targets and the antibody conjugated Fe_3O_4/Au-MNPs was used for sandwich format. Based on these properties, CFP10-ESAT6 antigen can be effectively detected by the differential pulse voltammetry (DPV) technique. Unlike the common electrochemical detection using potentiostat conducted in the laboratory, this portable reader is small in size, easily handled, and can be used for on-site monitoring. In addition, the detection times for this method was only 55 min (including the time of sample pretreatment), which might allow very rapid diagnosis. This study involves the utilization of iron/gold core/shell magnetic nanoparticles (Fe_3O_4/Au MNPs) which would be strongly attracted to the Ab. The incorporation of gold (Au) coating on a magnetic core could combine the advantages of high chemical stability/biocompatibility of gold and high magnetic separation efficiency of Fe_3O_4. This strategy allows the detection of CFP10-ESAT6 antigen complex at a concentration range of 5–500 ng/ml to show a LOD of 1.5 ng/ml. Moreover, the specificity would not be easily disturbed by other proteins like BSA, MPT64, and human serum. Mohd Azmi et al. (2021) also proposed sandwich-type immunosensor with a portable, rapid, and simple properties for the detection of Mtb in sputum samples by targeting CFP10-ESAT6 complex. This strategy indicates almost 100% sensitivity and 91.7% specificity compared with the standard methods (culture and smear microscopy) for Mtb analysis in the sputum samples, which suggested the potential of the proposed device for practical screening. In clinical sample detection, these two methods showed positive DPV signal changes in TB positive samples and negative changes in negative samples, showing absolutely 100% specificity and sensitivity (Azmi et al., 2021; Mohd Azmi et al., 2021). However, more works need to be done on larger sizes of clinical samples to make sure the applicability of this nanobiosensors for clinical uses. And further investigations are still needed to be done, such as the improvement of the stability, sensitivity and robustness of the sensor.

In addition to biosensor modification, researchers also tried to develop a label-free method for biosensor preparation to detect the CFP10-ESAT6 fusion protein, which might allow more convenience for TB diagnosis (Sun et al., 2017). Metal-organic framework (MOF-rGO) was doped onto the reduced graphene oxide, which were further deposited onto a glassy carbon electrode (GCE). Platinum/gold core/shell (Pt@Au) based nanosystem was prepared to assemble thiolated ESAT-6 binding aptamer (EBA) on a modified electrode and to further amplify the response to TB. Firstly, P-MOF-rGO nanocomposite was employed to enhance the loading of electroactive toluidine blue (TB). Then, Platinum aurum core shell (Pt@Au) nanoparticles provided abundant active sites for the immobilization of thiolated ESAT-6 binding aptamer (EBA) and further amplified the electrochemical response signal of TB. After the specific recognition between ESAT-6 antigen and EBA, significant change of electrochemical signal indicated that the aptasensor was successfully constructed. In that method, GNrs contained the fusion protein of CFP10-ESAT6 was directly incubated with clinical serum samples to detect CFP10-ESAT6. After incubated with collected serum samples for 2 min, the biosensor indicated changes in the SPR properties of GNrs due to the specific antigen-antibody interactions. According to the detection results, the sensitivity was 79% and the specificity was up to 92%, which indicated the potentials of this method to be a valuable tool for diagnosis of TB.

There are also publications about ESAT6 or CEP10 detection separately. Li et al. (2018a) developed an electrochemical nanoaptasensor to measure ESAT-6 protein. In their strategy, GCE electrode was modified by rGO-metal-organic framework complex (MOF-rGO) and Toluidine Blue, which could enlarge the surface area and facilitate the electron transferation. Later, thiolated ESAT-6 binding aptamer was conjugated onto (EBA)-platinum/gold core/shell (Pt@G) nanoparticles complex, which were then deposited into the above modified GCE electrode. The electrochemical signal was originated from the changes of Toluidine Blue based on the specific interactions between EBA and ESAT-6. Results demonstrated that the developed electrochemical nanoaptasensor had a linear response in

0.1 pg/ml to 200 ng/ml ESAT-6 concentration range with a LOD of 0.033 pg/ml. Compared with the detection result of the same concentration of other interference molecules, like glucose, CFP-10 and BSA, the specific recognition and interaction of the targeted biomolecule and nanoaptamer led to significantly decreased electrochemical signals, indicating the high selectivity of the proposed nanobiosensor for ESAT-6 detection. In another study, a new and one-step approach based nanobiosenser was designed to measure ESAT-6 (Wang et al., 2018). Within that detection system, AuNPs would change its colors from red to blue followed by the salt-induced aggregation if anti-ESAT-6 antibody was pre-mixed with ESAT-6, whereas the color did not change in control system (CFP-10). The red spectral shift could be visualized or measured by a UV-spectroscopy with a LOD value of 1.25 pM. Nevertheless, the sensitivity was easily influenced if the concentration of antibody and salt were not optimized. Further, this assay can be expanded with a small molecule complexed with an appropriate antibody to be possible for potential point-of-care diagnosis. This strategy could definitely work in proteins and peptides with small molecular weight, while the large proteins might introduce variations due to the amino acid charges.

Similarly, nanobiosensors can also be designed to detect CFP-10 alone. Researchers used Fe_3O_4@Ag/GPQDs to modify the GCE electrode for the formation of a sandwich complex on the electrode surface, which could be used for DPV signal collection. This nanoscale sensing platform allows synergetic electrochemical performance based on the properties of the three nanomaterials: Firstly, Fe_3O_4 nanomaterials could increase the surface/volume ratio of the nanobiosensor; then, Ag nanomaterials could enhance the electrical conductivity of the nanobiosensor; and GQD could load more anti-CFP-10 antibody onto the nanobiosensor. But the electrochemical nanoimmunosensor showed a linear range (5–5.0 × 10^5 ng/ml) and a LOD value of 0.33 ng/ml, which was a relatively low sensitivity comparing with other nanobiosensors (Tufa et al., 2018). These results suggest that this proposed nanobiosensor with good performance and high selectivity might also be used for the analysis of other kind of biomolecules of Mtb. However, how to extend this strategy for the much more complicated clinical sample analysis remain a big challenge.

The electrochemical nanobiosensor detection method developed by Azmi et al. (2021) was also used to detect CFP-10 using CFP-10 antibody. However, compared to the results for the fusion CFP-10-ESAT6 protein detection, analysis of CEP-10 alone by this method didn't show similar good linear range (20–100 ng/ml) and LOD (15 ng/ml) value (Mohd Azmi et al., 2018). CFP-10 aptamer can also be designed to capture CFP-10 antigen (Li et al., 2019b). CFP-10 is specifically captured by its aptamer and then induces a DNA cross-linking click reaction, the release of CFP-10, and an amplification cycle of repeated CFP-10 release. High occurrence of CFP-10 would cause the more CFP-10 aptamer strands on the gold electrode surface to expose their 5′ overhang and to hybridize with the DNA complexes linked to the AuNPs. Consequently, large amounts of AuNPs, which were loaded with lots of quadruplex DNA motifs, could be bound onto the electrode surface to remarkably enhance the electrochemical signal. This assay shows high selectivity toward CFP-10 antigen due to its specific interactions with the aptamer. However, based on the clicking chemical reactions for the target proteins and the G-quadruplex DNA motifs, this assay indicated a very low detection limit against the targeted CFP-10 antigen. In optimal conditions, this method demonstrated linear range of 0.01–100 ng/ml and LOD value of 10 pg/ml for CFP-10 analysis. In sputum sample analysis, their nanobiosensor indicated that the DPV signal changes in TB patients was much higher than the DPV signal changes of healthy volunteers.

Nanobiosensors targeting MPT64

MPT64, a 24-kDa protein only secreted by *Mtb* in the early/middle growth stage (Yin et al., 2013; Jiang et al., 2014), can also be utilized for Mtb detection (Dahiya et al., 2020). The aptamers that can bind specifically with MPT64 have already been reported (Qin et al., 2009). Hence, Li's team developed a voltammetric nanobiosensor based on two aptamers for MPT64 detection using AuNPs and Zr(IV)/terephthalate MOF (metal-organic framework) to modify gold electrode (Li et al., 2018b). Firstly, amino-modified Zr(IV) MOF was synthesized and was then loaded with AuNPs and aptamers, which was then used for nanoprobe fabrication by casting horseradish peroxidase onto the nanomaterials. These two different aptamers loaded onto the gold electrode could show synergistic effects for MPT64 binding with highest differential pulse voltammetry when the aptamer ratio is 1:1. This method showed a wide linear response range (0.02–1000 pg/ml) and a 10 fg/ml detection limit. Moreover, DPV results demonstrated the fabricated aptamer-based nanobiosensor had satisfactory selectivity for MPT64 from BSA and CFP10-ESAT6. The biosensor do exist some defects such as it still has some difficulty on clinical application and the modification process of electrode will be affected by various factors.

Guo's team also developed an aptamer-based voltammetric nanobiosensor for MPT64 detection by using synergistic signal amplification strategy based on a novel GO@Fe_3O_4@Pt nanocomposite (Gou et al., 2018). Based on this strategy, the constructed nanobiosensor showed a wide linearity range (5.0 fg/ml to 1.0 ng/ml) and a LOD of 0.34 fg/ml with less than 4 h of detection time. More importantly, when the nanobiosensor was used for clinical serum samples analysis from TB patients to show high current signals, whereas the signal was negligible in healthy or non-TB group. These results indicated that this proposed nanobiosensor had strong potentials to provide the basis for rapid clinical diagnosis of *Mtb* infection, although a larger scale

clinical sample analysis are still needed. In addition, some researchers introduced a sandwich-like electrochemical aptasensor based on carbon nanocomposite formed by nitrogen-doped carbon nanotubes, fullerene nanoparticles and grapheme oxide, which introduced larger specific surface area to obtain high conductivity and electroactive property for redox biosensing (Chen et al., 2019). The above nanocomposite was further modified with AuNPs to bind with the MPT64 antigen aptamer, which could generate effective amplification of the signals. Moreover, polyethyleneimine (PEI) modified MOF was used to capture Au–Pt nanoparticles (Au@Pt), which significantly accelerated electron transfer and increased the immobilization efficiency of aptamer. The AuNPs. The AuNPs containing MPT64 aptamer were immobilized in the C60NPs-N-CNTs/GO and conductive polyethyleneimine (PEI)-functionalized Fe-based metal-organic framework (P-MOF), to form a sandwich composite with the MPT64 antigen. The proposed aptasensor showed a wide linear range (1 fg/ml–1 ng/ml) with a LOD as low as 0.33 fg/ml. Similarly, the biosensor also indicated excellent sensitivity and specificity, but the gap of current response between TB serum specimens and healthy controls was a little bit small (about 2-fold), which need to be further confirmed by more clinical sample analysis.

In addition, AuNPs-C_{60}-PAn was also used as a kind of nanoprobes for redox analysis by detecting MPT64 antigen with high sensitivity, which showed linear range of 0.02–1,000 pg/ml and a LOD value of 20 fg/ml. This strategy showed current response was up to 15.58 μA when the concentration of MPT64 in clinical samples was as low as 0.2 pg/ml, whereas the current response in negative control was almost negligible (Bai et al., 2017). More importantly, this biosensor also showed high specificity and sensitivity for the detection of MPT64 antigen in serum samples, which therefore allowed the ability to distinguish TB patients from healthy donors.

However, the synthesis processes of nanomaterial for these electrochemical nanobiosensors detection method, especially for the nanobiosensor fabrication processes, were relatively complicated and the detection sensitivity, efficacy and selectivity also need to be further confirmed by more clinical sample analysis. Conceivably, these nanobiosensor assays for MPT64 detection demonstrate large potentials in providing new evidences for the rapid diagnosis of *Mtb* infection.

Nanobiosensors targeting Ag85B

Ag85 proteins are one of the most immunogenic antigens obtained from *Mtb* culture filtrate (Malen et al., 2008). As one of the representative secreted proteins in Ag85 proteins, Ag85B plays critical roles in the physiology of Mtb and has been proposed as a promising marker for potential *Mtb* diagnosis (Che et al., 2016; Zhang et al., 2018). A sandwich assay detecting Ag85B combining GNrs) and silica coated QDs (SiQDs) was produced by Eun's team (Kim et al., 2017). In this nanobiosensor, genetically engineered recombinant antibody was bound onto the surfaces of GNrs and SiQDs respectively without any surface modification. These two biocomplexes showed quenching fluorescence intensity in the presence of the target antigen through a sandwich assay. At high Ag85B concentrations, the distance between GNrs and SiQDs got closer, which thus led to the decrease of fluorescence through fluorescence resonance energy transfer (FRET) with an assay response range of 10 pg/ml–1 ng/ml and a LOD of 13 pg/ml. When compared with some interfering proteins like BSA or CFP10, the obtained fluorescence intensities were almost the same with the fluorescence intensities obtained from control samples, whereas Ag85B led to significant decreases of fluorescence intensity, indicating the specificity and selectivity of the proposed method. Moreover, the recovery experiments showed 92%–104% through measuring different concentrations of spiked clinical urine samples. Although the authors stated that they developed a highly sensitive and selective nanobiosensor for better diagnosis of TB by Ag85B-expressing Mtb detecting compared with the existing methods, no clinical samples were used for analysis by this nanobiosensor. More works are needed to compare this nanobiosensor with the existing clinical strategy on a large scale clinical samples.

By analyzing the above Mtb-specific proteins, the sensitivity and accuracy of TB diagnosis can be significantly enhanced by combining with some other diagnostic tools. As these target proteins can be secreted into environments and further transfered into different parts of body, different kinds of samples, such as blood samples (serum or plasma) and sputum samples, can be applied for protein analysis. Due to the complicated protein contents in serum or plasma samples, the specificity of nanobiosensors is of vital importance for Mtb-specific protein analysis. However, there are some target proteins that might be disturbed by the TB vaccine-BCG vaccination, such as Ag85b, which is both expressed and secreted by BCG and Mtb. Thus, developing nanobiosensors that can simultaneously detect different kinds of Mtb-specific proteins might be an attractive strategy for more sensitive and accurate TB diagnosis.

Detection of cytokines by nanobiosensors

Cytokines, some small peptides or glycoproteins, are synthesized and secreted by immune cells and certain non-immune cells. Cytokines have a variety of biological functions, such as regulating cell growth, differentiation and maturation, immune response, inflammation, wound healing, tumor growth and function maintenance (Pourgholaminejad et al., 2016; Wang et al., 2021). Host cytokine levels are different at different stages of Mtb infection and may serve as markers of Mtb infection (Sudbury et al., 2020).Many teams evaluated candidate cytokines as biomarkers to distinguish LTBI infection from active TB, and their results were generally associated with IL-10, IFN-γ, IP10,

IL-2, TNF-α and VEGF5, with IFN-γ being the most popular cytokine by far (Gong and Wu, 2021).It has been mentioned above that the existing cytokine detection is not real-time, expensive and difficult to operate. However, the development of nanobiosensors provides a way for its development (Perez et al., 2022). And as the most important cytokine that involved in TB infection, IFN-γ detection will be taken as an example to summarize the current status of nanobiosensors in the diagnosis of TB.

In a fluorescence nanobiosensor, when biometric elements or targeted biomolecules are labeled by fluorescent labels, the fluorescence intensity is used to reveal how strong about the interactions between the biometric molecules and the target biomolecules. Chen et al. (2022) developed a novel aptamer sensor for IFN-γ analysis using PPI-CE CPNs (cerium pyrophosphate coordination polymer nanoparticles) as a signal reporter molecule and using double-stranded DNAs as probes. The sensor is implemented by spatially regulating polymeric extension of terminal deoxynucleotide transferase (TdT) as well as the selective recognition of PPiCe CPNs. This method allowed a detection limit of 0.25 fg/ml with a linear range of 1–100 fg/ml and high specificity. This IFN-γ biosensing method was further validated in 57 clinical samples, which were proved by some current clinical TB diagnostic methods, indicating the ability of this nanobiosensor as a more sensitive tool for potential early diagnosis of TB. However, this method can't allow the direct naked-eye visual readout analysis. This, ultrasensitive IFN-γ quantitative method is expected to effectively reduce the serum stimulation culture time, and provide a novel tool for the early and rapid diagnosis of TB.

In another study, biosensors based on hairpin structures of oligonucleotides, single-stranded DNA-binding proteins (SSB), copper nanoparticles (CuNPs), and silica nanoparticles coated with Streptavidin were synthesized (Taghdisi et al., 2017). The presence of double-stranded DNA (dsDNA) regions and polythymidine (T) in hairpin structures of oligonucleotide, SSB, and SNP streptavidin results in highly selective and sensitive IFN-γ assays. Here, the hairpin structure of the used oligonucleotide allowed high specificity of the proposed aptamer nanobiosensor. The addition of IFN-γ could disassemble the structure of oligonucleotide to result in a weak fluorescence signal. And if no IFN-γ was added, no structure changes would happen in oligonucleotide, which would result in stronger fluorescence signal. In optimal cases, IFN-γ was detectable at concentrations as low as to 1 pg/ml with a linear range of 10–4,000 pg/ml. The above method was further used in spiked human serum samples for IFN-γ analysis with recovery value about 92.52%–98.32%, which indicated the promising potential of this method in real biomedical analysis. However, no samples from TB patients were analyzed to test the ability of this nanobiosensor for potential TB diagnosis. Thus, further investigations about clinical samples from TB patients and health controls should be applied for this proposed nanobiosensors.

In addition to the above nanibiosensors, other teams have also designed different fluorescence aptamer sensors with excellent characteristics such as high sensitivity and strong specificity (Wen et al., 2018; Wen et al., 2019), as shown in Table 2. Both of these two works indicated a great potential in IFN-γ detection of real samples by these nanobiosensors with high selectivity, efficiency and stability. However, it is still need to further confirm the potentials of these nanobiosensors for natural human serum sample analysis, especially for their ability for the serum analysis from TB patients.

In addition to fluorescent aptamer sensors, there are electrochemical sensors, which are sensing devices that couple biometric elements to electrode sensors. The transducer then converts biometric events into electrical signals. A novel electrochemical aptamer sensor for IFN-γ detection was developed based on exonuclease-catalyzed target recycling and TdT mediated cascade signal amplification (Liu et al., 2015). Previously hybridized double-stranded DNA (trapping probe hybridized with complementary IFN-γ junction suitable body) was immobilized on Au nanoparticle-graphene nanocomposite (Au-GrA) membrane modified electrodes. When IFN-γ is presented in the tested samples, there would form aptamer-IFN-γ complexes, which would further result in the release of aptamers from the dsDNA. The aptamer is selectively and specifically digested using exonuclides to release IFN-γ for target recovery. A large number of probes with single-stranded capture ability would form and result in hybridization to introduce the probe labeled Au@ Fe3O4 system. The structures of long single-stranded DNA can be formed by catalyzing the labeled probe sequence by terminal deoxynucleotide transferase (TdT). Finally, the electron medium ruthenium (III) hexamines chloride ($[Ru(NH3)6]^{3+}$) can interact with DNA to generate a strong electrochemical signal for quantitative measurement of IFN-γ. And by using Au-Gra as substrate, the proposed aptamer nanobiosensor shows wide detection liner range with a very low detection limit of 0.003 ng/ml. And taking the advantages of highly effective amplification, this aptamer nanobiosensor is very easily to be operated without complicated labelling procedures. Additionally, with valid signal amplification ability and simple structures, the above aptamer nanobiosensor uses might allow the further development of more versatile methods for other biomolecule detection.

Additionally, Miao et al. (2017) also prepared a novel Iridium (III) complex for sensitive electrochemical detection of IFN-γ. Firstly, the electrode surface was immobilized by Nafion (Nf) and (+)AuNPs composite films, which were then conjugated with a IFN-γ interaction chain contained capture probe by Au-S binding. After addition of IFN-γ, the ring-shaped stem structure of CP is opened, and the newly exposed "sticky" region of CP is subsequently associated with DNA hairpin 1

TABLE 2 Comparison of the analytical performance of nanobiosensors for the analysis of cytokines.

Biosensor devices	Active analytical layer	Linear range	LOD/Sensitivity	Reaction time	References (publication years)
Fluorescent aptasensor	PPi-Ce CPNs/Cu NPs	1–100 fg/ml	0.25 fg/ml	—	Chen et al. (2022)
Fluorescent aptasensor	Oligonucleotide-SNPs-streptavidin-SSB-CuNPs	10–4,000 pg/ml –	1 pg/ml	55 min	Taghdisi et al. (2017)
Fluorescent aptasensor	Fe3O4-aptamer 1/IFN-γ/aptamer 2/dsDNA	0.169–169 × 10^5 pg/ml	2.95 × 10^{-3} pg/ml		Wen et al. (2018)
Fluorescent aptasensor	Fe3O4-aptamer 1/IFN-γ/aptamer 2-PBiB-pBIEM	3.38 × 10^{-5}–8.44 × 10^5 pg/ml	3 × 10^{-3} pg/ml		Wen et al. (2019)
Electrochemical aptasensor	*Au-Gra/dsDNA*/IFN-γ/[Ru(NH3)6]$^{3+}$/SP-Au@Fe3O4		0.003 ng/ml	1 h	Liu et al. (2015)
Electrochemical aptasensor	*{H2/H1} n/IFN-γ/CP/(+)AuNPs/Nf*	50 fM–3.0 pM	16.3 fM	200 min	Miao et al. (2017)
Electrochemical aptasensor	*GE/aptamer/IFN-γ/Exo I and Exo III*	16.9–8.44 × 10^5 pg/ml	11.8 pg/ml	—	Li et al. (2019b)
Electrochemical aptasensor	*Au IDE/ACP/HDT-MCH*	375–1860 pg/ml	195 pg/ml	35 min	(Ding et al., 2017)
Electrochemical DNAzyme biosensor	T-DNA/MCH/CP/AuNCs-Gr@ZIF-8/GCE	0.0169–844 pg/ml	0.01 pg/ml		Bao et al. (2019)
DNA photoacoustic nanosensor	Streptavidin-coated SPR chip-IFN-γR2-IFN-γR1-IFN-γ	10–2,000 pg/ml	KD1 2.8 × 10^6 pg/ml KD2 5.3 × 10^6 pg/ml		Morales et al. (2019)
Electrochemical immunosensor	AJP graphene IDE-anti-IFN-γ-BSA-Tween-20-fish gelatin	100–5,000 pg/ml	25 pg/ml	60 min	Parate et al. (2020)

(H1), which in turn opens its hairpin structure for hybridization with DNA hairpin 2 (H2). HCR (hybrid chain reaction) occurs between H1 and H2 to produce polymeric double-stranded DNA (dsDNA) strands. At the same time, the Iridium (III) complex can interact with the groove of the double-stranded DNA polymer to produce a strong current signal proportional to the concentration of IFN-γ. Based on this novel nanobiosensor, the detection of IFN-γ can be achieved with high sensitivity and a detection limit of 16.3 fM. Compared with the enzyme-assisted signal amplification technique, HCR could achieve high robustness and stability of the nanobiosensor without the use of enzymes. Moreover, iridium (III) complex in the nanobiosensor could interact with the unlabelled dsDNA polymers, which allows the detection of IFN-γ with low-cost. In addition, other teams have also designed different electrochemical sensors with excellent features such as high sensitivity, high specificity, and strong (Ding et al., 2017; Li et al., 2019a; Bao et al., 2019; Morales et al., 2019; Parate et al., 2020), as shown in Table 2.

To be honest, cytokine detection of IFN-γ is not a highly specific method for TB diagnosis as IFN-γ is widely involved in different diseases, which means that it is very difficult to distinguish TB from other diseases based on IFN-γ detection. Thus, it is very important to explore more specific strategies for TB diagnosis, which might be achieved by the simultaneous detection of several different kinds of cytokines.

Nanomaterial-based biosensors can also be developed for multiple cytokines detection at the same time. For example, a team synthesized a graphene immunosensor based on aerosol jet printing (AJP) that can monitor two different cytokines: IFN-γ and IL10 (Parate et al., 2020). A 40 μm wide interfinger electrode (IDE) was printed on a polyimide substrate using graphene-nitrocellulose ink. By annealing the IDE in CO_2, ROS (reactive oxygen species) can be introduced onto the graphene surface to serve as a chemical handle that can covalently and effectively attach IFN-γ/IL10 antibodies onto the surface. The resulting AJP electrochemical immunosensor can monitor serum cytokines with a sensing range for IFN-γ of 0.1–5 ng/ml and for IL-10 of: 0.1–2 ng/ml, which allows potential TB diagnosis. Moreover, these biosensors are mechanically flexible with minimal change in signal output after 250 bending cycles over a high curvature (Φ = 5 mm). Hence, this technology could be applied to numerous electrochemical applications that require low-cost electroactive circuits that are disposable and/or flexible. The combination of IL-10, IP-10, and IL-4 can distinguish tuberculosis patients from latent tuberculosis patients, with sensitivity and specificity of 77.1% and 88.1% (Korma et al., 2020), respectively. The combination detection of IL-1α, IP-10, McP-1, TNF-α, and IL-10 was also shown to be excellent in the

potential diagnosis of LTBI with high sensitivity and specificity (Luo et al., 2019). This also provides more directions for the subsequent development of nano-biosensors.

Up to now, the low contents of specific markers in human serum still dramatically restricted the diagnosis of LTBI. Yang's group have recently introduced several different methods based on nanobiosensors for potential LTBI diagnosis. Firstly, a novel ECL-biosensing platform was developed for the detection of multiple LTBI markers, including IFN-γ and IL-2 (Zhou et al., 2017b). This proposed ECL-sensing platform allowed the accurate and specific detection of IFN-γ and IL-2 in human serum with high sensitivity, which provided a valuable protocol to develop fast and precise diagnostic strategy by nanobiosensing of LTBI samples. Moreover, they also tried to develop more specific detection method based on the simultaneous detection of three different kind of cytokines by fabricating potential-resolved ECL nanoprobes (Zhou et al., 2017a). The AuNPs and magnetic beads were conjugated with luminol carbon quantum dots and CdS quantum dots, followed by the immobilization of IFN-γ, TNF-α and IL-2 antibody onto indium tin oxide electrode as a nanobiosensor system for LTBI marker capture. The obtained ECL immunosensor provides an effective and high specific approach for the simultaneous detection of IFN-γ, TNF-α and IL-2 in human serum, which might be beneficial to facilitate more accurate and reliable clinical diagnosis for LTBI. In addition to the above electrochemiluminescence method, they further introduced a method for continuous monitoring of multiple cytokines using nanobiosensors based on quartz crystal microbalance (QCM) detection (Zhou et al., 2019). Although QCM is able to detect the mass change in the nanogram range, it is still limited in the detection of low-level antigen. In this work, mass signal amplifier-silver nanoparticles acting were conjugated with specific antibodies to form a kind of novel mass nanoprobes, which could increase the loaded mass on the surface of QCM. Hydrogen peroxide can oxidatively dissolve the prepared nanoprobes, which could avoid the steric hindrance of the probes. This method could be used to monitor IFN-γ, TNF-α, and IL-2 serially, thus providing a novel strategy for real-time monitoring of multiple LTBI related cytokines. Compared to MQCM, the above QCM strategy could effectively avoid the acoustic interference and simplify the instrumental setup procedures for sensitive and accurate detecting of multiple cytokine-associated LTBI biomarkers.

There are also clinical TB diagnostic methods that targeting the cytokine analysis, such as the IGRAs test, which detects the IFN-γ releases with few cross reactions with non-Mycobacterial or BCG infections. But it is worth to note that this method might also introduce false results in some subjects with inherent high IFN-γ production. Thus, it is a trend to develop new methods for multiple cytokine analysis, and among the current techniques, nanobiosensing techniques provide strong potentials for multiple cytokine analysis in potential TB diagnosis. But how to screen new Mtb-specific cytokines as new targets for analysis combining with IFN-γ remains a big challange. In theory, the direct analysis of plasma or serum cytokines of patients without antigen stimulation would be more easily to be disturbed by other diseased conditions. Thus, the development of new nanobiosensors should also be directed to detect the cytokine released from the PBMC of patients upon Mtb antigen stimulation.

Direct whole cell detection of Mtb by nanobiosensors

In addition to DNA, secreted proteins and cytokines, researchers also introduced whole cell detection method for *Mtb* diagnosis. Teresa and co-workers used a magnetoresistive (MR) biosensors to detect BCG bacteria with magnetic nanoparticles (MNPs), functionalized with specific antibodies (Abs) and bioconjugated with BCG bacterial cells through three steps: A) capture Abs and control Abs were attached to the surface of MR-biochip, respectively; and then a baseline MR signal was registered; B) a immunoassay following a sandwich format labeled by MNPs and functionalized with polyclonal biotin was conjugated with anti-*Mtb* detection Abs to bioconjugate with the target bacterial cells; C) the non-bound MNPs were then washed out and the signals from labeled targets could be recorded. It is worth to note that the BCG binding specificity is not 100%, but there are significant differences for the MR voltages between positive sample and negative control (Barroso et al., 2018). Their results showed significant signals during sample detection with an estimated LOD value of 10^4 cells/ml. A similar LOD detectability of 10^3–10^4 cells/ml can also be obtained by using magnetic barcode for nanobiosensor development in sputum sample detection (Liong et al., 2013).

In addition, Zhang et al. (2019) also developed a MSPQC sensor system for rapid detection of *Mtb*. The electrochemical sensor contains an H37Rv aptamer that were sequentially hybridized with three designed AuNPs–DNAs. When H37Rv was presented in the detected samples, it could specifically bind with the specific aptamer, which would lead to the release of AuNPs–DNA from the electrode and the non-conductive complex of aptamer and bacteria would replace the conductive layer of the electrode for MSPQC system detection. The frequency shift values of interfering bacteria, such as BCG, *Pseudomonas aeruginosa* and *S. aureus*, were not more than 25 Hz, whereas the frequency shift values of H37Rv was up to 236 Hz. Therefore, this AuNPs-DNA based and H37Rv aptamer conjugated MSPQC sensor can distinguish pathogenic from non-pathogenic bacteria, indicating the high selectivity and specificity. Taking L-J slant culture method as gold standard method, the sensitivity of this proposed nanobiosensor was 91% and the specificity was 90% in clinical sample detection. However, the detection time of the proposed sensor was only 2 h

with a LOD of 10^2 cfu/ml. It is very useful to shorten the 21 days detection time for L-J slant culture method to 2 h. However, the low sensitivity (LOD of 10^2 cfu/ml) makes it very difficult to be used for real clinical sample analysis from TB patients as most samples from TB patients showing lower CFU than 100. Therefore, more works are needed to further improve the sensitivity of this nanobiosensing strategy.

In addition to the measure of electrical signal, magnetic nanoparticle based colorimetric biosensing assay (NCBA) can also be developed to detect acid-fast bacilli (AFB). Among that method, MNPs were coated by glycan, which allowed the effective capture of *Mtb* by glycan-glycoprotein interactions that didn't require the use of the much more expensive antibodies or aptamers. The detection procedure was greatly simplified when compared to other signal detection methods such as electrical and fluorometric signal. More importantly, the detection results based on NCBA method showed 100% agreement with the results obtained by Xpert Mtb/RIF for all 500 tested samples, however, with much shorter time (10–20 min) and much cheaper costs (almost $0.10 per test), which might be more easily used for TB diagnosis in some developing and undeveloped countries (Abubakar et al., 2013). Blakemore et al. (2010) found that the lowest detection limit of Xpert system's was nearly 131 CFU/ml. However, there is a disadvantage that this method can't be used to distinguish pathogenic AFB from non-pathogenic AFB, which urges the authors to further improve the selectivity of this nanobiosensors.

In theory, the detection of whole cell of Mtb requires the existence of Mtb in the anayzed samples. Thus, the clinical analysis of whole cell of Mtb always performed in the sputum from potential pulmonary TB, such as the Mycobacterial culture analysis of Mtb in clinic. We need to know that there indeed exist potential biosafty issues for the use of sputum samples with live Mtb inside, which therefore requires strict laboratory conditions with high biosafety levels. Therefore, unlike the analysis of DNA, proteins or cytokines in the blood samples, the whole cell of Mtb analysis from sputum samples need to be strictky done in BSL-3 or at least BSL2+ labs. If new nanobiosensors are developed for whole cell of Mtb analysis, these nanobiosensors and their corresponding detecting instruments should also be set in the high biosafety labs, which might introduce more costs and biosafet issues.

Perspectives and conclusion

As one of the most urgent public health issues, TB causes millions of deaths every year, ranking above AIDS. Thus, how to control the TB epidemic remains a big challenge. For rapid and effective therapy of TB patients, the diagnosis of TB is the most important issues, which therefore requires rapid and accurate TB diagnosis method. However, the current methods for TB, latent TB or drug-resistance TB diagnosis is not sensitive, rapid and accurate enough, which urges us to develop more sensitive, rapid and effective diagnosis strategy.

Taking the advantages of outstanding physical, chemical and biological properties, nanomaterials have been proved to show promising potentials for novel nanobiosensor construction. Here, we summarized the current progress of nanobiosensors for potential TB diagnosis application. Due to the unique properties of TB infection, most of the current diagnostic method based on nanotechnology is focused on the detection of Mtb components, such as the DNA and proteins released from Mtb. The positive signals for the nanobiosensor indicate the presence of DNA and proteins from Mtb in the sample and also indirectly indicate the infection of the sample sources. The detection of the DNA and protein of Mtb by nanobiosensor is much more specific for TB diagnosis than that of cytokine detection. Whole cell detection of Mtb is also more specific than cytokine-based detection methods. This is caused by the fact that cytokines are always involved in different diseases, which means that they are not specific for TB. Therefore, we prefer to suggest that the cytokine detection should act as a ancillary method combining with other methods, which would allow more accurate diagnosis of TB.

Another important issue is that the sample for analysis is also critical for the clinical application of nanobiosensors. The detection of the DNA contents and proteins of Mtb, or the detection of cytokines allow the analysis of some very easily obtained samples, such as serum, plasma or blood cells. However, the detection of whole cell of Mtb requires the samples containing Mtb, such as the alveolar lavage fluid or the tissues from the infection site. It is widely known that the tissue samples and the alveolar lavage fluid samples are much more difficult to be obtained. Additionally, the samples with Mtb inside are very dangerous infectious samples that should be carefully treated in specific labs, such as BSL3 labs or BSL2 labs with strict controlled conditions. Thus, although the whole cell detection method could provide direct evidences for the presence of Mtb in samples, it is still very difficult to be popularized in hospitals. It is worth to note that the sample collection and storage strategies are also very important for the rapid, accurate and sensitive analysis of TB by nanobiosensors. As different sample collection and storage strategies might result in different detection results, developing standardized sample collection and storage protocols should also be recognized as an important part for the furture clinical application of nanobiosensors for TB diagnosis.

In some countries with high TB burdens, access to fast, simple, cheap and reliable diagnostic strategies is one of the most important and urgent issues in controlling TB. The combination of nanotechnology and biosensing technology have indicated strong potentials to develop *Mtb* detection and for potential management in clinical diagnosis. In this review, we summarized a variety of nanobiosensors that are designed to detect different TB targets from nucleic acid to the whole bacteria. These methods offer great prospects in the development of rapid TB biosensing strategies with high sensitivity and accuracy. However, there are still some remaining shortcomings as following: 1) although the sensitivity and

specificity seem to be satisfactory, most of those methods are lack of clinical detection data which could directly verify their clinical application prospect; 2) most of the fabrication procedures for those nanobiosensors are too complicated, which might affect the repeatability and applicability of these methods for clinical uses; 3) due to more attentions are needed to be paid in the development of inexpensive devices with high efficiency for the diagnosis of TB in latent phase; 4) most of those assays contain only one detection target which might result in false negative results in clinical detection.

Moreover, although lots of different nanobiosensors have been developed in recent decades for laboratorial analysis of TB associated samples, we can't deny that the current progress of nanobiosensors is still far from the clinical application. The current clinical diagnostic methods, such as Ziehl-Neelsen (ZN) smear microscopy, Mycobacterial cultures, tuberculin skin testing (TST), interferon gamma release assays (IGRAs) and Xpert Mtb/RIF assay have been widely proved to be effective in TB diagnosis, which dramatically enhanced the ability of hospitals for the rapid treatment of TB, latent TB and drug-resistant TB. Some iconography techniques, such as X-ray and computerized tomography (CT), also significantly contribute to TB diagnosis by providing direct graphic evidences for active TB. Although some works have demonstrated the enhanced sensitivity of some novel nanobiosensors for clinical sample analysis beyond the current clinical strategy, their accuracy and sensitivity remain to be further confirmed in larger corhorts.

The current clinical diagnostic methods have developed very mature detection instruments that are suitable for clinical uses, however, the development of laboratorial instruments for nanobiosensors that are suitable for clinical uses also remain a critical issue for the future uses of nanobiosensors. Although some clinical detection strategies, such as IGRAs and Xpert Mtb/RIF assay, are restricted by the high cost issues for widely uses worldwide, the complicated materials and procedures in most reported nanobiosensing methods might also introduce the high cost issues for potential clinical uses of nanobiosensor in the future TB diagnosis. Thus, more attentions are still needed to be paid into the development of novel nanobiosensors with low cost and high sensitivity that are suitable for clinical uses.

We prospect that in the following decades, some simple and portable diagnostic strategies that are capable of multi-target detection will be evolved for TB diagnosis based on the nanobiosensing methods. With these expectations and hopes in mind, the final application of nanobiosensors from bench to clinical diagnosis would promote the pace on the road of global objectives for TB control.

Data availability statement

The original contributions presented in the study are included in the article/Supplementary Material, further inquiries can be directed to the corresponding authors.

Author contributions

XY, SF, and YM drafted and revised the manuscript and contributed equally to this work, HC and J-FX helped to revise the manuscript, JP, WW and GC were responsible for leading this work and revising the manuscript.

Funding

This work was supported by the Medical Research Funding of Guangdong (A2019286), Science and Technology Project of Zhongshan (2019B1056, to WW), National Natural Science Foundation of China (82272348), Natural Science Foundation of Guangdong Province (2022A1515011223), Project of Educational Commission of Guangdong Province of China (2021KTSCX038), Funds for Ph.D. researchers of Guangdong Medical University in 2021 (4SG21236G) and Discipline construction project of Guangdong Medical University (4SG21229GDGFY01).

Acknowledgments

We tender our apologies to those authors whose deserving research was not cited in this manuscript.

Conflict of interest

The authors declare that the research was conducted in the absence of any commercial or financial relationships that could be construed as a potential conflict of interest.

Publisher's note

All claims expressed in this article are solely those of the authors and do not necessarily represent those of their affiliated organizations, or those of the publisher, the editors and the reviewers. Any product that may be evaluated in this article, or claim that may be made by its manufacturer, is not guaranteed or endorsed by the publisher.

References

Aagaard, C., Govaerts, M., Meikle, V., Vallecillo, A. J., Gutierrez-Pabello, J. A., Suarez-Güemes, F., et al. (2006). Optimizing antigen cocktails for detection of Mycobacterium bovis in herds with different prevalences of bovine tuberculosis: ESAT6-CFP10 mixture shows optimal sensitivity and specificity. *J. Clin. Microbiol.* 44, 4326–4335. doi:10.1128/jcm.01184-06

Abu-Salah, K. M., Zourob, M. M., Mouffouk, F., Alrokayan, S. A., Alaamery, M. A., and Ansari, A. A. (2015). DNA-based nanobiosensors as an emerging platform for detection of disease. *Sensors (Basel)* 15, 14539–14568. doi:10.3390/s150614539

Abubakar, I., Pimpin, L., Ariti, C., Beynon, R., Mangtani, P., Sterne, J. A., et al. (2013). Systematic review and meta-analysis of the current evidence on the duration of protection by bacillus Calmette-Guérin vaccination against tuberculosis. *Health Technol. Assess.* 17, 1–372. v-vi. doi:10.3310/hta17370

Alotaibi, B., El-Masry, T. A., Elekhnawy, E., El-Kadem, A. H., Saleh, A., Negm, W. A., et al. (2022). Aqueous core epigallocatechin gallate PLGA nanocapsules: Characterization, antibacterial activity against uropathogens, and *in vivo* reno-protective effect in cisplatin induced nephrotoxicity. *Drug Deliv. (Lond).* 29, 1848–1862. doi:10.1080/10717544.2022.2083725

Arend, S. M., and Van Soolingen, D. (2018). Performance of Xpert Mtb/RIF ultra: A matter of dead or alive. *Lancet Infect. Dis.* 18, 8–10. doi:10.1016/s1473-3099(17)30695-3

Arora, J., Kumar, G., Verma, A. K., Bhalla, M., Sarin, R., and Myneedu, V. P. (2015). Utility of MPT64 antigen detection for rapid confirmation of *Mycobacterium tuberculosis* complex. *J. Glob. Infect. Dis.* 7, 66–69. doi:10.4103/0974-777x.154443

Azmi, U. Z. M., Yusof, N. A., Abdullah, J., Mohammad, F., Ahmad, S. a. A., Suraiya, S., et al. (2021). Aptasensor for the detection of *Mycobacterium tuberculosis* in sputum utilising CFP10-ESAT6 protein as a selective biomarker. *Nanomater. (Basel)* 11, 2446. doi:10.3390/nano11092446

Bai, L., Chen, Y., Bai, Y., Chen, Y., Zhou, J., and Huang, A. (2017). Fullerene-doped polyaniline as new redox nanoprobe and catalyst in electrochemical aptasensor for ultrasensitive detection of *Mycobacterium tuberculosis* MPT64 antigen in human serum. *Biomaterials* 133, 11–19. doi:10.1016/j.biomaterials.2017.04.010

Bai, L., Chen, Y., Liu, X., Zhou, J., Cao, J., Hou, L., et al. (2019). Ultrasensitive electrochemical detection of *Mycobacterium tuberculosis* IS6110 fragment using gold nanoparticles decorated fullerene nanoparticles/nitrogen-doped graphene nanosheet as signal tags. *Anal. Chim. Acta X.* 1080, 75–83. doi:10.1016/j.aca.2019.06.043

Bao, T., Wen, M., Wen, W., Zhang, X., and Wang, S. (2019). Ultrasensitive electrochemical biosensor of interferon-gamma based on gold nanoclusters-graphene@zeolitic imidazolate framework-8 and layered-branched hybridization chain reaction. *Sensors Actuators B Chem.* 296, 126606. doi:10.1016/j.snb.2019.05.083

Barroso, T. G., Martins, R. C., Fernandes, E., Cardoso, S., Rivas, J., and Freitas, P. P. (2018). Detection of BCG bacteria using a magnetoresistive biosensor: A step towards a fully electronic platform for tuberculosis point-of-care detection. *Biosens. Bioelectron. X.* 100, 259–265. doi:10.1016/j.bios.2017.09.004

Behr, M. A., Wilson, M. A., Gill, W. P., Salamon, H., Schoolnik, G. K., Rane, S., et al. (1999). Comparative genomics of BCG vaccines by whole-genome DNA microarray. *Science* 284, 1520–1523. doi:10.1126/science.284.5419.1520

Blakemore, R., Story, E., Helb, D., Kop, J., Banada, P., Owens, M. R., et al. (2010). Evaluation of the analytical performance of the Xpert Mtb/RIF assay. *J. Clin. Microbiol.* 48, 2495–2501. doi:10.1128/jcm.00128-10

Che, N., Qu, Y., Zhang, C., Zhang, L., and Zhang, H. (2016). Double staining of bacilli and antigen Ag85B improves the accuracy of the pathological diagnosis of pulmonary tuberculosis. *J. Clin. Pathol.* 69, 600–606. doi:10.1136/jclinpath-2015-203244

Chen, P., Peng, W., Qu, R., He, Y., Liu, T., Huang, J., et al. (2022). Fluorescence aptasensor of tuberculosis interferon-gamma in clinical samples regulated by steric hindrance and selective identification. *Anal. Chem.* 94, 9122–9129. doi:10.1021/acs.analchem.2c01530

Chen, Y., Li, Y., Yang, Y., Wu, F., Cao, J., and Bai, L. (2017). A polyaniline-reduced graphene oxide nanocomposite as a redox nanoprobe in a voltammetric DNA biosensor for *Mycobacterium tuberculosis*. *Microchim. Acta* 184, 1801–1808. doi:10.1007/s00604-017-2184-5

Chen, Y., Liu, X., Guo, S., Cao, J., Zhou, J., Zuo, J., et al. (2019). A sandwich-type electrochemical aptasensor for *Mycobacterium tuberculosis* MPT64 antigen detection using C(60)NPs decorated N-CNTs/GO nanocomposite coupled with conductive PEI-functionalized metal-organic framework. *Biomaterials* 216, 119253. doi:10.1016/j.biomaterials.2019.119253

Dahiya, B., Prasad, T., Singh, V., Khan, A., Kamra, E., Mor, P., et al. (2020). Diagnosis of tuberculosis by nanoparticle-based immuno-PCR assay based on mycobacterial MPT64 and CFP-10 detection. *Nanomedicine (Lond)* 15, 2609–2624. doi:10.2217/nnm-2020-0258

Desikan, P. (2013). Sputum smear microscopy in tuberculosis: Is it still relevant? *Indian J. Med. Res.* 137, 442–444.

Ding, S., Mosher, C., Lee, X. Y., Das, S. R., Cargill, A. A., Tang, X., et al. (2017). Rapid and label-free detection of interferon gamma via an electrochemical aptasensor comprising a ternary surface monolayer on a gold interdigitated electrode array. *ACS Sens.* 2, 210–217. doi:10.1021/acssensors.6b00581

Diouani, M. F., Ouerghi, O., Refai, A., Belgacem, K., Tlili, C., Laouini, D., et al. (2017). Detection of ESAT-6 by a label free miniature immuno-electrochemical biosensor as a diagnostic tool for tuberculosis. *Mater. Sci. Eng. C* 74, 465–470. doi:10.1016/j.msec.2016.12.051

Dolin, P. J., Raviglione, M. C., and Kochi, A. (1994). Global tuberculosis incidence and mortality during 1990-2000. *Bull. World Health Organ.* 72, 213–220.

El-Samadony, H., Althani, A., Tageldin, M. A., and Azzazy, H. M. E. (2017). Nanodiagnostics for tuberculosis detection. *Expert Rev. Mol. diagn.* 17, 427–443. doi:10.1080/14737159.2017.1308825

El-Samadony, H., Azzazy, H. M. E., Tageldin, M. A., Ashour, M. E., Deraz, I. M., and Elmaghraby, T. (2019). Nanogold assay improves accuracy of conventional TB diagnostics. *Lung* 197, 241–247. doi:10.1007/s00408-018-00194-0

Fukushima, M., Kakinuma, K., Hayashi, H., Nagai, H., Ito, K., and Kawaguchi, R. (2003). Detection and identification of Mycobacterium species isolates by DNA microarray. *J. Clin. Microbiol.* 41, 2605–2615. doi:10.1128/jcm.41.6.2605-2615.2003

Gong, W., and Wu, X. (2021). Differential diagnosis of latent tuberculosis infection and active tuberculosis: A key to a successful tuberculosis control strategy. *Front. Microbiol.* 12, 745592. doi:10.3389/fmicb.2021.745592

Gordon, S. V., Brosch, R., Billault, A., Garnier, T., Eiglmeier, K., and Cole, S. T. (1999). Identification of variable regions in the genomes of tubercle bacilli using bacterial artificial chromosome arrays. *Mol. Microbiol.* 32, 643–655. doi:10.1046/j.1365-2958.1999.01383.x

Gou, D., Xie, G., Li, Y., Zhang, X., and Chen, H. (2018). Voltammetric immunoassay for *Mycobacterium tuberculosis* secretory protein MPT64 based on a synergistic amplification strategy using rolling circle amplification and a gold electrode modified with graphene oxide, Fe(3)O(4) and Pt nanoparticles. *Microchim. Acta* 185, 436. doi:10.1007/s00604-018-2972-6

Gupta, S., and Kakkar, V. (2018). Recent technological advancements in tuberculosis diagnostics - a review. *Biosens. Bioelectron. X.* 115, 14–29. doi:10.1016/j.bios.2018.05.017

Guthula, L. S., Yeh, K. T., Huang, W. L., Chen, C. H., Chen, Y. L., Huang, C. J., et al. (2022). Quantitative and amplification-free detection of SOCS-1 CpG methylation percentage analyses in gastric cancer by fiber optic nanoplasmonic biosensor. *Biosens. Bioelectron. X.* 214, 114540. doi:10.1016/j.bios.2022.114540

Hatami, Z., Ragheb, E., Jalali, F., Tabrizi, M. A., and Shamsipur, M. (2020). Zinc oxide-gold nanocomposite as a proper platform for label-free DNA biosensor. *Bioelectrochemistry* 133, 107458. doi:10.1016/j.bioelechem.2020.107458

He, F., Xiong, Y., Liu, J., Tong, F., and Yan, D. (2016). Construction of Au-IDE/CFP10-ESAT6 aptamer/DNA-AuNPs MSPQC for rapid detection of *Mycobacterium tuberculosis*. *Biosens. Bioelectron. X.* 77, 799–804. doi:10.1016/j.bios.2015.10.054

Hopmeier, D., Lampejo, T., Rycroft, J., Tiberi, S., and Melzer, M. (2020). The limitations of the Cepheid GeneXpert® Mtb/Rif assay for the diagnosis and management of polyresistant pulmonary tuberculosis. *Clin. Infect. Pract.* 7-8, 100038. doi:10.1016/j.clinpr.2020.100038

Jiang, Y., Liu, H., and Wan, K. (2014). MPT64 polymorphisms of *Mycobacterium tuberculosis* strains suggest ongoing immune evasion. *Tuberc. (Edinb)* 94, 712–714. doi:10.1016/j.tube.2014.08.013

Khoder, R., and Korri-Youssoufi, H. (2020). E-DNA biosensors of *M. tuberculosis* based on nanostructured polypyrrole. *Mater. Sci. Eng. C* 108, 110371. doi:10.1016/j.msec.2019.110371

Kim, E. J., Kim, E. B., Lee, S. W., Cheon, S. A., Kim, H. J., Lee, J., et al. (2017). An easy and sensitive sandwich assay for detection of *Mycobacterium tuberculosis* Ag85B antigen using quantum dots and gold nanorods. *Biosens. Bioelectron. X.* 87, 150–156. doi:10.1016/j.bios.2016.08.034

Korma, W., Mihret, A., Chang, Y., Tarekegn, A., Tegegn, M., Tuha, A., et al. (2020). Antigen-specific cytokine and chemokine gene expression for diagnosing latent and active tuberculosis. *Diagn. (Basel)* 10, 716. doi:10.3390/diagnostics10090716

Li, F., Yu, Y., Li, Q., Zhou, M., and Cui, H. (2014). A homogeneous signal-on strategy for the detection of rpoB genes of *Mycobacterium tuberculosis* based on electrochemiluminescent graphene oxide and ferrocene quenching. *Anal. Chem.* 86, 1608–1613. doi:10.1021/ac403281g

Li, H., Song, S., Wen, M., Bao, T., Wu, Z., Xiong, H., et al. (2019a). A novel label-free electrochemical impedance aptasensor for highly sensitive detection of human interferon-gamma based on target-induced exonuclease inhibition. *Biosens. Bioelectron.* 142, 111532. doi:10.1016/j.bios.2019.111532

Li, J., Hu, K., Zhang, Z., Teng, X., and Zhang, X. (2019b). Click DNA cycling in combination with gold nanoparticles loaded with quadruplex DNA motifs enable sensitive electrochemical quantitation of the tuberculosis-associated biomarker CFP-10 in sputum. *Microchim. Acta* 186, 662. doi:10.1007/s00604-019-3780-3

Li, L., Yuan, Y., Chen, Y., Zhang, P., Bai, Y., and Bai, L. (2018a). Aptamer based voltammetric biosensor for *Mycobacterium tuberculosis* antigen ESAT-6 using a nanohybrid material composed of reduced graphene oxide and a metal-organic framework. *Microchim. Acta* 185, 379. doi:10.1007/s00604-018-2884-5

Li, N., Huang, X., Sun, D., Yu, W., Tan, W., Luo, Z., et al. (2018b). Dual-aptamer-based voltammetric biosensor for the *Mycobacterium tuberculosis* antigen MPT64 by using a gold electrode modified with a peroxidase loaded composite consisting of gold nanoparticles and a Zr(IV)/terephthalate metal-organic framework. *Microchim. Acta* 185, 543. doi:10.1007/s00604-018-3081-2

Lin, H. Y., Zeng, Y. T., Lin, C. J., Harroun, S. G., Anand, A., Chang, L., et al. (2022). Partial carbonization of quercetin boosts the antiviral activity against H1N1 influenza A virus. *J. Colloid Interface Sci.* 622, 481–493. doi:10.1016/j.jcis.2022.04.124

Liong, M., Hoang, A. N., Chung, J., Gural, N., Ford, C. B., Min, C., et al. (2013). Magnetic barcode assay for genetic detection of pathogens. *Nat. Commun.* 4, 1752. doi:10.1038/ncomms2745

Liu, C., Jiang, D., Xiang, G., Liu, L., Liu, F., and Pu, X. (2014). An electrochemical DNA biosensor for the detection of *Mycobacterium tuberculosis*, based on signal amplification of graphene and a gold nanoparticle-polyaniline nanocomposite. *Analyst* 139, 5460–5465. doi:10.1039/c4an00976b

Liu, C., Xiang, G., Jiang, D., Liu, L., Liu, F., Luo, F., et al. (2015). An electrochemical aptasensor for detection of IFN-γ using graphene and a dual signal amplification strategy based on the exonuclease-mediated surface-initiated enzymatic polymerization. *Analyst* 140, 7784–7791. doi:10.1039/c5an01591j

Liu, R., Wang, C., Hu, J., Su, Y., and Lv, Y. (2018). DNA-templated copper nanoparticles: Versatile platform for label-free bioassays. *TrAC Trends Anal. Chem.* 105, 436–452. doi:10.1016/j.trac.2018.06.003

Luo, J., Zhang, M., Yan, B., Li, F., Guan, S., Chang, K., et al. (2019). Diagnostic performance of plasma cytokine biosignature combination and MCP-1 as individual biomarkers for differentiating stages *Mycobacterium tuberculosis* infection. *J. Infect.* 78, 281–291. doi:10.1016/j.jinf.2018.10.017

Mahairas, G. G., Sabo, P. J., Hickey, M. J., Singh, D. C., and Stover, C. K. (1996). Molecular analysis of genetic differences between Mycobacterium bovis BCG and virulent M. bovis. *J. Bacteriol.* 178, 1274–1282. doi:10.1128/jb.178.5.1274-1282.1996

Malen, H., Softeland, T., and Wiker, H. G. (2008). Antigen analysis of *Mycobacterium tuberculosis* H37Rv culture filtrate proteins. *Scand. J. Immunol.* 67, 245–252. doi:10.1111/j.1365-3083.2007.02064.x

Mat Zaid, M. H., Abdullah, J., Yusof, N. A., Sulaiman, Y., Wasoh, H., Md Noh, M. F., et al. (2017). PNA biosensor based on reduced graphene oxide/water soluble quantum dots for the detection of *Mycobacterium tuberculosis*. *Sensors Actuators B Chem.* 241, 1024–1034. doi:10.1016/j.snb.2016.10.045

Miao, X., Ko, C. N., Vellaisamy, K., Li, Z., Yang, G., Leung, C. H., et al. (2017). A cyclometalated iridium(III) complex used as a conductor for the electrochemical sensing of IFN-γ. *Sci. Rep.* 7, 42740. doi:10.1038/srep42740

Miodek, A., Mejri, N., Gomgnimbou, M., Sola, C., and Korri-Youssoufi, H. (2015). E-DNA sensor of *Mycobacterium tuberculosis* based on electrochemical assembly of nanomaterials (MWCNTs/PPy/PAMAM). *Anal. Chem.* 87, 9257–9264. doi:10.1021/acs.analchem.5b01761

Mohd Azmi, U. Z., Yusof, N. A., Abdullah, J., Alang Ahmad, S. A., Mohd Faudzi, F. N., Ahmad Raston, N. H., et al. (2021). Portable electrochemical immunosensor for detection of *Mycobacterium tuberculosis* secreted protein CFP10-ESAT6 in clinical sputum samples. *Microchim. Acta* 188, 20. doi:10.1007/s00604-020-04669-x

Mohd Azmi, U. Z., Yusof, N. A., Kusnin, N., Abdullah, J., Suraiya, S., Ong, P. S., et al. (2018). Sandwich electrochemical immunosensor for early detection of tuberculosis based on graphene/polyaniline-modified screen-printed gold electrode. *Sensors (Basel)* 18, 3926. doi:10.3390/s18113926

Mohd Bakhori, N., Yusof, N. A., Abdullah, J., Wasoh, H., Ab Rahman, S. K., and Abd Rahman, S. F. (2019). Surface enhanced CdSe/ZnS QD/SiNP electrochemical immunosensor for the detection of Mycobacterium tuberculosis by combination of CFP10-ESAT6 for better diagnostic specificity. *Mater. (Basel)* 13, 149. doi:10.3390/ma13010149

Morales, J., Pawle, R. H., Akkilic, N., Luo, Y., Xavierselvan, M., Albokhari, R., et al. (2019). DNA-based photoacoustic nanosensor for interferon gamma detection. *ACS Sens.* 4, 1313–1322. doi:10.1021/acssensors.9b00209

Onyango, R. O. (2011). State of the globe: Tracking tuberculosis is the test of time. *J. Glob. Infect. Dis.* 3, 1–3. doi:10.4103/0974-777x.77287

Pahwa, R., Hedau, S., Jain, S., Jain, N., Arora, V. M., Kumar, N., et al. (2005). Assessment of possible tuberculous lymphadenopathy by PCR compared to non-molecular methods. *J. Med. Microbiol.* 54, 873–878. doi:10.1099/jmm.0.45904-0

Parate, K., Rangnekar, S. V., Jing, D., Mendivelso-Perez, D. L., Ding, S., Secor, E. B., et al. (2020). Aerosol-jet-printed graphene immunosensor for label-free cytokine monitoring in serum. *ACS Appl. Mat. Interfaces* 12, 8592–8603. doi:10.1021/acsami.9b22183

Perez, D. J., Patino, E. B., and Orozco, J. (2022). Electrochemical nanobiosensors as point-of-care testing solution to cytokines measurement limitations. *Electroanalysis* 34, 184–211. doi:10.1002/elan.202100237

Perumal, V., Saheed, M. S. M., Mohamed, N. M., Saheed, M. S. M., Murthe, S. S., Gopinath, S. C. B., et al. (2018). Gold nanorod embedded novel 3D graphene nanocomposite for selective bio-capture in rapid detection of *Mycobacterium tuberculosis*. *Biosens. Bioelectron. X.* 116, 116–122. doi:10.1016/j.bios.2018.05.042

Pourgholaminejad, A., Aghdami, N., Baharvand, H., and Moazzeni, S. M. (2016). The effect of pro-inflammatory cytokines on immunophenotype, differentiation capacity and immunomodulatory functions of human mesenchymal stem cells. *Cytokine* 85, 51–60. doi:10.1016/j.cyto.2016.06.003

Prabowo, B. A., Purwidyantri, A., Liu, B., Lai, H. C., and Liu, K. C. (2021). Gold nanoparticle-assisted plasmonic enhancement for DNA detection on a graphene-based portable surface plasmon resonance sensor. *Nanotechnology* 32, 095503. doi:10.1088/1361-6528/abcd62

Qin, L., Zheng, R., Ma, Z., Feng, Y., Liu, Z., Yang, H., et al. (2009). The selection and application of ssDNA aptamers against MPT64 protein in *Mycobacterium tuberculosis*. *Clin. Chem. Lab. Med.* 47, 405–411. doi:10.1515/cclm.2009.097

Rai, M., Ingle, A. P., Birla, S., Yadav, A., and Santos, C. A. (2016). Strategic role of selected noble metal nanoparticles in medicine. *Crit. Rev. Microbiol.* 42, 696–719. doi:10.3109/1040841X.2015.1018131

Renshaw, P. S., Panagiotidou, P., Whelan, A., Gordon, S. V., Hewinson, R. G., Williamson, R. A., et al. (2002). Conclusive evidence that the major T-cell antigens of theMycobacterium tuberculosis complex ESAT-6 and CFP-10 form a tight, 1: 1 complex and characterization of the structural properties of ESAT-6, CFP-10, and the ESAT-6·CFP-10 complex. *J. Biol. Chem.* 277, 21598–21603. doi:10.1074/jbc.m201625200

Saengdee, P., Chaisriratanakul, W., Bunjongpru, W., Sripumkhai, W., Srisuwan, A., Hruanun, C., et al. (2016). A silicon nitride ISFET based immunosensor for Ag85B detection of tuberculosis. *Analyst* 141, 5767–5775. doi:10.1039/c6an00568c

Sanjuan-Jimenez, R., Morata, P., Bermúdez, P., Bravo, M. J., and Colmenero, J. D. (2013). Comparative clinical study of different multiplex real time PCR strategies for the simultaneous differential diagnosis between extrapulmonary tuberculosis and focal complications of brucellosis. *PLoS Negl. Trop. Dis.* 7, e2593. doi:10.1371/journal.pntd.0002593

Smith, I. (2003). *Mycobacterium tuberculosis* pathogenesis and molecular determinants of virulence. *Clin. Microbiol. Rev.* 16, 463–496. doi:10.1128/cmr.16.3.463-496.2003

Steingart, K. R., Ng, V., Henry, M., Hopewell, P. C., Ramsay, A., Cunningham, J., et al. (2006). Sputum processing methods to improve the sensitivity of smear microscopy for tuberculosis: A systematic review. *Lancet Infect. Dis.* 6, 664–674. doi:10.1016/s1473-3099(06)70602-8

Sudbury, E. L., Clifford, V., Messina, N. L., Song, R., and Curtis, N. (2020). Mycobacterium tuberculosis-specific cytokine biomarkers to differentiate active TB and LTBI: A systematic review. *J. Infect.* 81, 873–881. doi:10.1016/j.jinf.2020.09.032

Sun, W., Yuan, S., Huang, H., Liu, N., and Tan, Y. (2017). A label-free biosensor based on localized surface plasmon resonance for diagnosis of tuberculosis. *J. Microbiol. Methods* 142, 41–45. doi:10.1016/j.mimet.2017.09.007

Taghdisi, S. M., Danesh, N. M., Ramezani, M., Yazdian-Robati, R., and Abnous, K. (2017). An amplified fluorescent aptasensor based on single-stranded DNA binding protein, copper and silica nanoparticles for sensitive detection of interferon-gamma. *Anal. Chim. Acta X.* 984, 162–167. doi:10.1016/j.aca.2017.06.032

Torati, S. R., Reddy, V., Yoon, S. S., and Kim, C. (2016). Electrochemical biosensor for *Mycobacterium tuberculosis* DNA detection based on gold nanotubes array electrode platform. *Biosens. Bioelectron. X.* 78, 483–488. doi:10.1016/j.bios.2015.11.098

Tsai, T. T., Chen, C. A., Yi-Ju Ho, N., Yang, S., and Chen, C. F. (2019). Fluorescent double-stranded DNA-templated copper nanoprobes for rapid diagnosis of tuberculosis. *ACS Sens.* 4, 2885–2892. doi:10.1021/acssensors.9b01163

Tufa, L. T., Oh, S., Tran, V. T., Kim, J., Jeong, K.-J., Park, T. J., et al. (2018). Electrochemical immunosensor using nanotriplex of graphene quantum dots, Fe3O4, and Ag nanoparticles for tuberculosis. *Electrochimica Acta* 290, 369–377. doi:10.1016/j.electacta.2018.09.108

Vinuesa, V., Borras, R., Briones, M. L., Clari, M. A., Cresencio, V., Gimenez, E., et al. (2018). Performance of a highly sensitive *Mycobacterium tuberculosis* complex real-time PCR assay for diagnosis of pulmonary tuberculosis in a low-prevalence setting: A prospective intervention study. *J. Clin. Microbiol.* 56, e00116 18. doi:10.1128/jcm.00116-18

Vordermeier, H. M., Whelan, A., Cockle, P. J., Farrant, L., Palmer, N., and Hewinson, R. G. (2001). Use of synthetic peptides derived from the antigens ESAT-6 and CFP-10 for differential diagnosis of bovine tuberculosis in cattle. *Clin. Diagn. Lab. Immunol.* 8, 571–578. doi:10.1128/cdli.8.3.571-578.2001

Wang, F. A., Lakshmipriya, T., and Gopinath, S. C. B. (2018). Red spectral shift in sensitive colorimetric detection of tuberculosis by ESAT-6 antigen-antibody complex: A new strategy with gold nanoparticle. *Nanoscale Res. Lett.* 13, 331. doi:10.1186/s11671-018-2753-5

Wang, H., Zheng, X., Zhang, Y., Huang, J., Zhou, W., Li, X., et al. (2021). The endocrine role of bone: Novel functions of bone-derived cytokines. *Biochem. Pharmacol.* 183, 114308. doi:10.1016/j.bcp.2020.114308

Wang, L., Zhang, H., Ruan, Y., Chin, D. P., Xia, Y., Cheng, S., et al. (2014). Tuberculosis prevalence in China, 1990-2010; a longitudinal analysis of national survey data. *Lancet* 383, 2057–2064. doi:10.1016/S0140-6736(13)62639-2

Wang, Q., Boshoff, H. I. M., Harrison, J. R., Ray, P. C., Green, S. R., Wyatt, P. G., et al. (2020). PE/PPE proteins mediate nutrient transport across the outer membrane of *Mycobacterium tuberculosis*. *Science* 367, 1147–1151. doi:10.1126/science.aav5912

Wang, W., Chen, C., Ying, Y., Lv, S., Wang, Y., Zhang, X., et al. (2022). Smart PdH@MnO(2) yolk-shell nanostructures for spatiotemporally synchronous targeted hydrogen delivery and oxygen-elevated phototherapy of melanoma. *ACS Nano* 16, 5597–5614. doi:10.1021/acsnano.1c10450

Weldingh, K., and Andersen, P. (2008). ESAT-6/CFP10 skin test predicts disease in M. tuberculosis-infected Guinea pigs. *PLoS One* 3, e1978. doi:10.1371/journal.pone.0001978

Welin, A., Björnsdottir, H., Winther, M., Christenson, K., Oprea, T., Karlsson, A., et al. (2015). CFP-10 from *Mycobacterium tuberculosis* selectively activates human neutrophils through a pertussis toxin-sensitive chemotactic receptor. *Infect. Immun.* 83, 205–213. doi:10.1128/iai.02493-14

Wen, D., Liu, Q., Cui, Y., Kong, J., Yang, H., and Liu, Q. (2018). DNA based click polymerization for ultrasensitive IFN-γ fluorescent detection. *Sensors Actuators B Chem.* 276, 279–287. doi:10.1016/j.snb.2018.08.122

Wen, D., Liu, Q., Li, L., Yang, H., and Kong, J. (2019). Ultrasensitive aptamer fluorometric detection of IFN-γ by dual atom transfer radical polymerization amplification. *Sensors Actuators B Chem.* 295, 40–48. doi:10.1016/j.snb.2019.05.036

World Health, O. (2015a). *Accelerating progress on HIV, tuberculosis, malaria, hepatitis and neglected tropical diseases: A new agenda for 2016-2030*. Geneva: World Health Organization.

World Health, O. (2015b). *Global tuberculosis report 2015*. Geneva: World Health Organization.

World Health, O. (2021). *Global tuberculosis report 2021*. Geneva: World Health Organization.

Xu, J. N., Chen, J. P., and Chen, D. L. (2012). Serodiagnosis efficacy and immunogenicity of the fusion protein of *Mycobacterium tuberculosis* composed of the 10-kilodalton culture filtrate protein, ESAT-6, and the extracellular domain fragment of PPE68. *Clin. Vaccine Immunol.* 19, 536–544. doi:10.1128/cvi.05708-11

Xue, H., Zhang, Z., Lin, Z., Su, J., Panayi, A. C., Xiong, Y., et al. (2022). Enhanced tissue regeneration through immunomodulation of angiogenesis and osteogenesis with a multifaceted nanohybrid modified bioactive scaffold. *Bioact. Mat.* 18, 552–568. doi:10.1016/j.bioactmat.2022.05.023

Yin, X., Zheng, L., Lin, L., Hu, Y., Zheng, F., Hu, Y., et al. (2013). Commercial MPT64-based tests for rapid identification of *Mycobacterium tuberculosis* complex: A meta-analysis. *J. Infect.* 67, 369–377. doi:10.1016/j.jinf.2013.06.009

Zhang, C., Lou, J., Tu, W., Bao, J., and Dai, Z. (2015). Ultrasensitive electrochemical biosensing for DNA using quantum dots combined with restriction endonuclease. *Analyst* 140, 506–511. doi:10.1039/c4an01284d

Zhang, W., Shu, Q., Zhao, Z., Fan, J., Lyon, C. J., Zelazny, A. M., et al. (2018). Antigen 85B peptidomic analysis allows species-specific mycobacterial identification. *Clin. Proteomics* 15, 1. doi:10.1186/s12014-017-9177-6

Zhang, X., Feng, Y., Duan, S., Su, L., Zhang, J., and He, F. (2019). *Mycobacterium tuberculosis* strain H37Rv electrochemical sensor mediated by aptamer and AuNPs-DNA. *ACS Sens.* 4, 849–855. doi:10.1021/acssensors.8b01230

Zhou, B., Hao, Y., Chen, S., and Yang, P. (2019). A quartz crystal microbalance modified with antibody-coated silver nanoparticles acting as mass signal amplifiers for real-time monitoring of three latent tuberculosis infection biomarkers. *Microchim. Acta* 186, 212. doi:10.1007/s00604-019-3319-7

Zhou, B., Zhu, M., Hao, Y., and Yang, P. (2017a). Potential-resolved electrochemiluminescence for simultaneous determination of triple latent tuberculosis infection markers. *ACS Appl. Mat. Interfaces* 9, 30536–30542. doi:10.1021/acsami.7b10343

Zhou, B., Zhu, M., Qiu, Y., and Yang, P. (2017b). Novel electrochemiluminescence-sensing platform for the precise analysis of multiple latent tuberculosis infection markers. *ACS Appl. Mat. Interfaces* 9, 18493–18500. doi:10.1021/acsami.7b03211

frontiers | Frontiers in Bioengineering and Biotechnology

TYPE Original Research
PUBLISHED 06 January 2023
DOI 10.3389/fbioe.2022.1098986

Check for updates

OPEN ACCESS

EDITED BY
Hasan Uludag,
University of Alberta, Canada

REVIEWED BY
Yuewu Zhao,
Suzhou Institute of Nano-tech and Nano-bionics (CAS), China
Tao Yang,
Soochow University, China
Zhimin Chang,
Suzhou Institute of Biomedical Engineering and Technology (CAS), China

*CORRESPONDENCE
Jing Wang,
wangjing001@jlu.edu.cn

SPECIALTY SECTION
This article was submitted to Biomaterials, a section of the journal Frontiers in Bioengineering and Biotechnology

RECEIVED 15 November 2022
ACCEPTED 14 December 2022
PUBLISHED 06 January 2023

CITATION
Zuo S, Wang Z, Zhao L and Wang J (2023), Gold nanoplatform for near-infrared light-activated radio-photothermal gas therapy in breast cancer.
Front. Bioeng. Biotechnol. 10:1098986.
doi: 10.3389/fbioe.2022.1098986

COPYRIGHT
© 2023 Zuo, Wang, Zhao and Wang. This is an open-access article distributed under the terms of the Creative Commons Attribution License (CC BY). The use, distribution or reproduction in other forums is permitted, provided the original author(s) and the copyright owner(s) are credited and that the original publication in this journal is cited, in accordance with accepted academic practice. No use, distribution or reproduction is permitted which does not comply with these terms.

Gold nanoplatform for near-infrared light-activated radio-photothermal gas therapy in breast cancer

Shuting Zuo[1], Zhenyu Wang[1], Liping Zhao[2] and Jing Wang[1]*

[1]Department of Breast Surgery, The Second Hospital of Jilin University, Changchun, China, [2]Gynecology and Obstetrics Department of the Second Hospital of Jilin University, Changchun, China

Although radiotherapy is one of the most common treatments for triple-negative breast cancer (TNBC), it frequently has unsatisfactory therapeutic outcomes due to the radiation resistance of tumor tissues. Therefore, a synergistic strategy is urgently needed to increase therapeutic responses and prolong patient survival. Herein, we constructed gold nanocages (GNCs) loaded with a hyperpyrexia-sensitive nitric oxide (NO) donor (thiolate cupferron) to integrate extrinsic radiosensitization, local photothermal therapy, and near-infrared-activated NO gas therapy. The resulting nanoplatform (GNCs@NO) showed a high photothermal conversion efficiency, which induced the death of cancer cells and facilitated rapid NO release in tumor tissues. The radiosensitizing efficacy of GNCs@NO was further demonstrated *in vitro* and *in vivo*. Importantly, the released NO reacted with the reactive oxide species induced by radiotherapy to produce more toxic reactive nitrogen species, exerting a synergistic effect to improve anticancer efficacy. Thus, GNCs@NO demonstrated excellent effects as a combination therapy with few adverse effects. Our work proposes a promising nanoplatform for the radio/photothermal/gas treatment of TNBC.

KEYWORDS

nitric oxide, gas therapy, radio-sensitization, combination therapies, breast cancer

1 Introduction

Triple-negative breast cancer (TNBC) is an extremely malignant tumor that threatens the lives of women worldwide (Lyons, 2019; Cortes et al., 2022). Although radiotherapy and chemotherapy after surgical resection are the standard treatments for TNBC, they often result in unsatisfactory outcomes due to radio/chemoresistance and severe side effects (James et al., 2019; Baranova et al., 2022). Thus, highly effective and safe treatment methods for TNBC are urgently needed to prolong patient survival and improve their quality of life.

Gas therapy has attracted considerable attention owing to its non-invasiveness and absence of drug tolerance (Dai et al., 2018; Freund and Bekeschus, 2020). More importantly, gas therapy often exerts synergistic effects with other treatment modalities, including radiotherapy, chemotherapy, and photodynamic therapy, because of the regulation of cancer cells and tumor microenvironment (Fan et al., 2018; Liu et al., 2020; Wu et al., 2021). For example, carbon monoxide (CO) gas can effectively decrease tumor resistance to chemotherapy or radiotherapy by inhibiting cytochrome c oxidase and cytochrome P450 enzymes, causing obstacles in respiratory chain transmission and difficulties in oxygen utilization (Giuffrè et al., 2020; Thakar et al., 2021). Nitric oxide (NO) is the first gasotransmitter in the gas family and has various physiological and pathological activities, including blood vessel relaxation, NO

poisoning, and macrophage activation (Yu et al., 2018; Ding et al., 2019). Furthermore, NO can react with reactive oxygen species (ROS) to produce more lethal reactive nitrogen species (RNS), which improves the effectiveness of radiotherapy as the treatment effect of radiotherapy is mainly due to ROS produced by the interaction between radiation and water (Zuo et al., 2022). Therefore, combining radiotherapy with NO therapy promises a synergistic effect with low side effects for the treatment of TNBC. However, it remains a challenge to deliver unstable NO to the target site for maximal efficacy.

Photothermal therapy (PTT) is a promising green treatment because of its non-invasiveness (Fernandes et al., 2020; Gao et al., 2021). PTT alleviates hypoxia in tumor tissues by increasing tumor blood perfusion, which may improve the radiosensitivity of tumor tissues (Wang et al., 2019). Gold nanocages (GNCs) with tunable optical properties matching the near-infrared region (NIR) are particularly attractive for PTT because of their excellent photothermal conversion effect (Wang et al., 2018; Alimardani et al., 2021). Furthermore, GNCs, as high-Z nanomaterials, have emerged as radiosensitizers owing to their enhanced radiation absorption (Chen et al., 2020; Penninckx et al., 2020). More importantly, GNCs are widely used as nanodrug delivery systems because of their unique porous walls, hollow structure, and surface that can be easily functionalized (Wang et al., 2018; Zhang et al., 2021). Therefore, GNCs are ideal nanocarriers for delivering NO donors to provide radiosensitization, PTT, and gas therapy for treatment with spatiotemporal consistency.

In this work, we prepared GNCs and preloaded them with a hyperpyrexia-sensitive NO donor, thiolate cupferron, through thiol–gold interactions to form GNCs@NO (Scheme 1). GNCs@NO showed a high loading ability of the NO donor, good photothermal conversion efficiency, and NIR-stimulated NO release. *In vitro* and *in vivo* experiments demonstrated multiple therapeutic effects, including PTT and NO poisoning, as well as radiosensitization. More importantly, the released NO showed a synergistic effect with radiotherapy through the production of RNS by reacting with ROS. Thus, the combination of GNCs@NO and X-rays induced a remarkable antitumor effect and low systemic toxicity. Overall, our work proposes a promising nanoplatform for the multimodal treatment of TNBC.

2 Methods

2.1 GNC synthesis

GNCs were fabricated using a galvanic replacement reaction between $HAuCl_4$ and silver nanocages as previously described (Tang et al., 2021). First, we prepared 5 ml of 0.2 mg/ml aqueous polyvinyl pyrrolidone (PVP). Subsequently, we added silver nanocages (5 mg) to the prepared PVP solution. The mixture was then heated at 100°C for 30 min. Subsequently, 1 mM $HAuCl_4$ was slowly added to the mixture and reacted for another 30 min. Finally, the solution was cooled to room temperature and centrifuged at 8000 rpm for 15 min to collect GNCs. The GNCs were repeatedly washed with ethyl alcohol and distilled water before storage at 4°C.

2.2 NO donor loading and NO release

First, 10 mg thiolate cupferron was dissolved in dimethyl sulfoxide (DMSO) (0.5 ml). Subsequently, the thiolate cupferron solution was mixed with 20 ml of 0.1 nM aqueous GNCs and stirred at 30°C for

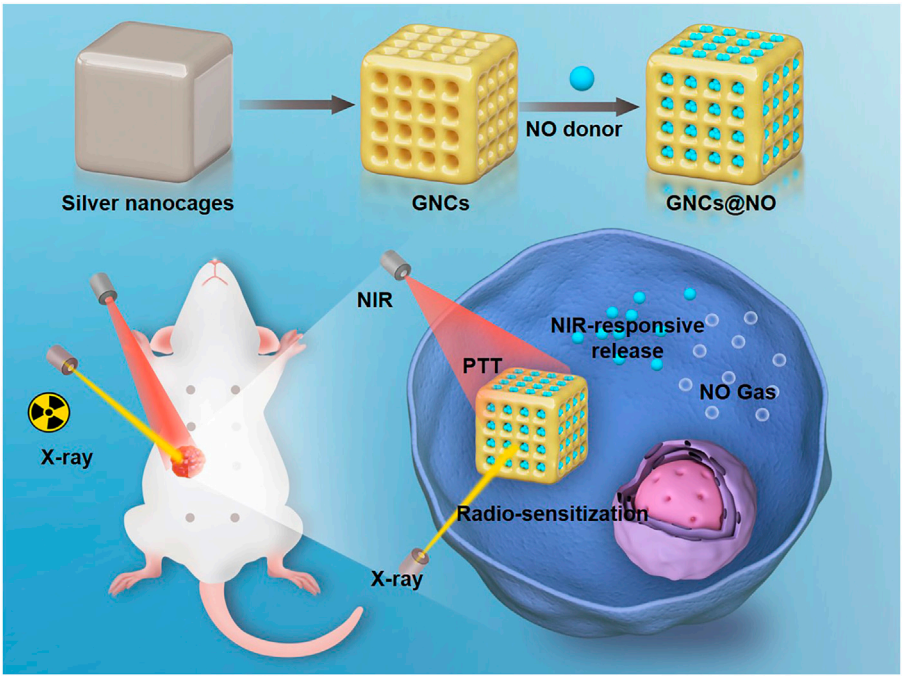

SCHEME 1
Fabrication of nitric oxide (NO) donor-loaded gold nanocages for radiosensitization, local photothermal therapy, and NIR-activated NO gas therapy for breast cancer.

48 h. The products were harvested after centrifugation at 8000 rpm for 10 min and washed multiple times with PBS. To explore the NIR-responsive release of NO, GNCs@NO (1 mg) were dispersed in phosphate-buffered saline (PBS) solution with or without exposure to 808 nm of NIR irradiation (1 W/cm^2) for 5 min. Then, the GNCs@NO were centrifuged at 8000 rpm for 10 min, and the supernatant was collected for the NO Griess assays. Briefly, 100 μL of the supernatant was added to Griess agent I and placed in the dark for 15 min. Subsequently, Griess agent II was slowly added to the mixture and allowed to react in the dark for 15 min to produce a diazo compound. We then quantified NO by measuring the UV absorbance of the solution of the generated diazo compound at 540 nm.

2.3 Cytotoxicity of GNCs and GNCs@NO

The cytotoxicity of GNCs and GNCs@NO toward human breast carcinoma MCF-7 cells and human breast epithelial MCF-10A cells was evaluated in the presence or absence of NIR irradiation using an SRB assay. Briefly, MCF-7 and MCF-10A cells were respectively seeded into 96-well plates (5×10^3 cells/well) and cultured overnight. GNCs or GNCs@NO were then added to these cells at various concentrations and co-incubated for 24 h. Next, 100 ml of 20% trichloroacetic acid was added to each well, followed by incubation at 4°C for 3 h. Then, the cell media were discarded and the cells were washed three times in PBS. Subsequently, 100 ml of 0.4% w/v SRB solution was added to each well. After 30 min, the unbound SRB was discarded, and 150 ml of 10 mM Tris-HCl was added to each well, followed by shaking for 5 min to solubilize the bound SRB. The optical density (OD) was measured at 570 nm, and the relative cell viability was calculated according to the ratio of the OD value to that of the control group. For the NIR irradiation group, GNCs and GNCs@NO (12.5 μg/ml) were respectively added to MCF-7 cells and co-cultured for 24 h and subsequently irradiated with NIR light (808 nm, 1 W/cm^2) for 5 min. To evaluate the radiosensitization effect of GNCs and GNCs@NO, the cells were treated with saline, GNCs, or GNCs@NO (12.5 μg/ml) for 24 h and irradiated with X-rays (1 Gy/min for 5 min). Subsequently, cell viability was assessed using an SRB assay.

2.4 ROS and RNS measurement

The MCF-7 cells were treated with GNCs or GNCs@NO (12.5 μg/ml) for 24 h and then exposed to 808 nm NIR light (1 W/cm^2) for 5 min or/and irradiated with 1 Gy/min of X-ray for 5 min. These MCF-7 cells were then mixed with dichlorodihydrofluorescein diacetate (DCFH-DA) and incubated for 20 min. Subsequently, the fluorescence intensity of DCFH-DA was measured by flow cytometry to measure intracellular ROS levels. To evaluate intracellular RNS levels, the cells were incubated with dihydrorhodamine (DHR) for 20 min after different treatments. The fluorescence intensity of DHR was determined by flow cytometry.

2.5 Colony formation assay

MCF-7 cells were seeded into 25 cm^2 flasks and cultured for 24 h. Then, these MCF-7 cells were co-incubated with GNCs or GNCs@NO or/and treated with NIR or/and X-ray irradiation. After 24 h of administration, the cells were trypsinized and cultured in 6 cm dishes for 7 days. The colonies were stained with 3-(4,5-dimethylthiazol-2-yl)-2-5-diphenyltetrazolium bromide. Colonies containing over 50 cells were counted.

2.6 *In vivo* combination therapies

We purchased six-week-old female nude mice from the Animal Experimental Center of Jilin University and kept them at a conventional animal housing facility in The Second Hospital of Jilin University. All the animal experimental protocols and experimental operations were approved by the Ethics Committee for the Use of Experimental Animals of The Second Hospital of Jilin University. To establish MCF-7 xenograft models, the nude mice were anesthetized by inhaling 2% isoflurane and subsequently injected with 5 × 10^6 MCF-7 cells into the mammary fat pads. When the tumor volume reached approximately 0.08 cm^3, the MCF-7 xenograft models were divided into seven groups: saline, NIR, X-ray, GNCs + X-rays, GNCs + NIR, GNCs@NO, and GNCs@NO + X-rays + NIR. Mice in the nanoparticle-treated groups were intravenously injected with GNCs or GNCs@NO at a dose of 5 mg/kg every 3 days for a total of four administrations. In the NIR-exposed groups, the tumor tissues were exposed to an 808 nm of NIR light (1 W/cm^2) for 5 min 6 h after the injection of nanoparticles or PBS. In the X-ray-irradiated groups, the tumor sites were irradiated with 1 Gy/min of X-ray for 5 min 6 h after the injection of nanoparticles or PBS. The tumor lengths and widths were measured using a digital caliper 2 days post-administration. We subsequently calculated the tumor volumes using the following equation: tumor volume = length × width^2 × 0.52. The experiment was terminated on day 18. All the mice were euthanized by carbon dioxide asphyxia and the tumors were collected for weighing. Serum was collected to assess biochemical parameters. The major organs, including the liver, spleen, kidney, lung, and heart, were harvested, fixed, and stained with hematoxylin and eosin.

2.7 Statistical analysis

The differences between two groups were analyzed using Student's t-tests. Differences between more than two groups were analyzed using one-way analysis of variance. Statistical significance was set at $p < 0.05$.

3 Results and discussion

GNCs were fabricated *via* a galvanic replacement reaction between $HAuCl_4$ and silver nanocages as previously reported (Tang et al., 2021). Transmission electron microscopy (TEM) images indicated the uniform morphology and good monodispersity of the prepared GNCs (Figure 1A). The dynamic light scattering assay showed an average GNC size of approximately 110.4 nm (Supplementary Figure S1), with a polydispersity index of 0.184. Additionally, the GNCs showed hollow structures and porous walls (Supplementary Figure S2). Subsequently, the surface of the prepared GNCs was modified with thiolate cupferron through thiol–gold interactions. The hydrodynamic size of the GNCs@NO was about 130.3 nm with a PDI value of 0.15

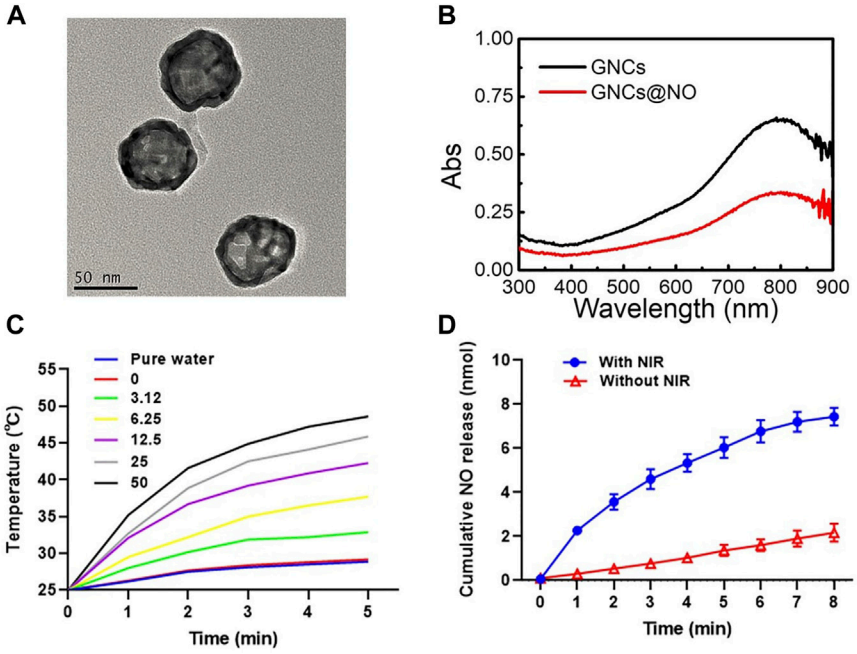

FIGURE 1
Characterization of GNCs@NO. **(A)** TEM image of GNCs. **(B)** UV-vis spectra of GNCs and GNCs@NO. **(C)** Temperature change curve of GNCs@NO suspensions with exposure to NIR irradiation. **(D)** Cumulative release of NO gas from GNCs@NO according to exposure to NIR irradiation.

(Supplementary Figure S3) and a GNCs@NO surface zeta-potential of −12.2 mV, which was higher than that of the GNCs (−15.4 mV) (Supplementary Figure S4). Furthermore, the localized surface plasmon resonance peak shifted from 792 to 800 nm (Figure 1B), suggesting the successful modification of thiolate cupferron. Moreover, the strong absorption of GNCs@NO in the NIR region implied that GNCs@NO had good photothermal conversion ability. To explore the photothermal conversion effect, cell culture media dispersions of GNCs@NO at different concentrations were irradiated by an 808 nm laser at a power density of 1 mW/cm^2. As shown in Figure 1C, after 5 min of continuous NIR irradiation, the changes in temperature in the water or cell culture medium were <6°C, whereas the GNCs@NO samples showed time- and concentration-dependent temperature increases. After irradiation with NIR light for 5 min, the temperature of the 12.5 μg/ml GNCs@NO sample was >43.2°C, a crucial temperature to induce tumor cell death without normal cell death. We then investigated the release of NO from GNCs@NO in the absence or presence of NIR irradiation. After NIR irradiation, GNCs@NO (12.5 μg/ml) showed a temperature change like that of GNCs at the same concentration (Supplementary Figure S5), indicating that the NO donor loading had a negligible effect on the photothermal conversion of GNCs. As illustrated in Figure 1D, NIR irradiation remarkably accelerated the release of NO from GNCs@NO, which was attributed to the slow decomposition of thiolate cupferron as an N-hydroxy-N-nitrosamine NO donor and release of NO under physiological conditions and rapid decomposition with the generation of NO at high temperature (Wang et al., 2002). The NIR-responsive NO release of GNCs@NO further confirmed their excellent photothermal conversion efficiency. To improve the biostability, GNCs@NO were functionalized with polyethylene glycol (PEG). GNCs@NO showed long-term stability in the cell culture media after PEGylation, whereas GNCs@NO without PEG modification showed an aggregate (Supplementary Figure S6).

Biosafety is particularly important for the biomedical application of nanoparticles (Yang et al., 2013; Xia et al., 2014; Kozics et al., 2021). Therefore, we investigated the cytotoxicity of various concentrations of GNCs and GNCs@NO toward MCF-7 and MCF-10A cells. As illustrated in Figure 2A and Supplementary Figure S7, GNCs and GNCs@NO both exhibited concentration-dependent cytotoxicity against the two cell lines. Additionally, the cytotoxicity of GNCs@NO was similar to that of GNCs, possibly because of the weak release of NO under physiological conditions. The viabilities of MCF-7 and MCF-10A cells were both >90% at GNC concentrations <12.5 μg/ml. Considering its lower cytotoxicity, a concentration of 12.5 μg/ml was chosen as the optimum dose in subsequent therapies. Additionally, both GNCs@NO and GNCs showed high cellular internalization efficiency in MCF-7 cells, indicating their good biocompatibility (Figure 2B and Supplementary Figure S8). Subsequently, we investigated the PTT effects of GNCs and GNCs@NO *in vitro*. Compared to the control groups, the viability of MCF-7 cells was <5% even 5 min after NIR irradiation (Figure 2C), confirming the biosafety of the applied NIR. In contrast, NIR irradiation induced time-dependent cytotoxicity toward MCF-7 cells after treatment with GNCs or GNCs@NO, indicating that our prepared nanoparticles could be used as effective photothermal agents for PTT. Notably, GNCs@NO showed a stronger killing effect compared to GNCs owing to NO-poisoning induced by the released NO gas. We subsequently explored the radiosensitizing effects of GNCs and GNCs@NO. MCF-7 cells irradiated with X-rays without nanoparticle treatment showed a high cell count (Figure 2D). In contrast, the viability of MCF-7 cells was reduced after treatment with nanoparticles combined with X-ray irradiation. Moreover, the killing effect of X-rays increased with

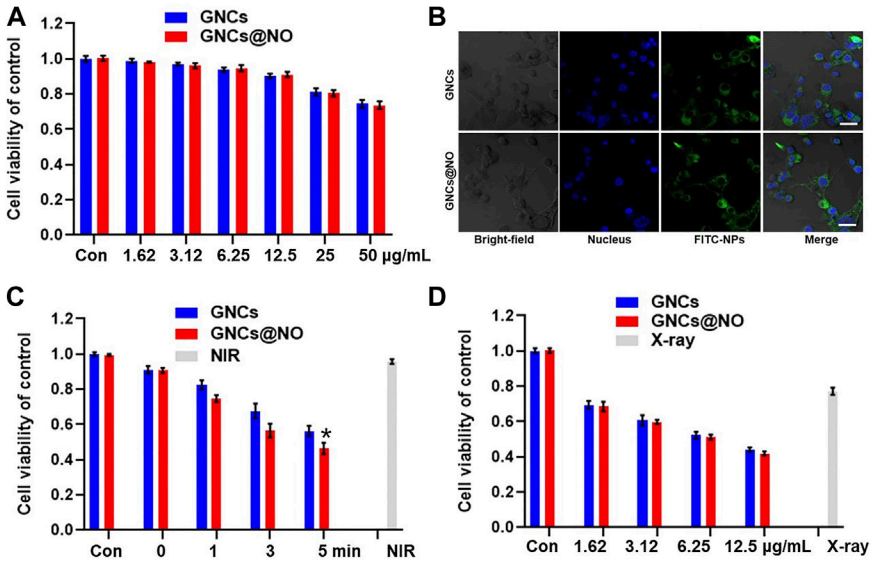

FIGURE 2
Photothermal therapy and radiosensitization of GNCs@NO. **(A)** Cytotoxicity of GNCs and GNCs@NO at various concentrations in MCF-7 cells. **(B)** CLSM images of MCF-7 cells co-incubated with GNCs or GNCs@NO for 3 h. Scale bar = 10 μm. **(C)** Viability of MCF-7 cells after incubation with GNCs or GNCs@NO with NIR irradiation. *$p < 0.05$ *versus* GNC group. **(D)** Viability of MCF-7 cells after incubation with GNCs or GNCs@NO with exposure to X-ray irradiation. The values represent mean values ±SD, $n = 5$.

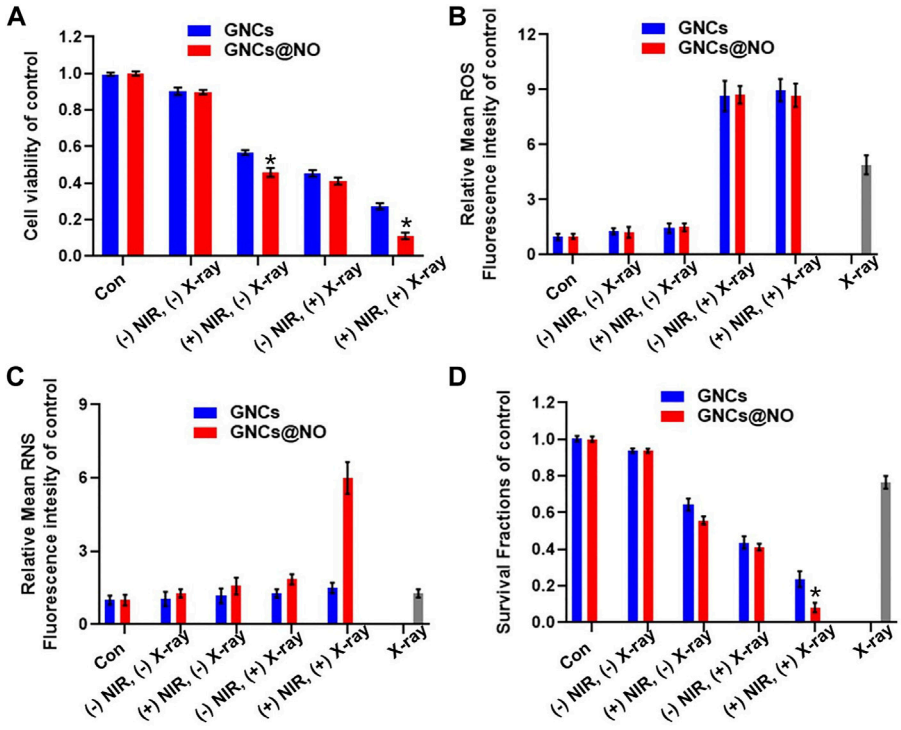

FIGURE 3
Combined GNCs@NO therapies *in vitro*. **(A)** Viability of MCF-7 cells after incubation with GNCs or GNCs@NO with (+) or without (-) NIR or/and X-ray irradiation, *$p < 0.05$ *versus* GNC group. **(B)** Quantitative analysis of ROS production by FACS. **(C)** Quantitative analysis of RNS production by FACS. **(D)** Colony formation assay of MCF-7 cells for various treatments, *$p < 0.05$ *versus* GNC group. The values represent mean values ±SD, $n = 5$.

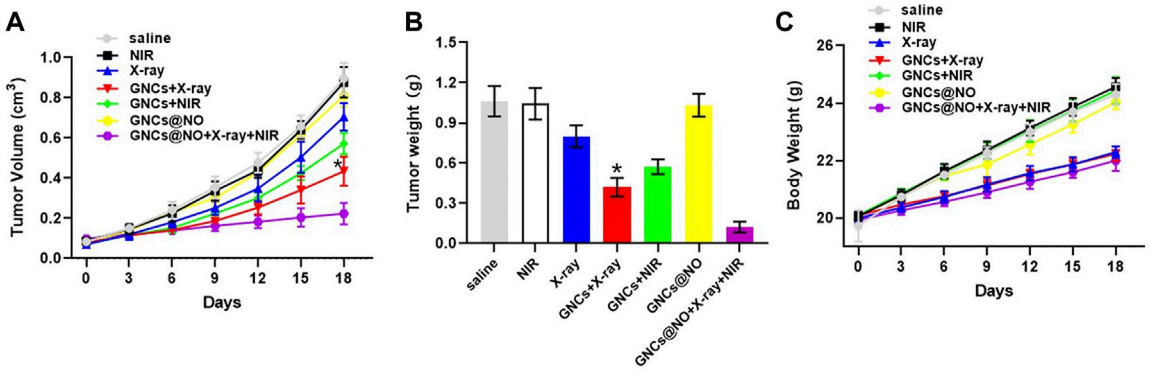

FIGURE 4
In vivo GNCs@NO combination therapies. **(A)** Tumor growth curve, $*p < 0.05$ *versus* X-ray group. **(B)** Tumor weight, $*p < 0.05$ *versus* X-ray group. **(C)** Body weight. The values represent mean values ±SD, $n = 5$.

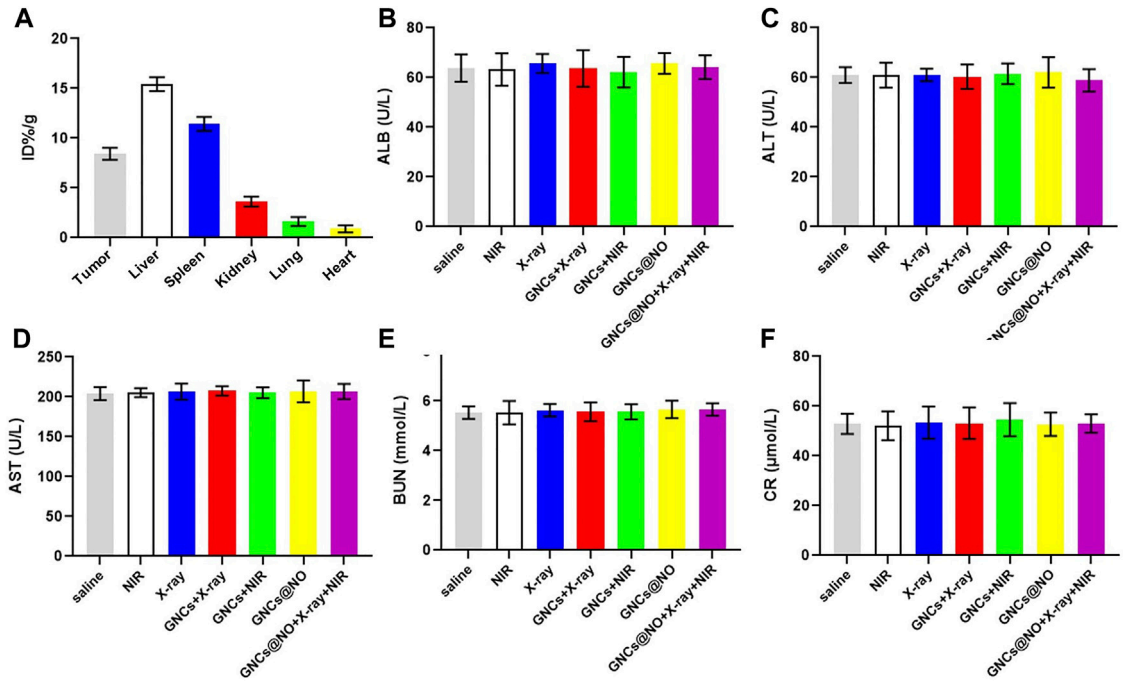

FIGURE 5
Biosafety evaluation. **(A)** Biodistribution of GNCs@NO. **(B–F)** Serum biochemistry indexes. Levels of ALB **(B)**, ALT **(C)**, AST **(D)**, BUN **(E)**, and CRE **(F)**. The values represent mean values ±SD, $n = 3$.

increasing concentration of GNCs or GNCs@NO, indicating the radiosensitizing effect of GNCs and GNCs@NO.

After demonstrating the PTT effect and NIR-responsive NO gas therapy, as well as the radiosensitizing effect of GNCs@NO, we explored the combined therapeutic efficacy of GNCs and GNCs@NO with exposure to X-rays and NIR light for 5 min *in vitro*. As shown in Figure 3A, nanoparticles combined with irradiation with both NIR light and X-rays destroyed significantly more MCF-7 cells compared to the combination with only NIR or X-ray irradiation, suggesting a good combination efficiency of radio-photothermal treatments. More importantly, GNCs@NO + X-rays + NIR treatment exhibited higher cytotoxicity toward MCF-7 cells than GNCs + X-rays + NIR. To explore the underlying mechanism, we measured the levels of intracellular ROS and RNS after various treatments. As shown in Figure 3B, neither GNCs@NO nor GNCs induced detectable ROS or RNS production with or without NIR irradiation. Additionally, X-ray irradiation led to the generation of ROS in MCF-cells, while both GNCs@NO and GNCs improved the ROS generation induced by X-ray irradiation, further confirming the radiosensitizing efficacy of GNCs and GNCs@NO. More importantly, a significant enhancement in RNS signal was observed in the GNCs@NO + X-rays + NIR treatment group, whereas few RNS were detected in the GNCs +

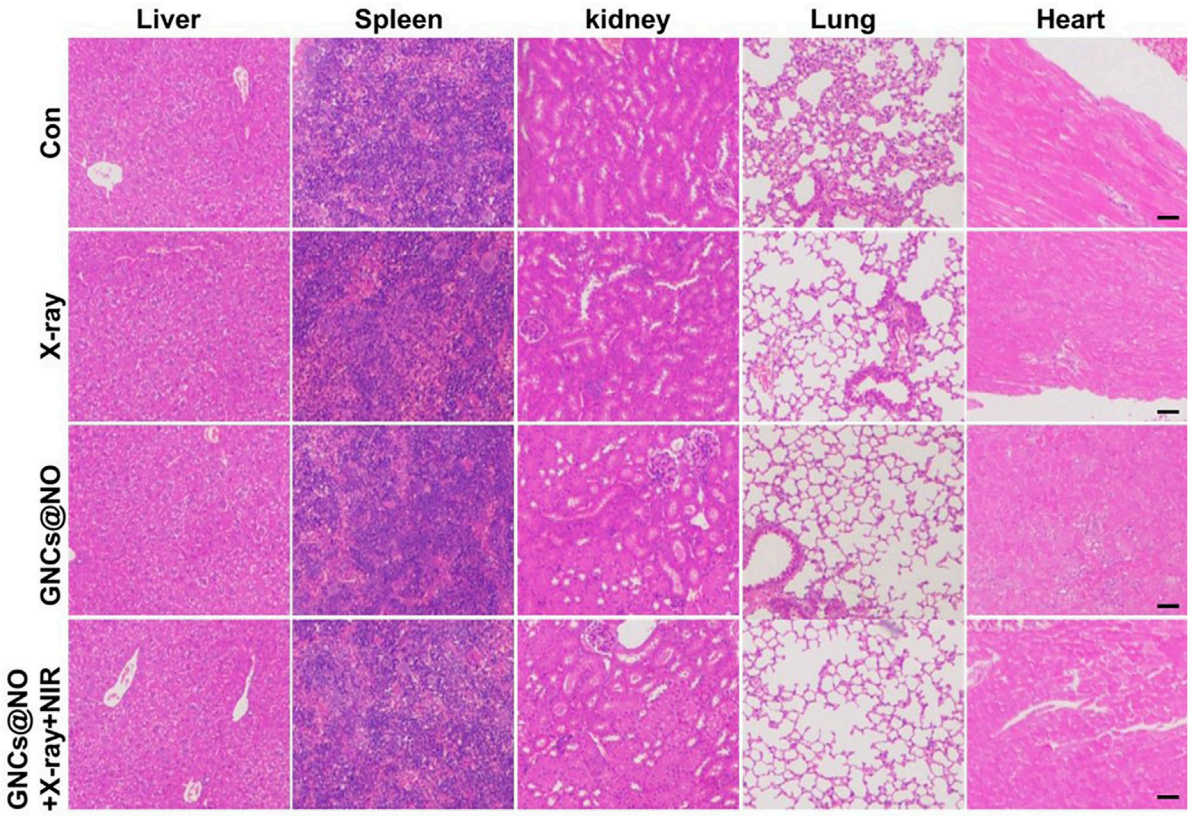

FIGURE 6
Histopathology of the livers, spleens, kidneys, lungs, and hearts from MCF-7 tumor-bearing mice from each group. Scale bar = 50 μm.

X-rays + NIR group (Figure 3C). The generation of more toxic RNS originates from the reaction of ROS with the released NO, suggesting the synergistic effects of NO therapy with radiotherapy. To further explore the long-term therapeutic efficacy of GNCs@NO, we investigated the clonal ability of MCF-7 cells after different treatments using a colony formation assay. As illustrated in Figure 3D, the number of MCF-7 colonies decreased after X-ray irradiation, whereas a smaller surviving fraction was observed in the GNCs + X-rays group owing to the radiosensitizing effect of GNCs. GNCs + X-ray + NIR exhibited a stronger inhibition of colony formation of MCF-7 cells compared to GNCs + X-rays owing to the combined effect of PTT. Consistent with the cell viability results, the smallest number of MCF-7 colonies was observed in the GNCs@NO + X-rays + NIR treatment group. These results confirmed that GNCs@NO, which integrates PTT, radiosensitization, and NIR-responsive NO gas therapy, were an effective combined therapy against TNBC.

Encouraged by the *in vitro* efficacy of PTT/radiotherapy/gas therapy, we explored the ability of the GNCs@NO + X-rays + NIR treatment to delay tumor progression *in vivo*. MCF-7 xenografts were replicated and divided into seven groups: saline, NIR, X-ray, GNCs + X-rays, GNCs + NIR, GNCs@NO, and GNCs@NO + X-rays + NIR; the treatments were administered by tail vein injection of drugs and/or X-ray irradiation in the absence or presence of NIR every 3 days for a total of six administrations. As illustrated in Figures 4A, B, tumors in mice treated with saline or NIR grew rapidly, whereas GNC + NIR treatment showed significant tumor growth inhibition compared to the NIR and control groups, indicating the PTT efficacy of GNCs. Additionally, GNCs@NO had a negligible inhibitory effect on tumor growth because of the weak release of NO gas. The X-ray group also showed an unsatisfactory inhibitory effect due to the radioresistance of the tumor tissues. However, the inhibitory effect of X-rays was improved in the GNCs + X-rays treatment group, further confirming the radiosensitization effect of GNCs. GNCs@NO + X-rays + NIR induced nearly complete inhibition of tumor growth. These findings demonstrate that GNCs@NO had excellent antitumor efficacy through the synergistic effects of PTT, radiosensitization, and gas therapy.

After confirming the outstanding anticancer efficiency, we evaluated the accumulation of GNCs@NO in tumors and major organs, including the heart, liver, spleen, lungs, and kidneys. As shown in Figure 5A, GNCs@NO predominantly accumulated in the reticuloendothelial system of the tumor tissues, liver, and spleen. Furthermore, the body weight of mice after treatment with X-rays decreased due to radiotherapy-induced gastrointestinal injury (Li et al., 2010; Li et al., 2019; Xie et al., 2020). In contrast, GNCs@NO did not induce a change in body weight compared to the saline group, while the body weight of the mice treated with GNCs + X-rays or GNCs@NO + X-rays + NIR showed no observable difference from the body weight of mice treated with X-rays (Figure 4C). These results suggested that GNCs@NO-based combination therapy might not aggravate radiotherapy-induced side effects. More importantly, blood biochemistry indices, including alkaline phosphatase (ALB), aspartate aminotransferase (AST), alanine aminotransferase (ALT), blood urea nitrogen (BUN), and creatinine (CR) (Figures 5B, F), do

not exhibit significant changes in any of the treatment groups compared to the saline group, indicating good liver and kidney functions during the combined treatment. Furthermore, no pathological changes were observed in the major organs of the mice after treatment with GNCs@NO + X-rays + NIR (Figure 6). Overall, these findings confirmed the low systemic toxicity of GNCs@NO-based combination therapies.

4 Conclusion

We designed a hyperpyrexia-sensitive NO donor (GNCs@NO) to integrate PTT, radiosensitization, and NIR-controlled NO gas therapy. GNCs@NO showed high drug loading of the NO donor and high photothermal conversion efficiency, which not only generated hyperpyrexia to induce cancer cell death but also facilitated rapid NO release under NIR irradiation. Additionally, we confirmed the radiosensitizing efficacy and NIR-activated NO gas therapy of GNCs@NO *in vitro* and *in vivo*. More importantly, GNCs@NO + X-ray + NIR treatment induced more lethal RNS production through the reaction of the released NO with the ROS induced by radiotherapy. Therefore, GNCs@NO + X-rays + NIR exerted outstanding anticancer efficacy due to synergistic effects. Furthermore, the body weight measurement, blood biochemistry analysis, and organ histopathology staining indicated the low systemic toxicity of GNCs@NO-based combination treatments. Consequently, GNCs@NO are a promising nanoplatform for combined radio/photothermal/gas therapy for TNBC.

Data availability statement

The original contributions presented in the study are included in the article/Supplementary Material. Further inquiries can be directed to the corresponding author.

Ethics statement

The animal study was reviewed and approved by the Ethics Committee for the Use of Experimental Animals of The Second Hospital of Jilin University.

Author contributions

SZ made substantial contributions to the study conception, methodology, funding, and investigation and also drafted the manuscript. ZW provided technical help, assisted with the data analysis and interpretation, and reviewed the manuscript critically for important intellectual content. LZ contributed to the investigation and edited the manuscript. JW supervised the study, revised the manuscript critically for important intellectual content, and provided final approval of the version to be published. All authors have read and agreed to the published version of the manuscript.

Funding

This work was supported by the Finance Department Program of Jilin Province (2020SCZT028).

Conflict of interest

The authors declare that the research was conducted in the absence of any commercial or financial relationships that could be construed as a potential conflict of interest.

Publisher's note

All claims expressed in this article are solely those of the authors and do not necessarily represent those of their affiliated organizations, or those of the publisher, the editors, and the reviewers. Any product that may be evaluated in this article, or claim that may be made by its manufacturer, is not guaranteed or endorsed by the publisher.

Supplementary material

The Supplementary Material for this article can be found online at: https://www.frontiersin.org/articles/10.3389/fbioe.2022.1098986/full#supplementary-material

SUPPLEMENTARY FIGURE S1
Hydrodynamic size of GNCs.

SUPPLEMENTARY FIGURE S2
HRTEM of GNCs.

SUPPLEMENTARY FIGURE S3
Hydrodynamic size of GNCs@NO.

SUPPLEMENTARY FIGURE S4
Surface zeta potential of GNCs and GNCs@NO.

SUPPLEMENTARY FIGURE S5
Temperature changes in GNC suspensions at 12.5 μg/mL with exposure to NIR irradiation.

SUPPLEMENTARY FIGURE S6
Long-term stability of GNCs@NO with or without PEG modification in cell media.

SUPPLEMENTARY FIGURE S7
Cytotoxicity of GNCs and GNCs@NO against MCF-10A at various concentrations.

SUPPLEMENTARY FIGURE S8
Quantitative analysis of the cellular internalization of GNCs and GNCs@NO in MCF-7 cells.

References

Alimardani, V., Farahavar, G., Salehi, S., Taghizadeh, S., Ghiasi, M. R., and Abolmaali, S. S. (2021). Gold nanocages in cancer diagnosis, therapy, and theranostics: A brief review. *Front. Mater. Sci.* 15, 494–511. doi:10.1007/s11706-021-0569-1

Baranova, A., Krasnoselskyi, M., Starikov, V., Kartashov, S., Zhulkevych, I., Vlasenko, V., et al. (2022). Triple-negative breast cancer: Current treatment strategies and factors of negative prognosis. *J. Med. Life* 15, 153–161. doi:10.25122/jml-2021-0108

Chen, Y., Yang, J., Fu, S., and Wu, J. (2020). Gold nanoparticles as radiosensitizers in cancer radiotherapy. *Int. J. Nanomedicine* 15, 9407–9430. doi:10.2147/ijn.s272902

Cortes, J., Rugo, H. S., Cescon, D. W., Im, S.-A., Yusof, M. M., Gallardo, C., et al. (2022). Pembrolizumab plus chemotherapy in advanced triple-negative breast cancer. *N. Engl. J. Med.* 387, 217–226. doi:10.1056/nejmoa2202809

Dai, X., Bazaka, K., Richard, D. J., Thompson, E. R. W., and Ostrikov, K. K. (2018). The emerging role of gas plasma in oncotherapy. *Trends Biotechnol.* 36, 1183–1198. doi:10.1016/j.tibtech.2018.06.010

Ding, Y., Du, C., Qian, J., and Dong, C.-M. (2019). NIR-responsive polypeptide nanocomposite generates no gas, mild photothermia, and chemotherapy to reverse multidrug-resistant cancer. *Nano Lett.* 19, 4362–4370. doi:10.1021/acs.nanolett.9b00975

Fan, W., Yung, B. C., and Chen, X. (2018). Stimuli-responsive no release for on-demand gas-sensitized synergistic cancer therapy. *Angew. Chem. Int. Ed.* 57, 8383–8394. doi:10.1002/anie.201800594

Fernandes, N., Rodrigues, C. F., Moreira, A. F., and Correia, I. J. (2020). Overview of the application of inorganic nanomaterials in cancer photothermal therapy. *Biomaterials Sci.* 8, 2990–3020. doi:10.1039/d0bm00222d

Freund, E., and Bekeschus, S. (2020). Gas plasma-oxidized liquids for cancer treatment: Pre-clinical relevance, immuno-oncology, and clinical obstacles. *IEEE Trans. Radiat. Plasma Med. Sci.* 5, 761–774. doi:10.1109/trpms.2020.3029982

Gao, G., Sun, X., and Liang, G. (2021). Nanoagent-promoted mild-temperature photothermal therapy for cancer treatment. *Adv. Funct. Mater.* 31, 2100738. doi:10.1002/adfm.202100738

Giuffrè, A., Tomé, C. S., Fernandes, D. G., Zuhra, K., and Vicente, J. B. (2020). Hydrogen sulfide metabolism and signaling in the tumor microenvironment. *Tumor Microenviron.* 1219, 335–353. doi:10.1007/978-3-030-34025-4_17

James, M., Dixit, A., Robinson, B., Frampton, C., and Davey, V. (2019). Outcomes for patients with non-metastatic triple-negative breast cancer in New Zealand. *Clin. Oncol.* 31, 17–24. doi:10.1016/j.clon.2018.09.006

Kozics, K., Sramkova, M., Kopecka, K., Begerova, P., Manova, A., Krivosikova, Z., et al. (2021). Pharmacokinetics, biodistribution, and biosafety of PEGylated gold nanoparticles *in vivo*. *Nanomaterials* 11, 1702. doi:10.3390/nano11071702

Li, G.-H., Wang, D.-L., Hu, Y.-D., Pu, P., Li, D.-Z., Wang, W.-D., et al. (2010). Berberine inhibits acute radiation intestinal syndrome in human with abdomen radiotherapy. *Med. Oncol.* 27, 919–925. doi:10.1007/s12032-009-9307-8

Li, X.-D., Wang, Z., Wang, X.-R., Shao, D., Zhang, X., Li, L., et al. (2019). Berberine-loaded Janus gold mesoporous silica nanocarriers for chemo/radio/photothermal therapy of liver cancer and radiation-induced injury inhibition. *Int. J. Nanomedicine* 14, 3967–3982. doi:10.2147/ijn.s206044

Liu, S., Li, W., Dong, S., Zhang, F., Dong, Y., Tian, B., et al. (2020). An all-in-one theranostic nanoplatform based on upconversion dendritic mesoporous silica nanocomposites for synergistic chemodynamic/photodynamic/gas therapy. *Nanoscale* 12, 24146–24161. doi:10.1039/d0nr06790c

Lyons, T. G. (2019). Targeted therapies for triple-negative breast cancer. *Curr. Treat. options Oncol.* 20, 82–13. doi:10.1007/s11864-019-0682-x

Penninckx, S., Heuskin, A.-C., Michiels, C., and Lucas, S. (2020). Gold nanoparticles as a potent radiosensitizer: A transdisciplinary approach from physics to patient. *Cancers* 12, 2021. doi:10.3390/cancers12082021

Tang, Y., Wang, T., Feng, J., Rong, F., Wang, K., Li, P., et al. (2021). Photoactivatable nitric oxide-releasing gold nanocages for enhanced hyperthermia treatment of biofilm-associated infections. *ACS Appl. Mater. Interfaces* 13, 50668–50681. doi:10.1021/acsami.1c12483

Thakar, S. B., Ghorpade, P. N., Shaker, B., Lee, J., and Na, D. (2021). Gas-mediated cancer therapy combined with starvation therapy, ultrasound therapy, chemotherapy, radiotherapy, and photodynamic therapy: A review. *Environ. Chem. Lett.* 19, 2981–2993. doi:10.1007/s10311-021-01218-7

Wang, C., Wang, Y., Zhang, L., Miron, R. J., Liang, J., Shi, M., et al. (2018). Pretreated macrophage-membrane-coated gold nanocages for precise drug delivery for treatment of bacterial infections. *Adv. Mater.* 30, 1804023. doi:10.1002/adma.201804023

Wang, P. G., Xian, M., Tang, X., Wu, X., Wen, Z., Cai, T., et al. (2002). Nitric oxide donors: Chemical activities and biological applications. *Chem. Rev.* 102, 1091–1134. doi:10.1021/cr000040l

Wang, Z., Chang, Z.-M., Shao, D., Zhang, F., Chen, F., Li, L., et al. (2019). Janus gold triangle-mesoporous silica nanoplatforms for hypoxia-activated radio-chemo-photothermal therapy of liver cancer. *ACS Appl. Mater. interfaces* 11, 34755–34765. doi:10.1021/acsami.9b12879

Wu, Y., Su, L., Yuan, M., Chen, T., Ye, J., Jiang, Y., et al. (2021). *In vivo* X-ray triggered catalysis of H2 generation for cancer synergistic gas radiotherapy. *Angew. Chem.* 133, 12978–12985. doi:10.1002/ange.202100002

Xia, D.-L., Wang, Y.-F., Bao, N., He, H., Li, X.-D., Chen, Y.-P., et al. (2014). Influence of reducing agents on biosafety and biocompatibility of gold nanoparticles. *Appl. Biochem. Biotechnol.* 174, 2458–2470. doi:10.1007/s12010-014-1193-7

Xie, J., Wang, C., Wang, N., Zhu, S., Mei, L., Zhang, X., et al. (2020). Graphdiyne nanoradioprotector with efficient free radical scavenging ability for mitigating radiation-induced gastrointestinal tract damage. *Biomaterials* 244, 119940. doi:10.1016/j.biomaterials.2020.119940

Yang, S. T., Liu, Y., Wang, Y. W., and Cao, A. (2013). Biosafety and bioapplication of nanomaterials by designing protein–nanoparticle interactions. *Small* 9, 1635–1653. doi:10.1002/smll.201201492

Yu, L., Hu, P., and Chen, Y. (2018). Gas-generating nanoplatforms: Material chemistry, multifunctionality, and gas therapy. *Adv. Mater.* 30, 1801964. doi:10.1002/adma.201801964

Zhang, H., Gao, Z., Li, X., Li, L., Ye, S., and Tang, B. (2021). Multiple-mRNA-controlled and heat-driven drug release from gold nanocages in targeted chemo-photothermal therapy for tumors. *Chem. Sci.* 12, 12429–12436. doi:10.1039/d1sc02017j

Zuo, S., Zhang, Y., Wang, Z., and Wang, J. (2022). Mitochondria-targeted mesoporous titanium dioxide nanoplatform for synergistic nitric oxide gas-sonodynamic therapy of breast cancer. *Int. J. Nanomedicine* 17, 989–1002. doi:10.2147/ijn.s348618

frontiers | Frontiers in Bioengineering and Biotechnology

TYPE Original Research
PUBLISHED 01 February 2023
DOI 10.3389/fbioe.2023.1132591

Check for updates

OPEN ACCESS

EDITED BY
Dan Shao,
South China University of Technology, China

REVIEWED BY
Jinbing Xie,
Southeast University, China
Zhe Chen,
Shanxi Medical University, China
Shuyue Ye,
University of Texas Southwestern Medical Center, United States

*CORRESPONDENCE
Gang Shen,
gshen119@163.com
Tao Yang,
tyang0920@suda.edu.cn

†These authors have contributed equally to this work

SPECIALTY SECTION
This article was submitted to Biomaterials, a section of the journal Frontiers in Bioengineering and Biotechnology

RECEIVED 27 December 2022
ACCEPTED 19 January 2023
PUBLISHED 01 February 2023

CITATION
Luo J, Miao Z, Huang X, Yang Y, Liu M, Shen G and Yang T (2023), Translational albumin nanocarrier caging photosensitizer for efficient cancer photodynamic therapy.
Front. Bioeng. Biotechnol. 11:1132591.
doi: 10.3389/fbioe.2023.1132591

COPYRIGHT
© 2023 Luo, Miao, Huang, Yang, Liu, Shen and Yang. This is an open-access article distributed under the terms of the Creative Commons Attribution License (CC BY). The use, distribution or reproduction in other forums is permitted, provided the original author(s) and the copyright owner(s) are credited and that the original publication in this journal is cited, in accordance with accepted academic practice. No use, distribution or reproduction is permitted which does not comply with these terms.

Translational albumin nanocarrier caging photosensitizer for efficient cancer photodynamic therapy

Jie Luo[1†], Zhijun Miao[1,2†], Xinglong Huang[1], Yifan Yang[1], Ming Liu[1], Gang Shen[2*] and Tao Yang[1*]

[1]Jiangsu Key Laboratory of Neuropsychiatric Diseases, College of Pharmaceutical Sciences, Soochow University, Suzhou, China, [2]Department of Urology, Dushu Lake Hospital Affiliated to Soochow University, Suzhou, China

It still remains a great challenge to efficiently treat malignant cancers which severely threaten human health. Photodynamic therapy (PDT) as a localized therapeutic modality has improved the therapeutic efficacy via chemical damage through reactive oxygen species (ROS). However, their efficacy is severely hampered by insufficient targeted delivery of photosensitizers owing to the lack of suitable carrier with facile preparation process and the clinical applicability. Herein, we applied clinically approved human serum albumin as the nanoreactor to encapsulate photosensitizers Chlorin e6 (Ce6) for enhancing their tumor accumulation and subsequently potent PDT effect against bladder cancer models. Albumin-loaded Chlorin e6 nanoparticles (CA-NPs) with rational nanoscale size exhibit increased reactive oxygen species production and excellent resistance to photobleaching. Moreover, CA-NPs could be efficiently internalized by tumor cells and locate in the lysosome, while they rapidly translocate to cytosol after irradiation to induce remarkable cytotoxicity (IC_{50} ~5.8 μg/ml). Furthermore, CA-NPs accumulate effectively in tumor tissue to afford total eradication of murine bladder tumor after single injection. More importantly, we also evidence the superior PDT effect in fresh human bladder tumor tissues via abundant reactive oxygen species generation and subsequent cell apoptosis. These findings demonstrate that human serum albumin acts as a universal tool to load small organic photoactivatable molecule with remarkable effectiveness and readiness for clinical translation.

KEYWORDS

human serum albumin, photosensitizer, target delivery, photodynamic therapy, bladder cancer

1 Introduction

Aggressive cancers have caused leading human death during the past few years, significant challenges still exist to explore effective solutions against various types of cancers to prolong the survival of cancer patients (Sung et al., 2021). Although chemotherapy and surgery are commonly applied in clinic settings (Nencioni et al., 2018; Joshi and Badgwell, 2021), the overall outcome remains relatively low due to their intrinsic limitations such as severe side effects, drug resistance, poor targeting ability, and rapid recurrence, finally leading to the failure of cancer treatment (Patel et al., 2020; Labrie et al., 2022).

Photodynamic therapy (PDT) as a localized therapeutic modality which activates photosensitizers specifically within targeted organs upon light irradiation to induce chemical damage *via* reactive oxygen species (ROS) has been used in clinic against various

cancers including superficial skin lesions and lung cancers for over 40 years (Li et al., 2020; Pham et al., 2021). However, existing PDT solutions suffer from poor blood circulation, limited tumor accumulation, and relatively short excitation wavelength of photosensitizers, thus severely hampering the *in vivo* therapeutic efficiency of PDT (Yang et al., 2021). With the development of nanotechnology, extensive efforts have been made to develop efficient nanocarriers incorporated with photosensitizer to improve their targeting ability (Xie et al., 2021). For example, polymeric materials with tunable surface properties (e.g., charge, size, and ligand installing) were applied to load photosensitizers for enhanced tumor delivery (Zhen et al., 2019; Zhu et al., 2020; Yi et al., 2021). Also, photosensitizer could be covalently conjugated to the surface of nanocarriers (e.g., inorganic nanomaterials, silica materials) *via* chemical modification to increase their tumor accumulation (Wang et al., 2019; Zheng et al., 2021). However, the potential clinic translation of these solutions is distinctly restricted by complex fabrication process and unapproved raw materials. Therefore, additional attentions should be focused to develop suitable nanocarriers with readiness for clinical translation and convenient preparation process.

Abraxane that is composed of human serum albumin (HSA) and paclitaxel with size around 130 nm has achieved huge success in clinic to reduce the side effects in diverse cancers (Yardley, 2013; Gianni et al., 2018). Inspired by this approach, we and other groups recently demonstrated that albumin and other proteins could be applied as a nanoreactor to allow the growth of theranostic inorganic nanocrystals such as tellurium (Yang et al., 2017), gadolinium oxide (Zhou et al., 2017; Lv et al., 2018), copper sulfide (Yang et al., 2016), manganese oxide (Li et al., 2022; Zhai et al., 2022) inside albumin or transferrin nanocage *via* precipitation reaction or redox reaction, exhibiting superior tumor targeting ability and high drug loading efficiency. However, incorporating small molecule photosensitizer inside albumin nanoreactor remains largely unexplored with limited solutions. Herein, we employed clinically approved HSA as the carrier to encapsulate photosensitizer Chlorin e6 (Ce6) *via* well-defined precipitation inside albumin nanocage for targeted delivery of Ce6 and potent PDT effect against murine bladder cancer and restricted human bladder tumor tissue. The albumin-loaded Ce6 nanoparticles (CA-NPs) with suitable size distribution showed improved photostability and photoactivity, as well as excellent resistance to photobleaching. Moreover, CA-NPs efficiently accumulated in tumor site and rapidly generate ROS after irradiation *in vivo*, resulting in an increased cytotoxicity to eradicate murine bladder cancer after single injection. Importantly, CA-NPs also exhibited abundant ROS production in freshly restricted human bladder tumor tissue to induce effective cell apoptosis upon irradiation. These results demonstrate the HSA as a universal nanocarrier to incorporate small molecule drugs with enhanced effectiveness and clinical applicability.

2 Materials and methods

2.1 Synthesis and characterization of CA-NPs

For the preparation of CA-NPs, Ce6 (Macklin, China) was dissolved in aqueous solution of pH 12 with concentration of 1 mg/ml. HSA (CSL Behring GmbH) was diluted to 10 mg/ml. Subsequently, Ce6 solution was added to HSA solution in a 5:1 (v/v) ratio under stirring. After the mixture was stirred for 5 min, hydrochloric acid (HCl) was used to adjust the pH to 5.5. The mixture was then stirred for another 2 h at room temperature. The resulting CA-NPs was transferred into Millipore and centrifuged at 2000 rpm for 10 min to remove free Ce6, and stored at PBS for further use.

For the characterization of CA-NPs, the morphology and size of CA-NPs were characterized by transmission electron microscope (Hitachi HT-7700, Japan) and dynamic light scattering (Malvern Zetasizer ZS90, England). The absorbance of CA-NPs was measured by UV-vis spectra (UV-2600, Shimadzu).

For determination of drug loading of CA-NPs, CA-NPs were prepared and purified as above, and concentration of Ce6 wad measured by ultraviolet spectrometer. Then, CA-NPs solution was freeze-dried and recorded the weight. The drug loading was calculated by the formula: loading efficiency (%) = weight of Ce6 encapsulated in CA-NPs/weight of CA-NPs × 100%.

2.2 ROS production photostability, and drug release

Free Ce6 and CA-NPs were diluted with the ultrapure water to 10 μg/ml, and then irradiated at the excitation wavelength of 660 nm with the power density of 0.15 W/cm^2 (FS-Optics, China). Simultaneously, the temperature was monitored with an electronic thermometer for 5 min. Besides, the stability of them were measured by UV-vis spectrophotometer under the same condition. The absorbance at the wavelength of 660 nm was monitored within 5 min.

1,3-diphenylisobenzofuran (DPBF) was employed as singlet oxygen probe to detect the generation of singlet oxygen. CA-NPs and free Ce6 with the concentration of 1.0 μg/ml (Ce6) were mixed with 30.0 μM DPBF under vigorous stirring, followed by 5 min irradiation (660 nm laser, 0.15 W/cm^2). Meanwhile, the absorbance of DPBF at 420 nm was monitored by UV-vis spectrophotometer during the irradiation.

The drug release behaviors of Ce6 from CA-NPs were evaluated using the dialysis method. CA-NPs with concentration of 100 μg/ml Ce6 was dialyzed in various media including pH 5.0 buffer, pH 6.5 buffer and pH 7.4 buffer and the same concentration of free Ce6 was served as the control group. The various formulations (1.0 ml for each sample) were separately added to dialysis bags incubated in 50 ml of release buffer. Then, the *in vitro* releases were performed in a contrast temperature oscillator shaker at 37°C. Each 0.5 ml sample was taken at 0.5, 1, 2, 4, 8, 12, 24, and 48 h with the replacement of an equal volume of fresh medium. The concentrations of Ce6 were measured using microplate reader (TECAN, Switzerland) at the wavelength of 660 nm.

2.3 Cell lines and cell culture

MB49-bladder carcinoma cells (ATCC, United States) were cultured in Dulbecco's modified Eagle's medium (DMEM, Gibco, America) supplemented with 10% fetal bovine serum (FBS, Bovogen Biological, Australia), 100 U/mL penicillin (Gibco, America) and 100 μg/ml streptomycin (Gibco, America). All the cells were grown in an atmosphere with 37°C and 5% CO_2.

2.4 Cellular uptake and endocytic pathways

To quantify the cellular uptake of Ce6, murine MB49 cells were seeded in 2×10^6 cells per well in 6-well plates and treated with PBS, free Ce6 and CA-NPs for 24 h at concentrations of 10 μg/ml (Ce6), respectively. Then, the cells were washed, harvested and suspended in a 2% bovine serum albumin in PBS solution and analyzed *via* flow cytometry (BD FACSVerse, America) using a 640 nm excitation laser and 780/15 filter configuration.

To determine the endocytic pathways of CA-NPs, MB49 cells were seeded in 6-well plates and treated with clathrin-dependent endocytosis inhibitor chlorpromazine (10 μg/ml), caveolin-dependent endocytosis inhibitor nystatin dihydrate (5.0 μg/ml) and macropinocytosis inhibitor amiloride (100.0 μg/ml) for 2 h. Then, CA-NPs (10.0 μg/ml) were added into the culture medium for further 24 h incubation, followed by the same procedure as used for cellular uptake. The data were processed and analyzed using FlowJo (v.10.5).

2.5 Cell viability assay

MTT assay (Macklin, China) was used to examine the cytotoxicity of free Ce6 and CA-NPs against MB49 cells. MB49 cells were seeded in a 96-well plate at the density of 5×10^3 cells per well and cultured overnight. After that, free Ce6 and CA-NPs with the concentration of 0, 2, 4, 6, 8, 10 and 12 μg/ml were added into the plate to co-incubate with cells for 24 h. Then, the medium was removed and the cells were washed with PBS, followed by adding fresh medium and 5 min irradiation (660 nm, 0.15 W/cm^2). After another 24 h incubation, the cell viability was evaluated using MTT assay. After 4 h of incubation at 37°C and 5% CO_2, the absorbance at 490 nm was measured by microplate reader (TECAN, Switzerland).

2.6 Intracellular distribution, ROS detection and lysosomal disruption

MB49 cells were seeded in the glass-bottom confocal dishes and treated with 5 μg/ml of rhodamine B-labeled CA-NPs (CA-NPs-RB) for 24 h, Then, the cells were washed, irradiated for 5 min (660 nm, 0.15 W/cm^2) and stained with 100 nM Lysotracker Green DND-26 (Beyotime, China) and Hoechst33342 (Beyotime, China). For ROS detection, 2′,7′-dichlorodihydrofluorescein diacetate (DCFH-DA) was used as singlet oxygen probe to examine the generation of ROS. After incubation with free Ce6 or CA-NPs (5 μg/ml), the cells were treated with 1 μM of DCFH-DA (Beyotime, China) for 30 min before irradiation. Then, the cells were irradiated for 5 min (660 nm, 0.15 W/cm^2), followed by staining with Hoechst33342 (1 μg/ml) for 8 min. To observe the disruption of lysosomal membranes, acridine orange (AO) was used as an intracellular indicator of acidic organelle integrity in cells. MB49 cells were treated with PBS, free Ce6 and CA-NPs at 5 μg/ml Ce6 for 12 h. Then, the cells were irradiated for 5 min (660 nm, 0.15 W/cm^2) and 2 mM vitamin C was incubated with cells before irradiation, followed by staining with AO working solution (5 μM) for 20 min, the cells were washed and further washed three times with PBS before being observation. The intracellular fluorescence was observed by confocal laser scanning microscope (CLSM) and the median fluorescence intensity (MFI) of cells was counted by ImageJ.

2.7 Measurement of mitochondrial membrane potential

Mitochondrial membrane potential was recorded by using the fluorescent indicator 5,5′,6,6′-tetrachloro-1,1′,3,3′-tetraethyl-imidacarbocyanine iodide (JC-1) molecular probes (Beyotime, China). MB49 cells treated with CA-NPs were irradiated for 5 min with the power density of 0.15 W/cm^2. After further incubation for 30 min, the cells were incubated with JC-1 working solution for 20 min and Hoechst33342 (1 μg/ml) for 8 min. Then, the cells were washed and observed by CLSM within 30 min. The MFI of JC-1 aggregates and monomers were counted by ImageJ.

2.8 Cell apoptosis detection

The proportion of cell apoptosis induced by CA-NPs was detected by Annexin V FITC/PI Apoptosis kit (Multi Science, China). MB49 cells treated with CA-NPs and irradiated (0.15 W/cm^2, 5 min) were harvested and suspended with binding buffer. Then, the cells were stained with Annexin V-FITC/PI working solution for 5 min and subjected to flow cytometry detection.

2.9 *In vivo* and *ex vivo* distribution

6–8 weeks C57BL/6J mice were subcutaneously injected with 1×10^6 MB49 cells (50 μl) to establish subcutaneous bladder tumor models. When the tumor volume reached to 100 mm^3 (tumor volumes were measured by a vernier caliper and were calculated as following: $V_{tumor} = 0.5 \times \text{length} \times \text{width}^2$), the mice were divided randomly into two groups (n = 3) and then were respectively injected with Ce6 and CA-NPs (5.0 mg/kg) *via* tail vein, followed by *in vivo* imaging at the excitation of 660 nm using IVIS spectrum (Perkin Elmer, United States) at 0, 2, 6, 12, 24, 48 h. For *ex vivo* distribution study, the mice bearing MB49 tumor models were sacrificed after 12 h post-injection of CA-NPs or free Ce6, then the major organs including heart, liver, spleen, lung, kidney and tumor were utilized for *ex vivo* imaging. The fluorescence intensities were obtained by Living Image software (4.5).

2.10 ROS production in tumor tissues

C57BL/6J mice bearing MB49 tumors were divided randomly into six groups and injected with PBS, free Ce6 and CA-NPs *via* tail vein at the dose of 5.0 mg/kg, respectively. Then the mice were suffered with or without 660 nm irradiation (0.15 W/cm^2, 5 min) after 12 h post-injection. In addition, DCFH-DA (10 μM) was prepared for intratumoral injection half an hour before irradiation. The mice were sacrificed after 1 h post-irradiation, then the MB49 tumors were cut into slices by freezing microtome for DCFH-DA staining assay. The tumors were washed with PBS three times, then treated with Hoechst33342 (1 μg/ml) for 10 min. We further acquired the images of slices using CLSM.

2.11 *In vivo* infrared imaging and anticancer efficacy

C57BL/6J mice bearing MB49 tumors were intravenously injected with PBS, free Ce6 and CA-NPs at the dose of 5.0 mg/kg. Then, the mice were irradiated at 0.15 W/cm^2 for 5 min at 12 h post injection. Temperature of the tumor region under irradiation were monitored using an infrared camera during 5 min. The temperature of tumor region was measured by Smartview4.3.

C57BL/6J mice bearing MB49 tumors were randomly divided into six groups and treated with PBS, PBS plus irradiation, free Ce6, free Ce6 plus irradiation, CA-NPs, CA-NPs plus irradiation at the dose of 5.0 mg/kg on day 0, followed by 660 nm laser after 12 h post-injection. The tumor size and body weight were measured during the next 21 days. Then the mice were scarified on the 21st day and tumor weight were measured by electronic balance (Sartorius, Germany).

2.12 *Ex vivo* ROS generation and apoptotic analysis of resected human bladder tumor tissue

Patients provided consent for the use of biospecimens for research as approved by the Clinical Trial Ethics Committee of Dushu Lake Hospital Affiliated of Soochow University. Within 30 min of surgical resection at Dushu Lake Hospital Affiliated of Soochow University, human bladder tumor tissues were submerged in Roswell Park Memorial Institute 1640 media (Gibco, America) supplemented with 10% FBS, 1% insulin-transferrin-selenium, 1% GlutaMAX (Gibco, America), and 1% penicillin-streptomycin (Gibco, America) and divided into twelve sections, followed by intratumoral injection with PBS and CA-NPs at the dose of 1 μg Ce6 for another incubation of 1 h. Then some of them were irradiated at the density of 0.15 W/cm^2 for 5 min. After another 1 h incubation, half of these samples were cut into slices by freezing microtome for immunofluorescence staining of TUNEL assay. And the others were dissociated with 1 mg/ml collagenase II and 0.1 mg/ml DNase I in 1640 medium at 37°C for 45 min after irradiation. The single cells were harvested and counted, and 1 × 10^6 cells suspended in staining buffer were used for TUNEL staining measured by flow cytometry.

2.13 Statistical analysis

All experiments were carried out at least three times and data were presented as mean ± standard deviation. The differences between two groups were evaluated using Student's t-test, whereas the statistical analysis of multiple groups was performed using the one-way ANOVA in GraphPad Prism 8. Significant differences are indicated as $^*p < 0.05$, $^{**}p < 0.01$, $^{***}p < 0.001$.

3 Results and discussion

3.1 Preparation and characterization of CA-NPs

In a typical synthesis process, HSA was applied as a nanoreactor to allow the precipitation reaction of Ce6 within the hollow albumin nanocage. Firstly, Ce6 dissolved in basic solutions (pH 12) was mixed with HSA to form the Ce6-HSA complex, and the pH of the solution was subsequently adjusted to 5.5 using HCl buffer with ionized Ce6 molecular tuning to be non-ionized, followed by vigorous stirring under room temperature for 4 h for the growth of CA-NPs (Figure 1A). Then the obtained solution was purified *via* ultrafiltration for further use. As shown in Figure 1B, the round-like CA-NPs exhibited uniform size of ~18.5 ± 3.2 nm upon the observation using transmission electron microscopy with the drug loading of 9.6 ± 1.1%, while the light scattering diameter of CA-NPs was slightly larger (~46.9 nm with the PDI value of 0.26) owing to the outer shell (Figure 1C). Furthermore, the diameter of CA-NPs remained relatively unchanged in aqueous solution, PBS and culture medium during 1 week, indicating the superior stability (Supplementary Figure S1). Meanwhile, CA-NPs was negatively charged after loading Ce6 into the HSA nanocage (Figure 1D). Next, typical absorbance of Ce6 at 660 nm and 410 nm confirmed the successful incorporation of Ce6 in CA-NPs, and the CA-NPs showed obvious red-shifted peak of Ce6, suggesting the *J*-type aggregation of Ce6 inside HSA nanocage (Figure 1E). Drug release behavior plays the vital role in their biological performance, and thus the drug releases from CA-NPs were evaluated in response to physiological environment and acidic tumor microenvironment. As shown in Supplementary Figure S2, the accumulative release of CA-NPs within 48 h was less than 10% due to the hydrophobic property of the Ce6, indicating a preferable ability to minimize their undesirable release during blood circulation.

According to the clinical setting for *in vivo* PDT against malignant diseases, we choose 0.15 W/cm^2 for 660 nm irradiation which is well tolerated for human and would not cause any significant side effects (Katsikanis et al., 2020). To measure photothermal effect and ROS production of CA-NPs under irradiation at human tolerance and clinically approved power density of 0.15 W/cm^2 with the wavelength of 660 nm, DPBF as applied as a specific probe to detect the ROS generation via monitoring the absorbance at 420 nm, which possesses a highly specific reactivity towards singlet oxygen forming an endoperoxide 1,2-dibenzoylbenzene, resulting a decrease absorbance at 420 nm. As shown in Figure 1F, CA-NPs exhibited higher ROS production as compared to free Ce6 without any increase of solution temperature (Supplementary Figure S3) and the ROS production of CA-NPs group was 1.6 times higher than that in the free group. Moreover, we then tested the photobleaching of CA-NPs and free Ce6 during irradiation for 5 min. Similarly, CA-NPs showed enhanced resistance against photobleaching as compared to free Ce6. It was indicated that the absorbance of free Ce6 underwent a sharp decrease within 5 min due to the rapid photobleaching of free Ce6 under irradiation. However, the absorbance of CA-NPs still exhibited sufficient absorbance owing to significant improvement of photostability of Ce6 in CA-NPs (Figure 1G). Collectively, the increased photostability and photoactivity confer the potential of CA-NPs to yield robust photodynamic therapeutic effect against intractable cancers both *in vitro* and *in vivo*.

3.2 Cellular uptake, endocytic pathway and subcellular translocation

To evaluate the ability of CA-NPs to be internalized by cancer cells, we applied flow cytometry to quantitatively measure the cellular

10.3389/fbioe.2023.1132591

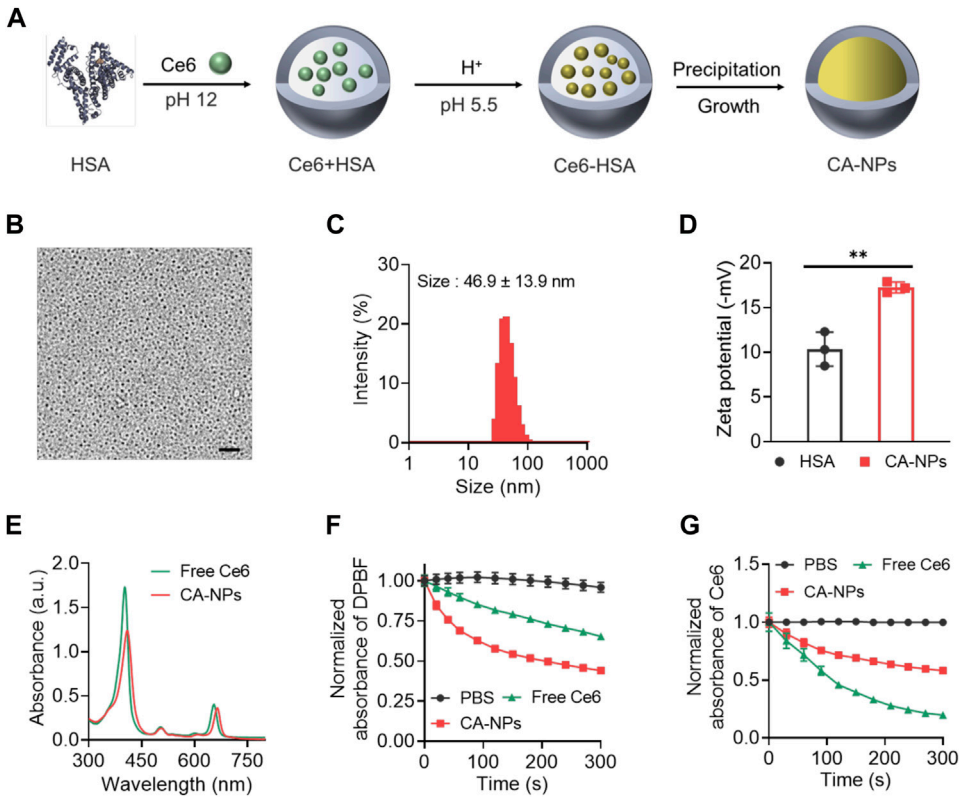

FIGURE 1
Synthesis and characterization of CA-NPs **(A)**. Preparation of CA-NPs through Albumin Nanoreactor. **(B)** Transmission electron microscope image of CA-NPs. Scale bar: 200 nm. **(C)** Size distribution of CA-NPs. **(D)** Zeta potential of HSA and CA-NPs. (n = 3; $^{**}p < 0.01$) **(E)** UV-Vis absorption spectrum of free Ce6 and CA-NPs at the concentration of 5 μg/ml Ce6. **(F)** ROS generation of free Ce6 and CA-NPs under 5 min irradiation (660 nm, 0.15 W/cm^2) using DPBF as a probe. **(G)** UV-Vis absorbance of PBS, free Ce6 and CA-NPs under irradiation during 5 min.

uptake of CA-NPs in murine bladder cancer cell lines (MB49) using free Ce6 as a control. At 24 h post-incubation of CA-NPs and free Ce6 at the dose of 5 μg/ml with MB49 cells, significantly increased internalization amount was observed in CA-NPs and was 3.5-fold higher than that of free Ce6 group (Figures 2A,Figures 2B). Moreover, chlorpromazine as an inhibitor of clathrin-dependent pathway distinctly decreased the cellular uptake of CA-NPs, indicating the internalization was depended on clathrin pathway. Meanwhile, when incubated CA-NPs with MB49 cells under 4°C, the intracellular amount of CA-NPs was declined to 55% as compared to PBS group (Figures 2C,D), confirming the energy also participated in the cellular uptake behavior. Next, we investigated the intracellular ROS production of CA-NPs upon irradiation using DCFH-DA as a probe. Both CA-NPs and free Ce6 showed negligible ROS production without irradiation, while durable green fluorescence from CA-NPs group emerged upon irradiation (Figure 2E) and was 1.6-fold higher than that of free Ce6 group (Figure 2F), reasonably owing to enhanced photoactivity and increased cellular uptake. We further verified the capacity of CA-NPs to induce lysosomal disruption under irradiation using AO staining. The acidic lysosomes in MB49 cells treated with PBS or PBS plus irradiation exhibited overlapped orange fluorescence between red and green fluorescence. And the red fluorescence was significantly decreased after the treatment of free Ce6 and CA-NPs upon irradiation. However, red fluorescence could be clearly observed in the MB49 cells pre-incubated with ROS scavenger (vitamin C), indicating that ROS production from CA-NPs upon irradiation participate in the disruption of lysosomal membranes upon irradiation (Supplementary Figure S4), which is in favor of the translocation of released Ce6 into cytoplasm for enhancing cytotoxicity. Considering the intracellular target of ROS to damage cancer cells is nucleus, we then investigated the subcellular location of CA-NPs with and without irradiation. MB49 cells were firstly labelled with Lysotracker Green and Hoechst33342 to distinguish lysosome and nucleus. At 6 h post-incubation of CA-NPs labelled with rhodamine B, preferable co-localization rate (92.1%) of CA-NPs with lysosome was observed as indicated by the merged yellow fluorescence, and CA-NPs rapidly translocated to cytosol upon irradiation with decreased co-localization rate (54.3%) *via* photo internalization effect (Figure 2G), which is favorable for causing cell damage.

3.3 Cytotoxicity and apoptotic level of CA-NPs

To evaluate the cytotoxicity of CA-NPs against MB49 cells, we firstly applied the JC-1 assay to test mitochondrial membrane potential (ΔΨm) that correlated with cytotoxicity under oxidized stress conditions *via* ROS, in which JC-1 emits strong red fluorescence for high ΔΨm and green fluorescence for low

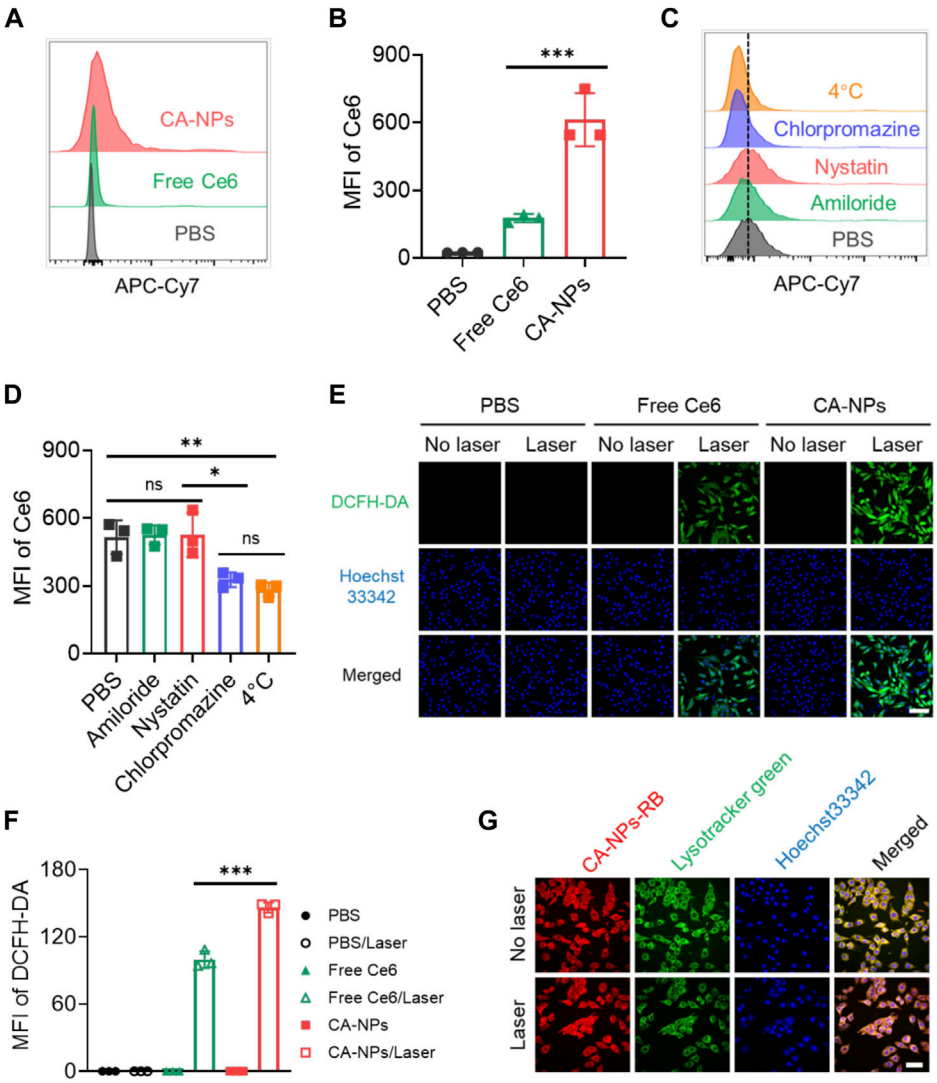

FIGURE 2
Cellular uptake, endocytic pathway and subcellular translocation of CA-NPs. **(A,B)** Flow cytometric quantification of the uptake of PBS, free Ce6 and CA-NPs at the dose of 10 μg/ml by MB49 cells for 24 h **(C,D)** Flow cytometric quantification of the uptake of CA-NPs by MB49 cells treated with PBS, amiloride, filipin and chlorpromazine at 37°C, and PBS at 4 °C. **(E,F)** Intracellular ROS generation and MFI of free Ce6 and CA-NPs under 660 nm irradiation (0.15 W/cm^2, 5 min) or not at the dose of 5 μg/ml detected by DCFH-DA probe. Scale bar: 100 μm. **(G)** Subcellular distribution of CA-NPs labelled with rhodamine B under irradiation or not. Scale bar: 50 μm. (n = 3; ns: no significance, *$p < 0.05$, **$p < 0.01$, ***$p < 0.001$).

ΔΨm, respectively. Ignorable change of red fluorescence was observed from the tumor cells treated with CA-NPs in the absence of irradiation, while CA-NPs showed minimal red fluorescence and emitted strong green fluorescence upon light exposure as compared to that of saline group and free Ce6 group (Figure 3A, Supplementary Figure S5), suggesting that CA-NPs possess a sharply decreased ΔΨm that reveals robust cytotoxicity against tumor cells. Subsequently, CA-NPs induced considerable photodynamic effect against MB49 cells with the IC_{50} value of 5.8 μg/ml upon irradiation, while free Ce6 with relatively decreased cellular uptake showed 1.5-fold higher IC_{50} value of 8.9 μg/ml (Figure 3C). Meanwhile, both free Ce6 and CA-NPs failed to arouse any toxicity in the absence of irradiation (Figure 3B). Next, Annexin V assay were used to measure the apoptotic levels of CA-NPs. As indicated in Figure 3D, CA-NPs led to significantly elevated apoptosis, especially the late stage, upon irradiation as compared with free Ce6 group (Figure 3E), further evidencing the potent PDT effect against MB49 cells.

3.4 *In vivo* targeting ability of CA-NPs

To unravel the *in vivo* targeting ability of CA-NPs, we firstly constructed the murine bladder tumor model via subcutaneous injection of MB49 cells (1×10^6) into C57BL/6J mice. When the tumor volume reaches 100 mm^3, CA-NPs at the dose of 5.0 mg/kg were intravenously injected into mice bearing MB49 bladder tumor model using free Ce6 as a control. Then, the mice were observed using IVIS imaging system to track the targeting behavior of CA-NPs by fluorescent signals from Ce6. Firstly, free Ce6 distributed quickly in the whole mice and were also cleared out of mice bearing

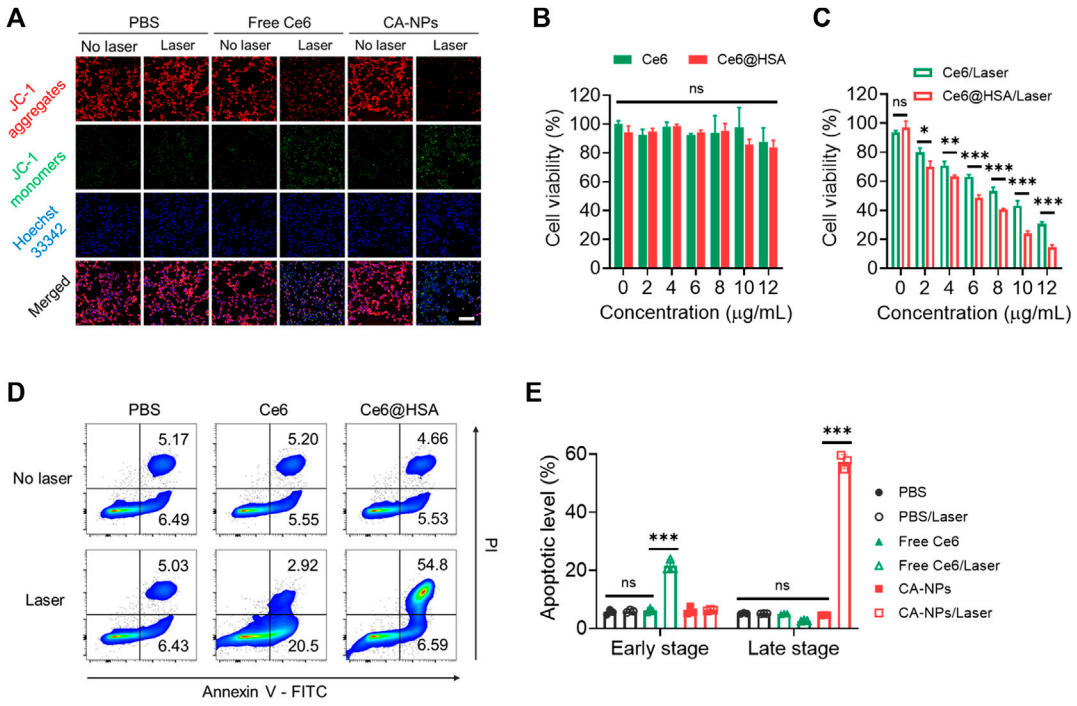

FIGURE 3
Cytotoxicity and tumor-killing mechanism of CA-NPs. **(A)** Mitochondrial membrane potential of MB49 cells treated with PBS, free Ce6 and CA-NPs at the dose of 5 μg/ml Ce6 detected by JC-1 assay. Scale bar: 100 μm. **(B,C)** Cell viability of MB49 cells treated with free Ce6, CA-NPs under 660 nm irradiation or not (0.15 W/cm^2, 5 min). **(D,E)** Flow cytometric measurement of the apoptotic percentages of MB49 cells after 24 h incubation with PBS, free Ce6 and CA-NPs under irradiation or not. (n = 3; ns: no significance, *$p < 0.05$, **$p < 0.01$, ***$p < 0.001$).

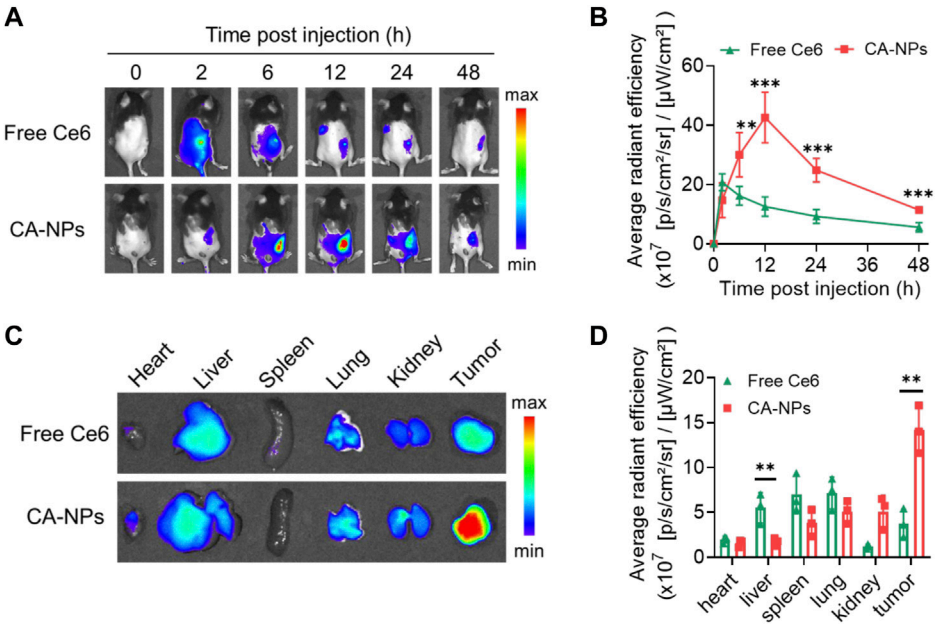

FIGURE 4
In vivo targeting ability of CA-NPs **(A,B)** *In vivo* fluorescence images and fluorescence intensities at tumor sites of MB49 tumor-bearing mice with intravenous injection of free Ce6 and CA-NPs at the dose of 5.0 mg/kg during 48 h (n = 4; **$p < 0.01$, ***$p < 0.001$). **(C,D)** *Ex vivo* fluorescence images and fluorescence intensities of various tissues extracted at 12 h from MB49 tumor-bearing mice with intravenous injection of free Ce6 and CA-NPs. (n = 3; **$p < 0.01$).

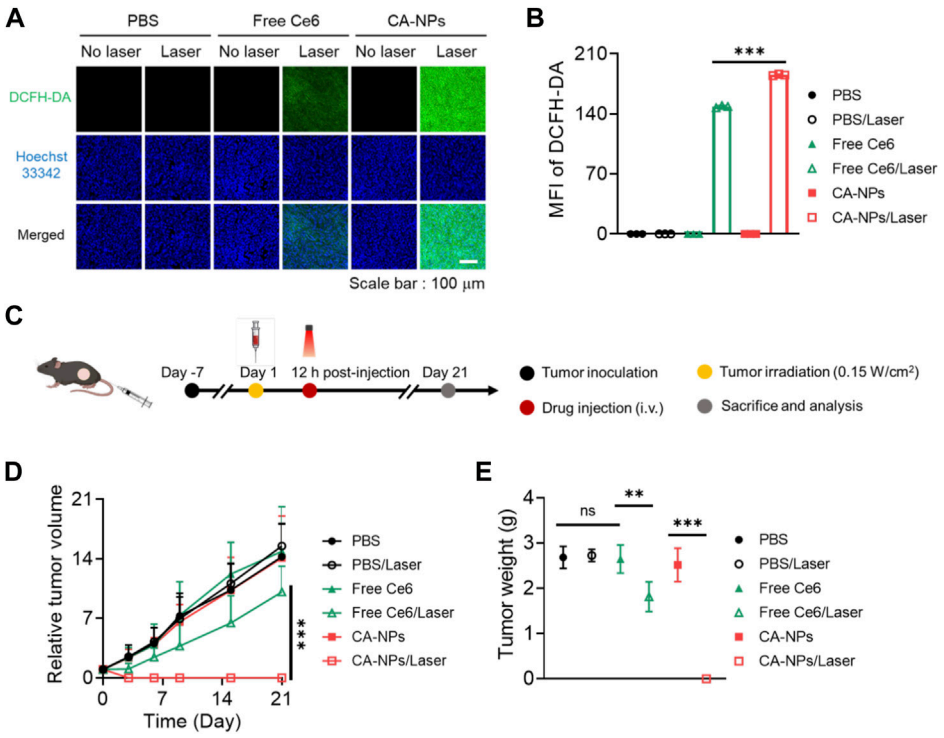

FIGURE 5
In vivo anti-tumor effect of CA-NPs. **(A,B)** Confocal images and fluorescence intensities of the MB49 tumor from the mice treated with PBS, Free Ce6 and CA-NPs at the dose of 5.0 mg/kg under irradiation or not (0.15 W/cm^2, 5min) and stained with DCFH-DA. Scale bar: 100 μm. **(C)**. Schematic illustration of therapeutic procedure of CA-NPs. **(D,E)** Tumor growth profiles and corresponding tumor mass (day 21) of the mice bearing MB49 tumors treated with PBS, Free Ce6 and CA-NPs at the dose of 5.0 mg/kg Ce6 under irradiation or not (660 nm, 0.15 W/cm^2, 5 min). (n = 7; ns: no significance, $^{**}p < 0.01$, $^{***}p < 0.001$).

MB49 bladder tumor model rapidly with minimal fluorescent signals observed at 12, 24 and 48 h post-injection (Figure 4A). While CA-NPs with suitable size distribution gradually accumulated in the tumor site (Figure 4A), possibly owing to enhanced permeability and retention effect as well as receptor-mediated active targeting ability of albumin (such as GP60). The highest amount of CA-NPs in the tumor site was detected at 12 h post-injection and was 2.8-fold higher than that of free Ce6 group (Figure 4B). We further collected major organs including heart, liver, spleen, lung, kidney and tumors to quantitatively measure the fluorescent intensities of CA-NPs. As shown in Figure 4C, although CA-NPs distributed in liver and kidney, significantly increased accumulation of CA-NPs was found in tumor tissues and was 3.0-fold and 2.8-fold higher than that of liver and kidney, respectively (Figure 4D), further confirming the superior targeting ability of CA-NPs for *in vivo* PDT effect.

3.5 *In vivo* anti-tumor effect of CA-NPs

Taking advantage of preferable photoactivity and targeting ability of CA-NPs, we then sought to investigate the *in vivo* anti-tumor effect against intractable bladder tumors. Firstly, we intravenously injected CA-NPs and free Ce6 at the dose of 5.0 mg/kg into mice bearing MB49 tumor models and the mice were suffered from irradiation at 12 h post-injection. Half an hour before irradiation, DCFH-DA was injected intratumorally at the dose of 10 μM. Then the tumor tissues were pick out at 30 min post-irradiation and were cut into 10 μm slices, followed by staining with Hoechst33342 to measure the *in vivo* ROS production. Both free Ce6 and CA-NPs induced ignorable ROS in the absence of irradiation as evidenced by the undetectable green fluorescence in the tumor sections (Figure 5A), while CA-NPs led to remarkable ROS generation upon irradiation and the amount of ROS was higher than that of free Ce6 group (Figure 5B), suggesting the enhanced tumor accumulation and elevated photoactivity cooperatively contributed to the abundant *in vivo* ROS production.

Next, we further evaluated the *in vivo* therapeutic effect of CA-NPs against subcutaneous MB49 tumor models. Briefly, CA-NPs and free Ce6 (5.0 mg/kg) were intravenously administrated into MB49 tumor model-bearing mice, and the mice were then treated with or without irradiation (660 nm, 0.15 W/cm^2, 5 min) at 12 h post-injection (Figure 5C). The tumor volume and mice weight were observed and recorded during 21 days as well as the tumor weight. During the observation time, the tumor volume was rapidly increased as compared to that at day 0, and the similar trend was also shown in PBS group upon irradiation, indicating that laser exposure alone didn't affect the growth of tumor. Meanwhile, the tumor growth profile in both CA-NPs and free Ce6 groups exhibited no significant change as compared to that of PBS group. And upon irradiation, a slight delay of tumor growth was clearly detected in the free Ce6 group, while the tumors were totally disappeared after treatment of CA-NPs under laser exposure during 21 days (Figure 5D). Consequently, the tumor weight was considerably decreased in the group of CA-NPs upon irradiation (Figure 5E). The excellent therapeutic effect of CA-NPs was attributed to the generation of ROS since there was no significant

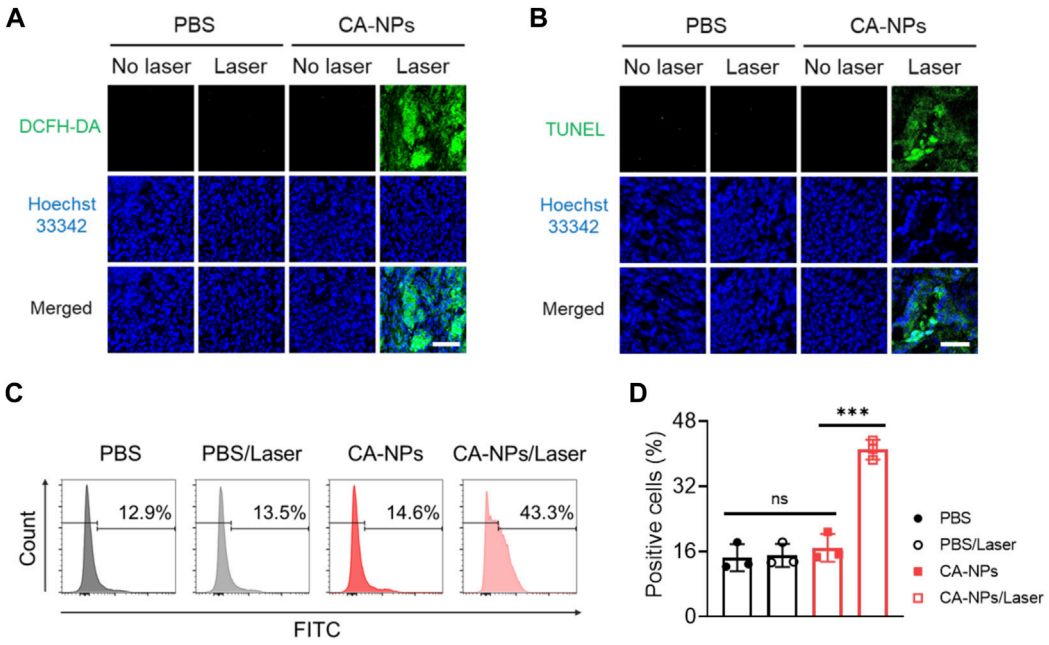

FIGURE 6
Anti-tumor effect of CA-NPs against bladder tumor sections from patients. **(A)** DCFH-DA staining of human bladder tumor treated with PBS and CA-NPs under irradiation or not (0.15 W/cm^2, 5min) post intratumoral injection of 1 μg Ce6. Scale bar: 100 μm. **(B)** TUNEL staining of human bladder tumor treated with PBS and CA-NPs under irradiation or not. Scale bar: 50 μm. **(C,D)**. Flow cytometric measurement of positive cells of TUNEL staining in human bladder tumor treated with PBS and CA-NPs under irradiation or not. (n = 3; ns: no significance, $^{**}p < 0.01$, $^{***}p < 0.001$).

temperature elevation at tumor region *in vivo* (Supplementary Figure S6). In addition, no significant decrease of the body weight was observed during 21 days for those treated mice, indicating that free Ce6 and CA-NPs have negligible side effects on the mice subjected to treatment (Supplementary Figure S7). Collectively, the abundant *in vivo* ROS production induced by CA-NPs via enhanced tumor accumulation and elevated photoactivity confers potent PDT effect against murine bladder tumor models.

3.6 Anti-tumor effect of CA-NPs against bladder tumor sections from patients

To further demonstrated the clinical applicability of CA-NPs, we selected bladder tumor sections from patients and assess the anti-tumor effect. Firstly, the freshly obtained bladder tumor tissues were intratumorally injected with CA-NPs (1 μg) and DCFH-DA, and suffered from 660 nm laser irradiation for 5 min at the density of 0.15 W/cm^2. Then the tumor tissues were cut into 10 μm slices and stained with Hoechst33342, followed by observation using confocal laser scanning microscopy. As shown in Figure 6A, emerged green fluorescence signals was detected in the tumor tissues treated with CA-NPs under light exposure. On the contrast, tumor tissues in other control groups showed negligible fluorescence signals (Supplementary Figure S8). Moreover, we also applied TUNEL assay to quantitatively measure the apoptosis of bladder tumor section after various treatments. In the group of CA-NPs under irradiation, strong green fluorescence was observed compared to compared to saline and CA-NPs without irradiation (Figure 6B, Supplementary Figure S9). Moreover, 41.0% apoptosis-positive cells were detected and were 2.8-fold and 2.4-fold higher as compared to that of PBS and CA-NPs group without irradiation, respectively (Figures 6C, D), revealing the superior PDT effect from CA-NPs against clinical bladder tumor tissues.

4 Conclusion

PDT was clinically approved for the treatment of bladder cancer in 1993 since it is feasible to insert the optical fiber into the urethra, showing the tremendous potential of PDT in the treatment of bladder cancer. To address current challenge of PDT against bladder cancers such as insufficient targeted delivery of photosensitizer, we present the CA-NPs that is accomplished *via* a well-defined precipitation reaction inside albumin nanoreactor for targeted delivery of Ce6 to induce potent PDT effect against murine bladder cancer and human restricted tumor tissues. CA-NPs shows enhanced ROS production and excellent resistance to photobleaching as compared to Ce6. Furthermore, CA-NPs are effectively internalized by cancer cells and allows rapid translocation from lysosome to cytosol to induce potent PDT effect against cancer cells. Owing to the suitable size, CA-NPs show the excellent capacity to accumulate and penetrate in the whole tumor sites. CA-NPs administered intravenously with single dose can generate ROS immediately after irradiation and produce strong anti-tumor efficacy to eradicate difficult-to-treat murine bladder cancer

models. Moreover, CA-NPs also induce severe apoptosis of tumor cells in freshly restricted human bladder cancer *via* abundant ROS generation. Therefore, these results indicate HSA as an emerging carrier for cancer treatment with tremendous clinic translational potential to expand the delivery of photosensitizers and other small molecule drugs.

Data availability statement

The raw data of this article will be made available by the authors, without undue reservation.

Ethics statement

The animal study was reviewed and approved by the Laboratory Animal Ethical and Welfare Committee of Soochow University. Resected human bladder tumor tissues were obtained from patients at Dushu Lake Hospital Affiliated of Soochow University. Ethical permission was approved by the Clinical Trial Ethics Committee of Dushu Lake Hospital Affiliated of Soochow University. The patients provided their informed consent to participate in this study.

Author contributions

JL and ZM designed and performed most of the experiments. XH constructed MB49 tumour models and performed biodistribution of CA-NPs. YY contributed to data statistics and analysis. ML helped prepare the nanoparticles. TY and GS conceived the idea, supervised the research and wrote the manuscript.

Funding

This work was supported by National Natural Science Foundation of China (82003671), Priority Academic Program Development of Jiangsu Higher Education Institutions (PAPD), Gusu Innovation and Entrepreneurship Leading Talent Plan (ZXL2022486), Suzhou Industrial Park clinical medical expert team introduction project (0202140004), and Jiangsu Key Laboratory of Translational Research and Therapy for Neuro-Psycho-Diseases.

Conflict of interest

The authors declare that the research was conducted in the absence of any commercial or financial relationships that could be construed as a potential conflict of interest.

Publisher's note

All claims expressed in this article are solely those of the authors and do not necessarily represent those of their affiliated organizations, or those of the publisher, the editors and the reviewers. Any product that may be evaluated in this article, or claim that may be made by its manufacturer, is not guaranteed or endorsed by the publisher.

Supplementary material

The Supplementary Material for this article can be found online at: https://www.frontiersin.org/articles/10.3389/fbioe.2023.1132591/full#supplementary-material

References

Gianni, L., Mansutti, M., Anton, A., Calvo, L., Bisagni, G., Bermejo, B., et al. (2018). Comparing neoadjuvant nab-paclitaxel vs paclitaxel both followed by anthracycline regimens in women with ERBB2/HER2-negative breast cancer-the evaluating treatment with neoadjuvant abraxane (ETNA) trial a randomized phase 3 clinical trial. *JAMA Oncol.* 4, 302–308. doi:10.1001/jamaoncol.2017.4612

Joshi, S. S., and Badgwell, B. D. (2021). Current treatment and recent progress in gastric cancer. *CA Cancer J. Clin.* 71, 264–279. doi:10.3322/caac.21657

Katsikanis, F., Strakas, D., and Vouros, I. (2020). The application of antimicrobial photodynamic therapy (aPDT, 670 nm) and diode laser (940 nm) as adjunctive approach in the conventional cause-related treatment of chronic periodontal disease: A randomized controlled split-mouth clinical trial. *Clin. Oral Investig.* 24, 1821–1827. doi:10.1007/s00784-019-03045-1

Labrie, M., Brugge, J. S., Mills, G. B., and Zervantonakis, I. K. (2022). Therapy resistance: Opportunities created by adaptive responses to targeted therapies in cancer. *Nat. Rev. Cancer* 22, 323–339. doi:10.1038/s41568-022-00454-5

Li, T., Tan, S., Li, M., Luo, J., Zhang, Y., Jiang, Z., et al. (2022). Holographically activatable nanoprobe via glutathione/albumin-mediated exponential signal amplification for high-contrast tumor imaging. *Adv. Mat.* 33, e2209603. doi:10.1002/adma.202209603

Li, X., Lovell, J. F., Yoon, J., and Chen, X. (2020). Clinical development and potential of photothermal and photodynamic therapies for cancer. *Nat. Rev. Clin. Oncol.* 17, 657–674. doi:10.1038/s41571-020-0410-2

Lv, X. Y., Wang, X., Li, T., Wei, C. G., Tang, Y. A., Yang, T., et al. (2018). Rationally designed monodisperse Gd_2O_3/Bi_2S_3 hybrid nanodots for efficient cancer theranostics. *Small* 14, e1802904. ARTN 1802904. doi:10.1002/smll.201802904

Nencioni, A., Caffa, I., Cortellino, S., and Longo, V. D. (2018). Fasting and cancer: Molecular mechanisms and clinical application. *Nat. Rev. Cancer* 18, 707–719. doi:10.1038/s41568-018-0061-0

Patel, V. G., Oh, W. K., and Galsky, M. D. (2020). Treatment of muscle-invasive and advanced bladder cancer in 2020. *CA Cancer J. Clin.* 70, 404–423. doi:10.3322/caac.21631

Pham, T. C., Nguyen, V. N., Choi, Y., Lee, S., and Yoon, J. (2021). Recent strategies to develop innovative photosensitizers for enhanced photodynamic therapy. *Chem. Rev.* 121, 13454–13619. doi:10.1021/acs.chemrev.1c00381

Sung, H., Ferlay, J., Siegel, R. L., Laversanne, M., Soerjomataram, I., Jemal, A., et al. (2021). Global cancer statistics 2020: GLOBOCAN estimates of incidence and mortality worldwide for 36 cancers in 185 countries. *CA Cancer J. Clin.* 71, 209–249. doi:10.3322/caac.21660

Wang, D. D., Wu, H. H., Lim, W. Q., Phua, S. Z. F., Xu, P. P., Chen, Q. W., et al. (2019). A mesoporous nanoenzyme derived from metal-organic frameworks with endogenous oxygen generation to alleviate tumor hypoxia for significantly enhanced photodynamic therapy. *Adv. Mat.* 31, e1901893. doi:10.1002/adma.201901893

Xie, J., Wang, Y., Choi, W., Jangili, P., Ge, Y., Xu, Y., et al. (2021). Overcoming barriers in photodynamic therapy harnessing nano-formulation strategies. *Chem. Soc. Rev.* 50, 9152–9201. doi:10.1039/d0cs01370f

Yang, H., Liu, R., Xu, Y., Qian, L., and Dai, Z. (2021). Photosensitizer nanoparticles boost photodynamic therapy for pancreatic cancer treatment. *Nano-micro Lett.* 13, 35. doi:10.1007/s40820-020-00561-8

Yang, T., Ke, H. T., Wang, Q. L., Tang, Y. A., Deng, Y. B., Yang, H., et al. (2017). Bifunctional tellurium nanodots for photo-induced synergistic cancer Therapy. *ACS Nano* 11, 10012–10024. doi:10.1021/acsnano.7b04230

Yang, T., Wang, Y., Ke, H. T., Wang, Q. L., Lv, X. Y., Wu, H., et al. (2016). Protein-nanoreactor-assisted synthesis of semiconductor nanocrystals for efficient cancer theranostics. *Adv. Mat.* 28, 5923–5930. doi:10.1002/adma.201506119

Yardley, D. A. (2013). Nab-paclitaxel mechanisms of action and delivery. *J. Control. Release* 170, 365–372. doi:10.1016/j.jconrel.2013.05.041

Yi, X., Hu, J. J., Dai, J., Lou, X., Zhao, Z., Xia, F., et al. (2021). Self-guiding polymeric prodrug micelles with two aggregation-induced emission photosensitizers for enhanced chemo-photodynamic therapy. *ACS Nano* 15, 3026–3037. doi:10.1021/acsnano.0c09407

Zhai, Y. H., Liu, M., Yang, T., Luo, J., Wei, C. G., Shen, J. K., et al. (2022). Self-activated arsenic manganite nanohybrids for visible and synergistic thermo/immuno-arsenotherapy. *J. Control. Release* 350, 761–776. doi:10.1016/j.jconrel.2022.08.054

Zhen, S., Yi, X., Zhao, Z., Lou, X., Xia, F., and Tang, B. Z. (2019). Drug delivery micelles with efficient near-infrared photosensitizer for combined image-guided photodynamic therapy and chemotherapy of drug-resistant cancer. *Biomaterials* 218, 119330. doi:10.1016/j.biomaterials.2019.119330

Zheng, Q., Liu, X., Zheng, Y., Yeung, K. W. K., Cui, Z., Liang, Y., et al. (2021). The recent progress on metal-organic frameworks for phototherapy. *Chem. Soc. Rev.* 50, 5086–5125. doi:10.1039/d1cs00056j

Zhou, L. J., Yang, T., Wang, J. X., Wang, Q. L., Lv, X. Y., Ke, H. T., et al. (2017). Size-tunable Gd_2O_3@albumin nanoparticles conjugating chlorin e6 for magnetic resonance imaging-guided photo-induced therapy. *Theranostics* 7, 764–774. doi:10.7150/thno.15757

Zhu, J., Xiao, T., Zhang, J., Che, H., Shi, Y., Shi, X., et al. (2020). Surface-charge-switchable nanoclusters for magnetic resonance imaging-guided and glutathione depletion-enhanced photodynamic therapy. *ACS Nano* 14, 11225–11237. doi:10.1021/acsnano.0c03080

frontiers | Frontiers in Bioengineering and Biotechnology

TYPE Original Research
PUBLISHED 06 March 2023
DOI 10.3389/fbioe.2023.1138601

Check for updates

OPEN ACCESS

EDITED BY
Mingqiang Li,
Third Affiliated Hospital of Sun Yat-sen University, China

REVIEWED BY
Shanyong Zhang,
Shanghai Jiao Tong University, China
Miao He,
School of Stomatology, Wuhan University, China

*CORRESPONDENCE
Kai Jiao,
kjiao1@163.com

†These authors have contributed equally to this work

SPECIALTY SECTION
This article was submitted to Biomaterials, a section of the journal Frontiers in Bioengineering and Biotechnology

RECEIVED 05 January 2023
ACCEPTED 24 February 2023
PUBLISHED 06 March 2023

CITATION
Han X, Ma Y, Lu W, Yan J, Qin W, He J, Niu L-N and Jiao K (2023), Bioactive semaphorin 3A promotes sequential formation of sensory nerve and type H vessels during *in situ* osteogenesis. *Front. Bioeng. Biotechnol.* 11:1138601. doi: 10.3389/fbioe.2023.1138601

COPYRIGHT
© 2023 Han, Ma, Lu, Yan, Qin, He, Niu and Jiao. This is an open-access article distributed under the terms of the Creative Commons Attribution License (CC BY). The use, distribution or reproduction in other forums is permitted, provided the original author(s) and the copyright owner(s) are credited and that the original publication in this journal is cited, in accordance with accepted academic practice. No use, distribution or reproduction is permitted which does not comply with these terms.

Bioactive semaphorin 3A promotes sequential formation of sensory nerve and type H vessels during *in situ* osteogenesis

Xiaoxiao Han[1,2†], Yuxuan Ma[2†], Weicheng Lu[2†], Jianfei Yan[2], Wenpin Qin[2], Jiaying He[2], Li-Na Niu[2] and Kai Jiao[2*]

[1]The College of Life Science, Northwest University, Xi'an, Shaanxi, China, [2]State Key Laboratory of Military Stomatology and National Clinical Research Center for Oral Diseases and Shaanxi Key Laboratory of Stomatology, School of Stomatology, The Fourth Military Medical University, Xi'an, Shaanxi, China

Introduction: Sensory nerves and vessels are critical for skeletal development and regeneration, but crosstalk between neurovascular network and mineralization are not clear. The aim of this study was to explore neurovascular changes and identify bioactive regulators during *in situ* osteogenesis.

Method: *In situ* osteogenesis model was performed in male rats following Achilles tenotomy. At 3, 6 and 9 weeks after surgery, mineralization, blood vessels, sensory innervation, and bioactive regulators expression were evaluated *via* micro-computed tomography, immunofluorescent staining, histology and reverse transcriptase-polymerase chain reaction analyses.

Result: In the process of *in situ* osteogenesis, the mineral density increased with time, and the locations of minerals, nerves and blood vessels were highly correlated at each time point. The highest density of sensory nerve was observed in the experimental group at the 3rd week, and then gradually decreased with time, but still higher than that in the sham control group. Among many regulatory factors, semaphorin 3A (Sema3A) was highly expressed in experimental model and its expression was temporally sequential and spatially correlated sensory nerve.

Conclusion: The present study showes that during *in situ* osteogenesis, innervation and angiogenesis are highly correlated, and Sema3A is associated with the position and expression of the sensory nerve.

KEYWORDS

semaphorin 3A, osteogenesis, nerves, vessels, neurovascular regulators

1 Introduction

Crosstalk between skeletal and neural tissues is critical for skeletal development and regeneration. Previous studies have demonstrated that nerve fibers and bone tissues interact during early embryonic development (Rajpar and Tomlinson, 2022). Increased sensory innervation was confirmed to precede the vascularization, ossification and mineralization of fracture callus (Li et al., 2019). Bone remodeling is regulated by neural signalling under both physiological and pathophysiological conditions (Brazill et al., 2019; Sayilekshmy et al., 2019; Wan et al., 2021). Neuropeptides from sensory nerves, such as substance P (SP) and calcitonin gene-related peptide (CGRP), increase significantly in the bone regeneration area,

suggesting that neurological substances play an important role in fracture healing and bone repair (Hofman et al., 2019; Sun et al., 2020). Tropomyosin receptor kinase A-expressing (TrKA-expressing) sensory nerve fibers drive abnormal osteochondral differentiation after soft tissue trauma (Lee et al., 2021). These observations have generated particular interest in sensory nerves related to bone formation.

Vascular network also plays a significant role in bone formation and repair. Blood vessels provide nutritional basis for the surrounding mineralized tissues, whether physiological or pathological (Zhu et al., 2020; Yin et al., 2021). The skeletal system is densely innervated by both neural and vascular networks and neurovascular unit has been identified (Qin et al., 2022a). In addition, innervation has been demonstrated to affect blood vessel assembly and endothelial cell proliferation in bone regeneration (Qin et al., 2022b). However, the role of sensory nerve correlated with vessels during *in situ* osteogenesis and its related mechanisms remain unclear.

Many bioactive regulators are involved in the neurovascular occurrence. Netrins and semaphorins are members of the neuronal guidance cue family (Feinstein and Ramkhelawon, 2017). Accumulating evidence suggests that netrins (Yamagishi et al., 2021) and semaphorins (Avouac et al., 2021; Limoni and Niquille, 2021) are neuronal guidance molecules that facilitate patterning of the nervous and vascular system. However, which bioactive factors influence the neurovascular unit during *in situ* osteogenesis are unknown.

Therefore, the primary aim of the present study was to identify the characteristics of sensory nerves and neovessels during *in situ* osteogenesis, and the secondary aim was to explore the bioactive factors that influence the neurovascular occurrence during bone formation. An *in situ* osteogenesis model was established using rat Achilles tenotomy (Zhang et al., 2020a). Bioactive factors that regulate angiogenesis and sensory innervation during osteogenesis were investigated *via* histology staining, immunofluorescent staining and reverse transcriptase-polymerase chain reaction analyses.

2 Materials and methods

2.1 Animal experiments

To examine the mechanism of *in situ* osteogenesis, an Achilles tenotomy model was utilized in the present study (EXP). The animal experiments were conducted in accordance with protocols approved by the Institutional Animal Care and Use Committee following the National Institute of Health Guidelines for the Care and Use of Laboratory Animals. All animals were housed in a pathogen-free room and fed with sterilized food and distilled water during the study. No more than 4 animals were housed in a single cage (measuring 50 × 40 × 25 cm) at ambient temperature of 20°C ± 2°C and humidity of 55% ± 5%, with good ventilation and 12-h dark/light cycles (4 W per square meter). Sterilized wood-chip bedding was replaced every other day. Animal health status was monitored twice daily. All animals were healthy from the beginning to the end of the study. No adverse events other than Achilles tendon pathology were observed. A total number of 72 male Sprague-Dawley rats (200–300 g) were randomly divided into following groups with a table of random numbers: (1) Sham; (2) EXP 3-week; (3) EXP 6-week and (4) EXP 9-week. For each animal, four different investigators were involved as follows: a first investigator was responsible for the randomized grouping design. A second investigator performed the surgical procedure, whereas a third investigator identified the characteristics of sensory nerves, vessels and bone formation during *in situ* osteogenesis. Finally, a fourth investigator analyzed data.

Anesthesia was performed by intraperitoneal injection of sodium pentobarbital (40 mg/kg) and pentobarbital overdose were provided to euthanize all rats. The heel of the both hind legs were shaved and sterilized, and then the skin and subcutaneous tissue near the Achilles tendon were incised. This was followed by a transverse disconnection along the midpoint of the Achilles tendon. Both ends of the tendon were clamped repeatedly with vascular clamps about five times and the Achilles tendon was not sutured. In the sham control group, only the skin and subcutaneous tissue were cut to expose the Achilles tendon. At 3, 6 and 9 weeks after surgery, the rats from sham (N = 36) and EXP groups (N = 36) were anesthetized and samples were taken to observe the distribution and content of sensory nerve, type H vessel, and bone. In experimental rats, no differences in bone formation were observed between the left and right legs. Hence, in the first run of the experiment, the left Achilles tendons with calcaneus and lower tibia dissected from rats were fixed with 4% paraformaldehyde for 24 h, then scanned and analyzed with micro-computed tomography (Micro-CT; Inveon, Siemens Preclinical, Knoxville, TN, United States) at high-resolution (N = 6). The right Achilles tendons with calcaneus and lower tibia were embedded in a mixture of methyl methacrylate and dibutyl phthalate and sectioned for hematoxylin-eosin (HE) staining (N = 6). In the second run of the experiment, the ankles with Achilles tendons from the left limbs were dissected, fixed, decalcified and dehydrated with 30% sucrose solution at 4°C for 48 h. Next, the specimens were embedded and processed into 10 μm-thick cryosections for immunofluorescence staining (N = 6). The cartoon-style drawing of section orientation/position was included in Supplementary Figure S1. In addition, the right Achilles tendons tissue from 3-week and 9-week groups were dissected and analyzed by quantitative real-time polymerase chain reaction (RT-PCR), and a single sample was obtained by pooling together every 2 out of 6 Achilles tendons samples (N = 3).

2.2 Micro-computed tomography

The Achilles tendons with calcaneus and lower tibia were scanned using micro-computed tomography (Micro-CT; Inveon, Siemens Preclinical, Knoxville, TN, United States) at high-resolution. Briefly, samples were scanned at 80 kV and 500 μA. Two-dimensional slices with 78 μm isotropic resolution were generated. A three-dimensional (3D) image was reconstructed based on the scanned information using the Inveon Research Workplace software (Siemens Medical Solutions United States, Inc., Hoffman Estates, IL, United States). A cylindrical region of interest was positioned over the injury site and the volume of the newly-formed bone was measured by assigning a threshold. Bone mineral density (BMD), bone volume to total volume ratio (BV/TV),

and bone surface to bone volume ratio (BS/BV) in the injury were measured using the Inveon Research Acquisition software.

2.3 Hematoxylin-eosin staining

The Achilles tendons with calcaneus and lower tibia of sham and experimental rats were excised, fixed in 4% paraformaldehyde for 24 h, dehydrated in ethanol, and embedded in a mixture of methyl methacrylate and dibutyl phthalate. Longitudinal sections (10 μm thickness) were made using a Leica SP1600 hard tissue-slicer. Sections were then used for HE staining. (Wuhan Servicebio Technology Co., Ltd., Wuhan, China).

2.4 Immunofluorescence

Specimens were collected from the rats with Achilles tendon injuries in the EXP and sham groups, and the specimens were excised, post-fixed using 4% paraformaldehyde overnight, and decalcified with 10% ethylenediaminetetraacetic acid (EDTA; pH 7.3) for 4 weeks. The demineralization medium was changed every 2 days. After decalcification, the specimens were dehydrated with 30% sucrose solution at 4°C for 48 h. L4 and L5 dorsal root ganglion (DRG) tissues were post-fixed with 1.5% glutaraldehyde for 6 h and cryo-protected with 30% sucrose solution at 4°C for 24 h.

The specimens were embedded in optimal cutting temperature compound (Leica, Germany) and stored at −80°C. Tissue was cut into 5-μm-thin longitudinal sections. The cryofilm (Section-lab, Japan) was mount onto the cut surface, and the specimen was tightly adhered to the cryofilm. Cryosections were stained using standard immunofluorescence methods. Briefly, the sections were permeabilized with 1% Triton X-100 (MilliporeSigma, Burlington, MA, United States) and blocked in 1.5% goat serum (MilliporeSigma, United States). The sections were then incubated overnight with the primary antibodies at 4°C. This was followed by incubation with Alexa Fluor™ fluorescent secondary antibodies (Molecular Probes, United States). All sections were rinsed and mounted with Prolong Diamond Antifade Mountant with 4',6-diamidino-2-phenylindole (DAPI; Invitrogen, San Diego, CA, United States). The images were captured under a fluorescence microscope (FV1000, Olympus, Tokyo, Japan) and the integrated fluorescence intensity was analyzed using ImageJ software (NIH, Bethesda, MD, United States).

The primary antibodies used were: anti-CGRP antibody (ab36001, Abcam, Cambridge, MA, United States; 14,959, Cell Signaling Technology, Inc. Danvers, MA, United States), anti-PGP9.5 (ab72911, Abcam), anti-platelet and endothelial cell adhesion molecule 1 (PECAM-1, also known as CD31) antibody (sc-376764, Santa Cruz Biotechnology, Inc., Santa Cruz, CA, United States), anti-endomucin (Emcn) antibody (343,158, United States Biological, Salem, MA, United States), and anti-semaphorin 3A (Sema3A) antibody (sc-74555, Santa Cruz Biotechnology). The biological replicates are six because in each group six specimens were embedded and processed for staining and quantification (N = 6). For each sample, three fields of view were selected randomly and the average fluorescence intensity was calculated as the data by Image J software. The control staining without primary or secondary antibody have been performed to confirm the positive staining (Supplementary Figure S2).

2.5 Quantitative real-time reverse transcription polymerase chain reaction (qRT-PCR)

To investigate the temporal relationship between sensory nerve and blood vessels during *in situ* osteogenesis, gene expression levels of *Cgrp*, *Sp*, *Cd31*, *Emcn*, *Osx* (osterix), *Ocn*, *Ntn1* (netrin1), *Ntn4* (netrin4), *Sema3a*, and *Sema3e* (semaphorin 3E) of the Achilles tendon tissue in trauma areas were evaluated using qRT-PCR. *Gapdh* (encoding glyceraldehyde-3-phosphate dehydrogenase) was used as the housekeeping gene. Results obtained after calibration using the *Gapdh* expression level were calculated using the $2^{-\Delta\Delta Ct}$ method and presented as fold increases relative to the non-stimulated control (technical replicates $n = 3$ for each group) (Livak and Schmittgen, 2001).

Briefly, total RNA was isolated using the Trizol reagent (Invitrogen). The concentration and purity of the extracted RNA were determined by measuring the absorbance at 260 and 280 nm (BioTek, Winooski, VT, United States). Complementary DNA (cDNA) was synthesized using a PrimeScript RT reagent kit (Takara Bio Inc., Shiga, Japan). The quantitative real-time polymerase chain reaction (qPCR) was performed using the cDNA as the template on a 7,500 Real Time PCR System (Applied Biosystems, Carlsbad, CA, United States). Sense and antisense primers were designed based on the published cDNA sequences using Primer Express 5.0 (Thermo Fisher Scientific, Waltham, MA, United States; Supplementary Table S1).

2.6 Statistical analyses

All data are presented as the means ± standard deviations. Data were examined for their normality and homoscedasticity assumptions before the use of parametric statistical methods. Comparisons were analyzed using one-factor analysis of variance (ANOVA) and Tukey's *post hoc* test. The GraphPad Prism 5 package (GraphPad Software, La Jolla, CA, United States) was employed for the analysis. Statistical significance was preset at $\alpha = 0.05$. For all charts, groups labeled with different lowercase letters are significantly different ($p < 0.05$).

3 Results

3.1 Sensory nerve infiltrated around the new bone formation during *in situ* osteogenesis

The Achilles tendon injury model has been widely used as a model of *in situ* osteogenesis. Micro-CT showed that bone began to form in the 6-week post Achilles tenotomy and continued to enlarge up to 9 weeks, while no obvious calcifications were found in the 3-week EXP group or the sham group. In addition, calcium deposition was evaluated using HE and Alizarin Red staining and the results showed that typical cancellous bone with marrow was noted at 6 and

10.3389/fbioe.2023.1138601

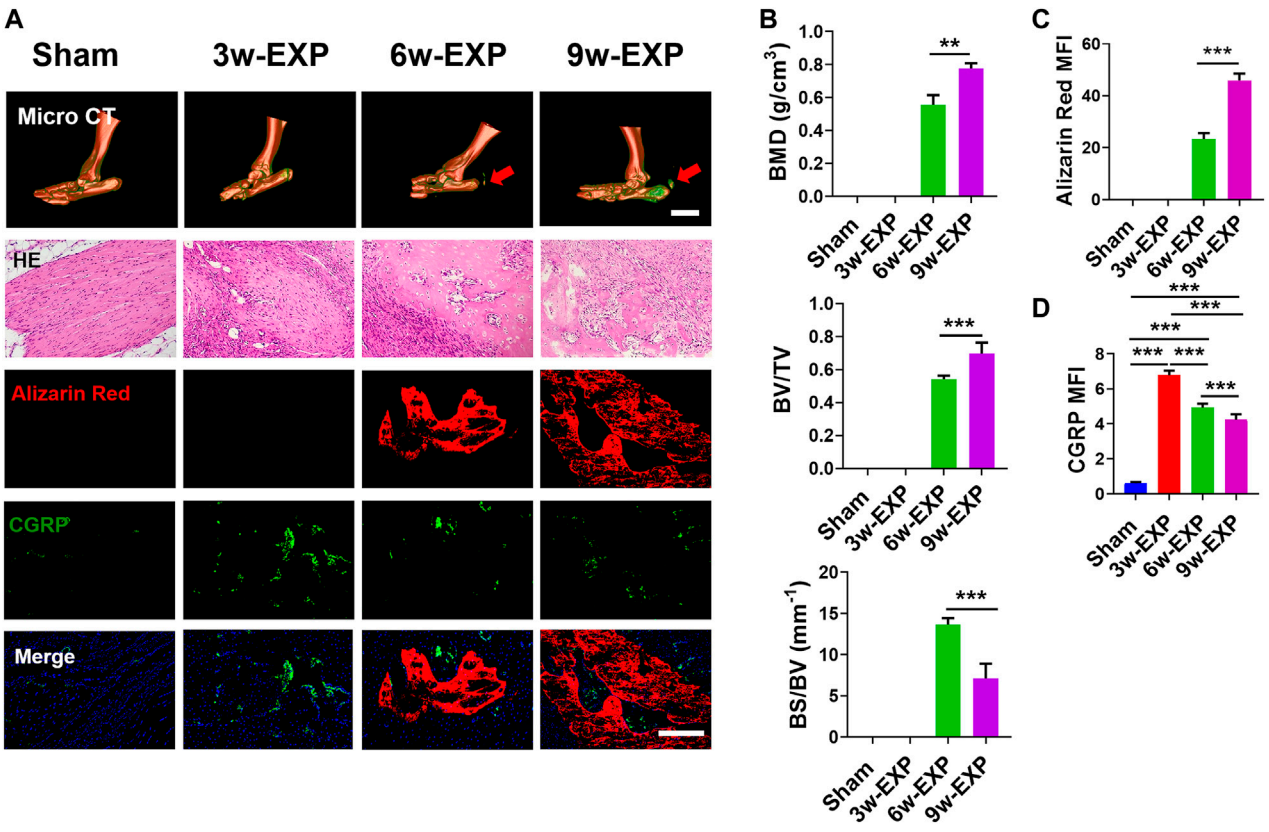

FIGURE 1
The bone formation and sensory innervation of trauma areas at 3 weeks after a sham operation or 3, 6 and 9 weeks after tenotomy. **(A)** Representative micro-CT images of 3D-reconstructed images of the Achilles tendon injury (bar: 5 mm) and HE, Alizarin Red and immunofluorescence staining of CGRP. Scale bar: 200 μm. **(B)** Quantitative analysis of bone mineral density (BMD), bone volume/total volume (BV/TV), and bone surface/bone volume (BS/BV). **(C)** Quantification of the MFI of Alizarin Red staining per field view. **(D)** Quantification of the MFI of CGRP expression per field view. Nuclei were stained with DAPI (blue). Data represent the means ± standard deviations. For all charts, groups labeled with different lowercase letters are significantly different ($p < 0.05$). CGRP, calcitonin gene-related peptide; DAPI, 4,6-diamidino-2-phenylindole.

9 weeks post tenotomy. To clarify the potential relationship between sensory innervation and bone regeneration during bone formation, immunofluorescent staining were conducted to detect calcium deposition and CGRP-positive sensory nerves (Figure 1A). Immunofluorescence staining of protein gene product 9.5 (PGP9.5) also was conducted to examine the presence and distribution of nerve fibers (Supplementary Figure S3).

Micro-CT analysis showed that the bone mineral density (BMD) and bone volume to total volume ratio (BV/TV) in the 9-week EXP group were significantly higher than those of the 6-week EXP group (0.78 ± 0.03 vs. 0.56 ± 0.06, $p < 0.01$; and 0.70 ± 0.07 vs. 0.54 ± 0.02, $p < 0.01$, respectively) (Figure 1B). Conversely, the bone surface to bone volume ratio (BS/BV) in the 9-week EXP group was significantly reduced compared with that in the 6-week EXP group (7.11 ± 1.80 vs. 13.66 ± 0.78; $p < 0.01$). The results suggest that the Achilles tenotomy model successfully simulated the occurrence and development of bone. Similar to the micro-CT analysis, the mineralization in the 9-week EXP group (45.95 ± 2.56) was significantly higher than that in the 6-week EXP group (23.31 ± 0.25) (Figure 1C). The highest MFI of CGRP and PGP9.5 was identified in the 3-week EXP group compared with that in other groups (all $p < 0.01$) (Figure 1D; Supplementary Figure S3). Notably, CGRP-positive sensory nerves co-localized with mineral deposition in both the 6-week and 9-week EXP groups and their distributions were significantly more extensive than that in the sham group ($p < 0.01$). These data suggested that sensory nerves might play an important role during *in situ* osteogenesis.

3.2 Infiltration of sensory nerve was followed by angiogenesis during *in situ* osteogenesis

Bone-associated nerves and blood vessels are thought to influence the propagation of one another as they grow within bone tissues. To investigate the potential relationship between sensory innervation and angiogenesis, immunofluorescence staining was conducted to show that $CD31^+$ and $Emcn^+$ vessels co-localized with $CGRP^+$ sensory nerves in areas of new bone formation (Figures 2A, 3A). The levels of CD31 and Emcn increased gradually with time (Figures 2B, 3B). Compared with the sham group, the MFI of CD31 and Emcn in the trauma areas increased significantly at 3 and 6 weeks (all $p < 0.01$), and reached

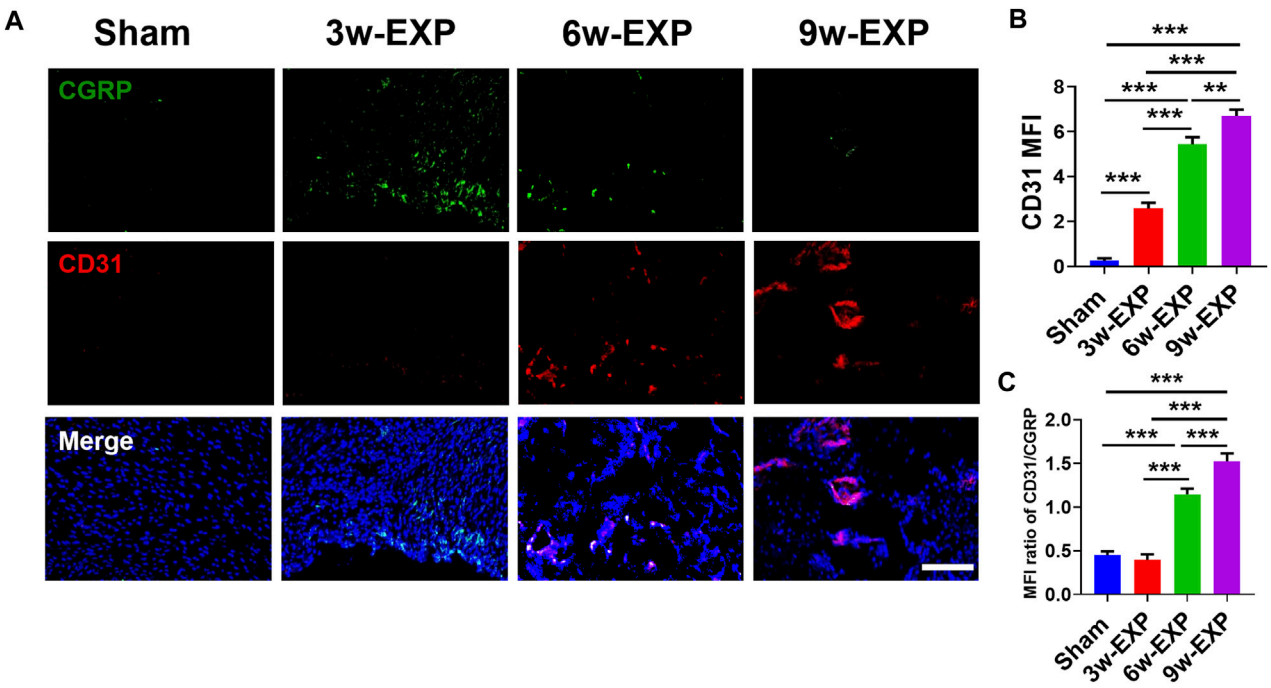

FIGURE 2
Immunofluorescence staining of trauma areas at 3 weeks after a sham operation or 3, 6 and 9 weeks after tenotomy. **(A)** Representative images of immunofluorescence staining of CGRP and CD31. **(B)** Quantification of the MFI of CD31 expression per field view. **(C)** Quantification of the MFI ratio of CD31/CGRP expression. Nuclei were stained with DAPI (blue). Scale bar: 100 μm. Data represent the means ± standard deviations. For all charts, groups labeled with different lowercase letters are significantly different ($p < 0.05$). CGRP, calcitonin gene-related peptide; DAPI, 4,6-diamidino-2-phenylindole.

the highest value at 9 weeks ($p < 0.01$). Co-staining of CD31 and Emcn representing type H vessels also increased gradually with time and reached the highest value at 9 weeks (all $p < 0.05$) (Supplementary Figure S4). In addition, the MFI ratios of CD31/CGRP and Emcn/CGRP showed no significant differences between the 3-week EXP group and the sham group (all $p > 0.05$), but gradually increased in the 6-week EXP group, reaching their highest levels in the 9-week EXP group, respectively, compared with those of the sham controls (Figures 2C, 3C; all $p < 0.01$).

3.3 Gene expression of factors was related to the infiltration of sensory nerves, type H vessels and osteogenesis during *in situ* osteogenesis

To confirm the formation of sensory nerves and type H vessels during *in situ* osteogenesis, qRT-PCR was used to detect the expression levels genes related to above processes in the trauma areas at different time points (Figure 4). The mRNA expression levels of sensory nerve-related genes (*Cgrp* and *Sp*), type H vessel-related genes (*Cd31* and *Emcn*), and bone formation related genes (*Osx* and *Ocn*) in the 3-week and 9-week EXP groups were increased significantly compared with those in time-matched sham controls (all $p < 0.05$). In accordance with the immunofluorescent results of the occurring features of sensory innervation and angiogenesis, the expression levels of *Cgrp* and *Sp* gradually decrease from the 3-week EXP group to the 9-week EXP group, while the levels of vessel and bone-related genes showed their higher expression in the 9-week EXP group compared with that in the 3-week EXP group (all $p < 0.05$). By comparison, no significant difference was observed between 3-week and 9-week sham control groups for all target genes (all $p > 0.05$).

3.4 Gene expression of factors was related to the infiltration of sensory nerves, type H vessels and osteogenesis during *in situ* osteogenesis

The immunofluorescence and qRT-PCR results both indicated that sensory nerve innervation occurred earlier than vascularization during *in situ* osteogenesis, we speculated that some neuronal guidance molecules from sensory nerves might induce angiogenesis and osteogenesis in the trauma areas (Figure 5A). Therefore, we detected the mRNA levels of those neuronal guidance molecules that related to angiogenesis and osteogenesis, such as *Ntn1, Ntn4, Sema3a*, and *Sema3e* (Sakurai et al., 2010; Yebra et al., 2011; van Gils et al., 2013). The results showed that the mRNA levels of *Sema3a* were significantly higher in the 3-week EXP group (7.83 ± 0.27) than in the 9-week EXP group (2.83 ± 0.27), and both levels were significantly higher than those in the sham controls (all $p < 0.05$). The cell bodies of afferent nerves are generally positioned in the dorsal root ganglia (DRG). Sema3A expression was significantly

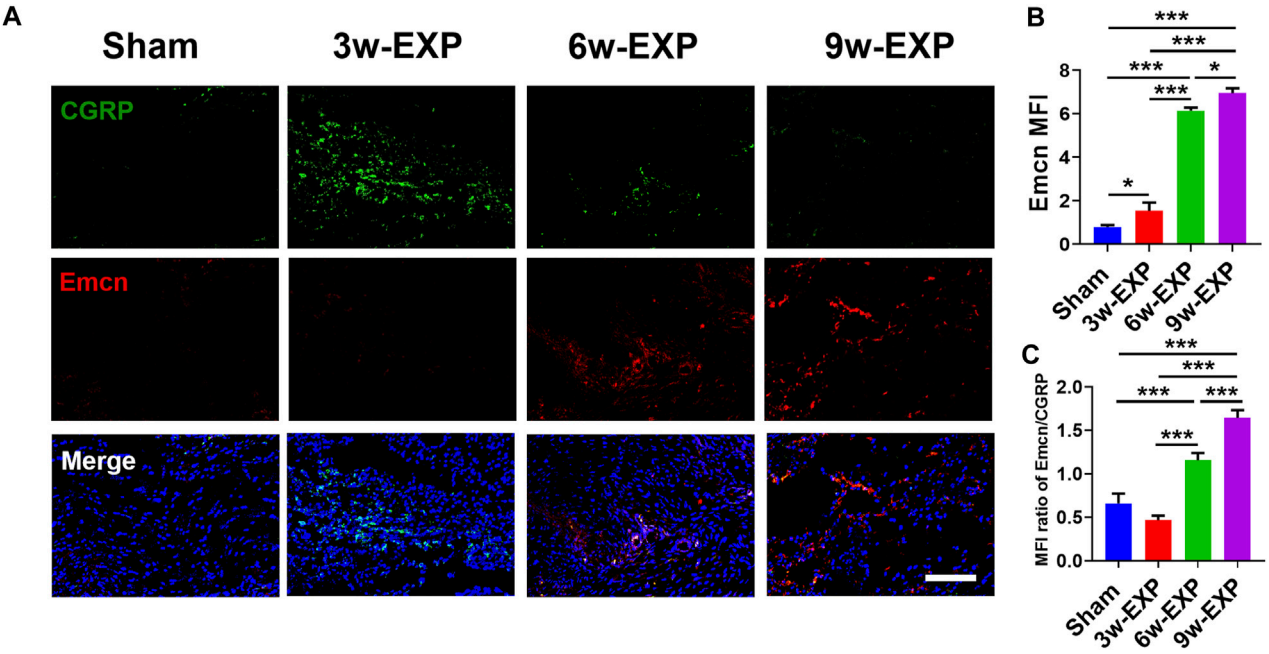

FIGURE 3
Immunofluorescence staining of trauma areas at 3 weeks after a sham operation or 3, 6 and 9 weeks after tenotomy. **(A)** Representative images of immunofluorescence staining of CGRP and Emcn. **(B)** Quantification of the MFI of Emcn expression per field view. **(C)** Quantification of the MFI ratio of Emcn/CGRP expression. Nuclei were stained with DAPI (blue). Scale bar: 100 μm. Data represent the means ± standard deviations. For all charts, groups labeled with different lowercase letters are significantly different ($p < 0.05$). CGRP, calcitonin gene-related peptide; Emcn, endomucin; DAPI, 4,6-diamidino-2-phenylindole.

higher for the DRG tissues obtained from the 3-week EXP group, compared with other groups (all $p < 0.05$) (Supplementary Figure S5). There was no significant difference in the mRNA levels of *Ntn1*, *Ntn4*, and *Sema3e* between the 3-week and 9-week EXP groups and the sham controls (all $p > 0.05$). Specimens stained for CGRP and Sema3A enabled simultaneous visualization of the location of sensory nerves and Sema3A expression (Figure 5B). CGRP-positive sensory nerves obviously co-localized with Sema3A in the 3-week and 6-week EXP groups and their distributions were more extensive than those in the sham controls, indicating the neural production of Sema3A in trauma areas. Similar to the CGRP quantification analysis, the highest MFI of Sema3A was identified in the 3-week EXP group (5.72 ± 0.28), compared with that in the 9-week EXP group (2.88 ± 0.66) and sham control groups (0.54 ± 0.12) (Figure 5C). The MFI ratios of Sema3A/CGRP were further used to confirm the presence of neural production of Sema3A in trauma areas. The ratios in all the EXP groups were around 1, and did not exhibit any significant difference among the EXP groups (all $p > 0.05$) (Figure 5D). Taken together, the results support the co-expression and co-localization of Sema3A and CGRP. Therefore, Sema3A might be an important signaling molecule that promotes osteogenesis and angiogenesis during *in situ* osteogenesis.

4 Discussion

The present study showed that the highest sensory innervation density was observed in the 3rd week after tendon injury, and then decreased gradually with time. At the same time, angiogenesis and osteogenesis both increased over time until the 9th week. In particular, sensory nerves, blood vessels and ectopic bone showed good spatiotemporal correlations. Furthermore, among many sensory nerve-derived regulators of angiogenesis and osteogenesis, Sema3A was observed to be highly expressed in the bone formation areas and thus might be an important signaling molecule that promotes bone formation. The present data show that sensory nerves and neovessels during *in situ* osteogenesis associates with Sema3A secretion.

In accordance with previous studies, our results showed that tendon injury caused bone formation, and the degree of ossification increased with time. The 9-week EXP group showed the highest BV/TV and BMD. In addition, the 6-week EXP group had a higher BS/BV compared with the 9-week group, which suggested that the new bone formed in the early stage of *in situ* osteogenesis is more interconnected and porous. No values for BV/TV and BMD were obtained for the 3-week EXP group *via* micro-CT analysis, which might have been caused by the level of minerals being too low to reach the scanning threshold. The distribution of either $CGRP^+$ or $PGP9.5^+$ nerves reached its peak at 3 weeks after tendon injury, and gradually decreased with increased time; however, it remained consistently higher than that in the sham controls. The correspondence between increased sensory innervation and early osteogenesis suggests that sensory nerves play an important role in bone formation, which is consistent with previous studies on embryonic skeleton growth and bone regeneration (Tomlinson et al., 2016; Marrella et al., 2018; Li

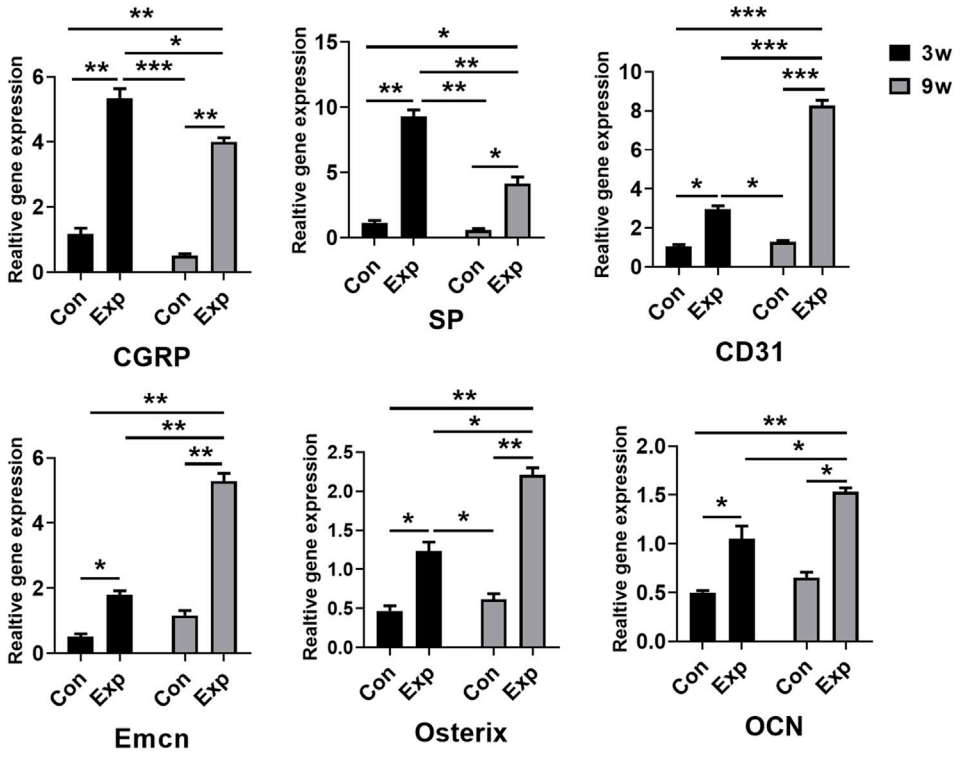

FIGURE 4
qRT-PCR analysis of genes expressed in the trauma areas after a sham operation or tenotomy at 3 and 9 weeks. For all charts, groups labeled with different lowercase letters are significantly different ($p < 0.05$). CGRP, calcitonin gene-related peptide; SP, substance P; Emcn, endomucin; OCN, osteocalcin.

et al., 2019; Tomlinson et al., 2020). However, male rats were used in the present and previous studies to exclude the effects of estrogen, so the translation of these results to females needs to be verified (Clarke, 2020).

It has been reported that peripheral nerves appear earlier than blood vessels during embryonic skeleton growth (Li et al., 2019). Nerve fibers appear initially in the vicinity of areas with high osteogenic activities and rich capillary networks in the developing skeleton (Tomlinson et al., 2016; Tomlinson et al., 2020). The present results showed that $CGRP^+$ sensory nerves were co-localized closely with $CD31^+$ or $Emcn^+$ blood vessels throughout the whole process of bone formation, and the numbers of $CD31^+$ or $Emcn^+$ blood vessel cells increased simultaneously until the end of the 9th week after injury. H-type vascular endothelial cells, with high expression of CD31 and Emcn, are tightly related to the function of osteoblastic cells and have a strong ability to induce new bone formation (Zhang et al., 2020b). The MFI ratios of CD31/CGRP and Emcn/CGRP in the 6-week and 9-week EXP groups were both significantly higher than those in the 3-week EXP group. The changes of these ratios reflect the difference in the occurrence time between innervation and angiogenesis dynamically, i.e., sensory nerve fibers participate in the osteogenic activities earlier, while vascularization follows innervation and gradually increases during *in situ* osteogenesis.

Many signaling molecules are involved in the coupling of innervation and angiogenesis. Netrins and semaphorins are known as neuronal guidance molecules that facilitate patterning of the nervous and vascular system. Netrin-1 and Sema3A were demonstrated to repel leukocytes in response to laminar shear stress, thus acting as mediators of adaptation to hemodynamic environment (Yebra et al., 2011). Deprivation of Sema3A adversely affects skeletal vascularization and mineralization (Li et al., 2017; Hayashi et al., 2019). Mice lacking Sema3A in neurons displayed diminished bone mass, sensory innervation and vascularization (Fukuda et al., 2013). The present study found that the Sema3A level increased significantly in the bone formation model and was primarily co-localized with $CGRP^+$ nerves which were spatially correlated with the distribution of $CD31^+$ and $Emcn^+$ blood vessels. These results suggested that vessels maintain their responsiveness to Sema3A spatially and temporally, and the increased distribution of blood vessels during *in situ* osteogenesis may result from the increased expression of Sema3A from sensory nerve. SEMA3 proteins have been demonstrated to control integrin-mediated adhesion, allowing for vascular remodeling (Serini et al., 2003). Particularly, Sema3A can inhibit the binding of $VEGF_{165}$ to Neuropilin-1 (NRP1) and regulate angiogenesis (Neufeld and Kessler, 2008). These findings demonstrate that Sema3A is essential to form the more mature-appearing vascular patterns. To further study the interaction of nerves and vessels during *in situ* osteogenesis, the co-staining and proximity assay of $CGRP^+$, $CD31^+Emcn^+$ and $NRP1^+$ structures are required.

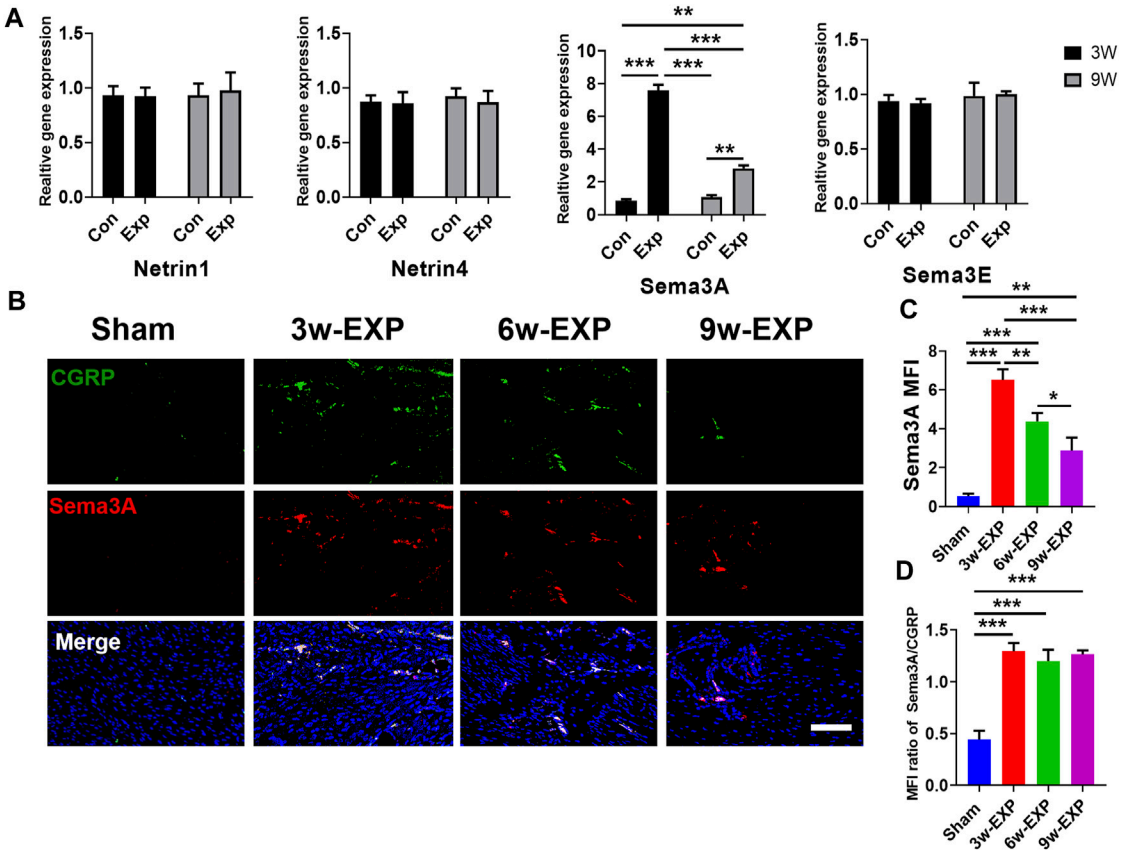

FIGURE 5
Immunofluorescence staining of trauma areas at 3 weeks after a sham operation or 3, 6 and 9 weeks after tenotomy. **(A)** qRT-PCR analysis of specific genes encoding neuronal guidance molecules in trauma areas in the sham controls and at 3 and 9 weeks in the EXP groups. **(B)** Representative images of immunofluorescence staining of CGRP and Sema3A in the trauma areas in the sham and EXP groups at 3, 6 and 9 weeks. **(C)** Quantification of the MFI of Sema3A expression. **(D)** Quantification of the MFI ratio of Sema3A/CGRP expression. Nuclei were stained with DAPI (blue). Scale bar: 100 μm. Data represent the means ± standard deviations. For all charts, groups labeled with different lowercase letters are significantly different ($p < 0.05$). Sema3A, semaphorin 3A; Sema3E, semaphorin 3E; CGRP, calcitonin gene-related peptide; DAPI, 4,6-diamidino-2-phenylindole.

The present study showed that abundant sensory fibers accompanied by increased Sema3A expression first appeared during *in situ* osteogenesis, followed by vascular formation and bone formation. During *in situ* osteogenesis, innervation and angiogenesis are spatially correlated; Sema3A is highly expressed and associated with the position of the sensory nerve. Based on above results, we proposed that the abnormal sensory innervation was one of the early events of bone formation, and thus targeting the sensory nerve ingrowth or Sema3A may be the potential targets for regulating bone formation.

Data availability statement

The original contributions presented in the study are included in the article/Supplementary Material, further inquiries can be directed to the corresponding author.

Ethics statement

The animal study was reviewed and approved by The Institutional Animal Care and Use Committee of the Fourth Military Medical University.

Author contributions

XH and YM contributed equally to the experimental performing, data acquisition and analysis and manuscript drafting. JY and L-NN contributed to data interpretation. WL contributed to animal experiments. WQ contributed to data analysis and interpretation. JH contributed to immunofluorescence experiments. KJ contributed to the study conception and design, data interpretation and manuscript revision. All authors have read and approved the current version of the manuscript.

Funding

This work was supported by grants 81870787, 82170978, and 81870805 from the National Nature Science Foundation of China, Distinguished Young Scientists Funds of Shannxi Province (2021JC-34), grant 2020TD-033 from the Shaanxi Key Scientific and Technological Innovation Team.

Conflict of interest

The authors declare that the research was conducted in the absence of any commercial or financial relationships that could be construed as a potential conflict of interest.

Publisher's note

All claims expressed in this article are solely those of the authors and do not necessarily represent those of their affiliated organizations, or those of the publisher, the editors and the reviewers. Any product that may be evaluated in this article, or claim that may be made by its manufacturer, is not guaranteed or endorsed by the publisher.

Supplementary material

The Supplementary Material for this article can be found online at: https://www.frontiersin.org/articles/10.3389/fbioe.2023.1138601/full#supplementary-material

References

Avouac, J., Pezet, S., Vandebeuque, E., Orvain, C., Gonzalez, V., Marin, G., et al. (2021). Semaphorins: From angiogenesis to inflammation in rheumatoid arthritis. *Arthritis Rheumatol.* 73 (9), 1579–1588. doi:10.1002/art.41701

Brazill, J. M., Beeve, A. T., Craft, C. S., Ivanusic, J. J., and Scheller, E. L. (2019). Nerves in bone: Evolving concepts in pain and anabolism. *J. Bone Min. Res.* 34 (8), 1393–1406. doi:10.1002/jbmr.3822

Clarke, S. A. (2020). The inadequate reporting of sex in research. *Bone Jt. Res.* 9 (10), 729–730. doi:10.1302/2046-3758.910.bjr-2020-0351.r1

Feinstein, J., and Ramkhelawon, B. (2017). Netrins & Semaphorins: Novel regulators of the immune response. *Biochim. Biophys. Acta Mol. Basis Dis.* 1863 (12), 3183–3189. doi:10.1016/j.bbadis.2017.09.010

Fukuda, T., Takeda, S., Xu, R., Ochi, H., Sunamura, S., Sato, T., et al. (2013). Sema3A regulates bone-mass accrual through sensory innervations. *Nature* 497 (7450), 490–493. doi:10.1038/nature12115

Hayashi, M., Nakashima, T., Yoshimura, N., Okamoto, K., Tanaka, S., and Takayanagi, H. (2019). Autoregulation of osteocyte Sema3A orchestrates estrogen action and counteracts bone aging. *Cell Metab.* 29 (3), 627–637.e5. doi:10.1016/j.cmet.2018.12.021

Hofman, M., Rabenschlag, F., Andruszkow, H., Andruszkow, J., Möckel, D., Lammers, T., et al. (2019). Effect of neurokinin-1-receptor blockage on fracture healing in rats. *Sci. Rep.* 9 (1), 9744. doi:10.1038/s41598-019-46278-6

Lee, S., Hwang, C., Marini, S., Tower, R. J., Qin, Q., Negri, S., et al. (2021). NGF-TrkA signaling dictates neural ingrowth and aberrant osteochondral differentiation after soft tissue trauma. *Nat. Commun.* 12 (1), 4939. doi:10.1038/s41467-021-25143-z

Li, Z., Hao, J., Duan, X., Wu, N., Zhou, Z., Yang, F., et al. (2017). The role of semaphorin 3A in bone remodeling. *Front. Cell Neurosci.* 11, 40. doi:10.3389/fncel.2017.00040

Li, Z., Meyers, C. A., Chang, L., Lee, S., Li, Z., Tomlinson, R., et al. (2019). Fracture repair requires TrkA signaling by skeletal sensory nerves. *J. Clin. Invest.* 129 (12), 5137–5150. doi:10.1172/JCI128428

Limoni, G., and Niquille, M. (2021). Semaphorins and plexins in central nervous system patterning: The key to it all? *Curr. Opin. Neurobiol.* 66, 224–232. doi:10.1016/j.conb.2020.12.014

Livak, K. J., and Schmittgen, T. D. (2001). Analysis of relative gene expression data using real-time quantitative PCR and the 2−ΔΔCT method. *Methods* 25 (4), 402–408. doi:10.1006/meth.2001.1262

Marrella, A., Lee, T. Y., Lee, D. H., Karuthedom, S., Syla, D., Chawla, A., et al. (2018). Engineering vascularized and innervated bone biomaterials for improved skeletal tissue regeneration. *Mater TodayKidlingt.* 21 (4), 362–376. doi:10.1016/j.mattod.2017.10.005

Neufeld, G., and Kessler, O. (2008). The semaphorins: Versatile regulators of tumour progression and tumour angiogenesis. *Nat. Rev. Cancer* 8 (8), 632–645. doi:10.1038/nrc2404

Qin, Q., Gomez-Salazar, M., Cherief, M., Pagani, C. A., Lee, S., Hwang, C., et al. (2022b). Neuron-to-vessel signaling is a required feature of aberrant stem cell commitment after soft tissue trauma. *Bone Res.* 10 (1), 43. doi:10.1038/s41413-022-00216-x

Qin, Q., Lee, S., Patel, N., Walden, K., Gomez-Salazar, M., Levi, B., et al. (2022a). Neurovascular coupling in bone regeneration. *Exp. Mol. Med.* 54 (11), 1844–1849. doi:10.1038/s12276-022-00899-6

Rajpar, I., and Tomlinson, R. E. (2022). Function of peripheral nerves in the development and healing of tendon and bone. *Semin. Cell Dev. Biol.* 123, 48–56. doi:10.1016/j.semcdb.2021.05.001

Sakurai, A., Gavard, J., Annas-Linhares, Y., Basile, J. R., Amornphimoltham, P., Palmby, T. R., et al. (2010). Semaphorin 3E initiates antiangiogenic signaling through plexin D1 by regulating Arf6 and R-Ras. *Mol. Cell Biol.* 30 (12), 3086–3098. doi:10.1128/MCB.01652-09

Sayilekshmy, M., Hansen, R. B., Delaissé, J. M., Rolighed, L., Andersen, T. L., and Heegaard, A. M. (2019). Innervation is higher above bone remodeling surfaces and in cortical pores in human bone: Lessons from patients with primary hyperparathyroidism. *Sci. Rep.* 9 (1), 5361. doi:10.1038/s41598-019-41779-w

Serini, G., Valdembri, D., Zanivan, S., Morterra, G., Burkhardt, C., Caccavari, F., et al. (2003). Class 3 semaphorins control vascular morphogenesis by inhibiting integrin function. *Nature* 424 (6947), 391–397. doi:10.1038/nature01784

Sun, S., Diggins, N. H., Gunderson, Z. J., Fehrenbacher, J. C., White, F. A., and Kacena, M. A. (2020). No pain, no gain? The effects of pain-promoting neuropeptides and neurotrophins on fracture healing. *Bone* 31, 115109. doi:10.1016/j.bone.2019.115109

Tomlinson, R. E., Christiansen, B. A., Giannone, A. A., and Genetos, D. C. (2020). The role of nerves in skeletal development, adaptation, and aging. *Front. Endocrinol. (Lausanne).* 11, 646. doi:10.3389/fendo.2020.00646

Tomlinson, R. E., Li, Z., Zhang, Q., Goh, B. C., Li, Z., Thorek, D. L. J., et al. (2016). NGF-TrkA signaling by sensory nerves coordinates the vascularization and ossification of developing endochondral bone. *Cell Rep.* 16 (10), 2723–2735. doi:10.1016/j.celrep.2016.08.002

van Gils, J. M., Ramkhelawon, B., Fernandes, L., Stewart, M. C., Guo, L., Seibert, T., et al. (2013). Endothelial expression of guidance cues in vessel wall homeostasis dysregulation under proatherosclerotic conditions. *Arterioscler. Thromb. Vasc. Biol.* 33 (5), 911–919. doi:10.1161/ATVBAHA.112.301155

Wan, Q. Q., Qin, W. P., Ma, Y. X., Shen, M. J., Li, J., Zhang, Z. B., et al. (2021). Crosstalk between bone and nerves within bone. *Adv. Sci.* 8 (7), 2003390. doi:10.1002/advs.202003390

Yamagishi, S., Bando, Y., and Sato, K. (2021). Involvement of netrins and their receptors in neuronal migration in the cerebral cortex. *Front. Cell Dev. Biol.* 8, 590009. doi:10.3389/fcell.2020.590009

Yebra, M., Diaferia, G. R., Montgomery, A. M., Kaido, T., Brunken, W. J., Koch, M., et al. (2011). Endothelium-derived Netrin-4 supports pancreatic epithelial cell adhesion and differentiation through integrins α2β1 and α3β1. *PLoS One* 6 (7), e22750. doi:10.1371/journal.pone.0022750

Yin, Y., Tang, Q., Xie, M., Hu, L., and Chen, L. (2021). Insights into the mechanism of vascular endothelial cells on bone biology. *Biosci. Rep.* 41 (1), BSR20203258. doi:10.1042/BSR20203258

Zhang, J., Pan, J., and Jing, W. (2020b). Motivating role of type H vessels in bone regeneration. *Cell Prolif.* 53 (9), e12874. doi:10.1111/cpr.12874

Zhang, J., Wang, L., Chu, J., Ao, X., Jiang, T., Yan, B., et al. (2020a). Macrophage-derived neurotrophin-3 promotes heterotopic ossification in rats. *Lab. Invest.* 100 (5), 762–776. doi:10.1038/s41374-019-0367-x

Zhu, S., Bennett, S., Kuek, V., Xiang, C., Xu, H., Rosen, V., et al. (2020). Endothelial cells produce angiocrine factors to regulate bone and cartilage via versatile mechanisms. *Theranostics* 10 (13), 5957–5965. doi:10.7150/thno.45422

frontiers | Frontiers in Bioengineering and Biotechnology

TYPE Review
PUBLISHED 27 April 2023
DOI 10.3389/fbioe.2023.1197974

Check for updates

OPEN ACCESS

EDITED BY
Jie Tang,
The University of Queensland, Australia

REVIEWED BY
Hao Song,
University of Queensland, Australia
Qianyu Zhang,
Chongqing Medical University, China

*CORRESPONDENCE
Liang Wang,
liang091@aliyun.com
Chao Yang,
charisyang@outlook.com

†These authors have contributed equally to this work

RECEIVED 31 March 2023
ACCEPTED 17 April 2023
PUBLISHED 27 April 2023

CITATION
Chen Y, He X, Chen Q, He Y, Chen F, Yang C and Wang L (2023), Nanomaterials against intracellular bacterial infection: from drug delivery to intrinsic biofunction.
Front. Bioeng. Biotechnol. 11:1197974.
doi: 10.3389/fbioe.2023.1197974

COPYRIGHT
© 2023 Chen, He, Chen, He, Chen, Yang and Wang. This is an open-access article distributed under the terms of the Creative Commons Attribution License (CC BY). The use, distribution or reproduction in other forums is permitted, provided the original author(s) and the copyright owner(s) are credited and that the original publication in this journal is cited, in accordance with accepted academic practice. No use, distribution or reproduction is permitted which does not comply with these terms.

Nanomaterials against intracellular bacterial infection: from drug delivery to intrinsic biofunction

Yinglu Chen[1,2†], Xiaoheng He[3†], Qiuhong Chen[1], Yi He[4], Fangman Chen[5], Chao Yang[1*] and Liang Wang[1*]

[1]Department of Orthopedics, Academy of Orthopedics-Guangdong Province, Orthopedic Hospital of Guangdong Province, Guangdong Provincial Key Laboratory of Bone and Joint Degenerative Diseases, The Third Affiliated Hospital, Southern Medical University, Guangzhou, China, [2]School of Biology and Biological Engineering, South China University of Technology, Guangzhou, China, [3]Department of Applied Chemistry, Xi'an University of Technology, Xi'an, China, [4]Department of Rheumatology and Immunology, The Third Affiliated Hospital, Southern Medical University, Guangzhou, China, [5]State Key Laboratory of Quality Research in Chinese Medicine, Institute of Chinese Medical Sciences, University of Macau, Macau, Macau SAR, China

Fighting intracellular bacteria with strong antibiotics evading remains a long-standing challenge. Responding to and regulating the infectious microenvironment is crucial for treating intracellular infections. Sophisticated nanomaterials with unique physicochemical properties exhibit great potential for precise drug delivery towards infection sites, along with modulating infectious microenvironment via their instinct bioactivity. In this review, we first identify the key characters and therapeutic targets of intracellular infection microenvironment. Next, we illustrate how the nanomaterials physicochemical properties, such as size, charge, shape and functionalization affect the interaction between nanomaterials, cells and bacteria. We also introduce the recent progress of nanomaterial-based targeted delivery and controlled release of antibiotics in intracellular infection microenvironment. Notably, we highlight the nanomaterials with unique intrinsic properties, such as metal toxicity and enzyme-like activity for the treatment of intracellular bacteria. Finally, we discuss the opportunities and challenges of bioactive nanomaterials in addressing intracellular infections.

KEYWORDS

intracellular infection, drug delivery, antibacterial, reactive oxygen species, bioactive nanomaterials

1 Introduction

In the territory of infectious disease, chronic and persistent infections caused by intracellular bacteria pose a thorny threat to public health (Kamaruzzaman et al., 2017). In these contexts, pathogens such as *Staphylococcus aureus* (*S. aureus*), *Mycobacterium tuberculosis* (*M. tuberculosis*), *Salmonella* and *Listeria* are able to nestle in professional phagocytic cells, particularly macrophages, which not only shield them from the host immune system's eradication but also from antibacterial agents. The most prominent intracellular infections in clinic are associated with *M. tuberculosis*, which can require prolonged and substantial antibiotic treatments. Over extended periods, intracellular bacteria can act as a 'Trojan horse', resulting in a secondary relapsing infection primarily due to their ability to survive and multiply rapidly within host cells. This

category includes obligate intracellular bacteria that can reproduce both inside and outside their cellular hosts, as well as facultative intracellular bacteria that depend on host cells for their reproduction (Briones et al., 2008).

To date, various families of antibiotics, such as rifampin, isoniazid, and linezolid, are commonly used in clinical settings to treat intracellular bacterial infections. However, these antibiotics are often ineffective in completely eradicating intracellular pathogens. This difficulty in treating intracellular infections is largely due to two factors: the inability of sufficient antibiotics to penetrate infected cells, and the various mechanisms by which bacteria can escape host cells. On the one hand, many antibiotics are hydrophilic and have poor intracellular permeability, which limits their effectiveness in treating intracellular infections. On the other hand, even antibiotics are able to diffuse into cells, they may be inactivated by several factors within cells, such as degradation by acidic, redox, or multi-enzymatic microenvironment, or discharge by efflux pumps (Wright, 2005). Accordingly, the restricted cellular penetration and intracellular instability of antibiotics cause sub-therapeutic concentrations within cells, resulting in the failure of anti-intracellular bacteria and the long-lasting persistence of pathogens.

Phagocytic systems are not only capable of killing invading pathogens, but also acting as a natural shield in some cases, preventing bacteria from being eliminated by antibiotics. However, intracellular bacteria develop some mechanisms to evade the innate immune response. These mechanisms include escaping from endosomal/lysosomal/phagolysosomal compartments to the cytoplasm, preventing the fusion of phagosomes and lysosomes, or developing resistance to the bactericidal microenvironments found in lysosomes/phagolysosomes. For instance, *Salmonella enterica* is usually located in late endosomes (Brouillette et al., 2003), while *Mycobacterium tuberculosis*, the typical intracellular bacterium, survives within phagosomes (Peng et al., 2016). This leads to those antibiotics that can penetrate the cell membranes are unable to eliminate evasive *M. tuberculosis* due to their failure to concentrate in phagosomes (Onyeji et al., 1994). Taken together, bacteria with different escape mechanisms survive in distinct cell compartments, making it difficult for antibiotics to locate within the appropriate compartments and resulting in inactive antibacterial effects.

Compared with the deficiency of traditional antibiotics against intracellular bacteria, targeted drug delivery systems show promising potentials for the management of intracellular infections through improving the cellular uptake and distribution of antibiotics. With the advances in nanotechnology, a wide variety of nanomaterials have been designed for controlled delivery of anti-bacterial agents, achieving maximal therapeutic efficiency along with minimizing potential adverse effects. Furthermore, the unique intracellular microenvironment at infected sites, with a low pH, redox potential, abundant H_2O_2, bacterial and cellular enzymes, can serve as responsive stimulus to realize spatiotemporal drug release of nanomaterials. Thus, exploring sophisticated nanomaterials with unique bioactivities in response to the factors or cues of intracellular microenvironment offers great potentials in eliciting specific responses and functions to kill intracellular bacteria. In these contexts, a deep understanding of the interactions between cells, intracellular bacteria and nanomaterials may provide guidance to develop intelligent nanomaterials with precise environmental responsiveness for efficient and safe management of intracellular infections.

In this review, we identify the key characters and therapeutic targets of intracellular infection microenvironment. We illustrate how the nanomaterials physicochemical properties, such as size, charge, shape and surface functionalization affect the interaction between nanomaterials, cells and bacteria. We introduce the recent progress of nanomaterial-based targeted delivery and controlled release of antibiotics in intracellular infection microenvironment. We highlight the nanomaterials with unique intrinsic properties, such as metal toxicity and enzyme-like activity for the treatment of intracellular bacteria (Figure 1). We discuss the opportunities and challenges of bioactive nanomaterials in addressing intracellular infections.

2 Intracellular bacteria and microenvironment

2.1 Host bactericidal mechanisms

When pathogens invade, macrophages, as one of the major immune cells, fight against infection by expressing a series of receptors to trigger innate immunity. This surveillance recognition is achieved through sensors called pattern recognition receptors (PRRs) that detect pathogen-associated molecular patterns (PAMPs) and damage-related molecular patterns (DAMPs) (Plüddemann et al., 2011; Broz and Monack, 2013). After the detection of pathogens, phagocytosis plays an essential role in anti-bacterial host defense, which is mainly manifested by the effective internalization of pathogens. In such a conversion, the engulfment of pathogens by macrophages and a series of sequent membrane remodeling leads to the formation of a membrane-bound vesicle named phagosome. Following the internalization, it is a clearance process in which the phagosome acquires bactericidal and degradative functions termed phagosomal maturation. At the terminal stage of its maturation, the microenvironment of the phagosome becomes highly acidic, degradative, and oxidative, which all contribute to clearing the invaded pathogens. The low pH in phagosomes is related to the progressive acidification within the vacuole, which is realized by the V-ATPase-mediated proton pump (Flannagan et al., 2009). Meanwhile, this acidic condition favors the subsequent formation of phagolysosomes and optimal enzymatic activity of hydrolases in lysosomes.

Another mechanism to kill bacteria is the delivery of molecules with degradative functions, such as defensins, cathelicidins, lysozyme and hydrolases, into phagosomes. Defensins are able to permeabilize bacteria membranes due to the formation of ion transport channels. Cathelicidins, on the other hand, induce permeabilization acting on the cell wall as well as both the outer and inner membranes of bacteria. In addition, hydrolases targeting carbohydrates and lipids also exist in phagosomes, which degrade a wide range of invading bacterial components (Flannagan et al., 2009).

Phagocytes could also act through a large amount of reactive oxygen species (ROS) and reactive nitrogen species (RNS) produced by the NOX2 NADPH oxidase (Quinn and Gauss, 2004; Minakami

and Sumimoto, 2006) and NOS2 nitric oxide synthase (Fang, 2004). The transfer of electrons from NADPH to molecular oxygen results in the formation of superoxide radicals ($O_2\cdot^-$), which are released into phagosomes (Quinn and Gauss, 2004; Mizushima et al., 2011). After that, $O_2\cdot^-$ in phagosomes react with H_2O_2 to produce hydroxyl radicals (·OH) and singlet oxygen ($^1O_2$) (Minakami and Sumimoto, 2006). It is worth noting that the fusion of the lysosomes and vacuoles leads to partial disruption of the membrane connection, releasing the contents, such as myeloperoxidase, into the phagosomes. Myeloperoxidase within the phagosomes can catalyze abundant H_2O_2 and halogen ions to highly bactericide hypochlorous acid (HClO) and chloramines (Thomas, 1979; Shepherd, 1986). RNS is also essential antimicrobial effectors, which reacts with ROS to destroy pathogens, causing nitrosative stress. The production of RNS starts with NOS catalyzing *L*-arginine and citrulline to produce nitric oxide (NO), which begins with superoxide to form peroxynitrite ($ONOO^-$), which is a highly reactive species that can directly act with several biological targets and cell components, including lipids, amino acid residues, and DNA bases (Webb et al., 2001). Besides, peroxynitrite also has the ability to get across cell membranes to some subcompartments like phagosomes through anion channel (Fang, 2004).

Accordingly, those produced free radicals and oxidation-state components contribute to protein denaturation and lipid peroxidation by oxidative damage, which leads to irreversible damage to the invading bacteria (Boyle and Randow, 2013). This natural defense process provides ideas for biomimetic strategies to eliminate intracellular bacteria.

2.2 Bacterial defensive mechanisms

Unlike extracellular bacteria, intracellular bacteria that can survive and replicate in host cells, especially macrophages, adapt to challenging intracellular microenvironment and evolve intelligent mechanisms to evade host clearance. Those intracellular bacteria are typically divided into two categories: phagosomal and cytosolic bacteria. Most intracellular bacteria studied to date are stored in phagosomes. In detail, the phagosomes provide a safe haven for bacteria, shielding them from immune system detection, and facilitating their replication using the components within the phagosomes (Cullinane et al., 2008; Lamkanfi and Dixit, 2010). Alternatively, cytosolic bacteria benefit from rich nutrient conditions and a relatively spacious microenvironment, enabling them to survive in the host cell cytoplasm despite the presence of immune defenses. In general, treatments that can eliminate bacteria in phagosomes can also act on cytosolic bacteria. It is much thornier to treat phagosome bacteria than cytosolic ones, so our review focus on phagosome bacteria.

Survival of intracellular bacteria presents three main challenges: evading immune system surveillance, resisting the microenvironment, and evading the phagolysosomal pathway. Numerous strategies, including actin-based cell-to-cell spread, low expression of flagellin, avoidance, blockage and adaptation to the phagolysosomal pathway, are utilized by intracellular pathogens.

Different species of bacteria have their own intracellular lifestyles. The majority of phagosome bacteria have abilities to prevent phagosomes maturation, the terminal stage before lysosomes fusion (Ray et al., 2009). For instance, some bacteria have evolved metabolic pathways to prevent acidification in phagosomes, or express specific proteins to withstand low pH microenvironment (Park et al., 1996; Vandal et al., 2008; Huang et al., 2009; Martinez et al., 2011). In addition, some bacteria are able to express detoxifying enzymes (Schmidtchen et al., 2002) like catalase or superoxide dismutase to balance ROS/RNS levels within phagosomes (John et al., 2001; Ng et al., 2004), or interfere with the biological function of enzymes that catalyze ROS/RNS production (Mott et al., 2002). As a result, bacteria protect themselves from being destroyed and eliminated by ROS/RNS (Rudel et al., 2010; Ashida et al., 2011).

Other bacteria escape into the cytoplasm, which constitutes a wild and favorable microenvironment, through sophisticated mechanisms, such as escaping from vesicles, and permeabilizing phagosomes. For those bacteria, it is essential to escape the phagosome subcompartments as early as possible after internalization to avoid fusion with lysosomes. In this process, protein secretion plays a key role in allowing bacteria to cross the cytoplasmic membranes, cell walls, vacuole and host cell membranes, to achieve both intracellular vacuole spread and cell-to-cell spread. Among them, the four major protein secretion ssystems are the type III secretion system (T3SS) (Cornelis, 2006), type IV secretion systems (T4SSs) (Vogel et al., 1998; Christie and Cascales, 2005), type VI secretion systems (T6SSs) (Coulthurst, 2013; Kudryashev et al., 2015) and type VII secretion system (T7SS) (Abdallah et al., 2007), which hold the potential to serve as inhibitory targets for treatment design.

With these findings in mind, a comprehensive understanding of the mechanisms by which intracellular pathogens evade host cells and respond to the innate immune systems are critical to elucidate the pathogenesis of intracellular infections. Moreover, systematically deciphering the interactions between host cells and intracellular pathogens may provide clues for designing advanced nanotherapeutics against intracellular infections.

3 Interactions between bacteria, cells, and nanomaterials

As discussed above, most intracellular bacteria spend their whole lifestyles within phagosomes. Internalization and phagosomal maturation are essential to keep phagocytosis effective. After being detected and taken up by phagocytes, bacteria undergo a series of membrane fusions and interactions, resulting in their entrapments in sub-compartments such as phagosomes or vacuoles. However, since bacteria may be located in different phagosomes, tailored designed nanomaterials against intracellular pathogens require coexisting in the same compartments. Therefore, a deep understanding of the interactions among bacteria, phagocyte cells, and nanomaterials is essential for the principle of material design.

Different nanomaterials may be located in different sites relative to cells, such as the inner or outer cell membranes, and can influence cell proliferation, apoptosis, and migration. Therefore, understanding the relevant parameters in nanomaterials interactions with cell membranes is essential in regulating

nanomaterials internalization. Nanomaterials can be internalized into cells via phagocytosis, diffusion, and fluid phase endocytosis (He et al., 2009). The endocytosis refers to the process by which the plasma membrane invaginates and forms vesicles, thereby transporting extracellular compositions into cells. It is categorized into four major types, including clathrin/caveolae-dependent endocytosis, phagocytosis, pinocytosis, and macropinocytosis (Doherty and McMahon, 2009; Howes et al., 2010; Sahay et al., 2010; Sandvig et al., 2011). Most nanoparticles enter cells through endocytosis, while relatively few enter via other mechanisms. Several factors, including size, shape, surface charge and functionalization, have influence on the uptake of materials by cells.

3.1 Size-dependent cellular uptake

Unlike non-phagocytes, which tend to engulf spherical nanoparticles in the 20–50 nm range, phagocytes preferentially take up micro scale particles (González et al., 1996; Champion et al., 2008; Jiang et al., 2008). Experimental results for silver nanoparticles have shown that well-dispersed 20–200 nm particles were internalized better by non-phagocytes than phagocytes (Lankoff et al., 2012), whereas aggregated silver particles were more likely to be internalized by phagocytes (Wang et al., 2012). The same phenomenon has been found for smaller nanoparticles like iron oxide particles, where small iron oxide particles exhibited a higher level of phagocytic accumulation than ultra-small particle size particles (Raynal et al., 2004).

This difference in internalization may be attributed to the influence of size on internalization pathways. Normally ultra-small particles are not recognized as exogenous agents by macrophages and can enter directly into cells based on pores in the cell membranes, whereas microscale particles are more likely to be absorbed by the reticuloendothelial system. Besides, smaller sizes possess larger surface areas, which contributes to particles diffuse into cells. When the diameter of the nanospheres is less than 200 nm, their penetration is mainly regulated by the clathrin pathway, but when the size increases to 500 nm, their internalization is mainly mediated by caveolae pathway (Rejman et al., 2004). The effect of size is also significant in the uptake of different sized anionic polystyrene particles, with smaller particles being taken up mainly through clathrin-independent cavelae-independent pathways, while larger particles are uptaken via clathrin-mediated endocytosis (Lai et al., 2007). This distinction can be explained by the fact that the clathrin-mediated pathway has a higher uptake rate than clathrin-independent cavelae-independent pathways, resulting in particles internalized through this pathway exhibiting faster accumulation within cells.

3.2 Charge-dependent cellular uptake

Surface charges also play a key role in cellular uptake. It is mainly manifested in the fact that the neutral surface charge nanomaterials have a lower plasma protein adsorption rate, accompanied by a longer blood circulation time, which results in a higher cell uptake due to a longer margin from the phagocytes.

Positively charged nanomaterials bind to negatively charged cell membranes through electrostatic interactions (Tahara et al., 2009; Duceppe and Tabrizian, 2010). A mass of works has demonstrated that positively charged particles were internalized into cells at a higher degree than their respective anionic particles, such as gold and silver particles, iron oxide particles, silicon dioxide, chitosan, liposome, and polymers. Besides, for negatively charged nanomaterials, the internalization decreases with increasing surface charge, while positively ones, on the contrary, performs a positive correlation with a certain range of surface charge. Surprisingly, a representative example is antibacterial silver nanoparticles coated with chitosan (CS-AgNPs) with enhanced antibacterial effect (Jena et al., 2012). The designed CS-AgNPs exhibited a significantly improved therapeutic effect on intracellular bacteria mainly due to their strong cell internalization.

Several other researches have shown some contradictory results, which might contribute to negatively charged nanoparticles can promote cellular uptake via regulating the formation of aggregation and cluster after initial electrostatic repulsion. Taking the uptake of liposome with different surface charges as an example, a negatively charged PLGA-lipid hybrid system performed better uptake behavior compared to a positively charged system (Maghrebi et al., 2020). Another hypothesis is that bacterial surfaces also present a negative charge, and phagocytes may preferentially take up anionic particles (Fröhlich, 2012). Moreover, some surface groups with negative charges, such as citrate groups, can improve the stability of nanoparticles in culture media and increase their affinity for cell membranes (Kolosnjaj-Tabi et al., 2013).

3.3 Shape-dependent cellular uptake

Shape is another important factor influencing the internalization of nanomaterials, especially when endocytosis pathways of nanomaterials need to be mediated by receptors. Although the surface area of rod-shaped nanomaterials is smaller than that of spherical particles, the limited binding sites on its surface can more efficiently recognize and bind to target cell surface receptors due to its aspect ratio. This allows rod-shaped nanomaterials to exhibit higher cell adhesion efficiency than spherical ones (Kolosnjaj-Tabi et al., 2013; Shao et al., 2017). On the other hand, nanomaterials with sharp shapes such as spines are able to locate in the cytoplasm due to their better ability to penetrate membranes, which enables them to remain in cells benefiting from low exocytosis (Chu et al., 2014).

3.4 Surface functionalization-dependent cellular uptake

Surface functionalization of nanomaterials not only regulates surface charge, but also improves properties such as hydrophobicity and softness. The most common strategy is surface polyethylene glycolation (PEGylation), which is mainly used to reduce the hydrophobicity of nanomaterials and alter their biological characteristics. PEGylation forms a hydrated layer that reduces the adsorption of serum proteins, increases the hydrophilicity, and reduces macrophage uptake, which is often referred to the "stealth effect" (Figures 2A, B) (Yang et al., 2014; Sanchez et al.,

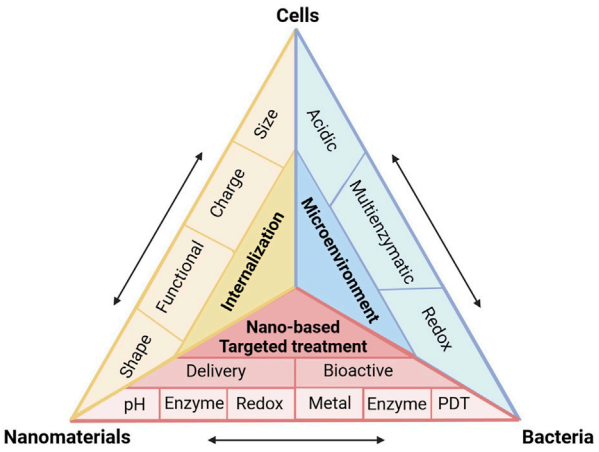

FIGURE 1
Schematic of interactions between cells, intracellular bacteria and nanomaterials during employing multifunctional nanomaterials against intracellular infections.

nanomaterials. For example, nanoparticles modified with polysaccharides could interact with specific receptors on cell membranes, resulting in active targeting for more precise internalization. Surface arginine-modified mesoporous silica nanoparticle (MSN) was able to co-localize with intracellular *Salmonella*, leading to efficient antibiotic delivery (Figures 2C–E) (Mudakavi et al., 2017).

4 Nanoparticulate materials against intracellular bacteria

Due to the particularity of intracellular bacteria, three subjects, cells, bacteria and nanomaterials included, should be taken into consideration at the same time for nano-therapy design. For instance, positively charged materials have a higher likelihood of being taken up by cells and can also bind to negatively charged bacterial surfaces through electrostatic interactions. Yang et al. utilized this strategy by designing surface cation-targeted peptide-modified MSN to deliver gentamicin, and the results proved the

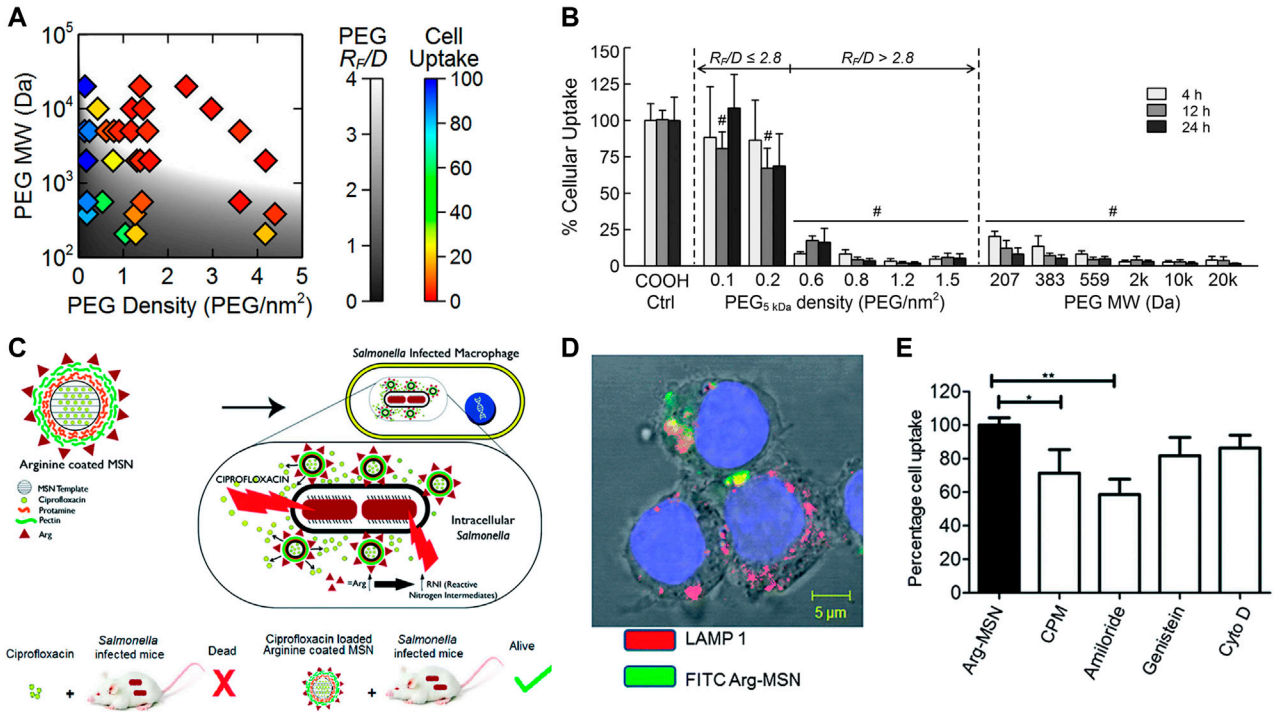

FIGURE 2
(A,B) Internalization probability of PEG functionalized nanoparticles with various grafting densities by differentiated human THP-1 cells. **(C)** Schematic illustration of the surface arginine-modified MSN co-localized with intracellular *Salmonella*, resulting in efficient antibiotic delivery. **(D)** Cellular trafficking and mechanism of endocytosis of Arg-MSN in RAW 264.7 cells. **(E)** Cellular uptake of Arg-MSN particles in the presence of pharmacological inhibitors of endocytosis. Reproduced with permission from Yang et al. (2014) (Copyright 2014 American Chemical Society) and Mudakavi et al. (2017).

2017). Additionally, the difference in uptake may also be related to the change in particle softness by functionalized modification, where softer particles are more likely to be taken up by macrophages. Surface functionalization also enables active targeting of ability of nanoparticles to specifically target *S. aureus* and internalize into RAW 264.7 cells, indicating potentials for fighting against intracellular infections (Yang et al., 2018). Similarly, Maya et al. developed *o*-carboxymethyl-coated chitosan to achieve tetracycline

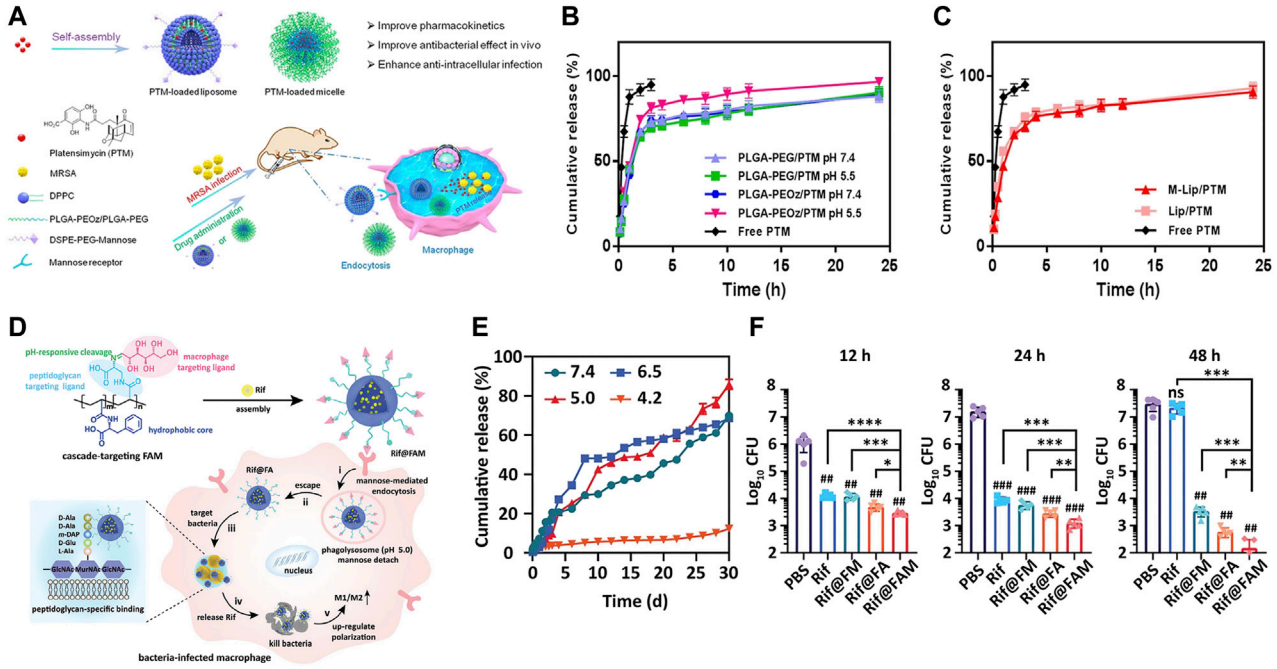

FIGURE 3
(A) Schematic illustration of PTM-loaded liposomes and micelles with pH-responsive release demonstrating a notably high antibacterial efficacy. **(B,C)** The pH-dependent release characteristics. **(D)** Schematic illustration of pH-triggered cascade release of rifampicin from DDS to eliminate intracellular MRSA. **(E)** The pH-sensitive release profile of DDS. **(F)** The intracellular bactericidal effect of different treatments. Reproduced with permission from Wang et al. (2020) (Copyright 2020 American Chemical Society) and Feng et al. (2022).

targeted delivery to the infectious sites of intracellular *S. aureus* (Maya et al., 2012).

Currently, the strategies of targeting infected cells involve non-specific electrostatic interactions and specific receptor-ligand interactions, the most representative of which are mannose receptor, CD44 receptor, tuftsin receptor, and hyaluronic acid ligand. On the other hand, direct targeting of bacteria is mainly achieved through non-specific electrostatic interactions, ligand-receptor recognition, and antigen-antibody specific binding.

4.1 Nanocarriers

According to the above discussion, bacteria invade cells and locate in different sub-compartments, making it crucial for nanotherapeutics to deliver antibiotics in on-demand manner. This approach can improve treatment efficacy and reduce toxicity to normal tissues. Furthermore, bacterial invasion creates a unique infection microenvironment characterized by low pH, related enzyme secretion, and slight temperature changes. These conditions can be leveraged as stimulus to achieve drug targeting and release.

4.1.1 pH-responsive release

Progressive acidification of phagosomes and the acidic microenvironment of lysosomes are the most common stimulus for antibiotic release (Ninan et al., 2016; Pei et al., 2017; Pei et al., 2017; Lu et al., 2018; Qu et al., 2018; Su et al., 2018; Mohebali and Abdouss, 2020; Wang et al., 2020). Platensimycin (PTM), a promising natural product drug, was designed to be loaded in pH responsive release polymers, which demonstrate significantly reduce residual methicillin-resistant *Staphylococcus aureus* (MRSA) in macrophage cells (Figures 3A–C). Antituberculosis drug-loaded MSNs equipped with a pH-sensitive valve (β-cyclodextrin) were constructed to optimize loading and achieve specific intracellular delivery of drug for the treatment of tuberculosis (TB) (Clemens et al., 2012). Greater therapeutic efficacy was achieved which may be attributed to the fact that it can only be released in acidified phagosomal conditions. Other drug delivery systems (DDS) were synthesized to realize cascade release of rifampicin after Schiff base cleavage in acidic phagolysosome (Figures 3D–F) (Feng et al., 2022). This DDS in a cascade manner performed outstanding targeting and killing activity against MRSA inside macrophages. In addition, some nanomaterials with tailored surface charge have been prepared. This particular type of nanoparticles typically perform positive surface charges only under acidic conditions, which allows them to better cross the cell membranes and bind to bacteria with negatively charged surfaces. In such a scenario, nanomaterials not only exhibit efficient internalization, but also have lower toxicity to normal cells. This is because cationic particles are more likely to cause hemolysis and cytotoxicity, which can lead to lysosomal and mitochondrial damage and cell membranes destruction.

4.1.2 Enzymes-responsive release

As mentioned earlier, during the process of phagosomes maturation, various enzymes like lipase (Jaeger et al., 1994; Jaeger and Reetz, 1998), phosphatase or phospholipase (DeVinney et al., 2000) are secreted and recruited into phagosomes. Accordingly,

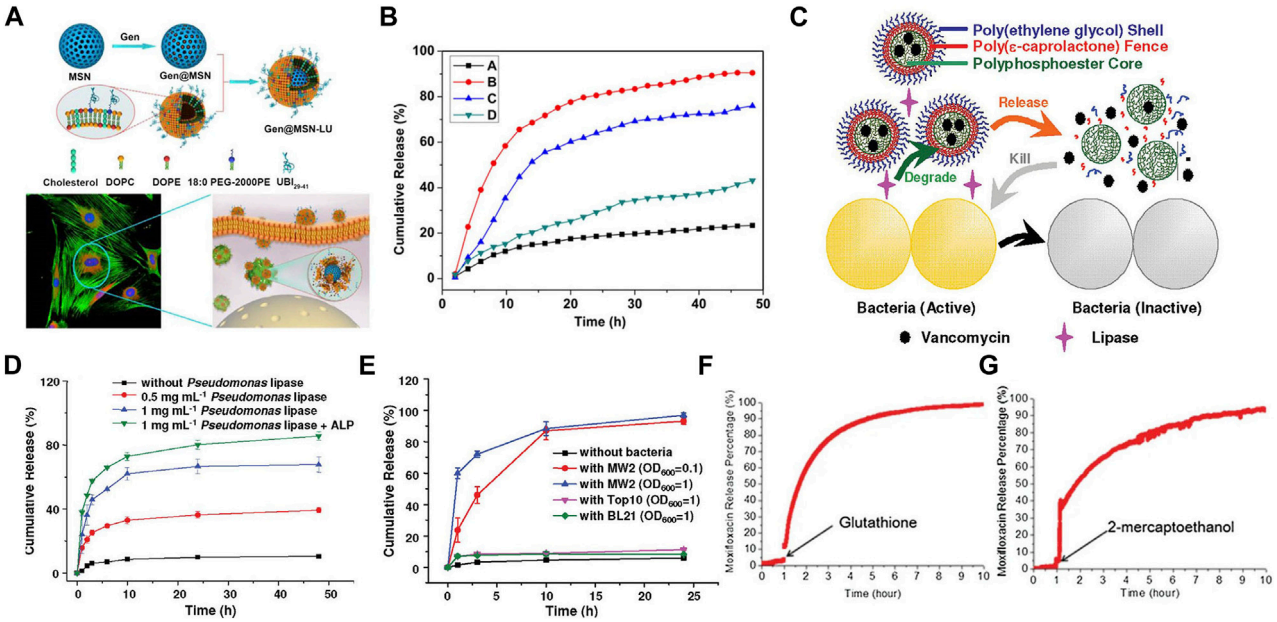

FIGURE 4
(A) Schematics of Gen@MSN-LU, in which the outer layer of liposomes can be degraded by the bacterium-secreted toxins, resulting in the Gen release. **(B)** The release profile of Gen from Gen@MSN-LU in different treatments (A control; B in the presence of *S. aureus*; C with lipase; D with lipase inhibitors in the presence of *S. aureus*). **(C)** Schematics of bacterial lipase triggered release of vancomycin to treat the bacterial infections. **(D,E)** Cumulative release of vancomycin from vancomycin-loaded TLN in different treatments. **(F,G)** The behavior of the redox-triggered release of Moxifloxacin. Reproduced with permission from Yang et al. (2018) (Copyright 2018 American Chemical Society), Xiong et al. (2012a) (Copyright 2012 American Chemical Society), and Lee et al. (2016).

these cellular enzymes (Alkekhia et al., 2022), bacterial enzymes (Sunnapu et al., 2022) and bacterium-secreted toxins (Figures 4A, B) (Yang et al., 2018) can also be used as stimulators for corresponding release. Peng et al. (2020) provided a practicable strategy to realize intracellular rapid release of antibiotics triggered by both enzymes and acid, thus promoting efficiency against intracellular infections. A rationally designed polymer, which was able to be degraded by bacterial lipase, significantly increased intracellular concentration of ciprofloxacin, thereby enhancing its therapeutic efficacy.

In addition, some nanogels were designed to respond to enzymes (Chen et al., 2020). Xiong et al. prepared two different feasible nanogels, a triple-layered polymer nanogel (Figures 4C–E) (Xiong et al., 2012a) and a core-shell mannose-modified nanogel (Xiong et al., 2012b), to inhibit the growth of intracellular *S. aureus*. In two systems, bacteria-secreting lipase and phosphatase or phospholipase were acted as triggers to release antibiotics, respectively.

4.1.3 Redox-responsive release

Nanomaterials that can respond to the redox environment could be a potential therapeutic strategy for the treatment of intracellular infections. A functionalized MSN was used to selectively release drugs intracellularly in response to the GSH/GSSG species (reduced glutathione/oxidized glutathione disulfide), which were commonly found intracellularly (Figures 4F, G) (Lee et al., 2016). The reducing microenvironment can also be utilized to break the disulfide bonds of red blood cell (RBC) nanogels, resulting in the rapid release of antibiotics (Zhang et al., 2017).

4.2 Bioactive nanomaterials

Beyond the application as drug delivery carriers, some nanomaterials with intrinsic antimicrobial bioactivities have recently shown promising aspects for potential clinical applications against intracellular bacteria.

4.2.1 Metal ion-based nanobactericides

Given that metals are traditionally used as drug delivery carriers, recent studies have also shown that some biomaterials with intrinsic antimicrobial bioactivity hold promise against intracellular infections. For example, gold nanomaterials can reduce the attachment of tRNA to ribosome units, decrease membrane viability and cause bacterial death. Copper ions can inhibit bacterial DNA replication and induce bacterial death through ROS production and lipid peroxidation. The release of metal ions, such as Ag^{+}, Cu^{2+}, and Fe^{2+}, also can enhance the antibacterial effect. For instance, ZnO has the ability to inhibit the formation of biofilms and catalyze the production of ROS. Besides, the release of Zn^{2+} can also increase the permeability and degradability of membranes.

The most widely used metal for antibacterial activity is silver, which exerts its effects through a variety of mechanisms, such as lipid peroxidation, ROS generation, interference with cell wall synthesis, and increasing membrane permeability. Besides, Ag^{+} hydrolyzes bacterial macromolecules by driving the generation of hydroxyl radicals. Aurore et al. (2018) designed Ag-NPs with synergistic antimicrobial effects against *S. aureus* in human

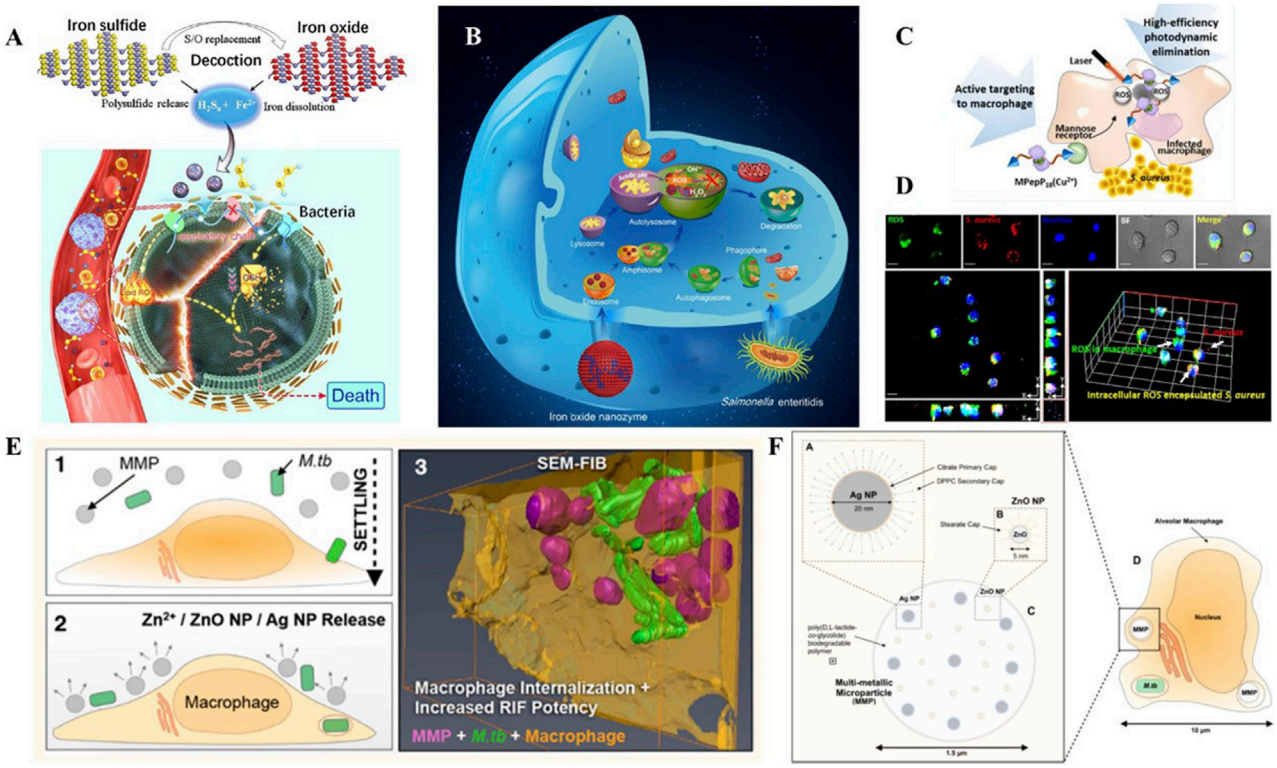

FIGURE 5
(A) Schematic illustration of the bioactive nanoparticles with collaborative bactericidal function depends on both ferrous iron and polysulfide. **(B)** Schematic illustration of the bacteriostatic effects of IONzymes with enzymes-like activity and mechanism responsible for the antibacterial activity. **(C)** Schematic illustration of the peptide-chlorophyll-based photodynamic therapy (PDT) agents to enhance the PDT effect and active targeting property to eliminate intracellular infections. **(D)** Confocal images of intracellular ROS production by $MPepP_{18}(Cu^{2+})$ in *S. aureus* infected macrophage. **(E)** Schematic illustration of the biodegradable multi-metallic particles (MMPs), containing Ag NPs and ZnO NPs, and its pulmonary delivery of anti-tuberculous drugs to the endosomal system of *M.tb*-infected macrophages. **(F)** MMPs embedded with Ag NPs and ZnO NPs within the endosome of an *M.tb*-infected alveolar macrophage. Reproduced with permission from Shen et al. (2020); Shi et al. (2018); Cai et al. (2018) (Copyright 2018 American Chemical Society) and Ellis et al. (2018).

osteoclasts. The promoted bactericidal activity not only came from the direct toxicity of silver itself but also from the ROS production in osteoclasts induced by Ag-NPs. Taken together, these surprising results indicate that silver nanoparticles can be used as an effective treatment for chronic long-term infections caused by intracellular bacteria, where conventional antibiotics are difficult to achieve equivalent therapeutic effects to their extracellular effects.

Ferrous ions are another type of metal ions that have shown great promise in terms of their antimicrobial biological activity, as they play a critical role in ferroptosis. In a recent study by Shen et al., discovered a multi-nanomaterials combined with ferrous iron and polysulfide ($Fe(II)S_n$aq) (Figure 5A) (Shen et al., 2020). The nanomaterials were found to be effective in killing both extracellular and intracellular bacteria, while only having slight toxicity towards host cells. In this system, the sulfur atoms were replaced by oxygen atoms to trigger the release of polysulfides and iron. The collaborative function depended on both ferrous iron and polysulfide. Ferrous irons were able to trigger lipid peroxidation and depress the respiratory chain, which induced ferroptosis-like death within bacteria. At the same time, polysulfide species prevented oxidation of ferrous ions, and demonstrated the ability to oxidize glutathione into GSSG, following with GSH depletion, which leads to DNA degradation and bacteria death.

4.2.2 Nanozymes

The natural process of scavenging pathogens by macrophages involves converting a large amount of hydrogen peroxide in phagosomes into more toxic ROS, catalyzed by enzymes such as oxidase, myeloperoxidase, lipid peroxidase, and other peroxidases. Inspired by this process, there are increased efforts devoted to build artificial enzymes with natural enzyme-like activity to combat extracellular bacteria. Based on their own instinct oxidase enzyme activity, nanozymes can provide various bactericidal ROS, including singlet oxygen, superoxide anion, hypochlorous acid and other oxidation-state components with non- or low-toxic substrates. These excess ROS are capable of damaging bacterial DNA, protein, or nucleic acid, along with breaking cell membranes. Nevertheless, development of nanozymes for efficient production of ROS against intracellular bacteria remains a significant challenge. With these findings in mind, the integration of ROS production and antibiotic delivery may be a promising strategy for efficient elimination both intracellular and extracellular pathogens, especially towards phagosomal bacteria.

Peroxidase is a series of enzymes that catalyze the substrates like hydrogen peroxide into hydroxyl radicals, which are essential in defending pathogens. Presently, enormous nanomaterials have been reported to exhibit the peroxidase-like catalytic activity, including metal, metal sulfide, metal oxide, metal organic frameworks, inorganic materials, and carbon-based materials. Shi et al. designed an iron oxide nanozyme (IONzymes) that can destroy structures, inhibit multiplication, and ultimately cause death of intracellular bacterial (Figure 5B) (Shi et al., 2018). In this work, IONzymes were able to co-localize with intracellular *S. enteritidis* in autophagic vacuoles and regulate ROS levels within acid vacuoles. Moreover, the increasing ROS levels suppressed the survival and reproduction of those pathogens hiding in Leghorn Male Hepatoma-derived cells (LMH).

Oxidases are the major enzymes in peroxisomes, accounting for almost half of the total ones. Generally, the catalytic process of oxidases requires the participation of oxygen, followed by the generation of superoxide anions (Wu et al., 2019). Therefore, nanozymes with oxidase-mimic activity can also be utilized as anti-bacterial materials. Haloperoxidase is another typical category of peroxidase in nature, divided into three subtypes: chloroperoxidase, bromoperoxidase, and iodoperoxidase (ten Brink et al., 2000). Particularly, haloperoxidase can catalyze halide ions in the physiologic environment to hypohalous acid in the presence of acidic and hydrogen peroxide (Hu et al., 2018). Hypohalous acid is a strong oxidizing agent, which can effectively damage bacterial structure (Butler, 1999). Accordingly, haloperoxidase-like nanozymes also have the promising potential for eliminating intracellular bacteria.

Collectively, a vast array of nanozymes present bi-enzymatic and even tri-enzymatic synergism activities, making it preferable to design them as functional components of composite materials.

4.2.3 Photo-active nanomaterials

Photodynamic therapy (PDT) is a method of using photosensitizers remaining in cells to produce singlet oxygen and free radicals to chemically eliminate bacteria. Some biomaterials with PDT effects are used for their active targeting properties to eliminate intracellular infections. Cai et al. (2018) presented a PDT-based strategy to clear *S. aureus* inside macrophages (Figures 5C, D). The dimer coated with peptide–chlorophyll was enabled to active targeting of macrophages, which can generate abundant ROS in infected macrophages with the laser, resulting in high-efficiency photodynamic elimination. This design demonstrated the potential of photodynamic and photothermal effects in intracellular bacterial clearance.

4.3 Multifunctional nanomaterials

From above mentioned findings, these bioactive nanomaterials can serve as alternative treatments to traditional antibiotics due to their multiple mechanisms involving intrinsic enzyme-mimic activities, metal toxicity, or physicochemical properties, making them less prone to cause antibiotic resistance. To achieve more efficient synergistic antibacterial effects, researchers are exploring the application of multifunctional nanomaterials integrating the functions of delivery with antibacterial activities (Chang et al., 2017a; Chang et al., 2017b; Lu et al., 2017; Lu et al., 2018; Zhang et al., 2020; Huo et al., 2021; Li et al., 2021; Liu et al., 2021).

Dube et al. presented nanoparticles with chitosan-functionalized shells and PLGA cores for the treatment of tuberculosis (Dube et al., 2014). This rationally designed nanoparticle showed a collaborative function between stimulation of ROS/RNS and delivery of rifampicin. In this case, the combined nanoparticles can not only regulate ROS/RNS levels but also modulate pro-inflammatory cytokine secretion. Meanwhile, it acted as a vehicle to transfer rifampicin inside alveolar macrophages. Similarly, Marwa et al. prepared Ag-coated PLGA particles loaded with pexiganan, which exhibited coordinated antibacterial functions, and were specifically uptaken by macrophages, but not by any non-phagocytic cells (Elnaggar et al., 2020). Additionally, Timothy et al. established composite materials containing Ag and ZnO for the targeted delivery of rifampicin (Figures 5E, F) (Ellis et al., 2018). The sophisticated nanoplatforms were developed to destabilize membranes, increase permeabilization of intracellular *Mycobacterium tuberculosis* and enhance penetration of rifampicin. As a result, multifunctional nanomaterials presented extraordinary bactericidal effects compared to free antibiotics.

5 Conclusion and future perspectives

Nanomaterials can enhance preferential accumulation and controlled release of bactericides within pathogens-infected host cells, resulting in increased therapeutic efficiency and reduced potential adverse effects. Size plays a crucial role in the ability of nanomaterial to permeate cells and reach the therapeutic concentration. Positively charged nanomaterials perform excellent interactions with negative-surface bacteria. Moreover, surface-functionalized nanomaterials with special ligands are conducive to an improving targeting of the infected cells. Responsive release at the diseased site can be triggered via pH, enzymes, and redox microenvironment. Beyond providing on-demand delivery of antibiotics, nanomaterials with intrinsic bioactivities, such as metal toxicity, enzyme-like activity and physicochemical properties also show promising potential in combating intracellular pathogens.

However, fabrication of multifunctional nanomaterials for eliminating bacteria is still in infancy, with several fundamental concerns unclear and numerous challenges to be addressed. Positively charged nanomaterials generally present a better cell uptake and adsorption with negative-surface bacteria, but cationic particles tend to cause hemolysis and cytotoxicity. Besides, there are also some examples of negative charged nanomaterials exhibit a higher internalization. Thus, it is worthy to clarify the detailed and wide functions of surface charge in different nanomaterials to balance cell uptake and safety. Despite the effects of size, charge, shape and surface modifications on internalization have been extensively studied, the mechanisms of other properties, such as smoothness and hydrophily, affecting internalization remain indistinct. A comprehensive understanding of the interactions between bacteria, nanomaterials and cellular microenvironment may provide insights into the development of intelligent nanomaterials with precise release property and high level of safety. Besides, nanozyme-based composite materials perform poor selectivity compared with natural enzymes, which might cause undesired toxicity. Additionally, most nanozymes, especially haloperoxidase-mimic ones, are only effective in an acidic microenvironment, limiting their further application. How to

compound bioactive and delivering materials to realize synergistic therapeutic effects is highly desired. Lastly, biosafety remains a major concern that determining the translation of nanomaterials against intracellular bacterial infection in clinic.

In summary, we review recent studies on employing multifunctional nanomaterials in treating intracellular infections through targeted delivery of anti-bacterial agents or utilizing their intrinsic bioactivities. We also discuss the opportunities and challenges that need to be focused on in future work. Broadening understanding of the interactions among macrophages, intracellular pathogens and nanoparticles contributes to inspire the development of the next-generation of nanomaterial-based therapeutics against intracellular bacterial infections.

Author contributions

YC and XH contributed equally to this work. YC and CY: conceptualization. YC and XH: original draft preparation. XH, QC, YH, FC, and CY: review and editing. LW: supervision and review. All authors contributed to the article and approved the submitted version.

Funding

This study was supported by the National Natural Science Foundation of China (Grant No. 82072433).

Conflict of interest

The authors declare that the research was conducted in the absence of any commercial or financial relationships that could be construed as a potential conflict of interest.

Publisher's note

All claims expressed in this article are solely those of the authors and do not necessarily represent those of their affiliated organizations, or those of the publisher, the editors and the reviewers. Any product that may be evaluated in this article, or claim that may be made by its manufacturer, is not guaranteed or endorsed by the publisher.

References

Abdallah, A. M., Gey van Pittius, N. C., DiGiuseppe Champion, P. A., Cox, J., Luirink, J., Vandenbroucke-Grauls, C. M., et al. (2007). Type VII secretion—Mycobacteria show the way. *Nat. Rev. Microbiol.* 5 (11), 883–891. doi:10.1038/nrmicro1773

Alkekhia, D., LaRose, C., and Shukla, A. (2022). β-Lactamase-Responsive hydrogel drug delivery platform for bacteria-triggered cargo release. *ACS Appl. Mater. Interfaces* 14 (24), 27538–27550. doi:10.1021/acsami.2c02614

Ashida, H., Mimuro, H., Ogawa, M., Kobayashi, T., Sanada, T., Kim, M., et al. (2011). Cell death and infection: A double-edged sword for host and pathogen survival. *J. Cell Biol.* 195 (6), 931–942. doi:10.1083/jcb.201108081

Aurore, V., Caldana, F., Blanchard, M., Hess, S. K., Lannes, N., Mantel, P.-Y., et al. (2018). Silver-nanoparticles increase bactericidal activity and radical oxygen responses against bacterial pathogens in human osteoclasts. *Nanomedicine Nanotechnol. Biol. Med.* 14 (2), 601–607. doi:10.1016/j.nano.2017.11.006

Boyle, K. B., and Randow, F. (2013). The role of 'eat-me'signals and autophagy cargo receptors in innate immunity. *Curr. Opin. Microbiol.* 16 (3), 339–348. doi:10.1016/j.mib.2013.03.010

Briones, E., Colino, C. I., and Lanao, J. M. (2008). Delivery systems to increase the selectivity of antibiotics in phagocytic cells. *J. Control. Release* 125 (3), 210–227. doi:10.1016/j.jconrel.2007.10.027

Brouillette, E., Grondin, G., Shkreta, L., Lacasse, P., and Talbot, B. G. (2003). *In vivo* and *in vitro* demonstration that *Staphylococcus aureus* is an intracellular pathogen in the presence or absence of fibronectin-binding proteins. *Microb. Pathog.* 35 (4), 159–168. doi:10.1016/s0882-4010(03)00112-8

Broz, P., and Monack, D. M. (2013). Newly described pattern recognition receptors team up against intracellular pathogens. *Nat. Rev. Immunol.* 13 (8), 551–565. doi:10.1038/nri3479

Butler, A. (1999). Vanadium haloperoxidases. *Bioinorg. Catal.* 1999, 71–96. doi:10.1016/S1367-5931(98)80070-7

Cai, Q., Fei, Y., An, H. W., Zhao, X.-X., Ma, Y., Cong, Y., et al. (2018). Macrophage-instructed intracellular *Staphylococcus aureus* killing by targeting photodynamic dimers. *ACS Appl. Mater. interfaces* 10 (11), 9197–9202. doi:10.1021/acsami.7b19056

Champion, J. A., Walker, A., and Mitragotri, S. (2008). Role of particle size in phagocytosis of polymeric microspheres. *Pharm. Res.* 25, 1815–1821. doi:10.1007/s11095-008-9562-y

Chang, Z., Wang, Z., Lu, M. m., Shao, D., Yue, J., Yang, D., et al. (2017a). Janus silver mesoporous silica nanobullets with synergistic antibacterial functions. *Colloids Surfaces B Biointerfaces* 157, 199–206. doi:10.1016/j.colsurfb.2017.05.079

Chang, Z., Wang, Z., Lu, M., Li, M., Li, L., Zhang, Y., et al. (2017b). Magnetic Janus nanorods for efficient capture, separation and elimination of bacteria. *RSC Adv.* 7 (6), 3550–3553. doi:10.1039/C6RA27296G

Chen, M., He, J., Xie, S., Wang, T., Ran, P., Zhang, Z., et al. (2020). Intracellular bacteria destruction via traceable enzymes-responsive release and deferoxamine-mediated ingestion of antibiotics. *J. Control. Release* 322, 326–336. doi:10.1016/j.jconrel.2020.03.037

Christie, P. J., and Cascales, E. (2005). Structural and dynamic properties of bacterial Type IV secretion systems (Review). *Mol. Membr. Biol.* 22 (1-2), 51–61. doi:10.1080/09687860500063316

Chu, Z., Zhang, S., Zhang, B., Zhang, C., Fang, C.-Y., Rehor, I., et al. (2014). Unambiguous observation of shape effects on cellular fate of nanoparticles. *Sci. Rep.* 4 (1), 4495. doi:10.1038/srep04495

Clemens, D. L., Lee, B.-Y., Xue, M., Thomas, C. R., Meng, H., Ferris, D., et al. (2012). Targeted intracellular delivery of antituberculosis drugs to Mycobacterium tuberculosis-infected macrophages via functionalized mesoporous silica nanoparticles. *Antimicrob. agents Chemother.* 56 (5), 2535–2545. doi:10.1128/AAC.06049-11

Cornelis, G. R. (2006). The type III secretion injectisome. *Nat. Rev. Microbiol.* 4 (11), 811–825. doi:10.1038/nrmicro1526

Coulthurst, S. J. (2013). The Type VI secretion system–a widespread and versatile cell targeting system. *Res. Microbiol.* 164 (6), 640–654. doi:10.1016/j.resmic.2013.03.017

Cullinane, M., Gong, L., Li, X., Adler, N.-L., Tra, T., Wolvetang, E., et al. (2008). Stimulation of autophagy suppresses the intracellular survival of Burkholderia pseudomallei in mammalian cell lines. *Autophagy* 4 (6), 744–753. doi:10.4161/auto.6246

DeVinney, R., Steele-Mortimer, O., and Finlay, B. B. (2000). Phosphatases and kinases delivered to the host cell by bacterial pathogens. *Trends Microbiol.* 8 (1), 29–33. doi:10.1016/s0966-842x(99)01657-1

Doherty, G. J., and McMahon, H. T. (2009). Mechanisms of endocytosis. *Annu. Rev. Biochem.* 78, 857–902. doi:10.1146/annurev.biochem.78.081307.110540

Dube, A., Reynolds, J. L., Law, W.-C., Maponga, C. C., Prasad, P. N., and Morse, G. D. (2014). Multimodal nanoparticles that provide immunomodulation and intracellular drug delivery for infectious diseases. *Nanomedicine Nanotechnol. Biol. Med.* 10 (4), 831–838. doi:10.1016/j.nano.2013.11.012

Duceppe, N., and Tabrizian, M. (2010). Advances in using chitosan-based nanoparticles for *in vitro* and *in vivo* drug and gene delivery. *Expert Opin. drug Deliv.* 7 (10), 1191–1207. doi:10.1517/17425247.2010.514604

Ellis, T., Chiappi, M., Garcia-Trenco, A., Al-Ejji, M., Sarkar, S., Georgiou, T. K., et al. (2018). Multimetallic microparticles increase the potency of rifampicin against intracellular *Mycobacterium tuberculosis*. *ACS Nano* 12 (6), 5228–5240. doi:10.1021/acsnano.7b08264

Elnaggar, M. G., Jiang, K., Eldesouky, H. E., Pei, Y., Park, J., Yuk, S. A., et al. (2020). Antibacterial nanotruffles for treatment of intracellular bacterial infection. *Biomaterials* 262, 120344. doi:10.1016/j.biomaterials.2020.120344

Fang, F. C. (2004). Antimicrobial reactive oxygen and nitrogen species: Concepts and controversies. *Nat. Rev. Microbiol.* 2 (10), 820–832. doi:10.1038/nrmicro1004

Feng, W., Li, G., Kang, X., Wang, R., Liu, F., Zhao, D., et al. (2022). Cascade-targeting poly (amino acid) nanoparticles eliminate intracellular bacteria via on-site antibiotic delivery. *Adv. Mater.* 34 (12), 2109789. doi:10.1002/adma.202109789

Flannagan, R. S., Cosío, G., and Grinstein, S. (2009). Antimicrobial mechanisms of phagocytes and bacterial evasion strategies. *Nat. Rev. Microbiol.* 7 (5), 355–366. doi:10.1038/nrmicro2128

Fröhlich, E. (2012). The role of surface charge in cellular uptake and cytotoxicity of medical nanoparticles. *Int. J. nanomedicine* 7, 5577–5591. doi:10.2147/IJN.S36111

González, O., Smith, R. L., and Goodman, S. B. (1996). Effect of size, concentration, surface area, and volume of polymethylmethacrylate particles on human macrophages *in vitro*. *J. Biomed. Mater. Res.* 30 (4), 463–473. doi:10.1002/(SICI)1097-4636(199604)30:4<463:AID-JBM4>3.0.CO;2-N

He, Q., Zhang, Z., Gao, Y., Shi, J., and Li, Y. (2009). Intracellular localization and cytotoxicity of spherical mesoporous silica nano- and microparticles. *Small* 5 (23), 2722–2729. doi:10.1002/smll.200900923

Howes, M. T., Mayor, S., and Parton, R. G. (2010). Molecules, mechanisms, and cellular roles of clathrin-independent endocytosis. *Curr. Opin. cell Biol.* 22 (4), 519–527. doi:10.1016/j.ceb.2010.04.001

Hu, M., Korschelt, K., Viel, M., Wiesmann, N., Kappl, M., Brieger, J. r., et al. (2018). Nanozymes in nanofibrous mats with haloperoxidase-like activity to combat biofouling. *ACS Appl. Mater. interfaces* 10 (51), 44722–44730. doi:10.1021/acsami.8b16307

Huang, J., Canadien, V., Lam, G. Y., Steinberg, B. E., Dinauer, M. C., Magalhaes, M. A., et al. (2009). Activation of antibacterial autophagy by NADPH oxidases. *Proc. Natl. Acad. Sci.* 106 (15), 6226–6231. doi:10.1073/pnas.0811045106

Huo, J., Jia, Q., Huang, H., Zhang, J., Li, P., Dong, X., et al. (2021). Emerging photothermal-derived multimodal synergistic therapy in combating bacterial infections. *Chem. Soc. Rev.* 50 (15), 8762–8789. doi:10.1039/D1CS00074H

Jaeger, K.-E., Ransac, S., Dijkstra, B. W., Colson, C., van Heuvel, M., and Misset, O. (1994). Bacterial lipases. *FEMS Microbiol. Rev.* 15 (1), 29–63. doi:10.1111/j.1574-6976.1994.tb00121.x

Jaeger, K.-E., and Reetz, M. T. (1998). Microbial lipases form versatile tools for biotechnology. *Trends Biotechnol.* 16 (9), 396–403. doi:10.1016/S0167-7799(98)01195-0

Jena, P., Mohanty, S., Mallick, R., Jacob, B., and Sonawane, A. (2012). Toxicity and antibacterial assessment of chitosancoated silver nanoparticles on human pathogens and macrophage cells. *Int. J. nanomedicine* 7, 1805–1818. doi:10.2147/IJN.S28077

Jiang, W., Kim, B. Y., Rutka, J. T., and Chan, W. C. (2008). Nanoparticle-mediated cellular response is size-dependent. *Nat. Nanotechnol.* 3 (3), 145–150. doi:10.1038/nnano.2008.30

John, G. S., Brot, N., Ruan, J., Erdjument-Bromage, H., Tempst, P., Weissbach, H., et al. (2001). Peptide methionine sulfoxide reductase from *Escherichia coli* and *Mycobacterium tuberculosis* protects bacteria against oxidative damage from reactive nitrogen intermediates. *Proc. Natl. Acad. Sci.* 98 (17), 9901–9906. doi:10.1073/pnas.161295398

Kamaruzzaman, N. F., Kendall, S., and Good, L. (2017). Targeting the hard to reach: Challenges and novel strategies in the treatment of intracellular bacterial infections. *Br. J. Pharmacol.* 174 (14), 2225–2236. doi:10.1111/bph.13664

Kolosnjaj-Tabi, J., Wilhelm, C., Clément, O., and Gazeau, F. (2013). Cell labeling with magnetic nanoparticles: Opportunity for magnetic cell imaging and cell manipulation. *J. nanobiotechnology* 11 (1), S7–S19. doi:10.1186/1477-3155-11-S1-S7

Kudryashev, M., Wang, R. Y.-R., Brackmann, M., Scherer, S., Maier, T., Baker, D., et al. (2015). Structure of the type VI secretion system contractile sheath. *Cell* 160 (5), 952–962. doi:10.1016/j.cell.2015.01.037

Lai, S. K., Hida, K., Man, S. T., Chen, C., Machamer, C., Schroer, T. A., et al. (2007). Privileged delivery of polymer nanoparticles to the perinuclear region of live cells via a non-clathrin, non-degradative pathway. *Biomaterials* 28 (18), 2876–2884. doi:10.1016/j.biomaterials.2007.02.021

Lamkanfi, M., and Dixit, V. M. (2010). Manipulation of host cell death pathways during microbial infections. *Cell host microbe* 8 (1), 44–54. doi:10.1016/j.chom.2010.06.007

Lankoff, A., Sandberg, W. J., Wegierek-Ciuk, A., Lisowska, H., Refsnes, M., Sartowska, B., et al. (2012). The effect of agglomeration state of silver and titanium dioxide nanoparticles on cellular response of HepG2, A549 and THP-1 cells. *Toxicol. Lett.* 208 (3), 197–213. doi:10.1016/j.toxlet.2011.11.006

Lee, B. Y., Li, Z., Clemens, D. L., Dillon, B. J., Hwang, A. A., Zink, J. I., et al. (2016). Redox-triggered release of moxifloxacin from mesoporous silica nanoparticles functionalized with disulfide snap-tops enhances efficacy against pneumonic tularemia in mice. *Small* 12 (27), 3690–3702. doi:10.1002/smll.201600892

Li, H., Li, D., Chen, F., Yang, C., Li, X., Zhang, Y., et al. (2021). Nanosilver-decorated biodegradable mesoporous organosilica nanoparticles for GSH-responsive gentamicin release and synergistic treatment of antibiotic-resistant bacteria. *Int. J. Nanomedicine* 16, 4631–4642. doi:10.2147/IJN.S315067

Liu, F., Sheng, S., Shao, D., Xiao, Y., Zhong, Y., Zhou, J., et al. (2021). Targeting multiple mediators of sepsis using multifunctional tannic acid-Zn2+-gentamicin nanoparticles. *Matter* 4 (11), 3677–3695. doi:10.1016/j.matt.2021.09.001

Lu, M.-m., Ge, Y., Qiu, J., Shao, D., Zhang, Y., Bai, J., et al. (2018). Redox/pH dual-controlled release of chlorhexidine and silver ions from biodegradable mesoporous silica nanoparticles against oral biofilms. *Int. J. nanomedicine* 13, 7697–7709. doi:10.2147/IJN.S181168

Lu, M.-m., Wang, Q.-j., Chang, Z.-m., Wang, Z., Zheng, X., Shao, D., et al. (2017). Synergistic bactericidal activity of chlorhexidine-loaded, silver-decorated mesoporous silica nanoparticles. *Int. J. nanomedicine* 12, 3577–3589. doi:10.2147/IJN.S133846

Maghrebi, S., Jambhrunkar, M., Joyce, P., and Prestidge, C. A. (2020). Engineering PLGA–lipid hybrid microparticles for enhanced macrophage uptake. *ACS Appl. Bio Mater.* 3 (7), 4159–4167. doi:10.1021/acsabm.0c00251

Martinez, J., Almendinger, J., Oberst, A., Ness, R., Dillon, C. P., Fitzgerald, P., et al. (2011). Microtubule-associated protein 1 light chain 3 alpha (LC3)-associated phagocytosis is required for the efficient clearance of dead cells. *Proc. Natl. Acad. Sci.* 108 (42), 17396–17401. doi:10.1073/pnas.1113421108

Maya, S., Indulekha, S., Sukhithasri, V., Smitha, K., Nair, S. V., Jayakumar, R., et al. (2012). Efficacy of tetracycline encapsulated O-carboxymethyl chitosan nanoparticles against intracellular infections of Staphylococcus aureus. *Int. J. Biol. Macromol.* 51 (4), 392–399. doi:10.1016/j.ijbiomac.2012.06.009

Minakami, R., and Sumimoto, H. (2006). Phagocytosis-coupled activation of the superoxide-producing phagocyte oxidase, a member of the NADPH oxidase (nox) family. *Int. J. Hematol.* 84, 193–198. doi:10.1532/IJH97.06133

Mizushima, N., Yoshimori, T., and Ohsumi, Y. (2011). The role of Atg proteins in autophagosome formation. *Annu. Rev. cell Dev. Biol.* 27, 107–132. doi:10.1146/annurev-cellbio-092910-154005

Mohebali, A., and Abdouss, M. (2020). Layered biocompatible pH-responsive antibacterial composite film based on HNT/PLGA/chitosan for controlled release of minocycline as burn wound dressing. *Int. J. Biol. Macromol.* 164, 4193–4204. doi:10.1016/j.ijbiomac.2020.09.004

Mott, J., Rikihisa, Y., and Tsunawaki, S. (2002). Effects of Anaplasma phagocytophila on NADPH oxidase components in human neutrophils and HL-60 cells. *Infect. Immun.* 70 (3), 1359–1366. doi:10.1128/IAI.70.3.1359-1366.2002

Mudakavi, R. J., Vanamali, S., Chakravortty, D., and Raichur, A. M. (2017). Development of arginine based nanocarriers for targeting and treatment of intracellular Salmonella. *RSC Adv.* 7 (12), 7022–7032. doi:10.1039/C6RA27868J

Ng, V. H., Cox, J. S., Sousa, A. O., MacMicking, J. D., and McKinney, J. D. (2004). Role of KatG catalase-peroxidase in mycobacterial pathogenesis: Countering the phagocyte oxidative burst. *Mol. Microbiol.* 52 (5), 1291–1302. doi:10.1111/j.1365-2958.2004.04078.x

Ninan, N., Forget, A., Shastri, V. P., Voelcker, N. H., and Blencowe, A. (2016). Antibacterial and anti-inflammatory pH-responsive tannic acid-carboxylated agarose composite hydrogels for wound healing. *ACS Appl. Mater. interfaces* 8 (42), 28511–28521. doi:10.1021/acsami.6b10491

Onyeji, C., Nightingale, C., Nicolau, D., and Quintiliani, R. (1994). Efficacies of liposome-encapsulated clarithromycin and ofloxacin against Mycobacterium avium-M. intracellulare complex in human macrophages. *Antimicrob. agents Chemother.* 38 (3), 523–527. doi:10.1128/AAC.38.3.523

Park, Y. K., Bearson, B., Bang, S. H., Bang, I. S., and Foster, J. W. (1996). Internal pH crisis, lysine decarboxylase and the acid tolerance response of *Salmonella typhimurium*. *Mol. Microbiol.* 20 (3), 605–611. doi:10.1046/j.1365-2958.1996.5441070.x

Pei, Y., Mohamed, M. F., Seleem, M. N., and Yeo, Y. (2017). Particle engineering for intracellular delivery of vancomycin to methicillin-resistant *Staphylococcus aureus* (MRSA)-infected macrophages. *J. Control. Release* 267, 133–143. doi:10.1016/j.jconrel.2017.08.007

Peng, H., Xie, B., Yang, X., Dai, J., Wei, G., and He, Y. (2020). Pillar [5] arene-based, dual pH and enzyme responsive supramolecular vesicles for targeted antibiotic delivery against intracellular MRSA. *Chem. Commun.* 56 (58), 8115–8118. doi:10.1039/D0CC02522D

Peng, X., Jiang, G., Liu, W., Zhang, Q., Qian, W., and Sun, J. (2016). Characterization of differential pore-forming activities of ESAT-6 proteins from *Mycobacterium tuberculosis* and Mycobacterium smegmatis. *FEBS Lett.* 590 (4), 509–519. doi:10.1002/1873-3468.12072

Plüddemann, A., Mukhopadhyay, S., and Gordon, S. (2011). Innate immunity to intracellular pathogens: Macrophage receptors and responses to microbial entry. *Immunol. Rev.* 240 (1), 11–24. doi:10.1111/j.1600-065X.2010.00989.x

Qu, J., Zhao, X., Ma, P. X., and Guo, B. (2018). Injectable antibacterial conductive hydrogels with dual response to an electric field and pH for localized "smart" drug release. *Acta biomater.* 72, 55–69. doi:10.1016/j.actbio.2018.03.018

Quinn, M. T., and Gauss, K. A. (2004). Structure and regulation of the neutrophil respiratory burst oxidase: Comparison with nonphagocyte oxidases. *J. Leukoc. Biol.* 76 (4), 760–781. doi:10.1189/jlb.0404216

Ray, K., Marteyn, B., Sansonetti, P. J., and Tang, C. M. (2009). Life on the inside: The intracellular lifestyle of cytosolic bacteria. *Nat. Rev. Microbiol.* 7 (5), 333–340. doi:10.1038/nrmicro2112

Raynal, I., Prigent, P., Peyramaure, S., Najid, A., Rebuzzi, C., and Corot, C. (2004). Macrophage endocytosis of superparamagnetic iron oxide nanoparticles: Mechanisms and comparison of ferumoxides and ferumoxtran-10. *Investig. Radiol.* 39 (1), 56–63. doi:10.1097/01.rli.0000101027.57021.28

Rejman, J., Oberle, V., Zuhorn, I. S., and Hoekstra, D. (2004). Size-dependent internalization of particles via the pathways of clathrin-and caveolae-mediated endocytosis. *Biochem. J.* 377 (1), 159–169. doi:10.1042/BJ20031253

Rudel, T., Kepp, O., and Kozjak-Pavlovic, V. (2010). Interactions between bacterial pathogens and mitochondrial cell death pathways. *Nat. Rev. Microbiol.* 8 (10), 693–705. doi:10.1038/nrmicro2421

Sahay, G., Alakhova, D. Y., and Kabanov, A. V. (2010). Endocytosis of nanomedicines. *J. Control. release* 145 (3), 182–195. doi:10.1016/j.jconrel.2010.01.036

Sanchez, L., Yi, Y., and Yu, Y. (2017). Effect of partial PEGylation on particle uptake by macrophages. *Nanoscale* 9 (1), 288–297. doi:10.1039/C6NR07353K

Sandvig, K., Pust, S., Skotland, T., and van Deurs, B. (2011). Clathrin-independent endocytosis: Mechanisms and function. *Curr. Opin. Cell Biol.* 23 (4), 413–420. doi:10.1016/j.ceb.2011.03.007

Schmidtchen, A., Frick, I. M., Andersson, E., Tapper, H., and Björck, L. (2002). Proteinases of common pathogenic bacteria degrade and inactivate the antibacterial peptide LL-37. *Mol. Microbiol.* 46 (1), 157–168. doi:10.1046/j.1365-2958.2002.03146.x

Shao, D., Lu, M.-m., Zhao, Y.-w., Zhang, F., Tan, Y.-f., Zheng, X., et al. (2017). The shape effect of magnetic mesoporous silica nanoparticles on endocytosis, biocompatibility and biodistribution. *Acta biomater.* 49, 531–540. doi:10.1016/j.actbio.2016.11.007

Shen, X., Ma, R., Huang, Y., Chen, L., Xu, Z., Li, D., et al. (2020). Nano-decocted ferrous polysulfide coordinates ferroptosis-like death in bacteria for anti-infection therapy. *Nano Today* 35, 100981. doi:10.1016/j.nantod.2020.100981

Shepherd, V. L. (1986). The role of the respiratory burst of phagocytes in host defense. *Semin. Respir. Infect.* 1 (2), 99–106.

Shi, S., Wu, S., Shen, Y., Zhang, S., Xiao, Y., He, X., et al. (2018). Iron oxide nanozyme suppresses intracellular Salmonella Enteritidis growth and alleviates infection *in vivo*. *Theranostics* 8 (22), 6149–6162. doi:10.7150/thno.29303

Su, F.-Y., Chen, J., Son, H.-N., Kelly, A. M., Convertine, A. J., West, T. E., et al. (2018). Polymer-augmented liposomes enhancing antibiotic delivery against intracellular infections. *Biomaterials Sci.* 6 (7), 1976–1985. doi:10.1039/c8bm00282g

Sunnapu, O., Khader, R., Dhanka, M., Kumar Vemula, P., and Karuppannan, S. (2022). Enzyme-responsive hydrogel for delivery of the anti-inflammatory agent Zingerone. *ChemNanoMat* 8 (11), e202200334. doi:10.1002/cnma.202200334

Tahara, K., Sakai, T., Yamamoto, H., Takeuchi, H., Hirashima, N., and Kawashima, Y. (2009). Improved cellular uptake of chitosan-modified PLGA nanospheres by A549 cells. *Int. J. Pharm.* 382 (1-2), 198–204. doi:10.1016/j.ijpharm.2009.07.023

ten Brink, H. B., Dekker, H. L., Schoemaker, H. E., and Wever, R. (2000). Oxidation reactions catalyzed by vanadium chloroperoxidase from Curvularia inaequalis. *J. Inorg. Biochem.* 80 (1-2), 91–98. doi:10.1016/s0162-0134(00)00044-1

Thomas, E. L. (1979). Myeloperoxidase-hydrogen peroxide-chloride antimicrobial system: Effect of exogenous amines on antibacterial action against *Escherichia coli*. *Infect. Immun.* 25 (1), 110–116. doi:10.1128/iai.25.1.110-116.1979

Vandal, O. H., Pierini, L. M., Schnappinger, D., Nathan, C. F., and Ehrt, S. (2008). A membrane protein preserves intrabacterial pH in intraphagosomal *Mycobacterium tuberculosis*. *Nat. Med.* 14 (8), 849–854. doi:10.1038/nm.1795

Vogel, J. P., Andrews, H. L., Wong, S. K., and Isberg, R. R. (1998). Conjugative transfer by the virulence system of *Legionella pneumophila*. *Science* 279 (5352), 873–876. doi:10.1126/science.279.5352.873

Wang, H., Wu, L., and Reinhard, B. r. M. (2012). Scavenger receptor mediated endocytosis of silver nanoparticles into J774A. 1 macrophages is heterogeneous. *Acs Nano* 6 (8), 7122–7132. doi:10.1021/nn302186n

Wang, Z., Liu, X., Peng, Y., Su, M., Zhu, S., Pan, J., et al. (2020). Platensimycin-encapsulated liposomes or micelles as biosafe nanoantibiotics exhibited strong antibacterial activities against methicillin-resistant *Staphylococcus aureus* infection in mice. *Mol. Pharm.* 17 (7), 2451–2462. doi:10.1021/acs.molpharmaceut.0c00194

Webb, J., Harvey, M., Holden, D. W., and Evans, T. (2001). Macrophage nitric oxide synthase associates with cortical actin but is not recruited to phagosomes. *Infect. Immun.* 69 (10), 6391–6400. doi:10.1128/IAI.69.10.6391-6400.2001

Wright, G. D. (2005). Bacterial resistance to antibiotics: Enzymatic degradation and modification. *Adv. Drug Deliv. Rev.* 57 (10), 1451–1470. doi:10.1016/j.addr.2005.04.002

Wu, J., Wang, X., Wang, Q., Lou, Z., Li, S., Zhu, Y., et al. (2019). Nanomaterials with enzyme-like characteristics (nanozymes): Next-generation artificial enzymes (II). *Chem. Soc. Rev.* 48 (4), 1004–1076. doi:10.1039/C8CS00457A

Xiong, M. H., Bao, Y., Yang, X.-Z., Wang, Y.-C., Sun, B., and Wang, J. (2012a). Lipase-sensitive polymeric triple-layered nanogel for "on-demand" drug delivery. *J. Am. Chem. Soc.* 134 (9), 4355–4362. doi:10.1021/ja211279u

Xiong, M. H., Li, Y. J., Bao, Y., Yang, X. Z., Hu, B., and Wang, J. (2012b). Bacteria-responsive multifunctional nanogel for targeted antibiotic delivery. *Adv. Mater.* 24 (46), 6175–6180. doi:10.1002/adma.201202847

Yang, Q., Jones, S. W., Parker, C. L., Zamboni, W. C., Bear, J. E., and Lai, S. K. (2014). Evading immune cell uptake and clearance requires PEG grafting at densities substantially exceeding the minimum for brush conformation. *Mol. Pharm.* 11 (4), 1250–1258. doi:10.1021/mp400703d

Yang, S., Han, X., Yang, Y., Qiao, H., Yu, Z., Liu, Y., et al. (2018). Bacteria-targeting nanoparticles with microenvironment-responsive antibiotic release to eliminate intracellular *Staphylococcus aureus* and associated infection. *ACS Appl. Mater. interfaces* 10 (17), 14299–14311. doi:10.1021/acsami.7b15678

Zhang, Y., He, Y., Shi, C., Sun, M., Yang, C., Li, H., et al. (2020). Tannic acid-assisted synthesis of biodegradable and antibacterial mesoporous organosilica nanoparticles decorated with nanosilver. *ACS Sustain. Chem.* 8 (3), 1695–1702. doi:10.1021/acssuschemeng.9b07576

Zhang, Y., Zhang, J., Chen, W., Angsantikul, P., Spiekermann, K. A., Fang, R. H., et al. (2017). Erythrocyte membrane-coated nanogel for combinatorial antivirulence and responsive antimicrobial delivery against *Staphylococcus aureus* infection. *J. Control. Release* 263, 185–191. doi:10.1016/j.jconrel.2017.01.016

frontiers | Frontiers in Bioengineering and Biotechnology

TYPE Review
PUBLISHED 08 June 2023
DOI 10.3389/fbioe.2023.1185520

Check for updates

OPEN ACCESS

EDITED BY
Dan Shao,
South China University of Technology, China

REVIEWED BY
Tao Yang,
Soochow University, China
Yingshuai Wang,
Weifang Medical University, China

*CORRESPONDENCE
Kai Zhou,
zhoukai_bone@163.com

†These authors have contributed equally to this work and share first authorship

RECEIVED 13 March 2023
ACCEPTED 26 May 2023
PUBLISHED 08 June 2023

CITATION
Yu S, You M, Zhou K and Li J (2023), Progress of research on graphene and its derivatives in bone and cartilage repair. *Front. Bioeng. Biotechnol.* 11:1185520. doi: 10.3389/fbioe.2023.1185520

COPYRIGHT
© 2023 Yu, You, Zhou and Li. This is an open-access article distributed under the terms of the Creative Commons Attribution License (CC BY). The use, distribution or reproduction in other forums is permitted, provided the original author(s) and the copyright owner(s) are credited and that the original publication in this journal is cited, in accordance with accepted academic practice. No use, distribution or reproduction is permitted which does not comply with these terms.

Progress of research on graphene and its derivatives in bone and cartilage repair

Shilong Yu[1†], Mingke You[2,3†], Kai Zhou[2,3*] and Jian Li[2,3]

[1]West China School of Medicine, West China Hospital, Sichuan University, Chengdu, China, [2]Sports Medicine Center, West China Hospital, Sichuan University, Chengdu, China, [3]Department of Orthopedics, Orthopedic Research Institute, West China Hospital, Sichuan University, Chengdu, China

In recent years, graphene and its derivatives have gained wide attention in the biomedical field due to their good physicochemical properties, biocompatibility, and bioactivity. Its good antibacterial, osteoinductive and drug-carrying properties make it a promising application in the field of orthopedic biomaterials. This paper introduces the research progress of graphene and its derivatives in bone tissue engineering and cartilage tissue engineering and presents an outlook on the future development of graphene-based materials in orthopedics.

KEYWORDS

graphene-based materials, bone, cartilage, tissue engineering, nanobiocatalysis

1 Introduction

Artificial joint replacement is mainly used for serious deformities of joint structures caused by arthritis, fractures, benign and malignant tumors, etc., which can relieve pain, correct deformities, and restore or improve function. Among all replacement procedures, the demand for knee and hip replacements is the strongest. In mainland China, there were 2,531,341 cases of total hip arthroplasty (THA) and 1,369,950 cases of total knee arthroplasty (TKA) between 2011 and 2019 (Feng B. et al., 2021). In the US, 2,244,587 primary and revision hip and knee arthroplasties were performed from 2012 to 2020 (Siddiqi et al., 2022). The strong demand for artificial joint replacement has also brought attention to the innovation of artificial joint materials, in which bone and cartilage tissue engineering is closely related to providing safer, more stable and functional artificial joints *in vivo*. As an emerging excellent nanobiomaterial, graphene-based materials have received great attention in major fields such as chemistry, physics, materials, and medical biology (Geim and Novoselov, 2007). Boccaccini *et al.* discovered that carbon nanotubes (CNTs) have great applications in biomedicine (Boccaccini and Gerhardt, 2010). Graphene-based materials in cardiac, neural, skeletal muscle, and skin/adipose tissue engineering have drawn particular attention in recent years (Shin et al., 2016). In regard to bone and cartilage tissue engineering specifically, hybrid scaffolds based on graphene nanomaterials have shown great potential in osteogenesis and chondrogenesis (Kang et al., 2022). These all attract more study on graphene and its derivatives in bone and cartilage tissue engineering.

Graphene is a two-dimensional hexagonal planar polycyclic aromatic hydrocarbon atomic crystal with sp2 hybridized carbon atoms arranged in a honeycomb shape, whose unique atomic structure gives it special chemical, physical, mechanical, thermal, electronic and optical properties. In 2004, Geim and Novoselov isolated graphene from graphite by micromechanical forces, for which they received the Nobel Prize in Physics in 2010 (Novoselov et al., 2004).

Graphene-based materials broadly refer to 2D carbon materials related to graphene, including graphene and its derivatives, such as graphene oxide (GO) and reduced graphene oxide (rGO). Meanwhile, other carbon materials, such as metal carbides and/or nitrides (MXenes) and fullerene (C60) also play an important role. Because of their physicochemical properties of high biocompatibility, low toxicity, high specific surface area, and strong adsorption ability to small molecules, graphene materials are an ideal material for tissue engineering (Nejabat et al., 2017). However, single-layer defect-free graphene is difficult to prepare, while derivatives of graphene, while maintaining the properties of graphene itself, solve the problem of its difficult dispersion in aqueous solutions and organic solvents by introducing functional group modifications (e.g., hydroxyl, carboxyl, epoxy groups, etc., and can be used more widely in biomedical fields by forming biocomposites with other materials. This paper focuses on the latest research progress of graphene materials in the field of bone and cartilage tissue engineering (Table 1).

1.1 Special biological properties of graphene and its derivatives

1.1.1 Antibacterial ability

Postoperative periprosthetic infection is a catastrophic complication of bone implant materials. Therefore, the design of

TABLE 1 Summary of the application of graphene and its derivatives in bone and cartilage tissue engineering and nanobiocatalysis.

Materials	Graphene and its derivatives attatched	Characteristics	Function	Application	References
chitosan	GO	improved elastic modulus, tensile strength, and elongation	promoting cellular proliferation	artificial bone materials	Liu et al. (2008), Gao et al. (2014)
polydimethylsiloxane (PDMS)	RGO	good mechanical strength and voids ranging from 10 to 600 μm in diameter	stimulating the differentiation of human ADSCs to the osteoblast lineage		Dinescu et al. (2014)
hydroxyapatite (HA)	rGO	better mechanical strength, hardness and Young's modulus	enhancing the osteogenic differentiation of cells and new bone formation		Dinescu et al. (2014), Li et al. (2017)
	GO (modified by sulfate groups)		promoting calcium ion aggregation and driving HA mineralizatio	bone repair	Fan et al. (2014)
hierarchical porous HA	rGO		accelerating bone growth and the repair of critical bone defects		Zhou et al. (2019)
poly-methyl methacrylate (PMMA)	GO	enhanced mechanical properties, promoted cell proliferation	binding the bone cement to the adjacent bone		Gonçalves et al. (2013)
ultrahigh molecular weight polyethylene (UHMWPE)	G	increased fracture toughness and tensile strength	reducing aseptic loosening after arthroplasty	arthroplasty	Lahiri et al. (2012)
protenis	G	high nanoscale porosity, excellent protein-bearing capacity	improving cell survival and chondrocyte differentiation	cartilage tissue engineering	Yoon et al. (2014)
chondroitin sulfate/ethylene glycol	GO	bionic three-dimensional environment	improving survival rate of chondrocyte growth		Liao et al. (2015)
N-doped rGO (N-rGO)		good biocompatibility and great stability	enhanceing peroxidase-mimicking activities	tumor catalytic therapy	Hu et al. (2018), Liang et al. (2020)
G encapsulated with TiO2		scavenging free radicals, protecting cells against oxidative stress		anti-oxidation treatment	Qiu et al. (2014)
reactive oxygen species (ROS)-based nanomaterials					Zhou et al. (2020), Zhao et al. (2022)
graphene quantum dots (GQDs)		anti-inflammation abilities		intestinal bowel diseases (IBDs) treatment	Lee et al. (2020)
Metal carbides and/or nitrides (MXenes)		high metallic conductivity, excellent hydrophilicity and a large surface area	oxidase, peroxidase, superoxide dismutase, and catalase activities	nanobiocatalysis	Feng W. et al. (2021), Liu et al. (2022)
tris-malonic acid derivative of fullerene (C60)		superoxide dismutase activities		cardiac damage treatment	Ali et al. (2004), Hao et al. (2017)
GO in gold nanoreaction between HAuCl4 and H2O2		high reaction rate	surface-enhanced Raman scattering (SERS) activity	detection of HCG	Liang et al. (2017)

bone implant materials with good antibacterial properties and osteogenic function is extremely important in the field of bone tissue engineering. However, the traditional method of loading antibiotics into bone implant materials is increasingly limited by the problems of bacterial biofilms on the surface of the prosthesis blocking the action of drugs and the development of bacterial resistance. Here, the discovery of graphene materials has brought a chance to solve the problem.

Hu *et al.* found that GO has a significant antibacterial effect. It could inactivate *Escherichia coli* within 2 h (Hu et al., 2010). Subsequent studies have reported that GO also shows excellent antibacterial activity against other common Gram-negative or Gram-positive bacteria (Liu et al., 2011; Krishnamoorthy et al., 2012; Tu et al., 2013; Yin et al., 2013). The specific antibacterial mechanism of GO is still inconclusive, but it is generally attributed to two main mechanisms: damage to the cell structure integrity of the exposed bacteria and oxidative stress. The former is mainly a physical damage mechanism: when bacteria come into contact with the GO surface, GO can kill bacteria by damaging the cell membrane through the sharp structure of the edge, extracting phospholipid molecules from the bacterial cell membrane and destroying its structural integrity (Hu et al., 2010; Tu et al., 2013). The latter is mainly a chemical mechanism: after contact with GO, bacterial intracellular reactive oxygen species (ROS) and reduced glutathione (GSH) ratios are imbalanced, resulting in lipid peroxidation, mitochondrial dysfunction, and protein inactivation, which lead to cell apoptosis (Gurunathan et al., 2013).

1.1.2 Bone tissue regeneration promotability

In the process of repair and reconstruction of defective bone tissue, biomaterials not only need to provide the mechanical and physiological environment required for cell adhesion, growth, proliferation, and metabolism but also play an essential role in regulating the differentiation of stem cells to osteoblasts. The good physicochemical properties, biocompatibility and pro-stem cell osteogenic differentiation properties of graphene make it show promising applications in osteoconduction (Kim et al., 2013).

Graphene material coatings are biocompatible and provide good conditions for the adhesion and proliferation of osteogenic-associated fibroblasts, osteoblasts, and mesenchymal stem cells (MSCs) (Ryoo et al., 2010). The stiffness and strain of the stem cell culture substrate are important factors affecting stem cell differentiation (Jang et al., 2011), and the extremely high Young's modulus and good flexibility to cope with out-of-plane deformation of graphene contribute to its role in promoting osteogenic differentiation of stem cells. McBeath *et al.* have grown human osteoblasts and MSCs on GO and silica surfaces, respectively. After 48 h of culture, they found that the number of proliferations on the graphene surface was significantly higher than the latter, and the morphology of MSCs on graphene was spindle-shaped, different from the irregular polygonal cells on the surface of SiO2 plates (Jang et al., 2011). Considering that MSCs with spindle morphology tend to have a higher potential to differentiate into osteoblasts, this suggests a tendency of osteogenic differentiation of MSCs in the graphene medium (McBeath et al., 2004). Nayak *et al.* found that BMSCs in graphene medium showed significant expression of the osteoblast marker osteocalcin (OCN) and more calcium deposition after alizarin red staining. The effect was similar to that of the classical pro-osteo-differentiation factor bone morphogenetic protein 2 (BMP2) (Kalbacova et al., 2010).

1.1.3 Drug delivery capacity

Graphene has a large specific surface area and can assume a larger drug loading capacity. In addition, the noncovalent π-π bonds and hydrogen bonds in the structure allow graphene to adsorb more proteins and drugs.

In 2008, Liu *et al.* were the first to realize the drug-carrying function of graphene. They loaded an anticancer drug camptothecin derivative (SN38) into PEG-modified GO and demonstrated the good biosafety of graphene materials as drug carriers (Nayak et al., 2011). Yang *et al.* successfully loaded GO with a large amount of adriamycin and demonstrated that the drug-carrying effect of GO was mainly accomplished by π-π stacking (Liu et al., 2008). Zhang *et al.* were the first to report that loading GO with multiple anticancer drugs for mixed transport reduced tumor drug resistance (Yang et al., 2010).

La *et al.* loaded BMP-2 onto GO-coated titanium (Ti) substrates and found that they released a significant amount of BMP-2. The GO-coated Ti substrates were found to promote osteoblast differentiation more than the pure Ti substrates. The study also found that there was more new bone formation in the Ti/GO-BMP2 group after implantation in a mouse cranial defect model. The above study showed that graphene has a large drug loading and controlled release capacity. It can also be used as an excellent drug carrier and slow release material in bone tissue engineering (Yang et al., 2010).

1.2 Progress in the application of graphene and its derivatives in bone tissue engineering

The purpose of tissue engineering is to restore or improve the morphology and function of damaged tissues and organs to achieve ultimate reconstruction. Among the three major elements of bone tissue engineering, scaffold material, growth factors and seed cells, scaffold material is an extremely important part. The three-dimensional structure of the material scaffold can provide an ideal microenvironment for cell adhesion and proliferation, mechanically supporting bone regeneration. The main problems of conventional bone tissue engineering scaffold materials currently include insufficient strength and low osteogenic induction capacity. Graphene (G) is a new carbon nanomaterial with great application potential that was discovered recently. The good mechanical strength and electrical conductivity, promotion of cell proliferation and differentiation, and many other biological functions make it a hot research topic in biomedical fields such as tumor therapy and neuromuscular regeneration (Kalbacova et al., 2010).

Graphene-based materials compounded with conventional bone tissue engineering scaffolds can increase toughness

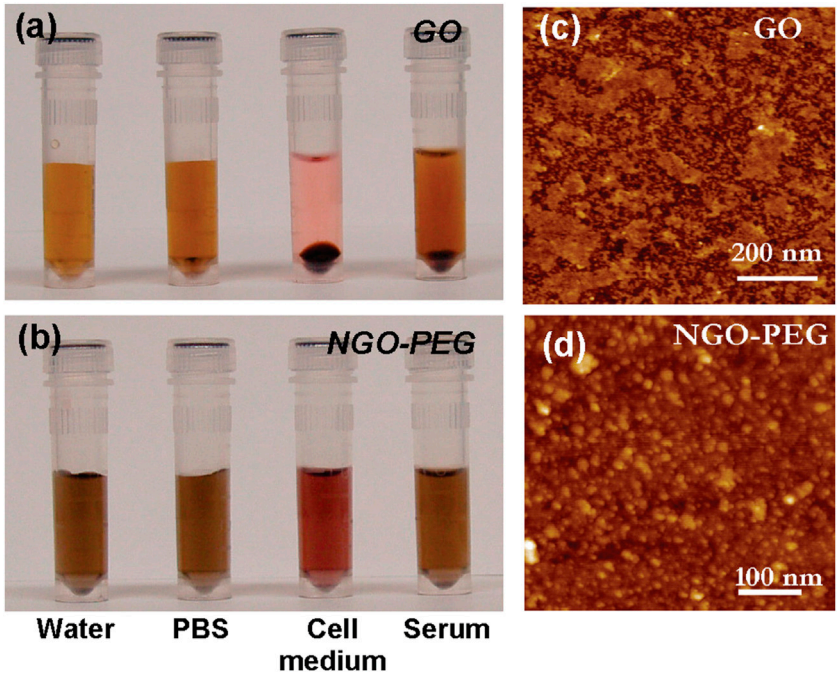

FIGURE 1
PEGylation of graphene oxide: photos of GO **(A)** and NGO–PEG **(B)** in different solutions recorded after centrifugation at 10000 *g* for 5 min. GO crashed out slightly in PBS and completely in cell medium and serum (top panel). NGO–PEG was stable in all solutions; AFM images of GO **(C)** and NGO-PEG **(D)** (Liu et al., 2008).

through crack bridging, crack deflection, and crack tip shielding, improving the mechanical properties of conventional materials, thus better helping the original materials achieve bone tissue engineering functions (Zhang et al., 2010). Chitosan is a natural polymer material with good biocompatibility and bioactivity that is rich in functional groups and is highly regarded among biomaterials. However, its poor mechanical properties and low strength limit its application. Recently, a study prepared composites by adding a 1% GO sheet layer to chitosan, which improved the elastic modulus, tensile strength, and elongation by 51%, 93%, and 41%, respectively, compared to pure chitosan (Figure 1 inserted) (Liu et al., 2008). Dinescu *et al.* added chitosan at 0.5% and 3% mass ratios of GO and discovered improvements in scaffold void formation, mechanical properties, and bioactivity. *In vitro* experiments revealed that the material containing 3% GO was more cytocompatible and better able to promote cellular proliferation, which has potential as a 3D scaffold material for bone tissue engineering (Gao et al., 2014).

Polydimethylsiloxane (PDMS) is a widely used silicon-based organic polymer material whose biocompatibility and high solubility of oxygen make it an ideal material for cell transplantation. However, its high hydrophobicity inhibits PDMS bioactivity, limiting its use in tissue engineering. Recently, a study coated PDMS 3D scaffolds with RGO, which formed RGO/PDMS 3D scaffolds with good mechanical strength and voids ranging from 10 to 600 μm in diameter. The composite 3D scaffold was found to stimulate the differentiation of human adipose stem cells (ADSCs) to the osteoblast lineage, suggesting that the RGO/PDMS 3D scaffold may be a potential osteointegration graft (Figure 2 inserted) (Dinescu et al., 2014).

As a bioceramic material, hydroxyapatite (HA), the main component of the inorganic part of bone in the human skeleton, can be firmly bonded to natural bone and has biological activity to promote bone regeneration and thus has promising applications in bone defect repair. However, its poor tensile strength and crack resistance limit its application in bone tissue engineering. The incorporation of graphene material in the preparation of HA material can improve its mechanical strength without destroying its structure and biocompatibility. It has been reported that the hardness and Young's modulus were significantly improved in graphene-HA composites (Li et al., 2017). Another study found that the complex of HA combined with rGO can greatly enhance the osteogenic differentiation of cells and new bone formation (Dinescu et al., 2014). If GO is modified by sulfate groups, it can further promote calcium ion aggregation and drive HA mineralization (Fan et al., 2014). HA with a hierarchical pore structure is beneficial for cell adhesion, fluid transfer, and cell ingrowth. The composite scaffolds of hierarchical porous HA combined with rGO can improve adhesion and promote the proliferation and spontaneous osteogenic differentiation of bone marrow mesenchymal stem cells, greatly accelerating bone growth in the scaffold and the repair of critical bone defects (Figure 3 inserted) (Zhou et al., 2019).

Poly-methyl methacrylate (PMMA) bone cement is widely used in arthroplasty and vertebroplasty as a molding material with good injectability and high mechanical strength. However, it is not biologically active and cannot form good osseointegration with

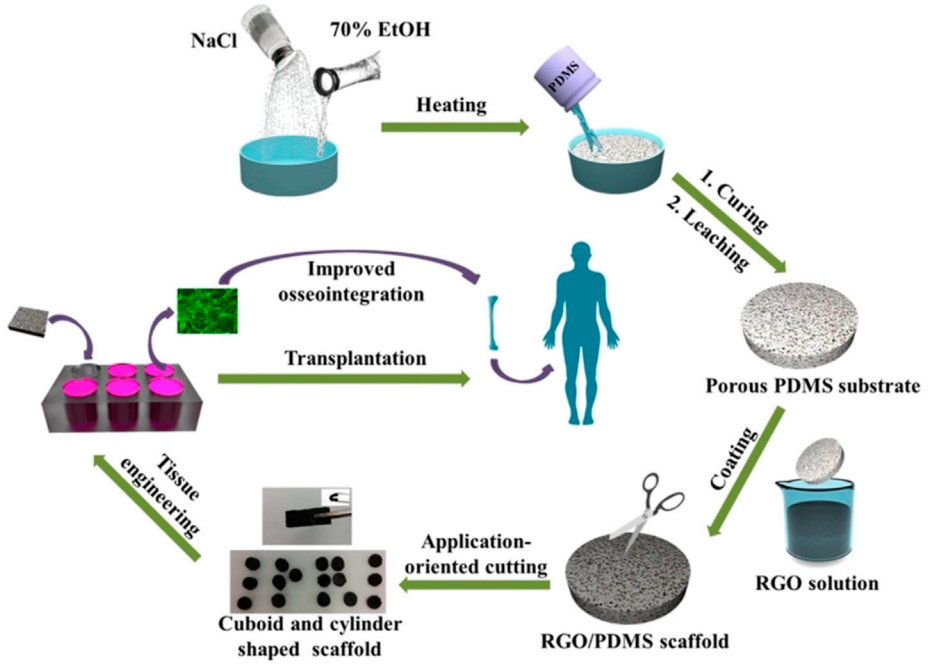

FIGURE 2
Schematic illustration of the fabrication process and application for improved osseointegration of porous rGO/PDMS scaffold (Li et al., 2017).

adjacent bone, which may lead to prosthetic loosening after implantation. In one study, GO at a mass fraction of 0.5% was added to PMMA/HA bone cement. The addition of GO increased the growth of the calcium phosphate layer, enhanced the mechanical properties of the material, and promoted cell proliferation on its surface (Gonçalves et al., 2013) (Figure 4 inserted). These results together increased the binding of the bone cement to the adjacent bone and reduced the risk of potential postoperative prosthetic loosening.

Ultrahigh molecular weight polyethylene (UHMWPE) is widely used as prosthetic liners for artificial hip and knee replacements because of its good biocompatibility, low coefficient of friction, and high impact toughness. However, its low surface hardness produces polyethylene abrasive debris in long-term use, which leads to periprosthetic osteolysis and is an important cause of aseptic loosening of the prosthesis after arthroplasty. By adding a thin layer of 0.1% graphene in the preparation of UHMPE, Lahiri *et al.* increased the fracture toughness and tensile strength of the composite by 54% and 71%, respectively. This finding could help reduce aseptic loosening after arthroplasty (Lahiri et al., 2012).

1.3 Progress in the application of graphene and its derivatives in cartilage tissue engineering

Human cartilage tissue is composed of chondrocytes, fibers, and extracellular matrix. Unlike other tissues, cartilage tissue is difficult to recover quickly on its own once damaged because of its lack of vessels and other cells. Currently, cellular therapy using MSCs can induce chondrocyte differentiation and regeneration and is now widely used to regenerate cartilage tissue. In recent years, graphene has been used as a complex scaffold for cartilage stem cell therapy by taking advantage of its ability to stimulate cell growth and differentiation and its excellent mechanical properties.

In cartilage tissue engineering, graphene biomaterials play the role of a "growth factor factory". With the high nanoscale porosity of graphene and its excellent protein-bearing capacity, aggregated proteoglycans, type II collagen, and aminoglucan are assembled with MSCs and graphene sheets to form graphene-cellular biocomposites. Meanwhile, GO can also adsorb fibronectin (FN) and TGF-β proteins through π-π and electrostatic interactions without damaging the protein structure. This composite can improve cell survival as well as chondrocyte differentiation (Figure 5 inserted) (Yoon et al., 2014).

In addition, a cartilage scaffold (CSMA/PECA/GO), synthesized from chondroitin sulfate, ethylene glycol, and GO, has been used to provide a bionic three-dimensional environment. Liao *et al.* found that chondrocytes grown on this composite scaffold had an extremely high survival rate, demonstrating the biocompatibility of the GO composite scaffold. In animal models, when the CSMA/PECA/GO composite scaffold was implanted into models with cartilage tissue defects, better cartilage morphology, more continuous subchondral bone and a thicker neochondral layer were discovered compared to the normal scaffold group (Liao et al.,

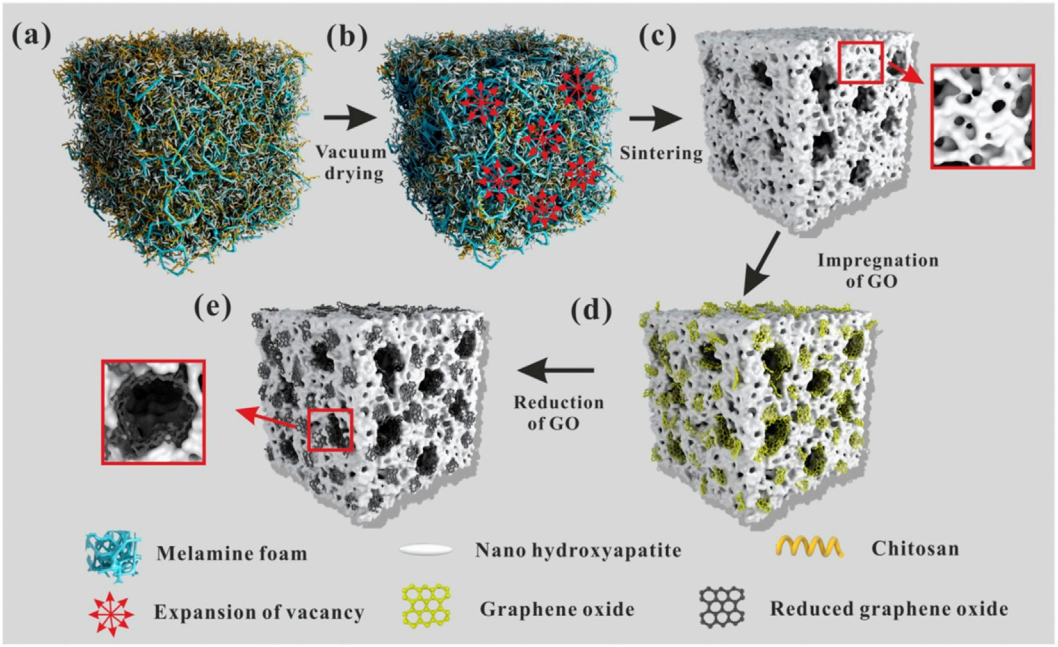

FIGURE 3
The formation mechanism of the hierarchical pore structure is schematically given in Figure 3. Firstly, melamine foam was immersed in HA/Chitosan (CS) composite slurry until the sponge was full of the slurry **(A)**. Then, the melamine foam full of the slurry was transferred into the vacuum oven. During vacuum drying, with the evaporation of the solvent, water, the volume of the filled slurry reduced, so the vacancy uniformly appeared in the foam. Vacuum suction guided the gradual and uniform expansion of vacancy during the evaporation of the solvent **(B)**. At last, the expanding vacancy connected with each other and formed a through-hole structure in the foam. During the solvent evaporation, CS molecular chains shrunk. Because of the strong hydrogen bonding between CS molecular chains and nano-HA, the shrinking of CS molecular chains dragged the nano-HA and made it tightly stuck to the frame of the melamine foam. Thus, uniform through-hole structure was formed in the melamine foam. The schematic diagram was shown in **(B)**. After sintering in air atmosphere, melamine foam and CS were burned out and pure porous HA ceramics were obtained as shown in **(C)**. During sintering, nano-HA was sintered together and porous HA ceramic formed. Simultaneously, the micropores formed on the through-hole structure because of the space occupied by needle-like nano-HA. After the introduction of GO, large GO sheets attached on the surface of the through-hole structure and small GO sheets embedded on the walls of the pores and wrapped into the internal of the micropores because of Van der Waals force **(D)**. Then, thermal reduction was carried out at 1000 °C under nitrogen atmosphere. After heat reduction, the reduced graphene sheets closely integrated with HA because of the shape changes of GO sheets during the reduction and the electrostatic interaction between graphene sheets and HA **(E)** (Zhou et al., 2019).

2015), suggesting that the CSMA/PECA/GO composite scaffold has good prospects in cartilage tissue engineering.

1.4 Progress in the application of graphene and its derivatives in nanobiocatalysis

In recent years, much research on nanobiocatalysis has revealed the great ability of nanomaterials to enhance the efficiency and stability of biocatalysts. Nanomaterial-based enzyme mimics (nanozymes), of all nanobiocatalysts, have gained great attention in clinical medicine, bioengineering, pharmaceuticals and many other fields. However, it is still difficult to control nanozymes to target and work more specifically *in vivo* (Liao et al., 2015; Fan et al., 2018). With graphene and its derivatives, researchers have developed nanozymes that can be well regulated and controlled intracellularly.

Liang *et al.* discovered that nitrogen (N), boron (B), phosphorus (P) and sulfur (S)-doped graphene materials have significant peroxidase-mimicking activity. Furthermore, the dual-doped graphene of P and N shows better mimicking activity because it increases the number of activity sites and has a synergistic effect (Fan et al., 2018). N-doped rGO (N-rGO) also demonstrates enhanced peroxidase-mimicking activities, with no great influence on oxidase-, superoxide dismutase-, or catalase-mimicking activities (Figure 6 inserted) (Hu et al., 2018). These N-doped graphene nanozymes have good biocompatibility and great stability, which is a promising strategy for tumor catalytic therapy (Hu et al., 2018; Liang et al., 2020). When loaded in isabgol nanocomposite scaffolds, rGO can heal wounds rapidly with magnified angiogenesis, collagen synthesis and deposition, especially in diabetic wounds (Thangavel et al., 2018). Qiu *et al.* also reported that graphene-based materials, especially those encapsulated with nanoparticles such as TiO_2, have a great ability to protect against oxidation (Qiu et al., 2014). In immunological regulation, graphene quantum dots (GQDs) have received much attention for their great anti-inflammatory properties for treating intestinal bowel diseases (IBDs) (Lee et al., 2020).

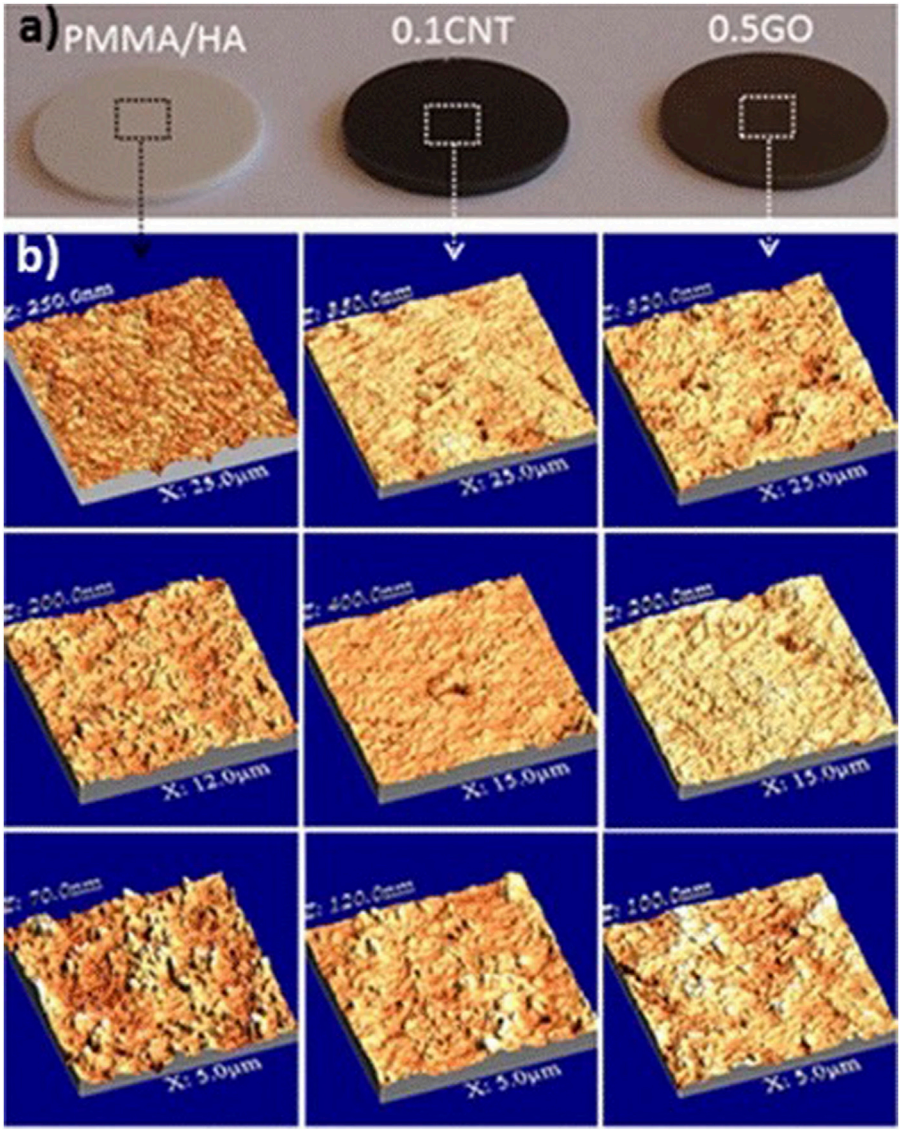

FIGURE 4
Photograph images of the polished cement disks **(A)** and AFM images of the disks surface recorded at different scales, from 5 to 25 µm **(B)** (Gonçalves et al., 2013).

Meanwhile, researchers discovered that other carbon materials might also play an important role in nanobiocatalysis. Metal carbides and/or nitrides (MXenes), a series of two-dimensional (2D) nanomaterials, have great physicochemical properties, including high metallic conductivity, excellent hydrophilicity and a large surface area (Liu et al., 2022). Feng *et al.* reported that a two-dimensional (2D) vanadium carbide (V2C) MXene nanoenzyme (MXenzyme) showed oxidase, peroxidase, superoxide dismutase, and catalase activities similar to those of natural enzymes (Figure 7 inserted) (Feng W. et al., 2021). Likewise, reactive oxygen species (ROS)-based nanomaterials, which are deeply related to cell signaling and tissue homeostasis, can scavenge free radicals, protecting cells against oxidative stress and leading to a possible treatment strategy (Zhou et al., 2020; Zhao et al., 2022). Similarly, Ali *et al.* found that a tris-malonic acid derivative of fullerene (C_{60}) showed approximate properties to superoxide dismutase (Ali et al., 2004), and the hydrogel of fullerene can be utilized to treat cardiac damage (Hao et al., 2017).

Apart from being used as a nanozyme, GO also has surface-enhanced Raman scattering (SERS) activity (Figure 8 inserted) (Liang et al., 2017). More GO added forms more gold nanoparticles (AuNPs) in the gold nanoreaction between $HAuCl_4$ and H_2O_2, resulting in linear enhancement of SERS, resonance Rayleigh scattering (RRS), and surface plasmon resonance (SPR) absorptions. This new strategy of immunocontrolling GO catalysis has been well adapted in the detection of HCG. The above discoveries of graphene and its derivatives being utilized in both clinical treatment and laboratory tests suggest more application in nanobiocatalysis.

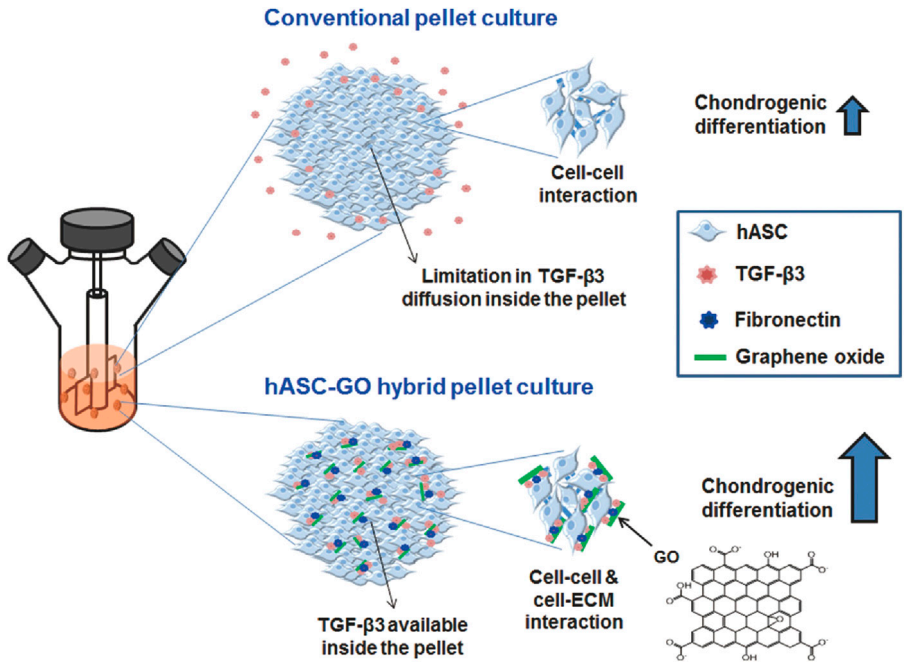

FIGURE 5
A schematic diagram describing the enhancement in chondrogenic differentiation of hASCs using GO. Conventional pellet culture provides only cell–cell interactions, and TGF-β3 diffusion inside the pellets is often limited; both of these factors limit the chondrogenic differentiation of stem cells. To improve chondrogenic differentiation, stem cells can be cultured in hybrid pellets of hASCs and GO. GO sheets are adsorbed with cell-adhesion proteins (e.g., FN) and TGF-β3 and dispersed in hASC pellets, providing cell-ECM interactions and TGF-β3 to enhance the chondrogenic differentiation of hASCs (Yoon et al., 2014).

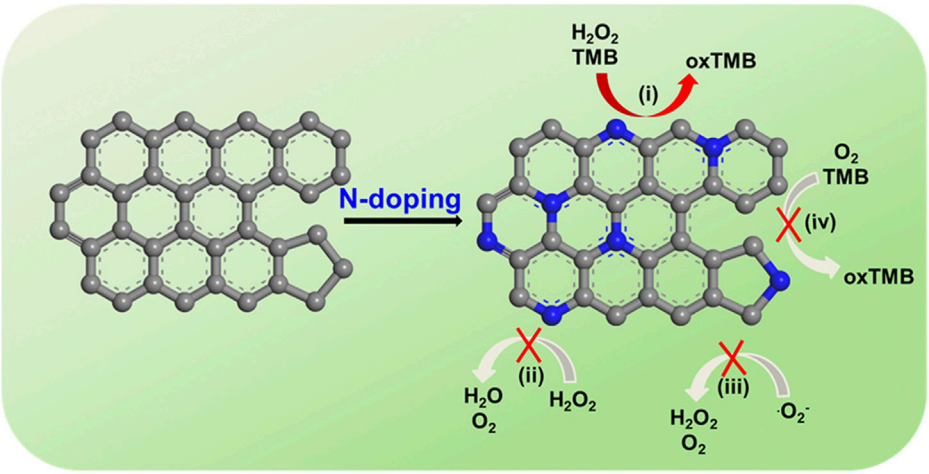

FIGURE 6
N-rGO exhibits specifically enhanced peroxidase-mimicking activity (i) but negligible catalase-, SOD-, and oxidase-mimicking activities (ii, iii, and iv, respectively). TMB: 3,3′,5,5′-tetramethylbenzidine dihydrochloride hydrate; oxTMB: oxidized TMB (Hu et al., 2018).

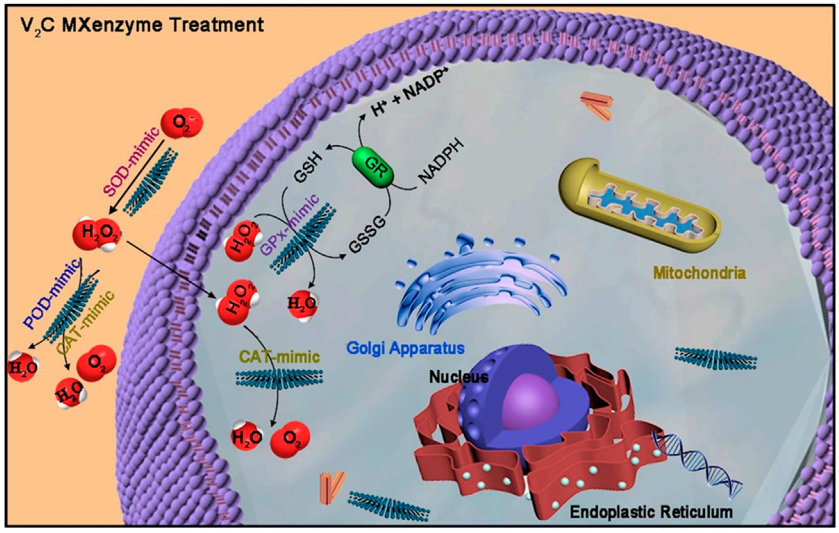

FIGURE 7
V2C MXenzyme effectively catalyzes $O_2^{-\cdot}$ into H_2O_2 and O_2, decomposes H_2O_2 into O_2 and H_2O, and gets rid of ·OH (Feng W. et al., 2021).

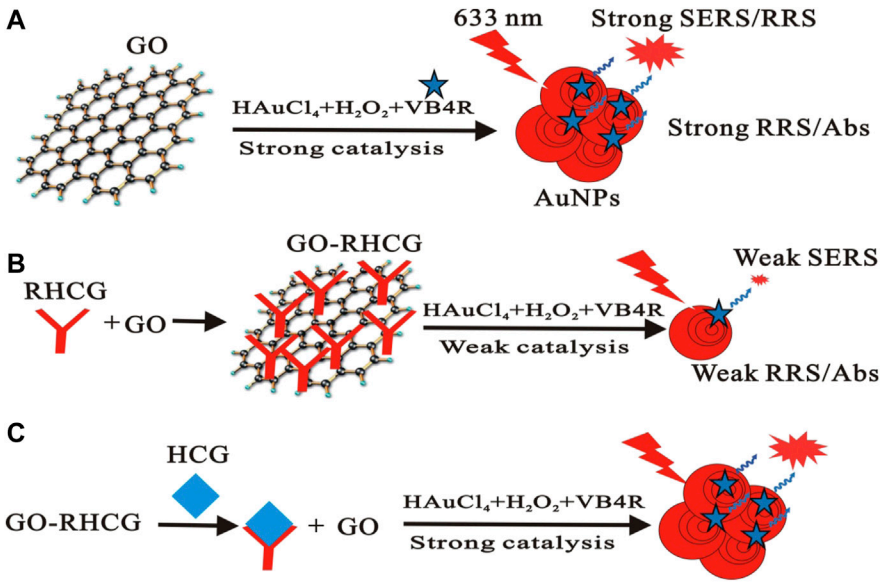

FIGURE 8
Scheme of the immunecontrolling GO catalytic activity–SERS detection of HCG. GO catalyzed the formed AuNPs with strong SERS **(A)**. RHCG inhabited the nanocatalytic reaction with weak SERS **(B)**. HCG recovered the nanocatalysis to form AuNPs with strong SERS **(C)** (Liang et al., 2017).

2 Conclusion

This review presented a wholesome picture of graphene and its derivatives, from their basic information to their special biological properties, including antibacterial ability, bone tissue regeneration promotability and drug delivery capacity. The application of graphene and its derivatives was then emphatically elaborated in bone and cartilage tissue engineering and nanobiocatalysis.

With a variety of unique biological functions, such as drug-carrying properties, antibacterial properties and osteoblast differentiation, graphene has not only become a new direction in the field of bone and cartilage tissue engineering but is also expected to bring new breakthroughs in clinical treatment. Although graphene has received widespread attention, it is still in its infancy, especially for the interaction between graphene and various cells, tissues and organs, and there is still a lack of

systematic and safe research. In the future, much basic and clinical research is still needed to break through the gap of graphene safety and degradability, making it a new application material in the field of bone and cartilage tissue engineering.

Author contributions

KZ and JL contributed to conception and design of the review. KZ and SY organized the structure of the manuscript. SY and MY wrote sections of the manuscript, All authors contributed to the article and approved the submitted version.

Funding

The authors would like to thank the following funding sources. The National Natural Science Foundation of China (82002304), Sichuan Science and Technology Department Key Research Projects (22ZDYF2639), Health Commission of Sichuan Province Program (21PJ038) and Sichuan University-Dazhou Municipal People's Government School-city Cooperation Special Fund Project (2022CDDZ-21).

Conflict of interest

The authors declare that the research was conducted in the absence of any commercial or financial relationships that could be construed as a potential conflict of interest.

Publisher's note

All claims expressed in this article are solely those of the authors and do not necessarily represent those of their affiliated organizations, or those of the publisher, the editors and the reviewers. Any product that may be evaluated in this article, or claim that may be made by its manufacturer, is not guaranteed or endorsed by the publisher.

References

Ali, S. S., Hardt, J. I., Quick, K. L., Sook Kim-Han, J., Erlanger, B. F., Huang, T. t., et al. (2004). A biologically effective fullerene (C60) derivative with superoxide dismutase mimetic properties. *Free Radic. Biol. Med.* 37, 1191–1202. doi:10.1016/j.freeradbiomed.2004.07.002

Boccaccini, A. R., and Gerhardt, L. C. (2010). Carbon nanotube composite scaffolds and coatings for tissue engineering applications. *Key Eng. Mater.* 441, 31–52. doi:10.4028/www.scientific.net/kem.441.31

Dinescu, S., Ionita, M., Pandele, A. M., Galateanu, B., Iovu, H., Ardelean, A., et al. (2014). *In vitro* cytocompatibility evaluation of chitosan/graphene oxide 3D scaffold composites designed for bone tissue engineering. *Bio-Med. Mater. Eng.* 24, 2249–2256. doi:10.3233/bme-141037

Fan, Z., Wang, J., Wang, Z., Ran, H., Li, Y., Niu, L., et al. (2014). One-pot synthesis of graphene/hydroxyapatite nanorod composite for tissue engineering. *Carbon* 66, 407–416. doi:10.1016/j.carbon.2013.09.016

Fan, K., Xi, J., Fan, L., Wang, P., Zhu, C., Tang, Y., et al. (2018). *In vivo* guiding nitrogen-doped carbon nanozyme for tumor catalytic therapy. *Nat. Commun.* 9, 1440. doi:10.1038/s41467-018-03903-8

Feng, B., Zhu, W., Bian, Y. Y., Chang, X., Cheng, K. Y., and Weng, X. S. (2021). China artificial joint annual data report. *Chin. Med. J.* 134, 752–753. doi:10.1097/cm9.0000000000001196

Feng, W., Han, X., Hu, H., Chang, M., Ding, L., Xiang, H., et al. (2021). 2D vanadium carbide MXenzyme to alleviate ROS-mediated inflammatory and neurodegenerative diseases. *Nat. Commun.* 12, 2203. doi:10.1038/s41467-021-22278-x

Gao, C., Liu, T., Shuai, C., and Peng, S. (2014). Enhancement mechanisms of graphene in nano-58S bioactive glass scaffold: Mechanical and biological performance. *Sci. Rep.* 4, 4712–4810. doi:10.1038/srep04712

Geim, A. K., and Novoselov, K. S. (2007). The rise of graphene. *Nat. Mater.* 6, 183–191. doi:10.1038/nmat1849

Gonçalves, G., Portolés, M. T., Ramírez-Santillán, C., Vallet-Regí, M., Serro, A. P., Grácio, J., et al. (2013). Evaluation of the *in vitro* biocompatibility of PMMA/high-load HA/carbon nanostructures bone cement formulations. *J. Mater. Sci. Mater. Med.* 24, 2787–2796. doi:10.1007/s10856-013-5030-2

Gurunathan, S., Han, J. W., Dayem, A. A., Eppakayala, V., Park, M. R., Kwon, D. N., et al. (2013). Antibacterial activity of dithiothreitol reduced graphene oxide. *J. Indust. Eng. Chem.* 19, 1280–1288. doi:10.1016/j.jiec.2012.12.029

Hao, T., Li, J., Yao, F., Dong, D., Wang, Y., Yang, B., et al. (2017). Injectable fullerenol/alginate hydrogel for suppression of oxidative stress damage in Brown adipose-derived stem cells and cardiac repair. *ACS Nano* 11, 5474–5488. doi:10.1021/acsnano.7b00221

Hu, W., Peng, C., Luo, W., Lv, M., Li, X., Li, D., et al. (2010). Graphene-based antibacterial paper. *ACS Nano* 4, 4317–4323. doi:10.1021/nn101097v

Hu, Y., Gao, X. J., Zhu, Y., Muhammad, F., Tan, S., Cao, W., et al. (2018). Nitrogen-doped carbon nanomaterials as highly active and specific peroxidase mimics. *Chem. Mater.* 30, 6431–6439. doi:10.1021/acs.chemmater.8b02726

Jang, J.-Y., Lee, S. W., Park, S. H., Shin, J. W., Mun, C., Kim, S. H., et al. (2011). Combined effects of surface morphology and mechanical straining magnitudes on the differentiation of mesenchymal stem cells without using biochemical reagents. *J. Biomed. Biotechnol.* 2011, 1–9. doi:10.1155/2011/860652

Kalbacova, M., Broz, A., Kong, J., and Kalbac, M. (2010). Graphene substrates promote adherence of human osteoblasts and mesenchymal stromal cells. *Carbon* 48, 4323–4329. doi:10.1016/j.carbon.2010.07.045

Kang, M. S., Jang, H. J., Lee, S. H., Shin, Y. C., Hong, S. W., Lee, J. H., et al. (2022). Functional graphene nanomaterials-based hybrid scaffolds for osteogenesis and chondrogenesis. *Adv. Exp. Med. Biol.* 1351, 65–87. doi:10.1007/978-981-16-4923-3_4

Kim, J., Choi, K. S., Kim, Y., Lim, K. T., Seonwoo, H., Park, Y., et al. (2013). Bioactive effects of graphene oxide cell culture substratum on structure and function of human adipose-derived stem cells. *J. Biomed. Mater. Res. Part A Off. J. Soc. Biomaterials* 101, 3520–3530. doi:10.1002/jbm.a.34659

Krishnamoorthy, K., Veerapandian, M., Zhang, L.-H., Yun, K., and Kim, S. J. (2012). Antibacterial efficiency of graphene nanosheets against pathogenic bacteria via lipid peroxidation. *J. Phys. Chem. C* 116, 17280–17287. doi:10.1021/jp3047054

Lahiri, D., Dua, R., Zhang, C., de Socarraz-Novoa, I., Bhat, A., Ramaswamy, S., et al. (2012). Graphene nanoplatelet-induced strengthening of ultrahigh molecular weight polyethylene and biocompatibility *in vitro*. *ACS Appl. Mater. interfaces* 4, 2234–2241. doi:10.1021/am300244s

Lee, B.-C., Lee, J. Y., Kim, J., Yoo, J. M., Kang, I., Kim, J. J., et al. (2020). Graphene quantum dots as anti-inflammatory therapy for colitis. *Sci. Adv.* 6, eaaz2630. doi:10.1126/sciadv.aaz2630

Li, J., Liu, X., Crook, J. M., and Wallace, G. G. (2017). Development of a porous 3D graphene-PDMS scaffold for improved osseointegration. *Colloids Surfaces B Biointerfaces* 159, 386–393. doi:10.1016/j.colsurfb.2017.07.087

Liang, A., Wang, X., Luo, Y., Wen, G., and Jiang, Z. (2017). Immunocontrolling graphene oxide catalytic nanogold reaction and its application to SERS quantitative analysis. *ACS omega* 2, 7349–7358. doi:10.1021/acsomega.7b01335

Liang, Q., Xi, J., Gao, X. J., Zhang, R., Yang, Y., Gao, X., et al. (2020). A metal-free nanozyme-activated prodrug strategy for targeted tumor catalytic therapy. *Nano Today* 35, 100935. doi:10.1016/j.nantod.2020.100935

Liao, J., Qu, Y., Chu, B., Zhang, X., and Qian, Z. (2015). Biodegradable CSMA/PECA/graphene porous hybrid scaffold for cartilage tissue engineering. *Sci. Rep.* 5, 9879. doi:10.1038/srep09879

Liu, Z., Robinson, J. T., Sun, X., and Dai, H. (2008). PEGylated nanographene oxide for delivery of water-insoluble cancer drugs. *J. Am. Chem. Soc.* 130, 10876–10877. doi:10.1021/ja803688x

Liu, S., Zeng, T. H., Hofmann, M., Burcombe, E., Wei, J., Jiang, R., et al. (2011). Antibacterial activity of graphite, graphite oxide, graphene oxide, and reduced graphene oxide: Membrane and oxidative stress. *ACS Nano* 5, 6971–6980. doi:10.1021/nn202451x

Liu, J., Lu, W., Lu, X., Zhang, L., Dong, H., and Li, Y. (2022). Versatile Ti 3 C 2 T x MXene for free-radical scavenging. *Nano Res.* 15, 2558–2566. doi:10.1007/s12274-021-3751-y

McBeath, R., Pirone, D. M., Nelson, C. M., Bhadriraju, K., and Chen, C. S. (2004). Cell shape, cytoskeletal tension, and RhoA regulate stem cell lineage commitment. *Dev. Cell* 6, 483–495. doi:10.1016/s1534-5807(04)00075-9

Nayak, T. R., Andersen, H., Makam, V. S., Khaw, C., Bae, S., Xu, X., et al. (2011). Graphene for controlled and accelerated osteogenic differentiation of human mesenchymal stem cells. *ACS Nano* 5, 4670–4678. doi:10.1021/nn200500h

Nejabat, M., Charbgoo, F., and Ramezani, M. (2017). Graphene as multifunctional delivery platform in cancer therapy. *J. Biomed. Mater. Res. Part A* 105, 2355–2367. doi:10.1002/jbm.a.36080

Novoselov, K. S., Geim, A. K., Morozov, S. V., Jiang, D., Zhang, Y., Dubonos, S. V., et al. (2004). Electric field effect in atomically thin carbon films. *Science* 306, 666–669. doi:10.1126/science.1102896

Qiu, Y., Wang, Z., Owens, A. C. E., Kulaots, I., Chen, Y., Kane, A. B., et al. (2014). Antioxidant chemistry of graphene-based materials and its role in oxidation protection technology. *Nanoscale* 6, 11744–11755. doi:10.1039/c4nr03275f

Ryoo, S.-R., Kim, Y.-K., Kim, M.-H., and Min, D.-H. (2010). Behaviors of NIH-3T3 fibroblasts on graphene/carbon nanotubes: Proliferation, focal adhesion, and gene transfection studies. *ACS Nano* 4, 6587–6598. doi:10.1021/nn1018279

Shin, S. R., Li, Y. C., Jang, H. L., Khoshakhlagh, P., Akbari, M., Nasajpour, A., et al. (2016). Graphene-based materials for tissue engineering. *Adv. Drug Deliv. Rev.* 105, 255–274. doi:10.1016/j.addr.2016.03.007

Siddiqi, A., Levine, B. R., and Springer, B. D. (2022). Highlights of the 2021 American joint replacement registry annual report. *Arthroplasty Today* 13, 205–207. doi:10.1016/j.artd.2022.01.020

Thangavel, P., Kannan, R., Ramachandran, B., Moorthy, G., Suguna, L., and Muthuvijayan, V. (2018). Development of reduced graphene oxide (rGO)-isabgol nanocomposite dressings for enhanced vascularization and accelerated wound healing in normal and diabetic rats. *J. Colloid interface Sci.* 517, 251–264. doi:10.1016/j.jcis.2018.01.110

Tu, Y., Lv, M., Xiu, P., Huynh, T., Zhang, M., Castelli, M., et al. (2013). Destructive extraction of phospholipids from *Escherichia coli* membranes by graphene nanosheets. *Nat. Nanotechnol.* 8, 594–601. doi:10.1038/nnano.2013.125

Yang, X., Tu, Y., Li, L., Shang, S., and Tao, X.-m. (2010). Well-dispersed chitosan/graphene oxide nanocomposites. *ACS Appl. Mater. interfaces* 2, 1707–1713. doi:10.1021/am100222m

Yin, S., Goldovsky, Y., Herzberg, M., Liu, L., Sun, H., Zhang, Y., et al. (2013). Functional free-standing graphene honeycomb films. *Adv. Funct. Mater.* 23, 2972–2978. doi:10.1002/adfm.201203491

Yoon, H. H., Bhang, S. H., Kim, T., Yu, T., Hyeon, T., and Kim, B. S. (2014). Dual roles of graphene oxide in chondrogenic differentiation of adult stem cells: Cell-adhesion substrate and growth factor-delivery carrier. *Adv. Funct. Mater.* 24, 6455–6464. doi:10.1002/adfm.201400793

Zhang, L., Xia, J., Zhao, Q., Liu, L., and Zhang, Z. (2010). Functional graphene oxide as a nanocarrier for controlled loading and targeted delivery of mixed anticancer drugs. *small* 6, 537–544. doi:10.1002/smll.200901680

Zhao, T., Wu, W., Sui, L., Huang, Q., Nan, Y., Liu, J., et al. (2022). Reactive oxygen species-based nanomaterials for the treatment of myocardial ischemia reperfusion injuries. *Bioact. Mater.* 7, 47–72. doi:10.1016/j.bioactmat.2021.06.006

Zhou, K., Yu, P., Shi, X., Ling, T., Zeng, W., Chen, A., et al. (2019). Hierarchically porous hydroxyapatite hybrid scaffold incorporated with reduced graphene oxide for rapid bone ingrowth and repair. *ACS Nano* 13, 9595–9606. doi:10.1021/acsnano.9b04723

Zhou, Z., Ni, K., Deng, H., and Chen, X. (2020). Dancing with reactive oxygen species generation and elimination in nanotheranostics for disease treatment. *Adv. Drug Deliv. Rev.* 158, 73–90. doi:10.1016/j.addr.2020.06.006

frontiers | Frontiers in Bioengineering and Biotechnology

TYPE Review
PUBLISHED 21 July 2023
DOI 10.3389/fbioe.2023.1191327

Check for updates

OPEN ACCESS

EDITED BY
Yuce Li,
Sungkyunkwan University, Republic of Korea

REVIEWED BY
Leopoldo Sitia,
University of Milan, Italy
Wooram Um,
Pukyong National University, Republic of Korea

*CORRESPONDENCE
Valle Palomo,
valle.palomo@imdea.org

†These authors share first authorship

RECEIVED 21 March 2023
ACCEPTED 23 May 2023
PUBLISHED 21 July 2023

CITATION
Fernández-Gómez P, Pérez de la Lastra Aranda C, Tosat-Bitrián C, Bueso de Barrio JA, Thompson S, Sot B, Salas G, Somoza Á, Espinosa A, Castellanos M and Palomo V (2023), Nanomedical research and development in Spain: improving the treatment of diseases from the nanoscale.
Front. Bioeng. Biotechnol. 11:1191327.
doi: 10.3389/fbioe.2023.1191327

COPYRIGHT
© 2023 Fernández-Gómez, Pérez de la Lastra Aranda, Tosat-Bitrián, Bueso de Barrio, Thompson, Sot, Salas, Somoza, Espinosa, Castellanos and Palomo. This is an open-access article distributed under the terms of the Creative Commons Attribution License (CC BY). The use, distribution or reproduction in other forums is permitted, provided the original author(s) and the copyright owner(s) are credited and that the original publication in this journal is cited, in accordance with accepted academic practice. No use, distribution or reproduction is permitted which does not comply with these terms.

Nanomedical research and development in Spain: improving the treatment of diseases from the nanoscale

Paula Fernández-Gómez[1†], Carmen Pérez de la Lastra Aranda[1,2†], Carlota Tosat-Bitrián[2,3], Jesús Alejandro Bueso de Barrio[1], Sebastián Thompson[1], Begoña Sot[1,4,5], Gorka Salas[1,6], Álvaro Somoza[1,6], Ana Espinosa[1,7], Milagros Castellanos[1] and Valle Palomo[1,3,6]*

[1]Instituto Madrileño de Estudios Avanzados en Nanociencia (IMDEA Nanociencia), Madrid, Spain, [2]Centro de Investigaciones Biológicas Margarita Salas-CSIC, Madrid, Spain, [3]Centro de Investigación Biomédica en Red de Enfermedades Neurodegenerativas (CIBERNED), Instituto de Salud Carlos III, Madrid, Spain, [4]Centro de Investigaciones Energéticas, Medioambientales y Tecnológicas (CIEMAT), Unidad de Innovación Biomédica, Madrid, Spain, [5]Advanced Therapies Unit, Instituto de Investigación Sanitaria Fundación Jiménez Díaz (IIS-FJ UAM), Madrid, Spain, [6]Unidad Asociada al Centro Nacional de Biotecnología (CSIC), Madrid, Spain, [7]Instituto de Ciencia de Materiales de Madrid, ICMM-CSIC, Madrid, Spain

The new and unique possibilities that nanomaterials offer have greatly impacted biomedicine, from the treatment and diagnosis of diseases, to the specific and optimized delivery of therapeutic agents. Technological advances in the synthesis, characterization, standardization, and therapeutic performance of nanoparticles have enabled the approval of several nanomedicines and novel applications. Discoveries continue to rise exponentially in all disease areas, from cancer to neurodegenerative diseases. In Spain, there is a substantial net of researchers involved in the development of nanodiagnostics and nanomedicines. In this review, we summarize the state of the art of nanotechnology, focusing on nanoparticles, for the treatment of diseases in Spain (2017–2022), and give a perspective on the future trends and direction that nanomedicine research is taking.

KEYWORDS

nanoparticles, therapy, Spain, nanotechnology, nanomedicine

1 Introduction

Nanoparticles (NPs) are small particles usually around 10–100 nm in size, that can be obtained from a broad class of materials, (Khan et al., 2019), and are classified according to their nature (Figure 1). Materials have different properties at a nanometric scale, such as higher reactivity, singular optical or magnetic properties, among others. These properties can be used as warheads against pathological conditions (Fratila et al., 2019), (Guisasola et al., 2018a). Nanomedicine takes advantage of these unique features, offering a new set of therapeutic and diagnostic tools. For example, in NP-mediated hyperthermia, each NP acts as a heat source, increasing the temperature specifically at localized areas, damaging specific tumor cells in a controlled manner and reducing side effects in healthy tissues (in contrast with the bulk heating of conventional hyperthermia) (Vilaboa et al., 2017), (Sanz et al., 2017).

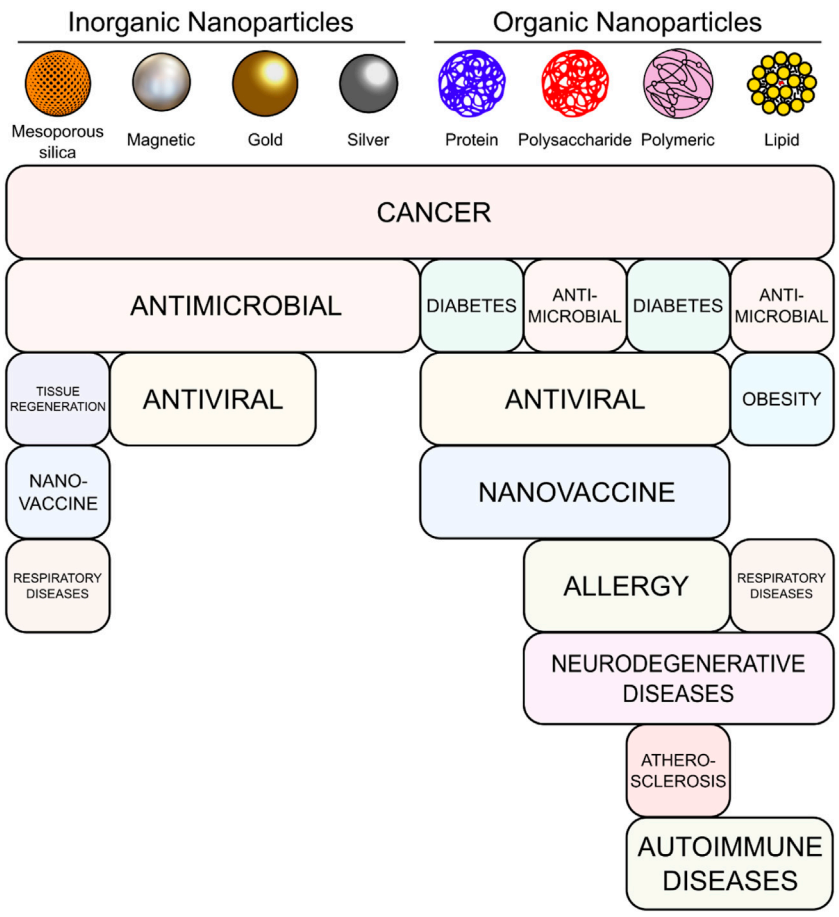

FIGURE 1
Main types of NPs and the therapeutic areas in which they are used in the articles included in this review.

A rise in temperature to 41°C–50°C induces cell death via necrosis and/or apoptosis, especially for the more thermosensitive cancer cells (Bass et al., 1978), (Sapareto and Dewey, 1984). In addition, hyperthermia increases blood irrigation preferentially within tumors (Elming et al., 2019), modifies the extracellular matrix of tumor tissue (Kolosnjaj-Tabi et al., 2017), and activates immunological responses by increasing the surface display of tumor antigens (Lee et al., 2018).

The shape, size, and surface of NPs are important properties to consider when using them for biological applications, since they determine the biocompatibility, biodistribution, cell-targeting, and uptake efficiency. NPs can be surface-modified with different biomolecules, including small proteins, antibodies, aptamers, oligonucleotides, oligosaccharides, polymers, or drugs. Therefore, by selecting suitable molecules, NPs can be tailored for the desired biological applications (Jindal, 2017), (Dolai et al., 2021), (Gatoo et al., 2014). In addition, the nanoformulation protects the cargo from degradation and improves its distribution in physiological media, facilitating oral administration and improving cell entry (Kim et al., 2021). Coating NPs with PEG, shields the surface from aggregation, opsonization, and phagocytosis, prolonging systemic circulation time and reducing their immunogenicity (Shi et al., 2021). Thus, different functionalization strategies make possible to enhance the pharmacokinetic properties of NPs, boosting the efficacy of therapy (Dacoba et al., 2017).

Another fundamental aspect is the protein corona formed on the surface of NPs, which plays a crucial role in the biological identity of NPs as it affects cytotoxicity, body distribution, endocytosis into specific cells, and biodegradation (Stepien et al., 2018), (Garcia-Alvarez and Vallet-Regi, 2021; Fleury et al., 2021). For these reasons, the proper identification and characterization of protein corona are essential in developing NPs-based therapeutics (Ritz et al., 2015; Di Silvio et al., 2018), (Alfranca et al., 2019).

NPs have a significant application as drug delivery systems (Miron-Barroso et al., 2021). Targeted therapies have at least three main advantages: reaching the target site specifically, not affecting other healthy organs, and reducing the dose needed to have the same therapeutic effect to the free drug. Biological barriers such as the blood-brain barrier (BBB) or mucus have a protective nature, hindering the simple diffusion of some therapeutic molecules, and a specific NP-mediated delivery can improve the permeability of therapeutic agents (Mulvihill et al., 2020), (Martin-Rapun et al., 2017). Finally, the possibility to encapsulate more than one drug that could provide synergistic effects showcases NPs versatility for delivery.

A significant example of the success of NPs as carriers is the drug Abraxane®. This nanomedicine, which comprises the chemotherapeutic paclitaxel (PTX) bound to albumin, has been approved for the treatment of metastatic breast cancer, advanced non-small cell lung cancer, late-stage pancreatic cancer, and metastatic triple-negative breast cancer. In several studies, it has increased patient survival and response rate significantly (De Luca et al., 2019).

Moreover, nanotechnology has also acquired a great interest in the immunological field. Vaccines are an extremely effective strategy to prevent several diseases, however their generation can be challenging since it is necessary to finely regulate the immunogenicity and the use of adjuvants as immunostimulatory agents can be critical to produce the desired effect. NPs have importance in vaccine generation because they are easily recognized by immune cells as they have a similar size to pathogens, and molecules can be anchored to their membrane to improve their recognition. In addition, new routes of administration, such as oral and nasal, can be used, and the possibility of multivalency enhances their activity (Miron-Barroso et al., 2021), (Gonzalez-Aramundiz et al., 2018).

Spain has emerged as a prominent player in the field of nanomedicine research in recent years. With numerous cutting-edge research centers and groups dedicated to this field, the country has made significant strides in the development of advanced treatments. Our review aims to provide a comprehensive overview of the latest breakthroughs in nanomedicine treatments in Spain over the past 5 years. By highlighting the capabilities of various research centers and groups, we hope to shed light on the role that Spain plays in advancing this exciting field.

2 Inorganic nanoparticles

Inorganic NPs encompass the nanoformulations that mainly contain inorganic elements. They include magnetic, metallic, gold, silver NPs and metallic quantum dots, among others, and have been studied as therapeutic systems against various diseases. For example, the plasmonic and optical properties of inorganic NPs have enabled to undertake innovative approaches to treat diseases, serving as improved contrast agents or thermo-photo-induced sources (Jaque et al., 2014), (Kim et al., 2018), (Borzenkov et al., 2019). Their tunable morphological properties and advantageous stability have promoted great promises in their nanomedical use. However, the long-term effects of the administration of these NPs in the human body still needs exhaustive characterization, which has resulted in a slower clinical translation of these NPs in comparison to their organic counterparts (Paul et al., 2020). In this review, recent advances in silica, magnetic, gold, and silver NPs, are summarized. At the end of each section, the studies are summarized in tables and categorized by NP type highlighting their purpose, therapeutic area, agent and functionalization strategy.

2.1 Mesoporous silica nanoparticles

Mesoporous silica NPs (MSNs) present several advantages that have qualified them as ideal carriers for drug delivery (Manzano and Vallet-Regi, 2019), (Manzano and Vallet-Regi, 2018), (Iturrioz-Rodriguez et al., 2019). They have large pores (0.6–1 cm^3) to encapsulate molecules of different sizes (including proteins), an easily modifiable surface that allows controlling drug loading and release, a very high surface-to-volume ratio, and good biocompatibility (Villegas et al., 2018), (Vallet-Regi et al., 2022). In addition, they can be prepared at different sizes (50–200 nm) and present a large surface area (Vallet-Regi et al., 2017). The group of Vallet-Regí was the first one to report the use of ordered mesoporous silica for drug delivery using the mesoporous material MCM-41 for the controlled release of ibuprofen using a simulated body fluid (Vallet-Regi et al., 2001). After that, tailored strategies have been developed for an efficient and smart delivery of therapeutic molecules, mainly for cancer treatment. For example, MSNs can be tuned to be responsive to a specific pH through an acid-sensitive linker, increasing tumor selectivity and efficacy, (Martinez-Carmona et al., 2018), and they can also be tuned to target specific organelles (Table 1) (Gisbert-Garzaran et al., 2020).

The delivery of the specific agent of MSNs can be controlled in different manners (Vallet-Regi et al., 2022). For example, Poyatos-Racionero et al. prepared MSNs loaded with essential oil components and covered by lactose that functioned as a molecular gate. They explored the properties of these particles loaded with different active agents in cellular and animal models, confirming the potential of this strategy for controlled delivery (Poyatos-Racionero et al., 2021). With regard to toxicity, mesoporous silica rods (MSR) have been less investigated in terms of biodistribution, biocompatibility, and cellular uptake, however in this case they presented improved characteristics when compared to their spherical counterparts in animal models. In this scenario, MSRs were functionalized with magnetic and fluorescent elements for diagnosis and treatment of fibrotic liver diseases (Grzelak et al., 2022).

Jimenez-Falcao et al. brought further the strategy of on-command delivery engineering loaded MSNs with a layer-by-layer supramolecular architecture, each with a specific role. The particles were first functionalized by benzimidazole and β-cyclodextrin gold NPs that act as a pH-sensitive gate. Then, a final coating was performed with glucose oxidase modified with an adamantine moiety linked to the free cyclodextrins. In that manner, these conjugates delivered their cargo upon the addition of glucose and were able to reduce HeLa cell viability (Jimenez-Falcao et al., 2019). A different delivery strategy was developed by Muñoz-Espín et al. to target senescent cells. They used MSNs coated with galacto-oligosaccharides, taking advantage of the high activity of lysosomal β-galactosidase activity in senescent cells. The nanoconjugates showed a preferential accumulation in senescent cells in animal models, improving tumor regression in mice and reducing the side effect of toxic drugs (Munoz-Espin et al., 2018).

To enhance delivery and exploit different ways of cellular entry, Navarro-Palomares et al. took advantage of cytoplasmatic entry of the toxic Shiga protein. They prepared fluorescent MSNs conjugated to a safe fragment of the protein that enabled to deliver the NPs intracellularly by a non-canonical pathway and thus avoiding the endolysosomal entry and its associated degradation (Navarro-Palomares et al., 2021).

Llinas et al. prepared a pH responsive nanosystem to deliver several drugs. First, they developed a nanosystem capable of

TABLE 1 Summary of MSNs with their therapeutic area and functionalization strategy.

NP Type	Purpose	Therapeutic area	Therapeutic agent	Functionalization strategy	Ref.
Gated MSNs	Delivery	Antimicrobial	Essential Oils	Lactose as molecular gate	Poyatos-Racionero et al. (2021)
Multifunctional MSNs		Cancer	DOX	Layer by layer functionalization with benzimidazole and β-cyclodextrin gold NPs as pH sensitive gate	Jimenez-Falcao et al. (2019)
MSNs				Galacto-oligosaccharides covered MSNs to target senescent tumoral cells	Munoz-Espin et al. (2018)
Nanovehicle MSNs			Camptothecin and DOX	pH responsive PEG linker	Llinas et al. (2018)
MCM-41/Pt			$Ru(Bpy)_3Cl_2$/DOX	Catalytic self-propulsion and oligoethylenglycol containing a disulfide element as redox dependent gating system	Diez et al. (2021)
TNFR-Dex-MSN		Pulmonary diseases	Dexamethasone	Functionalized with a peptide targeting TNFR1 that avoids cargo release. After internalization and peptide hydrolysis, the cargo is released	Garcia-Fernandez et al. (2021a), Garcia-Fernandez et al. (2021b)
Monodisperse silica spheres		-	-	Particles were functionalized with carbon nanotubes and linked to fluorophores	Iturrioz-Rodriguez et al. (2017)
Au-MSNs Janus	Development of an enzyme-controlled NP to release DOX in cancer cells	Cancer	DOX	MSNs capped with a thiol sensitive gate and glutathione reductase on the gold face, that controls cargo release	Mayol et al. (2021)
MSN loaded with iron oxide	Synergy of hyperthermia and drug delivery			SPIONS in MSNs covered with small PEG chains and a shell of polymer sentitive to temperature	Guisasola et al. (2018b)
Janus MSNs	Improve controlled targeting and current nanomedicines		Topotecan	Asymmetrically functionalized with two targeting moieties, folic acid and triphenylphosphine to target tumor cells and mitochondria respectively	Lopez et al. (2017)
MSNs	Overcoming biofilm barrier	Antibacterial	Levofloxacin	Concanavalin A was attached to carboxylic groups grafted on the MSNs surface forming covalent amide bonds	Martinez-Carmona et al. (2019)
AuNR@MSNs-SNO	Develop NIR activated MSNs combinade with photothermal and antimicrobial ccapabilities			Gold nanorods were covered in a silica shell functionalized with PEG and thiol groups to be attached to tert-butylnitrite	García et al. (2021)
MSNs	Induce biofilm disaggregation		Moxifloxacin, rifampicin	Gelatin/colistin coated MSNs to avoid premature antibiotic release	Aguilera-Correa et al. (2022a)
MSNs-AgBr and AG@ MSNs	Improve AgNPs effect	Tuberculosis	-	-	Montalvo-Quiros et al. (2021)
MSNs@PEI	Silence genes to stimulate bone regeneration	Bone regeneration	Osteostatin	Polyethylenimine grafted MSNs on phosphonate-modified MSNs	Mora-Raimundo et al. (2019)
MSNs	Induce osteogenesis and bone repair		Ipriflavone	Spherical NPs with a porous core-shell structure synthesized by double template method	Arcos et al. (2022)
Mesoporous nanospheres	Promote vascularization	Tissue regeneration		-	Casarrubios et al. (2021)
	Study NPs effects on osteoprogenitor cells	Periodontal		-	Casarrubios et al. (2020)
MSNs	Vaccine development	Tuberculosis	-	MSNs loaded with immunomodulatory proteins	Montalvo-Quiros et al. (2020)
SiO_2@ShTxB:FITC and Fe_3O_4@SiO_2:RBITC@ ShTxB		Head and Neck Cancer	-	Particles were functionalized with fluorophores and with the protein through sonication methodology	Navarro-Palomares et al. (2021)

delivering camptothecin (CPT) and doxorubicin (DOX) (Llinas et al., 2018), and, in a further step, they developed a new system for the delivery of CPT, DOX, and zinc (II) phthalocyanine (Pc). They labelled (Pc-CPT)@MSN-hyd-PEG-hyd-DOX, which sequentially releases DOX, linked on the MSNs surface through a pH-sensitive PEG linker that gradually delivers the Pc-CPT conjugate loaded inside the MSNs. In this manner, they combined chemotherapy and photosensitizers for photodynamic therapy (PDT). Upon irradiation of the samples, the Pc phototoxicity enhances the chemotoxicity of DOX and CPT (Martinez-Edo et al., 2021).

In a further step, self-propelled NPs also enable a more efficient manner to reach their target site without the need for external stimuli. Diez et al. designed MSNs coupled with platinum nanodendrites as a self-propulsion element (Figure 2). The particles were designed with an oligoethylenglycol containing a disulfide element that acts as a gating system that can be opened under specific redox conditions. This is a successful proof of concept of a nanomaterial that can autonomously reach its target and deliver the cargo upon specific and controllable conditions (Diez et al., 2021).

Another complicated site for drug delivery are the lungs, which present several pulmonary barriers that prevent the effective delivery of traditional drugs. In this regard, García-Fernández et al. addressed this issue using MSNs (Garcia-Fernandez et al., 2021a), (Garcia-Fernandez et al., 2021b). In this case, the nanostructures were loaded with dexamethasone, which is the standard corticoid used for the treatment of this disease, and decorated with a peptide with a dual objective, targeting TNFR1 receptors and avoiding the release of the cargo. TNFR1 receptors are expressed in pro-inflammatory macrophages, and indeed the particles showed a selective uptake by these cells and released the drug. The conjugates were also effective in animal models, demonstrating lung accumulation and the reduction of the damage.

As seen by now, the versatility of NP development with therapeutic approaches enables infinite combinations of coatings, particle size, shape, and biomolecule incorporation. In addition, one can combine several NPs into new assemblies that enable to take advantage of several properties simultaneously (Redolfi Riva et al., 2017). When NPs display two or more physical properties divided on their surface, they are called Janus particles, due to their asymmetric geometry. They can also be prepared with the combination of different kinds of NPs that enable them to take advantage of both materials, and even unlock undiscovered synergistic effects. Mayo et al. developed mesoporous silica-gold Janus NPs linked to glutathione reductase. These assemblies resulted highly efficient in delivering their cargo when presented with NADPH and glutathione disulfide as triggers (Mayol et al., 2021).

Similarly, Guisasola et al. developed innovative MSNs loaded with iron oxide NPs coated with a polymer sensitive to temperature. Upon the application of alternating magnetic fields (AMF), DOX was effectively released in animal models without increasing global tissue temperature, provoking a synergistic effect of drug and hyperthermia antitumoral activities (Guisasola et al., 2018b). In another example of Janus-type MSNs, Lopez et al. designed particles selective for tumor cells that, once internalized, specifically targeted mitochondria organelles, showcasing the utility of this strategy (Lopez et al., 2017).

Bacterial resistance to common antimicrobials is growing, and many efforts are being dedicated to the development of new antibiotic tools. Biofilm formation is especially problematic because it requires much higher antibiotic doses. MSNs can be designed to deliver antimicrobials in a localized and efficient way (Bernardos et al., 2019), (Vallet-Regi et al., 2019), (Colilla and Vallet-Regi, 2020). This approach has been used in MSNs functionalized with concanavalin A, which promotes the internalization of the NPs into the biofilm matrix to deliver levofloxacin (Martinez-Carmona et al., 2019). Also, in a sophisticated example, the release of levofloxacin and nitric oxide in biofilms was enhanced by near-infrared (NIR) irradiation using core-shell Au-MSN NPs (García et al., 2021). Aguilera-Correa et al. developed gelatin/colistin coated MSNs to treat osteomyelitis, a bone infection with poor prognosis. The functional coating prevented premature antibiotic release and induced biofilm disaggregation, showing the potential of these NPs to treat bone infections (Aguilera-Correa et al., 2022a). Finally, Montalvo-Quirós et al. explored the antimicrobial activity of MSNs loaded with silver bromide NPs and silver NPs with a mesoporous silica shell, confirming the great potential of MSNs for this application (Montalvo-Quiros et al., 2021).

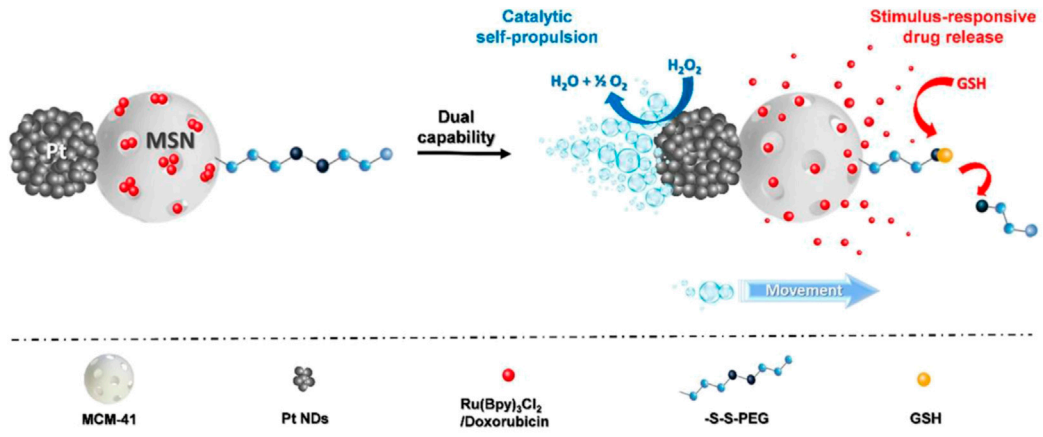

FIGURE 2
Design of Janus Pt-MSN motors. Reprinted from Diez et al. (Diez et al., 2021), and licensed under the Creative Commons Attribution.

Another prominent field of nanomedicine is the use of MSNs in bone regeneration. Mora-Raimundo et al. engineered particles to simultaneously deliver siRNA, to silence genes that inhibit osteoblasts differentiation, and osteostatin, which stimulates bone regeneration in animal models, taking advantage of the high loading capacity of MSNs (Mora-Raimundo et al., 2019). Further, Arcos et al. developed a methodology to inject MSNs loaded with an antiosteoporotic drug, ipriflavone, for the first time in rabbits, by suspending them in a hyaluronic acid hydrogel. The particles induced osteogenesis and bone repair (Arcos et al., 2022). In the same field, Casarrubios et al. decided to take advantage of the essential role that angiogenesis plays in vascularization and tissue regeneration. They loaded mesoporous nanospheres with ipriflavone, showing its release in endothelial cells by the increase of VEGFR2 expression indicating angiogenesis (Casarrubios et al., 2021). In another publication, the authors explored the potential of ipriflavone MSNs for periodontal treatment. They confirmed the clathrin-mediated entrance of the NPs, showing an osteogenesis activity (Casarrubios et al., 2020).

An original manner to deliver NPs was developed by Iturrioz-Rodriguez et al. that coated silica NPs with carbon nanotubes that enabled a cytoplasmic delivery and opens an innovative pathway to reach the cytoplasm of cells (Iturrioz-Rodriguez et al., 2017).

Finally, MSNs have also ideal properties to become a platform for vaccine development. Montalvo-Quirós et al. engineered MSNs loaded with immunomodulatory proteins that showed to have protective effects against infection of tuberculosis, (Montalvo-Quiros et al., 2020), and that could be used for dual delivery of immunomodulatory proteins and antitubercular drugs.

2.2 Magnetic nanoparticles

Magnetic NPs (MNPs) are an exceptional tool for biomedical treatment. They can deeply internalize in tissues, and have magnetic-heating capability. The most explored MNPs for nanomedicine are, by far, superparamagnetic iron oxide NPs (SPIONs) and related ferrites (Roca et al., 2019), (Pardo et al., 2020), (Mazario et al., 2012), (Garcia-Soriano et al., 2020), (Rubia-Rodriguez et al., 2021a). In clinical practice and biomedical research, they are used as iron supplements, contrast agents, and magnetic hyperthermia therapeutics (Polo et al., 2018), (de la Presa et al., 2012). Through the later application, localized heat is generated, which increases gene expression (Moros et al., 2019), particularly of the heat shock protein family, and the formation of reactive oxygen species (ROS), while inducing apoptosis and several cellular stresses such as endoplasmic reticular stress or mitochondrial damage. Interestingly, cancer cells are more sensitive to heat than healthy ones, and therefore, this approach can present reduced toxicity in healthy cells and tissues. On the other hand, the requirement to use this therapy is the application of an alternating magnetic field (AMF), which has a high penetration and negligible effect on the tissues, compared with other antitumoral techniques that present toxic side effects for nearby healthy cells and tissues. Finally, magnetic hyperthermia can be used to promote drug release and therefore it can be used alone or in combination with drugs, for synergistic combinatory therapy, or with specific molecules for active targeting (Table 2). For example, Fe_3O_4 NPs were synthesized by a seed growth method with defined shapes and sizes and were functionalized with an arginine-glycine-aspartate (RGD)-type peptide to target αvβ3 integrin receptors over-expressed in angiogenic cancer cells. NPs showed a good heating response, lower toxicity and better biocompatibility with improved magnetic properties (Arriortua et al., 2018). Sanz et al. extensively studied and compared conventional hyperthermia and the therapeutic advantage of using MNPs, confirming the improved effectiveness of the nanoheaters (Sanz et al., 2017). In case of other type of hyperthermia, Lozano-Pedraza et al. explored the optical heat losses using iron oxide NPs and identified the parameters that influence the NIR-heating effects for therapeutic purposes (Lozano-Pedraza et al., 2021).

Remarkably, iron oxide and other NPs can be obtained in a wide variety of morphologies and anisometric properties (Figure 3) (Roca et al., 2019) including, rods, cubes, stars, rings or as flower-shaped NPs among others (Gavilán et al., 2017). It is worth mentioning that the biological properties (e.g., internalization, toxicity) and response to AMF vary upon specific morphology (Ovejero et al., 2021a), (Simeonidis et al., 2016).

MNPs can be also combined with other nanostructures to yield nanostructures with additional properties. In this regard, Paterson et al. engineered self-assembled gold suprashells around dextran-coated SPION cores, which allowed them to obtain nanostructures with plasmonic and magnetic properties. The use of magnetic fields can be used to promote the accumulation of these nanostructures in cancer cells, and then exploit the plasmonic properties to induce heat by a light source, leading to the death of the tumoral cells (Paterson et al., 2017). In another work, MNPs were functionalized with dextran and crocin, which has antiproliferative properties. Crocin-coated dextran-MNPs showed greater anti-tumor effects and a higher rate of early apoptosis on MCF-7 breast tumor cells than free crocin was obtained, suggesting an effective alternative to traditional cancer treatments (Saravani et al., 2020).

Mejias et al., have worked in hyperthermia that improves tumor antigen presentation, activation of dendritic cells and natural killer cells, and leukocyte trafficking through endothelium. Probably due to NP aggregation, the contact of MNPs with cells could affect the heating capacity, highlighting the importance of NP coating to avoid cell-induced aggregation (Mejias et al., 2019). Similarly, Cabrera et al. studied intracellular MNP clustering, that led to a reduction of the magnetic hyperthermia ability. This work allowed to predict the magnetic thermal response of several NPs sizes in the cellular media (Cabrera et al., 2018).

Beola et al. investigated MNPs activity in 3D cell cultures, showing that magnetic hyperthermia can trigger necrosis or disruption of the extracellular matrix depending if the MNPs are inside or outside the cells (Beola et al., 2018). They studied the cell death mechanisms and the influence of the number of internalized particles to the cytotoxic effect testing several concentrations up to 7.5 pg Fe/cell. They showed that different apoptotic routes are triggered depending on the number of internalized NPs (Beola et al., 2020). In another work, they selected the conditions that caused the largest effect in cell viability for testing the NPs in animal models (Beola et al., 2021). AMF promoted MNPs migration into

TABLE 2 Summary of MNPs with their therapeutic area and functionalization strategy.

NP Type	Purpose	Therapeutic area	Therapeutic agent	Functionalization strategy	Ref.
Iron oxide (magnetite/maghemite)	Study of cell internalization and effects of IONPs	Cancer	-	Citric acid-coated IONPs	Cabrera et al. (2018)
	MHT: cytotoxicity study		-	3-aminopropyl-triethoxysilane and dimercaptosuccinic acid coated MNPs	Mejias et al. (2019)
	MHT control		DOX	Silica coated MNPs functionalized with hydroxyl groups	Fuentes-García et al. (2021)
	MHT with 3D cultures		-	MNPs coated with poly(maleic anhydride-alt-1-octadecene) modified with TAMRA functionalized with glucose	(Beola et al., 2018), (Beola et al., 2020)
	MHT: conditions for improving treatment effectiveness *in vivo*	Pancreatic cancer	-	MNPs coated with poly(maleic anhydride-alt-1-octadecene) modified with carboxytetramethylrhodamine functionalized with glucose	Beola et al. (2021)
	Multi-Hot-Spot magnetic inductive nanoheating	Selective regulation of multienzymatic reactions	-	Dimercaptosuccinic acid, poly(maleic anhydride-alt-1-octadecene) or poly(acrylic acid) coated MNPs	Ovejero et al. (2021b)
	MHT in mice. Study on the reliability of NP synthesis and how to control T increase	Pancreatic cancer	-	Dextran or starch coated MNPs	Luengo et al. (2022)
	MHT: chemotherapeutic synergy with drug delivery	Cancer	Gemcitabine	N6L ligand and gemcitabine functionalized on albumin coated MNPs	Aires et al. (2017)
	MHT and chemotherapeutic drug nanocarriers	Breast cancer	DOX	Dimercaptosuccinic acid coated MNPs functionalized with DOX using three different linkers-disulfide, imine or both	Lazaro-Carrillo et al. (2020)
	Selective multimodal treatment of pancreatic cancer	Pancreatic cancer	Gemcitabine	Dimercaptosuccinic acid coated MNPs functionalized with Gemcitabine and anti-CD47 antibody	Trabulo et al. (2017)
	Antiproliferative properties	Cancer	Crocin	Dextran and crocin coated MNPs	Saravani et al. (2020)
	Cell retention to improve cell therapy, EMF	Cell therapy in cancer	-	Dimercaptosuccinic acid, 3-aminopropyl-triethoxysilane or dextran coated MNPs	Sanz-Ortega et al. (2019a)
	Adoptive T cell-transfer, EMF		Antibodies	3-aminopropyl-triethoxysilane coated MNPs functionalized with antibodies	Sanz-Ortega et al. (2019b)
	Improve adoptive cell transfer therapy, EMF		-	Dimercaptosuccinic acid, 3-aminopropyl-triethoxysilane or dextran coated MNPs	Sanz-Ortega et al. (2019c)
	Gene transfection, pro-inflammation, magnetic targeting and anti-angiogenesis	Cancer	Polyethylenimine	Polyethylenimine-coated SPIONs	Mulens-Arias et al. (2019)
	Smart miRNA delivery system for immunotherapy		miRNA155, miRNA125b and miRNA146a	Dextran, carboxymethyldextran or dimercaptosuccinic acid coated NPs	Lafuente-Gomez et al. (2022)
Iron oxide (magnetite/maghemite)	PTT using iron oxide NPs	Cancer	-	IONPs with different sizes and coatings for biocompatibility	Lozano-Pedraza et al. (2021)
	PEI-MNPs	Cancer	-	Polymer coated NPs (PEI)	Sanz et al. (2017)
Iron oxide (magnetite) NPs and iron oxyhydroxide NPs	Prophylactic or therapeutic treatments for SARS-CoV-2	SARS-CoV-2	-	Dimercaptosuccinic acid, 3-aminopropyl-triethoxysilane or carboxydextran coated IONPs and sucrose coated iron oxyhydroxy NPs	DeDiego et al. (2022)

(Continued on following page)

TABLE 2 (*Continued*) Summary of MNPs with their therapeutic area and functionalization strategy.

NP Type	Purpose	Therapeutic area	Therapeutic agent	Functionalization strategy	Ref.
Ferrites $M_xFe_{3-x}O_4$ (M = metal other than iron)	Develop microswimmers with MHT capacity	Sarcoma (collagen-rich ECM)	-	PLL and collagenase coated polystyrene particles containing manganese ferrite NPs	Ramos-Docampo et al. (2019)
	Describe MHT and NPs uptake in cancer cells	Glioblastoma	-	cRGD peptide conjugation in dimercaptosuccinic acid manganese ferrite NPs	Del Sol-Fernandez et al. (2019)
	Promote heterogeneous catalysis for ROS production	Cancer	-	Copper-iron oxide spinel NPs. BSA templated synthesis with ethylene glycol	Bonet-Aleta et al. (2022a), Bonet-Aleta et al. (2022b)
Hybrid magnetic nanomaterials[1]					
Iron oxide-MnO_2	Intracellular response for switchable MRI contrast and magnetic hyperthermia	Cancer	-	Core-shell NPs with a tunable Mn oxide shell growth over iron oxide NPs	Garcia-Soriano et al. (2022)
Iron oxide-gold	Multifunctional photothermal therapy (PTT)		-	Gold suprashells around dextran coated SPIONS	Paterson et al. (2017)
	Multimodal cancer theranostics		-	Iron oxide-gold nanoflowers with PEGylated ligand	Christou et al. (2022)
	PTT, MHT and magneto-photothermal treatment with Janus NPs		-	Polyvinylpyrrolidone-coated iron oxide-gold magnetic Janus nanostars	Espinosa et al. (2020)
	PTT, MHT and magneto-photothermal treatment		-	Au-coated rod-shaped magnetite NPs in agarose hydrogels	Rincon-Iglesias et al. (2022)
Iron oxide-silver	Synergy between Ag and MHT	Antibacterial	-	γ-Fe_2O_3-Ag nanocomposites	Luengo et al. (2020)
	MHT *in vivo* real time feedback	Cancer	-	Phospholipid encapsulated Iron oxide-Ag_2S nanocomposites	Ximendes et al. (2021)

[1]Hybrid here refers to nanostructures combining two types of inorganic materials in which both are clearly distinguishable (e.g., core-shell, aggregates/encapsulates of individual NPs of both materials) and both provide a relevant function for the application (i.e., are not used just as a coating or as a platform).

the tumor and confirmed that NP biodistribution is essential for hyperthermia effectiveness, and is affected by surface coating, playing the protein corona a significant role (Stepien et al., 2018).

Also employing 3D cell cultures, the group of V. Salgueiriño and co-workers described the assembly of magnetic microswimmers, composed of 500 nm polystyrene particles containing ferrite NPs. The motion of the self-propelled microswimmers was triggered by calcium, and they were able to penetrate spheroid models for heat delivery under AMF (Ramos-Docampo et al., 2019).

Luengo et al. synthesized maghemite NPs with different coatings to determine the best properties to use in clinical applications. The NPs were injected into animals with pancreatic cancer, and the results determined that modulating the field intensity can control the temperature rise during magnetic hyperthermia protocols in animal models (Luengo et al., 2022).

The combination of experimental and simulation approaches might be a useful tool for better engineering NPs. In this regard, a model has provided quantitative predictions to fit the properties of iron NPs, including a targeting agent and a drug. Particularly, it allowed the design of NPs with a pseudopeptide Nucant-6L, which induced a significant accumulation in tumors. The studies revealed the synergy of Nucant-6L, the chemotherapeutic drug gemcitabine, and the NPs, together with the importance of fine tuning the functionalization (Aires et al., 2017).

Christou et al. developed a seed-assisted methodology for the synthesis of gold and iron oxide nanoflowers. The particles were functionalized with PEG, greatly enhancing the colloidal stability of the conjugates. The nanoflowers performed highly as contrast agents and exhibited a considerable conversion of energy to heat, having ideal properties to be used as theragnostic agents (Christou et al., 2022).

Del Sol-Fernandez et al. also developed flowerlike manganese iron oxide cRGD-functionalized NPs that, when exposed to the appropriate AMF conditions, induced intracellular magnetic hyperthermia resulting in *hsp70* transcription and strong ROS production leading to cell death in a glioblastoma cell line (Del Sol-Fernandez et al., 2019).

Espinosa et al. developed Janus magneto-plasmonic NPs, using gold nanostars and iron oxide nanospheres subjected to an external magnetic field and NIR light. With this strategy, a synergistic cytotoxic effect on cancer cells was achieved based on the combination of the two thermal effects into a magneto-photothermal modality. Moreover, experiments in animal models confirmed the high efficiency of magnetically enhanced photothermal therapy (PTT) that led to tumor growth inhibition, and the delivery was highly improved by magnetic targeting (Espinosa et al., 2020). Another type of magneto-plasmonic materials that display magneto- and photothermal anisotropic transductions for cancer ablation has been proposed by Rincon-

Iglesias et al., that incorporated Fe_3O_4@Au nanorods in an agarose hydrogel, resulting in free-standing anisotropic materials (Rincon-Iglesias et al., 2022).

Mulens-Arias et al., investigated the modulation of angiogenesis as an antitumor therapy. They used MNPs and a magnetic field for this approach. PEI-SPIONs, (SPIONs coated with polyethylenimine) showed anti-angiogenic and antitumoral effects as these NPs were able to reduce tumor vessel numbers and promoted intratumor macrophage infiltration in a tumor model after administration and application of magnetic field (Mulens-Arias et al., 2019). As another strategy against cancer, Sanz Ortega et al. developed NPs-based drug delivery systems to increase immunotherapy effectiveness. They showed that MNPs and the use of AMF can guide and retain T lymphocytes to a target region of interest and can be magnetically retained there (Sanz-Ortega et al., 2019a), (Sanz-Ortega et al., 2019b). In addition, they took advantage of the role of natural killer cells in antitumor immunity by binding MNPs coated with 3-aminopropyl triethoxysilane (APTES) to the surface of natural killer cells. They reported the retention of the cells at the specific target site by using external magnetic fields as the magnetic guiding effect (Sanz-Ortega et al., 2019c).

While hyperthermia has been exploited using several conjugates, an unsolved problem in this field is the lack of real time information on the temperature achieved locally, which complicates a fine control of therapeutic parameters *in situ*. Ximendes et al. combined in a recent work MNPs with infrared nanothermometers of Ag_2S NPs that provided an efficient solution to this problem by monitoring the subcutaneous temperatures in real time, to build 2D thermal maps, which were used to accurately assess the therapeutic effect of the MNPs (Ximendes et al., 2021). Alternatively, the temperature at the surface of

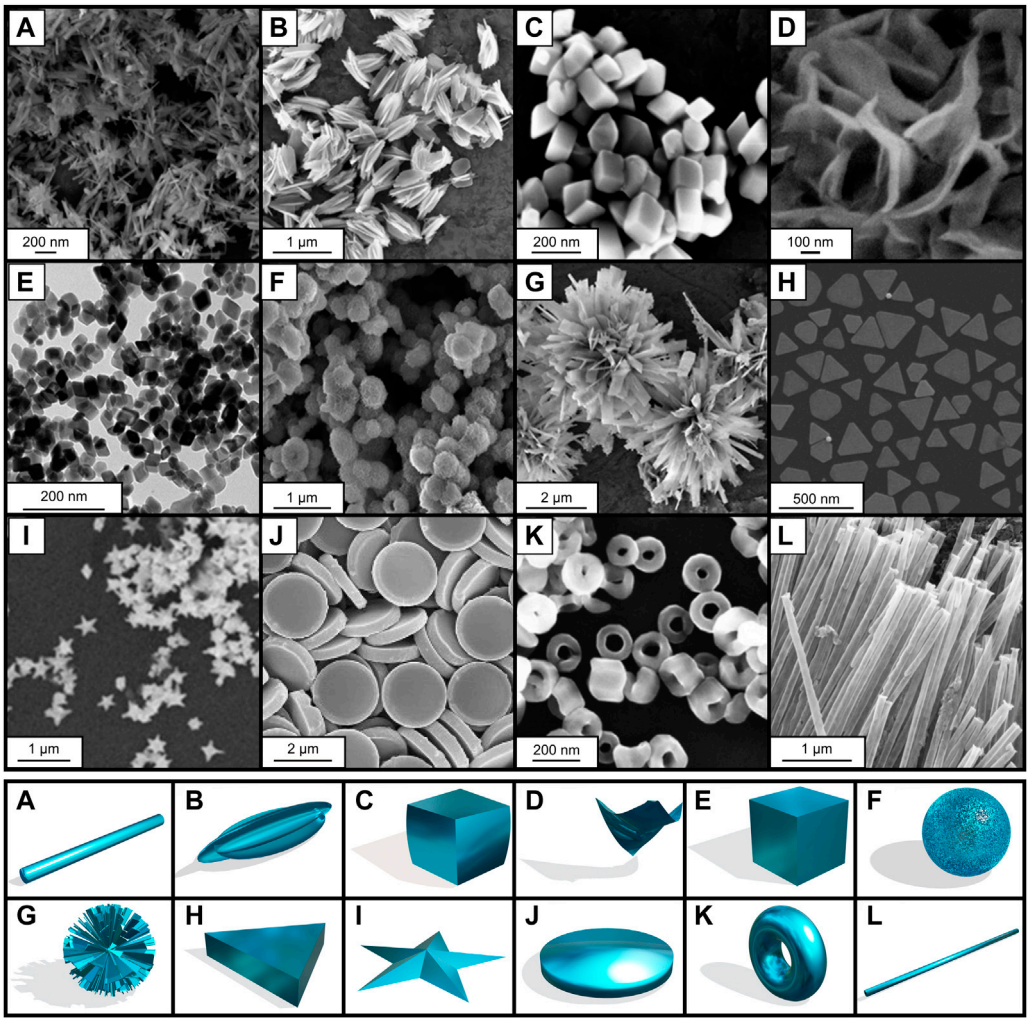

FIGURE 3
Different shapes and morphologies of iron oxide and other NPs. Scanning and transmission electron microscopy images on the upper part and morphology representation on the lower part. **(A)** nanorod, **(B)** nanohusk, **(C)** distorted cubes, **(D)** nanosheets, **(E)** distorted cubes, **(F)** porous spheres, **(G)** self-oriented flowers, **(H)** prismatic IONPs, **(I)** nanostar, **(J)** nanodiscs, **(K)** nanorings and **(L)** nanotubes. **(A, B, C, E, F, G)** adapted from Sayed and Polshettiwar (2015), **(D)** adapted from Chin et al. (2007), **(I)** adapted from Becerril-Castro et al. (2022), **(J)** adapted from Qu et al. (2021), **(H)** adapted from Ramirez-Jimenez et al. (2020), **(K)** adapted from Jia et al. (2008), **(L)** adapted from Zhang et al. (2016). Licensed under a Creative Commons Attribution.

AMF-activated MNPs was also obtained with fluorescence probes by J. Ovejero et al. (Ovejero et al., 2021b). Moreover, to guarantee an efficient thermal treatment in tumors in a safe window of applicability in the clinical practice, a modelling of the heat distribution in tissues (*in silico* studies) is crucial. Rubia-Rodriguez et al. have explored collateral heating effects on prostheses that can affect the safety and efficiency of magnetic hyperthermia treatments of localized tumors (Rubia-Rodriguez et al., 2021b).

Luengo et al. enhanced the antibacterial properties of silver NPs in combination with iron oxide and its magnetic hyperthermia properties. The authors showed how the introduction of silver in the iron oxide particles had bactericidal activity against *Staphylococcus aureus* and *Escherichia coli*, and in addition, how the external magnetic fields enhanced this activity, demonstrating the synergistic properties of both materials when used in the same composite (Luengo et al., 2020).

In a recent study, MNPs were coated by a sonochemical method with a mesoporous silica surface in which the drug, DOX, could be loaded. The release of the drug used was dependent on pH, which showed effectiveness at acidic pH, proving the ultrasound synthesis as successful (Fuentes-García et al., 2021). In another strategy for DOX delivery, Lazaro-Carrillo et al. engineered a release mechanism based on iron oxide MNPs controlled by pH. The reductive environment of the cell was critical to diminish the side effects of the chemotherapy, increasing the effect against cancer cells (Lazaro-Carrillo et al., 2020).

Trabulo et al. developed a nanoformulation of MNPs with gemcitabine (chemotherapeutic drug) and anti-CD47 (adjuvant). The anti-CD47 antibody formulation showed efficient induction of apoptosis in cancer cells compared to free antibodies. In addition, the NPs were covered with BSA and polyethylene glycol (PEG) avoiding their rapid clearance and leading to a better efficacy (Trabulo et al., 2017).

MNPs can also be employed as smart delivery system for miRNAs. Lafuente-Gómez et al. developed maghemite core NPs loaded with immunomodulatory miRNA that induced a pro-inflammatory response in macrophages due to their load and specific coating (Lafuente-Gomez et al., 2022).

A promising strategy against cancer delivered by NPs is heterogeneous catalysis, which aims to target key chemical species of the tumor and generate *in situ* harmful biomolecules. Bonet-Aleta et al. engineered copper-iron oxide spinel NPs that effectively reduced glutathione levels and increased ROS and apoptotic pathways in cancer cells (Bonet-Aleta et al., 2022a). Furthermore, they investigated in depth the selective homo- and heterogenous catalytic processes undergoing in the tumor microenvironment, in which the higher glutathione levels are the main driving factor (Bonet-Aleta et al., 2022b). Glutathione is in a much higher concentration inside the cells than on the outside and it is largely responsible of the redox environment of the intracellular medium. This has also been exploited using iron oxide-MnO_2 core-satellite shell NPs that undergo a chemical dissolution of the manganese dioxide shell when they are internalized by cells (Garcia-Soriano et al., 2022). This stimuli-responsive behavior changes the MRI contrast mode of the NPs and, at the same time, the iron oxide cores preserve their ability to kill cells through magnetic hyperthermia.

Another interesting property of MNPs is their antiviral activity, de Diego et al. showed that iron oxide NPs impair SARS-CoV-2 infection, highlighting their repurposing value as prophylactic agents against this viral infection (DeDiego et al., 2022).

Finally, the ultimate goal of research in nanomedical development is to reach clinical trials and improve current therapies. In this regard, it is worth highlighting the work done within the European project NoCanTher, where several Spanish institutions were involved. The consortium has been able to test the magnetic hyperthermia approach at Vall d'Hebron hospital (Barcelona) for the treatment of locally advanced pancreatic cancer. These types of studies are essential to make nanomaterial-based treatments a reality in the near future (Nanoscience, 2020).

2.3 Gold nanoparticles

Gold NPs (AuNPs) are especially relevant due to their ease of preparation, surface reactivity and unique optical properties (Garcia, 2011), (Goesmann and Feldmann, 2010; Wolfram and Ferrari, 2019). The small size of AuNPs, their biocompatibility, low toxicity and the possibility of simultaneous assembly of different molecular functionalities are attractive for biomedical use in therapy and sensing (Giner-Casares et al., 2016), (Saha et al., 2012), (Fabrizio et al., 2016), (Amendola et al., 2017), (Sperling et al., 2008), (Soenen et al., 2015). They are excellent candidates for PTT, biological imaging and optical sensing applications based on the localized surface plasmon resonance (LSPR) phenomenon, in terms of intrinsic properties as well as loading of different molecules, and they can also serve as contrast agents in computed tomography. Here we give an overview of the field given some examples of different AuNPs types but focusing on spherical colloids (Table 3).

The group of Liz-Marzan is a recognized reference in the synthesis of gold-based nanomaterials for multiple biomedical applications, including sensing, photothermia, and preparation of 3D scaffolds (Garcia-Lojo et al., 2019). For instance, they systematically investigated the synthesis of gold-branched nanostructures, such as nanostars with interesting optical properties related to LSPR and surface-enhanced spectroscopies, as excellent candidates for biomedical purposes (Barbosa et al., 2010). They are considered state-of-the-art NPs to be used as efficient agents for photothermal treatment at the NIR range employed as a single modality or combination with other therapeutic functionalities (Quintanilla et al., 2019), (Espinosa et al., 2016), (Villaverde et al., 2018).

In order to enhance the cellular adherence of AuNPs, some strategies have been explored. For instance Artiga et al. encapsulated AuNPs inside a mucoadhesive chitosan hydrogel using polyoxometalates and phosphotungstic acid, showing that these containers can adhere to the cytoplasmic membrane of cells, enabling the thermoablating effect of the AuNPs without the need of cellular internalization (Artiga et al., 2018) (Figure 4). Gonzalez-Pastor et al. explored an interesting modification of Adenoviral vectors (Ad) for improving their uptake in resistant cells and their biodistribution. The authors proposed a strategy

based on the modification of the Ad surface with 14 nm PEGylated AuNPs with quaternary ammonium groups and arginine-glycine-aspartic acid peptide motifs (or RGD-motif (Alipour et al., 2020)) to promote the attachment to cells via alternative cellular surface receptors, helped by the increase in positive charges. Modified vectors were tested in cellular models and in mice demonstrating their biocompatibility, high transduction efficiency, and antitumor activity (Gonzalez-Pastor et al., 2021).

As highlighted in MNPs, the shape of AuNPs also affects their biological behavior and therapeutic properties, and therefore a controlled synthesis with optimized purification methodologies is critical to obtain homogeneous NPs. Ramírez-Martínez et al. developed an efficient method to synthesize gold nanoprisms that showed reduced non-specific interactions with cells (Ramirez-Jimenez et al., 2020).

Enzyme prodrug therapy consists of selectively delivering an enzyme that activates a nontoxic prodrug into an active agent. Vivo-Llorca et al. functionalized the NPs with horseradish peroxidase, able to oxidize indole-3-acetic acid into toxic agents, and showed that this strategy presented high activity in 3D tumor models in which the three components on their own exhibit no therapeutic action (Vivo-Llorca et al., 2022).

Garcia-Garrido et al. studied drug delivery systems based on gold NPs tailored with low molecular weight polymers branched polyethylenimine and PEG. The system was able to deliver Gapmers targeting p53, reducing the chemoresistance to gemcitabine in mutant p53 cancer cells (Garcia-Garrido et al., 2021).

As is the case with every NP, the protein corona formed around NPs in biological media, modulates several key properties, including cellular internalization or clearance. Therefore, it is essential to study its formation, stability, and composition to understand NPs dynamics in cell and animal experiments. In this regard, Barbero et al. have studied the impact of common cell culture media elements in the formation of protein corona, and the mechanisms behind cellular penetration (Barbero et al., 2019), (Barbero et al., 2017), (Barbero et al., 2022). In this same subject, Mosquera et al. developed a strategy to control protein corona formation. The authors used AuNPs covered by an anionic dye (pyranine), which disrupts protein binding when a positively charged macromolecular cage is present. Zwitterionic surface ligands containing positive and negative charges will favor the formation of a protective hydration layer around the NPs. The authors demonstrate the reversibility of the system, which allows the control of corona formation through external additives. Applying this strategy the authors also increased (30-fold) the cellular uptake due to a synergistic effect between corona suppression and the charge switch from negative to positive at the NP surface. Finally, they explored its use in PTT, exploiting the conditional and enhanced cellular uptake of the system, this time using gold nanorods, with promising results (Mosquera et al., 2020).

Given the advantages of hybrid NPs, Encinas-Basurto et al. used DOX with gold NPs for PTT using human serum albumin NPs. When HeLa cells were treated with HSA-AuNR-DOX NPs, the cell viability was lower than the nanoplatform without DOX decreasing even further when the cells were irradiated (Encinas-Basurto et al., 2018a). Villar-Alvarez et al. also developed an hybrid nanocarrier based on human serum albumin/chitosan NPs that encapsulated free docetaxel and DOX-modified gold nanorods (DOX-GNRs) aiming to combine the chemotherapeutic properties of docetaxel and DOX with the plasmonic optical properties of GNRs for plasmonic-based PTT. This nanoformulation produced high cytotoxicity in breast cancer cells, and PTT enhances the cytostatic efficacy, with apoptosis being the main activated pathway (Villar-Alvarez et al., 2019). In a similar approach, Paris et al. engineered gold nanorods coated with a mesoporous silica shell to deliver two antivascular drugs with different mechanisms of action. The NPs also released heat and ROS through photothermal and PDT upon NIR light irradiation yielding remarkable results in a chicken embryo xenograft model (Paris et al., 2020).

In order to combine therapeutic plasmonic hyperthermia and DOX chemoaction, nanotransporters consisting of gold nanorods coated with poly(sodium-4-styrenesulfonate) (PSS)/DOX/hydrolyzed polylysine (PLL)/hyaluronic acid and (PSS/DOX/PLL)2/hyaluronic acid were developed by Villar-Alvarez et al. Hyaluronic acid targets CD44 receptors, which are overexpressed in some cancers. PTT induced cell necrosis, and apoptosis was promoted by DOX, resulting in a significant synergistic effect provided by a nano-based platform of targeted and multimodal controlled delivery (Villar-Alvarez et al., 2018). Astorga-Gamaza et al. also developed the synthesis of multivalent bispecific AuNPs to enhance the immune response towards HIV-expressing cells. They developed a cooperative adsorption methodology that allows the production of NPs with a 50:50 conjugation with two different antibodies that recognize the HIV gp120 protein and the CD16 receptor of natural killer cells. They performed a thorough characterization of the particles, which were able to promote specific cell-to-cell contact and induce a potent cytotoxic response (Astorga-Gamaza et al., 2021).

Martin-Saavedra et al. designed an hydrogel to incorporate AuNPs and thermosensitivie liposomes loaded with DOX. Upon NIR irradiation, the temperature rose locally releasing active DOX, whose delivery was dependent on the hydrogel composition and irradiation characteristics. Finally, the authors refined the system by incorporating copper sulfide NPs to create an easily biodegradable composite (Martin-Saavedra et al., 2017).

With the aim of controlling and monitoring the temperature of NPs reached during photothermal procedures in the tumor environment and, therefore, minimizing collateral effects during thermal treatments, plasmonic-mediated intracellular hyperthermia generated by Au nanomaterials has been tracked by nanothermometry methods. For instance, Rocha et al. have used Nd-doped Infrared-emitting NPs to monitor the light-to-heat conversion of Au nanorods during PTT (Rocha et al., 2016). Quintanilla et al. designed a hybrid probe for simultaneous plasmonic heating and NIR nanothermometry in glioma cells (Quintanilla et al., 2019). Finally, X-rays were also used to probe the local temperature of photoexcitated Au-based nanomaterials under NIR light for PTT, revealing significant nanothermal gradients (Espinosa et al., 2021).

Guasch et al., also investigated adoptive T cell therapy as a treatment for cancer, in an attempt to overcome the challenge of activating and expanding primary human T cells *in vitro*. They performed a method for activating primary human $CD4^+$ T cells *in vitro* functionalizing nanostructured surfaces. These surfaces consist of covalently functionalized RGD on rigid TiO_2 surfaces

TABLE 3 Summary of AuNPs with their therapeutic area and functionalization strategy.

Purpose	Cargo	Therapeutic area	Functionalization strategy	Ref.
Improve NP's properties	Increase the cellular attachment	-	Gelation with polyoxometalates for encapsulation of Gold Nanorods into mucoadhesive hydrogel, allowing the attachment to the cytoplasmic membranes	Artiga et al. (2018)
	Enhance Adenovirus cellular uptake, distribution and therapeutic effect via surface modification with NPs	Cancer	Adenovirus decoration with PEGylated AuNPs carrying quaternary ammonium groups and RGD-motifs	Gonzalez-Pastor et al. (2021)
	To gain control over protein corona formation	-	Zwitterionic ligands based on oligocationic cages and negatively charged pyranine	Mosquera et al. (2020)
	Study physicochemical changes by tracking the spectral signatures using Hyperspectral-enhanced dark field microscopy	-	Polymer-coated gold/copper sulfide NPs	Zamora-Perez et al. (2021)
Enhance biological processes	Enhance immune response	HIV infection	AuNPs dually conjugated with IgG anti-HIVgp120 and IgG anti-human CD16, bringing together virus and NK cells to reinforce the immune response against virus	Astorga-Gamaza et al. (2021)
	Activation and expansion of T cells against tumors	Cancer	Nanostructured surfaces functionalized with the stimulating anti-CD3 antibody and the RGD peptide, plus costimulatory agents	Guasch et al. (2018)
Control hyperthermia	Monitor light-to-heat conversion of gold nanorods	-	Encapsulation of gold nanorods together with Nd-doped fluorescent NPs in a PLGA polymer	Rocha et al. (2016)
	Control local heating and nanothermometry	Brain cancer	Gold Nanostars (photothermal) combined with CaF_2:Nd^{3+}-Y^3 luminescence NPs (thermometer)	Quintanilla et al. (2019)
	Nanothermometry Method	-	Gold nanorods and gold-iron oxide magnetic nanostars	Espinosa et al. (2021)
	Intercellular trafficking of gold nanostars as photothermal agents in cancer therapy		Gold nanostars functionalized with PEG-SH	Ahijado-Guzman et al. (2020)
Sustainable synthesis	Green synthesis of NPs for different purposes	Antimicrobial	Au and Ag NPs stabilized with "safely-obtained" biosurfactants	Gomez-Grana et al. (2017)
		Antiproliferative and Immunostimulative	Synthesis using an extract of *Saccorhiza polyschides* conferring a protective NP environment	Gonzalez-Ballesteros et al. (2021a)
		Cancer	Green synthesis of AuNPs with carrageenan from seaweed	Gonzalez-Ballesteros et al. (2021b)
Hyperthermia-triggered gene expression	Generation of cellular scaffolds and controlled gene expression	Cell therapy	AuNPs coated with poly-L-lysine through COOH-PEG-SH as covalent linker and thrombin to generate photothermal matrices	Escudero-Duch et al. (2019)
Purpose	**Cargo**	**Therapeutic area**	**Functionalization strategy**	**Ref.**
Drug delivery	Horseradish peroxidase	Cancer	Covalent functionalization with horseradish peroxidase which oxidizes the prodrug indole-3-acetic acid (IAA) to release toxic oxidative species	Vivo-Llorca et al. (2022)
	Gemcitabine/gapmers		Combination of PEG, PEI and oligonucleotides electrostatically bound and released in reducing ambient	Garcia-Garrido et al. (2021)
	DOX		DOX into Gold Nanorods loaded-HSA NPs prepared through desolvation	Encinas-Basurto et al. (2018a)
	Docetaxel and DOX		HSA/Chitosan NPs to encapsulate docetaxel and DOX-gold nanorods for chemotherapy and photothermal therapy	Villar-Alvarez et al. (2019)
	Antivascular drugs		Gold nanorods coated with mesoporous silica functionalized with aminopropyl groups and coupled to ICG photosensitizer. PEGylation with NHS-PEG-RGD	Paris et al. (2020)

(Continued on following page)

TABLE 3 (*Continued*) Summary of AuNPs with their therapeutic area and functionalization strategy.

Purpose	Cargo	Therapeutic area	Functionalization strategy	Ref.
Drug delivery	DOX	Cancer	Nanorods coated with PSS DOX/PLL/human serum albumin layer-by-layer for chemotherapy and photothermal therapy	Villar-Alvarez et al. (2018)
	DOX		Fibrin hydrogel imbibing AuNPs and thermosensitive liposomes with DOX	Martin-Saavedra et al. (2017)
	DOX and SN38		Albumin-stabilized gold nanoclusters modified with drugs	Latorre et al. (2019)
	miRNA and SN38		Conjugation of therapeutic oligonucleotides and SN38 using thiol moieties on AuNPs	Milan Rois et al. (2018)
	NK-Extracellular vesicles miRNAs		AuNPs functionalized with miRNAs via thiol modifications	Dosil et al. (2022)
	Calcein	-	Listeriolysin conjugated to the surface of AuNPs by functionalization with nitrile acetic acid	Plaza-Ga et al. (2019)
	Amikacin	Microbicidal	Gold nanostars functionalized with mercapto-poly(ethylene glycol)amino by ligand exchange and loaded with amikacin	Aguilera-Correa et al. (2022b)
	siRNA	Viral infection	AuNPs with cationic carbosilane dendrone coating	Pena-Gonzalez et al. (2017)
Smart delivery	Plasmid DNA	Gene therapy	Plasmonic PEGylated gold nanostars and gemini cationic lipoplexes	Sanchez-Arribas et al. (2021)
	Proteins	Biological therapy	PEGylated gold nanorods functionalized with a fluorescently labelled BSA cell penetrating peptide, and mixed with therapeutic proteins	Garcia et al. (2021)
	Antibodies	Cell-based therapies	Cell-derived NPs containing PEGylated gold nanorods for intracellular delivery of antibodies	Soprano et al. (2020)
	DOX	Cancer	Janus gold nanostars-mesoporous silica NP functionalized with a thiolated photolabile molecule	Hernandez Montoto et al. (2019)
	DOX in combination with PTT		Gold nanorods coated with silica and a thermosensitive polymer for drug delivery on demand upon irradiation	Villaverde et al. (2018)
	Bisbenzimide molecules		Thermoresponsive gold nanostars coated with ZIF-8 in combination with an amphiphilic polymer	Carrillo-Carrion et al. (2019)

decorated with arrays of AuNPs cell-linked to the stimulating antibody anti-CD3. They demonstrated that the combination of prestimulatory steps, nanostructure surfaces, and costimulatory compounds has an effect on the activation and proliferation of cells (Guasch et al., 2018).

Multidrug resistance is one of the problems of chemotherapy that reduces the efficacy of treatment, and nanocarriers can be used to enhance permeability and retention effect at the target site. Latorre et al. selected two chemotherapeutic drugs, DOX and the camptothecin analogue (CPT) SN38, for the functionalization of albumin-stabilized gold nanoclusters (AuNCs) using tailored linkers. The drugs were released when exposed to different stimuli, such as glutathione and acid pH, leading to a potent antitumor activity. Furthermore, this system showed antineoplastic activity against cancer stem cells (Latorre et al., 2019).

Recently, there has been wide interest in the nanomaterials community to synthesize NPs in a sustainable manner, reducing the use of toxic chemicals and solvents. In this regard, Gomez-Graña et al. explored the possibility of synthesizing gold and silver NPs using a lipopeptide biosurfactant extracted from corn steep liquor. The silver NPs showed antimicrobial properties against *Escherichia coli* that was greater than similar citrate-stabilized NPs, enhancing the application of sustainable methodologies in NP synthesis (Gomez-Grana et al., 2017). Gonzalez-Ballesteros et al. also synthesized gold and silver NPs in bionanofactories, aiming at developing environmentally friendly processes for NPs synthesis. They characterized the NPs obtained and demonstrated that the particles showed antiproliferative properties and could also serve as immunostimulant agents (Gonzalez-Ballesteros et al., 2021a). In another related work, Gonzalez-Ballesteros and colleagues performed a green synthesis of AuNPs that were decorated with carrageenan extracted from red seaweed. The NPs showed relevant antioxidant and antitumoral properties, highlighting the beneficial effect of NP loading of the active compound (Gonzalez-Ballesteros et al., 2021b).

Regarding delivery, AuNPs have demonstrated to be effective carriers for a wide variety of oligonucleotides. For example, siRNAs are interesting molecules capable of modulating gene expression. One of the critical factors for this strategy to be effective is choosing

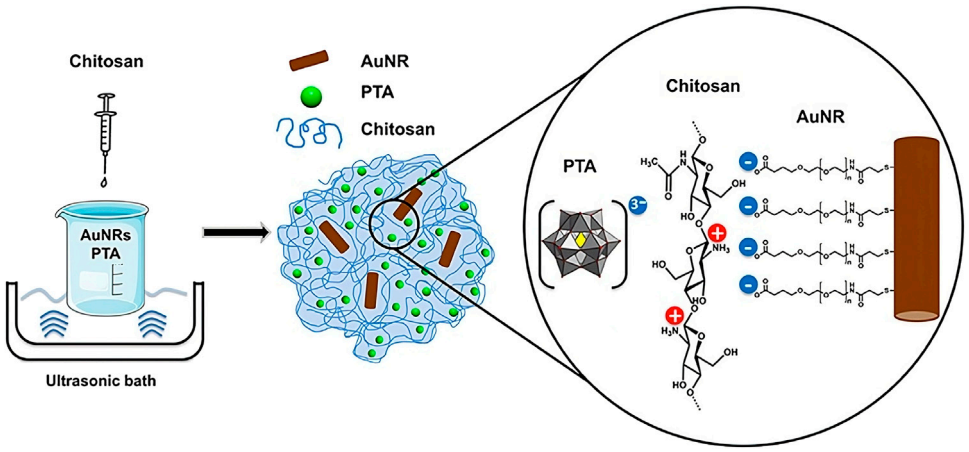

FIGURE 4
Synthesis of AuNR@CS hydrogel. Reprinted from Artiga et al. (2018)and licensed under the Creative Commons Attribution.

an optimal strategy to link the siRNA to the AuNPs, and several chemistries have been developed to form stable complexes with proven activity in cellular and animal models (Tortiglione and de la Fuente, 2019). Sánchez-Arribas et al. developed a strategy combining plasmonic gold nanostars and gemini cationic lipoplexes to release plasmid DNA upon irradiation (Sanchez-Arribas et al., 2021). Interestingly, this strategy exploits the release of a DNA plasmid "on demand" upon external stimuli.

Similarly, Milan-Rois et al., developed a strategy for the delivery of four miRNA downregulated in uveal melanoma, and other cancers, in combination with SN38, a topoisomerase I inhibitor. The study showed a synergistic effect between the four oligonucleotides and chemotherapeutic drug conjugated to the AuNPs (Milan Rois et al., 2018). In the same pathology, Ahijado-Guzman et al. explored the potential of gold nanostars as efficient plasmonic PTT using a non-harmful laser irradiation (Ahijado-Guzman et al., 2020). Their results show how these cancer cells can release and uptake the NPs achieving effective PTT even in non-preloaded cells.

Dosil et al. have demonstrated how AuNP-based delivery of specific NK-extracellular vesicles-miRNAs regulates immune responses related to Th1 and recapitulated this phenomenon in animal models. Th1 cells directly killed tumor cells via the release of cytokines that activate death receptors on the tumor cell surface, representing a potential immunomodulatory strategy against diseases (Dosil et al., 2022).

Endosomal escape of the transported cargo is another important feature of NP delivery, to guarantee active functionality in the cytosol. In a recent work, Plaza Ga et al. (Plaza-Ga et al., 2019), explored a mechanism used by the bacterial pathogen *Listeria monocytogenes* through a toxin called Listeriolysin O. They conjugated this protein to the surface of AuNPs and observed how upon endosomal acidification, the protein disassembles from the NPs to form a pore in the endosomal lipid bilayer enabling the escape of NPs. Within the same focus, and to improve the delivery of proteins, Garcia et al. developed gold nanorods modified with a cell-penetrating peptide that, upon NIR irradiation in the safe second biological window, releases the protein cargo in a controlled spatial and temporal manner (Garcia et al., 2021).

Smart delivery or delivery after external stimuli offers exciting methodologies for delivering cargo into the cytosol on demand. Soprano et al. developed cell-derived NPs that contained gold nanorods in their structure that enabled the release of non-permeant antibodies into the cytosol of cells. The nanocarriers were responsive to NIR irradiation, which proved safe for cells at the conditions needed for cytosolic delivery (Soprano et al., 2020).

Escudero-Duch and collaborators developed a NIR responsive hydrogel based on fibrin, and hollow poly-L-lysine covered gold NPs. The *in-situ* polymerization of fibrin upon NIR irradiation yields a hydrogel potentially suitable for its use as a scaffold in regenerative medicine. This hydrogel tested in cellular and animal models showed good biocompatibility and allowed the spatial patterning of transgene expression triggered by heat (Escudero-Duch et al., 2019).

Hernández-Montoto et al. prepared Janus gold nanostars MSNs loaded with DOX, and equipped with a cyclodextrin supramolecular gatekeeper. NIR light triggered the release of succinic acid that enabled gate opening and cargo delivery. This strategy enables to use AuNPs as photochemical transducers able to release a chemical messenger upon NIR irradiation. The Janus NPs showed a reduction in cell viability, proving their potential as smart delivery materials (Hernandez Montoto et al., 2019).

In an attempt to improve the available treatments for melanoma, which is highly resistant to cytotoxic agents after metastasis, Villaverde et al. engineered gold nanorods coated with silica and a thermosensitive polymer conjugated to NAPamide, a selective targeting agent for alpha melanocytes. Thus, these NPs exerted a synergistic effect of the cytotoxic DOX and PTT (Villaverde et al., 2018).

Carrillo-Carrión et al. investigated the combination of gold nanostars with metal organic frameworks based on zeolitic imidazole and an amphiphilic polymer to afford thermoresponsive nanocomposites. They demonstrated their stability and the release of cargo inside cells (Carrillo-Carrion et al., 2019).

Zamora-Pérez et al. employed Hyperspectral-Enhanced Dark Field Microscopy (HEDFM) to test the dynamics of

Au/CuS NPs directly, based on the changes in the scattering of the nanomaterial in different physiological conditions. Changes in the scattering profiles of NPs could be used as indicators of their performance as photothermal probes. The authors demonstrated how the combination of plasmonic NPs with HEDFM informs of the behavior of intracellular NPs to optimize their functionality for nanomedical applications (Zamora-Perez et al., 2021).

Aguilera-Correa et al. also developed gold nanostars and tested their antimicrobial properties alone and loaded with a potent and widely used antibiotic. The gold nanostars *per se* did not show antimicrobial activity, however in combination with amikacin inhibited the growth of bacterial biofilm of carbapenem-resistant *Klebsiella pneumoniae* strain, suggesting that the NPs facilitate the entrance of the therapeutic agent into the biofilm (Aguilera-Correa et al., 2022b).

Finally, Peña-Gonzalez et al. engineered AuNPs and AgNPs with a cationic carbosilane dendrone coating that improved their delivering capabilities, and characterized their interactions with erythrocytes, platelets, and peripheral blood mononuclear cells. The NPs showed to have a safe profile in these systems and proved successful in cell delivery of siRNA against HIV (Pena-Gonzalez et al., 2017).

2.4 Silver nanoparticles

Similar to gold NPs, silver NPs (AgNPs) have unique and useful properties and are being used in several consumer products such as textiles or home appliances (Ahamed et al., 2010). The antibacterial properties of silver have been known for centuries (McGillicuddy et al., 2017), and colloidal silver has been used by humans for more than 150 years for the treatment of wounds and infections (Reidy et al., 2013). Interestingly, this biological activity is gaining significant interest among researchers due to the resistance developed by different pathogens to current antibiotics. In this regard, some developments carried out by Spanish scientists are mentioned below (Table 4).

Silvan et al. designed AgNPs stabilized with glutathione and evaluated their efficacy against multidrug-resistant *Campylobacter* strains that were extracted from chicken samples. While the NPs were able to inhibit bacterial growth, the mean minimal inhibitory concentration resulted cytotoxic for three different human intestinal cell lines tested. This effect highlights the importance of further safety experiments to assess the practical potential of AgNPs therapeutic effects (Silvan et al., 2018).

TABLE 4 Summary of AgNPs with their therapeutic area and functionalization strategy.

NP Type	Purpose	Therapeutic area	Therapeutic agent	Functionalization strategy	Ref
AgNPs	Anti-amoebic contact lens solution	Keratitis	-	Commercially available AgNPs	Hendiger et al. (2021), (Hendiger et al. (2020)
	Anti-amoebic contact lens solution	Keratitis, encephalitis	Tannic acid	Tannic acid-modified AgNPs	Padzik et al. (2018)
	Prevention of implant-associated infection	Antibacterial	-	AgNPs were synthesized by laser ablation in de-ionized water	Perez-Tanoira et al. (2022)
	Low cost antitumor tool	Cancer	Acetogenin rich extracts	Extracts from leaves and peel of *A. muricata* were used to synthesize AgNPs	Gonzalez-Pedroza et al. (2021)
	Anti-biofilm treatments in chronic wound infections	Antibacterial	Enzymes (α-amylase, cellulose, DNase I and proteinase K)	Enzyme-coated AgNPs	Rubio-Canalejas et al. (2022)
	Combination of two antibacterial agents (probiotics and AgNPs)	Antibacterial (topical)	Probiotics	Probiotics and AgNPs in a matrix as bacterial cellulose	Sabio et al. (2021)
GSH-Ag NPs	Improve efficacy for multidrug resistant bacteria	Antibacterial	-	Glutathione for stabilization	Silvan et al. (2018)
AgNP@ nanoMOF	Combating bacterial biofilms		-	Silver impregnated nanoMOF thin film functionalized with DNase I	Arenas-Vivo et al. (2019)
Silver nanorings	Study a novel type of AgNPs as an antimicrobial therapy	Antifungal, antiamoebic	-	Silver nanorings which have a filament diameter of 80 nm and a ring diameter of between 12 and 18 μm	Gonzalez-Fernandez et al. (2022)
PLGA@Ag_2S and PLGA@ Ag_2S@SPION	Hybrid system for chemotherapy	Cancer	Maslinic acid	Combination of Ag_2S NPs and SPIONs by electrospraying into a PLGA matrix loaded with maslinic acid (PLGA@Ag2S@maslinic acid)	Alvear-Jimenez et al. (2022)
AgNPs and AuNPs	Nanoparticles as delivery systems for cancer cells	Cancer	Raltitrexed	AuNPs and AuNPs functionalized with raltitrexed	Morey et al. (2021)
AgNPs nanofluid	Photothermal agent acting as nanothermometer		-	AgNPs were functionalized with HS-PEG-OMe	Mendez-Gonzalez et al. (2022)

Sabio et al. designed a two-sided material combining AgNPs on one side and living probiotics on the other, with antibacterial capacity against *Pseudomonas aeruginosa* (Sabio et al., 2021). AgNPs have also been explored for their anti-amoebotic properties against pathogens responsible for keratitis. In this regard, Hendiger et al. evaluated the activity, cytotoxicity, and anti-adhesive properties of AgNPs included in contact lens solutions against the *Acanthamoeba castellanii Neff* strain (Hendiger et al., 2021), (Hendiger et al., 2020). The presence of the AgNPs showed a significant increase in anti-amoebic activity, without increasing the overall cytotoxicity, decreasing the risk of *Acanthamoeba keratitis* infection. Padzik et al. also employed AgNPs conjugated with tannic acid as potential agents against *Acanthamoeba spp* (Padzik et al., 2018).

In the case of peri-implantitis due to biofilm deposits, Pérez-Tanoira et al. immobilized AgNPs in titanium, demonstrating its beneficial effect in reducing the biofilms stablished by *S. aureus* and by mixed oral bacterial flora (Perez-Tanoira et al., 2022). Other anti-biofilm strategies involve the use of silver-containing nanoscaled Metal Organic Frameworks (MOFs) against *S. aureus* biofilm. Arenas-Vivo et al. demonstrated the use of AgNPs functionalized with DNase I decreasing the *S. aureus* biofilm viability more than using the antibiotics alone (Arenas-Vivo et al., 2019). Rubio-Canalejas et al. pointed out that clinical treatment combining antibiofilm enzymes and antibiotics may be essential to eliminating chronic wound infections (Rubio-Canalejas et al., 2022). Finally, González-Fernández et al. demonstrated how silver nanorings are capable of totally inhibiting the germination of *A. castellanii* cysts (Gonzalez-Fernandez et al., 2022).

In regards to drug delivery, the formation of hybrid Ag_2S NPs with poly(lactic-co-glycolic acid) (PLGA) by electrospray allows for the encapsulation of drugs such as maslinic acid (MA). The anticancer drug showed an efficient encapsulation and controlled release in cellular models (Alvear-Jimenez et al., 2022).

Morey et al., modified silver and gold NPs using cysteine to bind raltitrexed to the surface of NPs and tested them in A549 and HTC-116 cells lines. Silver raltitrexed NPs inhibited cancer cell viability (Morey et al., 2021). Other modifications, such as the functionalization of AgNPs with *Annona muricata* plant antitumoral extracts, have been prepared and tested by González-Pedroza et al. as promising antitumoral nanoformulations (Gonzalez-Pedroza et al., 2021).

Finally, AgNPs can be used as luminescent biofluids capable of acting as photothermal agents and nanothermometers. Mendez-Gonzalez et al. showed how a nanofluid containing AgNPs had improved properties compared to a combination with magnetic nanoflowers and showcases their use for hyperthermia in brain tumors (Mendez-Gonzalez et al., 2022).

3 Organic nanoparticles

Organic NPs have synthetic or natural organic components such as carbohydrates, proteins, peptides, or lipids (Romero et al., 2012). Their biodegradable composition, together with the relatively simple encapsulation of drugs, make them the preferred drug delivery systems. The current advances in the use of protein, polysaccharide, polymeric and lipid NPs carried out in Spanish institutions are discussed below, and summarized in tables at the end of each section.

3.1 Protein nanoparticles

Protein NPs are of great interest in nanomedicine due to the intrinsic properties of proteins, such as their biocompatibility and biodegradability. Proteins possess different functional groups located in the side chains of amino acids that can be exploited for chemical conjugation. They also contain hydrophilic and hydrophobic regions that can be used to interact with hydrosoluble or insoluble compounds. Finally, they have tunable structures that can be obtained by protein engineering, expanding their applications (Table 5).

Several proteins have been used to create NPs for their use in nanomedicine, being albumin one of the most successful ones. It is naturally present in the blood, so it can avoid immunogenic reactions, increasing the circulation time of their cargoes. It is a natural vehicle especially suited for the interaction with hydrophobic molecules. Furthermore, human cells present albumin receptors, namely, gp60 and SPARC (Prajapati and Somoza, 2021). As these receptors are overexpressed in cancer cells, albumin NPs can be used to target tumor sites. This strategy has been successfully used in the formulation of Abraxane, which has been approved for the treatment of several tumors (Trabulo et al., 2017). Albumin is a monomeric protein unable to form NPs by itself, therefore several methods have been used to form albumin nanostructures, being desolvation the most common one. For example, Prajapati et al. used this method to encapsulate DOX, a drug limited by its toxicity. Its encapsulation inside of NPs enabled to target tumor cells specifically, increased the drug efficacy, and decreased its toxicity. Furthermore, they stabilized the NPs employing several cross-linkers, showing that a redox-dependent crosslinker (SPDP, N-succinimidyl 3-(2-pyridyldithio) propionate) increased drug release in cancer cells, due to their enhanced redox environment compared to non-cancer cells. Their nanoformulation showed toxicity in breast cancer cells and a negligible effect in non-tumoral cells, presenting a potential use for the treatment of breast cancer (Prajapati et al., 2021) (Figure 5). The same group also used albumin-based nanostructures for uveal melanoma treatment. In another article, they studied the use of albumin to deliver AZD8055, a potent inhibitor of the mTOR pathway that is overexpressed in the pathology and is critical in tumorgenesis. They produced gold nanoclusters stabilized by albumin, while the drug was conjugated externally using disulphide bonds. The lately thiol-dependent conjugation of the drug allowed its specific release in the cytoplasm of cancer cells. The authors showed that their nanostructures had anti-tumoral activity in mice models, using a dose 23-fold lower than previously reported (Latorre et al., 2021). The conjugation of folate to NPs based on BSA and alginate as an active targeting strategy for the delivery of PTX was showed by Martinez-Relimpio et al. which resulted in an increased uptake of the NPs by cancer cell lines, as there is an overexpression of folate receptors (Martinez-Relimpio et al., 2021). To exploit BSA NPs delivery possibilities Gerke et al. developed a simple methodology with clickable anti-PD-L1 antibodies, showcasing the versatility of this bioorthogonal design (Gerke et al., 2022).

Hydrophilic proteins with multiple arginine residues, such as protamine and polyarginine, are widely used to form NPs as their positive charge confers membrane-translocation properties (Thwala et al., 2018). Similarly to albumin, it does not form NPs by itself, so a solvent displacement method must be used to create protamine nanocapsules. NPs contain an oily

TABLE 5 Summary of protein NPs with their therapeutic area and synthesis strategy.

Protein	Purpose	Therapeutic area	Therapeutic Agent	Synthesis/Encapsulation strategy	Ref
Albumin	Drug delivery/smart release	Cancer	DOX	NPs stabilized by redox crosslinker to increase drug release in cancer cells	Prajapati et al. (2021)
	Increase efficacy and biodisponibility of AZD8055	Uveal melanoma	AZD8055	Gold nanoculsters stabilized by albumin. Cargo conjugation by disulfide bonds	Latorre et al. (2021)
	Increase selectivity of nanoparticle delivery against tumor	Cancer	PTX	Folate-targeted NPs based on BSA and alginate and stabilized by amide bonds using ethylenediamine	Martinez-Relimpio et al. (2021)
	Develop tumor-targeted BSA NPs		-	BSA NPs functionalized with chlorosydnone to click with anti-PD-L1 antibodies with dibenzocyclooctyne moeities	Gerke et al. (2022)
Protamine	Insulin oral delivery	Diabetes	Insulin	Nanocarriers with oily core and protamine/PSA shell	Thwala et al. (2018)
	Vaccine adjuvant	Influenza	Different antigens	Nanocarriers with oily core and protamine shell	Gonzalez-Aramundiz et al. (2017), Gonzalez-Aramundiz et al. (2018)
Polyarginine	Oral peptide delivery	Diabetes	Insulin and oleic acid	Nanocapsules with oily core and polyarginine shell	Niu et al. (2017)
Zein	Insulin delivery		Insulin	Zein NPs coated with PEG and synthetic polymers	Reboredo et al. (2021), Inchaurraga et al. (2020)
				Zein NPs coated with PEG and Gantrez AN-PEG	Martinez-Lopez et al. (2021)
Engineered peptides	Toxic proteins delivery	Cancer	Diphteria and *P.aeruginosa* toxins	Toxic peptides self-assembled in NPs with specific targeting regions	Sanchez-Garcia et al. (2018), Volta-Duran et al. (2021)
			29 amino acid-segment of the helix α5 from the human BAX protein		Sanchez-Garcia et al. (2020)
			Exotoxin A from *P.aeruginosa*		Falgas et al. (2020)
			Diphteria toxin		Pallares et al. (2021)
			Monometyl Auristatin E (MMAE)		Pallares et al. (2020)

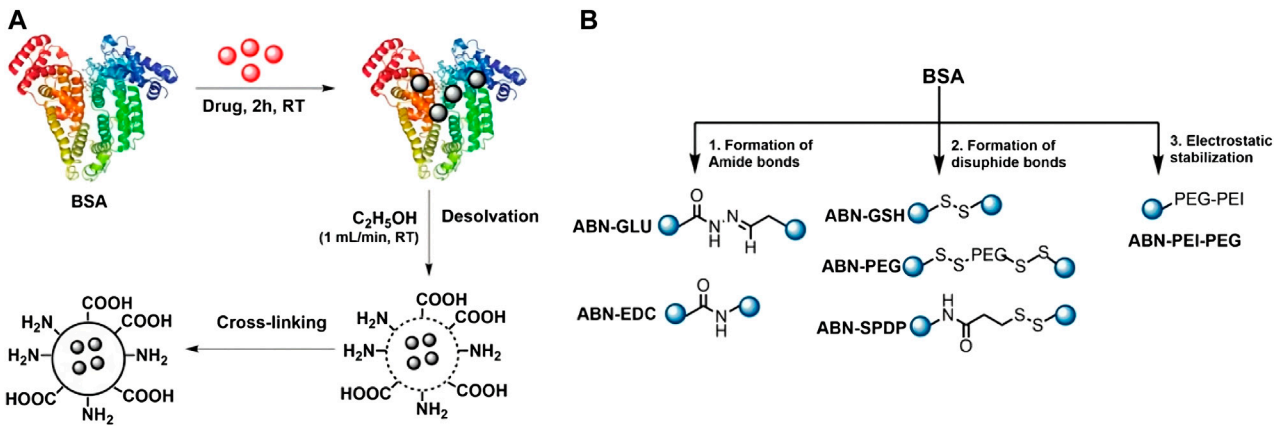

FIGURE 5
Albumin NPs synthesis. Reprinted from Prajapati et al. (2021) and licensed under the Creative Commons Attribution.

core and a protamine coating. Thwala et al. used them for the delivery of insulin, a highly used protein that cannot be administered orally. The authors used a protamine/PSA shell that controls the release of insulin from the moment the NPs are administered orally until reaching the intestine (Thwala et al., 2018). Furthermore, the insulin transport across mucus layers can be increased by incorporating in the formulation penetration enhancers such as oleic acid (Niu et al., 2017). The same group used protamine nanocapsules loaded with antigens as an alternative to vaccine adjuvants. This system can load multiple antigens, be lyophilized, and trigger the immune response. These properties have been shown in particles loaded with influenza hemagglutinin antigen, and particles containing hepatitis B virus surface antigen (Gonzalez-Aramundiz et al., 2017; Gonzalez-Aramundiz et al., 2018). According to the results, the protamine nanocapsules showed the ability to enter macrophages without toxicity and produced an important immune response against influenza (Gonzalez-Aramundiz et al., 2017).

Zein is a small hydrophobic protein that, in contrast to albumin and protamine, can easily self-assemble, forming colloidal NPs in the aqueous phase. Zein NPs coated with PEG and Gantrez AN-thiamine have been used to deliver insulin. They have an enhanced permeation within the mucus and intestinal absorption, which decreases the glucose level in blood (Inchaurraga et al., 2020; Reboredo et al., 2021). In particular, the Gantrez conjugate reduced the accumulated fat in *Caenorhabditis elegans* (Martinez-Lopez et al., 2021). Given this promising results a double blind clinical trial has been designed by Clínica Universidad de Navarra to determine whether this particles are able to provide glycemic control in patients (NT: 05560412) (Clinica Universidad de Navarra UdN, 2022b).

Another interesting kind of proteins are the ones considered self-delivered nanoscale drugs that, at the same time, can self-assemble in NPs. With this in mind, Sanchez-García et al. fused bacterial toxin peptides to a N-terminal cationic T22 peptide and a C-terminal region with 6 histidines. These engineered peptides self-assemble in nanostructures by the interaction of the N- and C-terminal regions. T22 peptide can recognize CXCR4, a receptor overexpressed in cancer cells, providing specific tumor targeting, while the toxin peptide promotes general cell death (Sanchez-Garcia et al., 2018). The bacterial toxins can be exchanged for human pro-apoptotic peptides with similar results (Sanchez-Garcia et al., 2020). These nanostructures were successfully applied to several cancer models in mice, such as colon, (Sanchez-Garcia et al., 2018), lymphoma, (Falgas et al., 2020), and leukemia (Pallares et al., 2021). Volta-Duran et al. (Volta-Duran et al., 2021) designed a method to deliver anticancer drug pairs that consist of a tumor-targeted protein NP based on two microbial toxins, exotoxin A and diphtheria toxin, chemically coupled with oligo-floxuridine and monomethyl auristatin E respectively. These nanoformulations were able to internalize into target cells and had a biological impact. Unfortunately, the chemical conjugation annulled the activity of the toxins. Pallares et al. synthesized a nanoconjugate that contained GFP instead of a bacterial toxin, covalently labelled with auristatin, a potent antimitotic agent. With this treatment, they were able to significantly reduce and control myeloid leukemia dissemination (Pallares et al., 2020).

3.2 Polysaccharide nanoparticles

Polysaccharides are biomacromolecules formed by sugars found in every living organism. They are non-toxic or immunogenic and are a better biocompatible alternative to synthetic polymers. In addition, they are highly versatile, varying in molecular weight, branch degree, and functional groups, and can be tuned to deliver different cargo (Serrano-Sevilla et al., 2019; Shokrani et al., 2022). In Spain, many polysaccharides have been used to form nanostructures with biomedical applications, such as chitosan, hyaluronic acid or cellulose as reviewed here (Table 6).

Chitosan is a derivative of the natural polysaccharide chitin, which is the second most abundant polysaccharide in the world after cellulose. Chitosan has many interesting properties, including biocompatibility, biodegradability, antibacterial effect, and muco-adhesion, and it is widely used in food, cosmetics, and biomedical applications. Chitosan has a high concentration of reactive amino groups along its backbone, conferring a high positive charge that promotes its interaction with biological tissues (Frigaard et al., 2022). The excellent properties of chitosan NPs for intracellular delivery have been exploited by Ambrossone et al. They showed that oily core chitosan nanocapsules synthesized by nanoemulsion efficiently delivered alsterpaullone, a Wnt signaling agonist, into the model organism *Hydra vulgaris*. They also studied the characteristics of the intracellular delivery with Nile red-loaded NPs. Their methodology resulted in a more efficient manner of activating Wnt pathway than free alsterpaullone at the same concentration (Ambrosone et al., 2020). Similarly, Montero et al. developed chitosan-BSA NPs and studied their potential as vehicles with different combinations, demonstrating their potential for drug delivery (Montero et al., 2019).

Chitosan NPs also enable the transportation of agents into the brain, given the difficulty to target this organ. As a proof of concept, Casadomé-Perales et al. demonstrated the inhibition of p38 MAPK, an enzyme that is commonly dysregulated in several neurodegenerative diseases. They encapsulated PH797804, an inhibitor of this enzyme, in NPs with a nanoemulsion core. The intranasal delivery of the NPs enabled the inhibition in different parts of the brain in animal models, showing that it could be an efficient strategy for brain delivery (Casadome-Perales et al., 2019).

Marciello et al. used chitosan NPs to deliver a model peptide through vaginal mucosa, given the interest of microbicides delivery for the prevention and treatment of sexually transmitted diseases. The NPs contained chitosan and ascorbate, with insulin as the model cargo. Then, the NPs were incorporated in sponge-like cylinders made of mannitol, sucrose, and gelatin B to control their release in the vaginal environment (Marciello et al., 2017).

The fact that chitosan NPs can encapsulate peptides opens the possibility of their use as nanovaccines. As mentioned previously, using NPs as vaccines improves both the administration and the activation of the targeted immune cells, which results in greater efficacy. The role of chitosan in these formulations has shown to

TABLE 6 Summary of polysaccharide NPs with their therapeutic area and synthesis strategy.

Saccharide	Purpose	Therapeutic area	Therapeutic Agent	Synthesis/Encapsulation strategy	Ref.
Chitosan	Drug delivery	Wnt signaling	Alsterpaullone	Oily core chitosan NPs formed by nanoemulsion	Ambrosone et al. (2020)
	Drug delivery to brain	Neurodegenerative diseases	PH797804	Oily core chitosan NPs formed by nanoemulsion	Casadome-Perales et al. (2019)
	Delivery to vaginal mucosa	Microbicidal	Peptide	NPs formed by inotropic gelation of chitosan with TPP method	Marciello et al. (2017)
	Nanovaccine	HIV	HIV antigen	NPs formed by ionic complexation of positive chitosan with negative hyaluronic acid or dextran	Dacoba et al. (2019), Dacoba et al. (2020a)
Mannose dendrons	Tolerance for allergens	Immune response modulation	Prup3 allergen peptide	Prup3 peptide bound to a mannose dendron structure (D_1ManPrup3 and D_4ManPrup3)	Rodriguez et al. (2019)
Hyaluronic acid	Tumor penetration	Cancer	Docetaxel	Hyaluronic acid modified with maleimide and with peptide tLyp1 on the shell	Teijeiro-Valino et al. (2019)
	Drug delivery	Cancer	Docetaxel	Hyaluronic acid functionalized by hydrophobic side chains	Cadete et al. (2019)
	Intraocular Drug delivery	Ocular inserts	Ferulic acid and peptide ε-polylysine	Electrospunned Hyaluronic acid by using PVP as excipient	Grimaudo et al. (2020)
	Drug delivery	Inflammatory joint diseases	Anti-inflammatory drugs	Hydrogels formed by Hyaluronic acid and fibrin with Hyaluronic acid NPs	Storozhylova et al. (2020)
	Drug delivery at infection site	Antibacterial	Clarithromycin	Clarithromycin-loaded papain-modified ureido-conjugated thiolated hyaluronic acid-co-oleic acid (CLR-PAP-Ur-thHyaluronic acid-co-OA) nanomicelles	Qaiser et al. (2022)
Cellulose	Drug delivery	Cancer	DOX	CNC modified with APTES and functionalized with FA, followed by incorporating Carbon dots and DOX	Do et al. (2021)
Cyclodextrin	Delivery of DNA to spleen	Gene therapy	DNA	Cyclodextrin-based molecular NPs through covalent dimerization	Gallego-Yerga et al. (2018)
Inulin	Improve lymphatic accumulation	Nanovaccine development	-	Small and negatively charged inulin nanocapsules	Crecente-Campo et al. (2019)

enhance the activation of the adaptive immune response (Moran et al., 2018).

The generation of an effective HIV vaccine is still an important health challenge, to which several nanotechnological approaches are being developed. According to previous works, the peptide sequences around the protease cleavage sites have been proposed as a target for HIV vaccines. Dacoba et al. developed different chitosan NPs loaded with the HIV peptide PCS5. The NPs were formed by ionic complexation, mixing the positive polysaccharide chitosan with negative ones like Hyaluronic acid or dextran. Furthermore, they tested if the presence of poly (I:C), an immunomodulatory molecule, had any effect. All the NPs were able to induce humoral responses against the antigen (Dacoba et al., 2019). However, they showed that the binding of the antigen, the presence of poly (I:C), and the nature of the polysaccharides influence the type of immune response, such as the kinetics of the effector T cell responses. The results suggest the possibility of developing a nanovaccine against HIV and its translation into clinical trials (Dacoba et al., 2020a). The same group showed that NPs made of chitosan and the anionic carboxymethyl-β-glucan, which accumulate in the lymph nodes, promoted the accumulation of the NPs in draining lymph nodes and exerted an immune response. The NPs were formed using the ionic complexation method, and loaded with ovalbumin (Frigaard et al., 2022).

Polysaccharide NPs loaded with antigens can also be used to induce tolerance for allergens. Rodriguez et al. explored the capabilities of several mannose nanostructures to serve as an efficient platform to generate specific recognition without the need for additional adjuvants. In this particular case the treatment developed prolonged protection against allergen exposure without any sign of anaphylaxis (Rodriguez et al., 2019).

Hyaluronic acid is an anionic polysaccharide, a glycosaminoglycan, consisting of disaccharide repeating units of β-1,4-D-glucuronic acid-β-1,3-N-acetyl-D-glucosamine. It has a high binding affinity towards the CD44 receptor, highly expressed in cancer cells (Liu and Huang, 2022). It can be used as shell in oil-based NPs, by the solvent displacement technique. Teijeiro-Valino et al. used this kind of NPs for the encapsulation of the anti-cancer drug docetaxel. Furthermore, they decorated the hyaluronic acid shell with the tumor homing peptide tLyp1. Their formulation increased penetration in the tumor and anti-cancer activity in lung and pancreatic cancer mice models (Teijeiro-Valino et al., 2019).

Cadete et al. used a modification of hyaluronic acid consisting of the addition of hydrophobic side chains, like dodecyl, to promote the

TABLE 7 Summary of polymeric NPs with their therapeutic area and functionalization strategy.

Polymer type	Purpose	Therapeutic area	Therapeutic Agent	Functionalization strategy	Ref.
Arginine based	Macrophages polarization from M2 to M1 profiles	Cancer	Toll-like receptor 3 agonist poly(I:C)	Poly(I:C) arginine-rich polypeptide was enveloped with an anionic polymeric layer by film hydration or incubation	Dacoba et al. (2020b)
Polyethylemine	Intratumoral immunotherapy			Nanoplexed formulation of Poly I:C complexed with polyethylenimine	Aznar et al. (2019)
Polyglutamic acid	Enhance the efficacy of first-line chemotherapeutics	Cancer (Triple negative breast cancer)	DOX	Nanogel particles were formed by Cu catalyzed azide-alkyne cycloaddition of polyglutamic acid and subsequently loaded with DOX	Duro-Castano et al. (2021a)
	Improve treatment of unresectable cancer by controlled release	Cancer	Gemcitabine	The low molecular weight nanogel N4-Octanoyl-2-deoxycytidine was loaded with hyaluronic acid and polyglutamic acid nanocapsules prepared by a self-emulsifying method	Staka et al. (2019)
	To develop zwitterionic pDNA delivery systems	-	Plasmid DNA delivery	Derivatization with oligoaminoamide residues for an efficient assembly containing five units of succinyl tetraethylene pentamine to develop a zwitterionic nonviral vectors	Nino-Pariente et al. (2017)
Polyglutamate	Develop multimodal NPs for AD	Neurodegenerative diseases	Bisdemethoxycurcumin or Genistein	80–100 nm sphere-like cross-linked self-assembled star-shaped Polyglutamic acid functionalized with Angiopep-2 to promote BBB permeation	Duro-Castano et al. (2021b)
Tert-Ser polyacetal	pH dependent and controlled release of drug	Cancer (prostate)	PTX	PTX was incorporated to the side-chains of the pH-susceptible and biodegradable tert-serinol polymer by a one-pot synthetic procedure	Fernandez et al. (2022)
Polyarginine	Delivery of two therapeutic agents for reverting MDSC-mediated immunosuppression	Cancer immunotherapy	RNAi and CCL2 chemokine	RNAs were associated to the nanocapsules through the RNA condensing capacity of the polyarginine shell. The chemokine was encapsulated in the aqueous domains of a glyceryl-monooleate (GMO)-based liquid-crystal core where	Ledo et al. (2019)
	miRNA delivery to the hippocampus	Neurodegenerative diseases	Specific miRNA mimic, miR-132	D-octaarginine was covalently conjugated to lauric acid and subsequently to RNA through electrostatic interactions of interest. Finally, the nanocomplexes were enveloped with protective polymers such as polyethyleneglycol - polyglutamic acid or hyaluronic acid to enhance stability and diffusion through the olfactory nasal mucosa	Samaridou et al. (2020)
	Oral delivery of insulin	Diabetes	Insulin	Polyarginine NPs were coated with PEGylated polyaminoacids to protect insulin	Niu et al. (2018)
Poly(N-vinyl caprolactam)	Develop microgels for drug delivery	Cancer	DOX	(PVCL)-based thermoresponsive microgels prepared by copolymerization of N-vinylcaprolactam monomer and ethylene glycol dimethacrylate stabilized by a reactive [poly(2-(acryloyloxy)ethyl] trimethylammonium chloride) cationic shell and loaded with DOX	Etchenausia et al. (2019)
Chitosan, polyarginine, and		Vaccine development	-	Chitosan nanocapsulse were functionalized with positively charged	Cordeiro et al. (2019)

(Continued on following page)

TABLE 7 (*Continued*) Summary of polymeric NPs with their therapeutic area and functionalization strategy.

Polymer type	Purpose	Therapeutic area	Therapeutic Agent	Functionalization strategy	Ref.
carboxymethyl-β-glucan	Improve targeting specific immune cells in the lymphatics			(polyarginine) and negatively charged (carboxymethyl-beta-glucan) polymeric shells	
Polyanionic carbosilane dendrimers	Inhibits the infection of human cytomegalovirus	Antiviral therapy		Polyanionic carbosilane dendrimers that present several sulfonate or sulfate groups in their periphery	Relano-Rodriguez et al. (2021)
Nanocapsules with a polymeric shell	Development of intranasal vaccination against *Mycobacterium tuberculosis*	Vaccine development	Imiquimod and a fusion protein formed by two antigens of *Mycobacterium tuberculosis*	Imiquimod was encapsulated in the oily core of the nanocapsules together with a fusion protein. Nanocapsules were functionalized with a polymer shell made of chitosan or inulin/polyarginine	Diego-Gonzalez et al. (2020)
Poly(β-amino esters)	Improve vaccine development		mRNA	mRNA NPs based on poly(beta aminoester) polymers	Fornaguera et al. (2021)
Poly(lactic-co-glycolic acid)	Improve BBB permeability and pharmacokinetics of compounds	Neurodegenerative diseases	PDE7 inhibitor	NPs were prepared in two different manners, by single emulsion and nanoprecipitation	Nozal et al. (2021)
			CDC7 inhibitor	Polymeric NPs were prepared by nanoprecipitation	Rojas-Prats et al. (2021)
	Enhance BBB penetration	Stroke	-	Functionalized with supramagnetic iron oxide NPs	Grayston et al. (2022)
	Improve antiretroviral therapy	HIV	HIV-1 peptide inhibitor	PLGA NPs were covered by glycol-chitosan to enhance delivery	Ariza-Saenz et al. (2017)
	Improve the delivery of bioactive peptides to inhibit HIV infection			PLGA NPs coated with glycol chitosan	Ariza-Saenz et al. (2018)
	Provide an efficient oral peptide administration	Diabetes	Hydrophobically modified insulin	Nanoemulsions and micelles formed by MPEG-2000-DSPE sodium tauocholate, Miglyol 812N and Polaxamer 407	Santalices et al. (2021)
	Improve pharmacokinetic properties of Licochalcone A	Ocular inflammation	Licochalcone A	PLGA was covalently bound to cell penetrating peptides through maleimide-PEG amine	Galindo et al. (2022)
	Deliver miRNA and atorvastatin simultaneously	Atherosclerosis	miRNA 124a and atorvastatin	Atorvastatin was loaded in PLGA NPs in the single emulsion synthesis, that were subsequently covered by chitosan to promote electrostatic interactions with the miRNA and finally functionalized with anti-VCAM and H4A3 antibodies	Leal et al. (2022)
	Improve tumor targeting	Cancer	Allyl-isothiocyanate	NPs were functionalized with an anti-EGFR antibody	Encinas-Basurto et al. (2018b)
1-vinylimidazole	Obtain a synergistic anti-inflammatory effect	Inflammation autoimmune diseases	Ketoprofen and dexamethasone	Copolymers were self-assembled by nanoprecipitation, and NPs presented a hydrophobic core formed by covalently linked ketoprofen and a hydrophilic shell mainly formed by vinylimidazole	Espinosa-Cano et al. (2020a), Espinosa-Cano et al. (2020b)
1-vinylimidazole and methacrylic derivative	Study the synergistic anti-inflammatory effect		Dexamethasone and naproxen	Polymeric NPs were self assembled incorporating covalently-linked naproxen and physically entrapped dexamethasone	Espinosa-Cano et al. (2020b)
$CaCO_3$ core stabilized by poly(vinylsulfonic acid)	Optimize *in vivo* delivery specificity	Acute ischemic stroke	Thrombolytic serine protease	Layer-by-layer structure of $CaCO_3$ cores later removed and stabilized by poly(vinylsulfonic acid). After macromolecule entrapment alternate layer of charged polyelectrolyte	Correa-Paz et al. (2019)

(Continued on following page)

TABLE 7 (*Continued*) Summary of polymeric NPs with their therapeutic area and functionalization strategy.

Polymer type	Purpose	Therapeutic area	Therapeutic Agent	Functionalization strategy	Ref.
				poly(sodium 4-styrenesulfonate) and poly(diallyldimethylammonium chloride) are added. Finally a coating with a layer of doped iron oxide NP or gelatin is performed	
Polyethylene and propylene glycol and ribose	Develop fuel-free propulsion NPs activatable by NIR	-	-	Micelles formed by polyethyleneglycol, polypropylenglycol copolymer and sodium oleate and then ribose was polymerized on the surface at high temperature yielding a bottle-structured particles	Xuan et al. (2018)

self-assembly of NPs without the use of surfactants. This strategy decreased the cytotoxicity of the NPs, while showing an improved intracellular drug delivery (Cadete et al., 2019).

Delivery of drugs on the eye surface can be achieved by flexible electrospun nanofibers, which are able to adapt and persist on the eye surface whilst the drug is released. Grimaudo et al. overcame the incapability of hyaluronic acid to be electrospunned, by using PVP as an excipient. This resulted in creating hyaluronan nanofibers, capable of delivering the antioxidant ferulic acid and the antimicrobial peptide ε-polylysine at the same time (Grimaudo et al., 2020).

In another study, Storozhylova et al. engineered hydrogels formed by Hyaluronic acid and fibrin, with hyaluronic acid nanocapsules loaded with anti-inflammatory drugs. They were used to improve intra-articular administration, showing a rapid efflux of the administered drugs. This system could relieve the inflammatory conditions of large joints (Storozhylova et al., 2020).

Qaiser et al. developed three types of nanomicelles formulations to synthesize a targeted, mucoadhesive and mucopenetrating drug delivery system. The goal was to encapsulate clarithromycin, an antibacterial drug, to improve its residence time at the *Helicobacter pylori* infection site. They concluded that clarithromycin-loaded papain-modified ureido-conjugated thiolated hyaluronic acid-co-oleic acid (CLR-PAP-Ur-thHA-co-OA) nanomicelles could be used as nanocarriers for the treatment of *H. pylori* infection, due to their mucopenetration, mucoadhesion properties, stability, and extended drug release (Qaiser et al., 2022).

Cellulose is the world's most abundant polysaccharide. It is a linear polymer composed of repeating units of two anhydroglucose rings. Its abundance and biocompatibility make nanocellulose a good candidate for biomedical applications (Nicu et al., 2021). Recently, Do et al. developed a modified cellulose nanocrystal (CNC) for the delivery of anti-cancer drugs. They engineered nanoplatforms based in modified CNCs with APTES to improve their dispersibility. These CNCs were covalently functionalized with folic acid (FA), followed by the incorporation of Carbon dots and the drug DOX, by electrostatic interaction. These CNCs may be promising nanoplatforms to be used both in chemotherapy and PTT against cancer (Do et al., 2021).

Gallego-Yerga et al. prepared DNA-cyclodextrin NPs to improve gene therapy. They controlled the morphology of the complexes to study how the shape affects the transfection properties. They found several complexes that exhibited highly efficient transgene expression and were able to deliver DNA to the spleen in a tissue-specific manner in animal models (Gallego-Yerga et al., 2018).

Finally, inulin is a fructan that has high structural flexibility and good biodegradability, which allows for its use as a drug delivery system. In a study comparing chitosan with inulin for drug delivery, the small inulin NPs showed less toxicity and a higher accumulation in the lymphatic nodes (Crecente-Campo et al., 2019).

3.3 Polymeric nanoparticles

The potential of polymeric NPs relies on their highly versatile structure, which can be altered depending on the therapeutic application, cargo, or type of administration. Moreover, the chemical reactivity of the polymers can be exploited for the controlled release of drugs at different pH or thermal environments. These properties in addition to good biocompatibility, make polymeric NPs great candidates in the biomedicine field (Table 7) (Elsabahy and Wooley, 2012; Sartaj et al., 2021).

Given their versatility, several anti-cancer strategies have been accomplished. Aznar et al. have studied the immunotherapeutic profile of BO-112, a nanoplexed form of Poly I:C coupled to polyethylemine that prevents its degradation from proteases. Poly I:C is a synthetic analog of double stranded RNA that activates innate immune receptors and several formulations with different polymers have been tested in the clinic. BO-112 was locally injected, leading to the death of tumoral cells. Also, this nanoplexed Poly I:C showed an antitumoral activity through the induction of type I Interferon and CD8 T-cell infiltrates in the tumor (Aznar et al., 2019). These promising results motivated the development of two clinical trials of BO-112 in combination with antiPD-1 therapies or with pembrolizumab showing encouraging clinical benefits in cancer patients. Dacoba et al. developed an arginine-based poly (I:C) nanocomplex that induces the accumulation of endosomal toll-like receptor 3 agonists, which affect the polarization of the profile M2 to M1 (pro-inflammatory and antitumoral) in endosomal compartments. This strategy has been explored in cancer, where the polarization to M1 profile of tumor-associated macrophages could be a promising approach

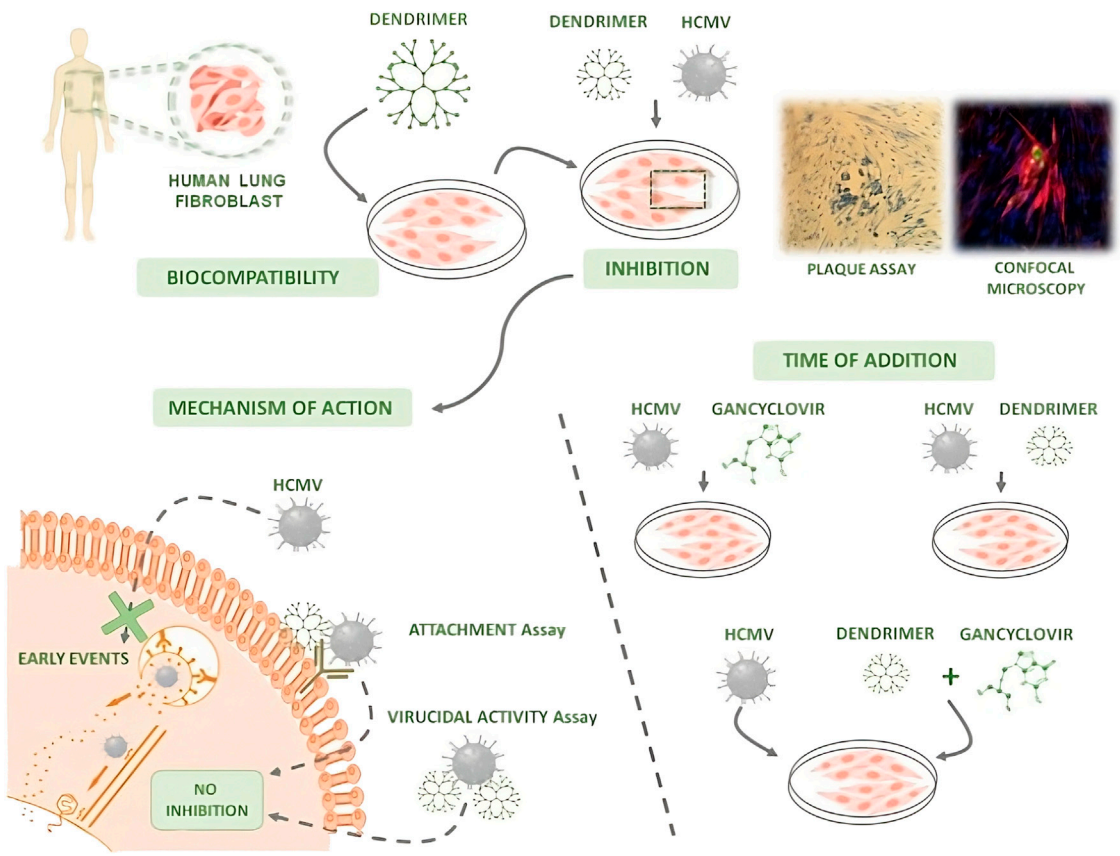

FIGURE 6
Dendrimer strategy as antiviral therapy. Reprinted from Relano-Rodriguez et al. (2021) and licensed under the Creative Commons Attribution.

against tumors (Dacoba et al., 2020b). Another study was based on the study of intratumoral immunotherapy.

Poly amino acid nanogels are also an interesting strategy in the delivery of cancer treatment. Interestingly, these agents can be developed to release the cargo specifically in the tumor microenvironment as pH responsive particles (Arroyo-Crespo et al., 2018). Duro-Castano et al. engineered polyglutamic acid nanogels loaded with DOX as an effective strategy for the treatment of triple-negative breast cancer metastases, which effectively reduced lung and lymph node metastases (Duro-Castano et al., 2021a). In another strategy, Fernández et al. developed a tert-Ser polyacetal loaded with PTX forming NPs of 10–70 nm, which showed a controlled release of drug dependent on pH. The nanomedicine thus inhibited an early release and reduced primary tumors in animal models while also inhibiting metastasis (Fernandez et al., 2022).

Staka et al. developed a low molecular weight hydrogel formed by a nucleoside (N4-octanoyl-2-deoxycytidine). The gel accommodated multiple polymeric NPs loaded with gemcitabine, a chemotherapeutic drug. The gel released the encapsulated drug for a month, which could be used as a treatment for unresectable cancer (Staka et al., 2019).

Myeloid-derived suppressor cells are a target in adoptive T cells transfer. Ledo et al. developed multilayer polymer nanocapsules to co-deliver two drugs: RNAi polynucleotides and chemokine CCL2. These NPs may help modulate the activity of myeloid derived suppressor cells (Ledo et al., 2019).

Etchenausia et al. studied poly(N-vinyl caprolactam) (PVCL)-based thermoresponsive microgels with polymer brushes as potential drug delivery nanocarriers. These microgels were biocompatible on HeLa and RAW cells. They tested DOX-loaded microgels and determined a sustained release of DOX from microgels as well as increased cell viability compared to free DOX, confirming the suitability of these microgels as safe drug delivery nanocarriers (Etchenausia et al., 2019).

Cordeiro et al. designed synthetic and natural polymer NPs and nanocapsules for antigen delivery. They observed that small-size cationic nanoclusters showed high accumulation in the lymph nodes and concluded that by modifying the physicochemical properties and composition of the nanocapsules, modulation of lymphatic uptake and biodistribution would be possible (Cordeiro et al., 2019).

Relano-Rodríguez et al. worked on human cytomegalovirus (HCMV), which infects and replicates in a wide variety of cells. They focused on the study of polyanionic carbosilane dendrimers (PCD). They tested two PCDs, G2-S16 and G2-S24P, which, alone or with current treatments, seemed to be a good tool against HCMV (Relano-Rodriguez et al., 2021) (Figure 6).

Polymeric nanocapsules are promising carriers for various antigens against different pathogens whose immunogenicity can be improved by including immunostimulatory molecules,

improving current vaccines. Imiquimod (IMQ) has been described as a good modulator of innate immunity and activator of the Th1 immune response, which is the target of most vaccines. Previous work showed that encapsulation of IMQ in chitosan (CS) NC induced protective antibody levels against recombinant hepatitis B surface antigen (HB) in mice immunized intranasally. In this work, two different IMQ-loaded NPs with a CS or inulin/pArg polymeric shell were synthesized for the development of a model vaccine containing a recombinant fusion protein (RFP) derived from the ESAT-6 antigen and CFP-10 from Mtb. The vaccine containing INU:pArg:Ag nanocapsules was the most immunogenic prototype against the ECH fusion protein (Diego-Gonzalez et al., 2020). The use of mRNA in vaccination has achieved great success in preventing the acute effects of COVID-19 after SARS-Cov-2 infection. Fornaguera et al. developed and described a protocol for the preparation of poly(β-amino esters) and their conjugation to mRNA and studies in cellular models (Fornaguera et al., 2021).

Poly amino acid particles are also excellent carriers able to cross the BBB when conjugated to brain penetrant peptides, demonstrating interesting properties in treating central nervous system disorders such as Alzheimer's disease (Duro-Castano et al., 2021b). Octaarginine conjugated with lauric acid forms a hydrophobic complex that can protect labile molecules by electrostatic and hydrophobic interactions, improving miRNA delivery in the hippocampus (Samaridou et al., 2020). Poly-I-glutamic acid complexes are also an efficient and non-toxic strategy to deliver oligonucleotides or DNA. Niño-Pariente et al. developed nanocomplexes with a poly-I-glutamic acid backbone that was derivatized with oligoaminoamide residues to efficiently assemble and deliver plasmid DNA (Nino-Pariente et al., 2017). Using PLGA-based polymeric NPs, Nozal et al., enhanced BBB permeation of NPs loaded with S14, a phosphodiesterase 7 (PDE7) inhibitor with great potential to treat Parkinson's disease. According to the studies, S14-loaded PLGA-NPs showed improved pharmacokinetic properties of S14 in animal models, as well as enhanced safety of this inhibitor (Nozal et al., 2021). The same group also encapsulated PHA-767491, a potent cell division cycle 7 (CDC7) kinase inhibitor in PLGA-NPs improving its permeability and CNS delivery properties (Rojas-Prats et al., 2021).

Grayston et al. tested biocompatible PLGA nanocapsules functionalized with superparamagnetic iron oxide NPs and Cy7.5 to improve brain targeting of drugs after stroke. According to the results, the intra-arterial route for the cerebral administration of new treatments showed an extraordinary advantage (Grayston et al., 2022).

Another active area of research belongs to anti-inflammatory agents. Interleukin-12 and interleukin-23 have a high interest as therapeutic targets to treat autoimmune/inflammatory diseases and chronic inflammatory diseases where T cells are the primary cells that are dysfunctional. Espinosa-Cano et al. prepared anti-inflammatory polymeric NPs that combine ketoprofen and dexamethasone (14Dx-KT), which are one of the most efficient cyclooxygenase-inhibitors. According to the results, a long-term treatment with 14Dx-KT NPs reduced the expression of Il12b and IL23a to normal cellular levels. The results suggest that the ketoprofen-based systems present an anti-inflammatory activity reducing the basal levels of pro-inflammatory markers and increasing the gene expression of anti-inflammatory cytokines (Espinosa-Cano et al., 2020a). Recent studies demonstrate the anti-inflammatory capacity of dexamethasone and naproxen. However, their use is limited by the rapid clearance of free drug. Espinosa-Cano et al. used polymeric NPs to administer these drugs in order to accumulate in pathological tissue, increasing the drugs' activity and reducing their adverse effects. The prepared naproxen-containing polymeric NPs loaded with dexamethasone were able to repress Il12b transcript levels, which would be an interesting treatment of autoimmune/anti-inflammatory diseases in which IL12 and IL23 are overexpressed (Espinosa-Cano et al., 2020b).

Oral delivery of insulin is also an attractive application for this type of NPs, since the acidity of intestinal fluids increases the risk of degradation. For instance, coating polyarginine insulin NPs with PEGylated polyaminoacids, protects insulin until it reaches the intestinal mucus (Niu et al., 2018), achieving the highest insulin uptake ever recorded in cellular models. Despite not resulting in a significantly increased systemic insulin uptake, the system showed a great potential for the delivery of peptides through the intestine mucosa. Santalices et al. also aimed at orally delivering hydrophobically modified insulin. They developed and extensively characterized nanoemulsions with selected components with improved properties on permeation, stability and mucodiffusion, such as miglyol, PEGylated phospholipids and poloxamer. The nanocomplexes showed promising results in cellular models and a moderate but significant hypoglycemic response in animals, highlighting key steps to take into consideration to overcome intestinal barriers (Santalices et al., 2021).

Similarly, Ariza-Saenz et al. used polymeric NPs of PLGA particles coated with glycol-chitosan (Ariza-Saenz et al., 2017) to enhance the delivery of a peptide inhibitor of the HIV-1 fusion protein that demonstrated to have enhanced permeability and efficacy of the peptide alone (Ariza-Saenz et al., 2018; Sanchez-Lopez et al., 2021).

As already showcased, polymeric NPs have been widely studied for the delivery of active compounds with poor pharmacokinetic properties. Here the delivery of licochalcone A was investigated using PLGA NPs and cell-penetrating peptides Tet and B6. Galindo et al. showed how the nanoconjugates with B6 showed increased activity for the treatment of ocular inflammation (Galindo et al., 2022).

Since combining drugs with miRNAs within a nanocarrier is a promising treatment for atherosclerosis, Leal et al., have developed polymeric PLGA NPs that simultaneously encapsulate and deliver miRNA-124a and the statin atorvastatin (ATOR). This combination reduced levels of proinflammatory cytokines and ROS. In addition, the dual-loaded NPs proved to be non-toxic to cells and prevent the accumulation of low-density lipoproteins inside macrophages and morphological changes, showing promise as a treatment for these types of diseases (Leal et al., 2022).

Encinas-Basurto et al., have developed allyl-isothiocyanate (AITC)-loaded PLGA NPs that target epithelial carcinoma cells due to anti-EGFR antibody binding to the surface. These NPs showed better anti-cancer properties compared to the free drug, suggesting that receptor-ligand binding could be used to target the NPs to tumor cells for improved drug delivery (Encinas-Basurto et al., 2018b).

TABLE 8 Summary of LNPs with their therapeutic area and functionalization strategy.

NP Type	Purpose	Therapeutic area	Therapeutic Agent	Functionalization strategy	Ref.
Solid lipid NPs (SLNs)	Edelfosine oral administration	Cancer	Edelfosine	NPs prepared with the homogenization and ultrasonication method	Gonzalez-Fernandez et al. (2018)
	Biodistribution study of edelfosine oral, intravenous and intraperitoneal administration			Edelfosine-LNS labeled with Technetium-99m	Lasa-Saracibar et al. (2022)
	Maslinic acid oral administration		Maslinic acid	Poloxamer407 (PMA), dicarboxylic acid-Poloxamer407 (PCMA) or Hialuronic Acid (Hyaluronic acid)-coated PCMA shell	Aguilera-Garrido et al. (2022)
	Improve the efficiency and the specificity of the SLN-loaded drug		Trans retinoic acid	SLNs composed of stearic acid, Epikuron 200 and sodium taurodeoxycholate coated with PE-PEG	Arana et al. (2019)
	Pulmonary administration	Tuberculosis	Rifabutin	RFB-loaded SLN based on glyceryl debehenate or glyceril tristearate	Gaspar et al. (2017)
	Drug administration	Tuberculosis	Bedaquiline	Chitosan-based nanocapsules with PEG layer	De Matteis et al. (2018)
	Local administration	Hearing loss	Dexamethasone and hydrocortisone	Stearic acid-based SLNs loaded with glucocorticoids	Cervantes et al. (2019)
	Oral drug delivery	Inflammatory bowel disease	Polyphenol oleuropein (OLE)	Olive oil-based NLCs	Huguet-Casquero et al. (2020)
		Antiparasitic (*Leishmania*)	Ammonium iodide derivative C6I	Glycerol tripalmitate and glyrerol tristearate SLNs obtained by emulsión-solvent evaporation method	Fernández et al. (2021)
	Nucleic acid delivery	-	Circular DNA and linear RNA	Combination of cationic and ionizable lipids	Fabregas et al. (2017)
			mRNA and pDNA	Combination of ionizable and cationic lipids (DOTAP)	Gomez-Aguado et al. (2020)
	Ocular drug delivery	Keratoconus	Lactoferrin	Double emulsion/solvent evaporation method	Varela-Fernandez et al. (2022)
	Gene therapy	Eye disease	IL-10	SLNs combined con protamine, dextran or hyaluronic acid and formulated with PVA.	Vicente-Pascual et al. (2020)
	Production of IL-10 in corneal cells		mRNA-based nanomedicinal products	Eye drops containing mRNA formulated in SLNs	Gomez-Aguado et al. (2021)
	Nucleic acid delivery (gene-silencing therapy)	-	siRNA	Cholesterol derivative cholesteryl oleate SLNs	Sune-Pou et al. (2018)
	Liver lipopolysaccharide-binding protein (LBP) downregulation	Obesity	Modified LBP siRNA	Four different lipid combination that interact with RNA and form non-charged NPs	Latorre et al. (2022)
	Downregulate metalloproteinase 9 (MPP-9)	Eye disease	Short-hairpin RNA (shRNA)	Nanocarriers formed by protamine, dextran and plasmids	Torrecilla et al. (2019)
Nanostructured lipid carriers (NLCs)	Characterization of IMT-loaded NLCs	Gastrointestinal stromal tumors	Imatinib	NLCs containing imatinib by emulsification-sonication methods	Gundogdu et al. (2022)
	Develop, characterize and assay Tripalm-NPs-PTX	Breast and Lung cancer	PTX	Glycerin tripalmitate NLCs loaded with PTX	Leiva et al. (2017)

(Continued on following page)

TABLE 8 (*Continued*) Summary of LNPs with their therapeutic area and functionalization strategy.

NP Type	Purpose	Therapeutic area	Therapeutic Agent	Functionalization strategy	Ref.
Nanostructured lipid carriers (NLCs)	Induce cancer cell death by apoptosis	Cancer	Apo2L/TRAIL	Binding TRAIL on a lipid nanoparticle surface	Gallego-Lleyda et al. (2018)
	Provide effective NLCs formulations for intramuscular or intraperitoneal administration	Resistant bacteria	Sodium colistumethate (SCM) and amikacin (AMK)	NLC formulations using trehalose and dextran as cryoprotectants and positive charged chitosan as coating	Vairo et al. (2020)
	Compare the efficacy of NLC-colistin vs. free colistin	Colistin-resistant *Pseudomonas aeruginosa* biofilm	Colistin	Hot melt homogenization technique. Precirol®ATO 5 and Miglyol 812 core mixed with colistin sulfate	Sans-Serramitjana et al. (2017a)
	Develop safer cationic NLCs using machine learning algorithms	Glioblastoma	Atorvastatin Coumarin	Glycerol based lipids NLCs produced by high-shear homogenization-ultrasonication	Basso et al. (2021)
	Drug oral administration	Antiparasitic (*Leishmania*)	Diselenide	Glyceryl palmitostearate and diethylene glycol monoethyl ether-based NLCs loaded with Diselenide	Etxebeste-Mitxeltorena et al. (2021)
	Increase EGFR gene expression	Cell culture and tissue engineering	Recombinant human epithelial growth factor (rhEGF)	NLCs prepared by hot melt homogenization	Chato-Astrain et al. (2021)
	Pulmonary and intramuscular administration	Respiratory infections	Sodium colistimethate		Pastor et al. (2019)
	Drug delivery across BBB	Neurodegenerative diseases	Growth factors	Polyunsaturated fatty acids-based NLC modulated with chitosan and TAT	Hernando et al. (2022)
Liposomes	Increase the granulysin concentration at the site of contact with the target cell	Cancer	Granulysin	Binding granulysin to the LNP surface through the complex formed by histidine tail of the protein and Ni^{2+} of a quelant lipid	Soler-Agesta et al. (2022)
Quatsomes and liposomes	Delivery	Fabry disease	α-galactosidase A	Incorporation of the cationic miristalkonium chloride (MKC) surfactant to nanoformulations	Tomsen-Melero et al. (2021)
Quatsomes	Parenteral administration	Cancer	Myristalkonium chloride (MKC) and cholesterol	Quatsomes prepared by depressurization on an expanded liquid organic solution-suspension method	Vargas-Nadal et al. (2020)
	Drug delivery	Chagas disease	Benznidazole	Quatsomes and LNPs prepared using CO_2 in a one-step procedure. Cyclodextrins by antisolvent precipitation	Vinuesa et al. (2017)
	miRNAs delivery	Cancer	miRNAs	Quatsomes composed of Chol and/or DC-Chol and quaternary ammonium surfactants	Boloix et al. (2022)
Lipoplexes	Cellular transfection		siRNA	Histidine-based gemini cationic lipids	Sanchez-Arribas et al. (2020a)
				Double-chain cationic lipid based on the argnine	Sanchez-Arribas et al. (2020b)
	pDNA delivery	-	pDNA	Mixture of a Gemini-Bolaamphiphilic Hybrid Lipid and DOPE	Martinez-Negro et al. (2018)

In another attempt to generate smart-delivery NPs, Correa-Paz et al. engineered polymeric templated $CaCO_3$ NPs with a layer-by-layer structure. The NPs were loaded with a fragile thrombolytic serine protease, labelled fluorescently and tagged with iron oxide NPs. The particles proved to efficiently release their protease cargo upon ultrasound application in cellular and animal models and maintained the activity after its delivery (Correa-Paz et al., 2019).

In another example of smart drug delivery using nanomaterials, Xuan et al. developed nanobottles formed from polyethylene glycol

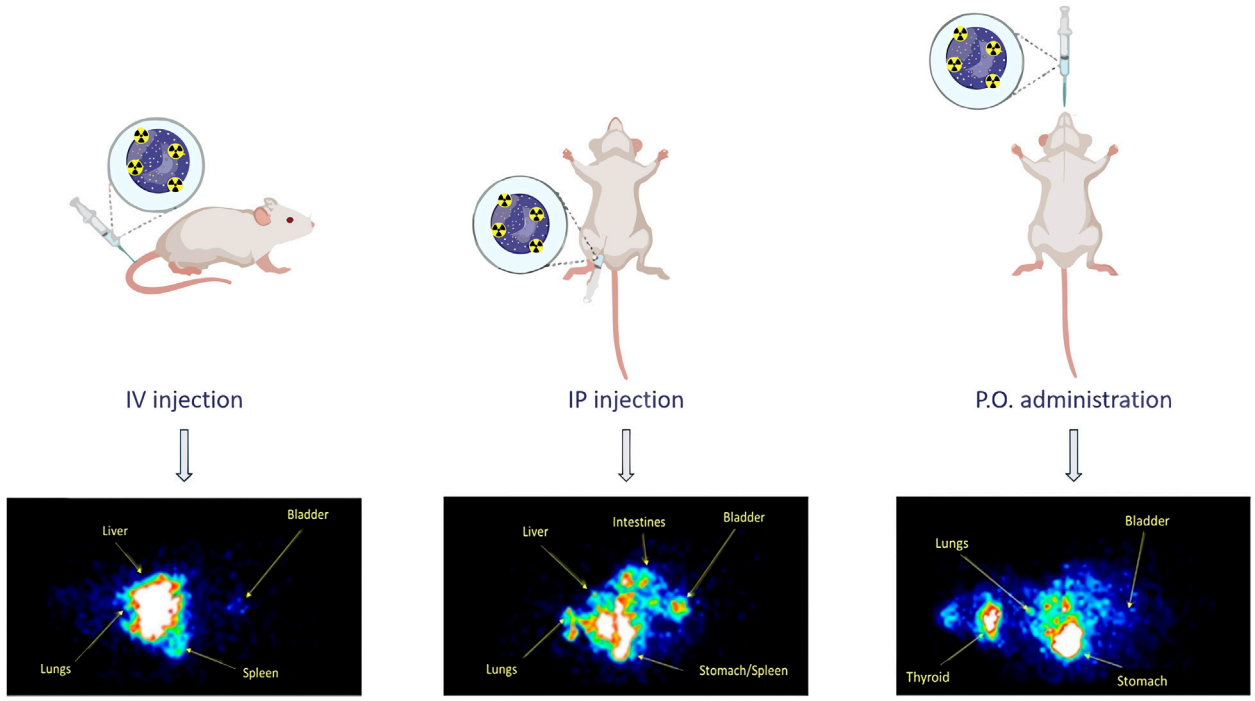

FIGURE 7
Distribution of LNPs loaded with edelfosine. Reprinted from Lasa-Saracibar et al. (2022), and licensed under the CReative Commons Attribution.

and ribose with a soft-template-based polymerization methodology. Using NIR light, the inner fluid of the bottle can be heated, resulting in its propulsion. The authors studied the trajectories, velocity and explosion events of the motors that could be controlled by modulating the NIR source and analyzed them through finite element analysis. This work is paving the road for the discovery and synthesis of new fuel-free based nanomotors (Xuan et al., 2018).

3.4 Lipid nanoparticles

Lipid NPs (LNPs) range from liposomes to solid LNPs (SLNs) and quatsomes (QS). The potential of these formulations relies on their stable structure and ability to cross biological barriers. LNPs constitute a good vehicle to transport both hydrophobic and hydrophilic drugs, providing protection for its cargo. For example, the complexation of lipids with nucleic acids allows their transport and prevents their degradation. They can be divided into four major types: liposomes, niosomes, SLNs, and nanostructured lipid carriers (NLCs) (Dhiman et al., 2021). SLNs and NLCs overcome liposomes and niosome due to their better performance under pH- and enzyme-dependent degradation. All of these formulations have been of research interest in Spain (Table 8) (Vargas-Nadal et al., 2020), (Tenchov et al., 2021)

LNPs are vastly used to treat cancer. Mitxelena-Iribarren et al. tested the effectiveness of nanoencapsulated methotrexate against human bone osteosarcoma cells U2OS using microfluidic platforms that allow cell culture and incubation under highly controlled dynamic conditions (Mitxelena-Iribarren et al., 2017; Mitxelena-Iribarren et al., 2021). Cacicedo et al. combined bacterial cellulose hydrogel (BC) and NLC, including cationic or neutral DOX as a drug model and tested in human breast adenocarcinoma MDA-MB-231 cells and orthotopic breast cancer mouse model. These carriers showed a significant reduction in tumor growth, metastasis incidence and local drug toxicities (Cacicedo et al., 2018). González-Fernández et al. tested the oral administration of edelfosine encapsulated SLNs in osteosarcoma cancer cell lines and animal models. They found that oral administration had a better effect against primary osteosarcoma tumors and successfully prevented the metastatic spread of cancer cells from the primary tumor to the lungs. In addition, Lasa-Saracíbar et al. labelled these SLNs with Tc and studied their biodistribution in mice after intraperitoneal and intravenous administration. Results showed that the drug could reach circulation and provide a more constant blood concentration after intraperitoneal administration (Gonzalez-Fernandez et al., 2018; Lasa-Saracibar et al., 2022) (Figure 7). Aguilera-Garrido et al. tested the delivery maslinic acid using SLNs with three different shell compositions: Poloxamer 407 (PMA), dicarboxylic acid-Poloxamer 407 (PCMA), and Hyaluronic acid-coated PCMA (PCMA-HA) in Caco-2/HT29-MTX co-cultures. Interestingly, they found that the SLNPs improved the solubility of MA up to 7.5 mg/mL, stable in a wide range of pH, and increased the bioaccessibility of MA after gastrointestinal digestion in a cellular model (Aguilera-Garrido et al., 2022). Arana et al. studied how different amounts of phosphatidylethanolamine polyethylene glycol (PE-PEG) influence SLNs composed of stearic acid, Epikuron 200, and sodium taurodeoxycholate. They observed that the presence of

TABLE 9 Summary of NPs classified by therapeutic area.

Therapeutic area	Purpose	NP type	Agent	Main results	Ref.
Antiamoebical activity (*A. castellani*)	Develop of anti-amoebic contact lens solution	AgNPs	-	A significant increase in anti-amoebic activity was observed	Hendiger et al. (2021), Hendiger et al. (2020)
			Tannic acid	AgNPs conjugated with tannic acid showed potential as an anti-amoebic agent	Padzik et al. (2018)
Antimicrobial activity	Lactose-gated delivery	MSNs	Essential Oil cinnamaldehyde	Improved delivery by decreasing volatility of compound and increasing its local concentration	Poyatos-Racionero et al. (2021)
Antibacterial activity	Overcome biofilm barrier		Levofloxacin	Therapeutic efficacy of levofloxacin was increased	Martinez-Carmona et al. (2019)
		AuNR@MSN		NIR activated MSNs with photothermal and antimicrobial properties	García et al. (2021)
Antibacterial activity	Provide effective NLCs formulations for intramuscular or intraperitoneal administration against resistant bacteria	Nanostructured lipid carriers (NLCs)	Sodium colistumethate (SCM) and amikacin (AMK)	NLC showed equal activity to the free drug. Intraperitoneal administration was observed to be superior than the intramuscular route	Vairo et al. (2020)
Antibacterial activity (Colistin-resistant *P. aeruginosa* biofilm)	Compare the efficacy of NLC-colistin vs. free colistin	Nanostructured lipid carriers (NLCs)	Colistin	Time dependent study of biofim viability upon treatment, showing colistin-NLC a more rapid biofilm killing with similar cellular death activity to the free drug	Sans-Serramitjana et al. (2017a)
Antibacterial activity (osteomyelitis)	Improve therapeutic effect	MSNs	Moxifloxacin, rifampicin	NPs treatment prevented the premature release of the antibiotics and induced biofilm disaggregation	Aguilera-Correa et al. (2022a)
Antibacterial activity (tuberculosis)	Pulmonary administration	SLNs	Rifabutin	Biodistribution study confirmed that pulmonary administered rifabutin NPs reached organs in 15–30 min timeframe, exerting their therapeutic activity	Gaspar et al. (2017)
	Drug administration	SLNs	Bedaquiline	NP encapsulation reduced drug toxicity while maintaining therapeutic activity	De Matteis et al. (2018)
	Drug delivery	MSNs-AgBr and Ag@MSNs	-	Good antimycobacterial capacity of both types of NPs was found *in vitro*	Montalvo-Quiros et al. (2021)
Antibacterial activity (*E. coli* infection)	Treatment of *E. coli* infection	AuNPs		Inhibition of *E. coli* infection was observed after treatment with the biosurfactant stabilized NPs	Gomez-Grana et al. (2017)
Antibacterial activity (*K. pneumoniae*)	Drug delivery		Amikacin	The combination of AuNPs and the antiobiotic evidenced a synergistic effect representing a potential anti-bacterial nanomaterial	Aguilera-Correa et al. (2022b)
Antibacterial activity (*Campylobacter*)	Improve drug efficacy against multidrug resistant strains	GSH-Ag NPs	-	Results evidenced that these NPs are highly effective against the infection of multidrug resistant strains	Silvan et al. (2018)
Antibacterial activity (*S. aureus* and *E. coli*)	Treatment against bacterial infection by *S. aureus* and *E. coli*	Hybrid γ-Fe_2O_3/Ag nanocomposites		Synergistic properties between AgNPs and IONPs were found for the treatment of bacterial infection of *S. aureus* and *E. coli*	Luengo et al. (2020)

(Continued on following page)

10.3389/fbioe.2023.1191327

TABLE 9 (*Continued*) Summary of NPs classified by therapeutic area.

Therapeutic area	Purpose	NP type	Agent	Main results	Ref.
Antibacterial activity (*P. aeruginosa*)	Treatment against bacterial infection by *P. aeruginosa*	AgNPs	Probiotics	Combination of AgNPs with living probiotics showed anti-bacterial activity against *P. aeruginosa*	Sabio et al. (2021)
Antibacterial activity (peri-implantitis)	Prevention of implant associated infection (*S. aureus* and mixed oral bacteria flora infection)		-	NPs prevented the formation of bacterial biofilms proving their potential to be used in dental implants to prevent pre-implantitis	Perez-Tanoira et al. (2022)
Antibacterial activity (*S. aureus*)	Anti-biofilm treatment	AgNP@nanoMIL-125(Ti)NH_2		Results showed a significant bacterial inhibition, proposing this composite as an active coating biofilm treatment	Arenas-Vivo et al. (2019)
Antibacterial activity (*S. aureus* and *P.aeruginosa*)	Improve antibiotic treatment of *S. aureus* and *P.aeruginosa* infection	AgNPs	Enzymes (α-amylase, cellulose, DNase I and proteinase K)	A potent anti-biofilm activity was found decreasing bacterial infection in combination with antibiotics	Rubio-Canalejas et al. (2022)
Antimicrobial activity (anti-fungal and anti-amoebic)	Treatment for fungal and amoebic infection	AgNRs and AgNws	-	AgNPs showed activity agains various fungals and *A. castellanii* infection	Gonzalez-Fernandez et al. (2022)
Antiparasitic (*Leishmania*)	Oral drug delivery	Solid lipid NPs (SLNs)	Ammonium iodide derivative C6I	Several NPs were tested in macrophages and PLGA based nanoformulationms improved antuiñlieshmanial activity on intracellular amastigotes	Fernández et al. (2021)
	Drug oral administration	Nanostructured lipid carriers (NLCs)	Diselenide	NLCs increased intestinal permeability providing higher plasmatic drug levels and reducing parasite burden after oral administration	Etxebeste-Mitxeltorena et al. (2021)
Chagas disease	Drug delivery	Quatsomes	Benznidazole	NPs enabled a safer administration of the drug without losing therapeutic activity	Vinuesa et al. (2017)
Antiviral activity (SARS-CoV-2)	Treat or prevent SARS-CoV-2 infection	Iron oxide NPs and iron oxyhydroxide NPs	-	IONPs and IOHNPs might be repurposed as a therapeutic treatment for SARS-CoV-2 infection	DeDiego et al. (2022)
Antiviral activity (HIV)	Enhance immune response in HIV infection	AuNPs	-	AuNPs coated with two different antibodies that recognize HIV protein and natural killer cells, promoting specific cell-to-cell contact and induced a potent cytotoxic response	Astorga-Gamaza et al. (2021)
	Drug delivery		siRNA-Nef	AuNPs were used for gene delivery against the HIV	Pena-Gonzalez et al. (2017)
	Improve antiretroviral therapy	Poly(lactic-co-glycolic acid)	HIV-1 Peptide inhibitor	NPs were successfully loaded with inhibitory peptides, permeated through the mucus reaching the vaginal epithelium and released the cargo	Ariza-Saenz et al. (2017)
	Improve the delivery of bioactive peptides to inhibit HIV infection			NPs successfully permeated vaginal tissue and released inhibitory peptides	Ariza-Saenz et al. (2018)
Antiviral therapy	Inhibits the infection of human cytomegalovirus	Polyanionic carbosilane dendrimers	-	Dendrimers reduced HCMV infection and enhanced the activity of ganciclovir	Relano-Rodriguez et al. (2021)

(Continued on following page)

10.3389/fbioe.2023.1191327

TABLE 9 (*Continued*) Summary of NPs classified by therapeutic area.

Therapeutic area	Purpose	NP type	Agent	Main results	Ref.
Cancer	Delivery	Multifunctional MSNs	DOX	Increase the efficacy of glucose dependent cargo delivery	Jimenez-Falcao et al. (2019)
		MSNs		A drug encapsulation system was designed using galacto-oligosaccharides to coat a silica scaffold containing the drug of interest, which is preferentially released in tissues with senescent cells	Munoz-Espin et al. (2018)
	Delivery	Nanovehicle MSNs	Camptothecin and DOX, Zn, and phtalocyanine	A pH-triggered nanovehicle with regioselectively bifunctionalized MSNs for the dual release of DOX and camptothecin was developed	Llinas et al. (2018)
		MCM-41/Pt	$Ru(Bpy)_3Cl_2$/DOX	Pt-MSNs nanomotors with stimuli-response drug release capabilities have been designed, synthetized and characterized	Diez et al. (2021)
		Au-MSNs Janus NPs	DOX	A nanodevice was designed for the autonomous release of DOX in specific cells triggered by NADPH and glutathione disulfide	Mayol et al. (2021)
	Synergy of hyperthermia and drug delivery	MSNs loaded with iron oxide NPs		The synergic effect of the intracellular hyperthermia and chemotherapy significantly reduced *in vivo* tumor growth without a global temperature rise of the tissue	Guisasola et al. (2018b)
	Photothermal therapy	Gold suprashells assembled around SPIONs	-	Development of multifunctional gold suprashell that can be magnetically accumulated and used for controlled plasmonic heat generation	Paterson et al. (2017)
	Delivery (drug nanocarrier)	Iron Oxide (magnetite) NPs	Crocin	Drug nanocarrier enhance therapy in comparison to free drug	Saravani et al. (2020)
	Magnetic hyperthermia (MHT) cytotoxicity		-	Cytotoxic effects caused by magnetic hyperthermia are reduced by the cell-promoted NP aggregation	Mejias et al. (2019)
	Cell internalization of IONPs			Magnetic thermal response can be predicted based on the type and size of the NP in the cellular media	Cabrera et al. (2018)
	Study of MHT in 3D cultures and a murine model			Localization of NPs inside or outside the cells can trigger different apoptotic routes. Best therapeutic conditions were tested in an animal model	Beola et al. (2018), Beola et al. (2020), Beola et al. (2021)
	To develop computational models to effectively design nanomedicine	Iron Oxide (maghemite) NPs	Gemcitabine	Rational design was successfully used to develop multifunctional NPs	Aires et al. (2017)
	Therasnotic agent	Au@Fe nanoflowers	-	Nanoflowers could be used as promising tools for diagnostics and hyperthermia therapy	Christou et al. (2022)

(Continued on following page)

10.3389/fbioe.2023.1191327

TABLE 9 (*Continued*) Summary of NPs classified by therapeutic area.

Therapeutic area	Purpose	NP type	Agent	Main results	Ref.
Cancer	MHT and NP uptake in cancer cells	Manganese ferrite nanoflowers	-	Improvement heating efficiency of magnetic NPs in a glioma cellular model	Del Sol-Fernandez et al. (2019)
	PTT, MHT and magneto-photothermal treatment	Gold-iron oxide Janus magnetic nanostars		A synergistic cytotoxic effect on cancer cells and in an animal model was observed	Espinosa et al. (2020)
	PTT, MHT and magneto-photothermal treatment	Gold coated magnetite nanorods		Proof of concept of the generation of free-standing anisotropic materials for magneto and photothermia applications	Rincon-Iglesias et al. (2022)
	Modulation of angiogenesis as an antitumor therapy	Super paramagnetic Iron oxide (maghemite) NPs		Anti-angiogenic and an-tumoral effects were observed after treatment with NPs	Mulens-Arias et al. (2019)
	Targeted cell therapy	Iron oxide (maghemite) NPs		Cell retention was favoured improving cell-based therapy for cancer treatment	Sanz-Ortega et al. (2019a)
	Targeted adoptive T-cell transfer therapy and EMF	Iron oxide NPs		T cells modified with the magnetic NPs were retained in lymph nodes after the use of an EMF despite their lower number	Sanz-Ortega et al. (2019b), Sanz-Ortega et al. (2019c)
	MHT *in vivo* feedback	Ag_2S-based NPs, Fe_3O_4 MNPs		Therapeutic effect of the MNPs was more accurately evaluated	Ximendes et al. (2021)
	Drug delivery, controlled release and MHT	$MNP@mSiO_2$	DOX	Drug was released at acidic pH showing promising results	Fuentes-García et al. (2021)
	Drug delivery, controlled release and MHT	MF66 iron oxide NPs		Drug release was controlled by pH reducing side effects of chemotherapy and increasing their therapeutic effect	Lazaro-Carrillo et al. (2020)
	Delivery	Iron oxide (maghemite) NPs	miRNA155, miRNA125b and miRNA146a	A pro-inflammatory response was induced after treatment with the loaded NPs	Lafuente-Gomez et al. (2022)
	Heterogeneous catalysis	Copper-iron oxide spinel NPs	-	NPs reduced the levels of glutathione and increased ROS and apoptotic pathways in cancer cells	Bonet-Aleta et al. (2022a), Bonet-Aleta et al. (2022b)
	Improve NP's properties	AuNPs	-	NPs uptake was improved using an adenovirus	Gonzalez-Pastor et al. (2021)
	Drug delivery		Gemcitabine/Gapmers	Delivery of both agents reduced the chemoresistence to gemcitabine in cancer cells	Garcia-Garrido et al. (2021)
	Drug delivery	AuNPs	DOX	A synergetic effect between chemo and photothermal therapy was observed reducing cell viability in cancer cells	Encinas-Basurto et al. (2018a)
			Docetaxel/DOX	Combination of the chemotherapeutic properties of the drugs with the photothermal therapy of the NPs produced high cytotoxic effects in breast cancer cells	Villar-Alvarez et al. (2019)
			Doxycicline/Fosbretabulin	Co-delivery of the two drugs in combination with photothermal and photodynamic therapy showed promising results in an embryo xenograph model	Paris et al. (2020)

(Continued on following page)

10.3389/fbioe.2023.1191327

TABLE 9 (*Continued*) Summary of NPs classified by therapeutic area.

Therapeutic area	Purpose	NP type	Agent	Main results	Ref.
Cancer			DOX	Controlled release of the drug in combination with photothermal therapy evidenced a synergistic effect in cancer cells	Villar-Alvarez et al. (2018)
	Drug delivery	AuNPs	DOX	A nanosystem for the controlled release of the drug was developed	Martin-Saavedra et al. (2017)
			DOX/SN38	Controlled drug release of both drugs showed a potent anti-tumoral activity as well as anti-neoplastic activity against cancer stem cells	Latorre et al. (2019)
	Biosynthesis of AuNPs with therapeutic properties		-	NPs synthetized using an aqueous extract of *Saccorhiza polyschides* showed both, immunostimulant and anti-proliferative activities, on immune and tumor cells	Gonzalez-Ballesteros et al. (2021a)
	Green synthesis of AuNPs with therapeutic properties			NPs synthetized using extracted carrageenan from red seaweed presented anti-oxidant and anti-tumoral activities	Gonzalez-Ballesteros et al. (2021b)
	miRNA delivery	AuNPs	Natural killer cells extracellular vesicle-miRNA	Specific delivery of the NPs regulated the immune response representing a potential immunomodulatory approach for cancer treatment	Dosil et al. (2022)
	Drug delivery	AuNPs	DOX	The therapeutic agent triggered by NIR light showed a reduction in the viability of cancer cells	Hernandez Montoto et al. (2019)
	Drug delivery	PLGA@Ag_2S and PLGA@Ag_2S@ SPION	Maslinic acid	An efficient encapsulation and controlled release of the therapeutic agent was observed in cellular models	Alvear-Jimenez et al. (2022)
		AgNPs and AuNPs	Raltitrexed	Drug modified NPs showed a strong inhibition on cancer cell viability	Morey et al. (2021)
	Drug delivery	Folate-targeted albumin-alginate NPs	PTX	Improved uptake of NPs by cells due to the overexpression of folate receptor	Martinez-Relimpio et al. (2021)
	Treatment of different types of tumors	AgNPs-LE AgNPs-PE	*A. muricata* extracts	Lower concentrations were found to have a potential antitumor activity with a better therapeutic index for the treatment of different types of tumors	Gonzalez-Pedroza et al. (2021)
	Macrophages polarization from M2 to M1 profiles	Arginine based	Toll-like receptor 3 agonist poly(I:C)	Nanocomplexes enabled a safe delivery of the Poly (i:C) that induced pro-inflammatory state macrophages	Dacoba et al. (2020b)
	Intratumoral immunotherapy	Polyethylenimine	Toll-like receptor 3 agonist poly(I:C)	Nanoplexed formulation of Poly I:C induced immunogenic cell death of tumoral cells	Aznar et al. (2019)

(Continued on following page)

10.3389/fbioe.2023.1191327

TABLE 9 (*Continued*) Summary of NPs classified by therapeutic area.

Therapeutic area	Purpose	NP type	Agent	Main results	Ref.
Cancer	Improve tumor targeting	Poly(lactic-co-glycolic acid)	Allyl-isothiocyanate	Antibody functionalized NP showed improved antitumoral properties than the free drug in cell co-cultures	Encinas-Basurto et al. (2018b)
	Develop microgels for drug delivery	Poly(N-vinyl caprolactam)	DOX	Sustained release of DOX through clathrin dependent internalization	Etchenausia et al. (2019)
	Improve treatment of unresectable cancer by controlled release	Polyglutamic acid	Gemcitabine	Lasting control release of loaded drug more than 1 month and effective cell growth inhibition in resistant cancer cell lines	Staka et al. (2019)
	Edelfosine oral administration	Solid lipid NPs (SLNs)	Edelfosine	NPs slowed down primary tumor growth and prevented metastatic spread. Combination with DOX did not show synergistic effects	Gonzalez-Fernandez et al. (2018)
	Biodistribution study of edelfosine oral, intravenous and intraperitoneal administration		Edelfosine	Biodistribution map of NPs after intravenous and intraperitounal administration showing that NPs presented quantifiable and constant levels in blood after intraperitoneal dose	Lasa-Saracibar et al. (2022)
	Maslinic acid oral administration		Maslinic acid	NPs improved solubility of the therapeutic agent, yielding delivery across *in vitro* gut barrier models, being able to inhibit the growth of pancreatic cancer cells	Aguilera-Garrido et al. (2022)
	Improve the efficiency and the specificity of the SLN-loaded drug		Trans retinoic acid	Phosphatidylethanolamine polyethylene glycol NPs improve active cellular internalization increasing the chemotoxic effect of the drug	Arana et al. (2019)
	Induce cancer cell death by apoptosis	Nanostructured lipid carriers (NLCs)	Apo2L/TRAIL	Nanoformulation development for apoptosis-inducing ligand with efficacy in sarcoma cell lines	Gallego-Lleyda et al. (2018)
	Increase the granulysin concentration at the site of contact with the target cell	Liposomes	Granulysin	Granulysin cytotoxicity is increased when formulated with liposomes and acts through the mitochondrial apoptotic pathway	Soler-Agesta et al. (2022)
	Parenteral administration	Quatsomes	Myristalkonium chloride (MKC) and cholesterol	Quatsomes are useful for biodistribution studies after intravenous administration and drug delivery applicability	Vargas-Nadal et al. (2020)
	miRNAs delivery		miRNAs	Quatsomes protect miRNA and provide a pH sensitive delivery platform	Boloix et al. (2022)
	Cellular transfection	Lipoplexes	siRNA	Remarkable silencing activity was obtained without associated toxicity	Sanchez-Arribas et al. (2020a)
				Cationic lipids with a helper lipid are a safe and biocompatible gene silencing strategy	Sanchez-Arribas et al. (2020b)
Cancer (Triple negative breast cancer)	Enhance the efficacy of first-line chemotherapeutics	Polyglutamic acid	DOX	Effective reduction of lung and lymph node metastases in triple-negative breast cancer	Duro-Castano et al. (2021a)

(Continued on following page)

10.3389/fbioe.2023.1191327

TABLE 9 (*Continued*) Summary of NPs classified by therapeutic area.

Therapeutic area	Purpose	NP type	Agent	Main results	Ref.
Cancer (prostate)	pH dependent and controlled release of drug	Tert-Ser polyacetal	PTX	Sustained release of PTX (2 weeks) reducing systemic toxicities while conserving tumor growth inhibitory activity	Fernandez et al. (2022)
Cancer immunotherapy	Delivery of two therapeutic agents for reverting MDSC-mediated immunosuppression	Polyarginine	RNAi and CCL2 chemokine	Nanocapsules modulated monocyte differentiation into tumour-associated macrophages and reduced significantly C/EBPβ mRNA levels	Ledo et al. (2019)
Cancer (pancreatic)	Development of targeted delivery chemotherapy	Iron oxide NPs	Gemcitabine and anti-CD47 antibody	Improved results and delivery were shown after treatment with the multifunctional NPs	Trabulo et al. (2017)
	MHT in mice model	Iron Oxide (maghemite) NPs	-	Temperature rise during MHT can be controlled by modulating the field intensity in animal models	Beola et al. (2021)
Cancer (sarcoma)	Microswimmers with MHT capacity	Manganese ferrite NPs	-	Microswimmers can be employed to enhance tissue penetration for specific cargo delivery	Ramos-Docampo et al. (2019)
Cancer (breast)	Enzyme prodrug therapy	AuNPs	Horseradish peroxidase	This combination strategy evidenced high anti-tumoral activity in 3D tumor models	Vivo-Llorca et al. (2022)
Breast and Lung cancer	Develop, characterize and assay Tripalm-NPs-PTX.	Nanostructured lipid carriers (NLCs)	PTX	PTX tumor activity was increased in breast and lung cancer cells through glyceryl triplamitate NPs formulation	Leiva et al. (2017)
Brain cancer	Hyperthermia control	AuNPs	-	Hybrid probes were internalized in 3D tumor spheroids and can induced cell death through photothermal effects, while measuring the local temperature *in situ*	Quintanilla et al. (2019)
Glioblastoma	Develop safer cationic NLCs using machine learning algorithms	Nanostructured lipid carriers (NLCs)	Atorvastatin Coumarin	Two novel glycerol lipids were studied showing that GLY1 circumvents the intrinsic cytotoxicity of common surfactant CTAB and shows anticancer activity	Basso et al. (2021)
Gastrointestinal stromal tumors	Characterization of IMT-loaded NLCs	Nanostructured lipid carriers (NLCs)	Imatinib	Imatinib loaded NPs were synthesized and characterized, showing a controlled release of the drug and thus being promising for tumor treatment	Gundogdu et al. (2022)
Eye disease	Gene therapy	Solid lipid NPs (SLNs)	IL-10	SLNs formulations were safe after topical administration and hyaluronic acid based ones reached endothelial layer	Vicente-Pascual et al. (2020)
	Production of IL-10 in corneal cells	Solid lipid NPs (SLNs)	mRNA-based nanomedicinal products	SLNs presented a high transfection efficiency when formulated as eye drops	Gomez-Aguado et al. (2021)
	Downregulate metalloproteinase 9 (MPP-9)	Solid lipid NPs (SLNs)	Short-hairpin RNA (shRNA)	NPs with non viral vectors downregulated MMP-9 expression in human corneal cells	Torrecilla et al. (2019)

(Continued on following page)

10.3389/fbioe.2023.1191327

TABLE 9 (*Continued*) Summary of NPs classified by therapeutic area.

Therapeutic area	Purpose	NP type	Agent	Main results	Ref.
Fabry disease	Delivery comparison by quatsomes and hybrid liposomes	Quatsomes and liposomes	α-galactosidase A	Improved efficacy was observed with hybrid liposomes having a good *in vitro/in vivo* safety profile	Tomsen-Melero et al. (2021)
Hearing loss	Local administration	Solid lipid NPs (SLNs)	Dexamethasone and hydrocortisone	Loaded NPs penetrated into auditory cells and protected them from cisplatin induced ototoxicity	Cervantes et al. (2019)
Inflammatory bowel disease	Oral drug delivery	Solid lipid NPs (SLNs)	Polyphenol oleuropein (OLE)	NPs ameliorated inflammation in macrophages and in a mouse model of acute colitis	Huguet-Casquero et al. (2020)
Keratoconus	Ocular drug delivery	Solid lipid NPs (SLNs)	Lactoferrin	Successful preparation of lactoferrin SLNs with a controlled release pattern	Varela-Fernandez et al. (2022)
Obesity	Liver lipopolysaccharide-binding protein (LBP) downregulation	Solid lipid NPs (SLNs)	Modified LBP siRNA	Nanoformulated siRNA against liver LBP is a promising therapy for faty liver associated to obesity	Latorre et al. (2022)
-	Increase EGFR gene expression	Nanostructured lipid carriers (NLCs)	Recombinant human epithelial growth factor (rhEGF)	NLCs improved EGF expression enhancing the efficiency of explant-based methodologies for primary cell culture	Chato-Astrain et al. (2021)
Respiratory diseases	Delivery	TNFR-Dex-MSN	Dexamethasone	A selective uptake by macrophages of the NPs was observed, demonstrating lung accumulation and reduction of the damage	Garcia-Fernandez et al. (2021a), Garcia-Fernandez et al. (2021b)
	Pulmonary and intramuscular administration	Nanostructured lipid carriers (NLCs)	Sodium colistimethate	NLC enabled a dose reduction of the drug to obtain a similar *in vivo* effect without apparent toxicity	Pastor et al. (2019)
Tissue regeneration (bone)	Delivery	MSN@PEI	Osteostatin and siRNA	Both therapeutic agents were efficiently delivered inside cells and consequently a synergistic effect in the increase in the osteogenic markers was observed	Mora-Raimundo et al. (2019)
	Induce osteogenesis and bone repair	MSNs	Ipriflavone	Results showed that both, bone regeneration and angiogenesis, were promoted after injection in an animal model	Arcos et al. (2022)
Tissue regeneration (angiogenesis)	Enhance angiogenesis			NPs evidenced a great potential to enhance angiogenesis after intracellular uptake	Casarrubios et al. (2021)
Tissue regeneration (periodontal)	Periodontal augmentation			NPs stimulated differentiation of pre-osteoblasts into mature osteoblasts after clathrin-dependent internalization	Casarrubios et al. (2020)
Vaccine development	Delivery	MSNs	Immunomodulatory and vesicle-associated proteins (Ag85B, LprG and LprA)	The designed nanosystems have been extensively characterized and their their immunostimulatory capacity demonstrated	Montalvo-Quiros et al. (2020)
	Improve targeting specific immune cells in the lymphatics	Chitosan, polyarginine, and carboxymethyl-β-glucan	-	Lymphatic uptake of polymeric NPs is dependent on particle size and charge	Cordeiro et al. (2019)

(Continued on following page)

10.3389/fbioe.2023.1191327

TABLE 9 (*Continued*) Summary of NPs classified by therapeutic area.

Therapeutic area	Purpose	NP type	Agent	Main results	Ref.
	Development of intranasal vaccination against *Mycobacterium tuberculosis*	Nanocapsules with a polymeric shell	Imiquimod and a fusion protein formed by two antigens of *Mycobacterium tuberculosis*	Inulin polyarginine produced an adequate IgA response *in vivo*	Diego-Gonzalez et al. (2020)
	Improve vaccine development	Poly(β-amino esters)	mRNA	Detailed description of a simple production of mRNA polymeric NPs with a proof of concept immunization	Fornaguera et al. (2021)
Neurodegenerative diseases	Develop multimodal NPs for AD	Polyglutamate	Bisdemethoxycurcumin or Genistein	Angiopep-2 conjugated NPs were efficiently delivered through the BBB and the treatment reduced β-amyloid peptides and rescued cognitive impairments in mice	Duro-Castano et al. (2021b)
	miRNA delivery to the hippocampus	Polyarginine	Specific miRNA mimic, miR-132	Successful production of a scalable nanoformulation that was efficiently delivered to the brain to exert its therapeutic action by nasal administration	Samaridou et al. (2020)
	Improve BBB permeability and pharmacokinetics of compounds	Poly(lactic-co-glycolic acid)	PDE7 inhibitor	Successful preparation of polymeric nanoparticle with efficient encapsulation and a sustained cargo release in mice brains after oral administration	Nozal et al. (2021)
			CDC7 inhibitor	Successful preparation of polymeric nanoparticle with efficient encapsulation and permeability through the BBB	Rojas-Prats et al. (2021)
	Drug delivery across BBB	Nanostructured lipid carriers (NLCs)	Growth factors	TAT-NLCs showed good BBB permeability *in vitro* and reduced the inflammatory response in human microglia	Hernando et al. (2022)
Diabetes	Oral delivery of insulin	Polyarginine	Insulin	Enhanced epithelial accumulation of insulin that did increase insulin transport	Niu et al. (2018)
	Provide an efficient oral peptide administration	Poly(lactic-co-glycolic acid)	Hydrophobically modified insulin	Nanoemulsions internalized Caco-2 monolayers yielding to a moderate hypoglycemic response in diabetic rats	Santalices et al. (2021)
Stroke	Enhance BBB penetration	Poly(lactic-co-glycolic acid)	-	Controlled brain delivery of polymeric NPs by endovascular administration and magnetic targeting	Grayston et al. (2022)
Ocular inflammaition	Improve pharmacokinetic properties of licochalcone A	Poly(lactic-co-glycolic acid)	Licochalcone A	Development of ocular inflammation targeted NPs with therapeutic efficacy *in vivo*	Galindo et al. (2022)
Atherosclerosis	Deliver miRNA and atorvastatin simultaneously	Poly(lactic-co-glycolic acid)	miRNA 124a and atorvastatin	NPs delivered simultaneously miRNA and atorvastatin that significantly reduced proinflammatory cytokines and prevented the accumulation of low-density lipoproteins inside macrophage	Leal et al. (2022)
Inflammation autoimmune diseases	Obtain a synergistic anti-inflammatory effect	1-vinylimidazole	Ketoprofen and dexamethasone	Synergistic anti-inflammatory effect of non-toxic polymeric NPs loaded with dexamethasone and naproxen. Coumarin loaded NPs showed to be rapidly uptaken by macrophages	Espinosa-Cano et al. (2020a)

(Continued on following page)

10.3389/fbioe.2023.1191327

TABLE 9 (*Continued*) Summary of NPs classified by therapeutic area.

Therapeutic area	Purpose	NP type	Agent	Main results	Ref.
	Study the synergistic anti-inflammatory effect	1-vinylimidazole and methacrylic derivative	Dexamethasone and naproxen		Espinosa-Cano et al. (2020b)
Acute ischemic stroke	Optimize *in vivo* delivery specificity	$CaCO_3$ cores stabilized by poly(vinylsulfonic acid)	Thrombolytic serine protease	Encapsulation of therapeutic agent precluded its inactivation promoting blood clots breakdown *in vitro*. Delivery upon ultrasound application was confirmed *in vivo*	Correa-Paz et al. (2019)
-	To develop zwitterionic pDNA delivery systems	Polyglutamic acid	Plasmid DNA delivery	Successful plasmid DNA complexes formation that yielded an effective transfection in N2a cells without apparent toxicity	Nino-Pariente et al. (2017)
	Develop fuel-free propulsion NPs activatable by NIR	Polyethylene and propylene glycol and ribose	-	Succesful development of NIR light powered carbonaceous nanobottles	Xuan et al. (2018)
	Gene therapy	AuNPs	Plasmid DNA	A novel strategy to control the release of plasmid DNA after sternal stimuli as irradiation was developed	Sanchez-Arribas et al. (2021)
	Multi-Hot-Spot magnetic inductive nanoheating	Iron oxide (magnetite/ maghemite) NPs	-	Creation of simultaneous and sequential multi hot spot conditions in a single pot	Ovejero et al. (2021b)
	Nucleic acid delivery	Solid lipid NPs (SLNs)	Circular DNA and linear RNA	Implementation of SLN formulation to efficiently transfect DNA and RNA	Fabregas et al. (2017)
	Nucleic acid delivery	Solid lipid NPs (SLNs)	mRNA and pDNA	Study of several SLNs for nucleic acid delivery analyzing stability and transfection efficieny	Gomez-Aguado et al. (2020)
	Nucleic acid delivery (gene-silencing therapy)	Solid lipid NPs (SLNs)	siRNA	Cholesteryl oleate SLNs represent a safe and efficient transfection tool for nonviral nucleic acid delivery	Sune-Pou et al. (2018)
	Increase the cellular attachment	AuNPs	-	Cellular adherence was increase enabling the thermoablating effect of AuNPs without cellular internalization	Artiga et al. (2018)
	Control protein corona formation			Protein corona formation was controlled and thus NPs cellular uptake increased	Mosquera et al. (2020)
	Inhibition of enzymatic activities			Local generation of plasmonic heat inhibited the horseradish peroxidase and the glucose oxidase which were coupled to AuNPs	Thompson et al. (2017)
	pDNA delivery	Lipoplexes	pDNA	Amphiphilic lipids and DOPE yieldied and efficient DNA transfection	Martinez-Negro et al. (2018)

10.3389/fbioe.2023.1191327

PE-PEG improved active cell internalization of the NPs in an oral adenocarcinoma cell line, reducing non-specific internalization mechanisms. Furthermore, they also tested the effect of surface coating on the efficiency of incorporated drugs finding that PE-PEG coated SLN increases its chemotoxic effect compared to non-coated SL (Arana et al., 2019). Gundogdu et al. rigorously studied the physical characteristics of imatinib-containing NLC for the treatment of gastrointestinal stroma tumors. They found that these NPs revealed a Korsmeyer-Peppas drug release model of 53% at 8 h with above 90% of cell viability. They also found an IC_{50} of 23.61 μM and induction of apoptosis in CRL-1739 cell lines (Gundogdu et al., 2022). Leiva et al. tested glyceryl tripalmitate NLCs loaded with PTX. The NPs-PTX significantly enhanced PTX antitumor activity in human breast (MCF7, MDAMB231, SKBR3, and T47D) and lung (A549, NCI-H520, and NCI-H460) cancer cells. They also decreased the volume of breast and lung multicellular tumor spheroids (Leiva et al., 2017).

To induce apoptosis in cancer cells, Gallego-Leyda et al. employed SLNs decorated with TNF-related apoptosis-inducing ligand (TRAIL). They found that the decorated NPs were more cytotoxic than soluble TRAIL in A673 cells, RD cells and HT-1080 cells (Gallego-Lleyda et al., 2018). Similarly, Solar-Agesta et al. developed LNPs whose surfaces can bind granulysin as an antitumoral treatment, increasing the concentration at the site of contact with the target cell. Granulysin binding to the liposomes significantly increased the cytotoxic potency, produced mainly by apoptosis (Soler-Agesta et al., 2022).

NLC can overcome the toxicity of some antibiotics with a current limited use. Vairo et al. encapsulated antibiotics in different NLC formulations through high pressure homogenization, and showed that negatively charged SCM-NLC, with trehalose as cryoprotectant, had the best efficacy in several bacteria strains (Vairo et al., 2020). With a similar aim, Vinuesa et al. explored different lipid nanoformulation options for benznidazole, a commercially available drug currently used for the treatment of Chagas disease with a high toxicity, finding balanced conjugates of activity/toxicity (Vinuesa et al., 2017).

LNPs are also used to destroy biofilms. Sans-Serramitjana et al. studied the viability of *P. aeruginosa* biofilms treated with both free and nanoencapsulated colistin finding a more rapid killing of *P. aeruginosa* bacterial biofilms by nanostructure lipid carrier-colistin than by free colistin (Sans-Serramitjana et al., 2017a). The same group investigated the encapsulation of Tobramycin and its effect on planktonic and biofilm forms of *Pseudomonas*. They found that the nanoencapsulation of tobramycin did not improve its efficacy against planktonic *P. aeruginosa* but did improve its ability to eradicate *P. aeruginosa* biofilms (Sans-Serramitjana et al., 2017b).

Machine learning algorithms can be used to unravel hidden patterns in NP. In this work by Basso et al., the effects of two novel glycerol-based lipids, GLY1 and GLY2, on the architecture and performance of NLC were evaluated. Results showed that GLY1 circumvents the intrinsic cytotoxicity, is effective at increasing glioblastoma uptake, and exhibits encouraging anticancer activity (Basso et al., 2021).

Diselenide loaded in NLCs were developed by Etxebeste-Mitxeltorena et al. to treat visceral leishmaniasis. In this work, Diselenide (2m), a trypanothione reductase inhibitor, was loaded in glyceryl palmitostearate and diethylene glycol monoethyl ether-based NLCs. They found that diselenide 2m-NLCs drastically enhanced its intestinal permeability and provided plasmatic levels higher than its effective concentration (IC_{50}). In *Leishmania infantum*-infected BALB/c mice, 2m-NLC reduced the parasite burden in the spleen, liver, and bone marrow by at least 95% after 5 doses (Etxebeste-Mitxeltorena et al., 2021).

SLNs can also be included in microspheres of appropriate size through a spray-drying technique. Gaspar et al. encapsulated SLNs containing rifabutin (pulmonary antibiotic) and tested their antimycobacterial activity in a murine model of infection with *Mycobacterium tuberculosis* (Gaspar et al., 2017). Moreover, tuberculosis was also treated using Bedaquiline encapsulation in SLNs and chitosan nanocapsules in a work performed by Matteis et al. The authors encapsulated this drug and found no cytotoxicity at the concentration needed to kill bacteria, (De Matteis et al., 2018), highlighting the great potential of this approach (Baranyai et al., 2021).

Another interesting application of SLNs was developed by Cervantes et al. to protect auditory cells from cisplatin-induced ototoxicity. SLNs were loaded with glucocorticoids (dexamethasone and hydrocortisone) and they were efficiently incorporated by auditory HEI-OC1. Their results showed that the encapsulation in SLNs increased the protective effect of low-doses of hydrocortisone and lengthened the survival of HEI-OC1 cells treated with cisplatin (Cervantes et al., 2019).

NLCs were also used to treat inflammatory bowel disease. Huguet-Casquero et al. loaded NLCs with polyphenol (antioxidant/antiinflammatory) oleuropein (OLE). NLC-OLE showed to be more effective in decreasing the TNF-α secretion and intracellular ROS by activated macrophages (J774) compared to the conventional form of OLE in a murine model (Huguet-Casquero et al., 2020)

Fernandez et al. developed a SLN to deliver N-iodomethyl-N, N-Dimethyl-N-(6,6-diphenylhex-5-en-1-yl) ammonium iodide (C6I). The SLNs were obtained by emulsion–solvent evaporation method. They were made of glycerol tripalmitate and glyceryl tristearate. They compared their performance with PLGA NPs. Although SLNs performed better than the free C6I, the SLNs were not capable of overcoming the performance of PLGA (Fernández et al., 2021).

Oligonucleotides are one of the biomolecules that reach their site of action less effectively. Thus, Fabregas et al. characterized the main physicochemical characteristics and binding capabilities of SLNs to oligonucleotides. They optimized the formulation of the NPs to efficiently transfect circular DNA and linear RNA molecules into cells (Fabregas et al., 2017). Gomez-Aguado et al. developed different SLNs by the combination of cationic and ionizable lipids, to deliver mRNA and pDNA. They evaluated their performance in human retinal pigment epithelial cells (ARPE-19) and human embryonic kidney cells (HEK-293). The results showed that SLNs containing only DOTAP (1,2-dioleoyl-3-trimethylammonium-propane) were the most promising formulations for nucleic acid delivery (Gomez-Aguado et al., 2020).

Similarly, Sanchez-Arribas et al. developed a strategy for siRNA delivery using cationic lipoplexes (Sanchez-Arribas et al., 2020a) enabling moderate to high gene lockdown levels. The authors also characterized the protein corona formed around these lipoplexes, that could have an influence on the silencing activity of these agents (Sanchez-Arribas et al., 2020b). Delivery of siRNAs was also performed by Suñé-Pou et al. The authors incorporated the

cholesterol derivative cholesteryl oleate to produce SLN–nucleic acid complexes with reduced cytotoxicity and more efficient cellular uptake. They found that intermediate concentrations of cholesteryl oleate exhibited good stability and spherical structures with no aggregation (Sune-Pou et al., 2018). Latorre J. et al. generated a LNP containing a siRNA with a chemically modified lipopolysaccharide-binding protein in order to reduce the levels of fat accumulated in the liver. The NPs showed to be effective *in vivo,* stressing the potential of this therapy against fatty liver disease (Latorre et al., 2022). In another work, Torrecillas et al. developed a SLN-based shRNA delivery system. This system was designed to downregulate metalloproteinase 9 (MMP-9), a proangiogenic factor, in corneal cells for the treatment of corneal neovascularization associated with inflammation. The non-viral vectors based on SLNs were able to downregulate the MMP-9 expression in HCE-2 cells via gene silencing, and, consequently, to inhibit cell migration and tube formation (Torrecilla et al., 2019).

Martinez-Negro et al. developed a multidisciplinary approach using a nanocarrier built with gemini-bolaamphiphilic hybrid lipids. This strategy resulted in a non-cytotoxic delivery of DNA plasmids in cellular models (Martinez-Negro et al., 2018). With the same goal, nanovesicles have proven to be effective carriers of miRNA in a recent work from Bloix et al. They engineered quatsomes, for the delivery of miRNAs and other small RNAs into the cytosol of tumor cells. The miRNAs delivered by this methodology were able to reach their target destination and thus providing a potential platform for the delivery of these molecules (Boloix et al., 2022).

LNPs have also been employed to cross the BBB to deliver drugs to the brain. Hernando et al. developed polyunsaturated fatty acids (PUFA)-based NLCs, namely, DHAH-NLC. The carriers were modulated with BBB-permeating compounds such as CS and trans-activating transcriptional activator (TAT) from HIV-1. They quantitatively assessed the permeability of DHAH-NLCs in endothelial cells (BMECs). Successfully, they reported that TAT-functionalized DHAH-NLCs successfully crossed the BBB in a cellular model (Hernando et al., 2022).

Improving ocular drug delivery is a milestone that can greatly impact the treatment of eye disorders. Varela-Fernandez et al. designed, developed and performed the physicochemical characterization of lactoferrin-loaded NLCs as a new therapeutic alternative for the keratoconus treatment. Based on the preclinical base obtained, they concluded that NLCs were stable, non-toxic and showed mucoadhesive properties (Varela-Fernandez et al., 2022). Vicente-Pascal et al. designed SLN-based eye drops as gene delivery system to induce the expression of interleukin 10 (IL-10). Two kinds of SLNs combined with different ligands (protamine, dextran, or hyaluronic acid) and formulated with polyvinyl alcohol (PVA) were prepared and tested in cellular and animal models. SLN-based vectors were capable of transfecting corneal epithelial cells. Animal model experiments show that IL-10 could reach even the endothelial layer (Vicente-Pascual et al., 2020; Gomez-Aguado et al., 2021).

To generate human keratinocyte primary cell cultures with potential in tissue engineering Chato-Astrain et al. developed EGF-loaded NLCs. After testing in skin keratinocytes and cornea epithelial cells, and in two epithelial cancer cell lines, gene expression analysis showed that the NLCs were able to increase EGFR gene expression (Chato-Astrain et al., 2021). Tomsen-Melero et al. investigated the potential of nanovesicles as carriers of α-galactosidase A, specifically quatsomes and hybrid liposomes. These structures provided improved colloidal stability in comparison to nanoliposomes and the conditions to preserve α-galactosidase A activity were also characterized, thus resulting in promising nanostructures for the delivery of this enzyme (Tomsen-Melero et al., 2021). In another study, MKC-Quatsomes formed by cholesterol and myristalkonium chloride were highly stable in different media and remained unaltered in human plasma for 24 h. After studying their biodistribution in a xenograft colorectal model they accumulated in tumors, liver, spleen, and kidneys (Vargas-Nadal et al., 2020). In fact, given their stability, they have also been used to efficiently incorporate different fluorophores (Ardizzone et al., 2018a), including diketopyrrolopyrroles, which promoted their photophysical properties and were used for imaging experiments in Saos-2 osteosarcoma cell line (Ardizzone et al., 2018b).

Pasto et al. prepared sodium colistimethate-loaded NLCs to treat respiratory infections (multiresistant *P. aeroginosa*). Biodistribution assessments showed a mild systemic absorption after nebulization and a notorious absorption after intramuscular route (Pastor et al., 2019).

4 Perspective

In this review, we aimed to provide an overview of the nanomedical research currently being performed in Spain. We organized the literature based on NP type and the most common materials employed in their preparation. There is a large number of researchers devoted to engineering NPs with nanomedical applications, and although here we have only focused on NPs with therapeutic applications, there is also a substantial amount of scientists engineering NPs for diagnostic purposes (Ortgies et al., 2016; Jornet-Martinez et al., 2019; Portela et al., 2020). Similarly, the thorough study of NPs and their properties is fundamental to future applications of these therapeutic agents. Here, we have reviewed a fraction of the work, due to space limitations, on the more popular nanoformulations and their therapeutic applications (Table 9). It is important to highlight the diverse applications of every type of NPs, that showcase the versatility of these nanomedical materials and their potential (Alfranca et al., 2016; Perez-Hernandez et al., 2017; Vallet-Regi, 2022).

Indubitably, one of the most explored abilities of NPs is their role as nanocarriers. In fact, in the last years the delivery function continues to improve, reaching a finely tuned controlled release that can be achieved through nanoformulation, and be sensitive to changes in the NPs' environment, i.e., temperature light, ultrasounds or pH (Xuan et al., 2018; Diez et al., 2021; Mayol et al., 2021; Aguilera-Correa et al., 2022a). Exquisitely controlled layer-by-layer design of NPs enables to control and achieve drug release with spatiotemporal resolution, improving currently available therapeutic options (Correa-Paz et al., 2019). In addition, targeting key pathological cells present in several diseases such as senescent cells through their high β-galactosidase activity was achieved through galacto-oligosaccharides encapsulated drugs, yielding a versatile strategy potentially effective for multiple pathologies (Munoz-Espin et al., 2018). This delivery function can be further improved with the combination of self-propelled materials, (Ramos-Docampo et al., 2019), or synergistic delivery of therapeutic agents as demonstrated by the delivery of siRNA and a

peptidic drug with remarkable potential against osteoporosis (Mora-Raimundo et al., 2019). The field however still shows important challenges ahead as highlighted in the aimed insulin oral delivery (Niu et al., 2018) that did not translate into an increased systemic absorption of insulin despite achieving a high retention in enterocytes.

The delivery of therapeutic agents and oligonucleotides based on polymeric nanocomplexes that stabilize and shield RNA analogs enabled the delivery of poly(I:C) to effectively treat several cancers. The preclinical data motivated clinical trials coordinated from Spain in which BO-112 was administered alone or in combinations treatments and performed in several hospitals with positive clinical benefits for some patients (Márquez-Rodas et al., 2022), (NCT: 02828098) (Therapeutics, 2016), (NCT: 05265650) (Clinica Universidad de Navarra UdN, 2022a), (NCT: 04570332) (Therapeutics, 2020). Interestingly, the same poly(I:C) agent in combination with polysaccharide based NPs has been employed for the development of another challenging therapeutic area: the creation of the HIV vaccine. Hyaluronic and chitosan NPs decorated with conserved HIV peptides as antigens and loaded with poly(I:C) yielded in a strong activation af antigen presenting cells (Dacoba et al., 2019).

Another clinical trial has its aim at evaluating antibiotic-containing alginate NPs for the treatment of *Pseudomonas aeruginosa* infection and biofilm formation in bronchiectasis patients. These type of NPs have shown to be efficient in treating pulmonary infections (Dhand, 2018).

Protein NPs also show promising characteristics for the delivery of insulin which yielded in clinical translation. Specifically the preclinical results obtained with Zein NPs has motivated the design of a clinical trial to verify in humans whether they could provide an efficient glycemic control in diabetic and obese patients through and orally administered therapeutic insulin derivative (NCT: 05560412) (Clinica Universidad de Navarra UdN, 2022b).

Regarding clinical applications, organic NPs and biodegradable MSNs have a competitive advantage over other metallic NPs. However, the remarkable properties that the metallic NPs have motivate their research for fighting complex diseases (Thompson et al., 2017). Thus, the combination of several cores in Janus–type NPs yields highly efficient conjugates that can not only combine complementary drugs or targeting agents but also synergistic effects simultaneously whith great potential to improve the treatment of several diseases (Lopez et al., 2017; Espinosa et al., 2020).

One of the hardest and more significant step in nanomedical development entails reaching clinical trials. This normally challenging road can have additional hurdles to achieve suitable nanoformulations. To translate nanomedicines into the clinic, multiple challenges should be taken into account to manufacture them under quality guidelines regulations (Foulkes et al., 2020). First, the results observed in research settings must be contextualized and standardized to prepare them for clinical translation. While small molecules are commonly evaluated for their efficacy, toxicity, and side effects, nanotherapies must also prove the biocompatibility for each of the components within the formulation. The use of specific nanomaterials for the development of personalized treatment requires in depth understanding of disease biology and the interaction between nanomaterials and the body. The potential of inorganic NPs in biomedicine is still in the preliminary stages of the clinic. Some important challenges in terms of biodistribution, pharmacokinetics, metabolism, biological barriers, safety, large-scale synthesis, patient heterogeneity or overall cost must be taken into account and optimized (Perez-Hernandez et al., 2017). In addition, several key parameters of the intrinsic NP-derived effects such as magnetic hyperthermia must be extensively studied and characterized to better understand its therapeutic operability and improve clinical translation (Beola et al., 2021; Luengo et al., 2022). On the objectives of the Spanish Scientific Network HIPERNANO stablished among different national groups was to consolidate the current scientific knowledge on hyperthermal therapies to enhance their practical implementation in clinical development (Spanish Scientific Network HiperNano, 2018). In addition, a key milestone was reached in 2022, where the first patient with pancreatic cancer was treated with magnetic hyperthermia in combination with the standard of care at Vall d'Hebron hospital (NoCanTher Project, 2022). This pilot study will guide future interventions and shed light on the steps needed to bring nanomedicines to the clinic. From this experience, it is worth highlighting that it is essential to involve multiple stakeholders, from scientists to clinicians, at every level (e.g., nanotherapy and clinical study design) from the beginning of the project to increase the success of this kind of study (Liz-Marzán et al., 2022). Furthermore collaborative nets and workshops such as NanomedSpain, Nanbiosis, Ciber-bbn and NanoSpain enable to promote collaborative studies with this goal.

Finally, while in this review we have only focused on the therapeutic role of NPs, there is another substantial part of nanomedicine that involves the diagnosis of diseases and in which an extensive amount of research groups in Spain are engaged. Both methods to diagnose *in vivo* (Ximendes et al., 2021), (Ximendes et al., 2017), (Pellico et al., 2021), (Santos et al., 2020) and *ex vivo* (Pelaez et al., 2018), (Litti et al., 2021), (Enshaei et al., 2021) enabled by several nanoformulations have revolutionized current medical practices and will continue to improve the crucial ability to diagnose diseases efficiently. In addition, the continuous effort of researchers to understand and exquisitely characterize the fate of NPs in biological system is a crucial foundation for all this work (Carregal-Romero et al., 2021; Areny-Balaguero et al., 2022).

Author contributions

VP, PF-G, CPA, and MC contributed to the concept and design of the manuscript. VP, PF-G, CPA, JAB, and CT-B contributed to the writing. BS, AS, ST, AE, GS, and MC critically revised the manuscript and contributed to the writing. All authors contributed to the article and approved the submitted version.

Funding

This work has been partially supported by MCIN/AEI /10.13039/501100011033 and European Union NextGenerationEU/PRTR (PID2021-128340OA-I00, PID2020-119352RB-I00, PID2021-127033OB-C21 and RTI2018-101050-J-I00), Comunidad de Madrid (S2022/BMD-7403 RENIM-CM and Talento program 2018-T1/IND-1005), European Union's Horizon 2020 research and innovation programme (grant agreement No 685795), la Caixa Foundation LCF/PR/HA21/52350003, Asociación Española Contra el Cáncer

IDEAS21989THOM, MCIN/AEI/10.13039/501100011033 and "ESF investing in your future" (RYC2019-027489-I, RYC2020-029282-I). CTB thanks Ministerio de Educación (FPU18/06310) for the predoctoral fellowship. IMDEA Nanociencia acknowledges support from the 'Severo Ochoa' Programme for Centers of Excellence in R&D (MINECO, CEX2020-001039-S).

Acknowledgments

The authors want to thank Prof. Dr. S. Ortega-Gutierrez and Prof. Dr. M. L. López-Rodríguez for the inspiration to start this review. Due to space restrictions, we made a selection of publications to be discussed in this review; we apologize to all of our colleagues whose work has not been cited here.

Conflict of interest

The authors declare that the research was conducted in the absence of any commercial or financial relationships that could be construed as a potential conflict of interest.

Publisher's note

All claims expressed in this article are solely those of the authors and do not necessarily represent those of their affiliated organizations, or those of the publisher, the editors and the reviewers. Any product that may be evaluated in this article, or claim that may be made by its manufacturer, is not guaranteed or endorsed by the publisher.

References

Aguilera-Correa, J. J., Garcia-Alvarez, R., Mediero, A., Esteban, J., and Vallet-Regi, M. (2022). Effect of gold nanostars plus amikacin against carbapenem-resistant *Klebsiella pneumoniae* biofilms. *Biol. (Basel).* 11 (2), 162. doi:10.3390/biology11020162

Aguilera-Correa, J. J., Gisbert-Garzaran, M., Mediero, A., Fernandez-Acenero, M. J., de-Pablo-Velasco, D., Lozano, D., et al. (2022). Antibiotic delivery from bone-targeted mesoporous silica nanoparticles for the treatment of osteomyelitis caused by methicillin-resistant *Staphylococcus aureus*. *Acta Biomater.* 154, 608–625. doi:10.1016/j.actbio.2022.10.039

Aguilera-Garrido, A., Arranz, E., Galvez-Ruiz, M. J., Marchal, J. A., Galisteo-Gonzalez, F., and Giblin, L. (2022). Solid lipid nanoparticles to improve bioaccessibility and permeability of orally administered maslinic acid. *Drug Deliv.* 29 (1), 1971–1982. doi:10.1080/10717544.2022.2086937

Ahamed, M., Alsalhi, M. S., and Siddiqui, M. K. (2010). Silver nanoparticle applications and human health. *Clin. Chim. Acta* 411 (23-24), 1841–1848. doi:10.1016/j.cca.2010.08.016

Ahijado-Guzman, R., Sanchez-Arribas, N., Martinez-Negro, M., Gonzalez-Rubio, G., Santiago-Varela, M., Pardo, M., et al. (2020). Intercellular trafficking of gold nanostars in uveal melanoma cells for plasmonic photothermal therapy. *Nanomater. (Basel).* 10 (3), 590. doi:10.3390/nano10030590

Aires, A., Cadenas, J. F., Guantes, R., and Cortajarena, A. L. (2017). An experimental and computational framework for engineering multifunctional nanoparticles: Designing selective anticancer therapies. *Nanoscale* 9 (36), 13760–13771. doi:10.1039/c7nr04475e

Alfranca, G., Artiga, A., Stepien, G., Moros, M., Mitchell, S. G., and de la Fuente, J. M. (2016). Gold nanoprism-nanorod face off: Comparing the heating efficiency, cellular internalization and thermoablation capacity. *Nanomedicine (Lond).* 11 (22), 2903–2916. doi:10.2217/nnm-2016-0257

Alfranca, G., Beola, L., Liu, Y., Gutierrez, L., Zhang, A., Artiga, A., et al. (2019). *In vivo* comparison of the biodistribution and long-term fate of colloids - gold nanoprisms and nanorods - with minimum surface modification. *Nanomedicine (Lond).* 14 (23), 3035–3055. doi:10.2217/nnm-2019-0253

Alipour, M., Baneshi, M., Hosseinkhani, S., Mahmoudi, R., Jabari Arabzadeh, A., Akrami, M., et al. (2020). Recent progress in biomedical applications of RGD-based ligand: From precise cancer theranostics to biomaterial engineering: A systematic review. *J. Biomed. Mater Res. A* 108 (4), 839–850. doi:10.1002/jbm.a.36862

Alvear-Jimenez, A., Zabala Gutierrez, I., Shen, Y., Villaverde, G., Lozano-Chamizo, L., Guardia, P., et al. (2022). Electrospraying as a technique for the controlled synthesis of biocompatible PLGA@Ag2S and PLGA@Ag2S@SPION nanocarriers with drug release capability. *Pharmaceutics* 14 (1), 214. doi:10.3390/pharmaceutics14010214

Ambrosone, A., Matteis, L., Serrano-Sevilla, I., Tortiglione, C., and De La Fuente, J. M. (2020). Glycogen synthase kinase 3β inhibitor delivered by chitosan nanocapsules promotes safe, fast, and efficient activation of Wnt signaling *in vivo*. *ACS Biomater. Sci. Eng.* 6 (5), 2893–2903. doi:10.1021/acsbiomaterials.9b01820

Amendola, V., Pilot, R., Frasconi, M., Marago, O. M., and Iati, M. A. (2017). Surface plasmon resonance in gold nanoparticles: A review. *J. Phys. Condens Matter* 29 (20), 203002. doi:10.1088/1361-648x/aa60f3

Arana, L., Bayon-Cordero, L., Sarasola, L. I., Berasategi, M., Ruiz, S., and Alkorta, I. (2019). Solid lipid nanoparticles surface modification modulates cell internalization and improves chemotoxic treatment in an oral carcinoma cell line. *Nanomater. (Basel)* 9 (3), 464. doi:10.3390/nano9030464

Arcos, D., Gomez-Cerezo, N., Saiz-Pardo, M., de Pablo, D., Ortega, L., Enciso, S., et al. (2022). Injectable mesoporous bioactive nanoparticles regenerate bone tissue under osteoporosis conditions. *Acta Biomater.* 151, 501–511. doi:10.1016/j.actbio.2022.07.067

Ardizzone, A., Blasi, D., Vona, D., Rosspeintner, A., Punzi, A., Altamura, E., et al. (2018). Highly stable and red-emitting nanovesicles incorporating lipophilic diketopyrrolopyrroles for cell imaging. *Chemistry* 24 (44), 11386–11392. doi:10.1002/chem.201801444

Ardizzone, A., Kurhuzenkau, S., Illa-Tuset, S., Faraudo, J., Bondar, M., Hagan, D., et al. (2018). Nanostructuring lipophilic dyes in water using stable Vesicles, quatsomes, as scaffolds and their use as probes for bioimaging. *Small* 14 (16), e1703851. doi:10.1002/smll.201703851

Arenas-Vivo, A., Amariei, G., Aguado, S., Rosal, R., and Horcajada, P. (2019). An Ag-loaded photoactive nano-metal organic framework as a promising biofilm treatment. *Acta Biomater.* 97, 490–500. doi:10.1016/j.actbio.2019.08.011

Areny-Balaguero, A., Mekseriwattana, W., Camprubi-Rimblas, M., Stephany, A., Roldan, A., Sole-Porta, A., et al. (2022). Fluorescent PLGA nanocarriers for pulmonary administration: Influence of the surface charge. *Pharmaceutics* 14 (7), 1447. doi:10.3390/pharmaceutics14071447

Ariza-Saenz, M., Espina, M., Bolanos, N., Calpena, A. C., Gomara, M. J., Haro, I., et al. (2017). Penetration of polymeric nanoparticles loaded with an HIV-1 inhibitor peptide derived from GB virus C in a vaginal mucosa model. *Eur. J. Pharm. Biopharm.* 120, 98–106. doi:10.1016/j.ejpb.2017.08.008

Ariza-Saenz, M., Espina, M., Calpena, A., Gomara, M. J., Perez-Pomeda, I., Haro, I., et al. (2018). Design, characterization, and biopharmaceutical behavior of nanoparticles loaded with an HIV-1 fusion inhibitor peptide. *Mol. Pharm.* 15 (11), 5005–5018. doi:10.1021/acs.molpharmaceut.8b00609

Arriortua, O. K., Insausti, M., Lezama, L., Gil de Muro, I., Garaio, E., de la Fuente, J. M., et al. (2018). RGD-Functionalized Fe3O4 nanoparticles for magnetic hyperthermia. *Colloids Surf. B Biointerfaces* 165, 315–324. doi:10.1016/j.colsurfb.2018.02.031

Arroyo-Crespo, J. J., Arminan, A., Charbonnier, D., Balzano-Nogueira, L., Huertas-Lopez, F., Marti, C., et al. (2018). Tumor microenvironment-targeted poly-L-glutamic acid-based combination conjugate for enhanced triple negative breast cancer treatment. *Biomaterials* 186, 8–21. doi:10.1016/j.biomaterials.2018.09.023

Artiga, A., Garcia-Embid, S., De Matteis, L., Mitchell, S. G., and de la Fuente, J. M. (2018). Effective *in vitro* photokilling by cell-adhesive gold nanorods. *Front. Chem.* 6, 234. doi:10.3389/fchem.2018.00234

Astorga-Gamaza, A., Vitali, M., Borrajo, M. L., Suarez-Lopez, R., Jaime, C., Bastus, N., et al. (2021). Antibody cooperative adsorption onto AuNPs and its exploitation to force natural killer cells to kill HIV-infected T cells. *Nano Today* 36, 101056. doi:10.1016/j.nantod.2020.101056

Aznar, M. A., Planelles, L., Perez-Olivares, M., Molina, C., Garasa, S., Etxeberria, I., et al. (2019). Immunotherapeutic effects of intratumoral nanoplexed poly I:C. *J. Immunother. Cancer* 7 (1), 116. doi:10.1186/s40425-019-0568-2

Baranyai, Z., Soria-Carrera, H., Alleva, M., Millán-Placer, A. C., Lucía, A., Martín-Rapún, R., et al. (2021). Nanotechnology-based targeted drug delivery: An emerging tool to overcome tuberculosis. *Adv. Ther.* 4 (1), 2000113. doi:10.1002/adtp.202000113

Barbero, F., Michelini, S., Moriones, O. H., Patarroyo, J., Rosell, J., Gusta, M. F., et al. (2022). Role of common cell culture media supplements on citrate-stabilized gold nanoparticle protein corona formation, aggregation state, and the consequent impact on

cellular uptake. *Bioconjug Chem.* 33 (8), 1505–1514. doi:10.1021/acs.bioconjchem.2c00232

Barbero, F., Moriones, O. H., Bastus, N. G., and Puntes, V. (2019). Dynamic equilibrium in the cetyltrimethylammonium bromide-Au nanoparticle bilayer, and the consequent impact on the formation of the nanoparticle protein corona. *Bioconjug Chem.* 30 (11), 2917–2930. doi:10.1021/acs.bioconjchem.9b00624

Barbero, F., Russo, L., Vitali, M., Piella, J., Salvo, I., Borrajo, M. L., et al. (2017). formation of the protein corona: The interface between nanoparticles and the immune system. *Semin. Immunol.* 34, 52–60. doi:10.1016/j.smim.2017.10.001

Barbosa, S., Agrawal, A., Rodriguez-Lorenzo, L., Pastoriza-Santos, I., Alvarez-Puebla, R. A., Kornowski, A., et al. (2010). Tuning size and sensing properties in colloidal gold nanostars. *Langmuir* 26 (18), 14943–14950. doi:10.1021/la102559e

Bass, H., Moore, J. L., and Coakley, W. T. (1978). Lethality in mammalian cells due to hyperthermia under oxic and hypoxic conditions. *Int. J. Radiat. Biol. Relat. Stud. Phys. Chem. Med.* 33 (1), 57–67. doi:10.1080/09553007714551491

Basso, J., Mendes, M., Silva, J., Cova, T., Luque-Michel, E., Jorge, A. F., et al. (2021). Sorting hidden patterns in nanoparticle performance for glioblastoma using machine learning algorithms. *Int. J. Pharm.* 592, 120095. doi:10.1016/j.ijpharm.2020.120095

Becerril-Castro, I. B., Calderon, I., Pazos-Perez, L., Guerrini, F., Schulz, N., Feliu, I., et al. (2022). Gold nanostars: Synthesis, optical and SERS analytical properties. *Anal. Sens.* 2, e202200005. doi:10.1002/anse.202200005

Beola, L., Asin, L., Fratila, R. M., Herrero, V., de la Fuente, J. M., Grazu, V., et al. (2018). Dual role of magnetic nanoparticles as intracellular hotspots and extracellular matrix disruptors triggered by magnetic hyperthermia in 3D cell culture models. *ACS Appl. Mater Interfaces* 10 (51), 44301–44313. doi:10.1021/acsami.8b18270

Beola, L., Asin, L., Roma-Rodrigues, C., Fernandez-Afonso, Y., Fratila, R. M., Serantes, D., et al. (2020). The intracellular number of magnetic nanoparticles modulates the apoptotic death pathway after magnetic hyperthermia treatment. *ACS Appl. Mater Interfaces* 12 (39), 43474–43487. doi:10.1021/acsami.0c12900

Beola, L., Grazu, V., Fernandez-Afonso, Y., Fratila, R. M., de Las Heras, M., de la Fuente, J. M., et al. (2021). Critical parameters to improve pancreatic cancer treatment using magnetic hyperthermia: Field conditions, immune response, and particle biodistribution. *ACS Appl. Mater Interfaces* 13 (11), 12982–12996. doi:10.1021/acsami.1c02338

Bernardos, A., Piacenza, E., Sancenon, F., Hamidi, M., Maleki, A., Turner, R. J., et al. (2019). Mesoporous silica-based materials with bactericidal properties. *Small* 15 (24), e1900669. doi:10.1002/smll.201900669

Boloix, A., Feiner-Gracia, N., Kober, M., Repetto, J., Pascarella, R., Soriano, A., et al. (2022). Engineering pH-sensitive stable nanovesicles for delivery of MicroRNA therapeutics. *Small* 18 (3), e2101959. doi:10.1002/smll.202101959

Bonet-Aleta, J., Encinas-Gimenez, M., Urriolabeitia, E., Martin-Duque, P., Hueso, J. L., and Santamaria, J. (2022). Unveiling the interplay between homogeneous and heterogeneous catalytic mechanisms in copper-iron nanoparticles working under chemically relevant tumour conditions. *Chem. Sci.* 13 (28), 8307–8320. doi:10.1039/d2sc01379g

Bonet-Aleta, J., Sancho-Albero, M., Calzada-Funes, J., Irusta, S., Martin-Duque, P., Hueso, J. L., et al. (2022). Glutathione-Triggered catalytic response of Copper-Iron mixed oxide Nanoparticles. Leveraging tumor microenvironment conditions for chemodynamic therapy. *J. Colloid Interface Sci.* 617, 704–717. doi:10.1016/j.jcis.2022.03.036

Borzenkov, M., Pallavicini, P., and Chirico, G. (2019). Photothermally active inorganic nanoparticles: From colloidal solutions to photothermally active printed surfaces and polymeric nanocomposite materials. *Eur. J. Inorg. Chem.* 2019 (41), 4397–4404. doi:10.1002/ejic.201900836

Cabrera, D., Coene, A., Leliaert, J., Artes-Ibanez, E. J., Dupre, L., Telling, N. D., et al. (2018). Dynamical magnetic response of iron oxide nanoparticles inside live cells. *ACS Nano* 12 (3), 2741–2752. doi:10.1021/acsnano.7b08995

Cacicedo, M. L., Islan, G. A., Leon, I. E., Alvarez, V. A., Chourpa, I., Allard-Vannier, E., et al. (2018). Bacterial cellulose hydrogel loaded with lipid nanoparticles for localized cancer treatment. *Colloids Surf. B Biointerfaces* 170, 596–608. doi:10.1016/j.colsurfb.2018.06.056

Cadete, A., Olivera, A., Besev, M., Dhal, P. K., Goncalves, L., Almeida, A. J., et al. (2019). Self-assembled hyaluronan nanocapsules for the intracellular delivery of anticancer drugs. *Sci. Rep.* 9 (1), 11565. doi:10.1038/s41598-019-47995-8

Carrillo-Carrion, C., Martinez, R., Navarro Poupard, M. F., Pelaz, B., Polo, E., Arenas-Vivo, A., et al. (2019). Aqueous stable gold nanostar/ZIF-8 nanocomposites for light-triggered release of active cargo inside living cells. *Angew. Chem. Int. Ed. Engl.* 58 (21), 7078–7082. doi:10.1002/anie.201902817

Casadome-Perales, A., Matteis, L., Alleva, M., Infantes-Rodriguez, C., Palomares-Perez, I., Saito, T., et al. (2019). Inhibition of p38 MAPK in the brain through nasal administration of p38 inhibitor loaded in chitosan nanocapsules. *Nanomedicine (Lond)* 14 (18), 2409–2422. doi:10.2217/nnm-2018-0496

Casarrubios, L., Gomez-Cerezo, N., Feito, M. J., Vallet-Regi, M., Arcos, D., and Portoles, M. T. (2020). Ipriflavone-loaded mesoporous nanospheres with potential applications for periodontal treatment. *Nanomater. (Basel)* 10 (12), 2573. doi:10.3390/nano10122573

Casarrubios, L., Polo-Montalvo, A., Serrano, M. C., Feito, M. J., Vallet-Regi, M., Arcos, D., et al. (2021). Effects of ipriflavone-loaded mesoporous nanospheres on the differentiation of endothelial progenitor cells and their modulation by macrophages. *Nanomater. (Basel)* 11 (5), 1102. doi:10.3390/nano11051102

Cervantes, B., Arana, L., Murillo-Cuesta, S., Bruno, M., Alkorta, I., and Varela-Nieto, I. (2019). Solid lipid nanoparticles loaded with glucocorticoids protect auditory cells from cisplatin-induced ototoxicity. *J. Clin. Med.* 8 (9), 1464. doi:10.3390/jcm8091464

Chato-Astrain, J., Sanchez-Porras, D., Garcia-Garcia, O. D., Vairo, C., Villar-Vidal, M., Villullas, S., et al. (2021). Improvement of cell culture methods for the successful generation of human keratinocyte primary cell cultures using EGF-loaded nanostructured lipid carriers. *Biomedicines* 9 (11), 1634. doi:10.3390/biomedicines9111634

Chin, K. C., Chong, G. L., Poh, C. K., Van, L. H., Sow, C. H., Lin, J., et al. (2007). Large-scale synthesis of Fe3O4 nanosheets at low temperature. *J. Phys. Chem. C* 111 (26), 9136–9141. doi:10.1021/jp070873g

Christou, E., Pearson, J. R., Beltran, A. M., Fernandez-Afonso, Y., Gutierrez, L., de la Fuente, J. M., et al. (2022). Iron-gold nanoflowers: A promising tool for multimodal imaging and hyperthermia therapy. *Pharmaceutics* 14 (3), 636. doi:10.3390/pharmaceutics14030636

Clinica Universidad de Navarra UdN (2022a). Study of BO-112 with radiotherapy and nivolumab for metastatic refractory NSCLC (noelia) clinicaltrials.gov2022. Available from: https://clinicaltrials.gov/ct2/show/NCT05265650?term=BO-112&draw=2&rank=1.

Clinica Universidad de Navarra UdN (2022b). Zein nanoparticles for glycemic control (GLUCOCAPS) clinicaltrials.gov2022. Available from: https://clinicaltrials.gov/ct2/show/NCT05560412?term=zein&cntry=ES&draw=2&rank=1.

Colilla, M., and Vallet-Regi, M. (2020). Targeted stimuli-responsive mesoporous silica nanoparticles for bacterial infection treatment. *Int. J. Mol. Sci.* 21 (22), 8605. doi:10.3390/ijms21228605

Cordeiro, A. S., Crecente-Campo, J., Bouzo, B. L., Gonzalez, S. F., de la Fuente, M., and Alonso, M. J. (2019). Engineering polymeric nanocapsules for an efficient drainage and biodistribution in the lymphatic system. *J. Drug Target* 27 (5-6), 646–658. doi:10.1080/1061186x.2018.1561886

Correa-Paz, C., Navarro Poupard, M. F., Polo, E., Rodriguez-Perez, M., Taboada, P., Iglesias-Rey, R., et al. (2019). *In vivo* ultrasound-activated delivery of recombinant tissue plasminogen activator from the cavity of sub-micrometric capsules. *J. Control Release* 308, 162–171. doi:10.1016/j.jconrel.2019.07.017

Crecente-Campo, J., Virgilio, T., Morone, D., Calvino-Sampedro, C., Fernandez-Marino, I., Olivera, A., et al. (2019). Design of polymeric nanocapsules to improve their lympho-targeting capacity. *Nanomedicine (Lond).* 14 (23), 3013–3033. doi:10.2217/nnm-2019-0206

Dacoba, T. G., Anfray, C., Mainini, F., Allavena, P., Alonso, M. J., Torres Andon, F., et al. (2020). Arginine-based poly(I:C)-Loaded nanocomplexes for the polarization of macrophages toward M1-antitumoral effectors. *Front. Immunol.* 11, 1412. doi:10.3389/fimmu.2020.01412

Dacoba, T. G., Olivera, A., Torres, D., Crecente-Campo, J., and Alonso, M. J. (2017). Modulating the immune system through nanotechnology. *Semin. Immunol.* 34, 78–102. doi:10.1016/j.smim.2017.09.007

Dacoba, T. G., Omange, R. W., Li, H., Crecente-Campo, J., Luo, M., and Alonso, M. J. (2019). Polysaccharide nanoparticles can efficiently modulate the immune response against an HIV peptide antigen. *ACS Nano* 13 (5), 4947–4959. doi:10.1021/acsnano.8b07662

Dacoba, T. G., Ruiz-Gaton, L., Benito, A., Klein, M., Dupin, D., Luo, M., et al. (2020). Technological challenges in the preclinical development of an HIV nanovaccine candidate. *Drug Deliv. Transl. Res.* 10 (3), 621–634. doi:10.1007/s13346-020-00721-8

de la Presa, P., Luengo, Y., Multigner, M., Costo, R., Morales, M. P., Rivero, G., et al. (2012). Study of heating efficiency as a function of concentration, size, and applied field in γ-Fe2O3 nanoparticles. *J. Phys. Chem. C* 116 (48), 25602–25610. doi:10.1021/jp310771p

De Luca, R., Profita, G., and Cicero, G. (2019). <p>Nab-paclitaxel in pretreated metastatic breast cancer: Evaluation of activity, safety, and quality of life</p>. *Onco Targets Ther.* 12, 1621–1627. doi:10.2147/ott.s191519

De Matteis, L., Jary, D., Lucía, A., García-Embid, S., Serrano-Sevilla, I., Pérez, D., et al. (2018). New active formulations against *M. tuberculosis*: Bedaquiline encapsulation in lipid nanoparticles and chitosan nanocapsules. *Chem. Eng. J.* 340, 181–191. doi:10.1016/j.cej.2017.12.110

DeDiego, M. L., Portilla, Y., Daviu, N., Lopez-Garcia, D., Villamayor, L., Mulens-Arias, V., et al. (2022). Iron oxide and iron oxyhydroxide nanoparticles impair SARS-CoV-2 infection of cultured cells. *J. Nanobiotechnology* 20 (1), 352. doi:10.1186/s12951-022-01542-2

Del Sol-Fernandez, S., Portilla-Tundidor, Y., Gutierrez, L., Odio, O. F., Reguera, E., Barber, D. F., et al. (2019). Flower-like Mn-doped magnetic nanoparticles functionalized with $\alpha_v\beta_3$-integrin-ligand to efficiently induce intracellular heat after

alternating magnetic field exposition, triggering glioma cell death. *ACS Appl. Mater Interfaces* 11 (30), 26648–26663. doi:10.1021/acsami.9b08318

Dhand, R. (2018). The rationale and evidence for use of inhaled antibiotics to control *Pseudomonas aeruginosa* infection in non-cystic fibrosis Bronchiectasis. *J. Aerosol Med. Pulm. Drug Deliv.* 31 (3), 121–138. doi:10.1089/jamp.2017.1415

Dhiman, N., Awasthi, R., Sharma, B., Kharkwal, H., and Kulkarni, G. T. (2021). Lipid nanoparticles as carriers for bioactive delivery. *Front. Chem.* 9, 580118. doi:10.3389/fchem.2021.580118

Diego-Gonzalez, L., Crecente-Campo, J., Paul, M. J., Singh, M., Reljic, R., Alonso, M. J., et al. (2020). Design of polymeric nanocapsules for intranasal vaccination against Mycobacterium tuberculosis: Influence of the polymeric shell and antigen positioning. *Pharmaceutics* 12 (6), 489. doi:10.3390/pharmaceutics12060489

Diez, P., Lucena-Sanchez, E., Escudero, A., Llopis-Lorente, A., Villalonga, R., and Martinez-Manez, R. (2021). Ultrafast directional Janus Pt-mesoporous silica nanomotors for smart drug delivery. *ACS Nano* 15 (3), 4467–4480. doi:10.1021/acsnano.0c08404

Di Silvio, D., Silvestri, A., Lay, L., Polito, L., and Moya, S. E. (2018). Impact of concanavalinA affinity in the intracellular fate of protein corona on Glucosamine Au nanoparticles. *Scientific Reports* 8 (1), 9046. doi:10.1038/s41598-018-27418-w

Do, T. T. A., Grijalvo, S., Imae, T., Garcia-Celma, M. J., and Rodriguez-Abreu, C. (2021). A nanocellulose-based platform towards targeted chemo-photodynamic/photothermal cancer therapy. *Carbohydr. Polym.* 270, 118366. doi:10.1016/j.carbpol.2021.118366

Dolai, J., Mandal, K., and Jana, N. R. (2021). Nanoparticle size effects in biomedical applications. *ACS Appl. Nano Mater.* 4 (7), 6471–6496. doi:10.1021/acsanm.1c00987

Dosil, S. G., Lopez-Cobo, S., Rodriguez-Galan, A., Fernandez-Delgado, I., et al. (2022). Natural killer (NK) cell-derived extracellular-vesicle shuttled microRNAs control T cell responses. *Elife* 11, e76319. doi:10.7554/elife.76319

Duro-Castano, A., Borras, C., Herranz-Perez, V., Blanco-Gandia, M. C., Conejos-Sanchez, I., Arminan, A., et al. (2021). Targeting Alzheimer's disease with multimodal polypeptide-based nanoconjugates. *Sci. Adv.* 7 (13), eabf9180. doi:10.1126/sciadv.abf9180

Duro-Castano, A., Sousa-Herves, A., Arminan, A., Charbonnier, D., Arroyo-Crespo, J. J., Wedepohl, S., et al. (2021). Polyglutamic acid-based crosslinked doxorubicin nanogels as an anti-metastatic treatment for triple negative breast cancer. *J. Control Release* 332, 10–20. doi:10.1016/j.jconrel.2021.02.005

Elming, P. B., Sorensen, B. S., Oei, A. L., Franken, N. A. P., Crezee, J., Overgaard, J., et al. (2019). Hyperthermia: The optimal treatment to overcome radiation resistant hypoxia. *Cancers (Basel)* 11 (1), 60. doi:10.3390/cancers11010060

Elsabahy, M., and Wooley, K. L. (2012). Design of polymeric nanoparticles for biomedical delivery applications. *Chem. Soc. Rev.* 41 (7), 2545–2561. doi:10.1039/c2cs15327k

Encinas-Basurto, D., Ibarra, J., Juarez, J., Pardo, A., Barbosa, S., Taboada, P., et al. (2018). Hybrid folic acid-conjugated gold nanorods-loaded human serum albumin nanoparticles for simultaneous photothermal and chemotherapeutic therapy. *Mater Sci. Eng. C Mater Biol. Appl.* 91, 669–678. doi:10.1016/j.msec.2018.06.002

Encinas-Basurto, D., Juarez, J., Valdez, M. A., Burboa, M. G., Barbosa, S., and Taboada, P. (2018). Targeted drug delivery via human epidermal growth factor receptor for sustained release of allyl isothiocyanate. *Curr. Top. Med. Chem.* 18 (14), 1252–1260. doi:10.2174/1568026618666180810150113

Enshaei, H., Puiggali-Jou, A., Del Valle, L. J., Turon, P., Saperas, N., and Aleman, C. (2021). Nanotheranostic interface based on antibiotic-loaded conducting polymer nanoparticles for real-time monitoring of bacterial growth inhibition. *Adv. Healthc. Mater* 10 (7), e2001636. doi:10.1002/adhm.202001636

Escudero-Duch, C., Martin-Saavedra, F., Prieto, M., Sanchez-Casanova, S., Lopez, D., Sebastian, V., et al. (2019). Gold nanoparticles for the *in situ* polymerization of near-infrared responsive hydrogels based on fibrin. *Acta Biomater.* 100, 306–315. doi:10.1016/j.actbio.2019.09.040

Espinosa, A., Castro, G. R., Reguera, J., Castellano, C., Castillo, J., Camarero, J., et al. (2021). Photoactivated nanoscale temperature gradient detection using X-ray absorption spectroscopy as a direct nanothermometry method. *Nano Lett.* 21 (1), 769–777. doi:10.1021/acs.nanolett.0c04477

Espinosa, A., Reguera, J., Curcio, A., Munoz-Noval, A., Kuttner, C., Van de Walle, A., et al. (2020). Janus magnetic-plasmonic nanoparticles for magnetically guided and thermally activated cancer therapy. *Small* 16 (11), e1904960. doi:10.1002/smll.201904960

Espinosa, A., Silva, A. K., Sanchez-Iglesias, A., Grzelczak, M., Pechoux, C., Desboeufs, K., et al. (2016). Cancer cell internalization of gold nanostars impacts their photothermal efficiency *in vitro* and *in vivo*: Toward a plasmonic thermal fingerprint in tumoral environment. *Adv. Healthc. Mater* 5 (9), 1040–1048. doi:10.1002/adhm.201501035

Espinosa-Cano, E., Aguilar, M. R., Portilla, Y., Barber, D. F., and San Roman, J. (2020). Anti-inflammatory polymeric nanoparticles based on ketoprofen and dexamethasone. *Pharmaceutics* 12 (8), 723. doi:10.3390/pharmaceutics12080723

Espinosa-Cano, E., Aguilar, M. R., Portilla, Y., Barber, D. F., and San Roman, J. (2020). Polymeric nanoparticles that combine dexamethasone and naproxen for the synergistic inhibition of Il12b transcription in macrophages. *Macromol. Biosci.* 20 (7), e2000002. doi:10.1002/mabi.202000002

Etchenausia, L., Villar-Alvarez, E., Forcada, J., Save, M., and Taboada, P. (2019). Evaluation of cationic core-shell thermoresponsive poly(N-vinylcaprolactam)-based microgels as potential drug delivery nanocarriers. *Mater Sci. Eng. C Mater Biol. Appl.* 104, 109871. doi:10.1016/j.msec.2019.109871

Etxebeste-Mitxeltorena, M., Moreno, E., Carvalheiro, M., Calvo, A., Navarro-Blasco, I., Gonzalez-Penas, E., et al. (2021). Oral efficacy of a diselenide compound loaded in nanostructured lipid carriers in a murine model of visceral leishmaniasis. *ACS Infect. Dis.* 7 (12), 3197–3209. doi:10.1021/acsinfecdis.1c00394

Fabregas, A., Prieto-Sanchez, S., Sune-Pou, M., Boyero-Corral, S., Tico, J. R., Garcia-Montoya, E., et al. (2017). Improved formulation of cationic solid lipid nanoparticles displays cellular uptake and biological activity of nucleic acids. *Int. J. Pharm.* 516 (1-2), 39–44. doi:10.1016/j.ijpharm.2016.11.026

Fabrizio, E. D., Schlücker, S., Wenger, J., Regmi, R., Rigneault, H., Calafiore, G., et al. (2016). Roadmap on biosensing and photonics with advanced nano-optical methods. *J. Opt.* 18 (6), 063003. doi:10.1088/2040-8978/18/6/063003

Falgas, A., Pallares, V., Serna, N., Sanchez-Garcia, L., Sierra, J., Gallardo, A., et al. (2020). Selective delivery of T22-PE24-H6 to CXCR4(+) diffuse large B-cell lymphoma cells leads to wide therapeutic index in a disseminated mouse model. *Theranostics* 10 (12), 5169–5180. doi:10.7150/thno.43231

Fernández, M., Holgado, M. Á., Cayero-Otero, M. D., Pineda, T., Yepes, L. M., Gaspar, D. P., et al. (2021). Improved antileishmanial activity and cytotoxicity of a novel nanotherapy for N-iodomethyl-N,N-dimethyl-N-(6,6-diphenylhex-5-en-1-yl)ammonium iodide. *J. Drug Deliv. Sci. Technol.* 61, 101988. doi:10.1016/j.jddst.2020.101988

Fernandez, Y., Movellan, J., Foradada, L., Gimenez, V., Garcia-Aranda, N., Mancilla, S., et al. (2022). *In vivo* antitumor and antimetastatic efficacy of a polyacetal-based paclitaxel conjugate for prostate cancer therapy. *Adv. Healthc. Mater* 11 (7), e2101544. doi:10.1002/adhm.202101544

Fornaguera, C., Diaz-Caballero, M., Garcia-Fernandez, C., Olmo, L., Stampa-Lopez Pinto, M., Navalon-Lopez, M., et al. (2021). Synthesis and characterization of mRNA-loaded poly(beta aminoesters) nanoparticles for vaccination purposes. *J. Vis. Exp.* 2021, 174.

Foulkes, R., Man, E., Thind, J., Yeung, S., Joy, A., and Hoskins, C. (2020). The regulation of nanomaterials and nanomedicines for clinical application: Current and future perspectives. *Biomater. Sci.* 8 (17), 4653–4664. doi:10.1039/d0bm00558d

Qu, N., Luo, Z., Zhao, S., and Liu, B. (2021). Frame-guided synthesis of polymeric colloidal discs. *J. Am. Chem. Soc.* 143 (4), 1790–1797. doi:10.1021/jacs.0c08627

Fleury, J. B., Werner, M., Guével, X. L., and Baulin, V. A. (2021). Protein corona modulates interaction of spiky nanoparticles with lipid bilayers. *Journal of Colloid and Interface Science* 603, 550–558. doi:10.1016/j.jcis.2021.06.047

Fratila, R. M., and de la Fuente, J. M. (2019). "Introduction to hyperthermia," in *Nanomaterials for magnetic and optical hyperthermia applications*. Editors R. M. Fratila and J. M. De La Fuente (Elsevier), 1–10.

Frigaard, J., Jensen, J. L., Galtung, H. K., and Hiorth, M. (2022). The potential of chitosan in nanomedicine: An overview of the cytotoxicity of chitosan based nanoparticles. *Front. Pharmacol.* 13, 880377. doi:10.3389/fphar.2022.880377

Fuentes-García, J. A. C. A, A., de Castro, C. E., Giacomelli, F. C., Ibarra, M. R., Bonvent, J., Fabián Goya, G., et al. (2021). Sonochemical route for mesoporous silica-coated magnetic nanoparticles towards pH-triggered drug delivery system. *J. Mater Res. Technol.* 15, 52–67. doi:10.1016/j.jmrt.2021.08.014

Galindo, R., Sanchez-Lopez, E., Gomara, M. J., Espina, M., Ettcheto, M., Cano, A., et al. (2022). Development of peptide targeted PLGA-PEGylated nanoparticles loading licochalcone-A for ocular inflammation. *Pharmaceutics* 14 (2), 285. doi:10.3390/pharmaceutics14020285

Gallego-Lleyda, A., De Miguel, D., Anel, A., and Martinez-Lostao, L. (2018). Lipid nanoparticles decorated with TNF-related aptosis-inducing ligand (TRAIL) are more cytotoxic than soluble recombinant TRAIL in sarcoma. *Int. J. Mol. Sci.* 19 (5), 1449. doi:10.3390/ijms19051449

Gallego-Yerga, L., Benito, J. M., Blanco-Fernandez, L., Martinez-Negro, M., Velaz, I., Aicart, E., et al. (2018). Plasmid-templated control of DNA-cyclodextrin nanoparticle morphology through molecular vector design for effective gene delivery. *Chemistry* 24 (15), 3825–3835. doi:10.1002/chem.201705723

García, A., González, B., Harvey, C., Izquierdo-Barba, I., and Vallet-Regí, M. (2021). Effective reduction of biofilm through photothermal therapy by gold core@shell based mesoporous silica nanoparticles. *Microporous Mesoporous Mater.* 328, 111489. doi:10.1016/j.micromeso.2021.111489

Garcia, J., Fernandez-Pradas, J. M., Llado, A., Serra, P., Zalvidea, D., Kogan, M. J., et al. (2021). The combined use of gold nanoparticles and infrared radiation enables cytosolic protein delivery. *Chemistry* 27 (14), 4670–4675. doi:10.1002/chem.202005000

Garcia, M. A. (2011). Surface plasmons in metallic nanoparticles: Fundamentals and applications. *J. Phys. D Appl. Phys.* 44 (28), 283001. doi:10.1088/0022-3727/44/28/283001

Garcia-Alvarez, R., and Vallet-Regi, M. (2021). Hard and soft protein corona of nanomaterials: Analysis and relevance. *Nanomater. (Basel).* 11 (4), 888. doi:10.3390/nano11040888

Garcia-Fernandez, A., Sancenon, F., and Martinez-Manez, R. (2021). Mesoporous silica nanoparticles for pulmonary drug delivery. *Adv. Drug Deliv. Rev.* 177, 113953. doi:10.1016/j.addr.2021.113953

Garcia-Fernandez, A., Sancho, M., Bisbal, V., Amoros, P., Marcos, M. D., Orzaez, M., et al. (2021). Targeted-lung delivery of dexamethasone using gated mesoporous silica nanoparticles. A new therapeutic approach for acute lung injury treatment. *J. Control Release* 337, 14–26. doi:10.1016/j.jconrel.2021.07.010

Garcia-Garrido, E., Cordani, M., and Somoza, A. (2021). Modified gold nanoparticles to overcome the chemoresistance to gemcitabine in mutant p53 cancer cells. *Pharmaceutics* 13 (12), 2067. doi:10.3390/pharmaceutics13122067

Garcia-Lojo, D., Nunez-Sanchez, S., Gomez-Grana, S., Grzelczak, M., Pastoriza-Santos, I., Perez-Juste, J., et al. (2019). Plasmonic supercrystals. *Acc. Chem. Res.* 52 (7), 1855–1864. doi:10.1021/acs.accounts.9b00213

Garcia-Soriano, D., Amaro, R., Lafuente-Gomez, N., Milan-Rois, P., Somoza, A., Navio, C., et al. (2020). The influence of cation incorporation and leaching in the properties of Mn-doped nanoparticles for biomedical applications. *J. Colloid Interface Sci.* 578, 510–521. doi:10.1016/j.jcis.2020.06.011

Garcia-Soriano, D., Milan-Rois, P., Lafuente-Gomez, N., Navio, C., Gutierrez, L., Cusso, L., et al. (2022). Iron oxide-manganese oxide nanoparticles with tunable morphology and switchable MRI contrast mode triggered by intracellular conditions. *J. Colloid Interface Sci.* 613, 447–460. doi:10.1016/j.jcis.2022.01.070

Gaspar, D. P., Gaspar, M. M., Eleuterio, C. V., Grenha, A., Blanco, M., Goncalves, L. M. D., et al. (2017). Microencapsulated solid lipid nanoparticles as a hybrid platform for pulmonary antibiotic delivery. *Mol. Pharm.* 14 (9), 2977–2990. doi:10.1021/acs.molpharmaceut.7b00169

Gatoo, M. A., Naseem, S., Arfat, M. Y., Dar, A. M., Qasim, K., and Zubair, S. (2014). Physicochemical properties of nanomaterials: Implication in associated toxic manifestations. *Biomed. Res. Int.* 2014, 1–8. doi:10.1155/2014/498420

Gavilán, H., Kowalski, A., Heinke, D., Sugunan, A., Sommertune, J., Varón, M., et al. (2017). Colloidal flower-shaped iron oxide nanoparticles: Synthesis strategies and coatings. *Part. Part. Syst. Charact.* 34 (7), 1700094. doi:10.1002/ppsc.201700094

Gerke, C., Zabala Gutierrez, I., Méndez-González, D., Cruz, M. C. I., Mulero, F., Jaque, D., et al. (2022). Clickable albumin nanoparticles for pretargeted drug delivery toward PD-L1 overexpressing tumors in combination immunotherapy. *Bioconjugate Chemistry* 33 (5), 821–828. doi:10.1021/acs.bioconjchem.2c00087

Giner-Casares, J. J., Henriksen-Lacey, M., Coronado-Puchau, M., and Liz-Marzán, L. M. (2016). Inorganic nanoparticles for biomedicine: Where materials scientists meet medical research. *Mater. Today* 19 (1), 19–28. doi:10.1016/j.mattod.2015.07.004

Gisbert-Garzaran, M., Lozano, D., and Vallet-Regi, M. (2020). Mesoporous silica nanoparticles for targeting subcellular organelles. *Int. J. Mol. Sci.* 21 (24), 9696. doi:10.3390/ijms21249696

Goesmann, H., and Feldmann, C. (2010). Cover picture: Nanoparticulate functional materials (angew. Chem. Int. Ed. 8/2010). *Angew. Chem. Int. Ed.* 49 (8), 1333. doi:10.1002/anie.200907226

Gomez-Aguado, I., Rodriguez-Castejon, J., Beraza-Millor, M., Vicente-Pascual, M., Rodriguez-Gascon, A., Garelli, S., et al. (2021). mRNA-based nanomedicinal products to address corneal inflammation by interleukin-10 supplementation. *Pharmaceutics* 13 (9), 1472. doi:10.3390/pharmaceutics13091472

Gomez-Aguado, I., Rodriguez-Castejon, J., Vicente-Pascual, M., Rodriguez-Gascon, A., Pozo-Rodriguez, A. D., and Solinis Aspiazu, M. A. (2020). Nucleic acid delivery by solid lipid nanoparticles containing switchable lipids: Plasmid DNA vs. Messenger RNA. *Mol.* 25 (24), 5995. doi:10.3390/molecules25245995

Gomez-Grana, S., Perez-Ameneiro, M., Vecino, X., Pastoriza-Santos, I., Perez-Juste, J., Cruz, J. M., et al. (2017). Biogenic synthesis of metal nanoparticles using a biosurfactant extracted from corn and their antimicrobial properties. *Nanomater. (Basel)* 7 (6), 139. doi:10.3390/nano7060139

Gonzalez-Aramundiz, J. V., Peleteiro, M., Gonzalez-Fernandez, A., Alonso, M. J., and Csaba, N. S. (2018). Protamine nanocapsules for the development of thermostable adjuvanted nanovaccines. *Mol. Pharm.* 15 (12), 5653–5664. doi:10.1021/acs.molpharmaceut.8b00852

Gonzalez-Aramundiz, J. V., Presas, E., Dalmau-Mena, I., Martinez-Pulgarin, S., Alonso, C., Escribano, J. M., et al. (2017). Rational design of protamine nanocapsules as antigen delivery carriers. *J. Control Release* 245, 62–69. doi:10.1016/j.jconrel.2016.11.012

Gonzalez-Ballesteros, N., Diego-Gonzalez, L., Lastra-Valdor, M., Grimaldi, M., Cavazza, A., Bigi, F., et al. (2021). Saccorhiza polyschides used to synthesize gold and silver nanoparticles with enhanced antiproliferative and immunostimulant activity. *Mater Sci. Eng. C Mater Biol. Appl.* 123, 111960. doi:10.1016/j.msec.2021.111960

Gonzalez-Ballesteros, N., Torres, M. D., Florez-Fernandez, N., Diego-Gonzalez, L., Simon-Vazquez, R., Rodriguez-Arguelles, M. C., et al. (2021). Eco-friendly extraction of Mastocarpus stellatus carrageenan for the synthesis of gold nanoparticles with improved biological activity. *Int. J. Biol. Macromol.* 183, 1436–1449. doi:10.1016/j.ijbiomac.2021.05.115

Gonzalez-Fernandez, S., Lozano-Iturbe, V., Menendez, M. F., Ordiales, H., Fernandez-Vega, I., Merayo, J., et al. (2022). A promising antifungal and antiamoebic effect of silver nanorings, a novel type of AgNP. *Antibiot. (Basel)* 11 (8), 1054. doi:10.3390/antibiotics11081054

Gonzalez-Fernandez, Y., Brown, H. K., Patino-Garcia, A., Heymann, D., and Blanco-Prieto, M. J. (2018). Oral administration of edelfosine encapsulated lipid nanoparticles causes regression of lung metastases in pre-clinical models of osteosarcoma. *Cancer Lett.* 430, 193–200. doi:10.1016/j.canlet.2018.05.030

Gonzalez-Pastor, R., Hernandez, Y., Gimeno, M., de Martino, A., Man, Y. K. S., Hallden, G., et al. (2021). Coating an adenovirus with functionalized gold nanoparticles favors uptake, intracellular trafficking and anti-cancer therapeutic efficacy. *Acta Biomater.* 134, 593–604. doi:10.1016/j.actbio.2021.07.047

Gonzalez-Pedroza, M. G., Argueta-Figueroa, L., Garcia-Contreras, R., Jimenez-Martinez, Y., Martinez-Martinez, E., Navarro-Marchal, S. A., et al. (2021). Silver nanoparticles from Annona muricata peel and leaf extracts as a potential potent, biocompatible and low cost antitumor tool. *Biocompatible Low Cost Antitumor Tool. Nanomater. (Basel).* 11 (5), 1273. doi:10.3390/nano11051273

Grayston, A., Zhang, Y., Garcia-Gabilondo, M., Arrue, M., Martin, A., Kopcansky, P., et al. (2022). Endovascular administration of magnetized nanocarriers targeting brain delivery after stroke. *J. Cereb. Blood Flow. Metab.* 42 (2), 237–252. doi:10.1177/0271678x211028816

Grimaudo, M. A., Concheiro, A., and Alvarez-Lorenzo, C. (2020). Crosslinked hyaluronan electrospun nanofibers for ferulic acid ocular delivery. *Pharmaceutics* 12 (3), 274. doi:10.3390/pharmaceutics12030274

Grzelak, J., Teles, M., Roher, N., Grayston, A., Rosell, A., Gich, M., et al. (2022). Bioevaluation of magnetic mesoporous silica rods: Cytotoxicity, cell uptake and biodistribution in zebrafish and rodents. *RSC Adv.* 12 (49), 31878–31888. doi:10.1039/d2ra05750f

Guasch, J., Hoffmann, M., Diemer, J., Riahinezhad, H., Neubauer, S., Kessler, H., et al. (2018). Combining adhesive nanostructured surfaces and costimulatory signals to increase T cell activation. *Nano Lett.* 18 (9), 5899–5904. doi:10.1021/acs.nanolett.8b02588

Guisasola, E., Asin, L., Beola, L., de la Fuente, J. M., Baeza, A., and Vallet-Regi, M. (2018). Beyond traditional hyperthermia: *In vivo* cancer treatment with magnetic-responsive mesoporous silica nanocarriers. *ACS Appl. Mater Interfaces* 10 (15), 12518–12525. doi:10.1021/acsami.8b02398

Guisasola, E., Baeza, A., Asín, L., de la Fuente, J. M., and Vallet-Regí, M. (2018). Heating at the nanoscale through drug-delivery devices: Fabrication and synergic effects in cancer treatment with nanoparticles. *Small Methods* 2 (9), 1800007. doi:10.1002/smtd.201800007

Gundogdu, E., Demir, E. S., Ekinci, M., Ozgenc, E., Ilem-Ozdemir, D., Senyigit, Z., et al. (2022). An innovative formulation based on nanostructured lipid carriers for imatinib delivery: Pre-formulation, cellular uptake and cytotoxicity studies. *Nanomater. (Basel).* 12 (2), 250. doi:10.3390/nano12020250

Hendiger, E. B., Padzik, M., Sifaoui, I., Reyes-Batlle, M., Lopez-Arencibia, A., Rizo-Liendo, A., et al. (2020). Silver nanoparticles as a novel potential preventive agent against Acanthamoeba keratitis. *Pathogens* 9 (5), 350. doi:10.3390/pathogens9050350

Hendiger, E. B., Padzik, M., Sifaoui, I., Reyes-Batlle, M., Lopez-Arencibia, A., Zyskowska, D., et al. (2021). Silver nanoparticles conjugated with contact lens solutions may reduce the risk of Acanthamoeba keratitis. *Pathogens* 10 (5), 583. doi:10.3390/pathogens10050583

Hernandez Montoto, A., Llopis-Lorente, A., Gorbe, M., Terrés, J. M., Cao-Milan, R., Diaz de Grenu, B., et al. (2019). Janus gold nanostars-mesoporous silica nanoparticles for NIR-light-triggered drug delivery. *Chemistry* 25 (36), 8471–8478. doi:10.1002/chem.201900750

Hernando, S., Nikolakopoulou, P., Voulgaris, D., Hernandez, R. M., Igartua, M., and Herland, A. (2022). Dual effect of TAT functionalized DHAH lipid nanoparticles with neurotrophic factors in human BBB and microglia cultures. *Fluids Barriers CNS* 19 (1), 22. doi:10.1186/s12987-022-00315-1

Huguet-Casquero, A., Xu, Y., Gainza, E., Pedraz, J. L., and Beloqui, A. (2020). Oral delivery of oleuropein-loaded lipid nanocarriers alleviates inflammation and oxidative stress in acute colitis. *Int. J. Pharm.* 586, 119515. doi:10.1016/j.ijpharm.2020.119515

Inchaurraga, L., Martinez-Lopez, A. L., Martin-Arbella, N., and Irache, J. M. (2020). Zein-based nanoparticles for the oral delivery of insulin. *Drug Deliv. Transl. Res.* 10 (6), 1601–1611. doi:10.1007/s13346-020-00796-3

Iturrioz-Rodriguez, N., Correa-Duarte, M. A., and Fanarraga, M. L. (2019). <p> Controlled drug delivery systems for cancer based on mesoporous silica nanoparticles</p>. *Int. J. Nanomedicine* 14, 3389–3401. doi:10.2147/ijn.s198848

Iturrioz-Rodriguez, N., Gonzalez-Dominguez, E., Gonzalez-Lavado, E., Marin-Caba, L., Vaz, B., Perez-Lorenzo, M., et al. (2017). A biomimetic escape strategy for cytoplasm invasion by synthetic particles. *Angew. Chem. Int. Ed. Engl.* 56 (44), 13924–13928. doi:10.1002/ange.201707769

Jaque, D., Martinez Maestro, L., del Rosal, B., Haro-Gonzalez, P., Benayas, A., Plaza, J. L., et al. (2014). Nanoparticles for photothermal therapies. *Nanoscale* 6 (16), 9494–9530. doi:10.1039/c4nr00708e

Jia, C. J., Sun, L. D., Luo, F., Han, X. D., Heyderman, L. J., Yan, Z. G., et al. (2008). Large-scale synthesis of single-crystalline iron oxide magnetic nanorings. *J. Am. Chem. Soc.* 130 (50), 16968–16977. doi:10.1021/ja805152t

Jimenez-Falcao, S., de Luis, B., Garcia-Fernandez, A., Llopis-Lorente, A., Diez, P., Sanchez, A., et al. (2019). Glucose-responsive enzyme-controlled mesoporous nanomachine with a layer-by-layer supramolecular architecture. *ACS Appl. Bio Mater* 2 (8), 3321–3328. doi:10.1021/acsabm.9b00338

Jindal, A. B. (2017). The effect of particle shape on cellular interaction and drug delivery applications of micro- and nanoparticles. *Int. J. Pharm.* 532 (1), 450–465. doi:10.1016/j.ijpharm.2017.09.028

Jornet-Martinez, N., Hakobyan, L., Argente-Garcia, A. I., Molins-Legua, C., and Campins-Falco, P. (2019). Nylon-supported plasmonic assay based on the aggregation of silver nanoparticles: *In situ* determination of hydrogen sulfide-like compounds in breath samples as a proof of concept. *ACS Sens.* 4 (8), 2164–2172. doi:10.1021/acssensors.9b01019

Khan, I., Saeed, K., and Khan, I. (2019). Nanoparticles: Properties, applications and toxicities. *Arabian J. Chem.* 12 (7), 908–931. doi:10.1016/j.arabjc.2017.05.011

Kim, D., Kim, J., Park, Y. I., Lee, N., and Hyeon, T. (2018). Recent development of inorganic nanoparticles for biomedical imaging. *ACS Cent. Sci.* 4 (3), 324–336. doi:10.1021/acscentsci.7b00574

Kim, W. J., Kwon, Y. J., Cho, C. H., Ye, S. K., and Kim, K. O. (2021). Insulin smart drug delivery nanoparticles of aminophenylboronic acid-POSS molecule at neutral pH. *Sci. Rep.* 11 (1), 21894. doi:10.1038/s41598-021-01216-3

Kolosnjaj-Tabi, J., Marangon, I., Nicolas-Boluda, A., Silva, A. K. A., and Gazeau, F. (2017). Nanoparticle-based hyperthermia, a local treatment modulating the tumor extracellular matrix. *Pharmacol. Res.* 126, 123–137. doi:10.1016/j.phrs.2017.07.010

Lafuente-Gomez, N., Wang, S., Fontana, F., Dhanjani, M., Garcia-Soriano, D., Correia, A., et al. (2022). Synergistic immunomodulatory effect in macrophages mediated by magnetic nanoparticles modified with miRNAs. *Nanoscale* 14 (31), 11129–11138. doi:10.1039/d2nr01767a

Lasa-Saracibar, B., El Moukhtari, S. H., Tsotakos, T., Xanthopoulos, S., Loudos, G., Bouziotis, P., et al. (2022). *In vivo* biodistribution of edelfosine-loaded lipid nanoparticles radiolabeled with Technetium-99 m: Comparison of administration routes in mice. *Eur. J. Pharm. Biopharm.* 175, 1–6. doi:10.1016/j.ejpb.2022.04.007

Latorre, A., Latorre, A., Castellanos, M., Lafuente-Gomez, N., Diaz, C. R., Crespo-Barreda, A., et al. (2021). Albumin-based nanostructures for uveal melanoma treatment. *Nanomedicine* 35, 102391. doi:10.1016/j.nano.2021.102391

Latorre, A., Latorre, A., Castellanos, M., Rodriguez Diaz, C., Lazaro-Carrillo, A., Aguado, T., et al. (2019). Multifunctional albumin-stabilized gold nanoclusters for the reduction of cancer stem cells. *Cancers (Basel)* 11 (7), 969. doi:10.3390/cancers11070969

Latorre, J., Diaz-Trelles, R., Comas, F., Gavalda-Navarro, A., Milbank, E., Dragano, N., et al. (2022). Downregulation of hepatic lipopolysaccharide binding protein improves lipogenesis-induced liver lipid accumulation. *Mol. Ther. Nucleic Acids* 29, 599–613. doi:10.1016/j.omtn.2022.08.003

Lazaro-Carrillo, A., Calero, M., Aires, A., Simoes, B. M., Latorre, A., et al. (2020). Tailored functionalized magnetic nanoparticles to target breast cancer cells including cancer stem-like cells. *Cancers (Basel)* 12 (6), 1397. doi:10.3390/cancers12061397

Leal, B. H., Velasco, B., Cambon, A., Pardo, A., Fernandez-Vega, J., Arellano, L., et al. (2022). Combined therapeutics for atherosclerosis treatment using polymeric nanovectors. *Pharmaceutics* 14 (2), 258. doi:10.3390/pharmaceutics14020258

Ledo, A. M., Sasso, M. S., Bronte, V., Marigo, I., Boyd, B. J., Garcia-Fuentes, M., et al. (2019). Co-delivery of RNAi and chemokine by polyarginine nanocapsules enables the modulation of myeloid-derived suppressor cells. *J. Control Release* 295, 60–73. doi:10.1016/j.jconrel.2018.12.041

Lee, S., Son, B., Park, G., Kim, H., Kang, H., Jeon, J., et al. (2018). Immunogenic effect of hyperthermia on enhancing radiotherapeutic efficacy. *Int. J. Mol. Sci.* 19 (9), 2795. doi:10.3390/ijms19092795

Leiva, M. C., Ortiz, R., Contreras-Caceres, R., Perazzoli, G., Mayevych, I., Lopez-Romero, J. M., et al. (2017). Tripalmitin nanoparticle formulations significantly enhance paclitaxel antitumor activity against breast and lung cancer cells *in vitro*. *Sci. Rep.* 7 (1), 13506. doi:10.1038/s41598-017-13816-z

Litti, L., Trivini, S., Ferraro, D., and Reguera, J. (2021). 3D printed microfluidic device for magnetic trapping and SERS quantitative evaluation of environmental and biomedical analytes. *ACS Appl. Mater Interfaces* 13 (29), 34752–34761. doi:10.1021/acsami.1c09771

Liu, K., and Huang, X. (2022). Synthesis of self-assembled hyaluronan based nanoparticles and their applications in targeted imaging and therapy. *Carbohydr. Res.* 511, 108500. doi:10.1016/j.carres.2022.108500

Liz-Marzán, L. M., Nel, A. E., Brinker, C. J., Chan, W. C. W., Chen, C., Chen, X., et al. (2022). What do we mean when we say nanomedicine? *ACS Nano* 16 (9), 13257–13259. doi:10.1021/acsnano.2c08675

Llinas, M. C., Martinez-Edo, G., Cascante, A., Porcar, I., Borros, S., and Sanchez-Garcia, D. (2018). Preparation of a mesoporous silica-based nano-vehicle for dual DOX/CPT pH-triggered delivery. *Drug Deliv.* 25 (1), 1137–1146. doi:10.1080/10717544.2018.1472678

Lopez, V., Villegas, M. R., Rodriguez, V., Villaverde, G., Lozano, D., Baeza, A., et al. (2017). Janus mesoporous silica nanoparticles for dual targeting of tumor cells and mitochondria. *ACS Appl. Mater Interfaces* 9 (32), 26697–26706. doi:10.1021/acsami.7b06906

Lozano-Pedraza, C., Plaza-Mayoral, E., Espinosa, A., Sot, B., Serrano, A., Salas, G., et al. (2021). Assessing the parameters modulating optical losses of iron oxide nanoparticles under near infrared irradiation. *Nanoscale Adv.* 3 (22), 6490–6502. doi:10.1039/d1na00601k

Luengo, Y., Diaz-Riascos, Z. V., Garcia-Soriano, D., Teran, F. J., Artes-Ibanez, E. J., Ibarrola, O., et al. (2022). Fine control of *in vivo* magnetic hyperthermia using iron oxide nanoparticles with different coatings and degree of aggregation. *Pharmaceutics* 14 (8), 1526. doi:10.3390/pharmaceutics14081526

Luengo, Y., Sot, B., and Salas, G. (2020). Combining Ag and gamma-Fe2O3 properties to produce effective antibacterial nanocomposites. *Colloids Surf. B Biointerfaces* 194, 111178. doi:10.1016/j.colsurfb.2020.111178

Manzano, M., and Vallet-Regi, M. (2018). Mesoporous silica nanoparticles in nanomedicine applications. *J. Mater Sci. Mater Med.* 29 (5), 65. doi:10.1007/s10856-018-6069-x

Manzano, M., and Vallet-Regi, M. (2019). Ultrasound responsive mesoporous silica nanoparticles for biomedical applications. *Chem. Commun. (Camb)* 55 (19), 2731–2740. doi:10.1039/c8cc09389j

Marciello, M., Rossi, S., Caramella, C., and Remunan-Lopez, C. (2017). Freeze-dried cylinders carrying chitosan nanoparticles for vaginal peptide delivery. *Carbohydr. Polym.* 170, 43–51. doi:10.1016/j.carbpol.2017.04.051

Márquez-Rodas, I., Dutriaux, C., Saiag, P., de la Cruz Merino, L., Castanon Álvarez, E., Robert, C., et al. (2022). Abstract CT014: Efficacy of intratumoral BO-112 with systemic pembrolizumab in patients with advanced melanoma refractory to anti-PD-1-based therapy: Final results of SPOTLIGHT203 phase 2 study. *Cancer Res.* 82, CT014. doi:10.1158/1538-7445.am2022-ct014

Martin-Rapun, R., De Matteis, L., Ambrosone, A., Garcia-Embid, S., Gutierrez, L., and de la Fuente, J. M. (2017). Targeted nanoparticles for the treatment of alzheimer's disease. *Curr. Pharm. Des.* 23 (13), 1927–1952. doi:10.2174/1381612822666161226151011

Martin-Saavedra, F., Ruiz-Hernandez, E., Escudero-Duch, C., Prieto, M., Arruebo, M., Sadeghi, N., et al. (2017). Lipogels responsive to near-infrared light for the triggered release of therapeutic agents. *Acta Biomater.* 61, 54–65. doi:10.1016/j.actbio.2017.08.010

Martinez-Carmona, M., Izquierdo-Barba, I., Colilla, M., and Vallet-Regi, M. (2019). Concanavalin A-targeted mesoporous silica nanoparticles for infection treatment. *Acta Biomater.* 96, 547–556. doi:10.1016/j.actbio.2019.07.001

Martinez-Carmona, M., Lozano, D., Colilla, M., and Vallet-Regi, M. (2018). Lectin-conjugated pH-responsive mesoporous silica nanoparticles for targeted bone cancer treatment. *Acta Biomater.* 65, 393–404. doi:10.1016/j.actbio.2017.11.007

Martinez-Edo, G., Xue, E. Y., Ha, S. Y. Y., Ponton, I., Gonzalez-Delgado, J. A., Borros, S., et al. (2021). Nanoparticles for triple drug release for combined chemo- and photodynamic therapy. *Chemistry* 27 (59), 14610–14618. doi:10.1002/chem.202101842

Martinez-Lopez, A. L., Gonzalez-Navarro, C. J., Vizmanos, J. L., and Irache, J. M. (2021). Zein-based nanocarriers for the oral delivery of insulin. *in vivo* evaluation in *Caenorhabditis elegans*. *Drug Deliv. Transl. Res.* 11 (2), 647–658. doi:10.1007/s13346-021-00919-4

Martinez-Negro, M., Guerrero-Martinez, A., Garcia-Rio, L., Domenech, O., Aicart, E., Tros de Ilarduya, C., et al. (2018). Multidisciplinary approach to the transfection of plasmid DNA by a nonviral nanocarrier based on a gemini-bolaamphiphilic hybrid lipid. *ACS Omega* 3 (1), 208–217. doi:10.1021/acsomega.7b01657

Martinez-Relimpio, A. M., Benito, M., Perez-Izquierdo, E., Teijon, C., Olmo, R. M., and Blanco, M. D. (2021). Paclitaxel-loaded folate-targeted albumin-alginate nanoparticles crosslinked with ethylenediamine. Synthesis and *in vitro* characterization. *Polym. (Basel)* 13 (13), 2083. doi:10.3390/polym13132083

Mayol, B., Diez, P., Sanchez, A., de la Torre, C., Villalonga, A., Lucena-Sanchez, E., et al. (2021). A glutathione disulfide-sensitive Janus nanomachine controlled by an enzymatic AND logic gate for smart delivery. *Nanoscale* 13 (44), 18616–18625. doi:10.1039/d0nr08282a

Mazario, E., Herrasti, P., Morales, M. P., and Menendez, N. (2012). Synthesis and characterization of CoFe2O4 ferrite nanoparticles obtained by an electrochemical method. *Nanotechnology* 23 (35), 355708. doi:10.1088/0957-4484/23/35/355708

McGillicuddy, E., Murray, I., Kavanagh, S., Morrison, L., Fogarty, A., Cormican, M., et al. (2017). Silver nanoparticles in the environment: Sources, detection and ecotoxicology. *Sci. Total Environ.* 575, 231–246. doi:10.1016/j.scitotenv.2016.10.041

Mejias, R., Hernandez Flores, P., Talelli, M., Tajada-Herraiz, J. L., Brollo, M. E. F., Portilla, Y., et al. (2019). Cell-promoted nanoparticle aggregation decreases nanoparticle-induced hyperthermia under an alternating magnetic field independently of nanoparticle coating, core size, and subcellular localization. *ACS Appl. Mater Interfaces* 11 (1), 340–355. doi:10.1021/acsami.8b18451

Mendez-Gonzalez, D., Lifante, J., Zabala Gutierrez, J., Marin, R., Ximendes, E., Sanz-de Diego, E., et al. (2022). Optomagnetic nanofluids for controlled brain hyperthermia: a critical study. *Nanoscale* 14 (43), 16208–16219. doi:10.1039/d2nr03413a

Milan Rois, P., Latorre, A., Rodriguez Diaz, C., Del Moral, A., and Somoza, A. (2018). Reprogramming cells for synergistic combination therapy with nanotherapeutics against uveal melanoma. *Biomimetics (Basel)* 3 (4), 28. doi:10.3390/biomimetics3040028

Miron-Barroso, S., Domenech, E. B., and Trigueros, S. (2021). Nanotechnology-based strategies to overcome current barriers in gene delivery. *Int. J. Mol. Sci.* 22 (16), 8537. doi:10.3390/ijms22168537

Mitxelena-Iribarren, O., Hisey, C. L., Errazquin-Irigoyen, M., Gonzalez-Fernandez, Y., Imbuluzqueta, E., Mujika, M., et al. (2017). Effectiveness of nanoencapsulated methotrexate against osteosarcoma cells: *In vitro* cytotoxicity under dynamic conditions. *Biomed. Microdevices* 19 (2), 35. doi:10.1007/s10544-017-0177-0

Mitxelena-Iribarren, O., Lizarbe-Sancha, S., Campisi, J., Arana, S., and Mujika, M. (2021). Different microfluidic environments for *in vitro* testing of lipid nanoparticles against osteosarcoma. *Bioeng. (Basel)* 8 (6), 77. doi:10.3390/bioengineering8060077

Montalvo-Quiros, S., Gomez-Grana, S., Vallet-Regi, M., Prados-Rosales, R. C., Gonzalez, B., and Luque-Garcia, J. L. (2021). Mesoporous silica nanoparticles containing silver as novel antimycobacterial agents against *Mycobacterium tuberculosis*. *Colloids Surf. B Biointerfaces* 197, 111405. doi:10.1016/j.colsurfb.2020.111405

Montalvo-Quiros, S., Vallet-Regi, M., Palacios, A., Anguita, J., Prados-Rosales, R. C., Gonzalez, B., et al. (2020). Mesoporous silica nanoparticles as a potential platform for vaccine development against tuberculosis. *Tuberc. Pharm.* 12 (12), 1218. doi:10.3390/pharmaceutics12121218

Montero, N., Pérez, E., Benito, M., Teijón, C., Teijón, J. M., Olmo, R., et al. (2019). Biocompatibility studies of intravenously administered ionic-crosslinked chitosan-BSA nanoparticles as vehicles for antitumour drugs. *International Journal of Pharmaceutics* 554, 337–351. doi:10.1016/j.ijpharm.2018.11.027

Mora-Raimundo, P., Lozano, D., Manzano, M., and Vallet-Regi, M. (2019). Nanoparticles to knockdown osteoporosis-related gene and promote osteogenic marker expression for osteoporosis treatment. *ACS Nano* 13 (5), 5451–5464. doi:10.1021/acsnano.9b00241

Moran, H. B. T., Turley, J. L., Andersson, M., and Lavelle, E. C. (2018). Immunomodulatory properties of chitosan polymers. *Biomaterials* 184, 1–9. doi:10.1016/j.biomaterials.2018.08.054

Morey, J., Llinas, P., Bueno-Costa, A., Leon, A. J., and Pina, M. N. (2021). Raltitrexed-modified gold and silver nanoparticles for targeted cancer therapy: Cytotoxicity behavior *in vitro* on A549 and HCT-116 human cancer cells. *Mater. (Basel)* 14 (3), 534. doi:10.3390/ma14030534

Moros, M., Idiago-Lopez, J., Asin, L., Moreno-Antolin, E., Beola, L., Grazu, V., et al. (2019). Triggering antitumoural drug release and gene expression by magnetic hyperthermia. *Adv. Drug Deliv. Rev.* 138, 326–343. doi:10.1016/j.addr.2018.10.004

Mosquera, J., Garcia, I., Henriksen-Lacey, M., Martinez-Calvo, M., Dhanjani, M., Mascarenas, J. L., et al. (2020). Reversible control of protein corona formation on gold nanoparticles using host-guest interactions. *ACS Nano* 14 (5), 5382–5391. doi:10.1021/acsnano.9b08752

Mulens-Arias, V., Rojas, J. M., Sanz-Ortega, L., Portilla, Y., Perez-Yague, S., and Barber, D. F. (2019). Polyethylenimine-coated superparamagnetic iron oxide nanoparticles impair *in vitro* and *in vivo* angiogenesis. *Nanomedicine* 21, 102063. doi:10.1016/j.nano.2019.102063

Mulvihill, J. J., Cunnane, E. M., Ross, A. M., Duskey, J. T., Tosi, G., and Grabrucker, A. M. (2020). Drug delivery across the blood-brain barrier: Recent advances in the use of nanocarriers. *Nanomedicine (Lond).* 15 (2), 205–214. doi:10.2217/nnm-2019-0367

Munoz-Espin, D., Rovira, M., Galiana, I., Gimenez, C., Lozano-Torres, B., Paez-Ribes, M., et al. (2018). A versatile drug delivery system targeting senescent cells. *EMBO Mol. Med.* 10 (9), e9355. doi:10.15252/emmm.201809355

Nanoscience, I. (2020). NoCanTher project 2020. Available from: http://www.nocanther-project.eu/.

Navarro-Palomares, E., Garcia-Hevia, L., Padin-Gonzalez, E., Banobre-Lopez, M., Villegas, J. C., Valiente, R., et al. (2021). Targeting nanomaterials to head and neck cancer cells using a fragment of the Shiga toxin as a potent natural ligand. *Cancers (Basel).* 13 (19), 4920. doi:10.3390/cancers13194920

Nicu, R., Ciolacu, F., and Ciolacu, D. E. (2021). Advanced functional materials based on nanocellulose for pharmaceutical/medical applications. *Pharmaceutics* 13 (8), 1125. doi:10.3390/pharmaceutics13081125

Nino-Pariente, A., Arminan, A., Reinhard, S., Scholz, C., Kos, P., Wagner, E., et al. (2017). Design of poly-l-glutamate-based complexes for pDNA delivery. *Macromol. Biosci.* 17 (10). doi:10.1002/mabi.201700245

Niu, Z., Samaridou, E., Jaumain, E., Coene, J., Ullio, G., Shrestha, N., et al. (2018). PEG-PGA enveloped octaarginine-peptide nanocomplexes: An oral peptide delivery strategy. *J. Control Release* 276, 125–139. doi:10.1016/j.jconrel.2018.03.004

Niu, Z., Tedesco, E., Benetti, F., Mabondzo, A., Montagner, I. M., Marigo, I., et al. (2017). Rational design of polyarginine nanocapsules intended to help peptides overcoming intestinal barriers. *J. Control Release* 263, 4–17. doi:10.1016/j.jconrel.2017.02.024

NoCanTher Project (2022). First patient is enrolled in the NoCanTher's clinical study 2022. Available from: http://www.nocanther-project.eu/index.php/news/70-first-patient-is-enrolled-in-the-nocanther-s-clinical-study.

Nozal, V., Rojas-Prats, E., Maestro, I., Gil, C., Perez, D. I., and Martinez, A. (2021). Improved controlled release and brain penetration of the small molecule S14 using PLGA nanoparticles. *Int. J. Mol. Sci.* 22 (6), 3206. doi:10.3390/ijms22063206

Ortgies, D. H., de la Cueva, L., Del Rosal, B., Sanz-Rodriguez, F., Fernandez, N., Iglesias-de la Cruz, M. C., et al. (2016). *In vivo* deep tissue fluorescence and magnetic imaging employing hybrid nanostructures. *ACS Appl. Mater Interfaces* 8 (2), 1406–1414. doi:10.1021/acsami.5b10617

Ovejero, J. G., Armenia, I., Serantes, D., Veintemillas-Verdaguer, S., Zeballos, N., Lopez-Gallego, F., et al. (2021). Selective magnetic nanoheating: Combining iron oxide nanoparticles for multi-hot-spot induction and sequential regulation. *Nano Lett.* 21 (17), 7213–7220. doi:10.1021/acs.nanolett.1c02178

Ovejero, J. G., Spizzo, F., Morales, M. P., and Del Bianco, L. (2021). Mixing iron oxide nanoparticles with different shape and size for tunable magneto-heating performance. *Nanoscale* 13 (11), 5714–5729. doi:10.1039/d0nr09121a

Padzik, M., Hendiger, E. B., Chomicz, L., Grodzik, M., Szmidt, M., Grobelny, J., et al. (2018). Tannic acid-modified silver nanoparticles as a novel therapeutic agent against Acanthamoeba. *Parasitol. Res.* 117 (11), 3519–3525. doi:10.1007/s00436-018-6049-6

Pallares, V., Nunez, Y., Sanchez-Garcia, L., Falgas, A., Serna, N., Unzueta, U., et al. (2021). Antineoplastic effect of a diphtheria toxin-based nanoparticle targeting acute myeloid leukemia cells overexpressing CXCR4. *J. Control Release* 335, 117–129. doi:10.1016/j.jconrel.2021.05.014

Pallares, V., Unzueta, U., Falgas, A., Sanchez-Garcia, L., Serna, N., Gallardo, A., et al. (2020). An Auristatin nanoconjugate targeting CXCR4+ leukemic cells blocks acute myeloid leukemia dissemination. *J. Hematol. Oncol.* 13 (1), 36. doi:10.1186/s13045-020-00863-9

Pardo, A., Pelaz, B., Gallo, J., Bañobre-López, M., Parak, W. J., Barbosa, S., et al. (2020). Synthesis, characterization, and evaluation of superparamagnetic doped ferrites as potential therapeutic nanotools. *Chem. Mater.* 32 (6), 2220–2231. doi:10.1021/acs.chemmater.9b04848

Paris, J. L., Villaverde, G., Gomez-Grana, S., and Vallet-Regi, M. (2020). Nanoparticles for multimodal antivascular therapeutics: Dual drug release, photothermal and photodynamic therapy. *Acta Biomater.* 101, 459–468. doi:10.1016/j.actbio.2019.11.004

Pastor, M., Basas, J., Vairo, C., Gainza, G., Moreno-Sastre, M., Gomis, X., et al. (2019). Safety and effectiveness of sodium colistimethate-loaded nanostructured lipid carriers (SCM-NLC) against *P. aeruginosa*: *In vitro* and *in vivo* studies following pulmonary and intramuscular administration. *Nanomedicine* 18, 101–111. doi:10.1016/j.nano.2019.02.014

Paterson, S., Thompson, S. A., Wark, A. W., and de la RicaGold, R. S. (2017). Gold suprashells: Enhanced photothermal nanoheaters with multiple localized surface plasmon resonances for broadband surface-enhanced Raman scattering. *J. Phys. Chem. C* 121 (13), 7404–7411. doi:10.1021/acs.jpcc.6b12792

Paul, W., and Sharma, C. P. (2020). "13 - inorganic nanoparticles for targeted drug delivery," in *Biointegration of medical implant materials*. Editor C. P. Sharma Second Edition (Woodhead Publishing), 333–373.

Pelaez, E. C., Estevez, M. C., Portela, A., Salvador, J. P., Marco, M. P., and Lechuga, L. M. (2018). Nanoplasmonic biosensor device for the monitoring of acenocoumarol therapeutic drug in plasma. *Biosens. Bioelectron.* 119, 149–155. doi:10.1016/j.bios.2018.08.011

Pellico, J., Fernandez-Barahona, I., Ruiz-Cabello, J., Gutierrez, L., Munoz-Hernando, M., Sanchez-Guisado, M. J., et al. (2021). HAP-multitag, a PET and positive MRI contrast nanotracer for the longitudinal characterization of vascular calcifications in atherosclerosis. *ACS Appl. Mater Interfaces* 13 (38), 45279–45290. doi:10.1021/acsami.1c13417

Pena-Gonzalez, C. E., Pedziwiatr-Werbicka, E., Shcharbin, D., Guerrero-Beltran, C., Abashkin, V., Loznikova, S., et al. (2017). Gold nanoparticles stabilized by cationic carbosilane dendrons: Synthesis and biological properties. *Dalton Trans.* 46 (27), 8736–8745. doi:10.1039/c6dt03791g

Perez-Hernandez, M., Moros, M., Stepien, G., Del Pino, P., Menao, S., de Las Heras, M., et al. (2017). Multiparametric analysis of anti-proliferative and apoptotic effects of gold nanoprisms on mouse and human primary and transformed cells, biodistribution and toxicity *in vivo*. *Part Fibre Toxicol.* 14 (1), 41. doi:10.1186/s12989-017-0222-4

Perez-Tanoira, R., Fernandez-Arias, M., Potel, C., Carballo-Fernandez, R., Perez-Castro, S., Boutinguiza, M., et al. (2022). Silver nanoparticles produced by laser ablation and Re-irradiation are effective preventing peri-implantitis multispecies biofilm formation. *Int. J. Mol. Sci.* 23 (19), 12027. doi:10.3390/ijms231912027

Plaza-Ga, I., Manzaneda-Gonzalez, V., Kisovec, M., Almendro-Vedia, V., Munoz-Ubeda, M., Anderluh, G., et al. (2019). pH-triggered endosomal escape of pore-forming Listeriolysin O toxin-coated gold nanoparticles. *J. Nanobiotechnology* 17 (1), 108. doi:10.1186/s12951-019-0543-6

Polo, E., del Pino, P., Pardo, A., Taboada, P., and Pelaz, B. (2018). "Magnetic nanoparticles for cancer therapy and bioimaging," in *Nanooncology: Engineering*

nanomaterials for cancer therapy and diagnosis. Editors G. Gonçalves and G. Tobias (Cham: Springer International Publishing), 239–279.

Portela, A., Calvo-Lozano, O., Estevez, M. C., Medina Escuela, A., and Lechuga, L. M. (2020). Optical nanogap antennas as plasmonic biosensors for the detection of miRNA biomarkers. *J. Mater Chem. B* 8 (19), 4310–4317. doi:10.1039/d0tb00307g

Poyatos-Racionero, E., Gonzalez-Alvarez, I., Sanchez-Moreno, P., Sitia, L., Gatto, F., Pompa, P. P., et al. (2021). Lactose-Gated mesoporous silica particles for intestinal controlled delivery of essential oil components: An *in vitro* and *in vivo* study. *Pharmaceutics* 13 (7), 982. doi:10.3390/pharmaceutics13070982

Prajapati, R., Garcia-Garrido, E., and Somoza, A. (2021). Albumin-based nanoparticles for the delivery of doxorubicin in breast cancer. *Cancers (Basel)* 13 (12), 3011. doi:10.3390/cancers13123011

Prajapati, R., and Somoza, A. (2021). Albumin nanostructures for nucleic acid delivery in cancer: Current trend, emerging issues, and possible solutions. *Cancers (Basel)*. 13 (14), 3454. doi:10.3390/cancers13143454

Qaiser, A., Kiani, M. H., Parveen, R., Sarfraz, M., Shahnaz, G., Rahdar, A., et al. (2022). Design and synthesis of multifunctional polymeric micelles for targeted delivery in *Helicobacter pylori* infection. *J. Mol. Liq.* 363, 119802. doi:10.1016/j.molliq.2022.119802

Quintanilla, M., Garcia, I., de Lazaro, I., Garcia-Alvarez, R., Henriksen-Lacey, M., Vranic, S., et al. (2019). Thermal monitoring during photothermia: Hybrid probes for simultaneous plasmonic heating and near-infrared optical nanothermometry. *Theranostics* 9 (24), 7298–7312. doi:10.7150/thno.38091

Ramirez-Jimenez, R., Artiga, A., Mitchell, S. G., Martin-Rapun, R., and de la Fuente, J. M. (2020). Surfactant-free synthesis and scalable purification of triangular gold nanoprisms with low non-specific cellular uptake. *Nanomater. (Basel)* 10 (3), 539. doi:10.3390/nano10030539

Ramos-Docampo, M. A., Fernandez-Medina, M., Taipaleenmaki, E., Hovorka, O., Salgueirino, V., and Stadler, B. (2019). Microswimmers with heat delivery capacity for 3D cell spheroid penetration. *ACS Nano* 13 (10), 12192–12205. doi:10.1021/acsnano.9b06869

Reboredo, C., Gonzalez-Navarro, C. J., Martinez-Oharriz, C., Martinez-Lopez, A. L., and Irache, J. M. (2021). Preparation and evaluation of PEG-coated zein nanoparticles for oral drug delivery purposes. *Int. J. Pharm.* 597, 120287. doi:10.1016/j.ijpharm.2021.120287

Redolfi Riva, E., Pastoriza-Santos, I., Lak, A., Pellegrino, T., Perez-Juste, J., and Mattoli, V. (2017). Plasmonic/magnetic nanocomposites: Gold nanorods-functionalized silica coated magnetic nanoparticles. *J. Colloid Interface Sci.* 502, 201–209. doi:10.1016/j.jcis.2017.04.089

Reidy, B., Haase, A., Luch, A., Dawson, K. A., and Lynch, I. (2013). Mechanisms of silver nanoparticle release, transformation and toxicity: A critical review of current knowledge and recommendations for future studies and applications. *Mater. (Basel)* 6 (6), 2295–2350. doi:10.3390/ma6062295

Relano-Rodriguez, I., Espinar-Buitrago, M. S., Martin-Canadilla, V., Gomez-Ramirez, R., Jimenez, J. L., and Munoz-Fernandez, M. A. (2021). Nanotechnology against human cytomegalovirus *in vitro*: Polyanionic carbosilane dendrimers as antiviral agents. *J. Nanobiotechnology* 19 (1), 65. doi:10.1186/s12951-021-00809-4

Rincon-Iglesias, M., Rodrigo, I. L. B. B., Serea, E. S. A., Plazaola, F., Lanceros-Mendez, S., et al. (2022). Core-shell Fe(3)O(4)@Au nanorod-loaded gels for tunable and anisotropic magneto- and photothermia. *ACS Appl. Mater Interfaces* 14 (5), 7130–7140. doi:10.1021/acsami.1c20990

Ritz, S., Schottler, S., Kotman, N., Baier, G., Musyanovych, A., Kuharev, J., et al. (2015). Protein corona of nanoparticles: Distinct proteins regulate the cellular uptake. *Biomacromolecules* 16 (4), 1311–1321. doi:10.1021/acs.biomac.5b00108

Roca, A. G., Gutierrez, L., Gavilan, H., Fortes Brollo, M. E., Veintemillas-Verdaguer, S., and Morales, M. D. P. (2019). Design strategies for shape-controlled magnetic iron oxide nanoparticles. *Adv. Drug Deliv. Rev.* 138, 68–104. doi:10.1016/j.addr.2018.12.008

Rocha, U., Hu, J., Rodriguez, E. M., Vanetsev, A. S., Rahn, M., Sammelselg, V., et al. (2016). Subtissue imaging and thermal monitoring of gold nanorods through joined encapsulation with Nd-doped infrared-emitting nanoparticles. *Small* 12 (39), 5394–5400. doi:10.1002/smll.201600866

Rodriguez, M. J., Ramos-Soriano, J., Perkins, J. R., Mascaraque, A., Torres, M. J., Gomez, F., et al. (2019). Glycosylated nanostructures in sublingual immunotherapy induce long-lasting tolerance in LTP allergy mouse model. *Sci. Rep.* 9 (1), 4043. doi:10.1038/s41598-019-40114-7

Rojas-Prats, E., Tosat-Bitrian, C., Martinez-Gonzalez, L., Nozal, V., Perez, D. I., and Martinez, A. (2021). Increasing brain permeability of PHA-767491, a cell division cycle 7 kinase inhibitor, with biodegradable polymeric nanoparticles. *Pharmaceutics* 13 (2), 180. doi:10.3390/pharmaceutics13020180

Romero, G., and Moya, S. E. (2012). "Chapter 4 - synthesis of organic nanoparticles," in *Frontiers of nanoscience*. Editors J. M. de la Fuente and V. Grazu (Elsevier), 4, 115–141.

Rubia-Rodriguez, I., Santana-Otero, A., Spassov, S., Tombacz, E., Johansson, C., De La Presa, P., et al. (2021). Whither magnetic hyperthermia? *A Tentat. Roadmap. Mater. (Basel)* 14 (4), 706. doi:10.3390/ma14040706

Rubia-Rodriguez, I., Zilberti, L., Arduino, A., Bottauscio, O., Chiampi, M., and Ortega, D. (2021). *In silico* assessment of collateral eddy current heating in biocompatible implants subjected to magnetic hyperthermia treatments. *Int. J. Hyperth.* 38 (1), 846–861. doi:10.1080/02656736.2021.1909758

Rubio-Canalejas, A., Baelo, A., Herbera, S., Blanco-Cabra, N., Vukomanovic, M., and Torrents, E. (2022). 3D spatial organization and improved antibiotic treatment of a Pseudomonas aeruginosa-Staphylococcus aureus wound biofilm by nanoparticle enzyme delivery. *Front. Microbiol.* 13, 959156. doi:10.3389/fmicb.2022.959156

Sabio, L., Sosa, A., Delgado-Lopez, J. M., and Dominguez-Vera, J. M. (2021). Two-sided antibacterial cellulose combining probiotics and silver nanoparticles. *Molecules* 26 (10), 2848. doi:10.3390/molecules26102848

Saha, K., Agasti, S. S., Kim, C., Li, X., and Rotello, V. M. (2012). Gold nanoparticles in chemical and biological sensing. *Chem. Rev.* 112 (5), 2739–2779. doi:10.1021/cr2001178

Samaridou, E., Walgrave, H., Salta, E., Alvarez, D. M., Castro-Lopez, V., Loza, M., et al. (2020). Nose-to-brain delivery of enveloped RNA - cell permeating peptide nanocomplexes for the treatment of neurodegenerative diseases. *Biomaterials* 230, 119657. doi:10.1016/j.biomaterials.2019.119657

Sanchez-Arribas, N., Diaz-Nunez, P., Osio Barcina, J., Aicart, E., Junquera, E., and Guerrero-Martinez, A. (2021). Controlled pDNA release in gemini cationic lipoplexes by femtosecond laser irradiation of gold nanostars. *Nanomater. (Basel)* 11 (6), 1498. doi:10.3390/nano11061498

Sanchez-Arribas, N., Martinez-Negro, M., Villar, E. M., Perez, L., Aicart, E., Taboada, P., et al. (2020). Biocompatible nanovector of siRNA consisting of arginine-based cationic lipid for gene knockdown in cancer cells. *ACS Appl. Mater Interfaces* 12 (31), 34536–34547. doi:10.1021/acsami.0c06273

Sanchez-Arribas, N., Martinez-Negro, M., Villar, E. M., Perez, L., Osio Barcina, J., Aicart, E., et al. (2020). Protein expression knockdown in cancer cells induced by a gemini cationic lipid nanovector with histidine-based polar heads. *Pharmaceutics* 12 (9), 791. doi:10.3390/pharmaceutics12090791

Sanchez-Garcia, L., Sala, R., Serna, N., Alamo, P., Parlade, E., Alba-Castellon, L., et al. (2020). A refined cocktailing of pro-apoptotic nanoparticles boosts anti-tumor activity. *Acta Biomater.* 113, 584–596. doi:10.1016/j.actbio.2020.06.033

Sanchez-Garcia, L., Serna, N., Alamo, P., Sala, R., Cespedes, M. V., Roldan, M., et al. (2018). Self-assembling toxin-based nanoparticles as self-delivered antitumoral drugs. *J. Control Release* 274, 81–92. doi:10.1016/j.jconrel.2018.01.031

Sanchez-Lopez, E., Gomara, M. J., and Haro, I. (2021). Nanotechnology-based platforms for vaginal delivery of peptide microbicides. *Curr. Med. Chem.* 28 (22), 4356–4379. doi:10.2174/0929867328666201209095753

Sans-Serramitjana, E., Jorba, M., Fuste, E., Pedraz, J. L., Vinuesa, T., and Vinas, M. (2017). Free and nanoencapsulated tobramycin: Effects on planktonic and biofilm forms of Pseudomonas. *Microorganisms* 5 (3), 35. doi:10.3390/microorganisms5030035

Sans-Serramitjana, E., Jorba, M., Pedraz, J. L., Vinuesa, T., and Vinas, M. (2017). Determination of the spatiotemporal dependence of *Pseudomonas aeruginosa* biofilm viability after treatment with NLC-colistin. *Int. J. Nanomedicine* 12, 4409–4413. doi:10.2147/ijn.s138763

Santalices, I., Vazquez-Vazquez, C., Santander-Ortega, M. J., Lozano, V., Araujo, F., Sarmento, B., et al. (2021). A nanoemulsion/micelles mixed nanosystem for the oral administration of hydrophobically modified insulin. *Drug Deliv. Transl. Res.* 11 (2), 524–545. doi:10.1007/s13346-021-00920-x

Santos, H. D. A., Zabala Gutierrez, I., Shen, Y., Lifante, J., Ximendes, E., Laurenti, M., et al. (2020). Ultrafast photochemistry produces superbright short-wave infrared dots for low-dose *in vivo* imaging. *Nat. Commun.* 11 (1), 2933. doi:10.1038/s41467-020-16333-2

Sanz, B., Calatayud, M. P., Torres, T. E., Fanarraga, M. L., Ibarra, M. R., and Goya, G. F. (2017). Magnetic hyperthermia enhances cell toxicity with respect to exogenous heating. *Biomaterials* 114, 62–70. doi:10.1016/j.biomaterials.2016.11.008

Sanz-Ortega, L., Portilla, Y., Perez-Yague, S., and Barber, D. F. (2019). Magnetic targeting of adoptively transferred tumour-specific nanoparticle-loaded CD8(+) T cells does not improve their tumour infiltration in a mouse model of cancer but promotes the retention of these cells in tumour-draining lymph nodes. *J. Nanobiotechnology* 17 (1), 87. doi:10.1186/s12951-019-0520-0

Sanz-Ortega, L., Rojas, J. M., Marcos, A., Portilla, Y., Stein, J. V., and Barber, D. F. (2019). T cells loaded with magnetic nanoparticles are retained in peripheral lymph nodes by the application of a magnetic field. *J. Nanobiotechnology* 17 (1), 14. doi:10.1186/s12951-019-0440-z

Sanz-Ortega, L., Rojas, J. M., Portilla, Y., Perez-Yague, S., and Barber, D. F. (2019). Magnetic nanoparticles attached to the NK cell surface for tumor targeting in adoptive transfer therapies does not affect cellular effector functions. *Front. Immunol.* 10, 2073. doi:10.3389/fimmu.2019.02073

Sapareto, S. A., and Dewey, W. C. (1984). Thermal dose determination in cancer therapy. *Int. J. Radiat. Oncol. Biol. Phys.* 10 (6), 787–800. doi:10.1016/0360-3016(84)90379-1

Saravani, R., Sargazi, S., Saravani, R., Rabbani, M., Rahdar, A., and Taboada, P. (2020). Newly crocin-coated magnetite nanoparticles induce apoptosis and decrease VEGF expression in breast carcinoma cells. *J. Drug Deliv. Sci. Technol.* 60, 101987. doi:10.1016/j.jddst.2020.101987

Sartaj, A., Qamar, Z., Qizilbash, F. F., Annu, Md S., Alhakamy, N. A., et al. (2021). Polymeric nanoparticles: Exploring the current drug development and therapeutic insight of breast cancer treatment and recommendations. *Polym. (Basel)* 13 (24), 4400. doi:10.3390/polym13244400

Sayed, F. N., and Polshettiwar, V. (2015). Facile and sustainable synthesis of shaped iron oxide nanoparticles: Effect of iron precursor salts on the shapes of iron oxides. *Sci. Rep.* 5, 9733. doi:10.1038/srep09733

Serrano-Sevilla, I., Artiga, A., Mitchell, S. G., De Matteis, L., and de la Fuente, J. M. (2019). Natural polysaccharides for siRNA delivery: Nanocarriers based on chitosan, hyaluronic acid, and their derivatives. *Molecules* 24 (14), 2570. doi:10.3390/molecules24142570

Sharma, G., and Jeevanandam, P. (2013). Synthesis of self-assembled prismatic iron oxide nanoparticles by a novel thermal decomposition route. *RSC Adv.* 3 (1), 189–200. doi:10.1039/c2ra22004k

Shi, L., Zhang, J., Zhao, M., Tang, S., Cheng, X., Zhang, W., et al. (2021). Effects of polyethylene glycol on the surface of nanoparticles for targeted drug delivery. *Nanoscale* 13 (24), 10748–10764. doi:10.1039/d1nr02065j

Shokrani, H., Shokrani, A., Sajadi, S. M., Khodadadi Yazdi, M., Seidi, F., Jouyandeh, M., et al. (2022). Polysaccharide-based nanocomposites for biomedical applications: A critical review. *Nanoscale Horiz.* 7, 1136–1160. doi:10.1039/d2nh00214k

Silvan, J. M., Zorraquin-Pena, I., Gonzalez de Llano, D., Moreno-Arribas, M. V., and Martinez-Rodriguez, A. J. (2018). Antibacterial activity of glutathione-stabilized silver nanoparticles against Campylobacter multidrug-resistant strains. *Front. Microbiol.* 9, 458. doi:10.3389/fmicb.2018.00458

Simeonidis, K., Morales, M. P., Marciello, M., Angelakeris, M., de la Presa, P., Lazaro-Carrillo, A., et al. (2016). *In-situ* particles reorientation during magnetic hyperthermia application: Shape matters twice. *Sci. Rep.* 6, 38382. doi:10.1038/srep38382

Soenen, S. J., Parak, W. J., Rejman, J., and Manshian, B. (2015). (Intra)cellular stability of inorganic nanoparticles: Effects on cytotoxicity, particle functionality, and biomedical applications. *Chem. Rev.* 115 (5), 2109–2135. doi:10.1021/cr400714j

Soler-Agesta, R., Guerrero-Ochoa, P., Marco-Brualla, J., Ibanez-Perez, R., Marzo, I., Martinez-Lostao, L., et al. (2022). Conjugation of the 9-kDa isoform of granulysin with liposomes potentiates its cytotoxicity. *Int. J. Mol. Sci.* 23 (15), 8705. doi:10.3390/ijms23158705

Soprano, E., Alvarez, A., Pelaz, B., Del Pino, P., and Polo, E. (2020). Plasmonic cell-derived nanocomposites for light-controlled cargo release inside living cells. *Adv. Biosyst.* 4 (3), e1900260. doi:10.1002/adbi.201900260

Spanish Scientific Network HiperNano (2018). *Spanish scientific Network HiperNano (RED2018-102626-T).*

Sperling, R. A., Rivera Gil, P., Zhang, F., Zanella, M., and Parak, W. J. (2008). Biological applications of gold nanoparticles. *Chem. Soc. Rev.* 37 (9), 1896–1908. doi:10.1039/b712170a

Spilde, M. N., Northup, D. E., Boston, P. J., Schelble, R. T., Dano, K. E., Crossey, L. J., et al. (2005). Geomicrobiology of cave ferromanganese deposits: A field and laboratory investigation. *Geomicrobiol. J.* 22 (3-4), 99–116. doi:10.1080/01490450590945889

Staka, I., Cadete, A., Surikutchi, B. T., Abuzaid, H., Bradshaw, T. D., Alonso, M. J., et al. (2019). A novel low molecular weight nanocomposite hydrogel formulation for intra-tumoural delivery of anti-cancer drugs. *Int. J. Pharm.* 565, 151–161. doi:10.1016/j.ijpharm.2019.04.070

Stepien, G., Moros, M., Perez-Hernandez, M., Monge, M., Gutierrez, L., Fratila, R. M., et al. (2018). Effect of surface chemistry and associated protein corona on the long-term biodegradation of iron oxide nanoparticles *in vivo*. *ACS Appl. Mater Interfaces* 10 (5), 4548–4560. doi:10.1021/acsami.7b18648

Storozhylova, N., Crecente-Campo, J., Cabaleiro, D., Lugo, L., Dussouy, C., Simões, S., et al. (2020). An *in situ* hyaluronic acid-fibrin hydrogel containing drug-loaded nanocapsules for intra-articular treatment of inflammatory joint diseases. *Regen. Eng. Transl. Med.* 6 (2), 201–216. doi:10.1007/s40883-020-00154-2

Sune-Pou, M., Prieto-Sanchez, S., El Yousfi, Y., Boyero-Corral, S., Nardi-Ricart, A., Nofrerias-Roig, I., et al. (2018). Cholesteryl oleate-loaded cationic solid lipid nanoparticles as carriers for efficient gene-silencing therapy. *Int. J. Nanomedicine* 13, 3223–3233. doi:10.2147/ijn.s158884

Carregal-Romero, S., Groult, H., Cañadas, O., A-Gonzalez, N., LechugaVieco, A. V., García-Fojeda, B., et al. (2021). Delayed alveolar clearance of nanoparticles through control of coating composition and interaction with lung surfactant protein A. *Materials Science and Engineering: C* 134, 112551. doi:10.1016/j.msec.2021.112551

Teijeiro-Valino, C., Novoa-Carballal, R., Borrajo, E., Vidal, A., Alonso-Nocelo, M., de la Fuente Freire, M., et al. (2019). A multifunctional drug nanocarrier for efficient anticancer therapy. *J. Control Release* 294, 154–164. doi:10.1016/j.jconrel.2018.12.002

Tenchov, R., Bird, R., Curtze, A. E., and Zhou, Q. (2021). Lipid nanoparticles-from liposomes to mRNA vaccine delivery, a landscape of research diversity and advancement. *ACS Nano* 15, 16982–17015. doi:10.1021/acsnano.1c04996

Therapeutics, H. (2020). BO-112 with pembrolizumab in unresectable malignant melanoma (SPOTLIGHT203) clinicaltrials.gov2020. Available from: https://clinicaltrials.gov/ct2/show/NCT04570332.

Therapeutics, H. (2016). *Exploratory study of BO-112 in adult patients with aggressive solid tumors clinicaltrials gov*. [Available from: https://clinicaltrials.gov/ct2/show/NCT02828098.

Thompson, S. A., Paterson, S., Azab, M. M., Wark, A. W., and de la Rica, R. (2017). Light-triggered inactivation of enzymes with photothermal nanoheaters. *Small* 13 (15), 1603195. doi:10.1002/smll.201603195

Thwala, L. N., Delgado, D. P., Leone, K., Marigo, I., Benetti, F., Chenlo, M., et al. (2018). Protamine nanocapsules as carriers for oral peptide delivery. *J. Control Release* 291, 157–168. doi:10.1016/j.jconrel.2018.10.022

Tomsen-Melero, J., Passemard, S., Garcia-Aranda, N., Diaz-Riascos, Z. V., Gonzalez-Rioja, R., Nedergaard Pedersen, J., et al. (2021). Impact of chemical composition on the nanostructure and biological activity of alpha-galactosidase-loaded nanovesicles for fabry disease treatment. *ACS Appl. Mater Interfaces* 13 (7), 7825–7838. doi:10.1021/acsami.0c16871

Torrecilla, J., Gomez-Aguado, I., Vicente-Pascual, M., Del Pozo-Rodriguez, A., Solinis, M. A., and Rodriguez-Gascon, A. (2019). MMP-9 downregulation with lipid nanoparticles for inhibiting corneal neovascularization by gene silencing. *Nanomater. (Basel)* 9 (4), 631. doi:10.3390/nano9040631

Tortiglione, C., and de la Fuente, J. M. (2019). Synthesis of gold nanoparticles for gene silencing. *Methods Mol. Biol.* 1974, 203–214. doi:10.1007/978-1-4939-9220-1_15

Trabulo, S., Aires, A., Aicher, A., Heeschen, C., and Cortajarena, A. L. (2017). Multifunctionalized iron oxide nanoparticles for selective targeting of pancreatic cancer cells. *Biochim. Biophys. Acta Gen. Subj.* 1861 (6), 1597–1605. doi:10.1016/j.bbagen.2017.01.035

Vairo, C., Basas, J., Pastor, M., Palau, M., Gomis, X., Almirante, B., et al. (2020). *In vitro* and *in vivo* antimicrobial activity of sodium colistimethate and amikacin-loaded nanostructured lipid carriers (NLC). *Nanomedicine* 29, 102259. doi:10.1016/j.nano.2020.102259

Vallet-Regi, M., Colilla, M., Izquierdo-Barba, I., and Manzano, M. (2017). Mesoporous silica nanoparticles for drug delivery: Current insights. *Molecules* 23 (1), 47. doi:10.3390/molecules23010047

Vallet-Regi, M., Gonzalez, B., and Izquierdo-Barba, I. (2019). Nanomaterials as promising alternative in the infection treatment. *Int. J. Mol. Sci.* 20 (15), 3806. doi:10.3390/ijms20153806

Vallet-Regi, M. (2022). Our contributions to applications of mesoporous silica nanoparticles. *Acta Biomater.* 137, 44–52. doi:10.1016/j.actbio.2021.10.011

Vallet-Regi, M., Rámila, A., del Real, R. P., and Pérez-Pariente, J. (2001). A new property of MCM-41: Drug delivery system. *Chem. Mater.* 13 (2), 308–311. doi:10.1021/cm0011559

Vallet-Regi, M., Schuth, F., Lozano, D., Colilla, M., and Manzano, M. (2022). Engineering mesoporous silica nanoparticles for drug delivery: Where are we after two decades? *Chem. Soc. Rev.* 51 (13), 5365–5451. doi:10.1039/d1cs00659b

Varela-Fernandez, R., Garcia-Otero, X., Diaz-Tome, V., Regueiro, U., Lopez-Lopez, M., Gonzalez-Barcia, M., et al. (2022). Lactoferrin-loaded nanostructured lipid carriers (NLCs) as a new formulation for optimized ocular drug delivery. *Eur. J. Pharm. Biopharm.* 172, 144–156. doi:10.1016/j.ejpb.2022.02.010

Vargas-Nadal, G., Munoz-Ubeda, M., Alamo, P., Mitjans, M., Cespedes, V., Kober, M., et al. (2020). MKC-quatsomes: A stable nanovesicle platform for bio-imaging and drug-delivery applications. *Nanomedicine* 24, 102136. doi:10.1016/j.nano.2019.102136

Vicente-Pascual, M., Gomez-Aguado, I., Rodriguez-Castejon, J., Rodriguez-Gascon, A., Muntoni, E., Battaglia, L., et al. (2020). Topical administration of SLN-based gene therapy for the treatment of corneal inflammation by de novo IL-10 production. *Pharmaceutics* 12 (6), 584. doi:10.3390/pharmaceutics12060584

Vilaboa, N., Bore, A., Martin-Saavedra, F., Bayford, M., Winfield, N., Firth-Clark, S., et al. (2017). New inhibitor targeting human transcription factor HSF1: Effects on the heat shock response and tumor cell survival. *Nucleic Acids Res.* 45 (10), 5797–5817. doi:10.1093/nar/gkx194

Villar-Alvarez, E., Cambon, A., Pardo, A., Arellano, L., Marcos, A. V., Pelaz, B., et al. (2019). Combination of light-driven co-delivery of chemodrugs and plasmonic-induced heat for cancer therapeutics using hybrid protein nanocapsules. *J. Nanobiotechnology* 17 (1), 106. doi:10.1186/s12951-019-0538-3

Villar-Alvarez, E., Cambon, A., Pardo, A., Mosquera, V. X., Bouzas-Mosquera, A., Topete, A., et al. (2018). Gold nanorod-based nanohybrids for combinatorial therapeutics. *ACS Omega* 3 (10), 12633–12647. doi:10.1021/acsomega.8b01591

Villaverde, G., Gómez-Graña, S., Guisasola, E., García, I., Hanske, C., Liz-Marzán, L. M., et al. (2018). Targeted chemo-photothermal therapy: A nanomedicine approximation to selective melanoma treatment. *Part. Part. Syst. Charact.* 35 (7), 1800148. doi:10.1002/ppsc.201800148

Villegas, M. R., Baeza, A., and Vallet-Regi, M. (2018). Nanotechnological strategies for protein delivery. *Molecules* 23 (5), 1008. doi:10.3390/molecules23051008

Vinuesa, T., Herraez, R., Oliver, L., Elizondo, E., Acarregui, A., Esquisabel, A., et al. (2017). Benznidazole nanoformulates: A chance to improve therapeutics for Chagas disease. *Am. J. Trop. Med. Hyg.* 97 (5), 1469–1476. doi:10.4269/ajtmh.17-0044

Vivo-Llorca, G., Morella-Aucejo, A., Garcia-Fernandez, A., Diez, P., Llopis-Lorente, A., Orzaez, M., et al. (2022). Horseradish peroxidase-functionalized gold nanoconjugates for breast cancer treatment based on enzyme prodrug therapy. *Int. J. Nanomedicine* 17, 409–422. doi:10.2147/ijn.s323802

Volta-Duran, E., Serna, N., Sanchez-Garcia, L., Avino, A., Sanchez, J. M., Lopez-Laguna, H., et al. (2021). Design and engineering of tumor-targeted, dual-acting cytotoxic nanoparticles. *Acta Biomater.* 119, 312–322. doi:10.1016/j.actbio.2020.11.018

Wolfram, J., and Ferrari, M. (2019). Clinical cancer nanomedicine. *Nano Today* 25, 85–98. doi:10.1016/j.nantod.2019.02.005

Ximendes, E., Marin, R., Shen, Y., Ruiz, D., Gomez-Cerezo, D., Rodriguez-Sevilla, P., et al. (2021). Infrared-emitting multimodal nanostructures for controlled *in vivo* magnetic hyperthermia. *Adv. Mater* 33 (30), e2100077. doi:10.1002/adma.202100077

Ximendes, E. C., Rocha, U., Sales, T. O., Fernández, N., Sanz-Rodríguez, F., Martín, I. R., et al. (2017). *In vivo* subcutaneous thermal video recording by supersensitive infrared nanothermometers. *Adv. Funct. Mater.* 27 (38), 1702249. doi:10.1002/adfm.201702249

Xuan, M., Mestre, R., Gao, C., Zhou, C., He, Q., and Sanchez, S. (2018). Noncontinuous super-diffusive dynamics of a light-activated nanobottle motor. *Angew. Chem. Int. Ed. Engl.* 57 (23), 6954–6958. doi:10.1002/ange.201801910

Zamora-Perez, P., Pelaz, B., Tsoutsi, D., Soliman, M. G., Parak, W. J., and Rivera-Gil, P. (2021). Hyperspectral-enhanced dark field analysis of individual and collective photo-responsive gold-copper sulfide nanoparticles. *Nanoscale* 13 (31), 13256–13272. doi:10.1039/d0nr08256b

Zhang, Y., Liu, M., Peng, B., Zhou, Z., Chen, X., Yang, S. M., et al. (2016). Controlled phase and tunable magnetism in ordered iron oxide nanotube arrays prepared by atomic layer deposition. *Sci. Rep.* 6, 18401. doi:10.1038/srep18401

frontiers | Frontiers in Bioengineering and Biotechnology

TYPE Original Research
PUBLISHED 27 July 2023
DOI 10.3389/fbioe.2023.1221458

Check for updates

OPEN ACCESS

EDITED BY
Mingqiang Li,
Third Affiliated Hospital of Sun Yat-Sen University, China

REVIEWED BY
Lesan Yan,
Wuhan University of Technology, China
Ruogu Qi,
Nanjing University of Chinese Medicine, China
Yingshuai Wang,
Weifang Medical University, China
Qingqing Xiong,
Tianjin Medical University Cancer Institute and Hospital, China

*CORRESPONDENCE
Lei Xu,
xul646@163.com

RECEIVED 12 May 2023
ACCEPTED 10 July 2023
PUBLISHED 27 July 2023

CITATION
Bao S, Sun S, Li L and Xu L (2023), Synthesis and antibacterial activities of Ag-TiO_2/ZIF-8.
Front. Bioeng. Biotechnol. 11:1221458.
doi: 10.3389/fbioe.2023.1221458

COPYRIGHT
© 2023 Bao, Sun, Li and Xu. This is an open-access article distributed under the terms of the Creative Commons Attribution License (CC BY). The use, distribution or reproduction in other forums is permitted, provided the original author(s) and the copyright owner(s) are credited and that the original publication in this journal is cited, in accordance with accepted academic practice. No use, distribution or reproduction is permitted which does not comply with these terms.

Synthesis and antibacterial activities of Ag-TiO_2/ZIF-8

Siqi Bao, Shuanghui Sun, Lin Li and Lei Xu*

School of Chemistry and Environmental Engineering, Changchun University of Science and Technology, Changchun, China

In recent years, massive bacterial infections have led to human illness and death, reminding us of the urgent need to develop effective and long-lasting antimicrobial materials. In this paper, Ag-TiO_2/ZIF-8 with good environmental friendliness and biological antibacterial activity was prepared by solvothermal method. The structure and morphology of the synthesized materials were characterized by XRD, FT-IR, SEM-EDS, TEM, XPS, and BET. To investigate the antibacterial activity of the synthesized samples, *Escherichia coli* and *Bacillus subtilis* were used as target bacteria for experimental studies of zone of inhibition, bacterial growth curves, minimum bactericidal concentration and antibacterial durability. The results demonstrated that 20 wt.%Ag-TiO_2/ZIF-8 had the best bacteriostatic effect on *E. coli* and *B. subtilis* under dark and UV conditions compared to TiO_2 and ZIF-8. Under the same conditions, the diameter of the inhibition circle of 20 wt% Ag-TiO_2/ZIF-8 is 8.5–11.5 mm larger than that of its constituent material 4 wt% Ag-TiO_2, with more obvious antibacterial effect and better antibacterial performance. It is also proposed that the excellent antibacterial activity of Ag-TiO_2/ZIF-8 is due to the synergistic effect of Ag-TiO_2 and ZIF-8 under UV light. In addition, the prepared material has good stability and durability with effective antimicrobial activity for more than 5 months.

KEYWORDS

antibacterial activity, bioactive organic materials, *Escherichia coli*, *Bacillus subtilis*, Ag-TiO_2, ZIF-8

1 Introduction

In recent years, the proliferation of microorganisms such as bacteria and viruses in the environment has posed a serious threat to the ecosystem and human health. Antibacterial materials are functional materials that can kill harmful bacteria or inhibit the growth and reproduction of harmful bacteria. The antibacterial effect of antimicrobial materials is generally evaluated by factors such as the diameter of the inhibition circle, the concentration of the minimum inhibition circle, and the bacterial growth curve. *E. coli* and *Bacillus subtilis* are two typical bacteria that are widespread in daily life and can cause health hazards such as abdominal pain, diarrhea, etc. However, the antimicrobial agents currently in use have disadvantages such as short expiration dates, high consumption, and specific hazards to the surrounding area, either by themselves or as by-products, which greatly limit the practical application. With the increasing human requirements for environmental health and recognition, the research and development of long-lasting, stable and environmentally friendly antimicrobial agents has become one of the hot spots of concern for many scholars.

TiO_2 has become a promising photocatalytic antibacterial agent due to its excellent characteristics such as green, stable, broad-spectrum antibacterial and simple preparation (Hayashi et al., 2020; Rodriguez-Gonzalez et al., 2020). However, it also has many drawbacks, such as: weak light capture ability and small specific surface area, which limit its application

in the field of photocatalytic antibacterial. To compensate for these drawbacks and obtain highly active photocatalytic antimicrobial agents, metal loading (e.g., Ag, Pt and Au) was used to modify the TiO_2 (Abadikhah et al., 2019; Ponomarev et al., 2019; Nasim et al., 2020; Xue et al., 2020). As we all know that silver nanoparticles are widely studied and used thanks to their excellent and long-lasting antibacterial activity as well as low induced drug resistance (Xu Y. et al., 2020). Dong et al. reported Ag-TiO_2 nanocomposites prepared by dielectric barrier discharge (DBD) cold plasma treatment could effectively inhibit the growth of *E. coli* and *Staphylococcus aureus* (Dong et al., 2019). The surface modified by Ag/TiO_2 nanoparticles prepared by Lu et al. was able to remove *E. coli* and *B. subtilis* under visible light induction (Lu et al., 2019). However, Ag/TiO_2 still has disadvantages such as aggregation phenomena and limited antibacterial activity.

Metal organic frameworks (MOFs) are porous crystalline materials with a periodic network structure composed of metal centers (metal ions or metal clusters) and bridging organic ligands, which have attracted increasing attention due to their large specific surface area, ease of separation, and structural and functional diversity (Zhu et al., 2019; Chen et al., 2021). Among the MOFs, ZIF-8 is a member of the zeolitic imidazolium framework (ZIF) family, which has been widely used in adsorption, catalysis, energy storage and separation processes due to its high specific surface area, special pore structure and good thermal stability (Zheng et al., 2020; Ahmad et al., 2021). Because of the central metal ion Zn^{2+} with antibacterial activity, ZIF-8 can also be used as an antibacterial agent (Xu W. et al., 2020). Combining MOFs with inorganic substances can effectively improve the antibacterial activity of the complexes. In this experiment, the bacterial inhibitory ability was enhanced by compounding ZIF-8 with TiO_2 and Ag. Nabi-pour et al. tested the antimicrobial activity of ciprofloxacin/ZIF-8 against *E. coli* and *S. aureus*, and the results exhibited that the synthetic agent could well inhibit the growth of a range of microorganisms such as bacteria (Nabipour et al., 2017). Guo et al. successfully fabricated core-shell Ag@ZIF-8 nanowires, which showed significant antibacterial activity against *E. coli* and *B. subtilis* (Guo et al., 2018). Malik et al. synthesized multifunctional CdSNPs@ZIF-8 with antimicrobial activity against *E. coli* and *S. aureus* (Malik et al., 2018).

Hence, based on the above discussion, Ag-TiO_2/ZIF-8 ternary composites with excellent biological antibacterial activity were successfully prepared by the solvothermal method. ZIF-8 was introduced into the material to increase the specific surface area, thereby increasing the contact area between the biocide and the bacteria. In addition, Ag^+ and Zn^{2+} can promote the separation of TiO_2 electron-hole pairs, enhance photocatalysis and generate more active substances to attack organic macromolecules in bacteria for their oxidative degradation (Younis et al., 2020; Ma et al., 2021). Then, the structure, morphology and elemental analysis of the prepared materials were studied in detail by XRD, FT-IR, XPS, TEM and EDS. Finally, *E. coli* and *B. subtilis* were selected for antibacterial activity evaluation experiments, such as inhibition zone, bacterial growth curve, minimum bactericidal concentration and antibacterial durability, and the antibacterial mechanism of Ag-TiO_2/ZIF-8 was further explored.

2 Materials and methods

2.1 Materials

Tetrabutyl titanate [$Ti(OBu)_4$], silver nitrate (99.8%, $AgNO_3$), absolute ethanol (99%), glacial acetic acid (98%), zinc nitrate hexahydrate, 2-methylimidazole, N,N-dimethylformamide (DMF), dichloromethane (DCM) and chloroform were purchased from Tianjin Guangfu Fine Chemical Research Institute Co., Ltd. China. *Escherichia coli (E. coli)* and *B. subtilis (B. subtilis)* were obtained from the private collection of the Biology Department, School of Life Science and Technology, Changchun University of Science and Technology. All biological reagents were purchased from Ob-xing Biological Co., Ltd. China. Deionized water was used throughout the experiments except for antibacterial activity evaluation experiments when sterile water was used. All chemicals were used directly without further purification.

2.2 Synthesis of Ag-TiO_2

Ag-TiO_2 was synthesized by the sol-gel method using $Ti(OBu)_4$ and $AgNO_3$ as the titanium source and dopant, respectively. Solution 1 was prepared by adding a few drops of $Ti(OBu)_4$ (8.5 mL) to absolute alcohol (20.0 mL). A certain amount of $AgNO_3$, acetic acid (2 mL), pure ethanol (6 mL) and a small amount of deionized water were mixed to obtain Solution 2. After the two solutions became abrasive, solution 1 was added dropwise to solution 2 under stirring conditions until a clear sol was produced and aged for 12 h to form a gel. Then, the gel was heated to 200°C at 2°C/min, maintained 120 min and cooled under ambient condition. The final product was obtained by washing three times in deionized water, baking at 70°Ctemperature overnight and then crushing into a purple-black powder. The theoretical content of Ag among the prepared Ag-TiO_2 was 1wt%~6wt%. For the sake of comparison, the above-mentioned steps were repeated in the absence of $AgNO_3$ to prepare TiO_2.

2.3 Synthesis of Ag-TiO_2/ZIF-8

The Ag-TiO_2/ZIF-8 ternary composites were synthesized by the solvothermal method. $ZnNO_3 \bullet 6H_2O$ (0.478 g), 2-methylimidazole (0.120 g) and Ag-TiO_2 (0.008 g) were dissolved in DMF (36 mL) and stirred thoroughly. A certain mass of 4 wt% Ag-TiO_2 was added into the above solution and stirred well to prepare a synthetic mixed solution. Then the mixture solution was heated to 140°C at 5°C/min and held for 24 h, then cooled to ambient temperature at 0.4°C/min. The final product was washed sequentially with chloroform, DMF and DCM, dried at 50°C, and ground to a brownish-yellow powder to finally obtain 4 wt% Ag-TiO_2/ZIF-8. In the synthesized Ag-TiO_2/ZIF-8, the theoretical content of Ag-TiO_2 ranged from 5 wt% to 70 wt%, and the specific modification amounts were shown in Supporting Material Supplementary Table S1. For the sake of contrast, the same procedure was followed for the preparation of ZIF-8 in the absence of Ag-TiO_2.

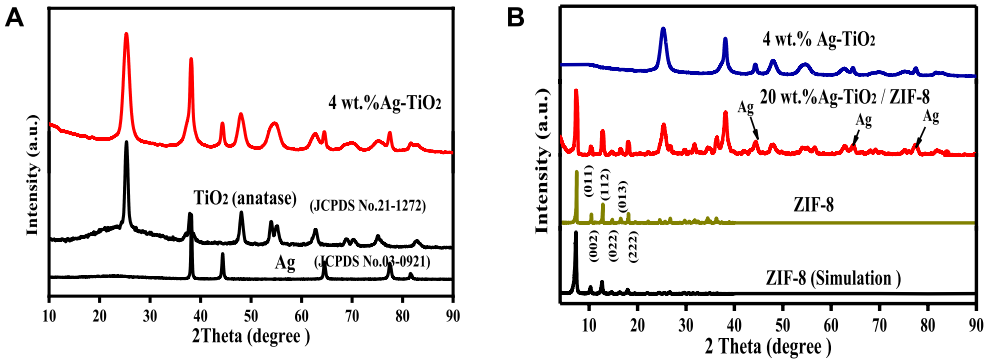

FIGURE 1
XRD patterns of as-synthesized TiO_2, 4 wt% Ag-TiO_2 **(A)** and ZIF-8, 4 wt% Ag-TiO_2, 20wt.%Ag-TiO_2/ZIF-8 **(B)**.

2.4 Characterization

The crystal structure of the material was studied on a Ricoh Y-2000 X-ray diffractometer with data recorded by powder X-ray diffractometer (XRD) in the range of 10° to 90°. The composition and chemical bonding of the materials were tested by Fourier transform infrared spectra (FT-IR, IFS 66V/S, Germany). The morphologies of the materials were carried out with transmission electron microscopy (TEM, Hitachi-H600). The elemental analysis was analyzed by energy dispersive spectroscopy (EDS) attached to SEM. X-ray photoelectron spectroscopy (XPS) results of materials were determined through Rigaku 2500/PC spectrometer. (In this experiment, Mg was chosen as the target source for the XPS test.) The surface area of each material was examined from the nitrogen adsorption-desorption isotherm using the Micromeritics ASAP 2020 system.

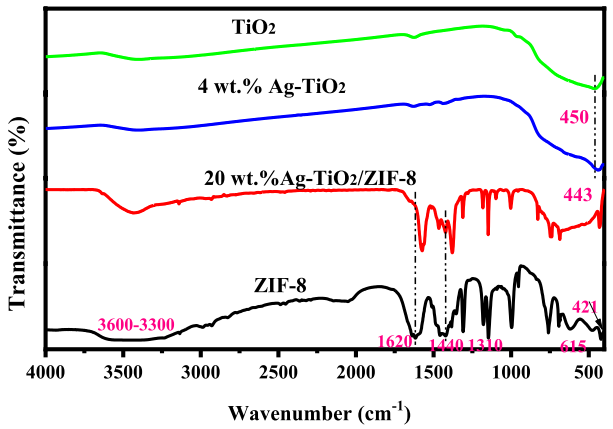

FIGURE 2
FT-IR spectra of ZIF-8, TiO_2, 4 wt.%Ag-TiO_2 and 20 wt.%Ag-TiO_2/ZIF-8.

2.5 Study of antibacterial activity

The antibacterial performance of the material was evaluated by measuring the zone of inhibition (ZOI), bacterial growth curve, minimum bactericidal concentration (MBC), and observing the antibacterial durability of the material. *E. coli* and *B. subtilis* were selected as test organisms and tested under dark and UV conditions. The specific experimental operations were as follows: (a) Zone of inhibition: The bacterial enrichment solution (80 μL) and the prepared material (100 mg) were put into the medium, then sealed and inverted in a shaker in a constant temperature incubator for 1 day, and the diameter of the zone of inhibition was measured with a ruler. (b) Bacterial growth curves: During the bacterial growth curve experiment, the prepared material was dissolved in fresh LB liquid medium (150 mL) and sterilized at 121°C for 20 min. After cooling, bacterial enrichment cultures (10 mL) were added and incubated at 37°C. The optical density (OD) of the bacteria was then measured using a UV-Vis spectrophotometer and the growth curve of the bacteria was plotted. (c) The MBC was obtained by preparing solid media with different amounts of preparation materials, adding bacterial enrichment, and measuring the number and condition of bacterial growth. (d) The durability of the antibacterial activity of the prepared materials was determined by observing changes in the zone of inhibition on the solid culture medium after 5 months.

3 Results and discussion

3.1 Characterization of the materials

The crystal structure and phase constitution of as-synthesized materials were identified by XRD, and the patterns are illustrated in Figure 1.

As shown in Figure 1A, the diffraction peaks (2θ) of Ag-TiO_2 at 25.3° (101), 37.8° (112), 48.0° (200), 62.7° (204), 68.8° (116), 75.3° (215) and 82.5° (303) are consistent with the standard XRD data of anatase phase TiO_2 (JCPDS No. 21-1272), showing that the TiO_2 used as a carrier has an obvious anatase structure, and the phase structure of TiO_2 did not change significantly after the silver modification. The

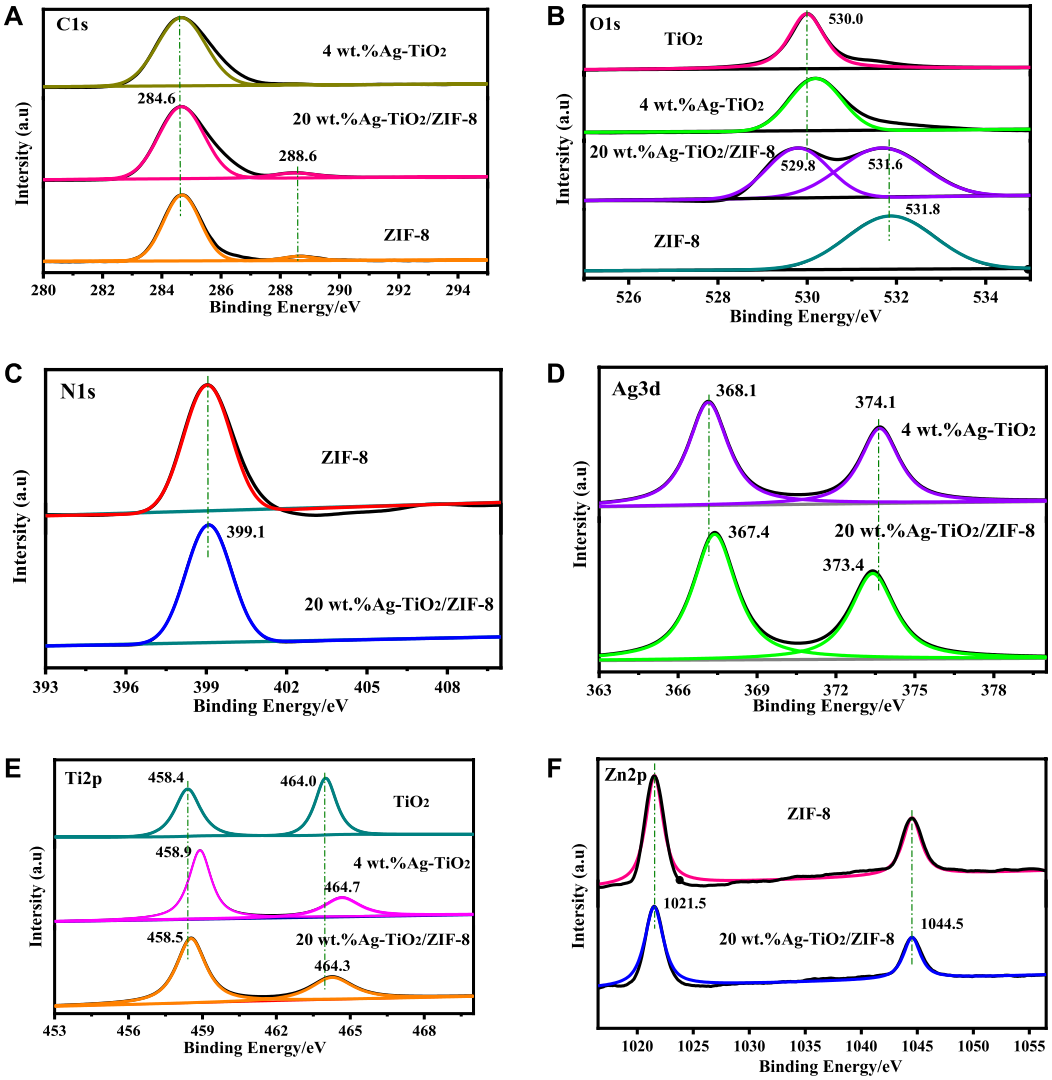

FIGURE 3
XPS: **(A)** C 1s XPS pattern, **(B)** O 1s XPS pattern, **(C)** N 1s XPS pattern, **(D)** Ti 2p XPS pattern, **(E)** Ag 3d XPS pattern, **(F)** Zn 2p XPS pattern.

other peaks of Ag-TiO_2 at 38.2° (111), 44.5° (200), 64.5° (220) and 77.5° (311) correspond to the cubic crystal form of pure silver (JCPDS No. 03-0921). The change from baryons to singletons at 2θ ≈ 54.4° may be due to the presence Ag^0 and AgO_x. Therefore, the peaks of Ag-TiO_2 matched well with Ag and TiO_2, proving that Ag-TiO_2 material was successfully prepared. Figure 1B suggests that the diffraction peaks of ZIF-8 is in good agreement with the previously published results (Jia et al., 2020), and the sharp diffraction peaks illustrated good crystal shape, confirming the formation of pure ZIF-8 phase. All the diffraction peaks of Ag-TiO_2/ZIF-8 can be associated with crystalline ZIF-8 and Ag-TiO_2, and no peaks of impurities are detected, which indicates the successful synthesis of Ag-TiO_2/ZIF-8. Moreover, Ag-TiO_2 doping into ZIF-8 does not affect the integrity of its crystal structure and framework.

The FT-IR spectra of the prepared materials are displayed in Figure 2. The FT-IR spectra of 20 wt% Ag-TiO_2 are shown in Supplementary Figure S1. The characteristic band of TiO_2 at 450 cm^{-1} is related to the vibrational mode of Ti-O-Ti bond, which shifts slightly to a lower frequency (443 cm^{-1}) after the silver modification (Li et al., 2019). In the spectrum of ZIF-8, the stretching pattern of the NH groups was discovered by analyzing the absorption band from 3300 to 3000 cm^{-1} (Troyano et al., 2019). The bands at 1620, 1440 and 421 cm^{-1} are attributed to the stretching modes of the C = N, C-N and Zn-N bonds, respectively (Abdi, 2020; Lia et al., 2020). The adsorption bands in the 600-1300 cm^{-1} region are attributed to stretching and bending vibrations of the imidazole ring (Li Y. Y. et al., 2020). These assignments are in common with the previously reported results (Vaidya et al., 2019). All characteristic bands of 4wt.%Ag-TiO_2 and ZIF-8 can be observed in the spectra of 20wt.%Ag-TiO_2/ZIF-8, indicating the successful construction of the complex. The smaller displacements at 1620 cm^{-1} and 1440 cm^{-1} may be due to the interaction of various functional groups among Ag-TiO_2/ZIF-8.

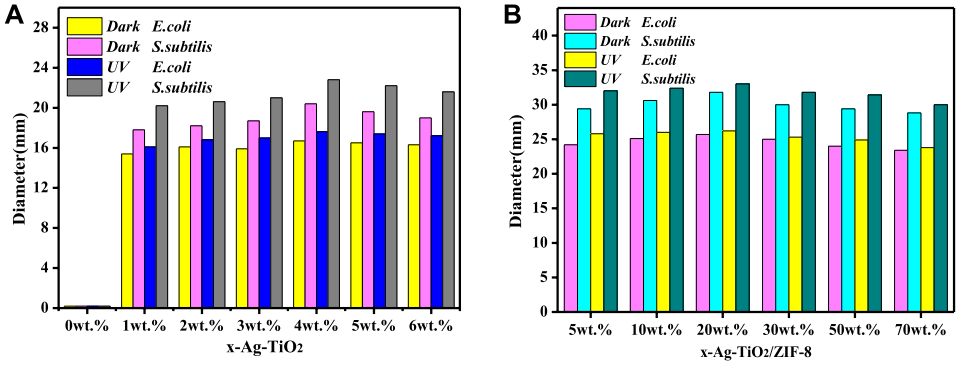

FIGURE 4
Diameters of ZOI of x-Ag-TiO_2 **(A)** and x-Ag-TiO_2/ZIF-8 **(B)**.

The TEM study the morphology and microstructure of the prepared materials. The results shows that pure ZIF-8 crystal has a dodecahedral sodalite structure with many hexagonal and quadrilateral planes (Supplementary Figure S2A), which is consistent with the previous report (Bin et al., 2020). In Supplementary Figure S2B, silver granules are well scattered on the surface of TiO_2, and this is because the radius of Ag^+ (12.6 nm) is larger than that of Ti^{4+} (7.45 nm), causing silver ions hardly enter the lattice of TiO_2 (Prabhu and Valan, 2020). Ag-TiO_2/ZIF-8 consists of Ag, TiO_2 and ZIF-8, and spherical Ag-TiO_2 particles are observed on the surface of the ternary complex (Supplementary Figure S2C), demonstrating the modification of Ag-TiO_2 makes no difference for the crystal structure and the integrity of framework. Furthermore, a typical EDS spectrum in Supplementary Figure S2D verifies the existence of C, O, N, Ag, Ti, Zn elements, and the silver content is 0.72 wt%. The Mapping of Ag-TiO_2/ZIF-8 is shown in Supplementary Figure S2E–J, and it can be found that the prepared materials have good dispersion properties.

The surface electronic elemental composition of the prepared materials is conducted by XPS. Supplementary Figure S3 confirms the existence C, N, O, Zn in ZIF-8, C, O, Ag, Ti in Ag-TiO_2 and C, N, O, Ag, Ti, Zn in Ag-TiO_2/ZIF-8. The element C is derived from the ligand of ZIF-8 and CO_2 adsorbed on the surface of the materials in the C 1s spectrum (Figure 3A). The main peaks located at 284.6 eV and 288.6 eV of 20 wt.%Ag-TiO_2/ZIF-8 are ascribed to C-C and C-N, respectively (Shwetharani et al., 2019; Ji et al., 2020). In comparison with the cohesive energy of O in TiO_2 and ZIF-8, two peaks are found and the binding energy display negative shifts after loading (Figure 3B), suggesting interactions exist ternary complex. The peak at 531.6 eV and 529.8 eV correspond to O 1s binding energy of C=O and lattice oxygen of anatase phase TiO_2, respectively (Singh and Mehata, 2019). The N 1s peak at 399.1 eV can originate from sp^2-hybridized nitrogen (C=N-C) (Figure 3C) (Wang et al., 2020). The 6.0 eV variance between the binding energy of $Ag3d_{5/2}$ and Ag $3d_{3/2}$ peak among Ag-TiO_2/ZIF-8 (Figure 3D) is characteristic of metallic Ag 3d state, implying that Ag exists as Ag^0 and AgO_x rather than Ag^+, which is consistent with the results of XRD. In Figure 3E, the binding energy located at 458.5 eV and 464.3 eV were put down to Ti $2p_{3/2}$ and Ti $2p_{1/2}$, respectively, which is consistent with the Ti 2p spectrum of TiO_2 (Rempel et al., 2020). By comparison, Ag-TiO_2/ZIF-8 (Figure 3D, E) displayed small shifts, revealing Ti-O-Ag chemical bonding exists. The Zn 2p peak splits into two peaks of Zn $2p_{3/2}$ (1021.5 eV) and Zn $2p_{1/2}$ (1044.5 eV) (Figure 3F) (Ren et al., 2019), demonstrating the state of Zn element remains unaltered after synthesizing Ag-TiO_2/ZIF-8.

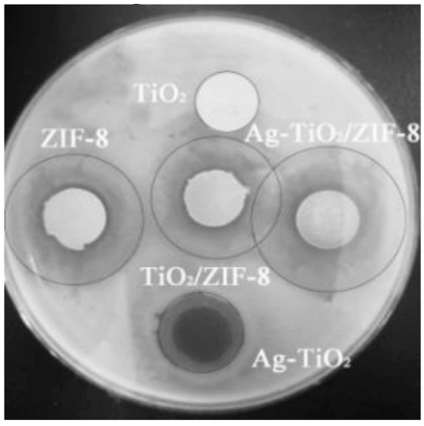

FIGURE 5
Images of ZOI of the prepared materials.

Supplementary Figure S4A displays the N_2 adsorption-desorption isotherms for 4 wt.%Ag-TiO_2, ZIF-8 and different loadings of Ag-TiO_2/ZIF-8. The Ag-TiO_2 shows type IV isotherms with hysteresis loops, demonstrating the prepared material is mesoporous. The ZIF-8 belongs to type I isotherm, indicating the presence of microporous, which is in line with the results published previously (Li C. E. et al., 2020). Meanwhile, the pore-size distributions also show that ZIF-8 was mainly microporous (Supplementary Figure S4B). Between different loadings of Ag-TiO_2 (20 wt%, 50 wt%), it was found that the increase of N_2 adsorption slowed down with increasing loading in the region of $P/P_0 < 0.01$, and a hysteresis loop appeared in the range of $P/P_0 = 0.4–0.8$, which indicated that the microporous structure characteristics became less pronounced and the mesoporous structure gradually became obvious. Therefore, a conclusion could be drawn from the above discussion that Ag-TiO_2 was attached to the surface of ZIF-8 and covered the microporous of ZIF-8. This assumption was consistent with the TEM image. Moreover, the average pore size of 20wt% Ag-

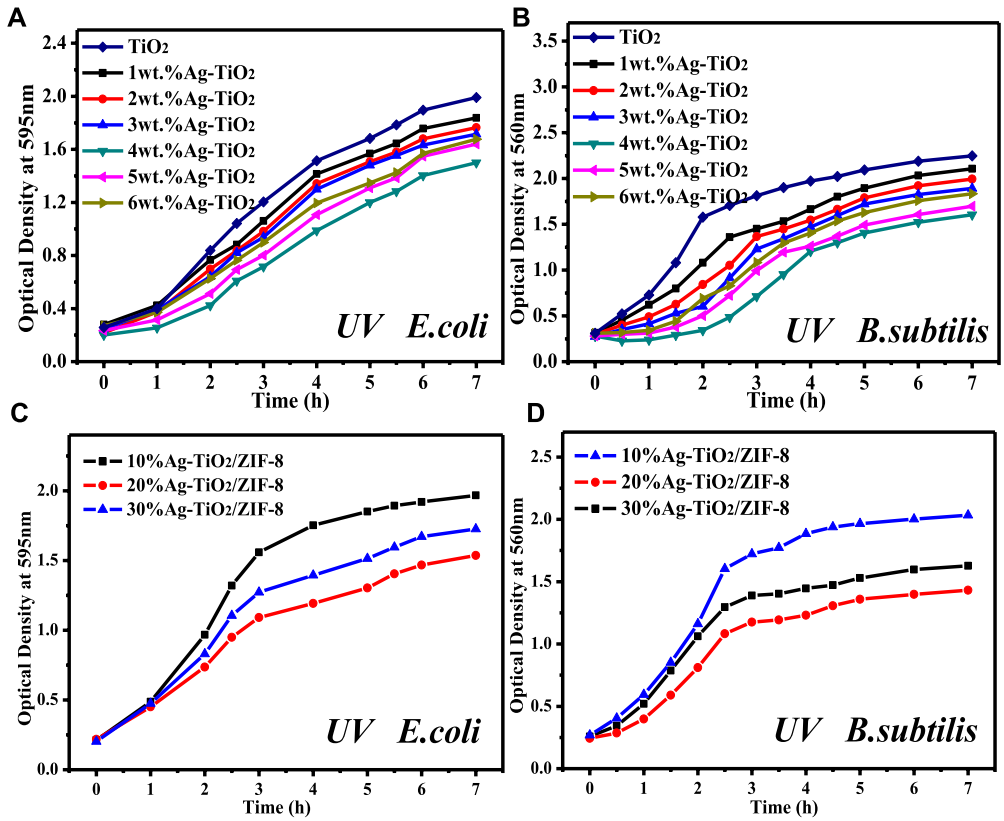

FIGURE 6
Growth curves of two kinds of bacteria under UV light **(A,C)**: *E. coli*; **(B,D)**: *B.subtilis*.

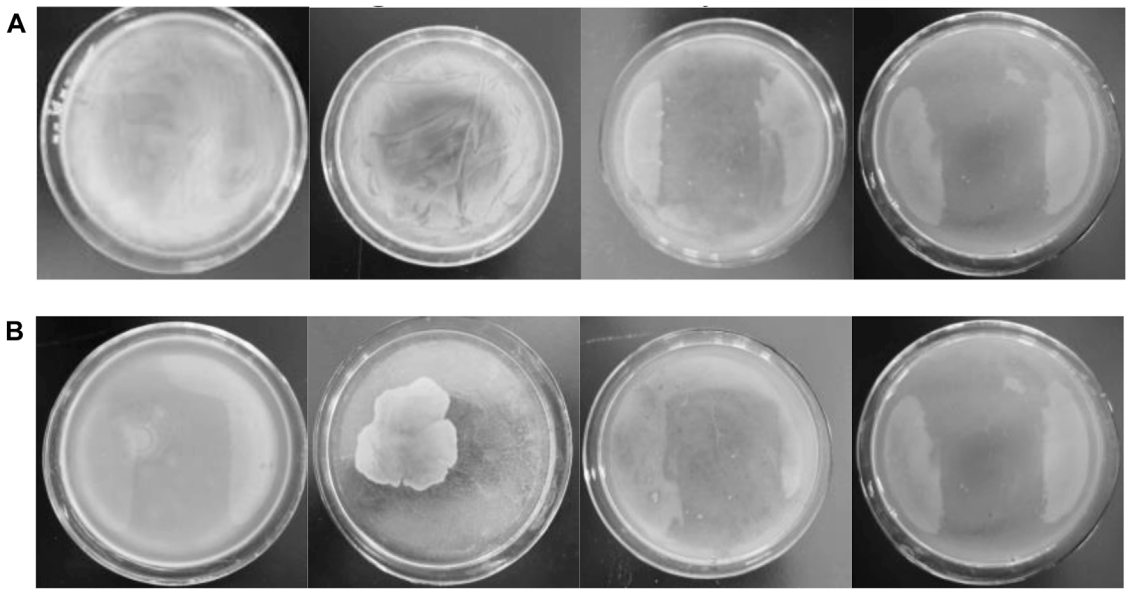

FIGURE 7
Images of MBC of 20 wt% Ag-TiO_2/ZIF-8 against *E coli* **(A)** and *B subtilis* **(B)** with the concentration of antibacterial agent increasing from left to right (3.50、3.65、3.70 and 3.80 mg/L) under UV light.

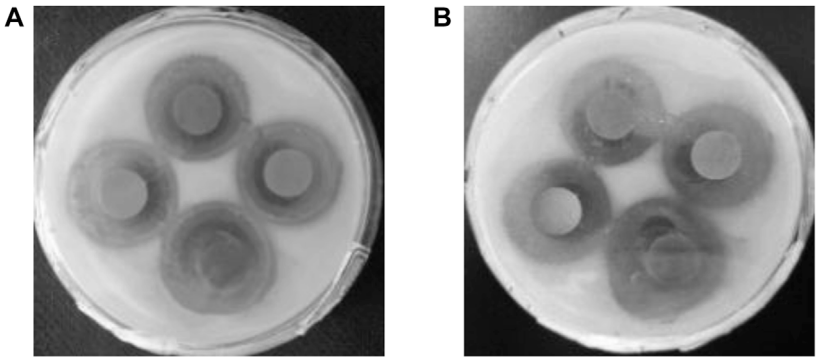

FIGURE 8
Images of ZOI of Ag-TiO_2/ZIF-8 against *B subtilis* after 1 day **(A)** and 5 months **(B)** under UV light.

TiO_2/ZIF-8 (4.46 nm) was larger than that of ZIF-8 (3.84 nm), and the BET surface areas was smaller than that of ZIF-8 (637.9 $m^2 \cdot g^{-1}$) (Supplementary Table S2), which demonstrated Ag-TiO_2 exists on the surface of ZIF-8, confirming the conclusion of N_2 adsorption-desorption isotherms.

3.2 Antibacterial activity evaluation

3.2.1 Zone of inhibition

The antibacterial activity of the prepared materials was evaluated through the ZOI assay (Zheng et al., 2023), and the results are summarized as follows. Combined with Figure 4A, Supplementary Figure S5, S6 and Supplementary Table S3, the control reactions show that no antibacterial activity was observed for pure TiO_2, while the antibacterial activity was significantly increased by the silver modification under dark and UV conditions. Moreover, the results show that the obtained 4 wt% Ag-TiO_2 at 4% silver deposition (mass ratio to pure TiO_2) had the best antibacterial activity against *E. coli* and *Bacillus subtilis* with ZOI diameters of 17.6 and 22.8 mm under UV light, respectively. As the degree of silver modification continues to increase, it readily agglomerates into large size silver particles, reducing its dispersibility and performance, thus weakening the antimicrobial activity of the material. Therefore, 4 wt.%Ag-TiO_2 was chosen for further experiments. Loading studies on different amounts of 4 wt.% Ag-TiO_2 reveals that the obtained 20wt% Ag-TiO_2/ZIF-8 has outstanding antibacterial activity against *E. coli* and *B. subtilis* when Ag-TiO_2 was deposited at 20% (mass ratio to pure ZIF-8), and the diameters of ZOI are 26.2 and 33.0 mm under UV light, respectively (Figure 4B, Supplementary Figure S7, S8 and Supplementary Table S4). Under equivalent conditions, the diameter of the inhibition circle of 20 wt% Ag-TiO_2/ZIF-8 is larger than that that of 4 wt% Ag-TiO_2, ZIF-8, TiO_2/ZIF-8 (Figure 5), which proves the antibacterial activity was significantly improved by loading Ag-TiO_2 and there is a synergetic effect between Ag-TiO_2 and ZIF-8.

3.2.2 Growth curve of bacteria

In order to investigate the effect of the prepared materials on bacterial growth, the growth curves of two types of bacteria were measured. Through preliminary experimental exploration, a loading of 30 mg Ag was selected to prepare 0.2 mg/L Ag-TiO_2 liquid culture medium. As revealed in Figure 6 and Supplementary Figure S9, pure TiO_2 inhibited the growth of bacteria, which is consistent with the photocatalytic antibacterial mechanism of TiO_2 (Jing et al., 2020). A comparative study of Ag-TiO_2 from 1 wt% to 6 wt% reveals that 4 wt% Ag-TiO_2 shows the strongest inhibitory effect on bacterial growth, and the smallest OD value was measured at 7 h under dark and UV conditions. In addition, it was found that the high concentration of Ag-TiO_2/ZIF-8 (0.2 mg/L) could completely inhibit the growth of bacteria used in experiments. Therefore, 15 mg of Ag-TiO_2/ZIF-8 was chosen to make 0.1 mg/L of liquid medium. Figure 6C, D and Supplementary Figure S10 show that 20 wt% Ag-TiO_2/ZIF-8 has the best antibacterial activity with the lowest OD values measured at 7 h under dark and UV conditions. When the amount of Ag-TiO_2/ZIF-8 is half of Ag-TiO_2, the OD measured at 7 h is smaller, and the concentration of bacteria solution is lower, indicating that the antimicrobial activity of Ag-TiO_2/ZIF-8 is superior to that of Ag-TiO_2, and Ag-TiO_2 has a positive effect on improving the antibacterial activity of Ag-TiO_2/ZIF-8. These findings are identical to those of the ZOI analysis.

3.2.3 Minimum bactericidal concentration

The MBC of the antibacterial agent refers to the minimum concentration needed to kill 99.9% of the test microorganisms. According to the experiment results of ZOI and bacteria growth curves, 20 wt% Ag-TiO_2/ZIF-8 has the optimum antibacterial activity. Therefore, 20 wt% Ag-TiO_2/ZIF-8 was chosen to explore a series of MBCs under dark and UV conditions.

As the concentration of antimicrobial agent increased from left to right, the last LB agar plate is almost free of bacteria after 24 h under dark and UV conditions (Figure 7 and Supplementary Figure S11), demonstrating that Ag-TiO_2/ZIF-8 possesses excellent antimicrobial activity. The MBS of Ag-TiO_2/ZIF-8 against *E. coli* and *B. subtilis* are 3.65 and 3.50 mg/L under UV light, which are lower than those under dark conditions (3.80 and 3.70 mg/L), showing the antibacterial activity under UV light is more apparent, and the bactericidal activity against *B.*

subtilis is stronger. These results are corroborated by the findings of ZOI and bacterial growth curve analysis.

3.2.4 Antibacterial durability

Antibacterial durability is an important indicator of the quality of antimicrobial agents. The ZOI was observed after 5 months of further incubation (Figure 8). The ZOI can visually expand outward while the contours are still noticeable. There are no colonies around, and the antibacterial activity does not diminish after 5 months, indicating the excellent antibacterial durability of Ag-TiO_2/ZIF-8. Due to its good antimicrobial durability, once it is put into use, it helps to reduce the cost of use. So, Ag-TiO_2/ZIF-8 is expected to become a long-lasting antimicrobial agent.

3.3 Probable antibacterial mechanism

Based on the above experimental results of antibacterial activity evaluation, it can be concluded that the antibacterial activity of Ag-TiO_2/ZIF-8 is better than that of Ag-TiO_2 and ZIF-8. The possible antibacterial mechanism of Ag-TiO_2/ZIF -8 was proposed as follows.

(i) When Ag-TiO_2/ZIF-8 is added to a solution containing bacteria, it can release Ag^+ and Zn^{2+} with low toxicity and biological antibacterial activity, these metal ions can come into direct contact with the bacteria and bind to component proteins in cell walls and membranes, denaturing and inactivating the component proteins (Chen et al., 2023; Wang et al., 2023). This causes the outer layer to lose its protection and the bacteria burst and die (Mariappan et al., 2022; Sun et al., 2023). In addition, the interaction between Ag^+ and DNA structures can prevent bacterial reproduction (Cao et al., 2020; Liu et al., 2022). (ii) TiO_2 itself has some photocatalytic antibacterial activity. When the energy provided by UV radiation is greater than 3.2 eV, the photogenerated electrons (e_{CB}^-) and holes (h_{VB}^+) generated by TiO_2 react with water and oxygen to form free ROS, which kill bacteria by destroying cell walls and solidifying viral proteins (Zerjav et al., 2017). Moreover, when TiO_2 is combined with Ag and ZIF-8 to form a ternary complex, the Ag^+ and Zn^{2+} in the material can actively inhibit the electron-hole pair recombination and further improve the photocatalytic antibacterial activity (Yang et al., 2019). And Ag-TiO_2 can also work in dark conditions where bacteria tend to multiply, so the application field of antibacterial agent will be further expanded without the limitation of light sources. (iii) On account of the high BET surface area and porous structure of ZIF-8, more Ag-TiO_2 is uniformly dispersed on its surface, which increases the contact area between the bactericidal agent and bacteria, thereby improving the antibacterial activity. In addition, Ag^+ and Zn^{2+} can be slowly released from Ag-TiO_2/ZIF-8 to achieve a long-term antibacterial effect. In summary, the high antibacterial activity of Ag-TiO_2/ZIF-8 comes from the synergetic effect between Ag-TiO_2 and ZIF-8.

4 Conclusion

In this paper, Ag-TiO_2/ZIF-8 ternary with excellent biological antibacterial activity was synthesized by solvothermal method. To evaluate its antibacterial activity against *E. coli* and *B. subtilis*, the experiments such as zone of inhibition, growth curve of bacteria, minimum bactericidal concentration and antibacterial durability were executed. The experimental results demonstrated that 20wt % Ag-TiO_2/ZIF-8 exhibits the best antibacterial activity under dark and UV conditions, where Ag-TiO_2 and ZIF-8 had a synergistic effect on antibacterial activity. Since its outstanding antibacterial activity against two ubiquitous bacteria, Ag-TiO_2/ZIF-8 is a broad-spectrum antibacterial agent. In addition, compared with other antimicrobial materials, the antimicrobial effect of Ag-TiO_2/ZIF-8 has good stability and durability, and can maintain its antimicrobial activity for more than 5 months without reducing its effectiveness (Liu et al., 2021; Wang et al., 2021). Therefore, Ag-TiO_2/ZIF-8 is expected to become a promising biological antibacterial material for electrical appliances, furniture coatings, medical facilities and other living fields.

Data availability statement

The raw data supporting the conclusions of this article will be made available by the authors, without undue reservation.

Author contributions

SB: writing—original draft; supervision; funding acquisition. SS: resources; investigation. LL: methodology; conceptualization. LX: writing—review and editing; validation. All authors contributed to the article and approved the submitted version.

Funding

This work was financially supported by Joint Fund Project of the Natural Science Foundation of Jilin Province (YDZJ202101ZYTS076).

Conflict of interest

The authors declare that the research was conducted in the absence of any commercial or financial relationships that could be construed as a potential conflict of interest.

Publisher's note

All claims expressed in this article are solely those of the authors and do not necessarily represent those of their affiliated organizations, or those of the publisher, the editors and the reviewers. Any product that may be evaluated in this article, or claim that may be made by its manufacturer, is not guaranteed or endorsed by the publisher.

Supplementary material

The Supplementary Material for this article can be found online at: https://www.frontiersin.org/articles/10.3389/fbioe.2023.1221458/full#supplementary-material

References

Abadikhah, H., Kalali, E. N., Khodi, S., Xu, X., and Agathopoulos, S. (2019). Multifunctional Thin-Film Nanofiltration Membrane Incorporated with reduced graphene oxide@TiO_2@Ag nanocomposites for high desalination performance, dye Retention, and antibacterial properties. *ACS Appl. Mater Inter* 11, 23535–23545. doi:10.1021/acsami.9b03557

Abdi, J. (2020). Synthesis of Ag-doped ZIF-8 photocatalyst with excellent performance for dye degradation and antibacterial activity. *Colloid Surf. A-physicochemical Eng. Aspects* 604, 125330. doi:10.1016/j.colsurfa.2020.125330

Ahmad, A., lqbal, N., Noor, T., Hassan, A., Khan, U. A., Wahab, A., et al. (2021). Cu-doped zeolite imidazole framework (ZIF-8) for effective electrocatalytic CO_2 reduction. *J. CO_2 Util.* 48, 101523. doi:10.1016/j.jcou.2021.101523

Bin, Q. Y., Wang, M., and Mwang, L. S. (2020). Ag nanoparticles decorated into metal-organic framework (Ag NPs/ZIF-8) for electrochemical sensing of chloride ion. *Nanotechnology* 31, 125601. doi:10.1088/1361-6528/ab5cde

Cao, S. W., Lin, C. H., Liang, S. N., Tan, C. H., and Xu, X. D. (2020). Enhancing chemotherapy by RNA interference. *BIO Integr.* 1 (2), 64–81. doi:10.15212/bioi-2020-0003

Chen, J. H., He, Z., Liu, J. M., Wang, Y. X., Hodgson, M., and Gao, W. (2023). Antibacterial anodic aluminium oxide-copper coatings on aluminium alloys: Preparation and long-term antibacterial performance. *Chem. Eng. J.* 461, 141873. doi:10.1016/j.cej.2023.141873

Chen, J., Gu, A., Miensah, E. D., Liu, Y., Wang, P., Mao, P., et al. (2021). Cu-Zn bimetal ZIFs derived nanowhisker zero-valent copper decorated ZnO nanocomposites induced oxygen activation for high-efficiency iodide elimination. *J. Hazard. Mater.* 416 (10), 126097. doi:10.1016/j.jhazmat.2021.126097

Dong, P. M., Yang, F. F., Cheng, X. D., Huang, Z., Nie, X., Xiao, Y., et al. (2019). Plasmon enhanced photocatalytic and antimicrobial activities of Ag-TiO_2 nanocomposites under visible light irradiation prepared by DBD cold plasma treatment. *Mater Sci. Eng. C* 96, 197–204. doi:10.1016/j.msec.2018.11.005

Guo, Y. F., Fang, W. J., Fu, J. R., Wu, Y., Zheng, J., Gao, G. Q., et al. (2018). Facile synthesis of Ag@ZIF-8 core-shell heterostructure nanowires for improved antibacterial activities. *Appl. Surf. Sci.* 435, 149–155. doi:10.1016/j.apsusc.2017.11.096

Hayashi, K., Nozaki, K., Tan, Z. Q., Fujita, K., Nemoto, R., Yamashita, K., et al. (2020). Enhanced antibacterial property of facet-engineered TiO_2 nanosheet in presence and absence of ultraviolet irradiation. *Mat* 13, 78. doi:10.3390/ma13010078

Ji, Q., Hou, Y. F., Wei, S. X., Liu, Y., Du, P., Luo, L., et al. (2020). Excellent energy storage performance in bilayer composites combining aligned TiO_2 nanoarray and random TiO_2 nanowires with poly(vinylidene fluoride). *J. Phys. Chem. C* 124 (5), 2864–2871. doi:10.1021/acs.jpcc.9b11212

Jia, M. M., Zhang, X. F., Feng, Y., Zhou, Y., and Yao, J. (2020). *In-situ* growing ZIF-8 on cellulose nanofibers to form gas separation membrane for CO_2 separation. *J. Membr. Sci.* 595, 117579. doi:10.1016/j.memsci.2019.117579

Jing, Y. S., Deng, Z. R., Yang, X. Y., Li, L. J., Gao, Y., and Li, W. L. (2020). Ultrathin two-dimensional polydopamine nanosheets for multiple free radical scavenging and wound healing. *Chem. Commun.* 56, 10875–10878. doi:10.1039/d0cc02888f

Li, C. E., Yu, H., Song, Y., Wang, M., and Liu, Z. (2020). A N-octadecane/hierarchically porous TiO_2 form-stable PCM for thermal energy storage. *Renew. Energy* 145, 1465–1473. doi:10.1016/j.renene.2019.06.070

Li, L. J., Li, L., Sun, T. T., Yu, X., Long, L., Xu, L., et al. (2019). Novel $H_3PW_{12}O_{40}$/TiO_2-g-C_3N_4 type-II heterojunction photocatalyst with enhanced visible-light photocatalytic properties. *J. Solid State Chem.* 274, 152–161. doi:10.1016/j.jssc.2019.03.005

Li, Y. Y., Li, K., Luo, Y. Y., Liu, B., Wang, H., Gao, L., et al. (2020). Synthesis of Co_3O_4/ZnO nano-heterojunctions by one-off processing ZIF-8@ZIF-67 and their gas-sensing performances for trimethylamine. *Sens. Actuat B. Chem.* 308, 127657. doi:10.1016/j.snb.2020.127657

Lia, X., Yua, S., Li, K., Ma, C., Zhang, J., Li, H., et al. (2020). Enhanced gas separation performance of Pebax mixed matrix membranes by incorporating ZIF-8 *in situ* inserted by multiwalled carbon nanotubes. *Sep. Purif. Technol.* 248, 117080. doi:10.1016/j.seppur.2020.117080

Liu, J. X., L Bao, X., Kolesnik, I., Jia, B., Yu, Z. H., Xing, C. X., et al. (2022). Enhancing the *in vivo* stability of polycation gene carriers by using PEGylated hyaluronic acid as a shielding system. *BIO Integr.* 10, 103–111. doi:10.15212/bioi-2021-0033

Liu, N., Ming, J., Sharma, A., Sun, X., Kawazoe, N., Chen, G., et al. (2021). Sustainable photocatalytic disinfection of four representative pathogenic bacteria isolated from real water environment by immobilized TiO2-based composite and its mechanism. *Chem. Eng. J.* 426, 131217. doi:10.1016/j.cej.2021.131217

Lu, Z., Zhou, H. F., Liao, J. J., Yang, Y. Y., Wang, K., Che, L. M., et al. (2019). A facile dopamine-assisted method for the preparation of antibacterial surfaces based on Ag/TiO_2 nanoparticles. *Appl. Surf. Sci.* 481, 1270–1276. doi:10.1016/j.apsusc.2019.03.174

Ma, X., Liu, H., Yang, W., Mao, G., Zheng, L., and Jiang, H. L. (2021). Modulating coordination environment of single-atom catalysts and their proximity to photosensitive units for boosting MOF photocatalysis. *J. Am. Chemiscal Soc.* 143, 12220–12229. doi:10.1021/jacs.1c05032

Malik, A., Nath, M., Mohiyuddin, S., and Packirisamy, G. (2018). Multifunctional CdSNPs@ZIF-8: Potential antibacterial agent against GFP-expressing *Escherichia coli* and staphylococcus aureus and efficient photocatalyst for degradation of methylene blue. *ACS Omega* 3, 8288–8308. doi:10.1021/acsomega.8b00664

Mariappan, A., Pandi, P., Rajeswarapalanichamy, R., Neyvasagam, K., Sureshkumar, S., Gatasheh, M. K., et al. (2022). Bandgap and visible-light-induced photocatalytic performance and dye degradation of silver doped HAp/TiO_2 nanocomposite by sol-gel method and its antimicrobial activity. *Environ. Res.* 211, 113079. doi:10.1016/j.envres.2022.113079

Nabipour, H., Sadr, M. H., and Bardajee, G. R. (2017). Synthesis and characterization of nanoscale zeolitic imidazolate frameworks with ciprofloxacin and their applications as antimicrobial agents. *New J. Chem.* 41, 7364–7370. doi:10.1039/c7nj00606c

Nasim, H., Vahid, V., Mohsen, S., and Nikjavan, Z. (2020). Preparation of a novel polyvinyl chloride (PVC) ultrafiltration membrane modified with Ag/TiO_2 nanoparticle with enhanced hydrophilicity and antibacterial activities. *Sep. Purif. Technol.* 237, 116374. doi:10.1016/j.seppur.2019.116374

Ponomarev, V. A., Sheveyko, A. N., Permyakova, E. S., Lee, J., Voevodin, A. A., Berman, D., et al. (2019). TiCaPCON-supported Pt- and Fe-based nanoparticles and related antibacterial activity. *ACS Appl. Mater Inter* 11, 28699–28719. doi:10.1021/acsami.9b09649

Prabhu, B., and Valan, A. (2020). Stability analysis of TiO_2-Ag nanocomposite particles dispersed paraffin wax as energy storage material for solar thermal systems. *Renew. Energy* 152, 358–367. doi:10.1016/j.renene.2020.01.043

Rempel, A. A., Valeeva, A. A., Vokhmintsev, A. S., and Weinstein, I. A. (2020). Titanium dioxide nanotubes: Synthesis, structure, properties and applications. *Russ. Chem. Rev.* 90 (11), 1397–1414. doi:10.1070/rcr4991

Ren, H., Yu, R., Qi, J., Zhang, L., Jin, Q., and Wang, D. (2019). Hollow multishelled heterostructured anatase/TiO_2(B) with superior rate capability and cycling performance. *Adv. Mater.* 31 (10), 1805754. doi:10.1002/adma.201805754

Rodriguez-Gonzalez, V., Obregon, S., Patron-Soberano, O. A., and Fujishima, A. (2020). An approach to the photocatalytic mechanism in the TiO_2-nanomaterials microorganism interface for the control of infectious processes. *Appl. Catal. B Environ.* 270, 118853. doi:10.1016/j.apcatb.2020.118853

Shwetharani, R., Sakar, M., Fernando, C. N., Binas, V., and Balakrishna, R. G. (2019). Recent advances and strategies to tailor the energy levels, active sites and electron mobility in titania and its doped/composite analogues for hydrogen evolution in sunlight. *Catal. Sci. Techology* 9 (1), 12–46. doi:10.1039/c8cy01395k

Singh, M. K., and Mehata, M. S. (2019). Phase-dependent optical and photocatalytic performance of synthesized titanium dioxide (TiO_2) nanoparticles. *Optik* 193, 163011. doi:10.1016/j.ijleo.2019.163011

Sun, M., Gao, P., Wang, B., Li, X. Y., Shao, D. H., Xu, Y., et al. (2023). Polydopamine-functionalized selenium nanoparticles as an efficient photoresponsive antibacterial platform. *RSC Adv.* 13, 9998–10004. doi:10.1039/d2ra07737j

Troyano, J., Carnee Sanchez, A., Avci, C., Imaz, I., and Maspoch, D. (2019). Colloidal metal-organic framework particles: The pioneering case of ZIF-8. *Chem. Soc. Rev.* 48 (23), 5534–5546. doi:10.1039/c9cs00472f

Vaidya, B. L., Nadar, S. S., and Rathod, V. K. (2019). Entrapment of surfactant modified lipase within zeolitic imidazolate framework (ZIF)-8. *Int. J. Biol. Macromol.* 146, 678–686. doi:10.1016/j.ijbiomac.2019.12.164

Wang, X., Huang, L., Wang, Y., Xuan, L., Li, W. W., and Tian, L. J. (2021). Highly efficient near-infrared photothermal antibacterial membrane with incorporated biogenic CuSe nanoparticles. *Chem. Eng. J.* 405, 126711. doi:10.1016/j.cej.2020.126711

Wang, X. Z., Wang, H., Cheng, J. F., Li, H., Wu, X., Zhang, D., et al. (2023). Initiative ROS generation of Cu-doped ZIF-8 for excellent antibacterial performance. *Chem. Eng. J.* 462, 143201. doi:10.1016/j.cej.2023.143201

Wang, Y., Chen, Y. X., Barakat, T., Wang, T. M., Krief, A., Zeng, Y. J., et al. (2020). Synergistic effects of carbon doping and coating of TiO_2 with exceptional photocurrent enhancement for high performance H_2 production from water splitting. *J. Energy Chem.* 56, 141–151. doi:10.1016/j.jechem.2020.08.002

Xu, W., Wang, J. C., Zhang, P., Klomkliang, N., Chaemchuen, S., and Verpoort, F. (2020). Hierarchical ZIFs@Al_2O_3 composite materials as effective heterogeneous catalysts. *Microporous Mesoporous Mater.* 297, 110009. doi:10.1016/j.micromeso.2020.110009

Xu, Y., Ma, J. X., Han, Y., Xu, H., Wang, Y., Qi, D., et al. (2020). A simple and universal strategy to deposit Ag/polypyrrole on various substrates for enhanced interfacial solar evaporation and antibacterial activity. *Chem. Eng. J.* 384, 123379. doi:10.1016/j.cej.2019.123379

Xue, P. P., Yuan, J. D., Yao, Q., Zhao, Y. Z., and L Xu, H. (2020). Bioactive factors-imprinted scaffold vehicles for promoting bone healing: The potential strategies and the

confronted challenges for clinical production. *BIO Integr.* 1 (1), 37–54. doi:10.15212/bioi-2020-0010

Yang, T., Oliver, S., Chen, Y., Boyer, C., and Chandrawati, R. (2019). Tuning crystallization and morphology of zinc oxide with polyvinylpyrrolidone: Formation mechanisms and antimicrobial activity. *J. Colloid Interface Sci.* 546, 43–52. doi:10.1016/j.jcis.2019.03.051

Younis, S. A., Kwon, E. E., Qasim, M., Kim, K. H., Kim, T., Kukkar, D., et al. (2020). Metal-organic framework as a photocatalyst: Progress in modulation strategies and environmental/energy applications. *Prog. Energy Combust. Sci.* 81, 100870. doi:10.1016/j.pecs.2020.100870

Zerjav, G., Arshad, M., Djinovic, P., Junkar, I., Kovač, J., Zavašnik, J., et al. (2017). Improved electron-hole separation and migration in anatase TiO_2 nanorod/reduced graphene oxide composites and their influence on photocatalytic performance. *Nanoscale* 9, 4578–4592. doi:10.1039/c7nr00704c

Zheng, Z. H., Liang, D. S., Deng, H. H., Chen, X. M., Luo, Y., and Zhang, C. Q. (2023). Castor oil-based, robust, non-leaching and durable antibacterial waterborne polyurethane/polyhexamethylene guanidine composites prepared via an electrostatic self-assembly strategy. *Chem. Eng. J.* 462, 142060. doi:10.1016/j.cej.2023.142060

Zheng, H., Wu, D., Wang, L. Y., Liu, X., Gao, P., Liu, W., et al. (2020). One-step synthesis of ZIF-8/ZnO composites based on coordination defect strategy and its derivatives for photocatalysis. *J. Alloys Compd.* 838, 155219. doi:10.1016/j.jallcom.2020.155219

Zhu, K., Fan, R. Q., Zheng, X. B., Wang, P., Chen, W., Sun, T., et al. (2019). Dual-emitting dye-CDs@MOFs for selective and sensitive identification of antibiotics and MnO_4^- in water. *J. Mater Chem. C* 7, 15057–15065. doi:10.1039/c9tc04700j

frontiers | Frontiers in Bioengineering and Biotechnology

TYPE Original Research
PUBLISHED 11 August 2023
DOI 10.3389/fbioe.2023.1226680

Check for updates

OPEN ACCESS

EDITED BY
Jie Tang,
The University of Queensland, Australia

REVIEWED BY
Bing Sun,
The University of Queensland, Australia
Zhengying Gu,
East China Normal University, China

*CORRESPONDENCE
Li Li,
lil@sibet.ac.cn
Zhimin Chang,
changzm@sibet.ac.cn

†These authors have contributed equally to this work

RECEIVED 22 May 2023
ACCEPTED 17 July 2023
PUBLISHED 11 August 2023

CITATION
Zhang F, Jia Y, Chen F, Zhao Y, Li L and Chang Z (2023), Tumor-targeted bioactive nanoprobes visualizing of hydrogen peroxide for forecasting chemotherapy-exacerbated malignant prognosis.
Front. Bioeng. Biotechnol. 11:1226680.
doi: 10.3389/fbioe.2023.1226680

COPYRIGHT
© 2023 Zhang, Jia, Chen, Zhao, Li and Chang. This is an open-access article distributed under the terms of the Creative Commons Attribution License (CC BY). The use, distribution or reproduction in other forums is permitted, provided the original author(s) and the copyright owner(s) are credited and that the original publication in this journal is cited, in accordance with accepted academic practice. No use, distribution or reproduction is permitted which does not comply with these terms.

Tumor-targeted bioactive nanoprobes visualizing of hydrogen peroxide for forecasting chemotherapy-exacerbated malignant prognosis

Fan Zhang[1,2†], Yong Jia[3†], Fangman Chen[1], Yawei Zhao[3], Li Li[1,2*] and Zhimin Chang[1,2*]

[1]CAS Key Laboratory of Bio Medical Diagnostics, Suzhou Institute of Biomedical Engineering and Technology Chinese Academy of Sciences, Suzhou, China, [2]Zhengzhou Institute of Biomedical Engineering and Technology, Zhengzhou, China, [3]School of Nursing, Jilin University, Changchun, Jilin, China

Introduction: Fluorescent visualization of hydrogen peroxide in the tumor microenvironment (TME) is conducive to predicting malignant prognosis after chemotherapy. Two photon microscopy has been employed for *in vivo* hydrogen peroxide detection owing to its advantages of deep penetration and low phototoxicity.

Methods: In this study, a two-photon fluorescent probe (TPFP) was protected by mesoporous silica nanoparticles (MSNs) and masked by cloaking the cancer cell membranes (CM), forming a tumor-targeted bioactive nanoprobe, termed MSN@TPFP@CM.

Results: This multifunctional nanoprobe allowed for the effective and selective detection of excessive hydrogen peroxide production in chemotherapeutic Etoposide (VP-16)-challenged tumor cells using two-photon microscopy. After specific accumulation in tumors, VP-16-MSN@TPFP@CM monitored tumor-specific hydrogen peroxide levels and revealed a positive correlation between oxidative stress in the TME and chemotherapy-exacerbated malignant prognosis.

Discussion: Given the recent translation of fluorescent imaging into early clinical trials and the high biocompatibility of bioactive nanoprobes, our approach may pave the way for specific imaging of oxidative stress in solid tumors after treatment and provide a promising technology for malignant prognosis predictions.

KEYWORDS

bioactive, nanoprobe, cancer, hydrogen peroxide, chemotherapy

1 Introduction

Reactive oxygen species (ROS) are considered secondary messengers in biological organisms and are critical for the regulation of pathological and physiological processes, such as cell growth and differentiation, immune response, and aging (Circu and Aw, 2010; Liou and Storz, 2010; Schieber and Chandel, 2014). Mounting evidence suggest that continuous production, transformation, and consumption of ROS can promote pro-survival and pro-proliferative pathways, and metabolic adaptation of tumor cells to the

tumor microenvironment (TME) (Jensen, 1966; Halliwell et al., 2000; Gupta and Massagué, 2006; Marcu, 2014; Liu et al., 2023). Recently, aberrant production of ROS in the TME has been associated with cancer malignant prognosis, especially in chemotherapy-exacerbated malignant prognosis (Lambert et al., 2017; Jiang et al., 2020). Under such conditions, sublethal levels of ROS induced by chemotherapeutics can help propagate, amplify, and effectively create a mutagenic and oncogenic field that facilitates tumor repopulation and acts as a springboard for metastatic tumor cells (Saggar and Tannock, 2015; Verma et al., 2016; Duy et al., 2021). Therefore, monitoring ROS levels in the TME is conducive for understanding cancer progression and developing novel therapeutics.

As the most stable ROS, hydrogen peroxide (H_2O_2) has a lifetime of up to a few minutes and can diffuse across biological membranes, thereby functioning as an ideal biomarker for cancer progression (Kamata et al., 2005; Lin and Beal, 2006; Guo et al., 2014; Jung et al., 2016). Electrochemistry and luminescence are the two major strategies for the quantification of H_2O_2 in living systems (Wang et al., 2022). The former measures extracellular H_2O_2 in an invasive manner and is affected by biofouling (Song et al., 2010; Aghamiri et al., 2019; Zhao et al., 2019). Whereas, the latter method is suitable for extracellular and intracellular H_2O_2 with the advantages of noninvasiveness, simple operation, high sensitivity, and excellent spatiotemporal resolution (Lu et al., 2021; Zhou et al., 2021; Hao et al., 2022; Zhan et al., 2022). To overcome limited light penetration depth, two-photon microscopy (TPM) has been employed for H_2O_2 detection with less phototoxicity and lower self-absorption, which facilitates real-time measurements *in vivo* (Chen et al., 2013; Guo et al., 2013; Li et al., 2017; Shi et al., 2018; Liaw et al., 2021). Additionally, as a benefit of nanotechnology, nanoparticulate probes have been widely developed for the efficient imaging of H_2O_2 in cancer owing to their specific tumoral targeting, higher penetration, and good stability (Maji et al., 2018; Shao et al., 2018; Wang et al., 2019; Zhang et al., 2019; Bondon et al., 2022). Therefore, it is necessary to develop a novel two-photon fluorescent nanoprobe with near-infrared (NIR) emission to monitor H_2O_2 during cancer chemotherapy.

In this study, we created a tumor-targeting bioactive nanoprobe which facilitated two-photon fluorescence imaging to visualize H_2O_2 during cancer chemotherapy (Scheme 1). We incorporated an H_2O_2-responsive two-photon fluorescent probe (TPFP) into mesoporous silica nanoparticles (MSNs), which were then coated with cancer cell membranes to form bioactive nanoprobes named MSN@TPFP@CMs. After loading with chemotherapeutic Etoposide (VP-16), this multifunctional nanoprobe allowed the effective and selective detection of excessive H_2O_2 production in chemotherapy-challenged tumor cells through two-photon microscopy. Importantly, VP-16-MSN@TPFP@CMs preferably accumulated in tumors and monitored tumor-specific H_2O_2 levels in a subcutaneous breast cancer mouse model without immediate or delayed toxic effect, revealing a positive correlation between endogenous H_2O_2 in the TME and chemotherapy-exacerbated repopulation and metastasis *in vitro* and *in vivo*. Two-photon fluorescence detection of H_2O_2 in the TME may be an appealing strategy for predicting poor prognosis after cancer chemotherapy, including recurrence and metastasis.

2 Materials and methods

2.1 Fabrication of VP-16-MSN@TPFP@CMs

A solution of the H_2O_2-responsive probe TPFP was prepared based on previous studies. MSNs were synthesized as follows: 0.12 g cetrimonium tosylate (CTAT), 0.03 g triethanolamine ($TEAH_3$), and 10 mL deionized water were mixed and stirred at 80°C for 30 min. Subsequently, a solution of 1.0 g tetraethyl orthosilicate (TEO) was added dropwise to the surfactant solution. The resulting mixture was stirred at 80°C for another 4 h at 1,000 rpm. The products were collected by centrifugation (10,000 rpm 30 min), washed three times with ethanol, and subsequently refluxed in an ethanol solution of NH_4NO_3 (1% w/v) for 12 h. Briefly, we used VP-16 and TPFP (1:20 mass ratio) dissolved in DMSO for the co-loading of the probes. To configure probes containing different ratios of chemotherapeutic components, the mass ratio of VP-16 to TPFP was adjusted to 0.5:20, 1:20, and 2:20 to prepare VP-16-MSN@TPFP (L), VP-16-MSN@TPFP (M), and VP-16-MSN@TPFP (H). The nanoparticles were collected by high-speed centrifugation and resuspended in the aqueous phase. Subsequently, VP-16-MSN@TPFP was mixed with CM derived from 4T1 cells, sonicated with heating for 5 min, and subsequently extruded through 200 nm polycarbonate membranes to obtain VP-16-MSN@TPFP@CMs.

2.2 Characterization of VP-16-MSN@TPFP@CMs

The morphology of the MSNs was characterized using a JEM-2100F transmission electron microscope (TEM; JEOL, Ltd., Japan) and a scanning electron microscope (SEM; FEI Quanta 200F). The hydrodynamic diameter and zeta potential of the nanoparticles in water and PBS were characterized using a Nano-ZS 90 Nanosizer (Malvern Instruments Ltd., Worcestershire, United Kingdom). UV-vis absorption spectra were recorded using a U-3310 spectrophotometer (Hitachi, Japan). Sodium dodecyl sulfate-polyacrylamide gel electrophoresis (SDS-PAGE) was used to characterize the protein composition of nanoparticles. Stability experiments were performed by measuring the nanoprobes in Dulbecco's Modified Eagle's medium (DMEM) plus 10% FBS for 7 days using dynamic light scattering (DLS).

2.3 Cell culture and *in vitro* analysis

The mouse breast cancer 4T1 cell line was cultured in DMEM supplemented with 10% FBS along with penicillin and streptomycin at 100–100 U/mL, respectively. Cells were incubated at 37°C in 5% CO_2-95% air atmosphere.

For the detection of exogenous H_2O_2, 4T1 cells were incubated with nanoprobes at 37°C for 30 min, images of VP-16-MSN@TPFP@CMs in live cells were investigated via spectral confocal multiphoton microscopy (Olympus FV1000-IX81) with a high-performance model titanium-sapphire laser source (Maitai, Spectra-Physics, United States), with the emission ranging from 575 to 630 nm. The excitation wavelength was 860 nm with a constant intensity.

2.3.1 Chemo-malignant prognosis cell model

Single-cell suspensions of chemotherapy-challenged cells were collected using trypsin after 12 h of treatment with VP-16 (2.5 μg/mL). The chemotherapy-challenged cells were re-inoculated in 6-well plates at a density of 5×10^4/well, and the cells were collected after 24 h to obtain whole cell protein lysates. After determining the protein concentration of the samples using the bicinchoninic acid (BCA)method, the Cyclooxygenase 2 (COX2) content in each treatment group was measured using a COX2 ELISA assay kit (ab210574). Additionally, the culture medium supernatant was collected for the determination of Prostaglandin E2 (PGE2) using an ELISA kit (ab287802).

2.3.2 Measurement of tumor cell repopulation with bioluminescence imaging

We constructed a chemo-repopulation cell model based on the fact that the luciferase activity of Fluc-labeled 4T1 cells was tightly correlated with cell number. The 4T1-Fluc cells (100 cells) were seeded with differentially agents-treated 4T1 cells (1×10^4) in 24-well plates. During the co-culture period (12–14 days), the culture medium was replaced with fresh 5% FBS DMEM every 3 days. Finally, to measure the luciferase activity of 4T1-Fluc, 0.15 mg/mL D-Luciferin potassium in PBS was added to each well before bioluminescence imaging.

2.3.3 Measurement of tumor cell metastasis with transwell assay

For the transwell assay, 4T1 cells were seeded into up-chamber of 8 μm pore size in six-well plates. Subsequently, 1.5 mL chemo-challenged 4T1 cell (5×10^4) medium was added into the lower chamber of every well and 500 μL serum free DMEM containing 4T1 cells (3×10^4) was added into the up-chamber. After 20–24 h, 4T1 cells remaining in the inserts were gently removed using cotton swabs. Migratory 4T1s were fixed in 90% ethanol and stained with crystal violet. The number of migratory 4T1s was measured by counting the cells from five random fields under a microscope.

2.3.4 Correlation analysis

The mean fluorescence intensity from flow cytometry of H_2O_2 levels in chemotherapy-challenged cells, PEG2 levels, and COX2 levels were plotted to analyze the correlation between H_2O_2 and chemo-repopulation/metastatic cells.

2.4 Animals and *in vivo* analysis

2.4.1 Chemo-malignant prognosis in 4T1 mouse model

All animal experimental procedures were approved by the Ethics Committee for the Use of Experimental Animals of the Suzhou Institute of Biomedical Engineering and Technology of the Chinese Academy of Science (Suzhou, Jiangsu, China). Initially, Balb/C NuNu approximately 18 g each) female mice ($n = 8$) aged four–six weeks were obtained from Cavens Biogle (suzhou) Model Animal Research Co., Ltd. A xenograft tumor model was established by subcutaneous injection of 1×10^6 4T1 cells into the right mammary fat pads.

When the tumor size reached approximately 150 mm^3, the nanoprobes (0.1 mg/kg based on VP-16) were administered intravenously. For the chemo-malignant prognosis in the 4T1 mouse model, tumor volumes and body weights were

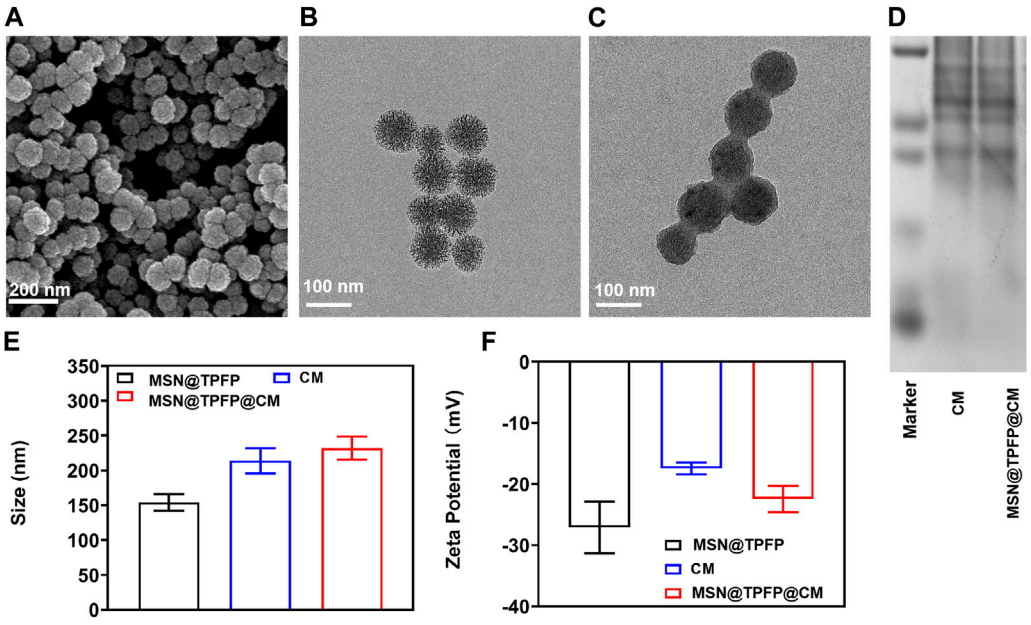

FIGURE 1
Spectroscopic studies of VP-16-MSN@TPFP@CMs. **(A)** UV-vis absorption of VP-16-MSN@TPFP@CMs. **(B)** Fluorescence spectra of VP-16-MSN@TPFP@CMs in the presence of H_2O_2 with excitation at 560 nm. **(C)** Fluorescence imaging of 4T1 cells incubated with TPFP or VP-16-MSN@TPFP@CMs for 30 min. Particle size **(D)**, Zeta potential **(E)**, and SDS-PAGE results **(F)** of VP16-MSN@TPFP@CM.

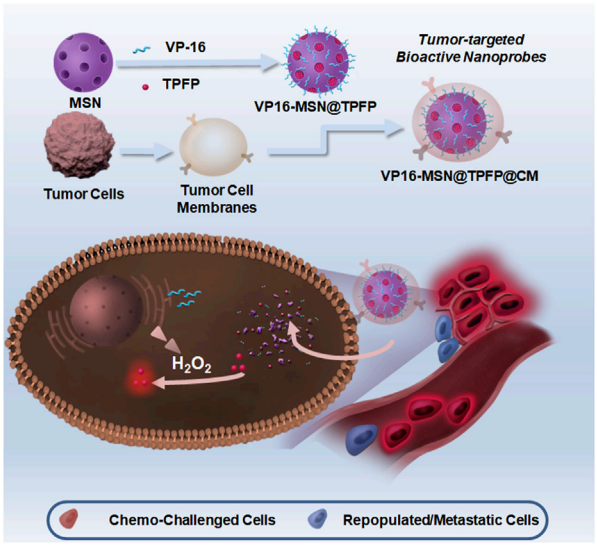

SCHEME 1
Schematic illustration of synthesis of VP-16-MSN@TPFP@CMs and their applications in visualizing hydrogen peroxide (H_2O_2) for forecasting chemotherapy-exacerbated malignant prognosis.

recorded every alternate day after the first injection. Mice were sacrificed 14 days after chemotherapeutic stimulation and lung tissue was collected to count the number of pulmonary metastatic nodules. Additionally, 12 h after the intravenous injection of nanoprobes, the tumor site fluorescence signal was monitored using *In-Vivo* Xtreme II™. Subsequently, the number of pulmonary metastatic nodules versus the *in vivo* fluorescence signal of the TPFP was plotted to analyze the correlation between chemo-malignant prognosis and H_2O_2 levels.

2.4.2 *In vivo* biodistribution and biosafety

The 4T1 tumor-bearing mice were injected with VP-16-MSN@TPFP or VP-16-MSN@TPFP@CM solutions (2 mg/kg based on TPFP). The fluorescence intensity of the TPFP in each organ sample was measured. The fluorescence intensity was converted to TPFP mass to investigate the organ distribution 12 h after administration. After treatment for 14 days, the mice were sacrificed, and the main organs (liver, spleen, kidneys, heart, and lungs) were collected for hematoxylin and eosin (H&E) stain to analyze the pathophysiology. Biochemical parameter indices were also tested for acute toxicological assay.

2.5 Statistical analysis

Student's *t*-test was used to analyze the differences between two groups. Differences between more than two groups were analyzed using a one-way analysis of variance. Simple linear regression was used to analyze the correlation between H_2O_2 signals and the expression level of COX2, PEG2 and their ratios. Sample sizes (n) and *p*-values (p) for all statistical analyses are indicated in

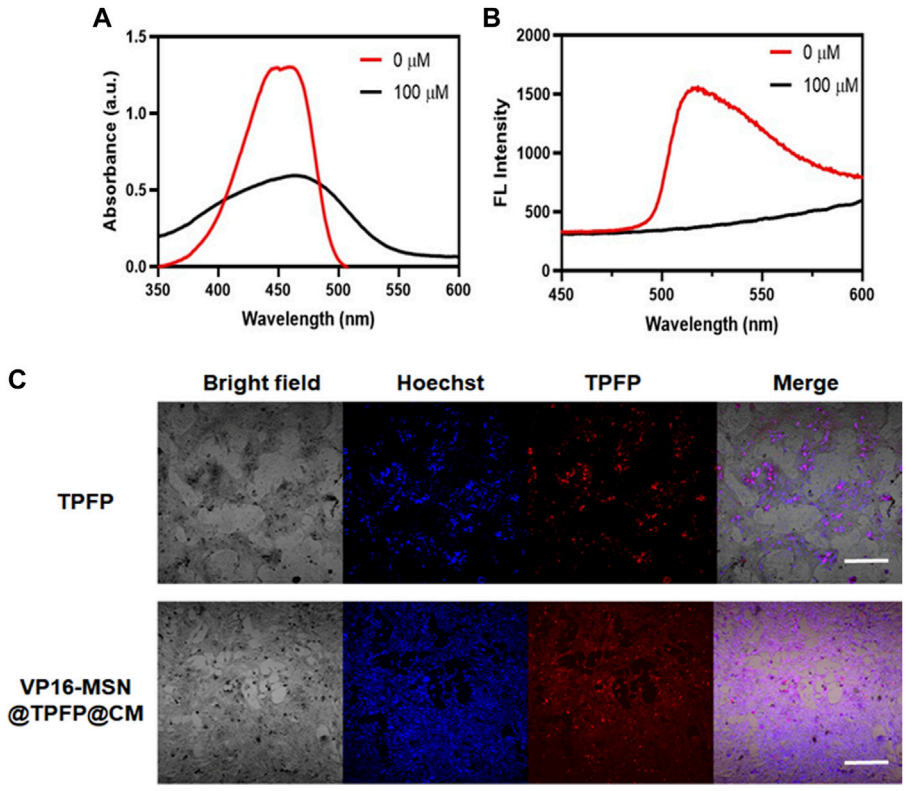

FIGURE 2
Spectroscopic studies of VP-16-MSN@TPFP@CMs. **(A)** UV-vis absorption of VP-16-MSN@TPFP@CMs. **(B)** Fluorescence spectra of VP-16-MSN@TPFP@CMs in the presence of H_2O_2 with excitation at 560 nm. **(C)** Fluorescence imaging of 4T1 cells incubated with TPFP or VP-16-MSN@TPFP@CMs for 30 min.

figures and figure legends. Data were analyzed using statistical software OriginPro 2021b. In all cases, $p < 0.05$ represents a statistically significant difference.

3 Results and discussion

3.1 Preparation and characterization of VP-16-MSN@TPFP@CMs

Mesoporous silica materials (MSNs) were prepared as previously reported. The SEM and TEM images revealed monodisperse spherical MSNs with a diameter of 80 nm (Figure 1A; Figure 1B). The prepared MSNs were loaded with the ROS-responsive fluorescent probe TPFP and chemotherapeutic VP-16 to form VP-16-MSN@TPFP. Release results show that simultaneous release of the two components can be achieved (Supplementary Figure S2). Subsequently, 4T1 breast cancer CM were isolated and coated with VP-16-MSN@TPFP to prepare VP-16-MSN@TPFP@CMs. As shown in Figure 1C, the bioactive materials possess a core–shell structure with an MSN core enclosed in a smooth membrane shell. Consistently, a slight increase in hydrodynamic diameter and a decrease in surface charge were observed after CM coating (Figure 1D; Figure 1E). Protein electrophoresis demonstrated the presence of membrane proteins on VP-16-MSN@TPFP@CMs (Figure 1F), suggesting the successful integration of the cell membrane-coated nanoplatforms. Additionally, stability experiments in 10% FBS-containing medium confirmed that VP-16-MSN@TPFP@CMs exhibited little aggregation after 7 days of incubation (Supplementary Figure S1).

3.2 Spectroscopic studies of VP-16-MSN@TPFP@CMs

Before the *in vitro* and *in vivo* experiments, a series of optical experiments were performed to evaluate VP-16-MSN@TPFP@CM for ROS-responsive imaging properties. The absorption spectra showed a characteristic absorption of VP-16-MSN@TPFP@CM in phosphate buffer saline at 428 nm and no significant absorption at 560 nm. After adding H_2O_2 (100 μM) to the solution for 30 min, the absorption spectra showed a decrease at 428 nm and concomitant absorption at 560 nm (Figure 2A). In contrast, the fluorescence emission spectra showed that excitation at 560 nm after the addition

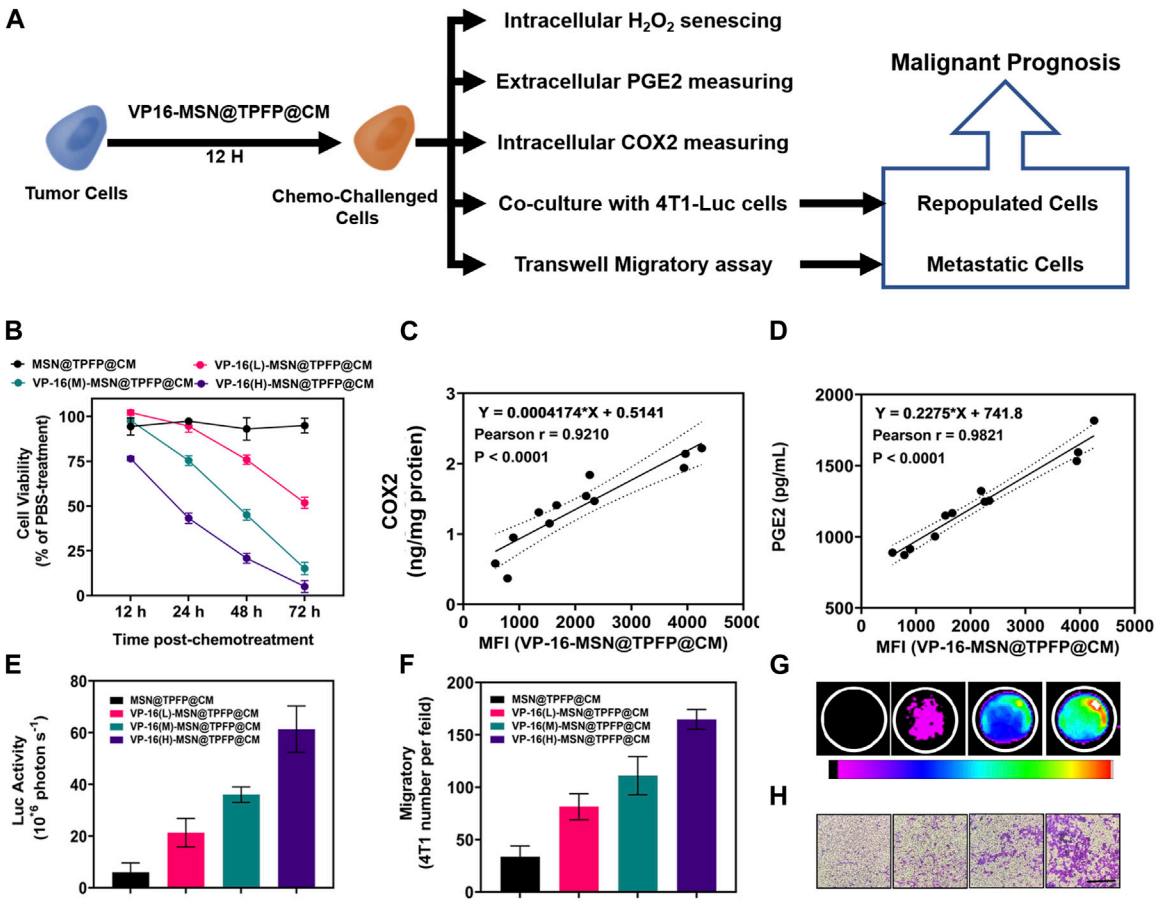

FIGURE 3
The correlation of post-chemotherapy ROS with chemo-exacerbated repopulation/metastasis cell models. **(A)** Schematic diagram. **(B)** Cell activity after treatment with different materials. The correlation analysis of ROS mean fluorescence intensity (MFI) with the expression levels of COX2 protein **(C)** or the ROS MFI with the level of PGE2 **(D)** Number of fluorescent cells in the cell repopulation model **(E,G)**. Migration rate results for each treatment group in the migration assay **(F,H)**.

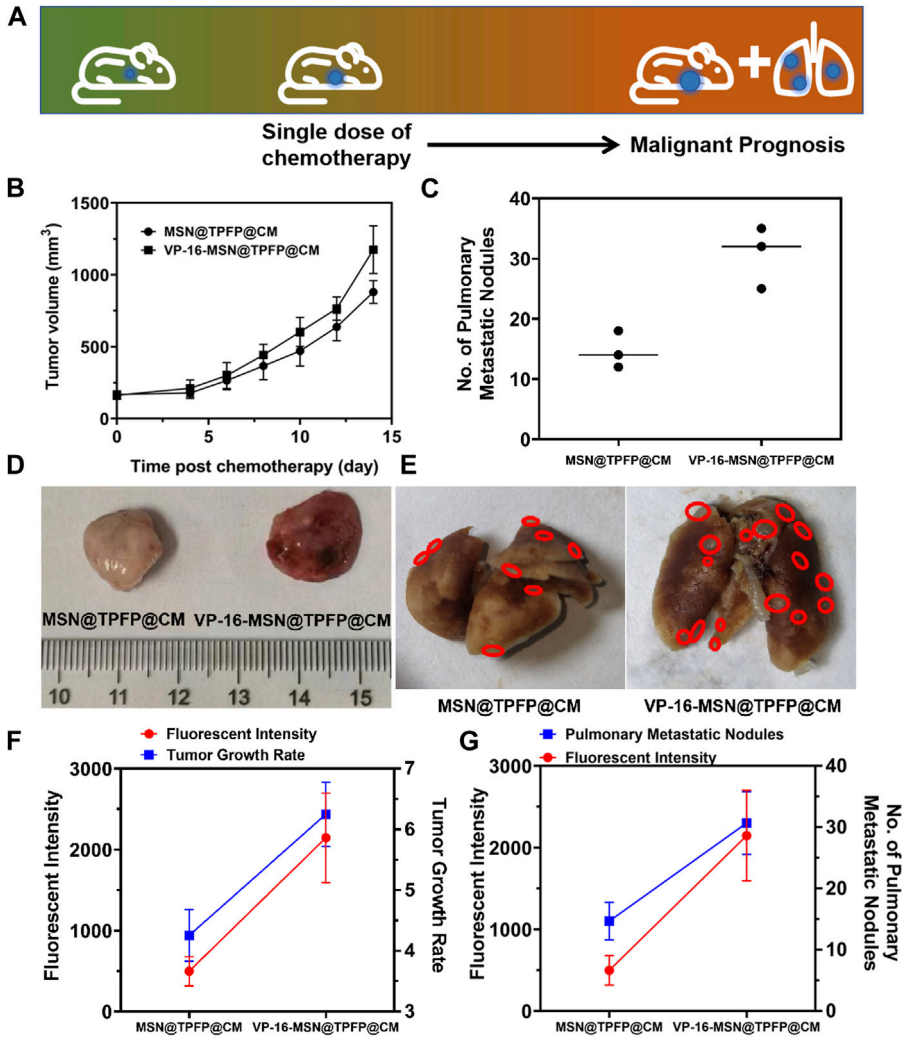

FIGURE 4
(A) Schematic diagram of tumor prognosis model. Orthotopic tumor growth curve **(B)** and pulmonary metastatic nodules **(C)** of chemotherapy-exacerbated model. Representative photographs of tumors **(D)** and lung tissue **(E)** from each group. The correlation analysis of the TGR(g) or pulmonary metastatic nodules **(G)** with the fluorescence intensity of orthotopic tumor.

of H_2O_2 resulted in an emission peak at 699 nm (Figure 2B). Quantitative studies have shown that the fluorescence intensity of VP-16-MSN@TPFP@CM can be used for the determination of *in vitro* and *in vivo* hydrogen peroxide concentration (Supplementary Figure S3, S4). Subsequently, we evaluated the imaging function of the prepared VP-16-MSN@TPFP@CM in 4T1 cells. As shown in Figure 2C, the fluorescence of TPFP and VP-16-MSN@TPFP@CM was found in the cytoplasm and represented H_2O_2 levels, indicating that VP-16-MSN@TPFP@CM was suitable for intracellular H_2O_2 analysis.

3.3 The correlation of H_2O_2 level in VP-16-treated cell with repopulation/metastasis *in vitro*

To ascertain the correlation between H_2O_2 levels and repopulation/metastasis *in vitro* in VP-16-treated cells, we conducted the chemotherapy-exacerbated repopulation/metastasis models *in vitro* by appropriate VP-16 stimulation (Figure 3A). Cell viability results showed that co-culturing 4T1 cells in six-well plates 12 h post-chemostimulation with all three materials caused significant cell death at 72 h (Figure 3B). The mean fluorescence intensity (MFI) of the VP-16-MSN@TPFP@CMs was measured using flow cytometry 12 h after the chemotherapeutic challenge (Supplementary Figure S5). The levels of intracellular COX2 and PGE2 in the culture medium were assayed on day 2. Increased levels of both the components were observed with increasing levels of VP-16 (Supplementary Figure S6, S7). Cell repopulation and cell migration assays showed that VP-16-stimulated cells shaped a microenvironment conducive to cell repopulation and metastasis by increasing components such as the inflammatory protein COX2 and cytokine PGE2 (Figures 3E–G). The intracellular fluorescence signal after treatment with nanoprobes was measured using flow cytometry. These data are consistent with

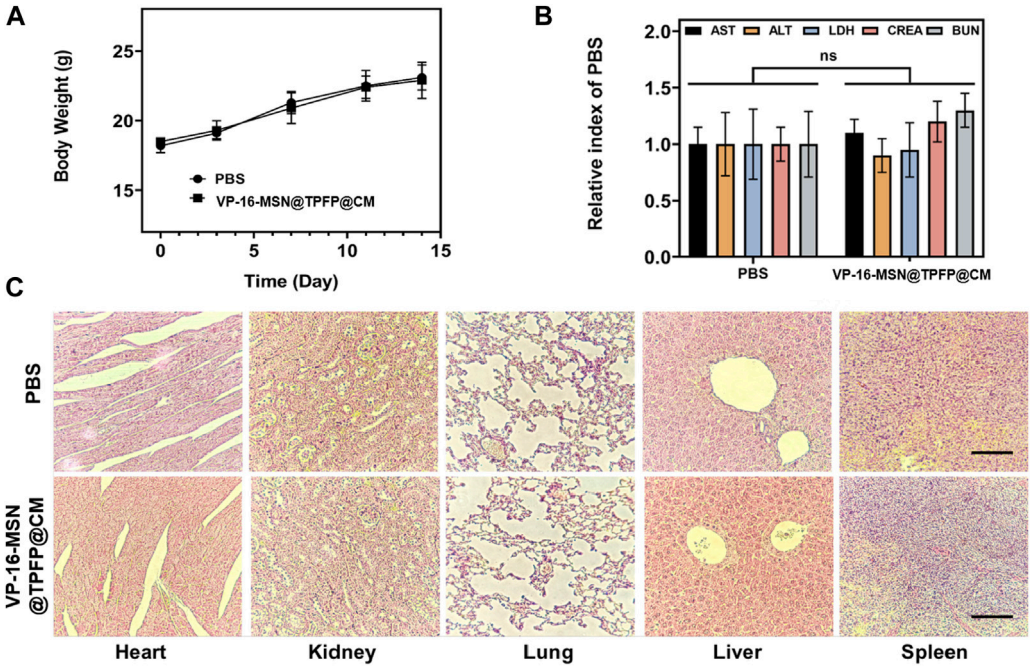

FIGURE 5
(A) Body weight and **(B)** biochemical parameters of 4T1 tumor-bearing mice 14 days after nanoprobe treatment. Data is represented as the mean ± SD (n = 3). **(C)** Histological evaluation from the major organs, including liver, spleen, kidney, heart, and lungs, of 4T1 tumor-bearing mice. Scale bars represent 50 μm.

the changes in COX2 protein expression and PGE2 secretion during chemotherapy. Correlation analysis showed that the MFI of VP-16-MSN@TPFP@CMs-treated cells was highly positively correlated with COX2 expression levels (Pearson r:0.9210, $p < 0.001$) (Figure 3D) and PGE2 levels (Pearson r:0.9821, $p < 0.001$) (Figure 3C), confirming that VP-16-MSN@TPFP@CMs might provide valuable information for the evaluation of repopulation/metastasis after chemotherapy.

3.4 The correlation of post-chemotherapy ROS with tumor prognosis

We established a 4T1 tumor-bearing mouse model to evaluate H_2O_2 detection using VP-16-MSN@TPFP@CM. We examined the H_2O_2 signals at the tumor site after intravenous treatment with VP-16-MSN@TPFP@CM or a mixture of VP-16 and TPFP. The results showed that, compared to free small molecules, VP-16-MSN@TPFP@CM could achieve up to 12 h of H_2O_2 monitoring at the tumor site owing to better tumor targeting and retention (Supplementary Figure S8). To further validate the advantages of the cell membrane-cloaked nanoprobe, we compared the distribution characteristics of VP-16-MSN@TPFP and VP-16-MSN@TPFP@CM. The results showed that the cell membrane-cloaked nanoprobes accumulated more at the tumor site after 12 h of i.v. administration, thus facilitating better *in vivo* monitoring (Supplementary Figure S8). We treated the tumor-bearing mice with a single dose of VP-16-MSN@TPFP@CM (Figure 4A). At the non-therapeutic stimulation dose, the growth rate of the tumor was higher than that of cells treated with MSN@TPFP@CM, and more metastatic nodules were found (Figure 4B; Figure 4C). Subsequently, the relationship between the H_2O_2 levels at the tumor site port-chemo with umor growth rate (TGR) or metastatic nodules was compared between MSN@TPFP@CM and VP-16-MSN@TPFP@CM. We observed more pulmonary metastatic nodules (PMN) in the lungs of VP-16-stimulated mice, and the TGRwas higher than in mice without chemotherapy (Figure 4D; Figure 4E). Both PMN and TGR fitted well when conducting correlation analysis with the H_2O_2 signal of the orthotopic tumor (Figure 4F; Figure 4G).

3.5 *In vivo* bio-safety assays

Biosafety is a prerequisite for the clinical translation of biomaterials. Therefore, we examined the body weight, serum biochemical index, and histology of the major organs to evaluate the systemic toxicity of VP-16-MSN@TPFP@CM. No weight loss was observed in the VP-16-MSN@TPFP@CM group compared to the saline control group (Figure 5A). The levels of serum chemistry indices, including albumin (ALB), alanine transaminase (ALT), aspartate aminotransferase (AST), blood urea nitrogen (BUN), and Serum creatinine (CRE), did not change remarkably in any of the VP-16-MSN@TPFP@CM groups (Figure 5B). Furthermore, H&E staining of the liver, spleen, kidney, lung, and heart indicated the absence of pathological damage to the major organs during exposure (Figure 5C). Collectively, these results indicated that VP-16-MSN@TPFP@CM is biologically safe.

4 Conclusion

In summary, we developed an MSN-protected H_2O_2 imaging system that preserved the responsiveness of TPFP to ROS and achieved spatiotemporal synergy between chemotherapy and malignant prognosis prediction in breast cancer. Notably, VP-16-MSN@TPFP@CM was highly specific towards H_2O_2. Furthermore, VP-16-MSN@TPFP@CM exhibited a higher fluorescence enhancement than VP-16-MSN@TPFP *in vivo*, which was achieved by homologous cancer membrane cloaking with better tumor targeting and immune system evasion. Our results suggest that this probe could enable the evaluation of H_2O_2 pathology in chemotherapeutic cancer models and provide new insights into oxidative stress during chemotherapy. Given the recent translation of fluorescent imaging into early clinical trials and the high biocompatibility of the nanoprobe with further refinement, our approach paved the way for specific imaging of oxidative stress in solid tumors after treatment and provided a promising technology for precise prognostic predictions.

Data availability statement

The raw data supporting the conclusion of this article will be made available by the authors, without undue reservation.

Ethics statement

The animal study was reviewed and approved by Ethics Committee for the Use of Experimental Animals of the Suzhou Institute of Biomedical Engineering and Technology of the Chinese Academy of Science (Suzhou, Jiangsu, China).

Author contributions

FZ and YJ contributed to the collection of experimental data. FZ, YJ, FC, and YZ analyzed the data. FZ, YJ, LL, and ZC contributed to writing and revising the manuscript. LL and ZC supervised the research. All authors contributed to the article and approved the submitted version.

Funding

This research was funded by the National Key R&D Program of China (No. 2021YFB3602200), the National Natural Science Foundation of China (No. 82172077, 22201298, 62027825, and 82071066), Natural Science Foundation of Shandong Province, China (No. ZR2022QB243), China Postdoctoral Science Foundation funded project (2021M702414), Jilin Scientific and Technological Development Program (20210508003RQ), the Innovation and Entrepreneurship Team of Jiangsu Province (JSSCTD202145), Cross disciplinary Research Fund of Shanghai Ninth people's Hospital, Shanghai JiaoTong university School of Medicine (JYJC202010).

Conflict of interest

The authors declare that the research was conducted in the absence of any commercial or financial relationships that could be construed as a potential conflict of interest.

Publisher's note

All claims expressed in this article are solely those of the authors and do not necessarily represent those of their affiliated organizations, or those of the publisher, the editors and the reviewers. Any product that may be evaluated in this article, or claim that may be made by its manufacturer, is not guaranteed or endorsed by the publisher.

Supplementary material

The Supplementary Material for this article can be found online at: https://www.frontiersin.org/articles/10.3389/fbioe.2023.1226680/full#supplementary-material

References

Aghamiri, Z. S., Mohsennia, M., and Rafiee-Pour, H.-A. (2019). Immobilization of cytochrome c on polyaniline/polypyrrole/carboxylated multi-walled carbon nanotube/glassy carbon electrode: biosensor fabrication. *J. Solid State Electrochem.* 23, 2233–2242. doi:10.1007/s10008-019-04300-x

Bondon, N., Durand, D., Hadj-Kaddour, K., Ali, L. M. A., Boukherroub, R., Bettache, N., et al. (2022). Photosensitivity of different nanodiamond-PMO nanoparticles in two-photon-excited photodynamic therapy. *Life (Basel)* 12, 2044. doi:10.3390/life12122044

Chen, Y., Guo, H. C., Gong, W., Qin, L. Y., Aleyasin, H., Ratan, R. R., et al. (2013). Recent advances in two-photon imaging: technology developments and biomedical applications. *Chin. Opt. Lett.* 11, 011703–011710. doi:10.3788/col201311.011703

Circu, M. L., and Aw, T. Y. (2010). Reactive oxygen species, cellular redox systems, and apoptosis. *Free Radic. Biol. Med.* 48, 749–762. doi:10.1016/j.freeradbiomed.2009.12.022

Duy, C., Li, M., Teater, M., Meydan, C., Garrett-Bakelman, F. E., Lee, T. C., et al. (2021). Chemotherapy induces senescence-like resilient cells capable of initiating AML recurrence. *Cancer Discov.* 11, 1542–1561. doi:10.1158/2159-8290.cd-20-1375

Guo, H., Aleyasin, H., Dickinson, B. C., Haskew-Layton, R. E., and Ratan, R. R. (2014). Recent advances in hydrogen peroxide imaging for biological applications. *Cell Biosci.* 4, 64. doi:10.1186/2045-3701-4-64

Guo, H., Aleyasin, H., Howard, S. S., Dickinson, B. C., Lin, V. S., Haskew-Layton, R. E., et al. (2013). Two-photon fluorescence imaging of intracellular hydrogen peroxide with chemoselective fluorescent probes. *J. Biomed. Opt.* 18, 106002. doi:10.1117/1.jbo.18.10.106002

Gupta, G. P., and Massagué, J. (2006). Cancer metastasis: building a framework. *Cell* 127, 679–695. doi:10.1016/j.cell.2006.11.001

Halliwell, B., Clement, M. V., and Long, L. H. (2000). Hydrogen peroxide in the human body. *FEBS Lett.* 486, 10–13. doi:10.1016/s0014-5793(00)02197-9

Hao, Y., Li, Z., Ding, N., Tang, X., and Zhang, C. (2022). A new near-infrared fluorescence probe synthesized from IR-783 for detection and bioimaging of hydrogen peroxide *in vitro* and *in vivo*. *Spectrochimica Acta Part A Mol. Biomol. Spectrosc.* 268, 120642. doi:10.1016/j.saa.2021.120642

Jensen, P. K. (1966). Antimycin-insensitive oxidation of succinate and reduced nicotinamide-adenine dinucleotide in electron-transport particles. I. pH dependency and hydrogen peroxide formation. *Biochim. Biophys. Acta* 122, 157–166. doi:10.1016/0926-6593(66)90057-9

Jiang, M.-J., Gu, D.-N., Dai, J.-J., Huang, Q., and Tian, L. (2020). Dark side of cytotoxic therapy: chemoradiation-induced cell death and tumor repopulation. *Trends Cancer* 6, 419–431. doi:10.1016/j.trecan.2020.01.018

Jung, H. S., Verwilst, P., Kim, W. Y., and Kim, J. S. (2016). Fluorescent and colorimetric sensors for the detection of humidity or water content. *Chem. Soc. Rev.* 45, 1242–1256. doi:10.1039/c5cs00494b

Kamata, H., Honda, S., Maeda, S., Chang, L., Hirata, H., and Karin, M. (2005). Reactive oxygen species promote TNFα-induced death and sustained JNK activation by inhibiting MAP kinase phosphatases. *Cell* 120, 649–661. doi:10.1016/j.cell.2004.12.041

Lambert, A. W., Pattabiraman, D. R., and Weinberg, R. A. (2017). Emerging biological principles of metastasis. *Cell* 168, 670–691. doi:10.1016/j.cell.2016.11.037

Li, H., Yao, Q., Fan, J., Du, J., Wang, J., and Peng, X. (2017). A two-photon NIR-to-NIR fluorescent probe for imaging hydrogen peroxide in living cells. *Biosens. Bioelectron.* 94, 536–543. doi:10.1016/j.bios.2017.03.039

Liaw, J. W., Kuo, C. Y., and Tsai, S. W. (2021). The effect of quasi-spherical gold nanoparticles on two-photon induced reactive oxygen species for cell damage. *Nanomater. (Basel)* 11, 1180. doi:10.3390/nano11051180

Lin, M. T., and Beal, M. F. (2006). Mitochondrial dysfunction and oxidative stress in neurodegenerative diseases. *Nature* 443, 787–795. doi:10.1038/nature05292

Liou, G.-Y., and Storz, P. (2010). Reactive oxygen species in cancer. *Free Radic. Res.* 44, 479–496. doi:10.3109/10715761003667554

Liu, W., Wang, B., Zhou, M., Liu, D., Chen, F., Zhao, X., et al. (2023). Redox dysregulation in the tumor microenvironment contributes to cancer metastasis. *Antioxid. Redox Signal.* [Advance online publication]. doi:10.1089/ars.2023.0272

Lu, J., Ji, L., and Yu, Y. (2021). Rational design of a selective and sensitive "turn-on" fluorescent probe for monitoring and imaging hydrogen peroxide in living cells. *RSC Adv.* 11, 35093–35098. doi:10.1039/d1ra06620j

Maji, S. K., Yu, S., Chung, K., Sekkarapatti Ramasamy, M., Lim, J. W., Wang, J., et al. (2018). Synergistic nanozymetic activity of hybrid gold bipyramid-molybdenum disulfide Core@Shell nanostructures for two-photon imaging and anticancer therapy. *ACS Appl. Mater Interfaces* 10, 42068–42076. doi:10.1021/acsami.8b15443

Marcu, L. G. (2014). Tumour repopulation and the role of abortive division in squamous cell carcinomas during chemotherapy. *Cell Prolif.* 47, 318–325. doi:10.1111/cpr.12108

Saggar, J. K., and Tannock, I. F. (2015). Chemotherapy rescues hypoxic tumor cells and induces their reoxygenation and repopulation-an effect that is inhibited by the hypoxia-activated prodrug TH-302. *Clin. Cancer Res.* 21, 2107–2114. doi:10.1158/1078-0432.ccr-14-2298

Schieber, M., and Chandel, N. S. (2014). ROS function in redox signaling and oxidative stress. *Curr. Biol.* 24, R453–R462. doi:10.1016/j.cub.2014.03.034

Shao, D., Li, M., Wang, Z., Zheng, X., Lao, Y. H., Chang, Z., et al. (2018). Bioinspired diselenide-bridged mesoporous silica nanoparticles for dual-responsive protein delivery. *Adv. Mater* 30, e1801198. doi:10.1002/adma.201801198

Shi, Y. J., Zhang, G. J., Lu, Z. Y., Ying, Y. C., Jia, H. L., and Xi, P. (2018). Advances in multiphoton microscopy technologies. *Chin. Opt.* 11, 296–306. doi:10.3788/co.20181103.0296

Song, M. J., Hwang, S. W., and Whang, D. (2010). Non-enzymatic electrochemical CuO nanoflowers sensor for hydrogen peroxide detection. *Talanta* 80, 1648–1652. doi:10.1016/j.talanta.2009.09.061

Verma, R., Foster, R. E., Horgan, K., Mounsey, K., Nixon, H., Smalle, N., et al. (2016). Lymphocyte depletion and repopulation after chemotherapy for primary breast cancer. *Breast Cancer Res.* 18, 10. doi:10.1186/s13058-015-0669-x

Wang, L., Hou, X., Fang, H., and Yang, X. (2022). Boronate-based fluorescent probes as a prominent tool for H_2O_2 sensing and recognition. *Curr. Med. Chem.* 29, 2476–2489. doi:10.2174/0929867328666210902101642

Wang, Z., Chang, Z. M., Shao, D., Zhang, F., Chen, F., Li, L., et al. (2019). Janus gold triangle-mesoporous silica nanoplatforms for hypoxia-activated radio-chemo-photothermal therapy of liver cancer. *ACS Appl. Mater Interfaces* 11, 34755–34765. doi:10.1021/acsami.9b12879

Zhan, X., Yu, X., Li, B., Zhou, R., Fang, Q., and Wu, Y. (2022). Quantifying H2O2 by ratiometric fluorescence sensor platform of N-GQDs/rhodamine B in the presence of thioglycolic acid under the catalysis of Fe3+. *Spectrochimica Acta Part A Mol. Biomol. Spectrosc.* 275, 121191. doi:10.1016/j.saa.2022.121191

Zhang, F., Jia, Y., Zheng, X., Shao, D., Zhao, Y., Wang, Z., et al. (2019). Janus nanocarrier-based co-delivery of doxorubicin and berberine weakens chemotherapy-exacerbated hepatocellular carcinoma recurrence. *Acta Biomater.* 100, 352–364. doi:10.1016/j.actbio.2019.09.034

Zhao, Y., Hu, Y., Hou, J., Jia, Z., Zhong, D., Zhou, S., et al. (2019). Electrochemical biointerface based on electrodeposition AuNPs on 3D graphene aerogel: direct electron transfer of Cytochrome c and hydrogen peroxide sensing. *J. Electroanal. Chem.* 842, 16–23. doi:10.1016/j.jelechem.2019.04.052

Zhou, R., Peng, Q., Wan, D., Yu, C., Zhang, Y., Hou, Y., et al. (2021). Construction of a lysosome-targetable ratiometric fluorescent probe for H2O2 tracing and imaging in living cells and an inflamed model. *RSC Adv.* 11, 24032–24037. doi:10.1039/d1ra04026j

frontiers | Frontiers in Bioengineering and Biotechnology

TYPE Review
PUBLISHED 14 August 2023
DOI 10.3389/fbioe.2023.1258666

Check for updates

OPEN ACCESS

EDITED BY
Yuce Li,
Sungkyunkwan University, Republic of Korea

REVIEWED BY
Linlong Li,
The Chinese University of Hong Kong, China
Tianlin Gao,
Qingdao University, China
Jinshan Guo,
Southern Medical University, China

*CORRESPONDENCE
Yi Zhang,
yizhang0502@jlu.edu.cn

RECEIVED 14 July 2023
ACCEPTED 02 August 2023
PUBLISHED 14 August 2023

CITATION
Duan L, Wang Z, Fan S, Wang C and Zhang Y (2023), Research progress of biomaterials and innovative technologies in urinary tissue engineering. *Front. Bioeng. Biotechnol.* 11:1258666. doi: 10.3389/fbioe.2023.1258666

COPYRIGHT
© 2023 Duan, Wang, Fan, Wang and Zhang. This is an open-access article distributed under the terms of the Creative Commons Attribution License (CC BY). The use, distribution or reproduction in other forums is permitted, provided the original author(s) and the copyright owner(s) are credited and that the original publication in this journal is cited, in accordance with accepted academic practice. No use, distribution or reproduction is permitted which does not comply with these terms.

Research progress of biomaterials and innovative technologies in urinary tissue engineering

Liwei Duan[1], Zongliang Wang[2], Shuang Fan[1], Chen Wang[1] and Yi Zhang[1]*

[1]The Second Hospital, Jilin University, Changchun, China, [2]Key Laboratory of Polymer Ecomaterials, Changchun Institute of Applied Chemistry, Chinese Academy of Sciences, Changchun, China

Substantial interests have been attracted to multiple bioactive and biomimetic biomaterials in recent decades because of their ability in presenting a structural and functional reconstruction of urinary tissues. Some innovative technologies have also been surging in urinary tissue engineering and urological regeneration by providing insights into the physiological behavior of the urinary system. As such, the hierarchical structure and tissue function of the bladder, urethra, and ureter can be reproduced similarly to the native urinary tissues. This review aims to summarize recent advances in functional biomaterials and biomimetic technologies toward urological reconstruction. Various nanofirous biomaterials derived from decellularized natural tissues, synthetic biopolymers, and hybrid scaffolds were developed with desired microstructure, surface chemistry, and mechanical properties. Some growth factors, drugs, as well as inorganic nanomaterials were also utilized to enhance the biological activity and functionality of scaffolds. Notably, it is emphasized that advanced approaches, such as 3D (bio) printing and organoids, have also been developed to facilitate structural and functional regeneration of the urological system. So in this review, we discussed the fabrication strategies, physiochemical properties, and biofunctional modification of regenerative biomaterials and their potential clinical application of fast-evolving technologies. In addition, future prospective and commercial products are further proposed and discussed.

KEYWORDS

biomaterials, technology, reconstruction, tissue engineering, urinary

1 Introduction

For decades, the major challenges that urologists are eager to overcome include the injury and function loss of urinary tissue caused by congenital disorders, inflammation, tumor, trauma, and degenerative diseases (Drewa et al., 2012; Zhang et al., 2020). For a long time, as a gold standard for clinical treatment, autologous tissue has played an important role in replacing damaged urinary system tissues, such as bladder mucosa, oral mucosa, and genital skin (Jiang et al., 2018). However, its prominent limitations lie in the insufficient source of donor tissue, immune rejection, the essential difference of structure and function between the donor site and the transplantation site, as well as related various complications, including infection, stone formation, metabolic disorder, excessive mucus production, and so on (Wang et al., 2021a; Chen et al., 2021). To address these problems, as a result of the rapid development of regenerative medicine and tissue engineering, damaged urinary tissues and organs can now be replaced and/or

regenerated. By means of biomaterials, cells, and growth factors, urologic tissue engineering technology aims to repair tissue defects, reconstruct new tissues, restore organ functions, and finally improve the life quality of patients (Chan et al., 2020).

There are two parts to the urinary system: the upper urinary tract and the lower urinary tract. The upper urinary tract consists of the kidney and ureter. The bladder and urethra make up the lower urinary tract (Liu et al., 2021). In the urinary system, urine is formed in kidney and then passes through ureter into bladder. Ureter is connected to bladder through the posterior lateral opening of bladder, while bladder is connected to urethra through its anterior opening. The bladder wall consists of four layers, including the urinary tract epithelial layer facing the bladder cavity, the connective tissue layer, the muscular layer, and the outer surface serosal layer (Sulob et al., 2021). The dysfunction or disorder of the normal urinary system requires reconstructive treatment to reduce urologic incontinence, preserve the storage function of the bladder, and minimize the risk of kidney injury (Shamout et al., 2023). Large or complex urinary injuries require surgical management and the choice of repair depends on the site of injury and timing of identification. Surgery treatment often include repairing urethral strictures or bladder damaged tissues, or repairing an abnormal bladder, and so on (Zelivianskaia et al., 2021; Fu et al., 2023). However, the repair of urinary bladder injury is often associated with some short- and long-term complications (Cohen et al., 2016). It is interesting to note that biomaterial scaffolds in tissue engineering have been presenting biomimetic substitutes for reconstructing the complex structure and function of the native urinary system. The ideal biomaterial scaffolds for the urinary system should first have appropriate mechanical strength and flexibility to resist the physiological pressure of continuous dynamic changes of urinary filling and emptying and facilitate cell migration and differentiation (Ajalloueian et al., 2018). Along with the ingrowth of newly formed tissue, the scaffolds would slowly degrade in a specific period. In addition, cells or growth factors can also be seeded or impregnated in the scaffolds to efficiently re-organize the native extracellular matrices physiologically (Adamowicz et al., 2019). Because of these aspects, kinds of acellular matrix, as well as natural and synthetic polymer scaffolds have been developed successively together with some advanced technologies towards urologic reconstruction.

This review aims to summarize the latest progress in functional biomaterials and fast-evolving technologies reported in the past 3 or 4 years for the repair and regeneration of the urinary system (Figure 1). The fabrication techniques and specific characteristics of a tissue-derived acellular matrix, natural and synthetic polymer scaffolds will be discussed first to address the urgent need of developing biomimetic materials and grafts for urinary reconstruction. Then, we try to pay special attention to the new strategy of biological modification of scaffolds using bioactive substances or inorganic components to improve the quality of reconstruction. Some innovative platform technologies for the regeneration of urologic tissues are also summarized. Finally, future prospects and clinical application potential of these biomaterials and techniques are given.

2 Biomaterials

Biomaterial-based urinary tissue engineering strategies are serving to address the growing demand for urological reconstruction (Sharma and Basu, 2022). Biomaterials and scaffolds should first stabilize structures with suitable mechanical properties, resist the physiological contraction and expansion pressure, and supporting cell migration (Lawkowska et al., 2022). Timely degradation is also necessary to promote the efficient ingrowth of new tissues (Lin et al., 2023). Regarding all these aspects, it includes acellular matrix, natural and synthetic polymer materials, and composite materials, etc.

2.1 Acellular matrix

Although acellular scaffolds have shown some limitations such as cytotoxic and inherent immune responses, many kinds of acellular matrices derived from various sources play a crucial role in urinary tissue regeneration by imitating natural extracellular matrix (ECM), including small intestinal submucosa (SIS), bladder acellular matrix (BAM), acellular corpus spongiosum (ACSM), and acellular amniotic membrane (Adamowicz et al., 2019). It is also common to use porcine SIS and BAM for urethra reconstruction in fundamental research and human clinical application (Ribeiro-Filho and Sievert, 2015; Cao et al., 2019). Chen and colleagues treated two patients with ureteral strictures using a semi-tubular 4-layer decellularized SIS matrix (Cook Co., Ltd. United States), and summarized its clinical effects (Xu et al., 2020a). They sutured the strip-shaped SIS matrix (4.0 cm long and 2.0 cm wide) onto the open ureter. Two months after surgery, ureteroscopic examination of the implanted SIS matrix showed that the internal surface of the implant was covered by mucosa, and the sutured lumen became narrow. After 4 months, the SIS matrix partially degraded, and the narrow ureteral stricture was covered by rough mucus. The SIS matrix was completely degraded after 6 months with rough mucosa covered on the ureteral stricture. Twelve months later, the SIS matrix was completely degraded, and no stricture was noted anymore with smooth and clean mucosal surfaces. No urinary leakage or infection was observed and the urography showed that ureteral anastomosis was no longer narrow. Serum creatinine levels returned to normal levels similar to those before surgery. The CT examinations of the urinary tract showed no signs of hydronephrosis. This SIS matrix is expected to serve as a substitute for ureteral reconstruction.

Recently, an emerging tissue engineering technology has been developed for the preparation of cell-free in-body tissue architecture (iBTA), which was used to produce autologous collagenous tissues with appropriate shape and mechanical properties via an alternative mold (Furukoshi et al., 2019; Makoto Komura et al., 2019; Terazawa et al., 2020). For this technique, decellularization is no longer required, thus avoiding the complex *in vitro* cell seeding processes in a clean laboratory environment. The tissue sheets obtained using the iBTA technique were named “Biosheet”, which was composed of fibroblasts and ECM rich in collagen type I (Col) (Takiyama et al., 2016). In one following study, Iimori et al. implanted porous cylindrical molds subcutaneously in dogs for 8 weeks to

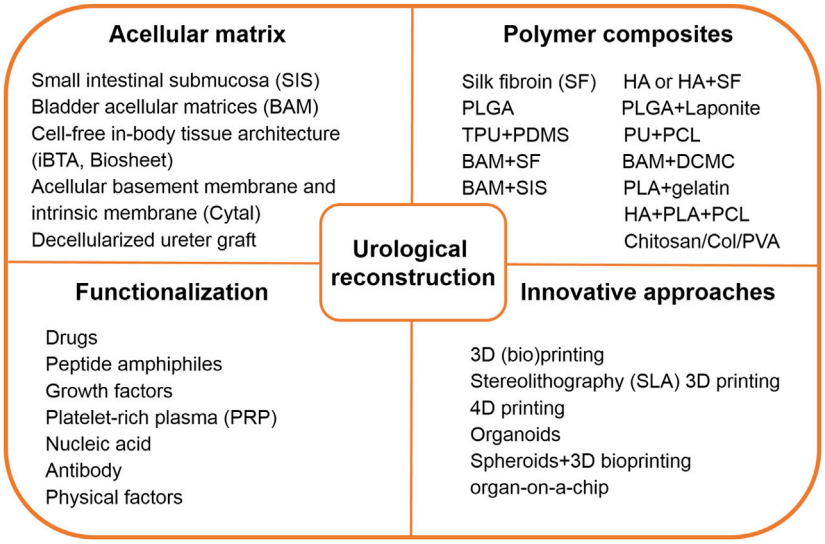

FIGURE 1
Brief summary of functional biomaterials and innovative technology toward urological reconstruction. Abbreviations: HA, hyaluronic acid; PLGA, poly (lactic-co-glycolic acid); TPU, thermoplastic polyurethane; PDMS, polydimethyl siloxane; PU, polydimethyl siloxane; PCL, poly (ε-caprolactone); BAM, bladder acellular matrix; SF, Silk fibroin; DCMC, dialdehyde carboxymethyl cellulose; SIS, small intestinal submucosa; PLA, poly (lactic acid); Col, collagen; PVA, polyvinyl alcohol.

prepare Biosheet implants for bladder reconstruction (Figure 2) (Iimori et al., 2020). The molds consisted of several stainless steel slits that were inserted into an acrylic tube with caps. After 8 weeks, flexible rectangular Biosheet implants composed of collagen and fibroblasts with a length of 3 × 5 cm and a thickness of 1 mm were harvested by longitudinally cutting the tubular tissues (Suzuki et al., 2018). Then, a piece of full-thickness ventral wall of the urinary bladder with a size of 2 × 2 cm was removed and immediately sutured with the same-sized freshly prepared autologous Biosheet implants. After 4 and 12 weeks post-implantation, the Biosheet implants were extracted for histological examination. During the entire observation period, no urine leakage, stones, hematoma, calcification, or metaplasia were found on urography and ultrasonography examination. At 4 weeks, the Biosheet implants were covered by a multicellular layer of regenerated transitional epithelium and new blood vessels, forming partially substituted mucosa. There were visible connective tissue, neovascularization, infiltration of lymphoid, macrophage, and inflammatory cells. After 12 weeks, the boundary between the Biosheet implants and the natural bladder was indistinguishable, retaining a deep submucosa. Well-differentiated urothelial layers and submucosa organization could be seen on the Biosheet implants, which were better than at 4 weeks. Alpha-smooth muscle actin (α-SMA) positive stained spindle cells infiltrated into the boundary between the Biosheet implants and the natural muscle tissues. Few inflammatory cells, no necrosis or calcification were noted for the Biosheet implants. The results of this study indicated that the autologous Biosheet implants had good biocompatibility, and its epithelium remodeling as well as neovascularization were beneficial for bladder reconstruction in dog models, without any harmful signs of chronic inflammation or rejection. The Biosheet implants would be applicable as a candidate substitute in the clinical reconstruction of full thickness bladder wall.

In addition, Cytal is one of the commercial acellular sheet scaffolds extracted from the basement membrane and intrinsic membrane of the porcine urinary bladder by ACell Inc. (Gilbert et al., 2005). Its ingredients include growth factors, glycosaminoglycans, and collagens. Initially, Cytal was designed to treat wounds of partial thickness and full thickness, such as surgical and traumatic wounds, pressure ulcers, and diabetic ulcers (Valerio et al., 2015). To understand its application in urethral tissue reconstruction, Huen et al. (2022) summarized their preliminary experience in implanting Cytal in children who underwent ventral curvature correction during the repair of proximal hypospadias. They reviewed surgeries during 2020 and 2021 within 4 surgeon hypospadias databases in a single institution. Ten male patients who were implanted with single-layer Cytal grafts through ventral curvature correction all showed straight erections. In addition, from the perspective of cost, the price of Cytal graft is favorable to patients compared with other commercial products. And donor site morbidity would also not be caused by the implantation of Cytal grafts.

Additionally, Sabetkish et al. (2020) prepared decellularized bladder scaffolds and an inverted hourglass technique was used to assess the feasibility of scaffolds for double-sized bladder augmentation in rabbits. For decellularization, harvested urinary bladders were administered with 2% sodium dodecyl sulfate (SDS) for 6 h, soaked in Triton X-100 for 4 h, and washed in phosphate-buffered saline (PBS) for 2 h. The hourglass technique involved suturing the bottom of the acellular scaffold to the bottom of the natural bladder through the serosal layer to prevent bladder exposure. The control group underwent resection of the dome muscle and mucosa of the bladder, and the acellular scaffold was directly sutured to the bladder wall for bladder augmentation. After

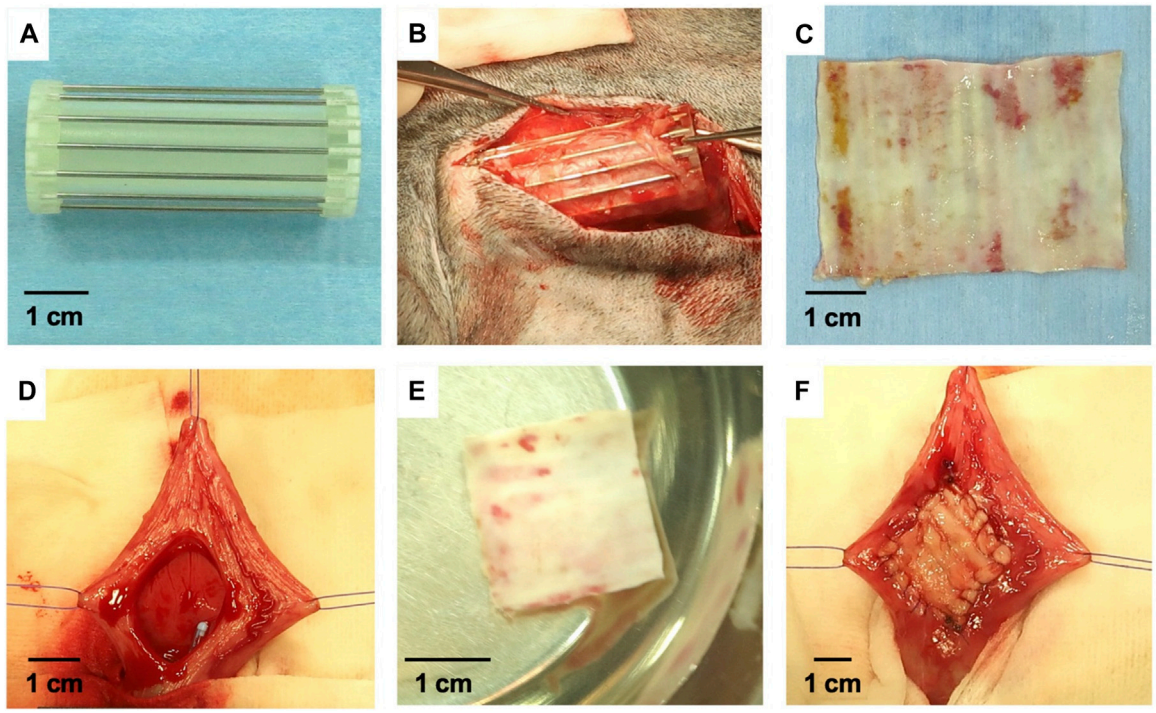

FIGURE 2
The preparation process and implantation of Biosheet implants. **(A)** Mold for the preparation of Biosheet. **(B)** Mold was completely encapsulated within the Biosheet tissues 8 weeks after implantation. **(C)** The fragile and redundant tissues covered on the Biosheet was clearly removed. **(D)** Urinary bladder wall after dissection (2 × 2 cm) **(E)** Trephined Biosheet (2 cm in diameter) **(F)** Urinary bladder after implantation of Biosheet. *Regenerative Therapy*. 2020; 15: 274–280. Copyright 2020, with permission from Elsevier (Iimori et al., 2020).

1, 3, and 9 months, no shrinkage, infections, and reactive were observed for macroscopic view in the hourglass technique group compared with the natural bladder tissue. However, macroscopic observation of the control group showed significant shrinkage, rejection, and fall from the bladder wall. After 3 months of implantation, the implanted scaffolds promoted epithelium and muscle regeneration, with high levels of immunohistochemistry (IHC) staining, and no significant difference compared to 9 months after surgery. On the contrary, a higher grade of fibrosis was observed for the control group from the histopathological evaluation. In all cases, the implantation of fully decellularized bladder scaffolds resulted in a successful double-sized bladder autoaugmentation for patients with a small bladder capacity. In comparison with synthetic materials and other natural scaffolds, this material has proven to be a significant alternative material.

Similarly, Moreno-Manzano et al. (2020) seeded human adipose-derived stem cells (ADSCs) on decellularized rat bladder matrices and then implanted them into rats with partial cystectomy to regenerate the bladders. The authors found that the implantation of the ADSC-contained bladder matrices significantly promoted the recovery of the urothelium, the organization of smooth muscle layers, the creation of new blood vessels and nerve innervation. The paracrine effect of ADSCs on the decellularized bladder matrices made the recellularized matrices to be a potentially effective bladder substitute. A similar strategy has also been performed by Vishwakarma et al. (2020), and the authors fabricated cell-laden decellularized goat bladder scaffolds for bladder reconstruction. Subsequently, human umbilical cord blood-derived mesenchymal stem cells (hUCBMSCs) were seeded to prepare bioactive decellularized bladder scaffolds for bladder augmentation. The composition, architecture and mechanical characteristics of the decellularized bladder scaffolds were well retained. The adhesion and proliferation of the seeded hUCBMSCs on the scaffolds were significantly improved at 14 days. So the prepared decellularized goat bladder scaffolds represented a simple and controlled fabrication process of biological tissue-specific substitutes and could provide a biocompatible microenvironment for transplanted MSCs in bladder reconstruction.

Correspondingly, decellularized ureter graft has also been developed by Sabetkish et al. (2022) for rat bladder augmentation. In this study, the ureteral samples were donated by four adult male patients who volunteered to donate their kidneys. The ureters were decellularized by successively using 2% SDS and 2% Triton X-100, PBS washed afterwards. The microstructure of the acellular extracellular matrix composed of well-organized type I and III collagen fibers was well maintained, with a tensile strength of 5.1×10^3 kN, similar to that of normal ureter (5.5×10^3 kN) and bladder tissue (5.8×10^3 kN), and no nucleus was retained. No contractions, infections, and stone formation were observed in the animals implanted with the decellularized ureters. It was worth noting that all the groups did not experience fibrosis or degeneration. After 9 months, complete regeneration of the bladder wall was achieved by implanting the decellularized

ureters, and the boundary between the host bladder and the decellularized ureter was no longer easily distinguished. The decellularized urethral grafts in this study have broad potential as biocompatible scaffolds for cell ingrowth and morphological formation of bladder tissues (Singh et al., 2018; Haeublein et al., 2022).

Undoubtedly, acellular tissue matrices have unique advantages as they possess the inherent components of natural ECM to support cell growth and differentiation. Natural proteins and growth factors, including collagen, vascular endothelial growth factor (VEGF), and fibroblast growth factor (FGF), etc., can be retained in the matrix. The problems they need to overcome are cytotoxic, fibrosis, infection, and immune response (Hughes et al., 2016; Wang et al., 2023a).

2.2 Natural and synthetic materials

The outstanding advantage of natural and synthetic materials is that they are easy to manipulate and process to achieve the required functions (Wang et al., 2023b; Sung et al., 2023). Many of them have been approved for commercial applications, including poly(glycolic acid) (PGA), poly(lactic acid) (PLA), and poly(lactic-co-glycolic acid) (PLGA), etc., (Alvarez-Mendez et al., 2023). The significant drawback lies in inducing foreign body reactions to the host and insufficient angiogenesis (Zhang et al., 2022).

Among them, silk is a natural protein fiber, and its superior mechanical properties, biocompatibility, as well as degradability make it very suitable for bladder reconstruction (Bhattacharjee et al., 2017; Nguyen et al., 2019; Li and Sun, 2022). Tavanai and others produced weft-knitted silk fibroin (SF) scaffolds (138, 182, and 245 loops/cm^2 of stitch density respectively), and evaluated their suitability for bladder regeneration (Figure 3) (Khademolqorani et al., 2021). Weft-knitted scaffolds have the following structure characteristics: perpendicular connecting wale and course loops (Eltahan et al., 2016; Cai et al., 2020; Meng et al., 2020). The authors knitted scaffolds with varying stitch densities using a knitting machine that can adjust tension. By increasing the stitch density, the porosity and pore size of the scaffolds decreased. The weft-knitted scaffolds showed an average tensile strength of 7–7.9 MPa and 8.1–8.8 MPa in the course and wale directions, respectively. After co-culturing with NIH-3T3 fibroblasts for 1, 2, 4 and 6 weeks, the tensile strength and ultimate strain of the weft-knitted scaffolds were higher than those of pure scaffolds at all time points. In addition, among all the three groups, the SF scaffolds with 182 loops/cm^2 stitch density exhibited the most similar stress-strain behavior to the natural porcine bladder, which meant it could simulate the process of bladder filling and urination. Therefore, its excellent performance makes it a promising candidate for bladder reconstruction.

Hyaluronic acid (HA) has been reported to have the ability to bind to cell surface receptors and recruit urethral stem cells to stimulate cell behavior and regulate tissue formation (Aruffo et al., 1990; Niu et al., 2021). In one study, a biomimetic tubular nanofiber scaffold with appropriate cell-binding motifs and sufficient mechanical properties was electrospun by integrating HA with natural SF protein to promote urethra epithelialization (Figure 4) (Niu et al., 2022). To further modulate the topological structure of SF and HA-SF nanofiber scaffolds, chemical crosslinking was carried out by immersing in ethanol and 1-ethyl-3-[3-dimethylaminopropyl] carbodiimide hydrochloride (EDC) solution. SF nanofibers showed a tightly interlinked nano-topography, while HA/SF nanofibers exhibited interconnected network decorating gel-like surface morphology, similar to the morphology of natural urethral epithelium. When urothelial cells (UCs) were cultured on the nanofibers, the cells preferentially adhered to the surface of HA/SF, with elongated morphology, uniform distribution, and ingrowth, which was confirmed by scanning electron microscopy (SEM) and cross-section observation of hematoxylin and eosin (HE) staining. The immunofluorescence staining for the proliferation marker, Ki67, and cell counting kit-8 (CCK-8) results showed that UCs proliferated well on the HA/SF nanofibers. The higher density positive green fluorescence of uropakin-3 on the HA/SF nanofibers confirmed its waterproof ability and anti-injury function for urothelial barrier restoration. Eight weeks after implantation in the rabbit transected urethral defect, the HA/SF group exhibited a slight lower urine flow rate (8.4 ± 0.2 mL/s) than that of before implantation (8.9 ± 0.2 mL/s), while the SF group showed the lowest level (6.6 ± 0.2 mL/s). By observing the Masson's trichrome staining of the regenerated urethral tissue, a dense UC layer and new collagen deposition were formed along the HA/SF scaffold. After 14 weeks, stratified epithelial remodeling occurred in the regenerated urothelium of the SF and HA/SF groups. While the thickness of the regenerated middle and surface layer in the HA/SF group (43 ± 3 μm) was similar to the normal urothelial epithelium and thicker than that of the SF group (26 ± 1 μm). The upregulation of double fluorescent staining for K5 and uroplakin-3 further confirmed that HA/SF nanofibers promoted the regeneration of K5 positive cubic cell layer in the urinary tract epithelium basal and outermost thin layer of uroplakin-3 positive flat cell, indicating that the effective remodeling of the blood urine barrier was similar to that of the healthy urothelial barrier. In addition, in the HA/SF nanofiber group, smooth muscle tissue remodeling and angiogenesis confirmed that lumen and myoepithelial cells were successfully recruited from adjacent areas, thus producing a higher proportion of smooth muscle bundles and α-SMA immunofluorescence staining positive areas, as well as higher levels of CD31 positivity in the regenerated urethra. This biomimetic scaffold provides a synergistic effect of nano-topography and biophysical cues, and promotes efficient endogenous regeneration by presenting meaningful aspects different from SF protein scaffolds.

As an alternative, PLGA-based nanofiber scaffold was electrospun to regulate the differentiation and regeneration of smooth muscle cells (SMCs) (Mirzaei et al., 2019a). After inducing and culturing the iPSCs on the PLGA scaffold for 2 and 3 weeks, genes related to SMCs were upregulated, such as myosin heavy chain (MHC), smooth muscle 22 alpha (SM-22α), Calponin-1, α-SMA, and Caldesmon1. This indicated that induced co-culturing of human iPSCs on the PLGA nanofibrous structure with an appropriate elasticity and strength, simulating the structure and function of natural bladder extracellular matrix, had great differentiation potential toward SMC, effectively promoting SMC differentiation and cellular penetration, and enhancing bladder tissue regeneration.

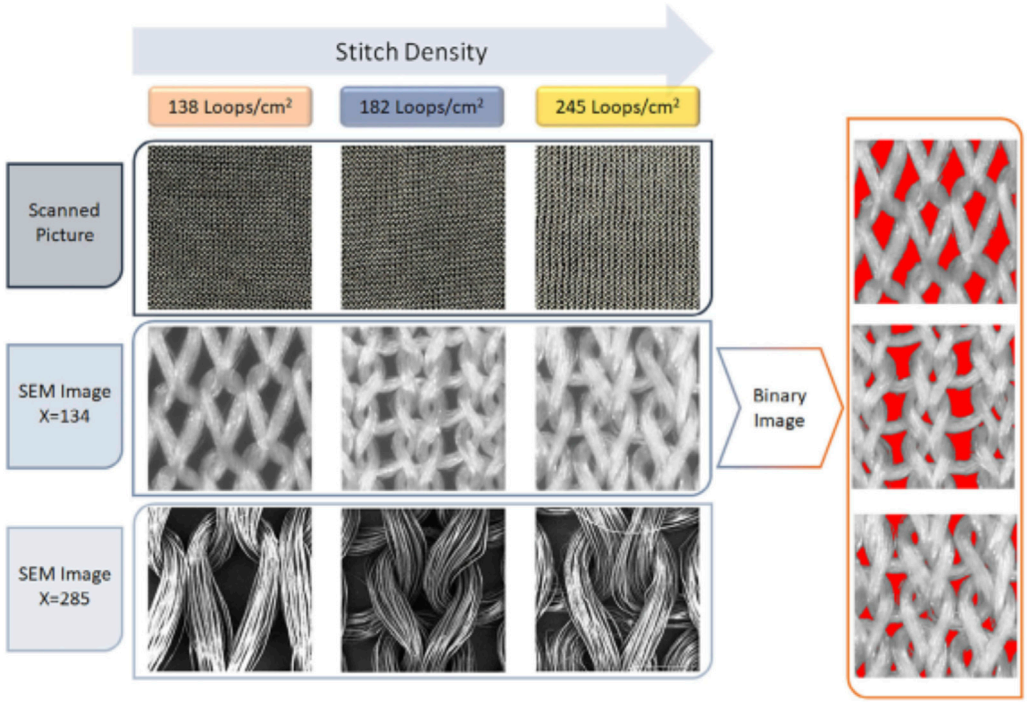

FIGURE 3
Scanning electron microscope (SEM) images of the silk fibroin weft-knitted scaffolds, and binary images of silk fibroin weft-knitted. *Polymers Advanced Technologies*. 2021; 32: 2367–2377. Copyright 2021, with permission from Wiley (Khademolqorani et al., 2021).

Similarly, Salem et al. prepared a tissue-engineered construct by seeding SMCs onto a commercial three-layer PLGA woven mesh (VICRYL, Ethicon Inc., United States) and then suturing it to rat bladder (Salem et al., 2020). After 90 days of surgery, radiography showed that the bladder reconstructed with the tissue-engineered construct presented a normal oval appearance and a smooth and regular outline. The newly reconstructed bladder was generally circular and full in shape, with a size and shape similar to a normal bladder. The PLGA mesh was completely degraded and no longer visible. Histological observation revealed complete regeneration of the bladder wall, consisting of layered urothelium, submucosal blood vessels, and muscle bundles. The results of this study demonstrated that the implanted materials and delivered cells contributed to the newly formed muscle tissues and the ingrowth of urethral epithelium, thereby fully restoring the volume and function of the regenerated bladder.

Different from polymers, as a two-dimensional (2D) smectite clay with high aspect ratio, Laponite is a biocompatible and safe nanomaterial, which is easy to degrade in physiological environment (Tomás et al., 2018). In a study, Laponite nanoparticles were electrospun into PLGA nanofiber scaffolds to replicate the porosity and microstructure of the natural urethra tissue microenvironment (Wang et al., 2020). The higher content of Laponite in the composite scaffolds, the smaller fiber diameter, which might be conducive to cell adhesion and migration. The spontaneous fluorescence of Laponite particles in the composite scaffolds indicated their uniform dispersion within the scaffolds. The mechanical characteristics of the scaffolds and the degradation of the PLGA matrix increased with the increase of Laponite content. Human umbilical vein endothelial cells (HUVECs) could attached, spread, and grew well on the surface of the scaffolds. After 3 days of co-culturing with 1% Laponite/PLGA composite urethral scaffolds, the cell proliferation rate exceeded 100%, indicating that the structural characteristics of the composite scaffolds were similar to the natural extracellular, which is very useful for cell adhesion and proliferation.

Polyurethane and silicone rubber have also been evaluated for their biological safety and low toxicity in urinary reconstruction (Chew and Denstedt, 2004; Cosentino et al., 2012). To obtain better structural integrity and antibacterial properties, thermoplastic polyurethanes (TPU) modified by polydimethyl siloxane (PDMS) was prepared by dynamic crosslinking method as thermoplastic vulcanizate for resistance to deformation and processing in clinical treatment (Sharma et al., 2021). Compared with the physical or van der Waal forces assisted melt mixing process, the interface adhesion between PDMS and molten TPU matrix became stronger due to the *in situ* three-dimensional (3D) cross-linking (Damrongsakkul et al., 2003; Drupitha and Nando, 2017). The interlinks formed in the silicone phase endowed the composite with rigidity. For example, the ultimate tensile strength and elastic modulus of the dynamically crosslinked 80/20 TPU/PDMS composite (DT8P2) increased up to 15.7 ± 0.5 MPa and 8.4 ± 0.1 MPa compared with that of T8P2 without crosslinking (10.9 ± 2.0 MPa and 8.0 ± 0.2 MPa). The suture retention force (SRF) of $T8P_{VP}2$, $DT_{bPEI}8P2$, and $DT_{PAP}8P2$ samples was 9.2 N, 14.1 N, and 13.8 N, respectively, which were far greater than the clinically acceptable minimum SRF value of 2 N to meet the reliable mechanical integration with the natural tissues (Billiar et al., 2001). Subsequently, a contact-killing

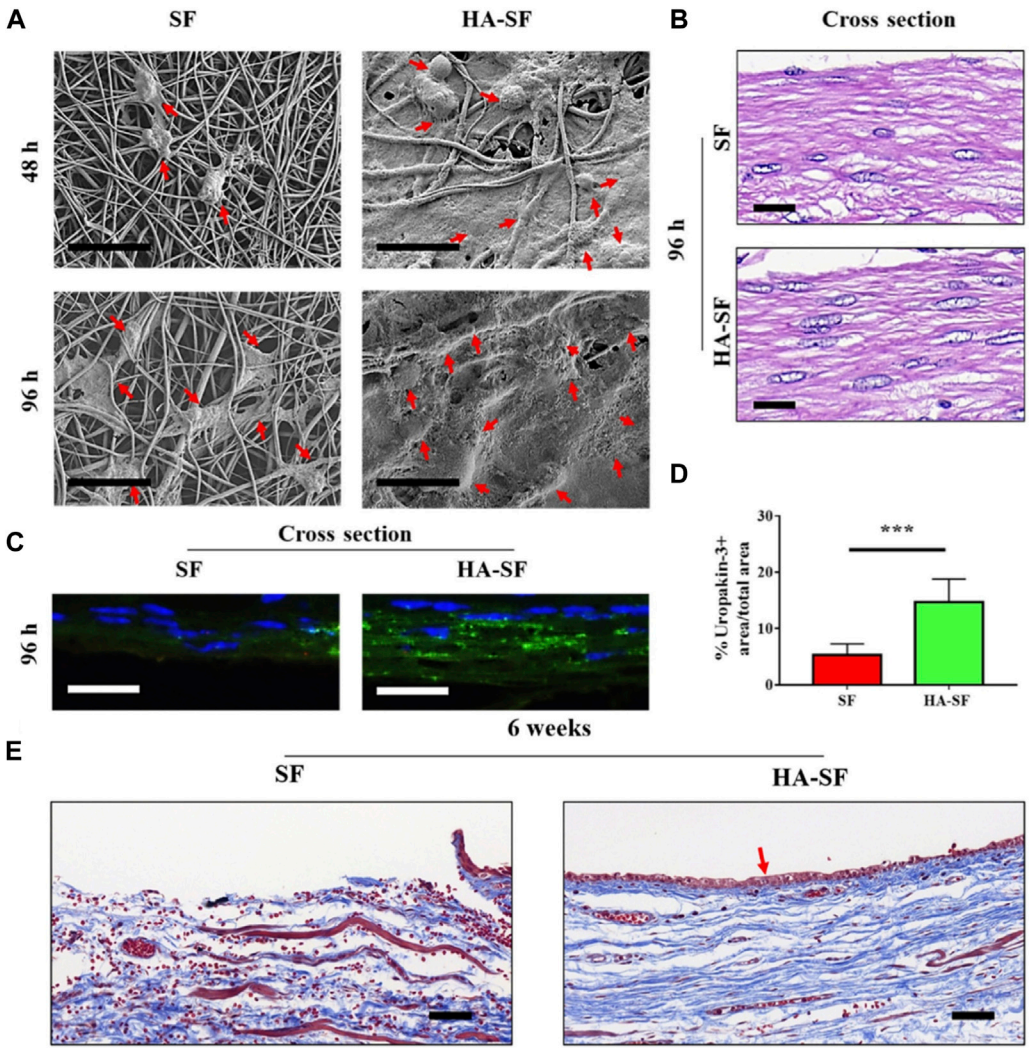

FIGURE 4
Cell behavior on silk fibroin (SF) and hyaluronic acid (HA)-SF nanofiber films. **(A)** SEM images of primary urothelial cells (UCs) on the inner wall surface of SF and HA-SF nanofiber after 48 and 96 h post-seeding. Red arrows indicate well-spread UCs. **(B)** Hematoxylin and eosin (HE) staining of the cross section of cellularized SF and HA-SF nanofiber films. **(C)** Fluorescence staining of the cross section of cellularized SF and HA-SF nanofiber thin films using uropakin-3 (green) and nuclei (blue). Scale bars: 20 μm **(A–C)**. **(D)** Statistical data of uropakin-3 positive expression of primary urethral UCs seeded on different nanofibers (three random fields per sample, n = 4 samples per group). ***$p < 0.01$. **(E)** Masson's trichrome staining of the cross section of the tubular SF and HA-SF nanofibers implanted for 6 weeks. Collagen (blue), smooth muscle, and erythrocytes (red). Red arrow indicates that the captured host endogenous urothelial cell (UC) is evenly distributed in the lumen of HA-SF scaffold. Scale bars, 20 μm. *Bioengineering and Translational Medicine*. 2022; 7: e10268. Copyright 2021, with permission from Wiley (Niu et al., 2022).

antibacterial surface was generated by covalent modification of quaternized compounds, which included branched polyethylenimine (bPEI), 4-vinyl pyridine (4-VP), and bPEI-grafted-(acrylic acid-co-vinylbenzyltriphenyl phosphonium chloride) (PAP), on the TPU/PDMS composites. Compared with the TPU group, the bactericidal efficiency of $T8P_{VP}2$ against *Escherichia coli* (*E. coli*), Methicillin-resistant *S. Aureus* (MRSA) and *Proteus mirabilis* (*P. mirabilis*) was 98.00%, 98.90%, and 99.37%, respectively, after 24 h of co-culture. The $DT_{bPEI}8P2$ samples exhibited corresponding bactericidal efficiency of 99.50%, 99.90%, and 99.90%. While the $DT_{PAP}8P2$ group showed 99.68%, 99.90%, and 99.84% of bactericidal efficiency, respectively. *E. coli* and *P. mirabilis* cultured on the $T8P_{VP}2$, $DT_{bPEI}8P2$, and $DT_{PAP}8P2$ composites showed distorted morphology and permanent damage characteristics. The integrity of the MRSA cell membrane was disrupted, leading to leakage of cytoplasmic contents. The superior surface energy and wettability of the $T8P_{VP}2$, $DT_{bPEI}8P2$, and $DT_{PAP}8P2$ samples contributed to the cell proliferation and characteristic morphology of L929 cells without inducing cytotoxicity. Therefore, the high-density cationic motifs functionalized surface of TPU/PDMS composites could inhibit the survival ability of bacteria in urinary tract infection and maintain appropriate *in vitro* cell behavior, serving as a potential biomaterial for developing medical urinary substitutes.

Broadly speaking, insufficient or slow vascularization of tissue-engineered urethral grafts often leads to complications such as urethral stricture and urethral obstruction, which hinder the success rate of urethral reconstruction in animal and clinical

studies (Rashidbenam et al., 2019). It has been reported that the appropriate weakly hydrophilic polyurethane scaffolds could not only improve the cell compatibility and histocompatibility, but also rapidly realize the tissue vascularization of the scaffolds (Niu et al., 2014; Niu et al., 2017). In one study, thanks to the rapid vascularization of biodegradable urethral scaffold made of linear amphiphilic block-copolymer of polyurethane (PU-ran), Niu et al. successfully achieved functional regeneration of the Beagle urethra (Niu et al., 2020). The structure backbone of PU-ran copolymer was solution polymerized from hydrophilic poly (ethylene glycol) (PEG) and hydrophobic poly(ε-caprolactone) (PCL) segments in a controlled manner. As the content of PEG in the backbone increased, the semi-crystalline of PU-ran copolymers changed to an amorphous state, and the tuning chain length of PEG promoted elasticity and mechanical characteristics. The coordinated segments of flexible PEG and rigid PCL prevented crystallization, thus promoting the flexible and stretchable copolymer of PU-ran. The electrospun nanofibers composed of PEG (0.4 kDa) and PCL-diol (2.8 kDa) segments, abbreviated as E10-ran-C20, were softer and smoother than pure PCL. The seeded primary bladder epithelial cells (ECs) and primary SMCs could quickly adhere, migrate, and grow on the PU-ran copolymer nanofiber scaffolds. The E10-ran-C20 nanofiber scaffolds were advantageous to the adhesion and proliferation of urothelial tissue-derived cells, and the construction of 3D morphology (Sharma and Cheng, 2015; Cheng et al., 2019). The authors later found that the E10-ran-C20 nanofibers could induce higher expression of the epithelial cytokeratin (AE1/AE3+) in ECs, α-SMA+ in SMCs, and secretion of elastin. Subsequently, the E10-ran-C20 layered tubular matrix was used to deliver cells for mimicking the natural urethra in space and dimension, and the thickness of the epithelial ECM in the tube was approximately 500 nm, indicating good cytocompatibility. The engineered E10-ran-C20 scaffolds were implanted into a partial urethral defectin Beagle puppies to simulate common urethral injuries in young male children with traffic accidents and medical injuries. After 60 days *in vivo*, the E10-ran-C20 scaffolds gradually degraded and absorbed, ECs and SMCs delivered on the scaffolds continued to proliferate and secrete ECM (Orabi et al., 2013; Kullmann et al., 2017; Wang et al., 2017), and finally formed tubular lumen epithelium in the nanofiber scaffolds. The formation of smooth muscle tissues was due to the biocompatibility of SMCs with surrounding tissues and its growth in the biodegradable scaffolds. After 3 months, the mean urinary flow rates (AFR) and the average urethral diameter (MUD) of the E10-ran-C20 scaffolds were similar to those of the autologous grafts, allowing the contrast agent to pass through the entire reconstructed lumen. Masson's trichrome staining showed that the newly formed epithelial cells in the urethral wall had a stratified epithelial morphology and were covered by smooth muscle tissue. A large amount of capillaries and small blood vessels were formed under the new epithelial basal. Collagen staining in the new urethra was more visible than that of autografts. The quantitate protein expression of smooth muscle (α-SMA+), urothelium (AE1/AE3+), and cell adhesion molecule (CD31) of the cell-seeded E10-ran-C20 scaffold implied that the regeneration of urethra was similar to that of the autograft group. The expression of cytokines and chemokines was elevated at the juction of the engineered E10-ran-C20 scaffolds, which facilitated the recruitment of host inflammatory cells, the neo-vessel formation, and the generation of regenerative microenvironment, contributing to the functional recovery of Beagles. This will help overcome potential difficulties, such as insufficient neovascularization within the grafts and associated urethral strictures, making it have great potential in treating many human urethral diseases (Lv et al., 2018; Sánchez et al., 2022).

2.3 Composite materials

To give full play to the high strength and elasticity of SF protein polymers and the preserved cellular components retained by BAM, Xiao et al. constructed a composite scaffold by combining double-layer SF film and sponge with BAM hydrogel and encapsulated ADSCs in the hydrogel for rat bladder augmentation (Xiao et al., 2021b). The composite scaffold was constructed by dropping the ASCs-encapsulated BAM hydrogel on the SF surface and continuing to incubate for 7 days. The biological components preserved in the bladder ECM provided a fluid and viscosity microenvironment for the uniform distribution of ASCs in the SF pores of the composite scaffold. It was worth noting that previously wrapping the constructed scaffold in the omentum for 7 days before anastomosing to repair the bladder defect achieved efficient vascularization and promoted the structural regeneration of the bladder wall. At 12 weeks after implantation, the SF/BAM/ASCs group formed a continuous urothelium layer and a large amount of smooth muscles. In addition, the ACSs delivered in the matrix hydrogel significantly regenerated smooth muscles, neurons, and blood vessels, thus restoring the function of rat bladder, which was proved by the immunofluorescence observation. The loaded ASCs also accelerated the degradation of the SF sponge in the composite scaffold.

The rapid degradation of BAM and the cytotoxicity of glutaraldehyde crosslinking reagent attracted Peng et al. (2019) attention, they used dialdehyde carboxymethyl cellulose (DCMC) with an appropriate molecular weight to crosslink BAM materials for bladder tissue engineering. The fixation of BAM by 30 mg mL^{-1} of DCMC obtained a cross-linked D-BAM composite with lower cytotoxicity, better mechanical properties, and resistance to enzyme degradation, while retaining the microstructure and biological components, including transforming growth factor beta (TGF-β), human keratinocyte growth factor (KGF), and glycosaminoglycans (GAGs). The bladder transitional epithelial cells cultured on the D-BAM composite were stimulated to secrete epidermal growth factor (EGF) and platelet-derived growth factor (PDGF), which was conducive to re-epithelialization. The D-BAM composite could inhibit the deposition of minerals in BAM tissues and possessed a prominent anti-calcification ability.

In another study, to overcome the poor expansibility and rapid degradation of decellularized extracellular matrixes (dECMs), including SIS and BAM, the transient crosslinking between dECMs and long-chain aliphatic molecules was developed. And dECMs were covalently linked to one end of the polymeric chains, while other molecules could interact at the other end through weak interactions, such as dipole-dipole forces (Sharma et al., 2022). Additionally, some other composite nanofibrous patches or scaffolds composed of PLA/gelatin or HA/PLA/PCL have also been generated to evaluate the critical potential of replacing damaged or diseased bladder and urethra (Liu et al., 2020a; Wang et al., 2022).

Among so many materials, acellular matrix can preserve the natural structure and composition of natural urinary tissues, while the natural or synthetic polymers or composite materials help to withstand mechanical loads during tissue regeneration process, even when the bladder is filled with urine (Table 1) (Hanczar et al., 2021). More importantly, they are also suitable for surgical procedures by providing structural rigidity, thereby resisting very high urinary pressure conditions (Zhu et al., 2022). The flexibility and stretchability of acellular matrix and artificial scaffolds are also crucial for adapting to increasing urine volume and stress (Chowdhury et al., 2021). Last but not least, suture resistance and impermeability are necessary for temporary storage of urine to avoid urine leakage (Pal, 1998; Ajalloueian et al., 2018; Lee et al., 2021). It can be expected that the promotion of the advantages and overcoming the disadvantages of different types of scaffold will make urinary tissue engineering better.

3 Biological functionalization strategies

3.1 Drugs or bioactive molecules

Natural biomolecules have been utilized for functionalization of transplant materials to overcome the limitations of contracture, stone formation, and smooth muscle regeneration (Mokhames et al., 2020; Zhang et al., 2021).

As a biotic component, curcumin has been selected to functionalize bladder scaffolds for protecting organs, inhibiting protease, and eliminating free radicals due to its anti-inflammatory, antioxidant and other biological activities (Bengmark, 2006; Anand et al., 2007). For example, Mokhames et al. (2020) prepared chitosan, collagen, and polyvinyl alcohol (chitosan/Col/PVA) nanofiber scaffolds doped with curcumin (nanofibers/curcumin), which had a randomly oriented and interconnected porous structure. In this composite scaffold, chitosan and PVA provided structural support, while Col served as a natural matrix that mimicked natural bladder tissue. In addition to the initial burst release of about 20% on the first day, the cumulative release of curcumin in 21 days increased slowly, and the release of curcumin from the nanofibers was up to 90%. The curcumin-loaded nanofibers exhibited the highest level of protein adsorption, cell attachment, and proliferation. Compared with the nanofibers and tissue culture plate groups, the nanofibers/curcumin group upregulated the expression of genes related to smooth muscle cells, including Calponin1, Caldesmon1, SM-22α, and α-SMA. Furthermore, immunocytochemistry staining analysis showed that the curcumin-incorporated nanofibers promoted the expression of α-SMA protein. Therefore, the natural bioactive substance curcumin in this study improved the differentiation of stem cells into bladder SMCs.

Procyanidin (PC) is a natural polyphenol and it was used to crosslink collagen materials for enhancing mechanical stability by forming hydrogen bonds with amide groups and also inhibit calcification (Han et al., 2003; Liu et al., 2013; Zhai et al., 2014; Balalaie et al., 2018). PC can also resist inflammation and oxidation, so it has been used in tissue engineering and the development of bioprosthetic heart valves (Schmidt and Baier, 2000; Zhai et al., 2006; Wang et al., 2015a; Wang et al., 2015b). To reduce contracture, enhance smooth muscle regeneration, and avoid stone formation of small intestine submucosa (SIS) materials during bladder regeneration, Zhang et al. (2021) prepared a PC-functionalized SIS scaffold (PC-SIS) with PC as a crosslinking agent. After crosslinking with a proper amount of PC, the diameter of collagen fibers in PC-SIS slightly increased, showing a deep brownish red color and a porous surface structure. Due to the cross-linking of PC, the PC-SIS exhibited excellent mechanical properties, good biocompatibility, slower degradation, and less formation of mineralized nodules. For the behavior of SMCs, PC-SIS supported cell growth and spreading, promoted cell organization, bundle-like structure formation, filopodia-like connection with adjacent cells, extracellular matrix deposition, and the SMC-related gene expression. When applied to full-thickness bladder defects, histological examination showed that the bladder tissue generated by PC-SIS contained more smooth muscle bundles than the SIS groups. The urodynamics analysis revealed that the PC-SIS materials had the same peak pressure, bladder volume, elastic modulus, and maximum load as the natural bladder tissue. The phenolic hydroxyl structure of catechin-containing PC with intermolecular hydrogen bonding ability provided a meaningful choice for cross-linking of SIS as a patch in bladder repair and reconstruction.

Self-assembled peptide amphiphiles (PAs) were synthesized to regulate the inflammatory microenvironment of urinary tract injury sites (Bury et al., 2014; Chan et al., 2021). By combining the hydrophobic collapse of the alkyl domains and the hydrogen bond of the β-sheet domains, the bioactive peptide epitopes of PAs could be specifically formed on the assembled nanofibers, which could be recognized by cell receptors or bound to other biological molecules to enhance function, such as anti-inflammatory and tissue regeneration (Hartgerink et al., 2001; Sohn et al., 2003; Silva et al., 2004; Webber et al., 2011). In one study, Hartgerink et al. (2001) first synthesized anti-inflammatory PAs (AIF-PAs) using solid peptide synthesis methods. Then SIS scaffolds were separately dip-coated in the AIF-PAs and then transplanted into the cystectomized bladder defects (Ashley et al., 2010). Compared with the unmodified group or the group modified with control peptides of AIF-PA6, the SIS scaffolds modified with the anti-inflammatory AIF-PA1 peptides significantly reduced the level of myeloperoxidase positive (MPO^+) neutrophils, M1 proinflammatory macrophages ($CD86^+$), proinflammatory cytokines of IL-1β and TNFα, while increased the expression of M2 regenerative/anti-inflammatory macrophages ($CD206^+$) at the anastomotic site and regenerated wound region. The AIF-PA1-SIS scaffolds also facilitated higher levels of vascularization and collagen deposition, which meant faster progress of angiogenesis and urethral remodeling, and promoted the healing process of urethral defects. The same team also observed a similar regenerative effect of AIF-PA1 on bladder tissue regeneration. They found that the anti-inflammatory PA alternated the immune response of rat bladder augmentation, decreased the $CD68^+$ macrophage and MPO^+ neutrophil level, reduced the TNFα, IL-1β and M1 macrophage level, but increased angiogenesis (Bury et al., 2014). Therefore, the easy use of AIF-PAs nanofibers and their ability to regulate the inflammatory microenvironment have broad prospects in urethral reconstruction.

TABLE 1 The physical and mechanical properties of the biomaterials for uribary tissue engineering.

Biomaterials	Porosity (%) or diameter (nm)	Mechanical properties	Refs.
Decellularized bladders	None	~88 KPa (Tensile strength)	Vishwakarma et al. (2020)
Decellularized ureters	None	(5.1 ×10^3) kilonewtons (Young's modulus)	Sabetkish et al. (2022)
Silk plain-weft knitted scaffolds	(89.9 ± 1.1) %	(7.1 ± 0.6) MPa in course direction and (8.1 ± 1.9) MPa in wale direction (Tensile strength)	Khademolqorani et al. (2021)
Hyaluronic acid and silk fibroin (HA-SF) nanofibers	(254 ± 13) nm	(0.83 ± 0.4) MPa (Young's modulus)	Niu et al. (2022)
Poly(lactide-co-glycolide) nanofibers	(600 ± 400) nm	(11.32 ± 2.02) MPa (Tensile strength)	Mirzaei et al. (2019a)
Dynamically crosslinked thermoplastic polyurethanes modified by polydimethyl siloxane (TPU/PDMS)	None	(15.7 ± 0.5) MPa (Ultimate tensile strength)	Sharma et al. (2021)
Bi-layer silk fibroin skeleton	(62.67 ± 3.40)%, (81.98 ± 2.10)μm	None	Xiao et al. (2021b)

Bacterial infection and biofilm formation of implant materials are considered one of the main issues hindering tissue repair quality and affecting global health, and are receiving increasing attention (Sun et al., 2019; Gao W et al., 2021). Chrysophanol (CP) is a unique natural anthraquinone with broad-spectrum therapeutic effects. It was reported that CP of appropriate concentration could inhibit the formation of biofilm through bacterial quorum sensing (QS) (Ding et al., 2011; Prateeksha et al., 2019). Therefore, Singh and his colleagues utilized CP to biofunctionalize silver nanoparticles (AgNPs) to regulate the interaction between QS signals and AgNPs, reduce bacterial pathogenicity, and minimize the dosage of AgNPs that inhibited bacterial adhesion and colonization on the implanted catheter materials (Prateeksha et al., 2021). Under alkaline conditions, CP-AgNPs were synthesized by easily transferring electrons to form Ag^+ ions due to the ionization of the ketone group of CP (Polte et al., 2012). The loading efficiency of CP on AgNPs was about 21% ± 1.1%, and it could be continuously released from CP-AgNPs. Flow cytometry analysis showed that compared to the control groups, the internalization rate of CP-AgNPs in *Pseudomonas aeruginosa* PAO1 and *Escherichia coli* (*E. coli*) was higher. For bacteria treated only with CP, there was no CP in both bacteria, further proving that CP-AgNPs would be a potential cargo delivery platform that could modulate bacterial QS and biofilm formation. The downregulation of QS-related genes indicated that CP molecules effectively delivered through CP-AgNPs could resist QS. Subsequently, a stable and durable CP-AgNPs coating was prepared on the surface of commercial silicone and polystyrene urinary catheters, with a retention time of more than 10 days to avoid protein and cell adsorption and prevent QS effect. The mechanical characteristics of the coated urinary catheters were not affected by the CP-AgNPs coating, and they could be freely imported into and removed from the bladder. Their clinical application would not be limited by the surface roughness of CP-AgNPs coatings, so bacterial adhesion might be accordingly restricted. Finally, the authors also evaluated the anti-adhesion effect of the nanolayer coated-urinary catheters through *in vitro* and *in vivo* tests, and achieved satisfactory results.

Another promising bioactive molecule, periostin (POSTN), is a stromal cell protein found in some tissues in embryonic development and is believed to be able to continuously regenerate and repair human tissues (Kormann et al., 2020; Wang et al., 2021b). It was reported that POSTN could not only bind to integrin receptors to promote cell spreading, proliferation, and tissue repair, but also induce macrophage proliferation and M2-subtype macrophage polarization to enhance tissue regeneration and wound healing (Wu et al., 2015; Allard et al., 2018; Liao et al., 2020; Nikoloudaki et al., 2020). Chen et al. delivered POSTN into the bladder through gelatin methacryloyl (GelMA) granular hydrogel to evaluate the potential mechanism of bladder urothelial regeneration in acute cystitis induced by cyclophosphamide (CYP) (Zhihong et al., 2022). The authors first detected upregulation of the POSTN gene and protein in CYP-treated mouse bladder, indicating that POSTN could regenerate bladder tissues. While the lack of POSTN deteriorated the structure and function of CYP-treated mouse bladder, delayed the regeneration of umbrella cells, and thus hindered the repair of the bladder barrier. The immunofluorescence staining of proliferation markers (pHH3 and Ki67), mRNA expression of differentiation markers for urothelial stem cells (Wnt1, Wnt2, Wnt2b, etc., and c-Myc, CCND1, AXIN2), as well as Western blot and immunofluorescence of urothelial stem cell marker (Krt14), showed that POSTN promoted the proliferation of urothelial cells by inducing AKT and Wnt4 and hence activated the signal of β-catenin. A large amount of $CD68^+$, a lower level of CD86 (M1 marker) expression and a higher level of CD206 (M2 marker) in the bladder showed that POSTN promoted the proliferation of residual macrophages, and macrophages were polarized into the M2 subtype, providing a suitable microenvironment for regeneration after acute injury. After intravesical delivery of GelMA hydrogel loaded with POSTN into the CYP-treated bladders using a catheter, HE staining and immunostaining images demonstrated that the exfoliation of umbrella cells was reduced, and a large number of urothelial stem cells was observed, indicating that CYP treatment promoted the regeneration of urothelial and prevented bladder barrier injury. Therefore, this study concluded that POSTN could promote the proliferation of urothelial stem cells and macrophage polarization, and enhance the regeneration of CYP induced bladder injury. So it has a promising clinical application for patients with cystitis.

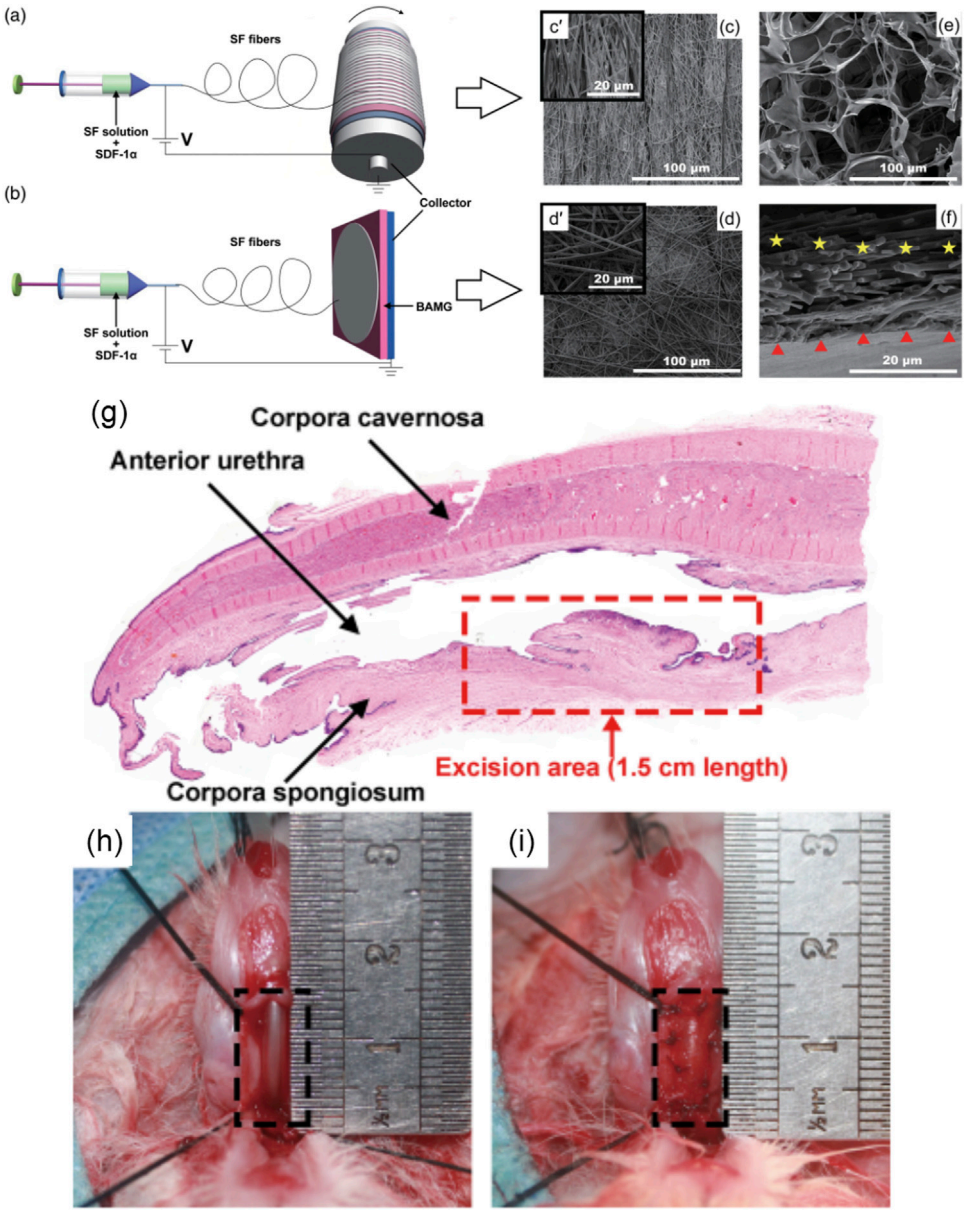

FIGURE 5
Schematic diagram showing electrospinning of the SF/3D-BAMG composite scaffolds with **(A)** aligned and **(B)** nonaligned fibers in aqueous solutions. Scanning electron microscopy images show the surfaces of [**(C)**, c'] aligned the SF microfiber and [**(D)**, d'] the nonaligned SF microfiber. **(E)** The surface of 3D-BAMG, and **(F)** cross section of the aligned SF/3D-BAMG composite scaffold. 3D-BAMG has been shown by a red triangle and silk microfiber has been indicated by yellow stars. **(G–I)** Substitution urethroplasty *in vivo* **(G)** Histological diagram of urethral defect rabbit model with an average length of a 1.5-cm ventral excision area. **(H)** Animal rabbit of the urethral defect. **(I)** Urethral reconstruction using composite scaffolds. Acta Biomaterialia. 2017; 61:101–113. Copyright 2020, with permission from Wiley (Liu et al., 2020b).

3.2 Growth factors

Angiogenesis involves the effective proliferation of endothelial cells and the formation of tubular structures (Herbert and Stainier, 2011). For example, VEGF can bind and activate the endothelial cell receptors, thereby enhancing cell migration and proliferation, and thus promoting the formation of blood vessels (Castro et al., 2018). Mokhames et al. (2021) fabricated electrospun polyvinylidene fluoride (PVDF) nanofibers, and further functionalized them with VEGF by neutralizing Col with sodium hydroxide. The prepared PVDF/Col/VEGF scaffold was fibrous and had interconnected pores with an average diameter of 900 ± 750 nm. After 168 h, the loaded VEGF continuously released up to 72%, and the PVDF/Col/VEGF scaffold exhibited significantly higher protein adsorption capacity than the PVDF/Col scaffold. The VEGF-loaded scaffold not only promoted the attachment and proliferation of primary bladder SMCs and HUVECs, but also significantly downregulated the apoptotic-related genes of SMCs (Bax, P53, P21, EP300, E2F5, and SMAD5) and upregulated angiogenesis-related genes of HUVECs (VEGFR1, VEGFR2, and CD31). The results indicated

that the loading of VEGF in the PVDF/Col nanofibrous scaffold was helpful to manufacture tissue-engineered grafts for bladder wall reconstruction.

As an important chemotactic, stromal cell-derived factor-1 alpha (SDF-1α) was incorporated and sustained released from a composite scaffold to recruit stem cells for homing and trigger self-repair ability after urethral tissue injury (Tang et al., 2017; Liu et al., 2020b). Liu et al. fabricated the composite scaffold through electrospinning aligned or nonaligned SF microfibers containing SDF-1α on porous 3D BAM graft (3D-BAMG) (Figure 5) (Liu et al., 2020b). The aligned SF microfibers were arranged in the same direction, which was conducive to the continuity of cell extension and distribution directional. The nonaligned silk microfibers were arranged in multiple directions. Both aligned and nonaligned SF were porous structures with high porosity. The aligned or randomly arranged SF microfibers attached on the highly porous 3D-BAMG graft, which facilitated cell infiltration and growth, as well as the formation of blood vessels and smooth muscles. The support of 3D-BAMG effectively enhanced the mechanical property of the SF fibrous scaffold. After immersing in PBS for 16 days, the maximum release rate of SDF-1α was up to 8.5%, and the release amount was about 9.9×10^3 pg. The controlled release of SDF-1α stimulated the migration of ADSCs and bone marrow stromal cells (BMSCs) cultured in a Transwell system for 16 days, showing the capacity to recruit and induce the chemotaxis of endogenous stem cells. Under urethroplasty, the aligned SF/3D-BAMG scaffolds functionalized by SDF-1α were implanted in a ventral urethral defect with a size of $1.5 \times 1\ cm^2$. Thicker epithelial layers and orderly arranged epithelial cells were formed in the group of SF/3D-BAMG scaffold containing SDF-1α. The number of smooth muscle fibers and vascularization in the submucosal area were also significantly promoted, delaying fibrosis as indicated by the decrease in collagen deposition in the SDF-1α-incorporated scaffold group. The findings from this study demonstrated that the successful loading of chemokine SDF-1α in the scaffolds efficiently regenerated urethral mucosa and activated the signaling pathway of SDF-1α/CXCR-4 to form new submucosal smooth muscles and microvessels (Yang et al., 2018; Sadri et al., 2022). It provided a promising candidate for reconstructing long urethral defects by accelerating *in situ* urethral regeneration without seeding any foreign cells. Furthermore, it was interesting to note that cytotoxicity was observed when the concentration of SDF-1α was up to 500 ng/mL. Therefore, it is necessary to further explore the effect of gradient concentrations of SDF-1α in the composite scaffolds on lone-term urethral regeneration and other related signaling pathways.

To overcome the fibrosis and graft contraction of traditional scaffolds, promote angiogenesis and the regeneration of smooth muscle, urothelial, and neuromuscular, and finally enhance bladder augmentation, a variety of growth factors, including basic fibroblast growth factor (bFGF), VEGF, and EGF, were utilized to functionalize gradient PCL scaffold (Freeman et al., 1997; Kanematsu et al., 2003; Nillesen et al., 2007; Kim et al., 2020b). In this study, Kim et al. (2020b) first produced gradient PCL scaffold by immersing them in a hot solution of 90°C PCL/tetraglycol in ethanol at 17 C for 1 h. The decrease in solubility led to the precipitation of PCL scaffolds, accompanied by the generation of gradient structure that became looser from bottom to top in a vertical direction, which was conducive to cell differentiation by providing a large surface area for cell growth (Di Luca et al., 2016). The loaded growth factors could be sustainedly released for 24 days without initial burst release from the complex path of the labyrinthine-like gradient structure, thus avoiding the chemical conjugation process using harmful reagents (Zhang et al., 2009; Gao W et al., 2021). After implanting into the bladder wall defect of partial cystectomy for 12 weeks, the growth factors-incorporated PCL scaffold almost restored the original volume of the bladder, with a maximum volume of 1,650 ± 300 μL, which was significantly larger than the volume of the PCL scaffold (1,291 ± 443 μL). Histological evaluation showed that compared to the scaffold without growth factors, the PCL scaffold containing growth factors regenerated well-organized urothelial layers, thicker and denser smooth muscle bundles, tighter connective tissue, and blood vessels. The results of immunohistochemistry staining and expression of genes related to the differentiation of smooth muscle and squamous urothelium further proved that the growth factors loaded in the PCL scaffold could induce the endogenous stem cells to differentiate towards urothelium and smooth muscle, which benefited from the paracrine effect of the functionalized scaffold. The bFGF and VEGF activities of the scaffold also greatly enhanced the regeneration of the neuromuscular junctions in contact with neurons, thereby maintaining homeostasis as evidenced by the high positive staining of α-bungarotoxin. In addition, anti-CD8 antibody staining revealed that the immune response of the growth factor-functionalized scaffold was lower than that of the PCL scaffold group, and the inflammatory level of the latter was similar to that of the partial cystectomy group. This study demonstrated that the continuous release of growth factors preserved the biological activity of the PCL scaffold and enhanced bladder regeneration and long-term *in vivo* safety.

Compared with the combination of growth factors and materials, Bates and his colleagues injected KGF directly into mice through subcutaneous injection to understand the regeneration mechanism of bladder injury caused by cyclophosphamide (Narla et al., 2020). That's because the administration of cyclophosphamide has a potential risk of inducing bladder fibrosis or urothelial carcinoma (Vlaovic and Jewett, 1999). The authors found that KGF could inhibit the apoptosis of bladder cells by activating AKT signaling, thus preventing apoptosis of extravesical cells after cyclophosphamide administration (Fehrenbach et al., 2000). Besides, the injection of KGF also promoted the proliferation of $KRT5^+/KRT14^-$ urothelial cells on the lumen surface composed of newly formed superficial cells driven by ERK signaling, thereby enhancing the regeneration of epithelial cells (Ornitz and Itoh, 2015). Altogether, KGF reduced damage, led to early urothelial regeneration, and recovered from cyclophosphamide-induced bladder injury.

As an effective mitogen, bFGF contributes to angiogenesis, wound healing, and tissue regeneration (Nakamichi et al., 2016; Abdelhakim et al., 2020; He et al., 2022). To overcome the shortcomings of short half-life and fast diffusion of bFGF in medical applications and improve its binding efficiency with biomaterials, researchers engineered a bFGF fusion protein containing collagen-binding domain (CBD-bFGF) using gene recombination technology. And thus due to the introduction of CBD motifs, bFGF acquired significant binding capacity with

collagen materials, while the biological activity of CBD-bFGF was not affected (Zhao et al., 2007; Wu et al., 2018). Dai and his colleagues first introduced von Willeband's factor (vWF)-derived WREPSFCALS and collagenase-derived TKKTLRT amino acid residues into natural bFGF to recombine two fusion proteins, V-bFGF and C-bFGF, respectively, for targeted therapy of wound repair with less dosage of growth factors (Desouza and Brentani, 1992; Nishi et al., 1998; Andrades et al., 2001; Zhao et al., 2007). Both V-bFGF and C-bFGF maintained similar biological activity and strong collagen binding activity similar to natural bFGF due to no intramolecular disulfide bonds were formed in the loosen 3D secondary structure composed of 11 β-sheets avoiding the interface between bFGF and CBD motifs (Eriksson et al., 1991). The collagen-binding ability of the fused C-bFGF was higher than that of V-bFGF, and it had better cell integration and angiogenesis, which was conducive to targeted cellular function and tissue regeneration.

Subsequently, Dai's team successively used the CBD-bFGF-modified collagen scaffolds to regenerate injury of bladder, uterine horns, abdominal wall, extrahepatic bile duct, sciatic nerve, and tympanic membrane perforation (Chen et al., 2010; Li et al., 2011; Shi et al., 2011; Li et al., 2012; Ma et al., 2014; Zhang et al., 2017). Among them, to establish a targeted delivery system of bFGF protein in clinical application, Chen et al. (2010) transplanted CBD-bFGF functionalized collagen scaffolds onto the residual bladders after partial cystectomy in rats. Histological examination showed that the regenerated bladder had good structure, newly formed blood vessels and ingrowth of SMCs. The recovery of bladder volume capacity and compliance as evidenced by urodynamics implied satisfied bladder tissue regeneration by the functional collagen materials. Further, to provide sufficient evidence for the regenerative ability of human bladder injuries, the same authors conducted *in vivo* repair of damaged bladder in large animals. In this work, Dai and his colleagues first prepared BAM scaffolds through decellularization, and then immobilized the fused CBD-bFGF containing a collagen-binding peptide of TKKTLRT onto the scaffolds (Shi et al., 2017). *In vitro* evaluations showed that CBD-bFGF efficiently bind to natural BAM in a dose-dependent manner, and could be sustainedly released for 14 days without burst release. The functional CBD-bFGF/BAM scaffolds were sutured to the rest half bladder of beagles that underwent hemicystectomy. The urodynamics test showed an improvement in bladder contractility, with a maximum bladder volume of 41.50 ± 5.35 for the CBD-bFGF/BAM regenerated bladder. The PBS/BAM group showed a statistical lower volume (28.28 ± 4.64, $p < 0.01$). Similar bladder compliance was observed in the CBD-bFGF/BAM group (0.94 ± 0.13), which was superior to the PBS/BAM group (0.55 ± 0.10, $p < 0.01$). The CBD-bFGF/BAM group obtained a smooth bladder similar to the sham operation group, but different from the PBS/BAM group, there were some rough texture areas. The CBD-bFGF/BAM group integrated with adjacent tissue, with a dense urinary epithelial cell layer, and formed well-arranged smooth muscle bundles on the bladder wall as in the sham operation group. It was worth noting that compared to the PBS/BAM group, the CBD-bFGF/BAM group showed a significant increase in neovascularization and regenerated nerve fibers, and no inflammatory reaction was detected. In summary, due to the targeted delivery and controlled release of bFGF at the target site, the functionalized CBD-bFGF/BAM scaffolds could more efficiently utilize bFGF to reconstruct bladder tissue and reduce side effects in the dog models.

Nevertheless, the exact mechanism of bladder regeneration using CBD-bFGF functionalized scaffolds is still unclear, and further research is needed on bladder repair to evaluate the histological and functional recovery of smooth muscle, nerves, blood vessels, and urothelium. More importantly, multiple growth factors and stem cells can be combined to better regenerate bladder tissue (Kim et al., 2021; Horii et al., 2022).

Scaffolds for efficient delivery and controlled release of TGF-β have also been developed to regulate stem cell differentiation and promote the regeneration of target injured tissues (Chen et al., 2020; Ye et al., 2022). For instance, Ardeshirylajimi et al. prepared electrospun nanofiber scaffolds composed of PVDF and chitosan nanoparticles loading with TGF-β for bladder regeneration (Ardeshirylajimi et al., 2018). Under SEM it was observed that the average diameter of the electrospun smooth nanofibers was 845 ± 456 nm. The plasma treatment increased the hydrophilicity of the nanofibrous scaffold, reducing the contact angle to 42°, much lower than 138° of untreated nanofibers. The MTT results showed that the proliferation of ADSCs cultured on the PVDF scaffold was significant better than that of tissue culture polystyrene (TCPS). The release kinetics showed that 70% of the loaded TGF-β continuously released from the nanofibers within 2 weeks, it significantly promoted the viability and proliferation of ADSCs. The anti-inflammatory function was observed for both the PVDF and PVDF/TGF-β nanofibers when HUVECs were monolayer cultured on the scaffolds using transwells and treated with lipopolysaccharide (LPS). The upregulated gene expression of SM-22α, calponin-1, α-SMA, and protein expression of α-SMA indicated that the TGF-β-functionalized PVDF nanofibrous scaffold had superior SMC differentiation potential in clinical bladder regeneration.

Platelet-rich plasma (PRP) is widely noticed by researchers and clinicians because it is rich in a variety of growth factors and cytokines, such as insulin-like growth factor 1 (IGF-1), bFGF, EGF, VEGF, TGF-β, and PDGF (Marques et al., 2015; Ziegler et al., 2019; Poulios et al., 2021; Khodamoradi et al., 2022). It has been reported that the injection of PRP could promote the proliferation of urothelial cells and the expression of cytoskeleton and urinary barrier function protein in the treatment of recurrent urinary tract infection (Jiang et al., 2021). PRP could also induce angiogenesis, promote the regeneration of bladder mucosal and nerves, improve the recovery of erectile function, and avoid SMC apoptosis (Mirzaei et al., 2019b). In one study, Juan and his colleagues prepared rat PRP and perfused it into the bladder of ketamine induced ulcerative cystitis once a week for 4 weeks (Chueh et al., 2022). Compared with the ketamine treatment group, the PRP treatment group significantly reduced the frequency of urination, decreased the peak pressure of urination, and expanded the bladder capacity, urine volume, and urination interval. In PRP-treated bladder tissues, the immunostaining distribution of the proliferation marker Ki67 in the basal layer of urinary tract epithelium demonstrated that PRP had a mitotic effect of stimulating mucosal proliferation and improving mucosal regeneration. What's more, the protein expression level of proliferation markers and urothelial tight junction markers was

upregulated by the PRP treatment. All these findings showed that PRP treatment could promote bladder regeneration by stimulating cell proliferation and differentiation. The expression of α-SMA, one of the angiogenesis-related proteins, was increased by the injection of PRP, and it could stimulate the angiogenesis of the bladder. PRP treatment also enhanced the regeneration of intramural nerve and alleviated the oxidative damage in ketamine-induced bladder injury. The perfusion of PRP *in vivo* verified the biosynthesis of inflammatory fibers, the transformation of fibroblasts into myofibroblasts, anti-inflammation, the promotion of cell proliferation, angiogenesis, and neurogenesis to restore bladder function and repair bladder. This preclinical trial of PRP in the treatment of bladder injury not only elucidated the potential pathophysiological therapeutic mechanisms of PRP on bladder dysfunction and tissue remodeling, but also provided reference for the clinical application of PRP, such as the concentration of growth factors and platelets, standardization and quality management of PRP formulations (Fadadu et al., 2019; Andia et al., 2020).

3.3 Antibody

The low survival rate of cells directly seeded on the implanted patch for urological repair has aroused increasing concern about the safety and even effectiveness of such cell-loading therapy (Amer et al., 2017; Pokrywczynska et al., 2019). Song et al. designed functional scaffolds by conjugating anti-CD29 antibody onto SIS patch (AC-SIS) to selectively capture autologous urine stem cells (USCs) *in situ* for bladder regeneration (Song et al., 2022). Specifically, two-step reaction effectively enabled the chemical binding of the anti-CD29 antibody and SIS patches. The grafting rate of anti-CD29 antibody on the AC-SIS scaffold was as high as 72%, and it did not affect the biocompatibility of the scaffold. After 1, 3, and 5 days of culture, the proliferation of USCs on the AC-SIS was superior to that of the pure SIS group. under dynamic conditions, the AC-SIS group captured more cells than the SIS group. After 8 weeks of implantation of the scaffolds into full-thickness bladder defect, the bladder wall of AC-SIS transplantation showed a thickness similar to that of a normal bladder wall. While the bladder wall in the control group was thinner, slightly larger in size, and less elastic than normal tissue. The bladder size in the AC-SIS group was about 5 cm × 5.3 cm, closest to a normal bladder. The histological analysis revealed that the implanted AC-SIS samples facilitated the regeneration of urothelium, forming a unique hierarchical structure similar to the natural bladder urothelium composed of loop fluctuations and smooth muscle fibers. The captured USCs captured by the AC-SIS scaffolds altered the microenvironment, leading to vascular growth, re-epithelization, collagen and smooth muscle bundle formation. All of these aspects presented important potential for structural reconstruction, bladder internal pressure maintenance, and bladder function integrity.

3.4 Nucleic acid

It has been noted that the number of stem cells that differentiated into SMCs was very small and most of the stem cells inoculated on the scaffolds remained undifferentiated (Pokrywczynska et al., 2018). To increase the myogenic differentiation of stem cells and help reconstruct bladder function, Jin et al. designed lipid nanoparticles containing RNA activation targeting the MyoD promoter (saRNA), and construct composite scaffolds [NP(saMyoD/BAMG)] to promote the upregulation of endogenous gene expression (Jin et al., 2020). In this study, the ADSCs transfected with NP(saMyoD) upregulated the expression of Desmin, SM-22α, and α-SMA. The efficient delivery and releasing of the saRNA through NPs regenerated bladder smooth muscle and enhanced neovascularization, as demonstrated by the well-regenerated urothelium, dense arrangement of smooth muscle fibers, and the formation of blood vessels, thereby improving bladder defect repair and urinary function. It provides a new perspective for developing alternatives for bladder defect repair.

In another work, microRNA-126 contained in the extracellular vesicles (EVs) derived from human ADSCs was incorporated into BAMG-based hydrogel scaffolds by Xiao et al. (2021a) to facilitate bladder regeneration (Figure 6). The bladder defect was reinforced by the sufficient mechanical characteristics of the degradable scaffold and accordingly regenerated by the effective delivery of the human EVs to the injury site. The internalization of miRNA-126 in HUVECs promoted angiogenesis by inhibiting G-protein signaling 16, and activated the CXCR4/SDF-1αpathway, thereby secreting VEGF through the phosphorylation of ERK1/2. Finally, the formation of well-organized urothelium, smooth muscle, tube-like structure, and neural fibers for bladder augmentation, improved the morphology of regeneration and functional recovery.

3.5 Physical factors

It was reported that low-intensity extracorporeal shock wave therapy (LiESWT) could promote penis tissue regeneration and regulate penis hemodynamics in patients with erectile dysfunction (ED) (Chung and Wang, 2017). Lin et al. evaluated the therapeutic effect of LiESWT on bladder tissue vascularization, inflammatory response regulation, and improvement of bladder hyperactivity in ovarian hormone deficiency (OHD)-induced overactive bladder (OAB) in the human body and rat model (Lin et al., 2021). After 8 weeks of treatment with LiESWT (0.25 mJ/mm^2 and 3,000 pulses), the authors found that an increase in regeneration of bladder urothelium, inhibition of interstitial fibrosis, promotion of cell proliferation, increased expression of angiogenesis-related proteins, and increased protein phosphorylation levels of Akt, P38, and ErK1/2. Accordingly, the frequency of urination decreased, residual urine volume after urination and urgent incontinence also reduced, while the maximal flow rate and urine volume increased. In this study, the potential molecular mechanism of applying LiESWT might be regulating bladder overactivity, reducing inflammatory reaction, increasing neovascularization, enhancing cell proliferation and differentiation, and thereby improving the life quality of postmenopausal patients.

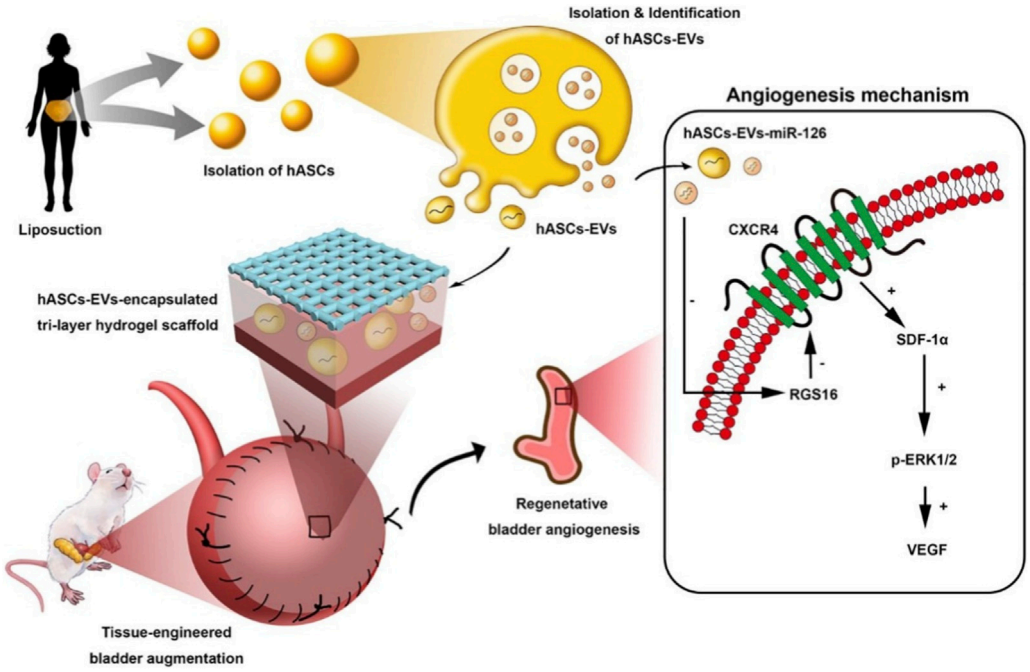

FIGURE 6
Schematic illustration of Human ASCs-EVs-encapsulated BAMG hydrogel scaffold delivers miR-126 to promote bladder regeneration angiogenesis through CXCR4/SDF-1α activation. *Chemical Engineering Journal.* 2021; 425:131624. Copyright 2021, with permission from Elsevier (Xiao et al., 2021a).

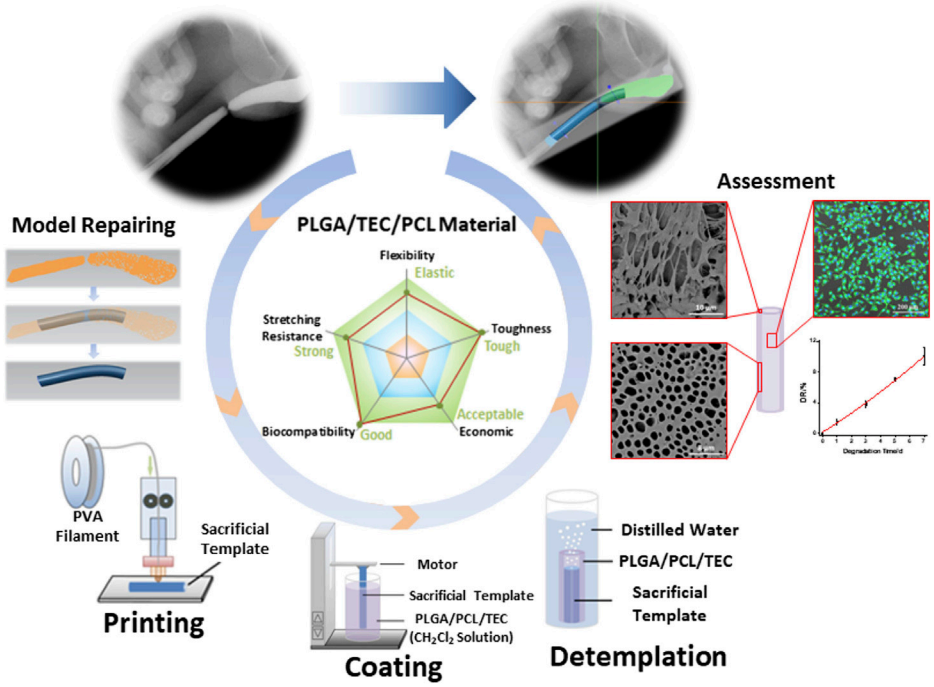

FIGURE 7
Manufacturing process of a biodegradable scaffold for urethra tissue engineering based on 3D printing. *ACS Applied Bio Materials.* 2020; 3: 2007–2016. Copyright 2020, with permission from American Chemical Society (Xu et al., 2020b).

4 Innovative approaches

4.1 3D printing

The diagnostic and therapeutic strategies for bladder dysfunction and tissue damage are often hampered by the lack of reliable *in vitro* 3D models to simulate the complex features of the human bladder. To overcome this problem and improve precision treatment, Xu et al. (2020b) prepared porous PLGA/PCL composite scaffolds incorporating different contents of triethyl citrate (TEC) using 3D printed polyvinyl alcohol (PVA) sacrificed templates for urethra tissue engineering (Figure 7). The mechanical characteristics of the PLGA/PCL scaffolds were influenced by different levels of PCL. Due to the inherent toughness of PCL and the poor phase interface between the two incompatible phases, the tensile strength of PLGA/PCL with higher PCL content (0%, 10%, 20%, 30%, 40%, and 50%) gradually reduced from 12.60 to 8.53 MPa. Meanwhile, due to the toughness of PCL, the Young's modulus of PLGA/PCL gradually increased from 121.08 to 178.88 MPa, making the materials more difficult to deform. Adding TEC into the PLGA/PCL (70:30) composite could effectively promote the compatibility between PLGA and PCL phases, with a maximum tensile strength of 11.11 MPa at 6% TEC. L929 cells with growth behavior similar to the urothelial cells were cultured on the PLGA/PCL/TEC (70:30:6) samples, and their fluorescence staining morphology and proliferation showed good biocompatibility and low cytotoxicity. The PLGA/PCL/TEC (70:30:6) materials also exhibited a moderate degradation rate between PLGA and PCL, indicating its suitability and feasibility as scaffolds for urethral tissue engineering.

In addition, 3D bioprinting and stereolithography (SLA) 3D printing techniques have also been utilized to create *in vitro* 3D urinary bladder models. In one study, Chae et al. reconstructed the physiological microenvironment of the bladder using a 3D bioprinting platform combined with decellularized bladder ECM and periodic mechanical stimulation (Chae et al., 2022). The created bladder models showed high cell viability and proliferation efficiency and enhanced the promotion of myogenic differentiation under dynamic mechanical stimulation. It envisions proposing a meaningful *in vitro* bladder model as a platform for drug screening, disease diagnosis and treatment. In another study, the authors used SLA 3D printing to prepare an elastic polymer-based indwelling bladder devices for the first time to achieve controlled local delivery of lidocaine hydrochloride (Xu et al., 2021). With the help of a urethral catheter, the hollow and solid bladder devices inserted into and retrieved from the bladder showed good blood compatibility, and the resistance to compression and tension was satisfactory, and they returned to their original shape immediately after removing the external force. Lidocaine was sustained released from the solid devices for 14 days. That is to say, as a revolutionary strategy, SLA 3D printing technology can manufacture drug delivery devices for the treatment and regeneration of bladder disease.

For urinary tissue engineering, 3D bioprinting using hydrogels containing cells as bioink is more suitable for manufacturing personalized biomimetic tissues than ink based only on biomaterials (Xu et al., 2022). Accordingly, 4D bioprinting invloving hydrogels based on intelligent stimulus response polymers as bioinks have been developed to manufacture urinary implants, as well as on demand stimulus responsive drug delivery. Various hydrogel materials with appropriate 4D bioprinting performance also have great potential in urinary tissue engineering, including poly(N-isopropylacrylamide) and poly(N,N-dimethylacrylamide), alginate, etc. (Dong et al., 2020; Imam et al., 2021).

4.2 Organoids

The characteristics of organoids simulated organs *in vitro* provides a novel approach for drug screening and precision medicine, and have become a research hotspot (Vasyutin et al., 2019; Jeong et al., 2023). Organoids derived from pluripotent stem cells, adult stem cells or tumor cells can be reconstructed to recapitulate the critical characteristics of organs and tissues. Kim et al. (2020a) created bladder assembloids to mimic bladder tissue regeneration and cancer microenvironments. In this study, multi-layered bladder "assembloids" were constructed using stromal stem cells, and well-organized architecture was represented with stroma surrounded by muscle and epithelium layer. The assembloids exhibited the characteristics of cellular compositional and single-cell transcriptome gene expression level of human mature bladder, and recapitulated tissue dynamics *in vivo* in response to tissue damage.

Human urothelial organoid models are of great significance for the long-term tolerance of human cells to urine, especially for the interaction of pathogens in urinary tract infections. Therefore, Horsley et al. developed a novel human organoid from progenitor cells, which reconstituted the important structure and biomarkers of urinary tract epithelium (Horsley et al., 2018). After 3 weeks of transwell culture with urine, multilayer organoids with umbrella-like cell connections, asymmetric membranes, as well as glycosaminoglycan layers were reconstructed. *Enterococcus faecalis* infection showed invasive results similar to those of patient cells, including urinary tract epithelial exfoliation and intracellular colony formation. Therefore, with the help of this bionic organoid model, which is helpful for diseases diagnosis and treatment, it is possible to elucidate the invasive behavior of urinary tract pathogens. Further, more progress in 3D tissue culture will increase the fundamental research and development of human organoid models related to bladder physiology.

Ureteral stricture is a common and frequently-occurring disease in adults and children, requiring ureteral reconstruction. Takagi et al. fabricated a novel type of artificial ureter grafts by combining spheroids and 3D bioprinting techniques (Takagi et al., 2022). The spheroids were generated by co-culturing human dermal fibroblasts and HUVECs, and were later laminated using a 3D bioprinter. Then, after the laminated spheroids matured, a tubular structure was formed, which was then transplanted into the rats as an artificial ureter. At 12 weeks after surgery, the ureteral epithelium and muscle layer regenerated well. This means that the ureteral structure based on the cell-only stacked spheroids is conducive to the regeneration of short ureters and lays the foundation for complete ureterregeneration (Ryosaka et al., 2022).

The design and manufacture of organoids based on cell extrusion bioprinting can describe specific events during the invasion of urinary diseases, and can also improve the

reproducibility of kidney organoid (Lawlor et al., 2021; Vandana et al., 2023). During this process, an organized urothelium model can completely regenerate with mature urothelial layer *in vitro*. By controlling the quality of kidney-like organ production, kidney tissue sheets with uniform patterns and tubular segments can also be produced (Jiang et al., 2023). Organoids also enables us to carry out further complex research by successfully simulating the tissue architecture and cellular disposition of normal bladder *in vivo*. In addition, organ-on-a-chip platforms combining organoids and microfluidic systems will help to establish more complex experimental models of multiple organ systems, and conduct efficient and economical toxicity tests, drug discovery, and drug screening (Berlo et al., 2021; Homan, 2023; Zhu et al., 2023).

5 Future prospects

Urinary system reconstruction is a medical mission with great challenges and far-reaching significance, because there are a large number of patients with complex tissue damage and dysfunction caused by congenital or acquired reasons in clinical need of repair. However, tissue engineering strategies involving functional biomaterials and biotechnology offer potential prospects for reconstructing damaged organs and tissues. Urologists urgently need to seek more technical and commercial product support from fields such as materials science, life sciences, biotechnology, and engineering. On the basis of vigorously promotig scientific and technological innovation in China, various tissue repair material products and biotechnology will increasingly benefit patients. One of the commercial products is a composite material composed of fibrinogen and poly(lactide-co-caprolactone) (PLCL) developed by Shanghai PINE&POWER Biotech Co., Ltd. This composite material was approved by the China Food and Drug Administration (CFDA) in August 2018 (Registration Certificate No. 20183130292), which is a tissue engineering electrospun scaffold similar to natural extracellular matrix. It has been successfully verified its good effect in bladder and ureter reconstruction and open, tension-free inguinal hernia repair (Li et al., 2019). Allium ureteral stent, developed by Allium Medical Solutions Ltd. (Allium®), is a self-expanding large caliber stent, made of a hyperelastic alloy covered by biocompatible polymer for preventing tissue ingrowth. The metal component provides radial and longitudinal strength, while the polymer bio-inertness prevents tissue from growing inward into the lumen and early encrustation (Gao CZ et al., 2021).

Significant efforts are still needed to achieve more successful commercial products for functional biomaterials and biotechnology. More attention should be paid to the biomimetic structure, appropriate mechanical properties, and biological functions of implants. What's more, in order to achieve satisfactory repair quality, it is also necessary to address the issues of *in situ* vascularization and integration between the implants and the host tissue. For these goals, it is required to continuously conduct high-quality clinical trials in accordance with laws and regulations. Although there is still a long way to go, people believe that the clinical transformation of functional biomaterials and biotechnology will ultimately overcome the risks and promote the structural and functional outcomes of the urinary bladder, urethra, and ureter.

6 Conclusion

In this review, we aim to summarize the latest advances of bioactive materials and biomimetic technologies in urinary tissue engineering. A series of biomaterials, including decellularized tissues, natural and synthetic biopolymers, as well as hybrid scaffolds, were discussed. Subsequently, the biological functions of biomaterials utilizing growth factors, drugs, inorganic nanomaterials, etc., were reviewed. In addition, the biomimetic approaches of 3D (bio)printing and organoids in urinary system structure and function regeneration were also discussed. This review will present new ideas and insights for the innovative development of bioactive materials and biomimetic technologies in the field of urological tissue engineering.

Author contributions

LD: Data curation, Investigation, Writing–original draft. ZW: Conceptualization, Funding acquisition, Writing–original draft, Writing–review and editing. SF: Methodology, Validation, Writing–review and editing. CW: Data curation, Validation, Writing–review and editing. YZ: Conceptualization, Validation, Writing–review and editing.

Funding

The author(s) declare financial support was received for the research, authorship, and/or publication of this article. This work was financially supported by Jilin Scientific and Technological Development Program (20210402025GH).

Conflict of interest

The authors declare that the research was conducted in the absence of any commercial or financial relationships that could be construed as a potential conflict of interest.

The author(s) declared that they were an editorial board member of Frontiers, at the time of submission. This had no impact on the peer review process and the final decision.

Publisher's note

All claims expressed in this article are solely those of the authors and do not necessarily represent those of their affiliated organizations, or those of the publisher, the editors and the reviewers. Any product that may be evaluated in this article, or claim that may be made by its manufacturer, is not guaranteed or endorsed by the publisher.

References

Abdelhakim, M., Lin, X. X., and Ogawa, R. (2020). The Japanese experience with basic fibroblast growth factor in cutaneous wound management and scar prevention: a systematic review of clinical and biological aspects. *Dermatology Ther.* 10, 569–587. doi:10.1007/s13555-020-00407-6

Adamowicz, J., Kuffel, B., Breda, S. V. V., Pokrwczynska, M., and Drewa, T. (2019). Reconstructive urology and tissue engineering: converging developmental paths. *J. Tissue Eng. Regen. Med.* 13, 522–533. doi:10.1002/term.2812

Ajalloueian, F., Lemon, G., Hilborn, J., Chronakis, I. S., and Fossum, M. (2018). Bladder biomechanics and the use of scaffolds for regenerative medicine in the urinary bladder. *Nat. Rev. Urol.* 15, 155–174. doi:10.1038/nrurol.2018.5

Allard, D. E., Wang, Y., Li, J. J., Conley, B., Xu, E. W., Sailer, D., et al. (2018). Schwann cell-derived periostin promotes autoimmune peripheral polyneuropathy via macrophage recruitment. *J. Clin. Investigation* 128, 4727–4741. doi:10.1172/jci99308

Alvarez-Mendez, S. J., Ramos-Suarez, J. L., Ritter, A., Mata Gonzalez, J., and Camacho Perez, A. (2023). Anaerobic digestion of commercial PLA and PBAT biodegradable plastic bags: potential biogas production and (1)H NMR and ATR-FTIR assessed biodegradation. *Heliyon* 9, e16691. doi:10.1016/j.heliyon.2023.e16691

Amer, M. H., Rose, F. R. A. J., Shakesheff, K. M., Modo, M., and White, L. J. (2017). Translational considerations in injectable cell-based therapeutics for neurological applications: concepts, progress and challenges. *Npj Regen. Med.* 2, 23. doi:10.1038/s41536-017-0028-x

Anand, P., Kunnumakkara, A. B., Newman, R. A., and Aggarwal, B. B. (2007). Bioavailability of curcumin: problems and promises. *Mol. Pharm.* 4, 807–818. doi:10.1021/mp700113r

Andia, I., Perez-Valle, A., Amo, C. D., and Maffulli, N. (2020). Freeze-drying of platelet-rich plasma: the quest for standardization. *Int. J. Mol. Sci.* 21, 6904. doi:10.3390/ijms21186904

Andrades, J. A., Wu, L. T., Hall, F. L., Nimni, M. E., and Becerra, J. (2001). Engineering, expression, and renaturation of a collagen-targeted human bFGF fusion protein. *Growth factors.* 18, 261–275. doi:10.3109/08977190109029115

Ardeshirylajimi, A., Ghaderian, S. M.-H., Omrani, M. D., and Moradi, S. L. (2018). Biomimetic scaffold containing PVDF nanofibers with sustained TGF-β release in combination with AT-MSCs for bladder tissue engineeringffold containing PVDF nanofibers with sustained TGF-β release in combination with AT-MSCs for bladder tissue engineering. *Gene* 676, 195–201. doi:10.1016/j.gene.2018.07.046

Aruffo, A., Stamenkovic, I., Melnick, M., Underhill, C. B., and Seed, B. (1990). CD44 is the principal cell surface receptor for hyaluronate. *Cell* 61, 1303–1313. doi:10.1016/0092-8674(90)90694-a

Ashley, R. A., Roth, C. C., Palmer, B. W., Kibar, Y., Routh, J. C., Fung, K.-M., et al. (2010). Regional variations in small intestinal submucosa evoke differences in inflammation with subsequent impact on tissue regeneration in the rat bladder augmentation model. *BJU Int.* 105, 1462–1468. doi:10.1111/j.1464-410x.2009.08965.x

Balalaie, A., Rezvani, M. B., and Basir, M. M. (2018). Dual function of proanthocyanidins as both mmp inhibitor and crosslinker in dentin biomodification: a literature review. *Dent. Mater. J.* 37, 173–182. doi:10.4012/dmj.2017-062

Bengmark, S. (2006). Curcumin, an atoxic antioxidant and natural NFκB, cyclooxygenase-2, lipooxygenase, and inducible nitric oxide synthase inhibitor: a shield against acute and chronic diseases. *J. Parenter. Enter. Nutr.* 30, 45–51. doi:10.1177/014860710603000145

Berlo, D. V., Nguyen, V. V. T., Gkouzioti, V., Leineweber, K., Verhaar, M. C., and Balkom, B. W. M. V. (2021). Stem cells, organoids, and organ-on-a-chip models for personalized *in vitro* drug testing. *Curr. Opin. Toxicol.* 28, 7–14. doi:10.1016/j.cotox.2021.08.006

Bhattacharjee, P., Kundu, B., Naskar, D., Kim, H.-W., Maiti, T. K., Bhattacharya, D., et al. (2017). Silk scaffolds in bone tissue engineering: an overview. *Acta Biomater.* 63, 1–17. doi:10.1016/j.actbio.2017.09.027

Billiar, K., Murray, J., Laude, D., Abraham, G., and Bachrach, N. (2001). Effects of carbodiimide crosslinking conditions on the physical properties of laminated intestinal submucosa. *J. Biomed. Mater. Res.* 56, 101–108. doi:10.1002/1097-4636(200107)56:1<101:aid-jbm1074>3.0.co;2-6

Bury, M. I., Fuller, N. J., Meisner, J. W., Hofer, M. D., Webber, M. J., Chow, L. W., et al. (2014). The promotion of functional urinary bladder regeneration using anti-inflammatory nanofibers. *Biomaterials* 35, 9311–9321. doi:10.1016/j.biomaterials.2014.07.057

Cai, J., Xie, X., Li, D., Wang, L., Jiang, J., Mo, X., et al. (2020). A novel knitted scaffold made of microfiber/nanofiber core-sheath yarns for tendon tissue engineering. *Biomaterials Sci.* 8, 4413–4425. doi:10.1039/d0bm00816h

Cao, G., Huang, Y., Li, K., Fan, Y., Xie, H., and Li, X. (2019). Small intestinal submucosa: superiority, limitations and solutions, and its potential to address bottlenecks in tissue repair. *J. Mater. Chem. B* 7, 5038–5055. doi:10.1039/c9tb00530g

Castro, P. R., Barbosa, A. S., Pereira, J. M., Ranfley, H., Felipetto, M., Goncalves, C. a. X., et al. (2018). Cellular and molecular heterogeneity associated with vessel formation processes. *Biomed Res. Int.* 2018, 1–32. doi:10.1155/2018/6740408

Chae, S., Kim, J., Yi, H.-G., and Cho, D.-W. (2022). 3D bioprinting of an *in vitro* model of a biomimetic urinary bladder with a contract-release system. *Micromachines* 13, 277. doi:10.3390/mi13020277

Chan, Y. Y., Bury, M. I., Fuller, N. J., Nolan, B. G., Gerbie, E. Y., Hofer, M. D., et al. (2021). Effects of anti-inflammatory nanofibers on urethral healing. *Macromol. Biosci.* 21, 2170011. doi:10.1002/mabi.202170011

Chan, Y. Y., Bury, M. I., Yura, E. M., Hofer, M. D., Cheng, E. Y., and Sharma, A. K. (2020). The current state of tissue engineering in the management of hypospadias. *Nat. Rev. Urol.* 17, 162–175. doi:10.1038/s41585-020-0281-4

Chen, B., Chen, X., Wang, W., Shen, J., Song, Z., Ji, H., et al. (2021). Tissue-engineered autologous peritoneal grafts for bladder reconstruction in a porcine model. *J. Tissue Eng.* 12, 204173142098679. doi:10.1177/2041731420986796

Chen, J., Liao, L. J., Lana, T. T., Zhang, Z. J., Gai, K., Huang, Y. B., et al. (2020). Treated dentin matrix-based scaffolds carrying TGF-beta 1/BMP4 for functional bio-root regeneration. *Appl. Mater. Today* 20, 100742. doi:10.1016/j.apmt.2020.100742

Chen, W., Shi, C., Yi, S., Chen, B., Zhang, W., Fang, Z., et al. (2010). Bladder regeneration by collagen scaffolds with collagen binding human basic fibroblast growth factor. *J. Urology* 183, 2432–2439. doi:10.1016/j.juro.2010.02.042

Cheng, F., Cao, X., Li, H., Liu, T., Xie, X., Huang, D., et al. (2019). Generation of cost-effective paper-based tissue models through matrix-assisted sacrificial 3D printing. *Nano Lett.* 19, 3603–3611. doi:10.1021/acs.nanolett.9b00583

Chew, B. H., and Denstedt, J. D. (2004). Technology insight: novel ureteral stent materials and designs. *Nat. Clin. Pract. Urol.* 1, 44–48. doi:10.1038/ncpuro0014

Chowdhury, S. R., Keshavan, N., and Basu, B. (2021). Urinary bladder and urethral tissue engineering, and 3D bioprinting approaches for urological reconstruction. *J. Mater. Res.* 36, 3781–3820. doi:10.1557/s43578-021-00255-w

Chueh, K.-S., Huang, K.-H., Lu, J.-H., Juan, T.-J., Chuang, S.-M., Lin, R.-J., et al. (2022). Therapeutic effect of platelet-rich plasma improves bladder overactivity in the pathogenesis of ketamine-induced ulcerative cystitis in a rat model. *Int. J. Mol. Sci.* 23, 5771. doi:10.3390/ijms23105771

Chung, E., and Wang, J. (2017). A state-of-art review of low intensity extracorporeal shock wave therapy and lithotripter machines for the treatment of erectile dysfunction. *Expert Rev. Med. Devices* 14, 929–934. doi:10.1080/17434440.2017.1403897

Cohen, A. J., Packiam, V. T., Nottingham, C. U., Pariser, J. J., Faris, S. F., and Bales, G. T. (2016). Iatrogenic bladder injury: national analysis of 30-day outcomes. *Urology* 97, 250–256. doi:10.1016/j.urology.2016.05.002

Cosentino, M., Gaya, J. M., Breda, A., Palou, J., and Villavicencio, H. (2012). Alloplastic bladder substitution: are we making progress? *Int. Urology Nephrol.* 44, 1295–1303. doi:10.1007/s11255-012-0249-2

Damrongsakkul, S., Sinweeruthai, R., and Higgins, J. S. (2003). Processability and chemical resistance of the polymer blend of thermoplastic polyurethane and polydimethylsiloxane. *Macromol. Symp.* 198, 411–420. doi:10.1002/masy.200350835

Desouza, S. J., and Brentani, R. (1992). Collagen binding-site in collagenase can Be determined using the concept of sense-antisense peptide interactions. *J. Biol. Chem.* 267, 13763–13767. doi:10.1016/s0021-9258(18)42279-x

Di Luca, A., Ostrowska, B., Lorenzo-Moldero, I., Lepedda, A., Swieszkowski, W., Van Blitterswijk, C., et al. (2016). Gradients in pore size enhance the osteogenic differentiation of human mesenchymal stromal cells in three-dimensional scaffolds. *Sci. Rep.* 6, 22898. doi:10.1038/srep22898

Ding, X., Yin, B., Qian, L., Zeng, Z., Yang, Z., Li, H., et al. (2011). Screening for novel quorum-sensing inhibitors to interfere with the formation of *Pseudomonas aeruginosa* biofilm. *J. Med. Microbiol.* 60, 1827–1834. doi:10.1099/jmm.0.024166-0

Dong, Y. T., Wang, S. C., Ke, Y. J., Ding, L. C., Zeng, X. T., Magdassi, S., et al. (2020). 4D printed hydrogels: fabrication, materials, and applications. *Adv. Mater. Technol.* 5, 2000034. doi:10.1002/admt.202000034

Drewa, T., Adamowicz, J., and Sharma, A. (2012). Tissue engineering for the oncologic urinary bladder. *Nat. Rev. Urol.* 9, 561–572. doi:10.1038/nrurol.2012.158

Drupitha, M. P., Nando, K. N. G. B., and Nando, G. B. (2017). Compatibilized TPU-PDMS blends: pros and cons of melt mixing and solution mixing techniques. *J. Appl. Polym. Sci.* 134, 45164. doi:10.1002/app.45164

Eltahan, E. A. E., Sultan, M., and Mito, A.-B. (2016). Determination of loop length, tightness factor and porosity of single Jersey knitted fabric. *Alexandria Eng. J.* 55, 851–856. doi:10.1016/j.aej.2016.02.006

Eriksson, A. E., Cousens, L. S., Weaver, L. H., and Matthews, B. W. (1991). Three-dimensional structure of human basic fibroblast growth factor. *Proc. Natl. Acad. Sci. U. S. A.* 88, 3441–3445. doi:10.1073/pnas.88.8.3441

Fadadu, P. P., Mazzola, A. J., Hunter, C. W., and Davis, T. T. (2019). Review of concentration yields in commercially available platelet-rich plasma (PRP) systems: a call for PRP standardization. *Regional Anesth. Pain Med.* 44, 652–659. doi:10.1136/rapm-2018-100356

Fehrenbach, H., Kasper, M., Koslowski, R., Pan, T., Schuh, D., Müller, M., et al. (2000). Alveolar epithelial type II cell apoptosis *in vivo* during resolution of keratinocyte

growth factor-induced hyperplasia in the rat. *Histochem. Cell Biol.* 114, 49–61. doi:10.1007/s004180000157

Freeman, M. R., Yoo, J. J., Raab, G., Soker, S., Adam, R. M., Schneck, F. X., et al. (1997). Heparin-binding EGF-like growth factor is an autocrine growth factor for human urothelial cells and is synthesized by epithelial and smooth muscle cells in the human bladder. *J. Clin. Investigation* 99, 1028–1036. doi:10.1172/jci119230

Fu, Z. Y., Xiao, S. W., Wang, P. C., Zhao, J., Ling, Z. Y., An, Z. Y., et al. (2023). Injectable, stretchable, toughened, bioadhesive composite hydrogel for bladder injury repair. *Rsc Adv.* 13, 10903–10913. doi:10.1039/d3ra00402c

Furukoshi, M., Tatsumi, E., and Nakayama, Y. (2019). Application of in-body tissue architecture–induced Biotube vascular grafts for vascular access: proof of concept in a beagle dog model. *J. Vasc. Access* 21, 314–321. doi:10.1177/1129729819874318

Gao, C. Z., Wang, Z. L., Jiao, Z. X., Wu, Z. X., Guo, M., Wang, Y., et al. (2021). Enhancing antibacterial capability and osseointegration of polyetheretherketone (PEEK) implants by dual-functional surface modification. *Mater. Des.* 205, 109733. doi:10.1016/j.matdes.2021.109733

Gao, W., Xing, T., and Ou, T. (2021). The Resonance and the Allium ureteral stents in the treatment of non-malignant refractory ureterostenosis. *BMC Urol.* 21, 53. doi:10.1186/s12894-021-00815-6

Gilbert, T. W., Stolz, D. B., Biancaniello, F., Simmons-Byrd, A., and Badylak, S. F. (2005). Production and characterization of ECM powder: implications for tissue engineering applications. *Biomaterials* 26, 1431–1435. doi:10.1016/j.biomaterials.2004.04.042

Haeublein, G., Lombardi, G., Caro, F., Guerrieri, D., Remolins, C., Incardona, C., et al. (2022). Human endothelial cell seeding in partially decellularized kidneys. *BioMed Res. Int.* 2022, 1–8. doi:10.1155/2022/9018074

Han, B., Jaurequi, J., Tang, B. W., and Nimni, M. E. (2003). Proanthocyanidin: a natural crosslinking reagent for stabilizing collagen matrices. *J. Biomed. Mater. Res. Part A* 65A, 118–124. doi:10.1002/jbm.a.10460

Hanczar, M., Moazen, M., and Day, R. (2021). The significance of biomechanics and scaffold structure for bladder tissue engineering. *Int. J. Mol. Sci.* 22, 12657. doi:10.3390/ijms222312657

Hartgerink, J. D., Beniash, E., and Stupp, S. I. (2001). Self-assembly and mineralization of peptide-amphiphile nanofibers. *Science* 294, 1684–1688. doi:10.1126/science.1063187

He, B., Zhang, M. Z., Yin, L. F., Quan, Z. X., Ou, Y. S., and Huang, W. (2022). bFGF-incorporated composite biomaterial for bone regeneration. *Mater. Des.* 215, 110469. doi:10.1016/j.matdes.2022.110469

Herbert, S. P., and Stainier, D. Y. R. (2011). Molecular control of endothelial cell behaviour during blood vessel morphogenesis. *Nat. Rev. Mol. Cell Biol.* 12, 551–564. doi:10.1038/nrm3176

Homan, K. A. (2023). Industry adoption of organoids and organs-on-chip technology: toward a paradox of choice. *Adv. Biol.* 7, e2200334. doi:10.1002/adbi.202200334

Horii, T., Jonin, K., Kageyama, S., Yoshida, T., Kobayashi, K., Minato, H., et al. (2022). Regeneration of functional bladder using cell-seeded amnion and P(LA/CL) scaffolds. *Tissue Eng. Part A* 28, 968–976. doi:10.1089/ten.tea.2022.0078

Horsley, H., Dharmasena, D., Malone-Lee, J., and Rohn, J. L. (2018). A urine-dependent human urothelial organoid offers a potential alternative to rodent models of infection. *Scentific Rep.* 8, 1238. doi:10.1038/s41598-018-19690-7

Huen, K. H., Macaraeg, A., Davis-Dao, C. A., Williamson, S. H., Boswell, T. C., Chuang, K.-W., et al. (2022). Single-layer acellular porcine bladder matrix as graft in corporoplasty for ventral curvature in pediatric proximal hypospadias repair: an initial experience. *Urology* 169, 196–201. doi:10.1016/j.urology.2022.07.025

Hughes, O. B., Rakosi, A., Macquhae, F., Herskovitz, I., Fox, J. D., and Kirsner, R. S. (2016). A review of cellular and acellular matrix products: indications, techniques, and outcomes. *Plastic Reconstr. Surg.* 138, 138s–147s. doi:10.1097/prs.0000000000002643

Iimori, Y., Iwai, R., Nagatani, K., Inoue, Y., Funayama-Iwai, M., Okamoto, M., et al. (2020). Urinary bladder reconstruction using autologous collagenous connective tissue membrane "Biosheet®" induced by in-body tissue architecture: a pilot study. *Regen. Ther.* 15, 274–280. doi:10.1016/j.reth.2020.10.006

Imam, S. S., Hussain, A., Altamimi, M. A., and Alshehri, S. (2021). Four-dimensional printing for hydrogel: theoretical concept, 4D materials, shape-morphing way, and future perspectives. *Polymers* 13, 3858. doi:10.3390/polym13213858

Jeong, E., Choi, S., and Cho, S. W. (2023). Recent advances in brain organoid technology for human brain research. *ACS Appl. Mater Interfaces* 15, 200–219. doi:10.1021/acsami.2c17467

Jiang, C., Wang, D., Ni, C., Li, X., Liu, X., Ge, X., et al. (2023). Generation of cynomolgus monkey airway, liver ductal, and kidney organoids with pharmacokinetic functions. *Organs-on-a-Chip* 5, 100031. doi:10.1016/j.ooc.2023.100031

Jiang, S.-W., Xu, Z.-H., Zhao, Y.-Y., Yan, L., Zhou, Z.-L., and Gu, G.-L. (2018). Autologous granulation tissue tubes for replacement of urethral defects: an experimental study in male rabbits. *J. Pediatr. Urology* 14, 14.e1–14.e7. doi:10.1016/j.jpurol.2017.07.019

Jiang, Y.-H., Jhang, J.-F., Hsu, Y.-H., Ho, H.-C., Lin, T.-Y., Birder, L. A., et al. (2021). Urothelial health after platelet-rich plasma injection in intractable recurrent urinary tract infection: improved cell proliferation, cytoskeleton, and barrier function protein expression. *Low. Urin. Tract. Symptoms* 13, 271–278. doi:10.1111/luts.12364

Jin, C. R., Cao, N. L., Ni, J. S., Zhao, W. X., Gu, B. J., and Zhu, W. D. (2020). A lipid-nanosphere-small MyoD activating RNA-bladder acellular matrix graft scaffold [NP(saMyoD)/BAMG] facilitates rat injured bladder muscle repair and regeneration [NP(saMyoD)/BAMG]. *Front. Pharmacol.* 11, 795. doi:10.3389/fphar.2020.00795

Kanematsu, A., Yamamoto, S., Noguchi, T., Ozeki, M., Tabata, Y., and Ogawa, O. (2003). Bladder regeneration by bladder acellular matrix combined with sustained release of exogenous growth factor. *J. Urology* 170, 1633–1638. doi:10.1097/01.ju.0000084021.51099.8a

Khademolqorani, S., Tavanai, H., and Ajalloueian, F. (2021). Mechanical properties of silk plain-weft knitted scaffolds for bladder tissue engineering applications. *Polym. Adv. Technol.* 32, 2367–2377. doi:10.1002/pat.5265

Khodamoradi, K., Dullea, A., Golan, R., Molina, M., Arora, H., Masterson, T. A., et al. (2022). Platelet rich plasma (PRP) growth factor concentration varies in men with erectile dysfunction. *J. Sex. Med.* 19, 1488–1493. doi:10.1016/j.jsxm.2022.06.003

Kim, E., Choi, S., Kang, B., Kong, J., Kim, Y., Yoon, W. H., et al. (2020a). Creation of bladder assembloids mimicking tissue regeneration and cancer. *Nature* 588, 664–669. doi:10.1038/s41586-020-3034-x

Kim, H. Y., Chun, S. Y., Lee, E. H., Kim, B., Ha, Y. S., Chung, J. W., et al. (2020b). Bladder regeneration using a polycaprolactone scaffold with a gradient structure and growth factors in a partially cystectomized rat model. *J. Korean Med. Sci.* 35, e374. doi:10.3346/jkms.2020.35.e374

Kim, J. H., Yang, H. J., Choi, S. S., Kim, S. U., Lee, H. J., and Song, Y. S. (2021). Improved bladder contractility after transplantation of human mesenchymal stem cells overexpressing hepatocyte growth factor into underactive bladder from bladder outlet obstruction models of rats. *PLoS ONE* 16, e0261402. doi:10.1371/journal.pone.0261402

Kormann, R., Kavvadas, P., Placier, S., Vandermeersch, S., Dorison, A., Dussaule, J.-C., et al. (2020). Periostin promotes cell proliferation and macrophage polarization to drive repair after AKI. *J. Am. Soc. Nephrol.* 31, 85–100. doi:10.1681/asn.2019020113

Kullmann, F. A., Clayton, D. R., Ruiz, W. G., Wolf-Johnston, A., Gauthier, C., Kanai, A., et al. (2017). Urothelial proliferation and regeneration after spinal cord injury. *Am. J. Physiology-Renal Physiology* 313, F85–F102. doi:10.1152/ajprenal.00592.2016

Lawkowska, K., Rosenbaum, C., Petrasz, P., Kluth, L., Koper, K., Drewa, T., et al. (2022). Tissue engineering in reconstructive urology-The current status and critical insights to set future directions-critical review. *Front. Bioeng. Biotechnol.* 10, 1040987. doi:10.3389/fbioe.2022.1040987

Lawlor, K. T., Vanslambrouck, J. M., Higgins, J. W., Chambon, A., Bishard, K., Arndt, D., et al. (2021). Cellular extrusion bioprinting improves kidney organoid reproducibility and conformation. *Nat. Mater.* 20, 260–271. doi:10.1038/s41563-020-00853-9

Lee, J. S., Katz, M., and Shah, O. J. (2021). Developments in ureteral stent technology. *Front. Surg.* 8, 764167. doi:10.3389/fsurg.2021.764167

Li, G., and Sun, S. (2022). Silk fibroin-based biomaterials for tissue engineering applications. *Molecules* 27, 2757. doi:10.3390/molecules27092757

Li, Q., Tao, L., Chen, B., Ren, H., Hou, X., Zhou, S., et al. (2012). Extrahepatic bile duct regeneration in pigs using collagen scaffolds loaded with human collagen-binding bFGF. *Biomaterials* 33, 4298–4308. doi:10.1016/j.biomaterials.2012.03.003

Li, S., Xiao, H., Yang, L., Hua, L., Qiu, Z., Hu, X., et al. (2019). Electrospun P(LLA-CL) nanoscale fibrinogen patch vs porcine small intestine submucosa graft repair of inguinal hernia in adults: a randomized, single-Blind,Controlled,Multicenter,NoninferiorityTrial. *J. Am. Coll. Surg.* 229, 541–551e1. doi:10.1016/j.jamcollsurg.2019.08.1446

Li, X. A., Sun, H., Lin, N., Hou, X., Wang, J., Zhou, B., et al. (2011). Regeneration of uterine horns in rats by collagen scaffolds loaded with collagen-binding human basic fibroblast growth factor. *Biomaterials* 32, 8172–8181. doi:10.1016/j.biomaterials.2011.07.050

Liao, Y., Li, G., Zhang, X., Huang, W., Xie, D., Dai, G., et al. (2020). Cardiac Nestin(+) mesenchymal stromal cells enhance healing of ischemic heart through periostin-mediated M2 macrophage polarization. *Mol. Ther.* 28, 855–873. doi:10.1016/j.ymthe.2020.01.011

Lin, K.-L., Lu, J.-H., Chueh, K.-S., Juan, T.-J., Wu, B.-N., Chuang, S.-M., et al. (2021). Low-intensity extracorporeal shock wave therapy promotes bladder regeneration and improves overactive bladder induced by ovarian hormone deficiency from rat animal model to human clinical trial. *Int. J. Mol. Sci.* 22, 9296. doi:10.3390/ijms22179296

Lin, M., Hu, Y., An, H., Guo, T., Gao, Y., Peng, K., et al. (2023). Silk fibroin-based biomaterials for disc tissue engineering. *Biomater. Sci.* 11, 749–776. doi:10.1039/d2bm01343f

Liu, C., Feng, S., Ma, L., Sun, M., Wei, Z., Wang, J., et al. (2021). An amphiphilic carbonaceous/nanosilver composite-incorporated urinary catheter for long-term combating bacteria and biofilms. *ACS Appl. Mater. interfaces* 13, 38029–38039. doi:10.1021/acsami.1c07399

Liu, G., Fu, M., Li, F., Fu, W., Zhao, Z., Xia, H., et al. (2020a). Tissue-engineered PLLA/gelatine nanofibrous scaffold promoting the phenotypic expression of epithelial

and smooth muscle cells for urethral reconstruction. *Mater. Sci. Eng. C* 111, 110810. doi:10.1016/j.msec.2020.110810

Liu, Y., Dusevich, V., and Wang, Y. (2013). Proanthocyanidins rapidly stabilize the demineralized dentin layer. *J. Dent. Res.* 92, 746–752. doi:10.1177/0022034513492769

Liu, Y., Huang, L., Yuan, W., Zhang, D. L., Gu, Y. B., Huang, J. W., et al. (2020b). Sustained release of stromal cell-derived factor-1 alpha from silk fibroin microfiber promotes urethral reconstruction in rabbits. *J. Biomed. Mater. Res. Part A* 108, 1760–1773. doi:10.1002/jbm.a.36943

Lv, X., Feng, C., Liu, Y., Peng, X., Chen, S., Xiao, D., et al. (2018). A smart bilayered scaffold supporting keratinocytes and muscle cells in micro/nano-scale for urethral reconstruction. *Theranostics* 8, 3153–3163. doi:10.7150/thno.22080

Ma, F., Xiao, Z., Chen, B., Hou, X., Dai, J., and Xu, R. (2014). Linear ordered collagen scaffolds loaded with collagen-binding basic fibroblast growth factor facilitate recovery of sciatic nerve injury in rats. *Tissue Eng. Part A* 20, 1253–1262. doi:10.1089/ten.tea.2013.0158

Makoto Komura, A., Yonekawa, H., Ikebukuro, K., Komuro, H., Hoshi, K., Takato, T., et al. (2019). Fabrication of an anatomy-mimicking BIO-AIR-TUBE with engineered cartilage. *Regen. Ther.* 11, 176–181. doi:10.1016/j.reth.2019.07.004

Marques, L. F., Stessuk, T., Camargo, I. C. C., Junior, N. S., Santos, L. D., and Ribeiro-Paes, J. T. (2015). Platelet-rich plasma (PRP): methodological aspects and clinical applications. *Platelets* 26, 101–113. doi:10.3109/09537104.2014.881991

Meng, C., Jiang, W., Huang, Z., Liu, T., and Feng, J. (2020). Fabrication of a highly conductive silk knitted composite scaffold by two-step electrostatic self-assembly for potential peripheral nerve regeneration. *ACS Appl. Mater. interfaces* 12, 12317–12327. doi:10.1021/acsami.9b22088

Mirzaei, A., Saburi, E., Islami, M., Ardeshirylajimi, A., Omrani, M. D., Taheri, M., et al. (2019a). Bladder smooth muscle cell differentiation of the human induced pluripotent stem cells on electrospun Poly(lactide-co-glycolide) nanofibrous structureifferentiation of the human induced pluripotent stem cells on electrospun Poly(lactide-co-glycolide) nanofibrous structure. *Gene* 694, 26–32. doi:10.1016/j.gene.2019.01.037

Mirzaei, M., Daneshpajooh, A., Farsinezhad, A., Jafarian, Z., Ebadzadeh, M. R., Saberi, N., et al. (2019b). The therapeutic effect of intravesical instillation of platelet rich plasma on recurrent bacterial cystitis in women: a randomized clinical trial. *Randomized Control. Trial* 16, 609–613. doi:10.22037/uj.v0i0.5239

Mokhames, Z., Rezaie, Z., Ardeshirylajimi, A., Basiri, A., Taheri, M., and Omrani, M. D. (2020). Efficient smooth muscle cell differentiation of iPS cells on curcumin-incorporated chitosan/collagen/polyvinyl-alcohol nanofibers. *Vitro Cell. Dev. Biol. - Animal* 56, 313–321. doi:10.1007/s11626-020-00445-6

Mokhames, Z., Rezaie, Z., Ardeshirylajimi, A., Basiri, A., Taheri, M., and Omrani, M. D. (2021). VEGF-incorporated PVDF/collagen nanofibrous scaffold for bladder wall regeneration and angiogenesis. *Int. J. Polym. Mater. Polym. Biomaterials* 70, 521–529. doi:10.1080/00914037.2020.1740985

Moreno-Manzano, V., Mellado-Lo´Pez, M., Morera-Esteve, M. J., Alastrue-Agudo, A., Bisbal-Velasco, V., Forteza-Vila, J. N., et al. (2020). Human adipose-derived mesenchymal stem cells accelerate decellularized neobladder regeneration. *Regen. Biomater.* 7, 161–169. doi:10.1093/rb/rbz049

Nakamichi, M., Akishima-Fukasawa, Y., Fujisawa, C., Mikami, T., Onishi, K., and Akasaka, Y. (2016). Basic fibroblast growth factor induces angiogenic properties of fibrocytes to stimulate vascular formation during wound healing. *Am. J. Pathology* 186, 3203–3216. doi:10.1016/j.ajpath.2016.08.015

Narla, S. T., Bushnell, D. S., Schaefer, C. M., Nouraie, M., and Bates, C. M. (2020). Keratinocyte growth factor reduces injury and leads to early recovery from cyclophosphamide bladder injury. *Am. J. Pathology* 190, 108–124. doi:10.1016/j.ajpath.2019.09.015

Nguyen, T. P., Nguyen, Q. V., Nguyen, V.-H., Le, T.-H., Huynh, V. Q. N., Vo, D.-V. N., et al. (2019). Silk fibroin-based biomaterials for biomedical applications: a review. *Polymers* 11, 1933. doi:10.3390/polym11121933

Nikoloudaki, G., Snider, P., Simmons, O., Conway, S. J., and Hamilton, D. W. (2020). Periostin and matrix stiffness combine to regulate myofibroblast differentiation and fibronectin synthesis during palatal healing. *Matrix Biol.* 94, 31–56. doi:10.1016/j.matbio.2020.07.002

Nillesen, S. T. M., Geutjes, P. J., Wismans, R., Schalkwijk, J., Daamen, W. F., and Van Kuppevelt, T. H. (2007). Increased angiogenesis and blood vessel maturation in acellular collagen-heparin scaffolds containing both FGF2 and VEGF. *Biomaterials* 28, 1123–1131. doi:10.1016/j.biomaterials.2006.10.029

Nishi, N., Matsushita, O., Yuube, K., Miyanaka, H., Okabe, A., and Wada, F. (1998). Collagen-binding growth factors: production and characterization of functional fusion proteins having a collagen-binding domain. *Proc. Natl. Acad. Sci. U. S. A.* 95, 7018–7023. doi:10.1073/pnas.95.12.7018

Niu, Y., Galluzzi, M., Deng, F., Zhao|, Z., Fu, M., Su, L., et al. (2022). A biomimetic hyaluronic acid-silk fibroin nanofiber scaffold promoting regeneration of transected urothelium. *Bioeng. Transl. Med.* 7, e10268. doi:10.1002/btm2.10268

Niu, Y. Q., Chen, K. V. C., He, T., Yu, W. Y., Huang, S. W., and Xu, K. T. (2014). Scaffolds from block polyurethanes based on poly(ε-caprolactone) (PCL) and poly(ethylene glycol) (PEG) for peripheral nerve regeneration. *Biomaterials* 35, 4266–4277. doi:10.1016/j.biomaterials.2014.02.013

Niu, Y. Q., He, T., Song, J., Chen, S. P., Liu, X. Y., Chen, Z. G., et al. (2017). A new AIE multi-block polyurethane copolymer material for subcellular microfilament imaging in living cells. *Chem. Commun.* 53, 7541–7544. doi:10.1039/c7cc02555f

Niu, Y. Q., Liu, G. C., Chen, C. B., Fu, M., Fu, W., Zhao, Z., et al. (2020). Urethral reconstruction using an amphiphilic tissue-engineered autologous polyurethane nanofiber scaffold with rapid vascularization function. *Biomaterials Sci.* 8, 2164–2174. doi:10.1039/c9bm01911a

Niu, Y., Stadler, F. J., Yang, X., Deng, F., Liu, G., and Xia, H. (2021). HA-coated collagen nanofibers for urethral regeneration via *in situ* polarization of M2 macrophages. *J. Nanobiotechnology* 19, 283. doi:10.1186/s12951-021-01000-5

Orabi, H., Aboushwareb, T., Zhang, Y., Yoo, J. J., and Atala, A. (2013). Cell-seeded tubularized scaffolds for reconstruction of long urethral defects: a preclinical study. *Eur. Urol.* 63, 531–538. doi:10.1016/j.eururo.2012.07.041

Ornitz, D. M., and Itoh, N. (2015). The fibroblast growth factor signaling pathway. *Wiley Interdiscip. Rev. Dev. Biol.* 4, 215–266. doi:10.1002/wdev.176

Pal, K. M. I. (1998). Urinary bladder wall repair: what suture to use? *Br. J. Urology* 82, 196–198. doi:10.1046/j.1464-410x.1998.00722.x

Peng, X., Yue, P., Zhou, X., Li, L., Li, S., and Yu, X. (2019). Development and characterization of bladder acellular matrix cross-linked by dialdehyde carboxymethyl cellulose for bladder tissue engineering. *RSC Adv.* 9, 42000–42009. doi:10.1039/c9ra07965c

Pokrywczynska, M., Jundzill, A., Rasmus, M., Adamowicz, J., Balcerczyk, D., Buhl, M., et al. (2018). Understanding the role of mesenchymal stem cells in urinary bladder regenerationa preclinical study on a porcine model. *Stem Cell Res. Ther.* 9, 328. doi:10.1186/s13287-018-1070-3

Pokrywczynska, M., Rasmus, M., Jundzill, A., Balcerczyk, D., Adamowicz, J., Warda, K., et al. (2019). Mesenchymal stromal cells modulate the molecular pattern of healing process in tissue-engineered urinary bladder: the microarray data. *Stem Cell Res. Ther.* 10, 176. doi:10.1186/s13287-019-1266-1

Polte, J., Tuaev, X., Wuithschick, M., Fischer, A., Thuenemann, A. F., Rademann, K., et al. (2012). Formation mechanism of colloidal silver nanoparticles: analogies and differences to the growth of gold nanoparticles. *ACS Nano* 6, 5791–5802. doi:10.1021/nn301724z

Poulios, E., Mykoniatis, I., Pyrgidis, N., Zilotis, F., Kapoteli, P., Kotsiris, D., et al. (2021). Platelet-rich plasma (PRP) improves erectile function: a double-blind, randomized, placebo-controlled clinical trial. *J. Sex. Med.* 18, 926–935. doi:10.1016/j.jsxm.2021.03.008

Prateeksha, P., Bajpai, R., Rao, C. V., Upreti, D. K., Barik, S. K., and Singh, B. N. (2021). Chrysophanol-functionalized silver nanoparticles for anti-adhesive and anti-biofouling coatings to prevent urinary catheter-associated infections. *ACS Appl. Nano Mater.* 4, 1512–1528. doi:10.1021/acsanm.0c03029

Prateeksha, Y. M. A., Singh, B. N., Sudheer, S., Kharwar, R. N., Siddiqui, S., Abdel-Azeem, A. M., et al. (2019). Chrysophanol: a natural anthraquinone with multifaceted biotherapeutic potential. *Biomacromolecules* 9, 68. doi:10.3390/biom9020068

Rashidbenam, Z., Jasman, M. H., Hafez, P., Tan, G. H., Goh, E. H., Fam, X. I., et al. (2019). Overview of urethral reconstruction by tissue engineering: current strategies, clinical status and future direction. *Tissue Eng. Regen. Med.* 16, 365–384. doi:10.1007/s13770-019-00193-z

Ribeiro-Filho, L. A., and Sievert, K.-D. (2015). Acellular matrix in urethral reconstruction. *Adv. Drug Deliv. Rev.* 82-83, 38–46. doi:10.1016/j.addr.2014.11.019

Ryosaka, M., Mae, S.-I., and Osafune, K. (2022). Protocol for the generation and expansion of human iPS cell-derived ureteric bud organoids. *Star. Protoc.* 3, 101484. doi:10.1016/j.xpro.2022.101484

Sabetkish, S., Sabetkish, N., and Kajbafzadeh, A.-M. (2020). *In-vivo* regeneration of bladder muscular wall with whole decellularized bladder matrix: a novel hourglass technique for duplication of bladder volume in rabbit model. *J. Pediatr. Surg.* 55, 2226–2232. doi:10.1016/j.jpedsurg.2019.11.020

Sabetkish, S., Sabetkish, N., and Kajbafzadeh, A.-M. (2022). Regeneration of muscular wall of the bladder using a ureter matrix graft as a scaffold. *Biotech. Histochem.* 97, 207–214. doi:10.1080/10520295.2021.1931448

Sadri, F., Rezaei, Z., and Fereidouni, M. (2022). The significance of the SDF-1/CXCR4 signaling pathway in the normal development. *Mol. Biol. Rep.* 49, 3307–3320. doi:10.1007/s11033-021-07069-3

Salem, S. A., Rashidbenam, Z., Jasman, M. H., Ho, C. C. K., Sagap, I., Singh, R., et al. (2020). Incorporation of smooth muscle cells derived from human adipose stem cells on poly(lactic-co-glycolic acid) scaffold for the reconstruction of subtotally resected urinary bladder in athymic rats. *Tissue Eng. Regen. Med.* 17, 553–563. doi:10.1007/s13770-020-00271-7

Sánchez, A. L., García-Perdomo, H. A., and Robayo, J. A. (2022). Alternatives to oral mucosa grafts for urethral reconstruction. *Nat. Rev. Urol.* 20, 259–260. doi:10.1038/s41585-022-00707-w

Schmidt, E. C., and Baier, M. (2000). Acellular vascular tissues: natural biomaterials for tissue repair and tissue engineering. *Biomaterials* 21, 2215–2231. doi:10.1016/s0142-9612(00)00148-4

Shamout, S., Nazha, S., Dragomir, A., Baverstock, R., Corcos, J., and Campeau, L. (2023). A cost-effectiveness analysis of bladder management strategies in neurogenic lower urinary tract dysfunction after spinal cord injury: a publicly funded health care perspective. *Spinal Cord.* 61, 269–275. doi:10.1038/s41393-023-00883-5

Sharma, A. K., and Cheng, E. Y. (2015). Growth factor and small molecule influence on urological tissue regeneration utilizing cell seeded scaffolds. *Adv. Drug Deliv. Rev.* 82-82, 86–92. doi:10.1016/j.addr.2014.11.008

Sharma, S., and Basu, B. (2022). Biomaterials assisted reconstructive urology: the pursuit of an implantable bioengineered neo-urinary bladder. *Biomaterials* 281, 121331. doi:10.1016/j.biomaterials.2021.121331

Sharma, S., Mandhani, A., Bose, S., and Basu, B. (2021). Dynamically crosslinked polydimethylsiloxane-based polyurethanes with contact-killing antimicrobial properties as implantable alloplasts for urological reconstruction. *Acta Biomater.* 129, 122–137. doi:10.1016/j.actbio.2021.04.055

Sharma, S., Rajani, S., Hui, J. S., Chen, A. R., Bivalacqua, T., and Singh, A. (2022). Development of enzymatic-resistant and compliant decellularized extracellular matrixes via aliphatic chain modification for bladder tissue engineering. *ACS Appl. Mater. Interfaces* 14, 37301–37315. doi:10.1021/acsami.2c06865

Shi, C., Chen, W., Zhao, Y., Chen, B., Xiao, Z., Wei, Z., et al. (2011). Regeneration of full-thickness abdominal wall defects in rats using collagen scaffolds loaded with collagen-binding basic fibroblast growth factor. *Biomaterials* 32, 753–759. doi:10.1016/j.biomaterials.2010.09.038

Shi, C. Y., Chen, W., Chen, B., Shan, T., Jia, W. S., Hou, X. L., et al. (2017). Bladder regeneration in a canine model using a bladder acellular matrix loaded with a collagen-binding bFGF. *Biomaterials Sci.* 5, 2427–2436. doi:10.1039/c7bm00806f

Silva, G. A., Czeisler, C., Niece, K. L., Beniash, E., Harrington, D. A., Kessler, J. A., et al. (2004). Selective differentiation of neural progenitor cells by high-epitope density nanofibers. *Science* 303, 1352–1355. doi:10.1126/science.1093783

Singh, A., Bivalacqua, T. J., and Sopko, N. (2018). Urinary tissue engineering: challenges and opportunities. *Sex. Med. Rev.* 6, 35–44. doi:10.1016/j.sxmr.2017.08.004

Sohn, J., Kim, T.-I., Yoon, Y.-H., Kim, J.-Y., and Kim, S.-Y. (2003). Novel transglutaminase inhibitors reverse the inflammation of allergic conjunctivitis. *J. Clin. Investigation* 111, 121–128. doi:10.1172/jci200315937

Song, Y. T., Li, Y. Q., Tian, M. X., Hu, J. G., Zhang, X. R., Liu, P. C., et al. (2022). Application of antibody-conjugated small intestine submucosa to capture urine-derived stem cells for bladder repair in a rabbit model. *Bioact. Mater.* 14, 443–455. doi:10.1016/j.bioactmat.2021.11.017

Sulob, R. C., Keshavan, N., and Basu, B. (2021). Urinary bladder and urethral tissue engineering, and 3D bioprinting approaches for urological reconstruction. *J. Mateirals Res.* 36, 3781–3820. doi:10.1557/s43578-021-00255-w

Sun, Y., Qin, H., Yan, Z., Zhao, C., Ren, J., and Qu, X. (2019). Combating biofilm associated infection *in vivo*: integration of quorum sensing inhibition and photodynamic treatment based on multidrug delivered hollow carbon nitride sphere. *Adv. Funct. Mater.* 29, 1808222. doi:10.1002/adfm.201808222

Sung, S., Steele, L. A., Risser, G. E., and Spiller, K. L. (2023). Biomaterial-assisted macrophage cell therapy for regenerative medicine. *Adv. Drug Deliv. Rev.* 199, 114979. doi:10.1016/j.addr.2023.114979

Suzuki, K., Komura, M., Terawaki, K., Kodaka, T., Gohara, T., Komura, H., et al. (2018). Engineering and repair of diaphragm using biosheet (a collagenous connective tissue membrane) in rabbits. *J. Pediatr. Surg.* 53, 330–334. doi:10.1016/j.jpedsurg.2017.11.035

Takagi, K., Matsumoto, K., Taniguchi, D., Machino, R., Uchida, F., Hara, R., et al. (2022). Regeneration of the ureter using a scaffold-free live-cell structure created with the bio-three-dimensional printing technique. *Acta Biomater.* S1742, 7061. doi:10.1016/j.actbio.2022.10.006. https://www.frontiersin.org.cn/authors-proof-support/#QA53

Takiyama, N., Mizuno, T., Iwai, R., Uechi, M., and Nakayama, Y. (2016). In-body tissue-engineered collagenous connective tissue membranes (BIOSHEETs) for potential corneal stromal substitution. *J. Tissue Eng. Regen. Med.* 10, E518–E526. doi:10.1002/term.1859

Tang, Q., Luo, C., Lu, B., Fu, Q., Yin, H., Qin, Z., et al. (2017). Thermosensitive chitosan-based hydrogels releasing stromal cell derived factor-1 alpha recruit MSC for corneal epithelium regeneration. *Acta Biomater.* 61, 101–113. doi:10.1016/j.actbio.2017.08.001

Terazawa, T., Kawashima, T., Umeno, T., Wada, T., Ozaki, S., Miyamoto, S., et al. (2020). Mechanical characterization of an in-body tissue-engineered autologous collagenous sheet for application as an aortic valve reconstruction material. *J. Biomechanics* 99, 109528. doi:10.1016/j.jbiomech.2019.109528

Tomás, H., Alves, C. S., and Rodrigues, J. (2018). Laponite®: a key nanoplatform for biomedical applications? *Nanomedicine Nanotechnol. Biol. Med.* 14, 2407–2420. doi:10.1016/j.nano.2017.04.016

Valerio, I. L., Campbell, P., Sabino, J., Dearth, C. L., and Fleming, M. (2015). The use of urinary bladder matrix in the treatment of trauma and combat casualty wound care. *Regen. Med.* 10, 611–622. doi:10.2217/rme.15.34

Vandana, J. J., Manrique, C., Lacko, L. A., and Chen, S. (2023). Human pluripotent-stem-cell-derived organoids for drug discovery and evaluation. *Cell Stem Cell* 30, 571–591. doi:10.1016/j.stem.2023.04.011

Vasyutin, I., Zerihun, L., Ivan, C., and Atala, A. (2019). Bladder organoids and spheroids: potential tools for normal and diseased tissue modelling. *Anticancer Res.* 39, 1105–1118. doi:10.21873/anticanres.13219

Vishwakarma, S. K., Sarwar, S., Adil, M. a. M., and Khan, A. A. (2020). Biofabrication of cell-laden allografts of goat urinary bladder scaffold for organ reconstruction/regeneration. *Tissue Cell* 67, 101443. doi:10.1016/j.tice.2020.101443

Vlaovic, P., and Jewett, M. A. S. (1999). Cyclophosphamide-induced bladder cancer. *Can. J. Urology* 6, 745–748.

Wang, B., Tang, Q. L., Yang, Q., Li, M. M., Zeng, S. Y., Yang, X. M., et al. (2023a). Functional acellular matrix for tissue repair. *Mater. Today Bio* 18, 100530. doi:10.1016/j.mtbio.2022.100530

Wang, C., Ross, W. T., and Mysorekar, I. U. (2017). Urothelial generation and regeneration in development, injury, and cancer. *Dev. Dyn.* 246, 336–343. doi:10.1002/dvdy.24487

Wang, J., Feng, C., Zhu, Y., Wang, Z., Ren, X., Li, X., et al. (2022). A multilayered nanofibrous patch functionalized with adipose tissue extract for the treatment of bladder regeneration. *Mater. Des.* 220, 110821. doi:10.1016/j.matdes.2022.110821

Wang, X., Ma, B., and Chang, J. (2015a). Preparation of decellularized vascular matrix by co-crosslinking of procyanidins and glutaraldehyde. *Bio-Medical Mater. Eng.* 26, 19–30. doi:10.3233/bme-151548

Wang, X., Zhai, W., Wu, C., Ma, B., Zhang, J., Zhang, H., et al. (2015b). Procyanidins-crosslinked aortic elastin scaffolds with distinctive anti-calcification and biological properties. *Acta Biomater.* 16, 81–93. doi:10.1016/j.actbio.2015.01.028

Wang, X., Zhang, F., and Liao, L. (2021a). Current applications and future directions of bioengineering approaches for bladder augmentation and reconstruction. *Front. Surg.* 8, 664404. doi:10.3389/fsurg.2021.664404

Wang, Y., Jin, S., Luo, D., He, D., Shi, C., Zhu, L., et al. (2021b). Functional regeneration and repair of tendons using biomimetic scaffolds loaded with recombinant periostin. *Nat. Commun.* 12, 1293. doi:10.1038/s41467-021-21545-1

Wang, Y., Wang, Z., and Dong, Y. (2023b). Collagen-based biomaterials for tissue engineering. *ACS Biomater. Sci. Eng.* 9, 1132–1150. doi:10.1021/acsbiomaterials.2c00730

Wang, Z., Hu, J., Yu, J., and Chen, D. (2020). Preparation and characterization of nano-laponite/PLGA composite scaffolds for urethra tissue engineering. *Mol. Biotechnol.* 62, 192–199. doi:10.1007/s12033-020-00237-z

Webber, M. J., Tongers, J., Newcomb, C. J., Marquardt, K.-T., Bauersachs, J., Losordo, D. W., et al. (2011). Supramolecular nanostructures that mimic VEGF as a strategy for ischemic tissue repair. *Proc. Natl. Acad. Sci. U. S. A.* 108, 13438–13443. doi:10.1073/pnas.1016546108

Wu, T. T., Luo, Q., and Ouyang, G. L. (2015). Periostin: a potent chemotactic factor for recruiting tumor-associated macrophage. *Protein & Cell* 6, 235–237. doi:10.1007/s13238-015-0141-9

Wu, Z. X., Zhou, Y. L., Chen, L., Hu, M. X., Wang, Y., Li, L. L., et al. (2018). Binding efficiency of recombinant collagen-binding basic fibroblast growth factors (CBD-bFGFs) and their promotion for NIH-3T3 cell proliferation. *Biopolymers* 109, e23105. doi:10.1002/bip.23105

Xiao, D. D., Yang, M. B., Zhang, M., Rong, L. D., Wang, Y. M., Cheng, H., et al. (2021a). MicroRNA-126 from stem cell extracellular vesicles encapsulated in a tri-layer hydrogel scaffold promotes bladder angiogenesis by activating CXCR4/SDF-1 alpha pathway. *Chem. Eng. J.* 425, 131624. doi:10.1016/j.cej.2021.131624

Xiao, S., Wang, P., Zhao, J., Ling, Z., An, Z., Fu, Z., et al. (2021b). Bi-layer silk fibroin skeleton and bladder acellular matrix hydrogel encapsulating adipose-derived stem cells for bladder reconstruction. *Biomaterials Sci.* 9, 6169–6182. doi:10.1039/d1bm00761k

Xu, K. L., Han, Y., Huang, Y. Y., Wei, P., Yin, J., and Jiang, J. H. (2022). The application of 3D bioprinting in urological diseases. *Mater. Today Bio* 16, 100388. doi:10.1016/j.mtbio.2022.100388

Xu, Q., Chen, C., Xu, Z., Chen, F., Yu, Y., Hong, X., et al. (2020a). Ureteral reconstruction with decellularized small intestinal submucosa matrix for ureteral stricture: a preliminary report of two cases. *Asian J. Urology* 7, 51–55. doi:10.1016/j.ajur.2019.03.004

Xu, X., Goyanes, A., Trenfield, S. J., Diaz-Gomez, L., Alvarez-Lorenzo, C., Gaisford, S., et al. (2021). Stereolithography (SLA) 3D printing of a bladder device for intravesical drug delivery. *Mater. Sci. Eng. C* 120, 111773. doi:10.1016/j.msec.2020.111773

Xu, Y., Meng, Q., Jin, X., Liu, F., and Yu, J. (2020b). Biodegradable scaffolds for urethra tissue engineering based on 3D printing. *ACS Appl. Bio Mater.* 3, 2007–2016. doi:10.1021/acsabm.9b01151

Yang, F., Xue, F., Guan, J., Zhang, Z., Yin, J., and Kang, Q. (2018). Stromal-cell-derived factor (SDF) 1-alpha overexpression promotes bone regeneration by osteogenesis and angiogenesis in osteonecrosis of the femoral head. *Cell. Physiology Biochem.* 46, 2561–2575. doi:10.1159/000489684

Ye, W. L., Yang, Z., Cao, F. Y., Li, H., Zhao, T. Y., Zhang, H., et al. (2022). Articular cartilage reconstruction with TGF-β1-simulating self-assembling peptide hydrogel-based composite scaffold. *Acta Biomater.* 146, 94–106. doi:10.1016/j.actbio.2022.05.012

Zelivianskaia, A., Bradley, S., and Morozov, V. (2021). 113 Best practices for repair of iatrogenic bladder injury in gynecologic surgery. *Am. J. Obstetrics Gynecol.* 224, S810–S811. doi:10.1016/j.ajog.2021.04.138

Zhai, W., Chang, J., Lin, K., Wang, J., Zhao, Q., and Sun, X. (2006). Crosslinking of decellularized porcine heart valve matrix by procyanidins. *Biomaterials* 27, 3684–3690. doi:10.1016/j.biomaterials.2006.02.008

Zhai, W., Zhang, H., Wu, C., Zhang, J., Sun, X., Zhang, H., et al. (2014). Crosslinking of saphenous vein ECM by procyanidins for small diameter blood vessel replacement. *J. Biomed. Mater. Res. Part B* 102, 1190–1198. doi:10.1002/jbm.b.33102

Zhang, D., Huang, Z., Sun, P., Huang, H., Zhang, Y., Dai, J., et al. (2017). Acceleration of healing of traumatic tympanic membrane perforation in rats by implanted collagen membrane integrated with collagen-binding basic fibroblast growth factor. *Tissue Eng. Part A* 23, 20–29. doi:10.1089/ten.tea.2016.0265

Zhang, M., Du, H., Guan, Y., Liu, J., Wang, S., Li, H., et al. (2022). Study on the effect of PDA-PLGA scaffold loaded with islet cells for skeletal muscle transplantation in the treatment of diabetes. *Front. Bioeng. Biotechnol.* 10, 927348. doi:10.3389/fbioe.2022.927348

Zhang, P. B., Hong, Z. K., Yu, T., Chen, X. S., and Jing, X. B. (2009). *In vivo* mineralization and osteogenesis of nanocomposite scaffold of poly (lactide-co-glycolide) and hydroxyapatite surface-grafted with poly(L-lactide). *Biomaterials* 30, 58–70. doi:10.1016/j.biomaterials.2008.08.041

Zhang, X.-Z., Jiang, Y.-L., Hu, J.-G., Zhao, L.-M., Chen, Q.-Z., Liang, Y., et al. (2021). Procyanidins-crosslinked small intestine submucosa: a bladder patch promotes smooth muscle regeneration and bladder function restoration in a rabbit model. *Bioact. Mater.* 6, 1827–1838. doi:10.1016/j.bioactmat.2020.11.023

Zhang, Y., Yoo, J. J., and Atala, A. (2020). "Chapter 46 - tissue engineering: bladder and urethra," in *Principles of tissue engineering* Editor E. Brown Fifth Edition (United Kingdom: Andre Gerhard Wolff), 845–862.

Zhao, W. X., Chen, B., Li, X. D., Lin, H., Sun, W. J., Zhao, Y. H., et al. (2007). Vascularization and cellularization of collagen scaffolds incorporated with two different collagen-targeting human basic fibroblast growth factors. *J. Biomed. Mater. Res. Part A* 82A, 630–636. doi:10.1002/jbm.a.31179

Zhihong, C., Liyong, L., Chen, Y., Liu, M., Xiang, A., Deng, C., et al. (2022). Periostin attenuates cyclophosphamide-induced bladder injury by promoting urothelial stem cell proliferation and macrophage polarization. *Stem Cells Transl. Med.* 11, 659–673. doi:10.1093/stcltm/szac025

Zhu, J., Ji, L., Chen, Y., Li, H., Huang, M., Dai, Z., et al. (2023). Organoids and organs-on-chips: insights into predicting the efficacy of systemic treatment in colorectal cancer. *Cell Death Discov.* 9, 72. doi:10.1038/s41420-023-01354-9

Zhu, Z. P., Yang, J. Y., Ji, X., Wang, Z. C., Dai, C. X., Li, S. K., et al. (2022). Clinical application of a double-modified sulfated bacterial cellulose scaffold material loaded with FGFR2-modified adipose-derived stem cells in urethral reconstruction. *Stem Cell Res. Ther.* 13, 463. doi:10.1186/s13287-022-03164-9

Ziegler, C. G., Sloun, R. V., Gonzalez, S., Whitney, K. E., Dephillipo, N. N., Kennedy, M. I., et al. (2019). Characterization of growth factors, cytokines, and chemokines in bone marrow concentrate and platelet-rich plasma: a prospective analysis. *Am. J. Sports Med.* 47, 2174–2187. doi:10.1177/0363546519832003

frontiers | Frontiers in Bioengineering and Biotechnology

TYPE Original Research
PUBLISHED 09 November 2023
DOI 10.3389/fbioe.2023.1308184

Check for updates

OPEN ACCESS

EDITED BY
Mingqiang Li,
Third Affiliated Hospital of Sun Yat-sen University, China

REVIEWED BY
Supeng Ding,
Johns Hopkins University, United States
Qiang Wei,
Sichuan University, China
Yang Zhang,
Shenzhen University, China

*CORRESPONDENCE
Qian Feng,
qianfeng@cqu.edu.cn
Xiufeng Xiao,
xfxiao@fjnu.edu.cn
Bobin Mi,
mibobin@hust.edu.cn

†These authors have contributed equally to this work

RECEIVED 06 October 2023
ACCEPTED 20 October 2023
PUBLISHED 09 November 2023

CITATION
Liu M, Zheng L, Zha K, Yang Y, Hu Y, Chen K, Wang F, Zhang K, Liu W, Mi B, Xiao X and Feng Q (2023), Cu(II)@MXene based photothermal hydrogel with antioxidative and antibacterial properties for the infected wounds.
Front. Bioeng. Biotechnol. 11:1308184.
doi: 10.3389/fbioe.2023.1308184

COPYRIGHT
© 2023 Liu, Zheng, Zha, Yang, Hu, Chen, Wang, Zhang, Liu, Mi, Xiao and Feng. This is an open-access article distributed under the terms of the Creative Commons Attribution License (CC BY). The use, distribution or reproduction in other forums is permitted, provided the original author(s) and the copyright owner(s) are credited and that the original publication in this journal is cited, in accordance with accepted academic practice. No use, distribution or reproduction is permitted which does not comply with these terms.

Cu(II)@MXene based photothermal hydrogel with antioxidative and antibacterial properties for the infected wounds

Mingxiang Liu[1†], Lei Zheng[2†], Kangkang Zha[3†], Yayan Yang[1], Yunping Hu[1], Kai Chen[1], Feng Wang[1], Kunyu Zhang[4], Wei Liu[5], Bobin Mi[3*], Xiufeng Xiao[1*] and Qian Feng[6*]

[1]Fujian Provincial Key Laboratory of Advanced Materials Oriented Chemical Engineering, College of Chemistry and Materials Science, Fujian Normal University, Fuzhou, China, [2]Department of Biochemistry and Molecular Biology, Key Laboratory of Neural and Vascular Biology, Ministry of Education, Hebei Medical University, Shijiazhuang, China, [3]Department of Orthopedics, Union Hospital, Tongji Medical College, Huazhong University of Science and Technology, Wuhan, China, [4]School of Biomedical Science and Engineering, South China University of Technology, Guangzhou, China, [5]Department of Neurosurgery, Renhe Hospital, Huashan North Hospital Baoshan Branch Affiliated to Fudan University, Shanghai, China, [6]Key Laboratory of Biorheological Science and Technology, Ministry of Education, College of Bioengineering, Chongqing University, Chongqing, China

The regeneration of skin tissue is often impeded by bacterial infection seriously. At the same time, reactive oxygen species (ROS) are often overexpressed in infected skin wounds, causing persistent inflammation that further hinders the skin repair process. All of these make the treatment of infected wounds is still a great challenge in clinic. In this study, we fabricate Cu(II)@MXene photothermal complex based on electrostatic self-assembly between Cu^{2+} and MXene, which are then introduced into a hyaluronic acid (HA) hydrogel to form an antibacterial dressing. The rapid adhesion, self-healing, and injectability of the dressing allows the hydrogel to be easily applied to different wound shapes and to provide long-term wound protection. More importantly, this easily prepared Cu(II)@MXene complex can act as a photothermal antibacterial barrier, ROS scavenger and angiogenesis promoter simultaneously to accelerate the healing rate of infected wounds. Our *in vivo* experiments strongly proved that the inflammatory condition, collagen deposition, vessel formation, and the final wound closure area were all improved by the application of Cu(II)@MXene photothermal hydrogel dressing.

KEYWORDS

hydrogel, MXene, antibacterial, angiogenesis, wound healing

Introduction

Skin, as the largest organ and the first defense of human body, often suffers from various kinds of injuries (Cui et al., 2022). Fortunately, skin shows a good ability of self-healing if the damages are not serious (Lee et al., 2022). The self-healing of wounds is a complex process, which includes the hemostatic phase, inflammatory phase, proliferative phase, and remodeling phase (Zhao et al., 2019). During the inflammatory phase, ROS secreted by leukocytes, macrophages, and other inflammatory cells prevent bacterial invasion and avoid

wound infection, playing an important role in regulating the inflammatory response and the wound healing process (Jin et al., 2020; Sawaya et al., 2020). However, the self-protection of the wounds does not always work to eliminate bacterial infection. Moreover, under long-term bacterial infection, ROS are often overexpressed in the wound to lead the overactivation of proinflammatory cytokines and matrix metalloproteinases (MMPs), thereby disrupting the intracellular homeostasis and prolonging the inflammation phase (Liu and Shi, 2019; Xuan et al., 2021). At the same time, the overexpressed ROS also can damage the endothelial cell and blood vessels (Zhao et al., 2020). All of these create a negative microenvironment to hinder the infected wound healing. Therefore, in order to reverse the negative microenvironment of infected wound, how to remove bacteria and scavenge excessive ROS simultaneously is a research direction which is worth of further pondering.

Until now, for the antibacterial treatment of wounds, antibiotics are still the first choice in clinic (Li et al., 2022a). For example, Suhaeri et al. (2018) loaded ciprofloxacin onto a skin patch for the treatment of infected wounds, and (Fu et al., 2022) introduced gentamicin into a hydrogel network to eliminate bacteria in infected wounds. However, the treatment methods involving loaded antibiotics are often characterized by cumbersome preparation and face challenges such as poor drug permeability, antibiotic resistance risks, and the need for frequent administration (Li et al., 2022b). Therefore, developing new types of antibacterial therapies, such as photothermal therapy (PTT) and photodynamic therapy (PDT), is extremely urgent. Especially, PTT means that the photothermal agent is activated to an excited singlet state by irradiation with near-infrared (NIR) light and subsequently recovered to the ground state by exotherm. The released heat during this process induces the damage to the bacterial membrane, which finally achieve bacterial clearance (Ma et al., 2021). Until now, PTT has received increasing attention because of its broad antibacterial spectrum, non-invasiveness and deep tissue penetration (Zeng et al., 2021). Various two-dimensional (2D) nanomaterials have been reported to be used as photothermal converters for PTT, including graphene or graphene derivatives (Altinbasak et al., 2018), molybdenum disulfide (MoS_2) (Venkata Subbaiah et al., 2016; Liu et al., 2017), black phosphorus (BP) (Qian et al., 2017; Yang et al., 2018), and transition metal carbides and nitrides (MXenes) (Lin et al., 2017). MXenes is an emerging 2D multifunctional ultra-thin nanomaterial (Li et al., 2017; Murali et al., 2021) with promising applications in biomedical engineering based on its excellent biocompatibility, excellent structural stability, and high photothermal conversion efficiency (Rasool et al., 2016). For example, Wu et al. (2022) developed a MXene photothermal microneedle patch to control the release of the biologic agent IL-17 mAbs through photothermolysis, making it a potential candidate for the treatment of inflamed skin. Li et al. (2018) reported a MXene based composite nanoplatform for efficient synergistic chemotherapy and photothermal therapy for the eradication and prevention of recurrence of hepatocellular carcinoma. More interestingly, MXenes also exhibit satisfactory antioxidative property, so it can scavenge ROS, such as hydrogen peroxide (H_2O_2), superoxide radicals ($\cdot O_2^-$), and hydroxyl radicals (·OH) effectively (Feng et al., 2021). For example, Ren et al. (2019) developed MXene protectants that significantly reduced IR-induced ROS production to reverse the damage of the hematopoietic system in irradiated mice. Therefore, MXene-based nanomaterials are actually a promising development direction for the treatment of infected wound. On the other hand, hydrogels, due to the biocompatibility and functionality, are the most rapidly developed wound dressing at present. Firstly, the porous three-dimensional (3D) network structure of hydrogels guarantees their good permeability, allowing the efficient oxygen and nutrient exchange in wound (Qi et al., 2022). At the same time, hydrogels can be easily endowed with special properties, such as injectable and self-healing, and bio-adhesive properties, through the well-design of the hydrogel crosslinking (Liang et al., 2021). Then, these special properties allowed the hydrogels to fill irregularly shaped wound defects easily to provide a lasting physical barrier for wound protection (Li et al., 2022c). Therefore, how to take advantages of 2D nanomaterials and hydrogels to develop the next-generation dressing for infected wound treatment should be an interesting research direction.

Herein, we designed a Cu(II)@MXene based photothermal hydrogel system and explored its potential application as a dressing for the infected wound (Scheme 1). The Cu(II)@MXene composite we have designed and prepared can simultaneously act as a photothermal converter and ROS scavenger. Under near-infrared triggering, the composite rapidly releases the loaded Cu^{2+} and exhibits good photothermal synergy with MXene against bacteria. The preparation of Cu(II)@ MXene photothermal hydrogel is simple, without the need for loading antibiotics, reducing the prevalence of drug-resistant pathogens, but its multifunctional characteristics, including injectability, self-healing, antioxidant, antibacterial, and long-term release of Cu^{2+}, meet the requirements of infection wound dressings. Our subsequent *in vitro* and *in vivo* studies strongly demonstrated the enormous potential of Cu(II)@ MXene-based photothermal hydrogel in treating infected wounds.

Materials and methods

Materials

Sodium hyaluronate (HA, MW: 10 kDa) was purchased from Shandong Focuschem Co., Ltd. (China) Adipic dihydrazide (ADH, 98%), sodium periodate ($NaIO_4$, AR), 2-morpholineethanesulfonic acid (MES, 99%), 1-(3-dimethylaminopropyl)-3-ethylcarbodiimide hydrochloride (EDC, 98.5%), copper chloride ($CuCl_2{\cdot}H_2O$, AR), lithium fluoride (LiF, AR), sodium hydroxide (NaOH, AR), ethylene glycol (EG, AR), hyaluronidase (300 U/mg) were purchased from Shanghai Macklin Biochemical Technology Co. Ltd. (China) Hydrochloric acid (HCl, AR, 37%), hydrogen peroxide (H_2O_2, AR, 30%), sulfuric acid (H_2SO_4, AR) were bought from Sinopharm Chemical Reagent Co., Ltd. (China) 1-Hydroxybenzotriazole (HOBT) was obtained from J&K Scientific. (China) Titanium aluminum carbide (Ti_3AlC_2, 400 mesh) purchased from Adamas Reagent Co. (China) Titanium sulfate ($Ti(SO_4)_2$, AR) was purchased from Shanghai Aladdin Biochemical Technology Co., Ltd. (China).

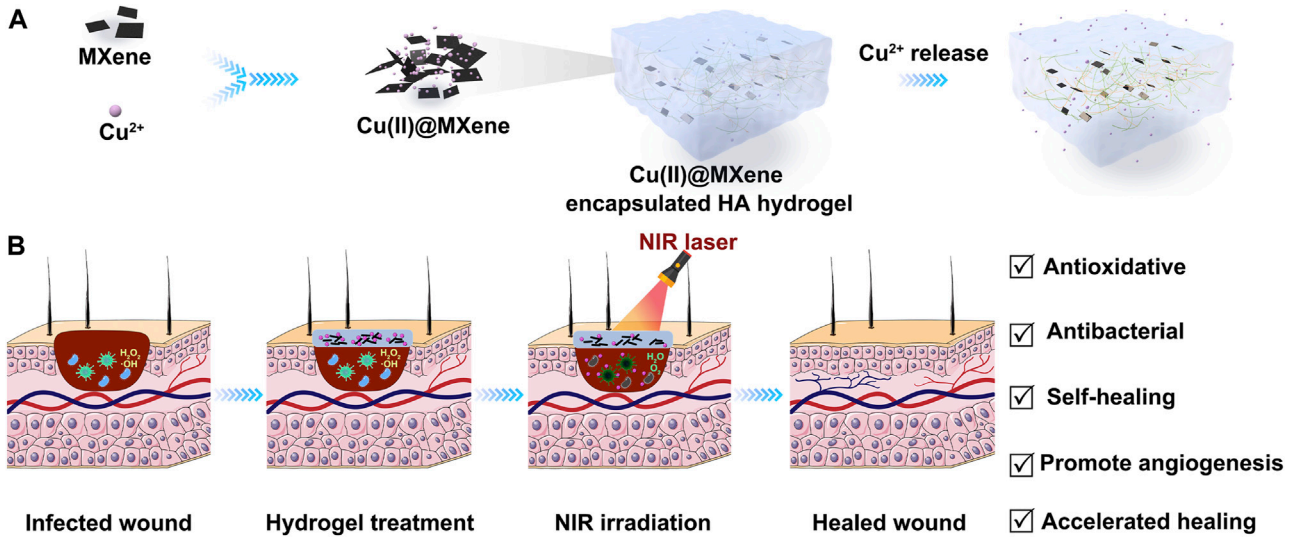

SCHEME 1
Schematic illustration of the preparation and application of Cu(II)@MXene photothermal hydrogel. **(A)** The Cu(II)@MXene complex were formed through the electrostatic aggregation and the Cu(II)@MXene photothermal hydrogels were prepared by the mixing of Cu(II)@MXene suspension, OHA solution, and HA-ADH solution. **(B)** The Cu(II)@MXene hydrogels could be injected to cover the infected wounds as a protective layer to promote the wound healing.

Electrostatic aggregation forms Cu(II) @MXene complex

Ti_3C_2 MXene was prepared according to previous reported method (Peng et al., 2021). Briefly, 1.6 g of LiF was dissolved in 20 mL of HCl (9 M) to form an etching solution. Then 1 g of Ti_3AlC_2 was added to the etching solution and stirring was continued for 24 h. Subsequently, the precipitates were rinsed with deionized water (DI water) and then centrifuged. This process was repeated several times until the pH of the supernatant was >6. Finally, the solid precipitates were continued to be sonicated in DI water for 1 h. The dark green supernatant was collected and stored at 4°C.

MXene suspension (10 mL, 0.5 g/mL) was sonicated and then added to 100 μL of $CuCl_2$ solution (5 wt%) and mixed thoroughly with a vortex shaker for 60 s to obtain the suspension of self-assembled Cu(II)@MXene complex (Scheme 1A).

Synthesis of hexanediyl dihydrazide modified hyaluronic acid (HA-ADH)

Dissolve 1 g of MES in 200 ml of DI water. Adjust the pH of the solution to 6.5 with 1 M NaOH. 2 g of HA was completely dissolved in the MES buffer. Then 2.5 g of EDC and 1.78 g of HOBT were added to the HA solution sequentially. After 1 h of reaction, 9 g of ADH was added into the solution, and then the reaction was continued at room temperature for another 24 h. Finally, the obtained solution was dialyzed against NaCl solution for 3 days and then further dialyzed against DI water for another 3 days (Mw = 14,000). The purified solution was freeze-dried to obtain the final product HA-ADH.

Synthesis of oxidized hyaluronic acid (OHA)

1 g of HA was completely solved in 100 mL of phosphate buffer solution (PBS) and the solution pH was adjusted to 5.0 with 1 M HCl. 0.5 g of $NaIO_4$ was added into the solution and the reaction was continued at room temperature under dark for 5 h. Then 1 mL of EG was added to the solution to terminate the reaction. Finally, the obtained solution was dialyzed against NaCl solution for 3 d, and then further dialyzed against deionized water for 3 days (Mw = 14,000). The purified solution was freeze-dried to obtain OHA.

Preparation of hydrogels

HA-ADH and OHA were dissolved in PBS (pH = 7.4), respectively. The HA hydrogel was prepared by the mixing of HA-ADH and OHA solution with specific concentration. The concentration of HA-ADH solution was fixed at 4 (w/v)% and the concentration of OHA solution was ranged from 0.6, 0.8, 1.0 to 1.2 (w/v)%. For the preparation of the Cu(II)@MXene hydrogel, the Cu(II)@MXene suspension was added directly to the aforementioned mixing process.at concentrations of 30, 90, and 150 μg/mL.

Chemical structure characterization

The microstructure of MXene was characterized by transmission electron microscopy (TEM, Tecnai F20, FEI, United States), atomic force microscopy (AFM, Dimension ICON, Bruker, Germany). The particle size distribution and zeta potential of MXene were characterized by laser particle sizer (Nano

ZSE, Malvern, United Kingdom) at 25°C. Each test was repeated three times. The crystal structure of MXene was characterized by X-ray diffractometry (XRD, X'Pert PXRD, PANalytical B.V., Netherlands). The molecular structure of MXene was characterized by X-ray photoelectron spectroscopy (XPS, ESCALAB Xi+, Thermo Fisher Scientific, United States) and Raman spectroscopy (Raman, LabRAM HR Evolution, HORIBA, Japan). The Cu^{2+} loading and releasing ability of Cu(II)@MXene complex were analyzed with an inductively coupled plasma spetrometer (ICP, Optima8000, Perkin Elmer, Singapore). The ability of MXene to scavenge ROS was evaluated by enzymatic calibrator (Multiskan Sky, Thermo Fisher Scientific, United States). Structural analysis of HA-ADH, OHA was performed by nuclear magnetic resonance spectrometry (NMR, AVANCE 400, Bruker, Germany). The coating formation and microstructure of the hydrogels were characterized by Fourier transform infrared spectroscopy (FT-IR, Nicolet IS50, Thermo Fisher Scientific, United States), scanning electron microscopy (SEM, Regulus 8100, HITACHI, Japan). The hydrogel samples were rapidly frozen in liquid nitrogen for 5 min and immediately freeze-dried for 48 h to remove moisture. The samples were plated by sputtering for 30 s.

In vitro photothermal effect of Cu(II)@MXene complex

The photothermal properties of Cu(II)@MXene complex were investigated by exposing NIR with a wavelength of 808 nm. Briefly, Cu(II)@MXene suspension with different concentration (30, 90, 150 μg/mL) were loaded in 1.5 mL centrifuge tubes and the solutions were irradiated with NIR with different power (0.5, 1.0, 1.3, 1.8 W/cm^2). The temperature change of the solution was then recorded with a temperature sensing recorder until the temperature stopped rising. The photothermal properties of the materials were evaluated by using temperature-time curves.

Swelling properties

Firstly, hydrogel samples were placed in centrifuge tubes containing 500 μL of PBS buffer (pH = 7.4, 37°C) to simulate physiological conditions. After that, the hydrogels were periodically removed, and after wiping the surface water with filter paper, the mass of the hydrogels was weighed, and the above process was repeated until the mass of the hydrogels was stable. Finally, the swelling rate of the hydrogel was calculated based on the swelling mass. The experiment was repeated three times for each sample and the average value was calculated. The swelling rate was calculated by the following equation: $SR=(W_t-W_0)/W_0\times100\%$, where SR-swelling rate; W_t-weight of hydrogel after specific time swelling; W_0-weight of initial hydrogel.

Biodegradation behavior

The biodegradation behavior of hydrogels in the wet state after reaching solubilization equilibrium was determined experimentally. Briefly, the hydrogels were placed in a PBS buffer containing hyaluronidase (enzyme concentration of 100 U/mL, pH = 7.4, 37°C) and replaced with fresh PBS buffer of hyaluronidase every 2 days to simulate physiological conditions. After that, the hydrogels were periodically removed and the mass of the hydrogels was weighed after wiping the surface water with filter paper, and the process was repeated until the hydrogels were completely biodegraded. Finally, the biodegradation rate of the hydrogel was calculated based on the residual amount of the hydrogel. The experiment was repeated three times for each sample and the average value was calculated. The biodegradation rate was calculated by the following equation: $DR=(W_s-W_d)/W_s\times100\%$, where, DR-biodegradation rate; W_d-weight of hydrogel after a specific time of biodegradation; W_s-weight of hydrogel with dissolution equilibrium.

Rheological performance characterization

The rheological properties of the hydrogels were evaluated using a TA rheometer (DHR 2, Waters, United States). Parallel plates of 8 mm diameter with a fixed gap size of 1 mm were used at 25°C. The time sweep at strain of 1% and a frequency of 0.1 Hz. Then strain sweep was performed at a frequency of 1 Hz and a strain range of 1%–600%. As for the shear thinning experiments, the hydrogels were subjected to alternating high strain (500%) and low strain (1%) with a time interval of 60 s.

Ion loading and release capacity testing

The Cu^{2+} loading efficiency was determined by measuring the Cu^{2+} content in the supernatant after Cu(II)@MXene self-assembly. The experiment was repeated three times for each sample and the average value was calculated. The loading rate was calculated as follows: $LR=(C_b-C_a)/C_b\times100\%$, where LR-loading rate of Cu^{2+}; C_b-the beginning concentration of Cu^{2+}; C_a-the final concentration of Cu^{2+} in the supernatant.

The ion release property of Cu(II)@MXene hydrogel was similarly investigated. Briefly, 80 μL of Cu(II)@MXene hydrogel was incubated in 1 mL of DI water at 37°C. The concentration of Cu^{2+} in the supernatant was measured at different time points. In addition, to investigate the effect of laser irradiation on the ion release properties of the hydrogels, NIR laser irradiation using a laser power density of 1.5 W/cm^2 was added for 10 min at 16 h. The experiment was repeated three times for each sample and the mean value was calculated.

Evaluation of reactive oxygen scavenging capacity

The ROS scavenging ability of the hydrogels was evaluated by the reaction of $Ti(SO_4)_2$ with hydrogen peroxide to form a complex. Briefly, and 80 μL of Cu(II)@Mxene hydrogel was immersed into 0.5 mL of the assay solution (2 M H_2SO_4 and 5 wt% $Ti(SO_4)_2$ and 1 mM H_2O_2). At different time points, the supernatant (180 μL) was collected and the absorbance at 408 nm was measured by an enzyme

marker, and the ability of the hydrogel to scavenge reactive oxygen species was evaluated by calculating the concentration of H_2O_2 in the solution.

In vitro cytocompatibility

L929 cells were seeded onto 24-well plates at 1×10^4 cells/well and cultured in DMEM/F12 supplemented with 10% FBS in 5% CO_2 at 37°C. Then, 100 μL PBS or sterile hydrogel was added into 24-well plates for another culture of 24 h. As for Cu(II)@MXene hydrogel-150+NIR group, the NIR was set as 1.5 W/cm^2 808 nm laser for 5 min. A CCK-8 kit (Dojindo, Kumamoto, Japan) was used to evaluate the proliferation rates of L929 cells treated by co-culturing with PBS or hydrogel at 24 h. The optical density (OD) value (absorbance at 450 nm) was measured with a plate reader. A Calcein-FITC/PI live-dead staining kit (Solarbio, Beijing, China) was used to evaluate the viability of L929 cells after treatment with PBS or hydrogels for 24 h. Images were obtained using a fluorescence microscope (Olympus).

Tube formation assay

HUVECs were treated with the extracts of PBS, HA hydrogel, Cu(II)@MXene for 24 h. Then, the cells (2×10^4/well) were cultured in 96-well plates pre-coated with Matrigel for 6 h. Three randomly-chosen fields were photographed using an inverted microscope (Olympus, Tokyo, Japan) and the branch points and tube length were determined by ImageJ software.

In vitro antibacterial properties

100 μL of hydrogel was co-cultured with 50 μL of bacterial solution with a concentration of 105 CFU/mL to the 96-well plate (the group without hydrogel is the positive control group). No NIR treatment for 5 min and NIR treatment (1.5 W/cm^2, 5 min) were given, respectively. Subsequently, 10 μL of treated bacterial solution was mixed with another 90 uL of Mueller-Hinton Broth (MHB) bacterial solution was added and incubated in 96-well plates for 12 h. The absorbance at 600 nm was then read using an enzyme marker. At the same time, another 10 μL of treated bacterial solution was resuspended in 1 mL of PBS and plated on LB agar for another 12 h of culture before taking pictures.

In vivo wound healing

The C57BL/6 male mice were anesthetized via intraperitoneal injection of 2% pentobarbital sodium (50 mg/kg; Sigma Aldrich) and full-thickness round skin wounds (d = 1 cm) were made by a sharp round pouch. Each wound was infected with *S. aureus* suspension (30 μL) with 3×10^8 CFU/mL for 10 min. The C57BL/6 mice were randomly divided into 5 groups and treated with 200 μL of PBS, HA hydrogel, and Cu(II)@MXene hydrogel, respectively (n = 5). Among them, a group of Cu(II)@MXene hydrogel were irradiated with 1.5 W/cm^2 808 nm laser for 5 min. The wounds were bandaged with gauze and were photographed on days 0, 3, 7, and 14 d.

Histological analysis

Wound sections from rats were stained with hematoxylin and eosin (H&E), Masson and CD31, and wound healing mechanisms were analyzed under standard procedures.

Statistical analysis

Pair groups were assessed with Student's t-test, while multiple group comparisons were performed with a one-way analysis of variance (ANOVA) with Tukey's *post hoc* test.

Results and discussion

Characterization of MXene nanosheets

The single-layer MXene was prepared by a classical liquid phase exfoliation and ultrasonic layering strategy for the MAX phase (Ti_3AlC_2), as shown in Figure 1A. The SEM images clearly demonstrated the etching progress from bulk MAX phase (Figure 1B) to multi-layer MXene (Figure 1C). Then, single-layer MXene was successful obatain via ultrasound exfoliation of multi-layer MXene as shown in TEM (Figure 1D) and AFM (Figure 1E) images. Both of these results show that the final exfoliated MXene nanosheets had an ultrathin and transparent structure with an average thickness of about 4 nm and lateral dimensions of about 150–300 nm (Supplementary Figure S1A). The phase composition of single-layer MXene was further analyzed by XRD (Figure 1F). Compared to the raw material MAX, the single-layered MXene showed a disappearance of the (104) characteristic peak, a left-shift of the (002) peak, and a widening of the (002) peak (Feng et al., 2017). All of these indicated that the Al phase was stripped, confirming the successful etching of MAX to produce MXene. Raman spectroscopy measurements (Supplementary Figure S2) were used to investigate structural defects and vibrational modes in the prepared samples. In the case of Ti_3AlC_2, a characteristic peak of out-of-plane stretching vibrations of Ti and C atoms was clearly observed at 271 cm^{-1}. After etching, this characteristic peak shifted to 202 cm^{-1}. The overall vibrational mode was significantly broadened due to the structural changes induced by the etching progress (Sarycheva and Gogotsi, 2020), confirming the results in agreement with the X-ray diffraction analysis. For the following experiments, we used MXene to represent single-layered MXene.

Characterization of Cu(II)@MXene complex

The 2D layered planar structure provides MXenes with abundant anchor points and an extremely high specific surface area. After etching by LiF-HCl solution, the MXene surface is distributed with a large number of negatively charged groups (-OH, -O and -F), which can serve as available sites for trapping cations. Due to the strong adsorption affinity of Ti-O and Ti-OH for metal ions, the positively charged Cu^{2+} could undergo the ion-exchange reactions with the negatively charged groups (-OH, -O) on the MXene surface, forming Cu(II)@MXene complex (Figure 2A). This self-assembly progress between Cu^{2+} and MXene could be

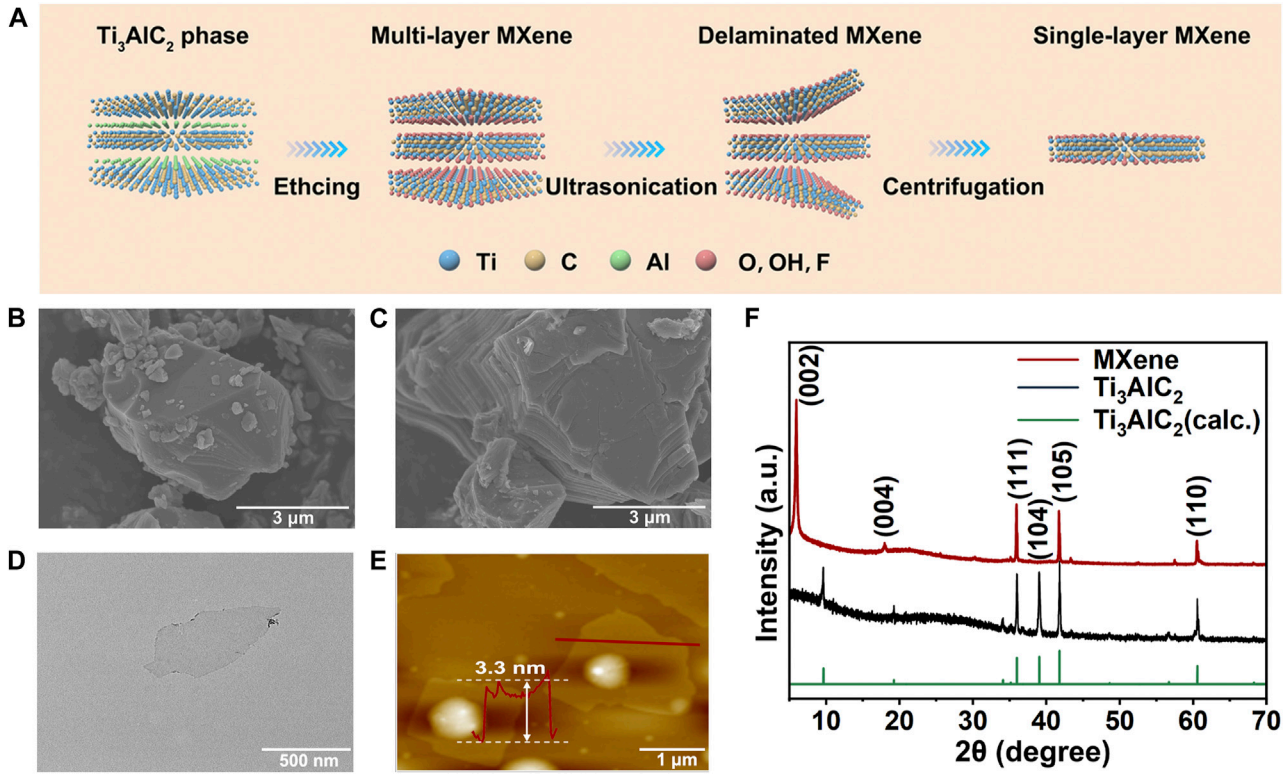

FIGURE 1
Synthesis and characterization of MXene nanosheets. **(A)** Schematic diagram of the synthesis process of 2D MXene nanosheets. SEM images of **(B)** Ti_3AlC_2 (MAX) phase and **(C)** multi-layer MXene. **(D)** TEM image of single-layer MXene. **(E)** AFM image of single-layer MXene. **(F)** XRD spectra of single-layer MXene and Ti_3AlC_2 powder.

observed by TEM (Supplementary Figure S3) and also proved by the Zeta potential change in Figure 2B. The pure MXene suspension exhibited a negative zeta potential (−38.9 mV) due to the strongly negatively charged groups in the surface, while the zeta potential of Cu(II)@MXene dramatically increased to a value (−1.5 mV) which was close to neutral because of the absorption of Cu^{2+} in the surface of MXene (Yin et al., 2020). In order to test the Cu^{2+} absorption efficiency, we tested the Cu^{2+} concentration in the supernatant before and after the Cu(II)@MXene formation as shown in Figure 2C. The loading efficiency of Cu^{2+} in the surface of MXene was about 22%. The SEM images (Figure 2D) showed that the self-assembly among Cu^{2+} and single-layer MXene rapidly occurred within the first 1 min. The EDS image (Supplementary Figure S4) indicates an effective binding between Cu^{2+} and MXene. The morphology of Cu(II)@MXene maintained stable at micron level, which was consistent with the dynamic light scattering (DLS) result (Supplementary Figure S1B). Although Cu(II)@MXene exhibited a certain degree of aggregation over time, simple shaking could relieve the aggregation effectively (Supplementary Figure S5). Therefore, we believed that the dispersibility and stability of the Cu(II)@MXene could meet our requirements for the wound dressing preparation. To understand the elemental composition and molecular structure of the complex, we used X-ray photoelectron spectroscopy (XPS) to further analyze MXene and Cu(II)@MXene. As for MXene, there was no obvious peak of Al, further indicating that the aluminum layer was effectively stripped (Supplementary Figure S6A), while the C 1s peak indicated that the primary structure of MXene was not damaged during the etching process (Supplementary Figure S6C). The characteristic Cu 2p3 peak can be easily observed for Cu(II)@MXene, strongly proving the successful Cu^{2+} doping in the surface of MXene (Figure 2E). Compared to the O 1s spectrum of Mxene (Figure 2F), except the similar 529.6, 531.7, and 532.1 eV peaks which were assigned to Ti-O, Ti-C-O and Ti-OH (Song et al., 2021), respectively, there was another newly appeared characteristic peak on 530.9 eV in the O 1s spectrum of Cu(II)@MXene associated with Cu-O (Figure 2G), confirming the adsorption of Cu^{2+} in the MXene surface. As shown in the Ti 2p spectrum of MXene (Figure 2H), five peaks located at 454.9, 460.8, 455.9, 461.9, and 458.5 eV correspond to Ti-C $2p_{3/2}$, Ti-C $2p_{1/2}$, Ti(II) $2p_{3/2}$, Ti(II) $2p_{1/2}$ and Ti-O $2p_{3/2}$, respectively (Zhang et al., 2020a). After introduction of Cu^{2+}, the peak of Ti-O $2p_{3/2}$ shifted to higher energy values and were significantly enhanced (Figure 2I), which indicated the interaction between Cu^{2+} and the oxygen-containing groups of MXene to form Cu-O bonds. The presence of Cu^{2+} was also further verified by the strong satellite lines located at 962.6 eV and between 940 eV and 946 eV besides the two main peaks at 934.5 and 954.4 eV in Figure 2J (Xu et al., 2022). All of the above-mentioned data strongly evidenced the successful fabrication of Cu(II)@MXene.

To investigate the photothermal conversion efficiency of the Cu(II)@MXene complex, the Cu(II)@MXene suspension with

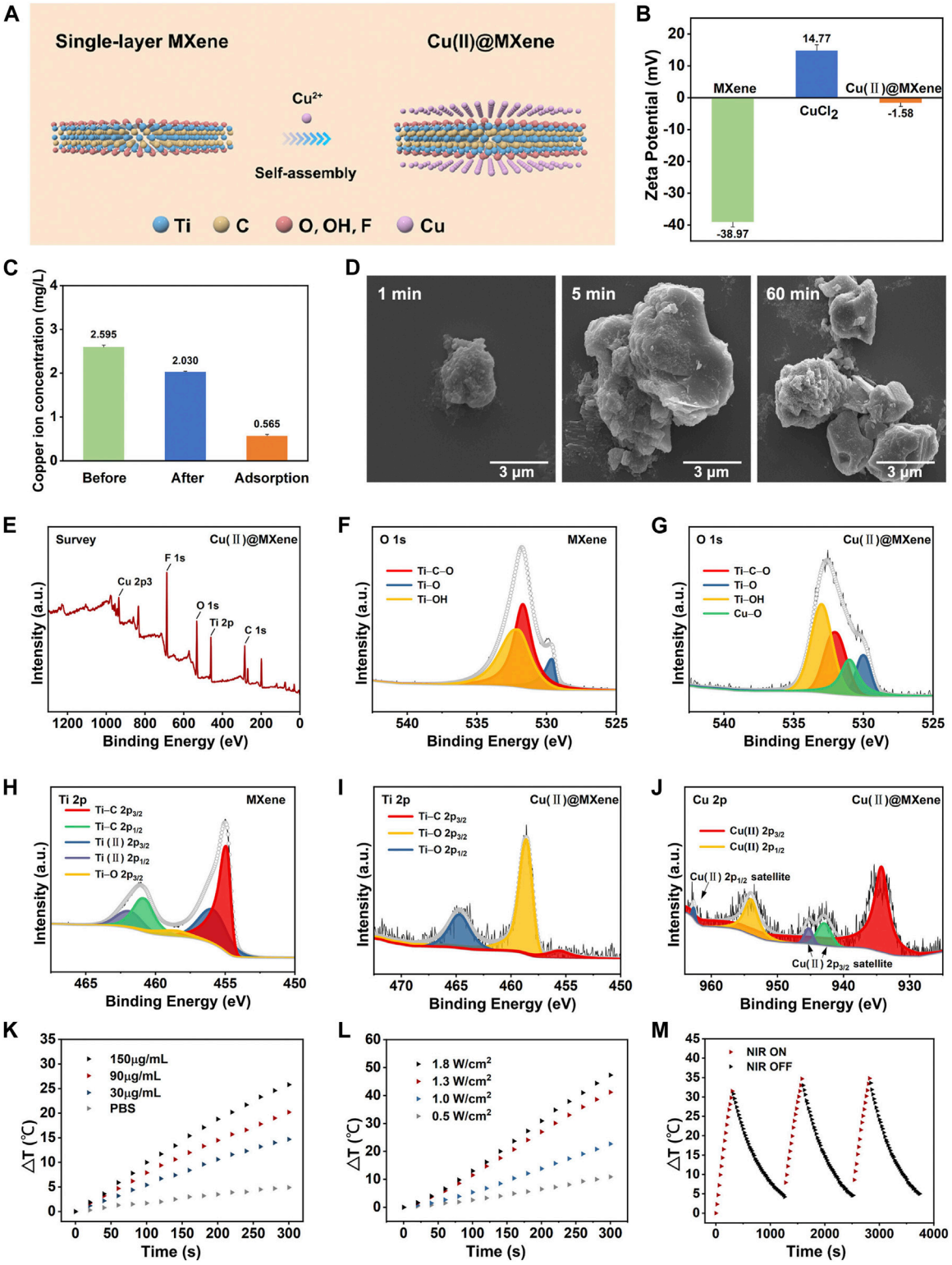

FIGURE 2
Synthesis and characterization of Cu(II)@MXene complex. **(A)** Schematic diagram of the synthesis process of Cu(II)@MXene complex. **(B)** Zeta potential of MXene, $CuCl_2$, and Cu(II)@MXene. **(C)** Concentration of Cu^{2+} in the supernatant before and after electrostatic self-assemble between Cu^{2+} and MXene. **(D)** The SEM images of Cu(II)@MXene at different time points. XPS spectral analysis, measured spectra of **(E)** Cu(II)@MXene, **(F)** O 1s of MXene, **(G)** Cu(II)@MXene, **(H)** Ti 2p of MXene **(I)** Cu(II)@MXene, and **(J)** Cu 2p of Cu(II)@MXene. **(K)** Photothermal conversion efficiency of the Cu(II)@MXene suspension with different concentrations under NIR irradiation with 1.0 W/cm^2. **(L)** The thermal increase curves of the Cu(II)@MXene suspension (150 μg/mL) under NIR irradiation with different power densities. **(M)** The recycling heating profile of Cu(II)@MXene suspension (150 μg/mL) under NIR light irradiation (1.0 W/cm^2) for three on/off cycles.

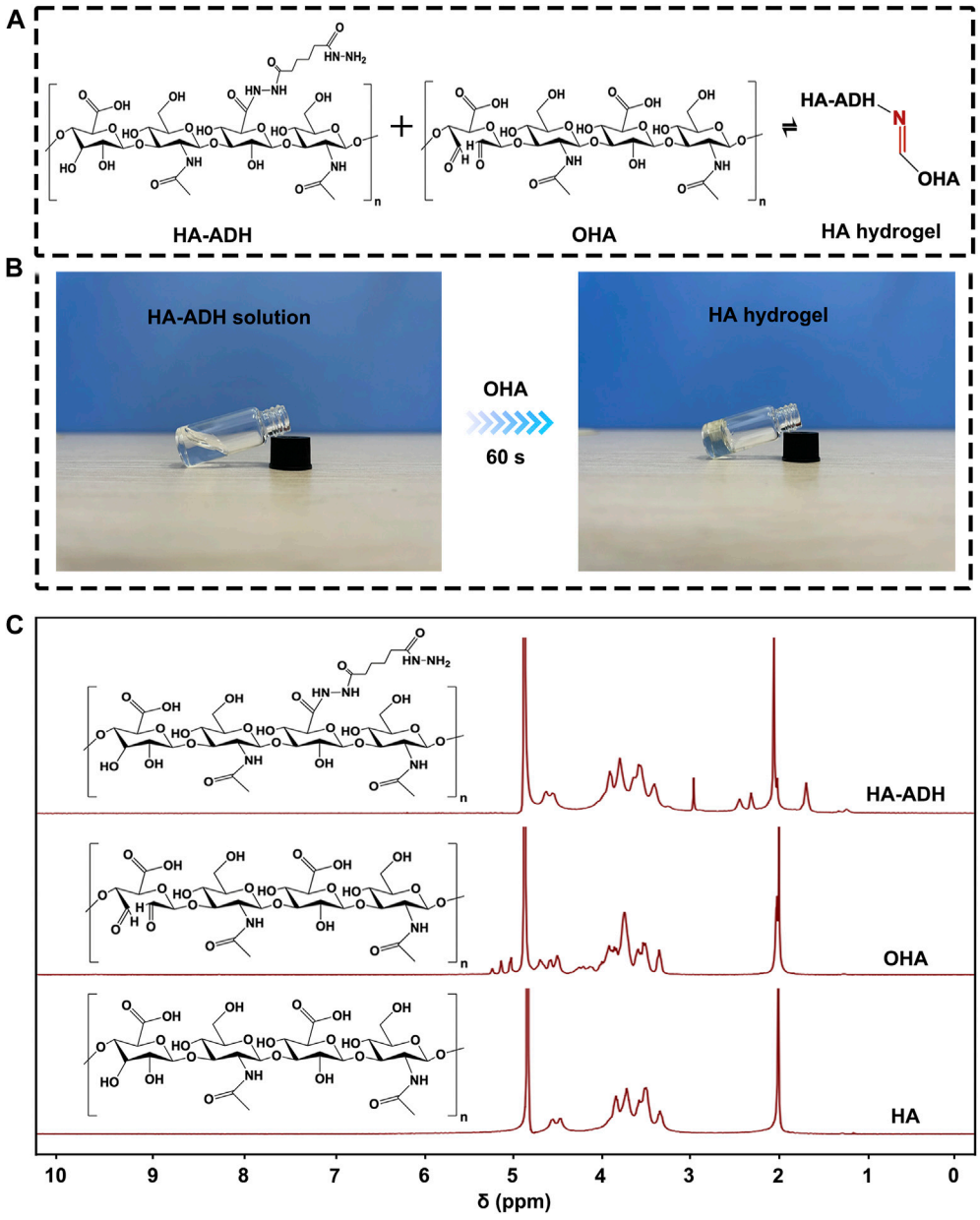

FIGURE 3
The preparation of HA hydrogel. **(A)** The crosslinking formation between HA-ADH and OHA inside the HA hydrogel. **(B)** Photograph of HA hydrogel formation by an equal volume mixing of OHA and HA-ADH solution at room temperature. **(C)** ^{1}H NMR of HA, OHA, and HA-ADH.

different concentration was exposed to 808 nm NIR irradiation with different power for 5 min. The results proved that the heating behavior of Cu(II)@MXene complex could be accelerated by increasing the suspension concentration (Figure 2K) and NIR power (Figure 2L). The real-time heating of Cu(II)@MXene under NIR was also visually reported by the thermal images in Supplementary Figure S7. All of these results demonstrated that the Cu(II)@MXene had an outstanding photothermal conversion efficiency. Compared to some previous studies about PTT nanomaterials for biotherapeutic use (Jiang et al., 2020; Ni et al., 2020), our Cu(II)@MXene complex could reach to a rapid heating behavior to 70°C under a such low concentration of 150 μg/mL and a mild NIR power of 1.8 W/cm^2 within 5 min. Based on the all above results, we chose Cu(II)@MXene concentration of 150 μg/mL and NIR power of 1.8 W/cm^2 for the following experiments. The heating cycle test (Figure 2M) showed the photothermal stability of the Cu(II)@MXene complex, indicating the cyclic PTT potential for the infected wounds of our Cu(II)@MXene based composite hydrogel wound dressing.

Synthesis and characterization of Cu(II) @MXene photothermal hydrogels

We chose HA hydrogel formed with Schiff base reaction as the main scaffold for our Cu(II)@MXene photothermal system

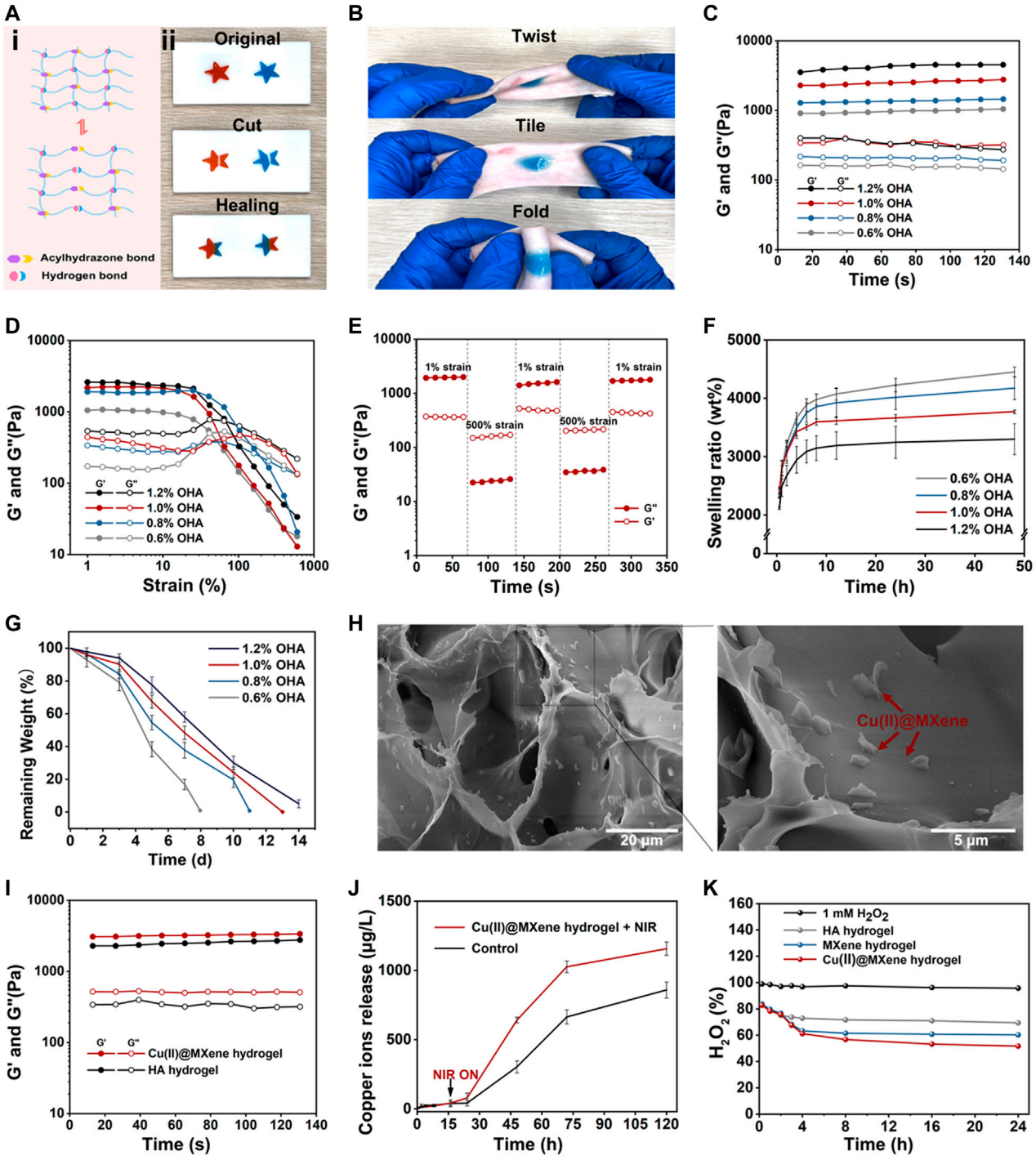

FIGURE 4
The characterizations of HA hydrogel and Cu(II)@MXene hydrogel. The **(A)** self-healing and **(B)** bio-adhesive properties of HA hydrogel. The rheological **(C)** time sweep and **(D)** strain sweep of HA hydrogel. **(E)** The time sweep of HA hydrogel under cyclic low-high strain. **(F)** Swelling properties of HA hydrogels in PBS. **(G)** *In vitro* degradation property of HA hydrogels in PBS under 37°C. **(H)** Cu(II)@MXene hydrogel and local magnified SEM images. **(I)** The rheological time sweep test comparison between HA hydrogel and Cu(II)@MXene hydrogel. The HA hydrogel groups was differentiated by the concentration of OHA. **(J)** Cu^{2+} release curves of Cu(II)@MXene hydrogels with and without NIR irradiation. **(K)** The ROS scavenging efficiency curve of Cu(II)@MXene hydrogel.

(Figure 3A). Therefore, the formed hydrazone crosslinking could meet the injectable, self-healing, and bio-adhesive requirements of wound dressing. As a natural polysaccharide inside the human body, HA possesses excellent biocompatibility and moisture absorption. Moreover, hyaluronic acid is capable of promoting wound healing through facilitating cell migration and mediating cell signaling. Before the HA hydrogel formation, HA should be modified to OHA and HA-ADH, respectively (Supplementary Figure S8). The

successful synthesis of OHA and HA-ADH were proved by ^{1}H NMR (Figure 3B) and FT-IR (Supplementary Figure S9A). Compared to pure HA, we could observe the methylene proton peaks in HA-ADH (1.66 ppm, 2.27–2.40 ppm) and the hemiacetal peaks (4.94–5.15 ppm) in OHA (Xu et al., 2017). These results were consistent with the FT-IR results (Supplementary Figure S9A) (Liu et al., 2022). Especially, the disappearance of the carbonyl peak at 1,735 cm^{-1} in the FT-IR spectrum of HA hydrogel indicated the Schiff base reaction between the aldehyde groups of OHA and the hydrazide groups of HA-ADH (Supplementary Figure S9B). Of course, the photographs in Figure 3C further demonstrated that the Schiff base reaction between OHA and HA-ADH could guarantee the HA hydrogel fabrication by one-step equal volume mixing of OHA and HA-ADH solution.

Thanks to the rapid Schiff base reaction between of OHA and HA-ADH, this HA hydrogel could be formed by a dual-syringe model injection as shown in Supplementary Figure S10 and Supplementary Video S1. In this way, this HA hydrogel could realize satisfactory covering for wounds of different shapes. Furthermore, as the hydrazone crosslinking of HA hydrogel was a kind of dynamic covalent bond (Yang et al., 2020), this HA hydrogel also had a good self-healing property (Figure 4A), which was conducive to keeping the integrity of the HA hydrogel to prolong the serves time of our Cu(II)@MXene wound dressing. Moreover, the aldehyde groups of OHA could react with the amino groups of the host tissue to reach the tight adhesion of the HA hydrogel to tissue (Figure 4B). This bio-adhesive property could further guarantee the effective protection of our designed Cu(II)@MXene based dressing for the infected wounds.

We further evaluated the viscoelastic properties of the HA hydrogels by rheological tests. In Figure 4C, the time sweep results of HA hydrogels showed that for all groups the storage modulus (G′) was higher than the loss modulus (G″), indicating the stable state of HA hydrogels. With the OHA/HA-ADH ratio increased, the G′ of the hydrogels subsequently increased from 900 to 3,500 Pa. This phenomenon indicated that the crosslinking density of HA hydrogel increased with the increase of the OHA content. The strain sweep results (Figure 4D) showed that the intersection of G′ and G″ which indicated the hydrogel fracture, was at about 100% strain for all HA hydrogel groups. Based on this data, we chose a high strain at 500% and a low strain at 1% to test the shear-thinning property of our HA hydrogel. Figure 4E demonstrated that the HA hydrogel had a rapid conversion between the “sol” (high strain) and “gel” (low strain) state, which was convincing evidence for the reversibility of the hydrazone crosslinking of the HA hydrogel. This was also the fundamental for the self-healing property of the HA hydrogel. We also observed the *in vitro* swelling (Figure 4F) and degradation (Figure 4G) behavior of the HA hydrogel. After 8 h, all the HA hydrogel groups could reach to the equilibrium swelling (Supplementary Figure S11) and the equilibrium swelling ratio presented a downward trend with the increase of the OHA content. Meanwhile, the changing of the degradation speed of HA hydrogel also presented a similar trend as that of the swelling ratio. These phenomena were due to the increase of crosslinking density with the increase of OHA content. Considering that the difference between 1% and 1.2% group was not significant, we chose 1% group as the substrate materials to be assembled with the prepared Cu(II)@MXene complex to form the final photothermal hydrogel system. In the SEM images of the Cu(II)@MXene hydrogel (Figure 4H), we could easily observe the aggregation of the doped Cu(II)@MXene nanosheets inside the network of the HA hydrogel. The EDS elemental mapping of Cu^{2+} further illustrated the uniform distribution of the Cu(II)@MXene nanosheets inside hydrogel. The further time sweep comparison between the HA hydrogel and the Cu(II)@MXene hydrogel demonstrated that the addition of Cu(II)@MXene had a positive effect on the modulus of hydrogel (Figure 4I). We speculated that it was related to the formation of hydrogen bonds inside the Cu(II)@MXene hydrogel (Zhang et al., 2020b). FT-IR spectra showed that a newly appeared absorption peak at 1,703 cm^{-1} in Cu(II)@MXene hydrogel which was related to the $\nu_{C=O}$ stretching vibration of the carboxyl group (Supplementary Figure S9B). This might represent the hydrogen bonds formed between the carboxyl group of HA backbones and the surface of Cu(II)@MXene complex.

The Cu^{2+} released from the Cu(II)@ MXene photothermal hydrogel system has a good synergistic antibacterial effect (Mitra et al., 2020). In addition, the long-term release of Cu^{2+} promotes blood vessel regeneration and collagen deposition (Xiao et al., 2017; Xiao et al., 2018). The results demonstrated that NIR irradiation could speed up the Cu^{2+} release (Figure 4J). This should be due to the accelerated Cu^{2+} motion induced by the increase temperature under NIR irradiation. Under the NIR condition, the sustained Cu^{2+} release was still able to last up to more than 120 h, which was helpful to the wound healing.

The presence of excess ROS in chronically infected wounds severely hinders the normal healing process. Because of its natural enzyme-like properties, MXene can effectively catalyze the decomposition of H_2O_2 into H_2O and O_2 (Ren et al., 2019; Feng et al., 2021). We used H_2O_2 as the demo specie of ROS. After the Cu(II)@MXene incubated with H_2O_2 solution for different time, UV-vis was applicated to test the solution absorption in 408 nm (Supplementary Figure S12). In the quantitative analysis (Figure 4K), during the first 120 min, the ROS elimination ratio was quite similar in these three groups [HA hydrogel, MXene hydrogel, and Cu(II)@MXene hydrogel]. It was because that the HA network reacted with H_2O_2 firstly to play the main role in the beginning (Stern et al., 2007). Whereafter, as H_2O_2 seeped into hydrogel, doped Cu(II)@MXene began to scavenge H_2O_2. Compared to pure HA hydrogel, the ROS scavenging ability of Cu(II)@MXene hydrogel was improved by 25%, indicating a good amelioration of oxidative stress microenvironment in infected wounds. The photothermal property of Cu(II)@MXene hydrogel was also tested. Although compared to free Cu(II)@MXene solution, the heating rate of Cu(II)@MXene hydrogel slowed down, it still met the antibacterial requirements for our research (Supplementary Figure S13).

In vitro and *in vivo* characterization of Cu(II)@MXene hydrogels

The L929 mouse fibroblast cell lines was cultured with the Cu(II)@MXene hydrogels to evaluate the cytocompatibility.

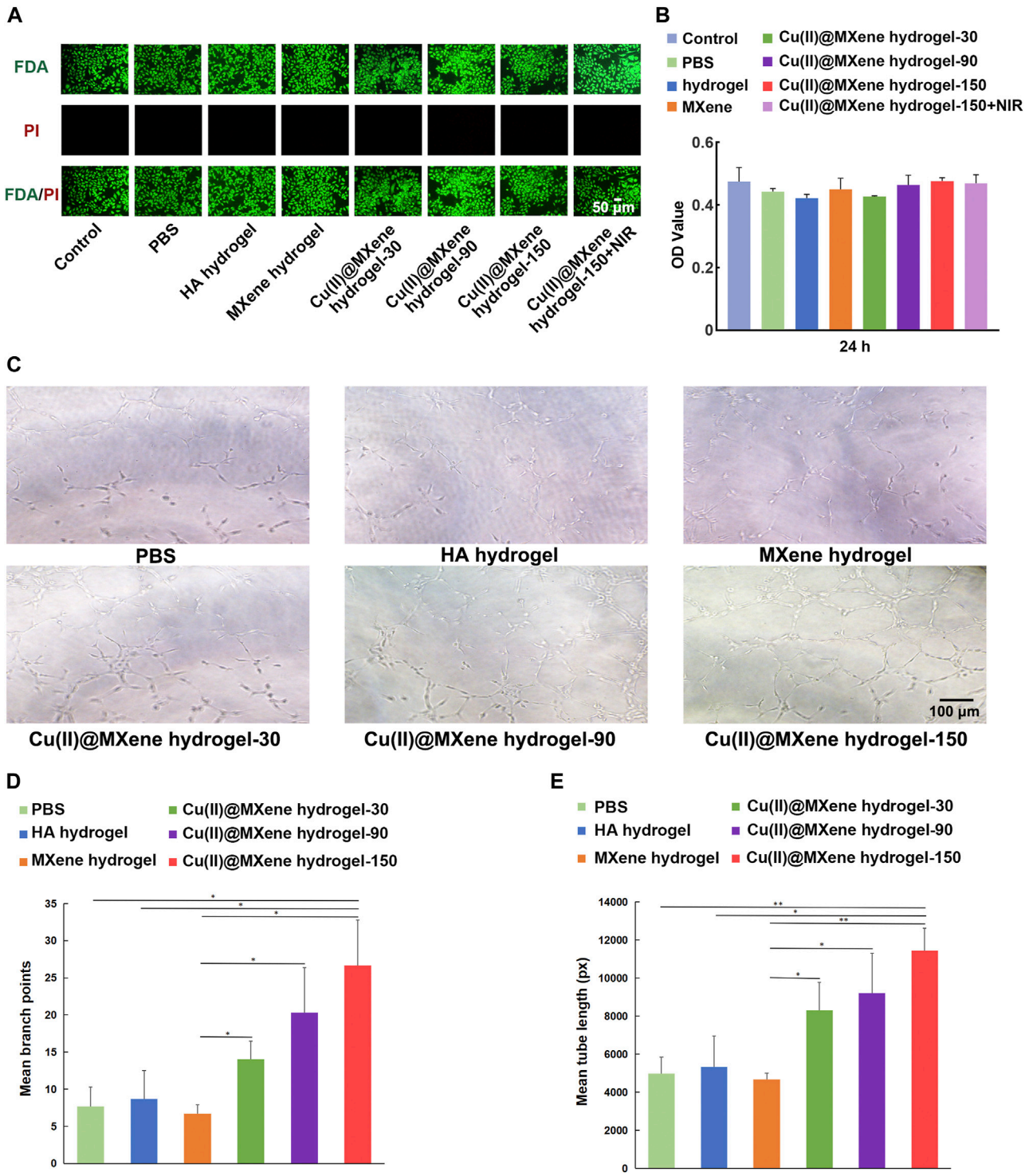

FIGURE 5
In vitro cytocompatibility and angiogenesis property of Cu(II)@MXene hydrogel. **(A)** Live/dead staining images of the L929 cells after being treated with different materials for 24 h. **(B)** CCK-8 results of the L929 cells after treatment with different materials for 24 h. **(C)** Tube formation assay of HUVECs treated by different materials. The quantitative analysis of formed **(D)** branch points and **(E)** tube length, respectively. Statistic results: $^{*}p < 0.05$. $^{**}p < 0.01$. $^{***}p < 0.001$.

The Live/dead staining images (Figure 5A) showed that all the groups had a satisfactory cell viability. This was also proved by the CCK-8 quantitative analysis (Figure 5B). All of these data demonstrated that our Cu(II)@MXene hydrogel had good biocompatibility. Furthermore, the NIR exposure (1.5 W/cm^2, 5 min, 45°C) did not show any negative effect on the cell viability

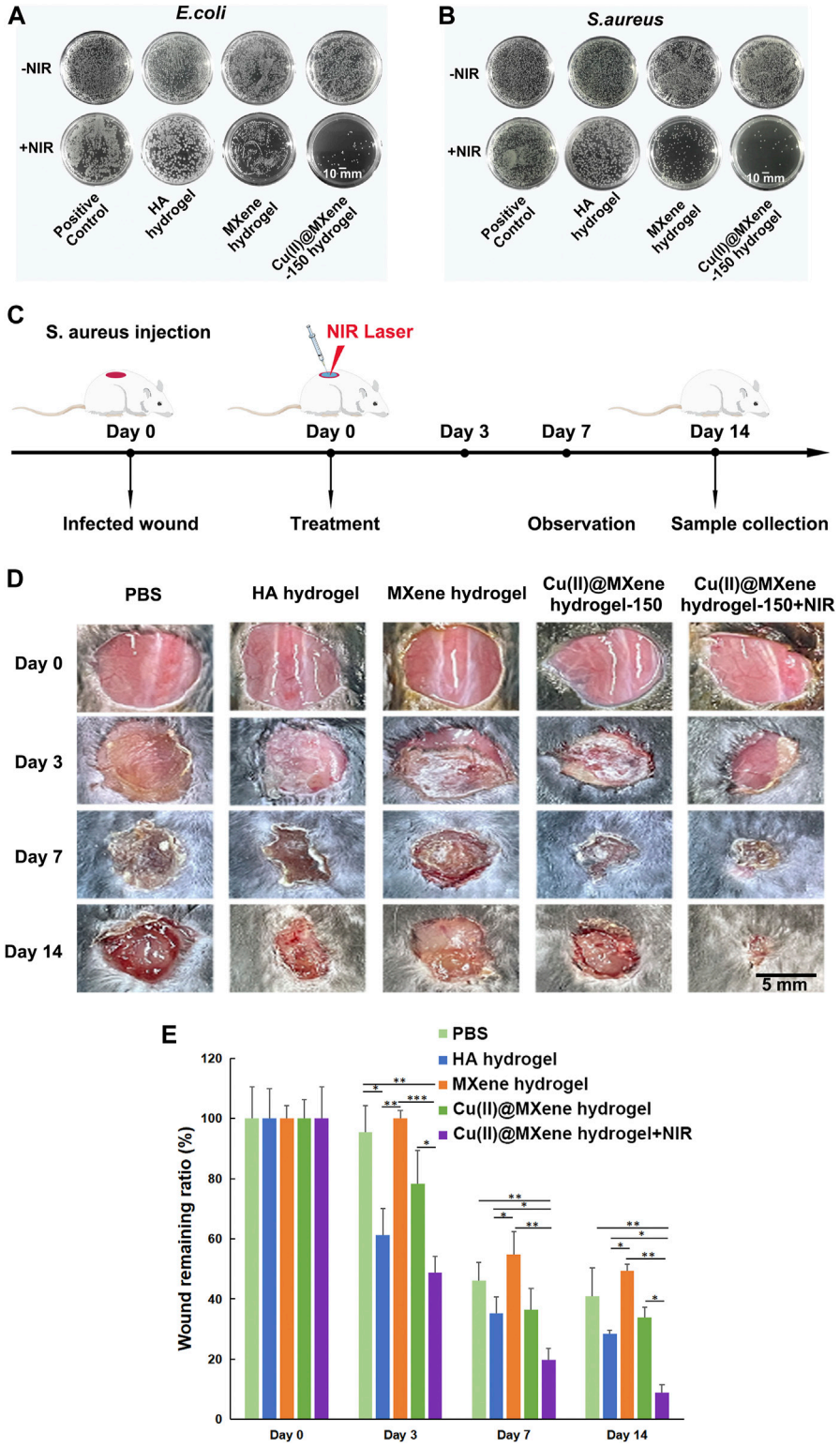

FIGURE 6
Antibacterial properties of Cu(II)@MXene hydrogel and promotion of infected wound healing *in vivo*. Total view of bacterial colonies formed by *E. coli* **(A)** and *S. aureus* **(B)** after different hydrogel treatments. **(C)** Schematic diagram of the construction of mouse skin infection model. **(D)** Representative images of the wounds at a given time. **(E)** Wound remaining ratios after treatment with different materials. Statistic results: $*p < 0.05$. $**p < 0.01$. $***p < 0.001$.

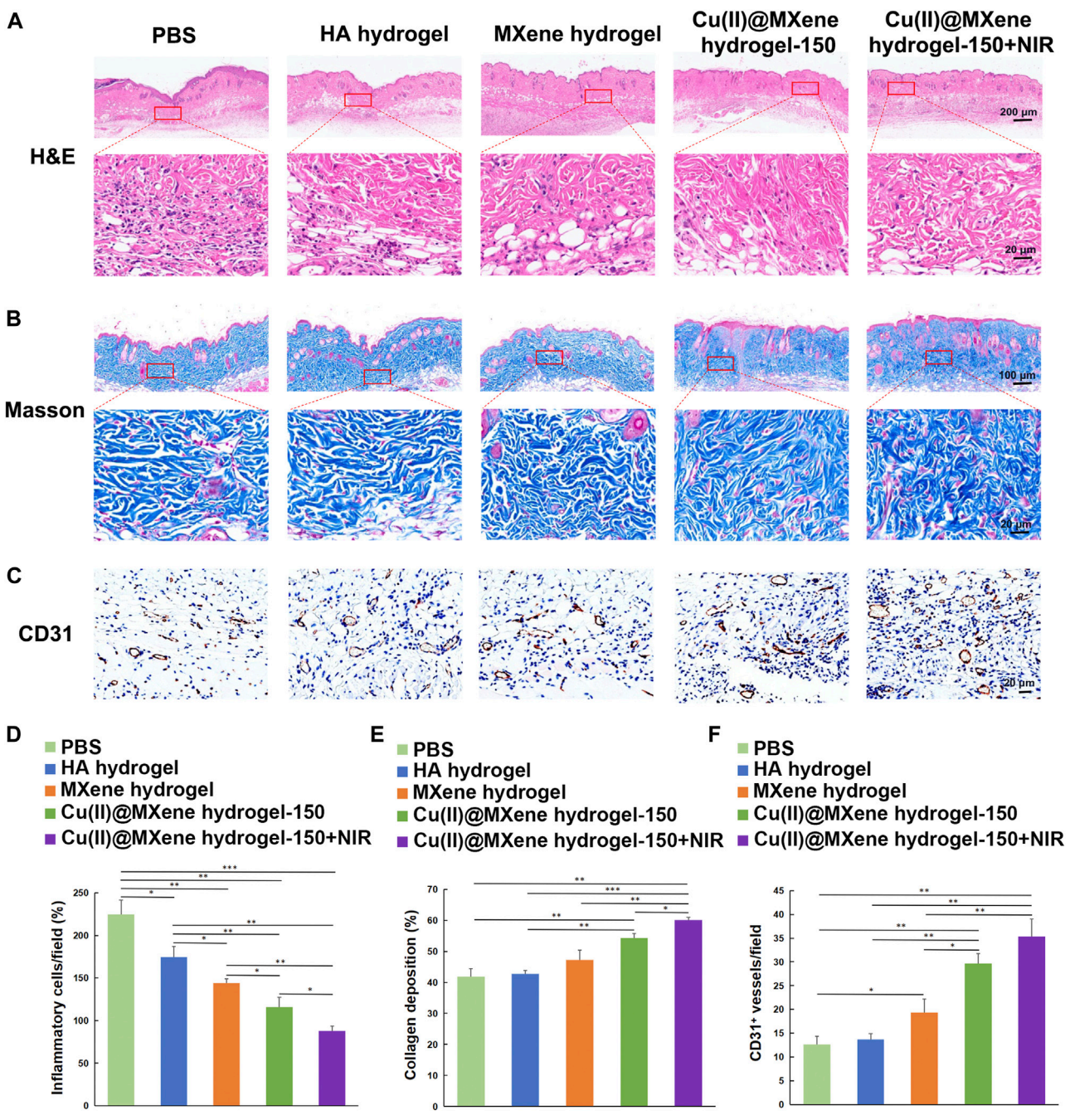

FIGURE 7
Histologic analysis of the wound tissues. **(A)** H&E and **(B)** Masson's trichrome staining of wound tissues of the five groups at the day 14. **(C)** IHC images of wound tissues stained for CD31. Quantitative analysis of the **(D)** inflammatory condition based on H&E staining, **(E)** collagen deposition on Masson's trichrome staining, and **(F)** vessel formation based on CD31 IHC staining. *$p < 0.05$. **$p < 0.01$. ***$p < 0.001$.

(Figure 5B). Angiogenesis is a vital process during the wound healing (Shao et al., 2023). However, endothelial cell dysfunction usually occurred under oxidative stress. To assess the role of Cu(II)@MXene hydrogel in angiogenesis, *in vitro* tube formation assays were obtained by co-culturing HUVECs with hydrogel extract on Matrigel substrates. As shown in Figures 5C–E, the tube formation was not obvious in PBS control group, HA hydrogel group, and MXene hydrogel group. In contrast, these three Cu(II)@MXene hydrogel groups showed a noticeable promoted trend of tube formation through the increase of the Cu(II)@MXene loading concentration. The quantitative analysis (Figures 5D, E) showed that the mean branch points and mean tube length in Cu(II)@MXene hydrogel group (150 μg/mL) was 3.5-fold and 2.3-fold higher than these in the PBS control group, respectively. These results suggested that the

Cu^{2+} release from Cu(II)@MXene hydrogel could play a vital facilitation role in angiogenesis in wound healing.

The photothermal antibacterial efficiency was evaluated by using *E. coli*, which represented for Gram-negative bacteria, and *S. aureus*, which represented for Gram-positive bacteria. The hydrogels were co-cultured with bacteria with or without NIR irradiation for 5 min, and then after another 12 h of culture. As shown in Figures 6A, B, the MXene hydrogel that only had photothermal effect (45°C) showed a quite low antibacterial effect. As for the Cu(II)@MXene hydrogel + NIR group, the antibacterial efficiency based on the collaboration of photothermal effect and released Cu^{2+} (Supplementary Figure S14) was obvious for *E. coli* and *S. aureus*. The OD_{600} value of the bacterial suspension (Supplementary Figure S15) was also tested to confirm that the antibacterial efficiency of the Cu(II)@MXene hydrogel under NIR irradiation could reach to about 80%. Considering that the concentration of Cu(II)@MXene was fixed at a low level, this result should be satisfactory. After this, an infected wound model of C57BL/6 mice was established for *in vivo* evaluation of wound healing (Figure 6C). Just as we suspected, the Cu(II)@MXene hydrogel NIR groups had the best wound healing efficiency among these four groups after 2 weeks (Figures 6D, E). Compared to Cu(II)@MXene hydrogel group, the wound closure rate increased about 30% in Cu(II)@MXene hydrogel + NIR group, indicating the importance of the bacteria removing during the wound healing.

Firstly, the collected skin samples were analyzed by H&E staining to observe the status of the neo-epidermis and the inflammatory condition. As shown in Figure 7A, after Cu(II)@MXene hydrogel and NIR treatment, the epithelialization in wound was more complete than the other three groups. Furthermore, fewer inflammatory cells were found in the neo-epidermis of all the MXene hydrogel, Cu(II)@MXene hydrogel, and Cu(II)@MXenehydrogel + NIR group than that in Control group and HA hydrogel group (Figures 7A, D; Supplementary Figure S16). This was because that the ROS removal by MXene was of great help to reduce the inflammation in the wound. From the Masson's trichrome staining, we further analyzed the collagen deposition in the regeneration skin tissue, with the Cu(II)@MXene hydrogel + NIR group showing the highest degree (Figures 7B, E; Supplementary Figure S17). Section staining of the wound edges further revealed differences in regenerated blood vessels and collagen in the new skin tissue (Supplementary Figures S18, S19). Meanwhile, both the Cu(II)@MXene hydrogel group and Cu(II)@MXene hydrogel + NIR group showed a stronger IHC staining of CD31, a marker for vessel regeneration, than the other groups (Figures 7C, F; Supplementary Figure S20), demonstrating the angiogenesis promopted by the Cu^{2+} release. All of these results proved our Cu(II)@MXene photothermal hydrogel system influenced every step in the infected wound healing positively.

Conclusion

In short, we successfully prepared a kind of Cu(II)@MXene nanosheet and then constructed the injectable, self-healing, and bio-adhesive Cu(II)@MXene photothermal hydrogel as the dressing for infected wounds. These properties allowed our hydrogels provide long-term protection for wounds. Moreover, after covering the wounds, this Cu(II)@MXene hydrogel effectively remove bacteria by its photothermal conversion under NIR. Meanwhile, this Cu(II)@MXene hydrogel scavenged the excess ROS to reduce inflammation and released the Cu^{2+} to promote angiogenesis. In this way, the Cu(II)@MXene hydrogel could rebuild a favorable microenvironment in infected wounds to accelerated the skin regeneration.

Data availability statement

The original contributions presented in the study are included in the article/Supplementary Material, further inquiries can be directed to the corresponding authors.

Ethics statement

The animal study was approved by the Institutional Animal Care and Use Committee at Tongji Medical College, Huazhong University of Science and Technology (HUST). The study was conducted in accordance with the local legislation and institutional requirements.

Author contributions

ML: Conceptualization, Data curation, Formal Analysis, Methodology, Writing–original draft, Writing–review and editing. LZ: Data curation, Formal Analysis, Methodology, Writing–review and editing. KZ: Data curation, Methodology, Writing–review and editing. YY: Data curation, Formal Analysis, Writing–review and editing. YH: Formal Analysis, Writing–review and editing. KC: Formal Analysis, Writing–review and editing. FW: Formal Analysis, Methodology, Writing–review and editing. KuZ: Investigation, Writing–review and editing. WL: Writing–review and editing, Funding acquisition. BM: Data curation, Funding acquisition, Supervision, Writing–review and editing. XX: Conceptualization, Data curation, Funding acquisition, Supervision, Writing–review and editing. QF: Conceptualization, Formal Analysis, Funding acquisition, Methodology, Supervision, Writing–original draft, Writing–review and editing.

Funding

The author(s) declare financial support was received for the research, authorship, and/or publication of this article. This work was supported by the National Natural Science Foundation of China (31900963), the Natural Science Foundation of Fujian Province (2020J02033, 2022Y0005, and 2023J011023), Fuzhou Science and Technology Project (2021-P-037 and 2022-Y-003), the Natural Science Foundation of Chongqing (cstc2021jcyj-cxttX0002), and Renhe Hospital Excellent Youth Program in Baoshan District (BSRHYQ-2021-07).

Conflict of interest

The authors declare that the research was conducted in the absence of any commercial or financial relationships that could be construed as a potential conflict of interest.

Publisher's note

All claims expressed in this article are solely those of the authors and do not necessarily represent those of their affiliated organizations, or those of the publisher, the editors and the reviewers. Any product that may be evaluated in this article, or claim that may be made by its manufacturer, is not guaranteed or endorsed by the publisher.

Supplementary material

The Supplementary Material for this article can be found online at: https://www.frontiersin.org/articles/10.3389/fbioe.2023.1308184/full#supplementary-material

References

Altinbasak, I., Jijie, R., Barras, A., Golba, B., Sanyal, R., Bouckaert, J., et al. (2018). Reduced graphene-oxide-embedded polymeric nanofiber mats: an "On-Demand" photothermally triggered antibiotic release platform. *ACS Appl. Mater Interfaces* 10 (48), 41098–41106. doi:10.1021/acsami.8b14784

Cui, L., Li, J., Guan, S., Zhang, K., Zhang, K., and Li, J. (2022). Injectable multifunctional CMC/HA-DA hydrogel for repairing skin injury. *Mater Today Bio* 14, 100257. doi:10.1016/j.mtbio.2022.100257

Feng, A., Yu, Y., Wang, Y., Jiang, F., Yu, Y., Mi, L., et al. (2017). Two-dimensional MXene Ti3C2 produced by exfoliation of Ti3AlC2. *Mater. Des.* 114, 161–166. doi:10.1016/j.matdes.2016.10.053

Feng, W., Han, X., Hu, H., Chang, M., Ding, L., Xiang, H., et al. (2021). 2D vanadium carbide MXenzyme to alleviate ROS-mediated inflammatory and neurodegenerative diseases. *Nat. Commun.* 12 (1), 2203. doi:10.1038/s41467-021-22278-x

Fu, M., Gan, Y., Jiang, F., Lv, X., Tan, N., Zhao, X., et al. (2022). Interpenetrating polymer network hydrogels formed using antibiotics as a dynamic crosslinker for treatment of infected wounds. *Adv. Healthc. Mater* 11 (15), e2200902. doi:10.1002/adhm.202200902

Jiang, W., Chen, Y., Zhao, L., Xu, J., Zhao, R., Serpe, M. J., et al. (2020). Bioinspired tissue-compliant hydrogels with multifunctions for synergistic surgery–photothermal therapy. *J. Mater. Chem. B* 8 (44), 10117–10125. doi:10.1039/d0tb01907k

Jin, X., Shang, Y., Zou, Y., Xiao, M., Huang, H., Zhu, S., et al. (2020). Injectable hypoxia-induced conductive hydrogel to promote diabetic wound healing. *ACS Appl. Mater. Interfaces* 12 (51), 56681–56691. doi:10.1021/acsami.0c13197

Lee, S. Y., Jeon, S., Kwon, Y. W., Kwon, M., Kang, M. S., Seong, K.-Y., et al. (2022). Combinatorial wound healing therapy using adhesive nanofibrous membrane equipped with wearable LED patches for photobiomodulation. *Sci. Adv.* 8 (15), eabn1646. doi:10.1126/sciadv.abn1646

Li, L., Cheng, X., Huang, Q., Cheng, Y., Xiao, J., and Hu, J. (2022a). Sprayable antibacterial hydrogels by simply mixing of aminoglycoside antibiotics and cellulose nanocrystals for the treatment of infected wounds. *Adv. Healthc. Mater.* 11 (20), 2201286. doi:10.1002/adhm.202201286

Li, R., Zhang, L., Shi, L., and Wang, P. (2017). MXene Ti3C2: an effective 2D light-to-heat conversion material. *ACS Nano* 11 (4), 3752–3759. doi:10.1021/acsnano.6b08415

Li, Y., Fu, R., Duan, Z., Zhu, C., and Fan, D. (2022c). Artificial nonenzymatic antioxidant MXene nanosheet-anchored injectable hydrogel as a mild photothermal-controlled oxygen release platform for diabetic wound healing. *ACS Nano* 16 (5), 7486–7502. doi:10.1021/acsnano.1c10575

Li, Z., You, S., Mao, R., Xiang, Y., Cai, E., Deng, H., et al. (2022b). Architecting polyelectrolyte hydrogels with Cu-assisted polydopamine nanoparticles for photothermal antibacterial therapy. *Mater. Today Bio* 15, 100264. doi:10.1016/j.mtbio.2022.100264

Li, Z., Zhang, H., Han, J., Chen, Y., Lin, H., and Yang, T. (2018). Surface nanopore engineering of 2D MXenes for targeted and synergistic multitherapies of hepatocellular carcinoma. *Adv. Mater.* 30 (25), 1706981. doi:10.1002/adma.201706981

Liang, Y., Li, Z., Huang, Y., Yu, R., and Guo, B. (2021). Dual-dynamic-bond cross-linked antibacterial adhesive hydrogel sealants with on-demand removability for post-wound-closure and infected wound healing. *ACS Nano* 15 (4), 7078–7093. doi:10.1021/acsnano.1c00204

Lin, H., Wang, X., Yu, L., Chen, Y., and Shi, J. (2017). Two-dimensional ultrathin MXene ceramic nanosheets for photothermal conversion. *Nano Lett.* 17 (1), 384–391. doi:10.1021/acs.nanolett.6b04339

Liu, B., Li, C., Chen, G., Liu, B., Deng, X., Wei, Y., et al. (2017). Synthesis and optimization of MoS2@ Fe3O4-ICG/Pt (IV) nanoflowers for MR/IR/PA bioimaging and combined PTT/PDT/chemotherapy triggered by 808 nm laser. *Adv. Sci.* 4 (8), 1600540. doi:10.1002/advs.201600540

Liu, P., Xiong, Y., Chen, L., Lin, C., Yang, Y., Lin, Z., et al. (2022). Angiogenesis-based diabetic skin reconstruction through multifunctional hydrogel with sustained releasing of M2 Macrophage-derived exosome. *Chem. Eng. J.* 431, 132413. doi:10.1016/j.cej.2021.132413

Liu, Y., and Shi, J. (2019). Antioxidative nanomaterials and biomedical applications. *Nano Today* 27, 146–177. doi:10.1016/j.nantod.2019.05.008

Ma, T., Zhai, X., Huang, Y., Zhang, M., Zhao, X., Du, Y., et al. (2021). A smart nanoplatform with photothermal antibacterial capability and antioxidant activity for chronic wound healing. *Adv. Healthc. Mater* 10 (13), e2100033. doi:10.1002/adhm.202100033

Mitra, D., Kang, E.-T., and Neoh, K. G. (2020). Antimicrobial copper-based materials and coatings: potential multifaceted biomedical applications. *ACS Appl. Mater. Interfaces* 12 (19), 21159–21182. doi:10.1021/acsami.9b17815

Murali, A., Lokhande, G., Deo, K. A., Brokesh, A., and Gaharwar, A. K. (2021). Emerging 2D nanomaterials for biomedical applications. *Mater. Today* 50, 276–302. doi:10.1016/j.mattod.2021.04.020

Ni, G., Yang, G., He, Y., Li, X., Du, T., Xu, L., et al. (2020). Uniformly sized hollow microspheres loaded with polydopamine nanoparticles and doxorubicin for local chemo-photothermal combination therapy. *Chem. Eng. J.* 379, 122317. doi:10.1016/j.cej.2019.122317

Peng, M., Wang, L., Li, L., Tang, X., Huang, B., Hu, T., et al. (2021). Manipulating the interlayer spacing of 3D MXenes with improved stability and zinc-ion storage capability. *Adv. Funct. Mater.* 32 (7). doi:10.1002/adfm.202109524

Qi, L., Zhang, C., Wang, B., Yin, J., and Yan, S. (2022). Progress in hydrogels for skin wound repair. *Macromol. Biosci.* 22 (7), e2100475. doi:10.1002/mabi.202100475

Qian, X., Gu, Z., and Chen, Y. (2017). Two-dimensional black phosphorus nanosheets for theranostic nanomedicine. *Mater. Horizons* 4 (5), 800–816. doi:10.1039/c7mh00305f

Rasool, K., Helal, M., Ali, A., Ren, C. E., Gogotsi, Y., and Mahmoud, K. A. (2016). Antibacterial Activity of $Ti_3C_2T_{<i>x</i>}$ MXene. *ACS Nano* 10 (3), 3674–3684. doi:10.1021/acsnano.6b00181

Ren, X., Huo, M., Wang, M., Lin, H., Zhang, X., Yin, J., et al. (2019). Highly catalytic niobium carbide (MXene) promotes hematopoietic recovery after radiation by free radical scavenging. *ACS Nano* 13 (6), 6438–6454. doi:10.1021/acsnano.8b09327

Sarycheva, A., and Gogotsi, Y. (2020). Raman spectroscopy analysis of the structure and surface chemistry of $Ti_3C_2T_x$ MXene. *Chem. Mater.* 32 (8), 3480–3488. doi:10.1021/acs.chemmater.0c00359

Sawaya, A. P., Stone, R. C., Brooks, S. R., Pastar, I., Jozic, I., Hasneen, K., et al. (2020). Deregulated immune cell recruitment orchestrated by FOXM1 impairs human diabetic wound healing. *Nat. Commun.* 11 (1), 4678. doi:10.1038/s41467-020-18276-0

Shao, Z., Yin, T., Jiang, J., He, Y., Xiang, T., and Zhou, S. (2023). Wound microenvironment self-adaptive hydrogel with efficient angiogenesis for promoting diabetic wound healing. *Bioact. Mater.* 20, 561–573. doi:10.1016/j.bioactmat.2022.06.018

Song, H., Zu, D., Li, C., Zhou, R., Wang, Y., Zhang, W., et al. (2021). Ultrafast activation of peroxymonosulfate by reduction of trace Fe3+ with Ti3C2 MXene under neutral and alkaline conditions: reducibility and confinement effect. *Chem. Eng. J.* 423, 130012. doi:10.1016/j.cej.2021.130012

Stern, R., Kogan, G., Jedrzejas, M. J., and Šoltés, L. (2007). The many ways to cleave hyaluronan. *Biotechnol. Adv.* 25 (6), 537–557. doi:10.1016/j.biotechadv.2007.07.001

Suhaeri, M., Noh, M. H., Moon, J.-H., Kim, I. G., Oh, S. J., Ha, S. S., et al. (2018). Novel skin patch combining human fibroblast-derived matrix and ciprofloxacin for infected wound healing. *Theranostics* 8 (18), 5025–5038. doi:10.7150/thno.26837

Venkata Subbaiah, Y., Saji, K., and Tiwari, A. (2016). Atomically thin MoS2: a versatile nongraphene 2D material. *Adv. Funct. Mater.* 26 (13), 2046–2069. doi:10.1002/adfm.201504202

Wu, D., Shou, X., Yu, Y., Wang, X., Chen, G., Zhao, Y., et al. (2022). Biologics-loaded photothermally dissolvable hyaluronic acid microneedle patch for psoriasis treatment. *Adv. Funct. Mater.* 32 (47), 5847. doi:10.1002/adfm.202205847

Xiao, J., Chen, S., Yi, J., Zhang, H., and Ameer, G. A. (2017). A cooperative copper metal-organic framework-hydrogel system improves wound healing in diabetes. *Adv. Funct. Mater* 27 (1), 1604872. doi:10.1002/adfm.201604872

Xiao, J., Zhu, Y., Huddleston, S., Li, P., Xiao, B., Farha, O. K., et al. (2018). Copper metal–organic framework nanoparticles stabilized with folic acid improve wound healing in diabetes. *ACS Nano* 12 (2), 1023–1032. doi:10.1021/acsnano.7b01850

Xu, P., Wang, P., Li, X., Wei, R., Wang, X., Yang, C., et al. (2022). Efficient peroxymonosulfate activation by CuO-Fe2O3/MXene composite for atrazine degradation: performance, coexisting matter influence and mechanism. *Chem. Eng. J.* 440, 135863. doi:10.1016/j.cej.2022.135863

Xu, W., Qian, J., Hou, G., Suo, A., Wang, Y., Wang, J., et al. (2017). Hyaluronic acid-functionalized gold nanorods with pH/NIR dual-responsive drug release for synergetic targeted photothermal chemotherapy of breast cancer. *ACS Appl. Mater. Interfaces* 9 (42), 36533–36547. doi:10.1021/acsami.7b08700

Xuan, Q., Jiang, F., Dong, H., Zhang, W., Zhang, F., Ma, T., et al. (2021). Bioinspired intrinsic versatile hydrogel fabricated by amyloidal toxin simulant-based nanofibrous assemblies for accelerated diabetic wound healing. *Adv. Funct. Mater.* 31 (49). doi:10.1002/adfm.202106705

Yang, B., Song, J., Jiang, Y., Li, M., Wei, J., Qin, J., et al. (2020). Injectable adhesive self-healing multicross-linked double-network hydrogel facilitates full-thickness skin wound healing. *ACS Appl. Mater. Interfaces* 12 (52), 57782–57797. doi:10.1021/acsami.0c18948

Yang, B., Yin, J., Chen, Y., Pan, S., Yao, H., Gao, Y., et al. (2018). 2D-black-phosphorus-reinforced 3D-printed scaffolds: a stepwise countermeasure for osteosarcoma. *Adv. Mater.* 30 (10), 1705611. doi:10.1002/adma.201705611

Yin, J., Han, Q., Zhang, J., Liu, Y., Gan, X., Xie, K., et al. (2020). MXene-based hydrogels endow polyetheretherketone with effective osteogenicity and combined treatment of osteosarcoma and bacterial infection. *ACS Appl. Mater. Interfaces* 12 (41), 45891–45903. doi:10.1021/acsami.0c14752

Zeng, Q., Qian, Y., Huang, Y., Ding, F., Qi, X., and Shen, J. (2021). Polydopamine nanoparticle-dotted food gum hydrogel with excellent antibacterial activity and rapid shape adaptability for accelerated bacteria-infected wound healing. *Bioact. Mater.* 6 (9), 2647–2657. doi:10.1016/j.bioactmat.2021.01.035

Zhang, J., Kong, N., Hegh, D., Usman, K. A. S., Guan, G., Qin, S., et al. (2020a). Freezing Titanium carbide aqueous dispersions for ultra-long-term storage. *ACS Appl. Mater. Interfaces* 12 (30), 34032–34040. doi:10.1021/acsami.0c06728

Zhang, K., Sun, J., Song, J., Gao, C., Wang, Z., Song, C., et al. (2020b). Self-healing Ti3C2 MXene/PDMS supramolecular elastomers based on small biomolecules modification for wearable sensors. *ACS Appl. Mater. Interfaces* 12 (40), 45306–45314. doi:10.1021/acsami.0c13653

Zhao, H., Huang, J., Li, Y., Lv, X., Zhou, H., Wang, H., et al. (2020). ROS-scavenging hydrogel to promote healing of bacteria infected diabetic wounds. *Biomaterials* 258, 120286. doi:10.1016/j.biomaterials.2020.120286

Zhao, Y., Li, Z., Song, S., Yang, K., Liu, H., Yang, Z., et al. (2019). Skin-inspired antibacterial conductive hydrogels for epidermal sensors and diabetic foot wound dressings. *Adv. Funct. Mater.* 29 (31), 1474. doi:10.1002/adfm.201901474

frontiers | Frontiers in Bioengineering and Biotechnology

TYPE Original Research
PUBLISHED 13 November 2023
DOI 10.3389/fbioe.2023.1300336

Check for updates

OPEN ACCESS

EDITED BY
Dan Shao,
South China University of Technology, China

REVIEWED BY
Tao Yang,
Soochow University, China
Jiying Liu,
University of Michigan, United States

*CORRESPONDENCE
Pengyu Pan,
panpengyu09@sina.com
Guobiao Liang,
liangguobiao6708@163.com

†These authors have contributed equally to this work and share first authorship

RECEIVED 23 September 2023
ACCEPTED 01 November 2023
PUBLISHED 13 November 2023

CITATION
Bi S, Lin H, Zhu K, Zhu Z, Zhang W, Yang X, Chen S, Zhao J, Liu M, Pan P and Liang G (2023), Chitosan-salvianolic acid B coating on the surface of nickel-titanium alloy inhibits proliferation of smooth muscle cells and promote endothelialization. *Front. Bioeng. Biotechnol.* 11:1300336. doi: 10.3389/fbioe.2023.1300336

COPYRIGHT
© 2023 Bi, Lin, Zhu, Zhu, Zhang, Yang, Chen, Zhao, Liu, Pan and Liang. This is an open-access article distributed under the terms of the Creative Commons Attribution License (CC BY). The use, distribution or reproduction in other forums is permitted, provided the original author(s) and the copyright owner(s) are credited and that the original publication in this journal is cited, in accordance with accepted academic practice. No use, distribution or reproduction is permitted which does not comply with these terms.

Chitosan-salvianolic acid B coating on the surface of nickel-titanium alloy inhibits proliferation of smooth muscle cells and promote endothelialization

Shijun Bi[1,2†], Hao Lin[3†], Kunyuan Zhu[1,4], Zechao Zhu[1], Wenxu Zhang[1], Xinyu Yang[1], Shanshan Chen[3], Jing Zhao[3], Meixia Liu[3], Pengyu Pan[1*] and Guobiao Liang[1*]

[1]Department of Neurosurgery, General Hospital of Northern Theater Command, Shenyang, China, [2]Graduate School, Dalian Medical University, Dalian, China, [3]Institute of Metal Research, Chinese Academy of Sciences, Shenyang, China, [4]Graduate School, China Medical University, Shenyang, China

Introduction: Intracranial stents are of paramount importance in managing cerebrovascular disorders. Nevertheless, the currently employed drug-eluting stents, although effective in decreasing in-stent restenosis, might impede the re-endothelialization process within blood vessels, potentially leading to prolonged thrombosis development and restenosis over time.

Methods: This study aims to construct a multifunctional bioactive coating to enhance the biocompatibility of the stents. Salvianolic acid B (SALB), a bioactive compound extracted from Salvia miltiorrhiza, exhibits potential for improving cardiovascular health. We utilized dopamine as the base and adhered chitosan-coated SALB microspheres onto nickel-titanium alloy flat plates, resulting in a multifunctional drug coating.

Results: By encapsulating SALB within chitosan, the release period of SALB was effectively prolonged, as evidenced by the *in vitro* drug release curve showing sustained release over 28 days. The interaction between the drug coating and blood was examined through experiments on water contact angle, clotting time, and protein adsorption. Cellular experiments showed that the drug coating stimulates the proliferation, adhesion, and migration of human umbilical vein endothelial cells.

Discussion: These findings indicate its potential to promote re-endothelialization. In addition, the bioactive coating effectively suppressed smooth muscle cells proliferation, adhesion, and migration, potentially reducing the occurrence of neointimal hyperplasia and restenosis. These findings emphasize the exceptional biocompatibility of the newly developed bioactive coating and demonstrate its potential clinical application as an innovative strategy to improve stent therapy efficacy. Thus, this coating holds great promise for the treatment of cerebrovascular disease.

KEYWORDS

cerebrovascular disease, stent stenosis, interventional therapy, salvianolic acid B, chitosan, surface modification, endothelialization, restenosis

1 Introduction

Cerebrovascular disease, following ischemic heart disease, is the second major factor in global mortality and morbidity (Diseases and Injuries, 2020). In the treatment of cerebrovascular diseases, intracranial stents hold a pivotal position. Over time, stent technology has improved to include drug-eluting stents (DES) (Lee et al., 2018). DES involve the application of a pharmaceutical coating onto the surface of a metallic stent. After implantation, these stents gradually release drugs, thereby assisting in the inhibition of scar tissue formation around the stent and the maintenance of vascular patency (Lyu et al., 2020). Currently, widely utilized DES predominantly encompass rapamycin-eluting and paclitaxel-eluting stents (Sabate, 2022). Furthermore, bioactive stent coatings also have made rapid advancements, including polymer-coated stents, fibrin-coated metal stents, and phosphatidylcholine-coated stents. Polymer-coated stents have garnered significant attention due to their intrinsic elasticity and their capacity to reduce coagulation system activation (Chen et al., 2021). This feature results in a lowered risk of acute thrombus formation. Fibrin-coated metal stents have demonstrated the potential to promote endothelialization during peripheral vascular grafting and facilitate hemostasis during surgery (Link et al., 2020). This contributes to the preservation of the structural integrity of local blood vessels and a reduced risk of restenosis. Additionally, phosphorylcholine-coated stents have gained prominence owing to their hydrogel properties, which hinder protein adhesion, reduce thrombus formation, and enhance cellular biocompatibility (Liu et al., 2020). However, there are still significant limitations associated with the current approaches. When solely employing polymer coatings, experimental outcomes have not been as promising. Consequently, they are increasingly regarded as carriers for anti-thrombotic and anti-proliferative agents (Tzafriri et al., 2019). Additionally, it's worth noting that DES can potentially incite local tissue inflammation and immune responses (Choe et al., 2020). An even more critical concern is, although DES have reduced in-stent restenosis, a downside accompanies their use: the delayed re-endothelialization of the vascular wall (Qiu et al., 2022). Delayed re-endothelialization is a potential component that contributes to the establishment of late thrombosis and restenosis (Joner et al., 2006). Arterial healing after stent implantation is crucial in preventing stent-related complications, and the rebuilding of endothelial cells (ECs) has a substantial impact on recovery following stent insertion (Inoue et al., 2011). Stent coating design should shift its focus from individual targets to addressing issues such as delayed re-endothelialization, thrombosis, and restenosis. Additionally, stent coatings must possess high biocompatibility and multifunctionality to provide a favorable biological environment for re-endothelialization (Tahir et al., 2013). Therefore, our research aims to construct a novel coating with dual functionality: inhibiting smooth muscle cell proliferation while promoting endothelialization.

Salvianolic acid B (SALB), is well-known for its antioxidant activity (Katary et al., 2019). Furthermore, recent research has emphasized its anti-inflammatory and anti-apoptotic properties, which are of particular importance in the context of cardiovascular and cerebrovascular diseases (Xiao et al., 2020). In addition to the aforementioned functions, SALB serves a crucial dual purpose of inhibiting excessive proliferation of smooth muscle cells (SMCs), which is the primary cause of restenosis, and promoting angiogenesis, which is indicative of healthy vascular repair and regeneration (Ji et al., 2019; Hu et al., 2021b). This dual function of SALB aligns with the aim of enhancing stent biocompatibility, making SALB an ideal choice for improving vascular stents to withstand restenosis and promote vascular healing. Therefore, we hypothesize that SALB can be utilized to modify vascular stents to enhance their biocompatibility. Currently, the scientific literature only documents a limited amount of research on the use of SALB to modify the surface of vascular stents (Ji et al., 2019). The maximum blood concentration (Cmax) of SALB is approximately 910 μg/ml, and its half-life ($t_{1/2}$) is approximately 105 min, which may not be sufficient for endothelial reconstruction (Wu et al., 2006). Chitosan has been demonstrated to be a drug delivery carriage and is increasingly being considered as a candidate material for tissue engineering (Khor and Lim, 2003). Chitosan demonstrates biodegradability, low toxicity, and antimicrobial activity, all of which are vital properties for implantable stents (Kim C. H. et al., 2018). Chitosan is frequently used as a carrier for sustained drug release in numerous routes of administration, such as oral, nasal, and mucosal delivery, aiming to achieve prolonged drug delivery (Mengatto et al., 2012). Our previous research on chitosan coating has shown that it has good biological activity and corrosion resistance (Eren et al., 2022). Additionally, the potential of chitosan to improve the biocompatibility of materials has been demonstrated (Venkatesan et al., 2014). This study optimized the surface of chitosan by utilizing its drug release function and its good biocompatibility and biodegradability (Abourehab et al., 2022). Therefore, our plan is to encapsulate chitosan on SALB to achieve the objective of prolonged drug release. Polydopamine (PDA) can essentially deposit on all types of organic and inorganic materials, forming functional coatings on their surfaces (Lee et al., 2007). To research the biological impacts of the stent on preventing restenosis and promoting endothelialization, nickel-titanium alloy flat plates were used in this experiment to imitate the stent. Therefore, our first step is to coat nickel-titanium alloy flat plates with a PDA layer. Subsequently, we will immobilize chitosan-encapsulated SALB microspheres onto the surface, thereby constructing a multifunctional drug coating.

To evaluate the promoting effect of this bioactive coating stent on endothelialization, we utilized methods such as biocompatibility experiments and cell experiments. This study aims to extend the current technology and enhance the material properties through an original approach.

2 Materials and methods

2.1 Materials

Salvianolic acid B (SALB) was acquired from Push Biotechnology (Chengdu, China). Dopamine hydrochloride, chitosan, and Crystal Violet Ammonium Oxalate Solution were acquired from Solarbio (Beijing, China). Nickel-titanium alloy flat plates were purchased from Yuyue Metal Products (Changzhou, China). Human umbilical vein endothelial cells (HUVECs) and smooth muscle cells (SMCs) were obtained from iCell Bioscience

(Shanghai, China). Transwell chambers were procured from Nest Biotechnology (Wuxi, China).

2.2 Sample preparation

1×1 cm^2 round nickel-titanium alloy flat plates were polished using sandpaper and then sequentially cleaned with acetone, anhydrous ethanol, and deionized water. A 2 mg/mL PDA solution was made by diluting dopamine hydrochloride in Tris-HCl buffer (10 mM, pH 8.5). The PDA solution was used to soak the nickel-titanium alloy samples, which were shaken for 24 h. To obtain nickel-titanium alloy samples coated with PDA, the samples were then washed with deionized water and allowed to air dry for 24 h.

The PDA-coated nickel-titanium alloy samples were submerged in a 2.0 mg/ml SALB solution at 4°C for 48 h. The samples were then air dried after being rinsed with PBS buffer solution. To create a solution containing 2.5 mg/ml of chitosan, add chitosan to an acetic acid solution and then raise the pH to 4.5. Stir the solution at room temperature until fully dissolved. Next, SALB was added to a solution of chitosan and stirred until complete dissolution. The final concentration of SALB was 2 mg/ml. Under high-speed magnetic stirring (4,000 rpm/min), a syringe was used to slowly add a 2 mg/ml solution of sodium tripolyphosphate (TPP) while stirring for a half-hour at room temperature. Finally, the chitosan-SALB nanoparticle solution underwent purification by passing through a membrane filter with a 0.22 μm micropore. The PDA-coated nickel-titanium alloy samples were then immersed in the purified chitosan-SALB nanoparticle solution at 4°C for 2 days. Following a thorough washing with PBS buffer solution, the samples were allowed to air-dry.

We used bare metal and dopamine-coated samples as the control group in all experiments to account for the potential biological reaction of dopamine. "BARE" refers to the unmodified nickel-titanium alloy flat plates, "PDA" refers to the single PDA coating, "SALB" refers to the coating of SALB on the PDA layer, and "CS-SALB" refers to the coating of chitosan-coated SALB on the PDA layer.

2.3 Surface characteristics

Scanning electron microscopy (SEM) (Quanta 450 FEG, FEI, Hillsboro, United States) was used to examine the nickel-titanium alloy plates' coated surfaces with nanoparticles. The water contact angle of the nickel-titanium alloy plates' surface was characterized using a water contact angle measurement device. The nickel-titanium alloy samples were fixed on the sample stage, and a droplet of distilled water was placed on the surface. After 2 s, the water contact angle was measured. Using ImageJ software, the samples' water contact angles at the surface were examined.

2.4 Drug release *in vitro*

The SALB and CS-SALB group samples were immersed in test tubes containing 3 ml of PBS solution and continuously shaken at 37°C and 60 rpm. 1 ml of the solution was taken out of the test tubes at predetermined intervals, and an equivalent volume of PBS solution was added to keep the total volume constant. Samples were collected at specific intervals: 6, 12, 18, 24, and 36 h, and 2, 4, 7, 14, and 28 days. The collected solution from the test tubes was subjected to ultrasound treatment, followed by filtration, and a microplate reader (Epoch, Biotek, Winooski, United States) was used to measure the absorbance at 280 nm. The release standard curve of SALB was constructed, and the release amount was calculated from the release absorbance value.

2.5 Hemocompatibility experiments

The automated blood coagulation analyzer (CS-5100, Sysmex, Kobe, Japan) conducted tests for activated partial thromboplastin time (APTT) and prothrombin time (PT). After soaking each set of samples in PBS solution for an hour, 500 μl of platelet-poor plasma were added, followed by a 30-min incubation at 37°C. APTT and PT tests were then conducted to analyze the clotting time of the samples.

The samples were submerged in a solution of PBS containing BSA (1 mg/ml) for 1 ml, and then incubated for 1 h at 37°C to determine the quantity of adsorbed protein. The difference in concentration of the BSA solution before and after immersion is used to calculate the adsorbed protein.

2.6 HUVECs and SMCs proliferation assay

HUVECs and SMCs were grown in DMEM with 10% FBS supplement and incubated at 37°C in a 5% CO_2 incubator (BC-J160S, Boxun, Shanghai, China) for the duration of the experiment. 24-well culture plates were used to hold the samples. Each well was then filled with a 1 mL solution of HUVECs or SMCs (2×10^3 cells/mL). The plates were incubated for 1, 3, and 5 days, respectively, at 37°C and 5% CO_2. After the allotted incubation time had passed, the culture media was carefully removed, and each well received 1 mL of DMEM with 100 μL of Cell Counting Kit-8 (CCK-8). After 2 h of incubation at 37°C, the samples were examined to determine the number of cells in each group by measuring the optical density (OD) at 450 nm with a microplate reader.

2.7 HUVECs and SMCs migration assay

The groups of samples underwent sterilization using ethylene oxide and were then immersed in 2 mL of DMEM for 72 h to obtain the respective extracts. HUVECs or SMCs were infused into 6-well plates at a density of 5×10^5 cells/ml and cultivated in 10% FBS DMEM until a monolayer of cells formed. A 200 μL pipette tip was used to scrape the cell layer's surface in order to produce a cell-free area. Subsequently, 10% FBS DMEM was changed to serum-free DMEM that included extracts from each sample group. The migration of cells in the scratched region was seen under a light microscope (CKX-53, Olympus, Tokyo, Japan) at the appropriate time intervals following a 24-h incubation period at 37°C with 5% CO_2. The ImageJ software was used to analyze each collection of scratches.

The transwell chamber was used to analyze the effect of each set of samples on the migration of HUVECs and SMCs. First, the samples were placed in the lower chamber of the transwell chamber. Then, serum-free DMEM culture medium containing HUVECs or SMCs (200 μL, 1.0×10^5 cells/mL) was added to the upper chamber. The culture medium was taken out after 24 h of incubation. After using a cotton swab to clean the upper chamber and washing it with PBS, the cells were fixed for 30 min with 4% paraformaldehyde. After PBS-rinsing, 0.1% crystal violet solution was used to stain the cells. Cell migration to the lower chamber was observed under the microscope (CKX-53, Olympus, Tokyo, Japan). The cell numbers migrating to the lower chamber of the transwell chamber were counted using ImageJ software.

2.8 HUVECs and SMCs adhesion assay

A suspension of HUVECs (1×10^4 cells/mL) or SMCs (2×10^4 cells/mL) was placed in each well of the 24-well plates containing the samples. The plates were kept in a 37°C, 5% CO_2 incubator. After the medium had been removed after 3 days, the samples had been cleaned with PBS, and the cells had been fixed with 4% paraformaldehyde for 30 min. Each well was added to an antifade mounting medium containing DAPI stain and incubated for 5 min in the dark. Cell adhesion levels were assessed by observing the cells under a fluorescence microscope (BX-53, Olympus, Tokyo, Japan).

The cell culture media was taken out of the well plates and PBS-washed after 3 days of incubation. Following that, the samples from each group were fixed for 30 min in 4% paraformaldehyde. Afterwards, PBS was used to rinse the samples. Triton X-100 0.2% solution was used to permeabilize cells for 15 min at 4°C. The samples were then treated with 1% BSA for an hour at 37°C. Furthermore, the cells were stained with 1% fluorescently labeled phalloidin for 60 min at room temperature, protected from light, followed by washing with PBS. Incubate the sample in the dark with antifade mounting medium containing DAPI for 5 min. Finally, using fluorescence microscopy (BX-53, Olympus, Tokyo, Japan), the cell morphology of the sample is analyzed and photographed.

2.9 Statistical analysis

Version 9.5.0 of GraphPad Prism for Windows (GraphPad Software) was used to conduct the statistical analysis. All data are presented as mean ± standard deviation (SD). The two-way ANOVA and one-way ANOVA with Tukey *post hoc* comparison were used to compare the results. The statistical significance level was determined using a minimum sample size of three. Values of $p < 0.05$ were considered significant.

3 Results

3.1 Surface characteristics of nickel-titanium alloy samples

The nickel-titanium alloy plates' surface morphology was examined using SEM (Figure 1A). The SEM images revealed a relatively smooth surface of the nickel-titanium plates with only fine polishing lines. After fixation, the SALB nanospheres were uniformly adhered to the surface, presenting spherical shapes with a uniform particle size distribution. Water contact angle measurements were used to evaluate the hydrophilicity of the material's surface. Smaller contact angles indicate better hydrophilicity. Figure 1B shows the images of water contact angle testing for each group, and Figure 1C presents the water contact angle values for the BARE group (90.57° ± 1.32°), PDA group (29.67° ± 4.21°), SALB group (46.57° ± 2.29°), and CS-SALB group (51.33° ± 0.83°). The PDA group exhibited the best hydrophilicity, while the CS-SALB group showed significantly enhanced hydrophilicity compared to the BARE group. The SALB group's and the CS-SALB group's levels of hydrophilicity were not significantly different.

3.2 *In vitro* drug release

A standard curve of SALB concentration was generated using GraphPad Prism software for linear fitting (Figure 2A). The amount of SALB released from the drug coating on the sample's surface during the duration of the experiment was calculated by contrasting the absorbance values to the standard curve. The drug-loaded microspheres released the drug over time, as shown by the *in vitro* drug release behavior. The drug release curves of the CS-SALB group are shown in Figure 2B. After the rapid release during the first 2 days, the release rate of SALB slowed significantly with increasing release time. More than 80% of SALB was released cumulatively within a period of 28 days.

3.3 Hemocompatibility experiments

The results of coagulation function tests conducted on the surface of each sample group are presented in Figure 2C. There was no statistically significant difference in PT between the samples from any group. However, APTT was significantly prolonged in the SALB and CS-SALB groups. Figure 2D shows the amount of protein adsorbed onto the surfaces of the samples, with values for the BARE group (890.92 ± 3.94), PDA group (814.66 ± 4.71), SALB group (752.27 ± 3.77), and CS-SALB group (775.82 ± 4.47). The CS-SALB group showed significantly lower protein adsorption, indicating better blood compatibility.

3.4 Effects of nickel-titanium alloy plates on HUVECs and SMCs

The effect of each group of samples on cell proliferation is shown in Figures 3A, B. All samples showed continuous proliferation of cells on their surfaces during the 5-day incubation period. After 1 day of culture, there were no significant variations in the proliferation of HUVECs and SMCs across groups. On days 3 and 5, the SALB and CS-SALB groups' surfaces had a much greater rate of HUVECs proliferation than the BARE and PDA groups' surfaces. On day 5, there was no discernible difference between the SALB and CS-SALB groups in the pace at which

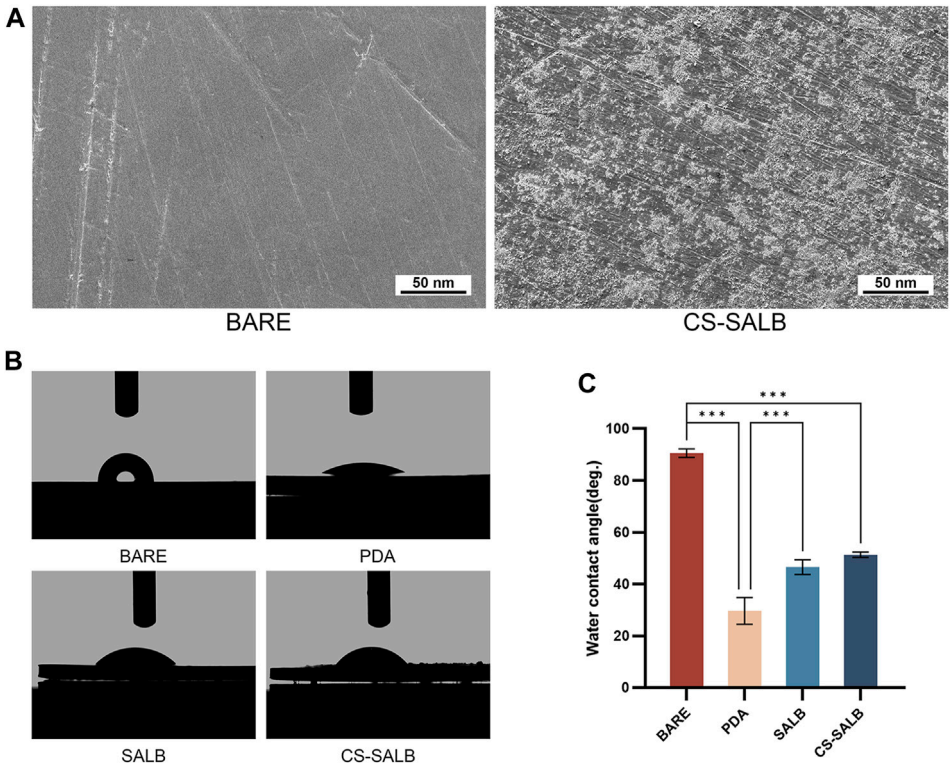

FIGURE 1
SEM and water contact angle analysis. **(A)** Scanning electron microscopy (SEM) images comparing the BARE group and CS-SALB group. **(B)** Representative images of water contact angle testing on different surfaces. **(C)** Quantification of water contact angles on different surfaces. Significance is indicated by asterisks: *$p < 0.05$, **$p < 0.01$, ***$p < 0.001$.

HUVECs proliferated. After the 3-day cultural phase, the CS-SALB group exhibited a higher inhibitory effect on SMCs proliferation than the BARE group, while no significant differences were observed for the remaining groups. After the 5-day culturing period, the proliferation rates of SMCs in the SALB and CS-SALB groups were not significantly different, but both groups showed significant inhibition of SMCs proliferation compared to the BARE and PDA groups.

Figures 4A, B shows the effect of each sample group on cell migration ability. After 24 h, the results for HUVECs showed no apparent distinction between the BARE and PDA groups. However, the number of migratory cells was greater in the SALB group compared to the BARE group and noticeably higher in the CS-SALB group compared to the SALB group. The number of migrating SMCs between the BARE group and the PDA group after 24 h of culture did not differ significantly. However, the CS-SALB group significantly inhibited the migration of SMCs compared with the BARE group (Figure 4C). After 24 h, there was no discernible difference between the SALB and CS-SALB groups in the quantity of HUVECs migrating to the lower chamber. In contrast to the BARE and PDA groups, both groups had a much higher number of migrating cells. Both the SALB and CS-SALB groups significantly inhibited the migration of SMCs from the upper to the lower chamber (Figure 4D).

As shown in Figure 5A, the cell growth was visualized by DAPI staining. The morphology of adherent cells in each sample group is depicted in Figure 5B. HUVECs displayed polygonal morphology on all surfaces. SMCs adhered well to the surfaces of the BARE group, PDA group, and SALB group. Conversely, SMCs in the CS-SALB group exhibited spindle-like narrowing. After 3 days, the SALB group and the CS-SALB group demonstrated significantly increased numbers of adherent HUVECs. Comparing the CS-SALB group to the other groups, the number of adherent SMCs dramatically decreased (Figure 5C).

4 Discussion

The research results demonstrate that the SALB coating surface on nickel-titanium alloy exhibits excellent biocompatibility and can effectively promote HUVECs proliferation, adhesion, and migration. Additionally, they can inhibit SMCs proliferation, adhesion, and migration. These findings suggest that the developed bioactive coating holds potential for promoting endothelialization and preventing restenosis.

ECs and SMCs are involved in vascular reconstruction following stent placement (Jin et al., 2019). ECs are responsible for maintaining vascular function, while SMCs regulate vascular contraction and expansion, which jointly influence the biocompatibility and functionality of stents (Chen et al., 2021). Diaz-Rodriguez discovered that the coating of CD31-mimetic peptide significantly reduced the activation of platelets and leukocytes *in vitro*, which proved advantageous to the growth of physiological ECs on the scaffold, thus accelerating the process of

10.3389/fbioe.2023.1300336

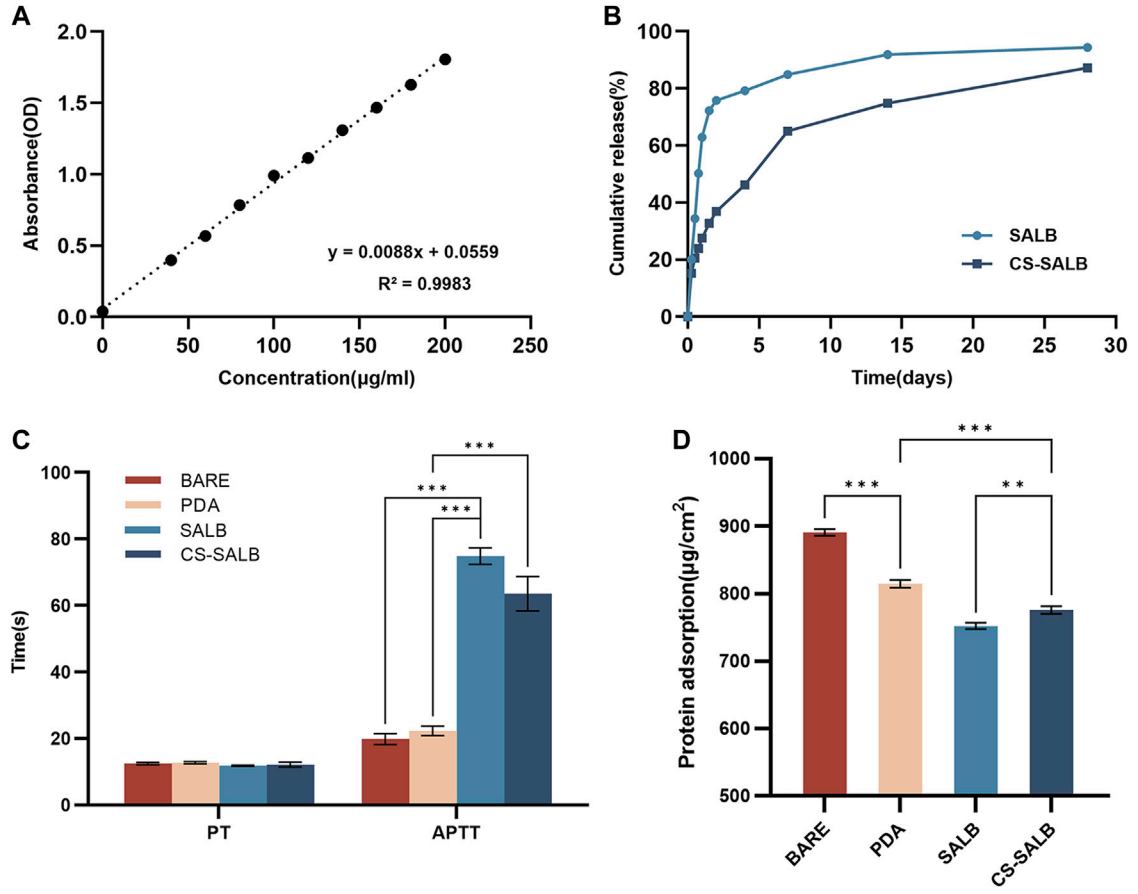

FIGURE 2
In vitro drug release and hemocompatibility experiments. **(A)** Standard curve showing the concentration of salvianolic acid B (SALB) drug. **(B)** Drug release curves of the SALB and CS-SALB group. **(C)** Activated partial thromboplastin time (APTT) and prothrombin time (PT) measurements. **(D)** Protein adsorption onto the surfaces of each group. Significance is indicated by asterisks: *$p < 0.05$, **$p < 0.01$, ***$p < 0.001$.

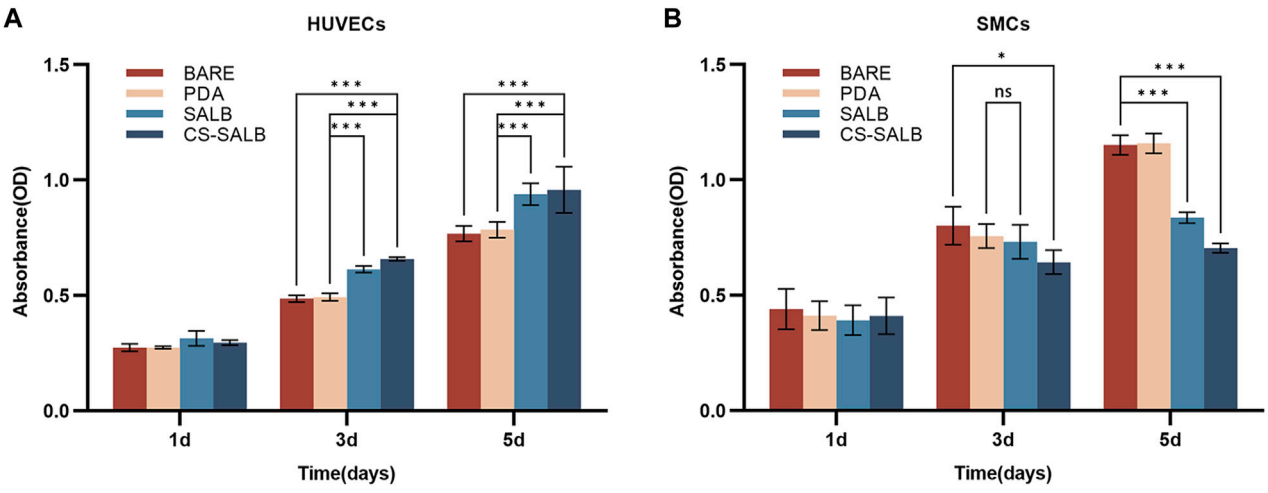

FIGURE 3
Cell viability assessed by CCK-8 assay. **(A)** Viability of HUVECs at 1, 3, and 5 days as determined by CCK-8 assay. **(B)** Viability of SMCs at 1, 3, and 5 days as determined by CCK-8 assay. Significance is indicated by asterisks: *$p < 0.05$, **$p < 0.01$, ***$p < 0.001$; ns means no statistical difference.

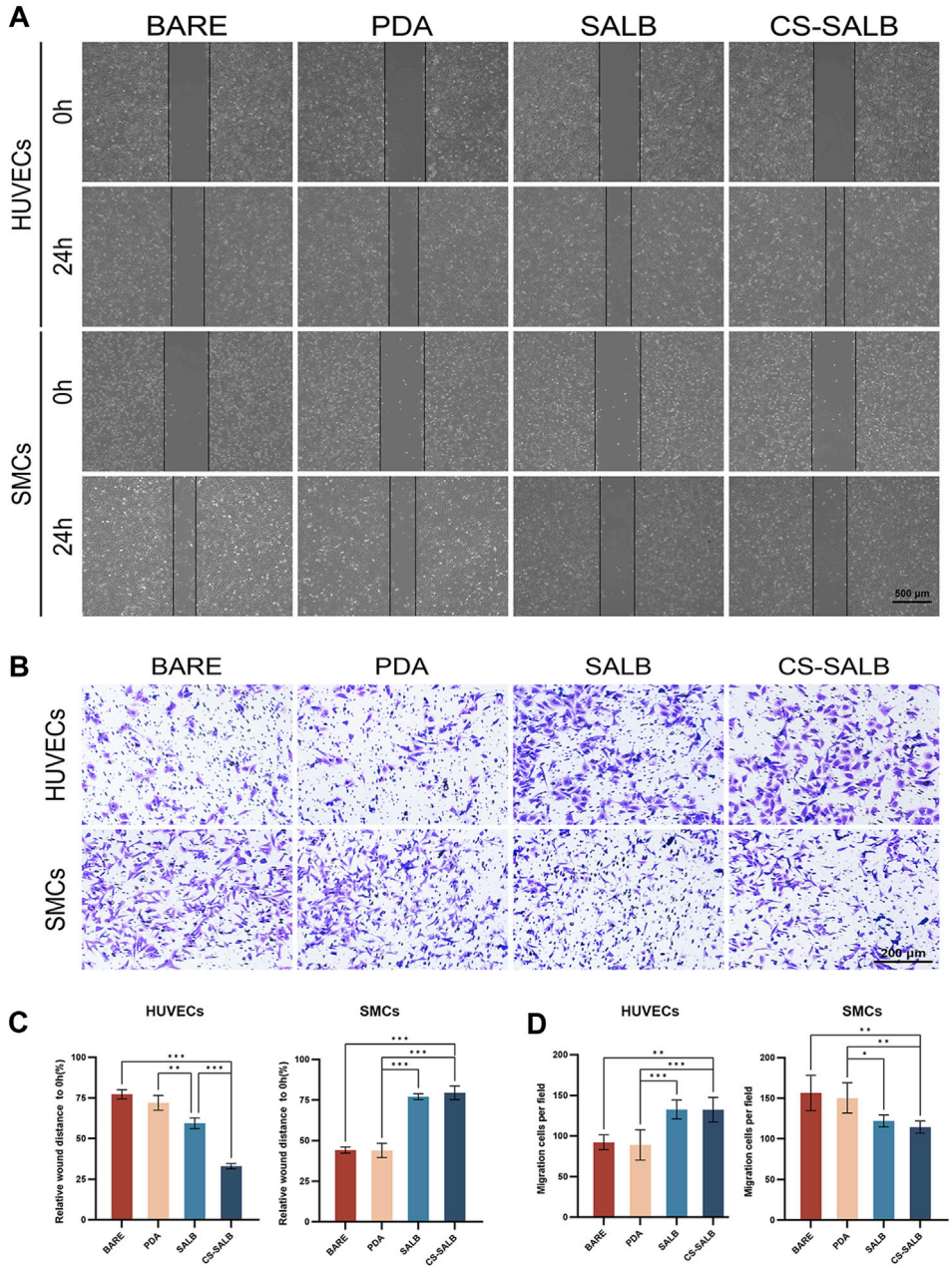

FIGURE 4
Cell migration capacity assessed by scratch assay and Transwell assay. **(A)** Impact of extracted eluates from each group after 3-day immersion on the migration of HUVECs and SMCs as measured by scratch assay. **(B)** Influence of co-culturing with each group's samples for 24 h on the invasiveness of HUVECs and SMCs as determined by Transwell assay. **(C)** Quantitative assessment of the effects of eluates from each group on the migration of HUVECs and SMCs. **(D)** Quantitative evaluation of the effects of eluates from each group on the invasiveness of HUVECs and SMCs. Significance is indicated by asterisks: $*p < 0.05$, $**p < 0.01$, $***p < 0.001$.

arterial wall healing (Diaz-Rodriguez et al., 2021). Exosome-eluting stents have been found to accelerate vascular healing, promote the formation of ECs, reduce restenosis, regulate macrophage polarization, minimize inflammation, and promote tissue repair after ischemic injury (Hu et al., 2021a). Moreover, a bionic modification method was successfully developed to treat the surface of degradable magnesium alloys by micropatterning the natural extracellular matrix (ECM) secreted by SMCs and ECs. The bionic ECM coating improves the endothelialization of the material's surface and exhibits better blood compatibility as well as anti-proliferation and anti-inflammatory effects (Liu et al., 2022). To summarize, drug coating can enhance vascular healing and repair by encouraging the creation of ECs or inhibiting the proliferation of SMCs. To achieve better results in specific clinical applications, further exploration and optimization of the coating's composition and characteristics are necessary.

At present, a lot of stent coating studies focus on a singular biological process, either preventing restenosis or promoting re-

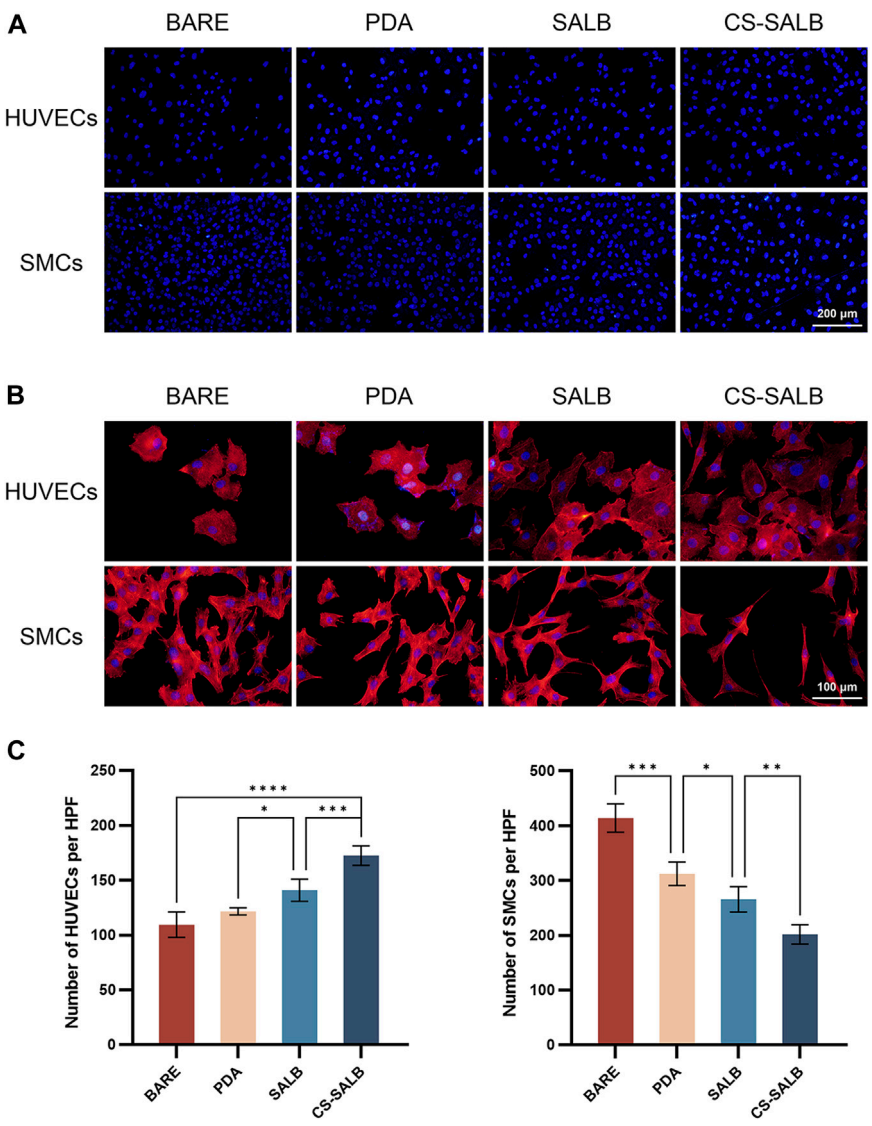

FIGURE 5
Cell adhesion capacity and cell morphology. **(A)** DAPI staining of HUVECs and SMCs attached to the surface of the samples. **(B)** Fluorescence images showing the adhesion of HUVECs and SMCs on the surface of the samples. Actin filaments are stained in red, and cell nuclei are stained in blue. **(C)** Quantification of cell proliferation by counting the number of DAPI-positive cells. Significance is indicated by asterisks: $*p < 0.05$, $**p < 0.01$, $***p < 0.001$.

endothelialization (Hu et al., 2021a; Diaz-Rodriguez et al., 2021). However, stents with dual functions of re-endothelialization and inhibiting SMCs proliferation show a high antithrombotic effect, rapid endothelialization, and long-term prevention of restenosis *in vivo* (Lyu et al., 2020). Consequently, it is highly significant to develop a drug coating that serves dual functions to enhance vascular reconstruction (Alexander et al., 2018). SALB, a phenolic carboxylic acid extracted from the water extract of Salvia miltiorrhiza, has been proven to possess two bioactivities: inhibiting SMCs proliferation and promoting angiogenesis (Lay et al., 2003; Pan et al., 2012). Consequently, our research endeavors to investigate a novel coating strategy, utilizing SALB as the fundamental element, to concurrently promote endothelialization and impede the proliferation of SMCs during metal surface modification to achieve overall better stent implanting performance. Nevertheless, one major challenge encountered at the beginning of the experiment was the rapid release of SALB *in vivo*. To overcome this issue, we developed a drug coating that could control the sustained release of SALB to leverage its biological effects on blood vessels. The use of chitosan as a nanocarrier system provides the advantages of sustained release, biodegradability, and modifiability (Cheng and Dai, 2022). For these reasons, chitosan is commonly employed in drug-sustained release systems to achieve prolonged drug release (Wu et al., 2006).

The analysis of the drug release curve data shows two distinct phases consisting of an initial burst phase and a sustained release phase (Figure 2B). During the first 24 h, the initial burst phase of the drug release curve exhibits a significant increase in the release rate, followed by a transition to the sustained release phase, where the release rate gradually decreases over the next 36 h to 28 days and

eventually stabilizes. The pronounced rapid release of the drug during the initial phase can be attributed to its physical adsorption onto the surface of the chitosan coating. Over time, the depletion of physically adsorbed drugs causes a gradual decline in the release rate, the stable biodegradability of chitosan mainly affects the slow-release stage (Bruinsmann et al., 2019). TPP is a commonly employed ionic crosslinking agent (Abdelgawad and Hudson, 2019). The positively charged R-NH3+ groups of chitosan engage with the negatively charged oxygen molecules of TPP's phosphate groups (R'-O-), facilitating proton exchange with the chitosan amino groups through electrostatic interactions (Saeedi et al., 2022). Physical crosslinking eliminates the need for chemical crosslinking agents and emulsifiers, which can be harmful to medications (Berger et al., 2004). SALB diffuses into the chitosan matrix through this ionic crosslinking reaction (Fan et al., 2012). Sustained release of SALB occurs during the degradation of chitosan particles, allowing the continuous diffusion of the drug into the surrounding environment.

PDA served as the interface between chitosan-SALB drug-loaded microspheres and the material surface in this study. PDA is a novel polymer known for its remarkable adhesive properties, making it suitable for deposition on both hydrophilic and hydrophobic surfaces. The polymerization process relies on the oxidative polymerization of dopamine under alkaline conditions (Mrowczynski et al., 2018). PDA-based coatings not only improve the solution stability of polymer nanoparticles but also provide an active platform for secondary reactions, enabling the immobilization of more functional components. This offers an opportunity for further improvement of material performance and functionality (Liu et al., 2016). PDA shows excellent biocompatibility due to its status as an important component of natural melanin widely present in the human body (Li et al., 2021). Moreover, it can decrease the frequency of unfavorable responses caused by introducing exogenous materials (Liu et al., 2014; Marinas et al., 2020).

Clear polishing marks could be seen on the BARE group's surface using SEM. However, in the CS-SALB group, the nanoparticles formed uniform clusters that successfully adhered to the PDA coating surface. The chitosan microspheres loaded with SALB were attached to the PDA coating surface through both physical adsorption and chemical cross-linking, effectively preventing the detachment of drug-loaded microspheres from the coating surface. A comparison of the water contact angles on the surfaces of the different groups showed differences in surface hydrophilicity. The contact angle significantly decreased in the PDA group, and after the fixation of CS-SALB microspheres on the surface, the contact angle slightly increased. Past research has thoroughly illustrated PDA's superhydrophilicity, the material can rapidly absorb water after being treated with a PDA coating, and this treatment causes the material's superhydrophilicity to endure for a minimum of 28 days (Kopec et al., 2020). It has been reported that materials having water contact angles within the range of 40°–70° are conducive to cell adhesion (He et al., 2022). The contact angle of the CS-SALB group exceeds that of the BARE group, facilitating cell adhesion. This shows that the sample surface's hydrophilicity is improved by the application of the chitosan-SALB coating.

Placement of the stent within the blood vessel leads to biocompatibility issues caused by its foreign body properties (Zhu et al., 2022). To tackle this issue, experiments related to blood compatibility were conducted. Once the stent comes into contact with blood, blood proteins adhere to the stent's surface, causing a protein layer to develop. One of the blood proteins, fibrinogen, may cause platelet activation, aggregation, and the start of the coagulation cascade (Rubic et al., 2022). BSA has been widely used in biomedical research due to its comparability and validation with existing literature and findings (Ribeiro et al., 2022). BSA exhibits several favorable properties, including biocompatibility and solution stability, when compared to HSA and other proteins (Sangra et al., 2017). Therefore, BSA is a suitable choice for modeling the interaction between blood and stents, so we chose BSA for the protein adsorption assay. The results of the protein adsorption test indicate that the chitosan-SALB coating significantly decreases the protein adsorption rate on the material's surface, with potential implications for reducing the incidence of thrombosis. The evaluation of coagulation time revealed that the CS-SALB group had a significant prolongation of APTT. Our results suggest that surface loading of materials with PDA, chitosan, and SALB coatings can improve biocompatibility and reduce coagulation activity, thereby potentially reducing thrombosis risk.

We carried out pertinent studies by culturing HUVECs and SMCs on the samples in order to assess the *in vitro* bioactivity of the coatings. We assessed cell proliferation activity using the CCK-8 assay, cell migration ability through scratch and transwell assays, and cell adhesion quantity and morphology through cell adhesion experiments.

While our study demonstrated its potential dual role in regulating both ECs and SMCs, further investigation is needed to understand the precise molecular mechanisms involved. Previous studies have shed light on the potential mechanisms underlying SALB's actions. SALB has been shown to increase the expression of phosphorylated STAT3 and VEGF signaling pathway-related proteins, upregulate the genes for VEGF and its receptors, and stimulate angiogenesis (Lay et al., 2003; Kim R. et al., 2018; Wang et al., 2018). Our *in vitro* research demonstrated that the SALB drug coating significantly affected the proliferative and migratory capacities of HUVECs. These findings indicate that drug coating may be a significant factor in encouraging re-endothelialization. In terms of SALB's effect on SMCs, it has been discovered that SALB can regulate cell cycle regulators and miR-146a, as well as inhibit the CXCR4 signal pathway molecule's expression level, thereby preventing the proliferation and migration of SMCs (Pan et al., 2012; Lee et al., 2014; Zhao et al., 2019). Our observation indicates that the SALB drug coating can potentially impede the proliferation of SMCs and reduce stenosis. Further study on the molecular biology mechanism of SALB on ECs and SMCs is needed.

In certain experiments, the SALB group exhibited slightly superior performance to the CS-SALB group. This could be explained by the burst release of the drug coating in the SALB group resulting from the lack of chitosan, leading to improved short-term effects. Long-term drug release from the coating is especially important in addressing the issue of late complications and restenosis after stent implantation. Based on relatively long-term experimental results, the CS-SALB group demonstrated similar or even better functional effects compared to the SALB group in this study.

Our focus was on exploring the potential of SALB in the field of vascular stents, where we conducted relevant experiments with only two cell types that are important for vascular reconstruction. To validate the effects of this novel coating, further long-term animal experiments are needed. Furthermore, for simulating the stent material, we used nickel-titanium alloy flat plates in this study. An investigation using the controlled and uniform coating of this formulation onto commercially available stents will be helpful to prove our opinion.

5 Conclusion

The combination of chitosan and SALB in the coating improved the biocompatibility of the bare metal surface. And those may promote the adhesion and migration of ECs while inhibiting the proliferation and migration of SMCs. This composite coating might have the potential to prevent stenosis in the field of vascular interventions.

Data availability statement

The original contributions presented in the study are included in the article/Supplementary Material, further inquiries can be directed to the corresponding authors.

Ethics statement

The animal study was approved by the Ethics Committee of General Hospital of Northern Theater Command. The study was conducted in accordance with the local legislation and institutional requirements.

Author contributions

SB: Writing–original draft, Writing–review and editing, Data curation, Formal Analysis, Investigation, Methodology. HL: Writing–original draft, Project administration, Supervision. KZ: Writing–original draft, Investigation, Methodology, Software, Formal Analysis. ZZ: Writing–original draft, Data curation, Software. WZ: Writing–original draft, Formal Analysis, Investigation. XY: Writing–original draft, Data curation, Formal Analysis. SC: Writing–original draft, Formal Analysis, Methodology. JZ: Investigation, Validation, Writing–original draft. ML: Formal Analysis, Methodology, Writing–original draft. PP: Funding acquisition, Methodology, Resources, Validation, Writing–original draft, Writing–review and editing. GL: Funding acquisition, Project administration, Resources, Supervision, Writing–original draft, Writing–review and editing.

Funding

The author(s) declare financial support was received for the research, authorship, and/or publication of this article. This work was sponsored by National Natural Science Foundation of China (Grant Nos 81971133, 82071481, and 82301487), Liaoning Revitalization Talents Program (XLYC2002109); Liaoning Key Research and Development Project (2021JH2/10300059); Research Project of Shenyang Bureau of Science and Technology (20-205-4-017).

Conflict of interest

The authors declare that the research was conducted in the absence of any commercial or financial relationships that could be construed as a potential conflict of interest.

Publisher's note

All claims expressed in this article are solely those of the authors and do not necessarily represent those of their affiliated organizations, or those of the publisher, the editors and the reviewers. Any product that may be evaluated in this article, or claim that may be made by its manufacturer, is not guaranteed or endorsed by the publisher.

References

Abdelgawad, A. M., and Hudson, S. M. (2019). Chitosan nanoparticles: polyphosphates cross-linking and protein delivery properties. *Int. J. Biol. Macromol.* 136, 133–142. doi:10.1016/j.ijbiomac.2019.06.062

Abourehab, M. A. S., Pramanik, S., Abdelgawad, M. A., Abualsoud, B. M., Kadi, A., Ansari, M. J., et al. (2022). Recent advances of chitosan formulations in biomedical applications. *Int. J. Mol. Sci.* 23 (18), 10975. doi:10.3390/ijms231810975

Alexander, G. C., Hwang, P. T. J., Chen, J., Kim, J., Brott, B. C., Yoon, Y. S., et al. (2018). Nanomatrix coated stent enhances endothelialization but reduces platelet, smooth muscle cell, and monocyte adhesion under physiologic conditions. *ACS Biomater. Sci. Eng.* 4 (1), 107–115. doi:10.1021/acsbiomaterials.7b00676

Berger, J., Reist, M., Mayer, J. M., Felt, O., Peppas, N. A., and Gurny, R. (2004). Structure and interactions in covalently and ionically crosslinked chitosan hydrogels for biomedical applications. *Eur. J. Pharm. Biopharm.* 57 (1), 19–34. doi:10.1016/s0939-6411(03)00161-9

Bruinsmann, F. A., Pigana, S., Aguirre, T., Dadalt Souto, G., Garrastazu Pereira, G., Bianchera, A., et al. (2019). Chitosan-coated nanoparticles: effect of chitosan molecular weight on nasal transmucosal delivery. *Pharmaceutics* 11 (2), 86. doi:10.3390/pharmaceutics11020086

Chen, Y., Gao, P., Huang, L., Tan, X., Zhou, N., Yang, T., et al. (2021). A tough nitric oxide-eluting hydrogel coating suppresses neointimal hyperplasia on vascular stent. *Nat. Commun.* 12 (1), 7079. doi:10.1038/s41467-021-27368-4

Cheng, M., and Dai, D. (2022). Inhibitory of active dual cancer targeting 5-Fluorouracil nanoparticles on liver cancer *in vitro* and *in vivo*. *Front. Oncol.* 12, 971475. doi:10.3389/fonc.2022.971475

Choe, J. C., Park, J. H., Lee, H. C., Park, T. S., Ahn, J., Park, J. S., et al. (2020). Histopathologic response after hydrophilic polyethylene glycol-coating stent and hydrophobic octadecylthiol-coating stent implantations in porcine coronary restenosis model. *J. Mater Sci. Mater Med.* 31 (12), 122. doi:10.1007/s10856-020-06452-z

Diaz-Rodriguez, S., Rasser, C., Mesnier, J., Chevallier, P., Gallet, R., Choqueux, C., et al. (2021). Coronary stent CD31-mimetic coating favours endothelialization and reduces local inflammation and neointimal development *in vivo*. *Eur. Heart J.* 42 (18), 1760–1769. doi:10.1093/eurheartj/ehab027

Diseases, G. B. D., Injuries, C., Abbafati, C., Abbas, K. M., Abbasi, M., Abbasifard, M., et al. (2020). Global burden of 369 diseases and injuries in 204 countries and territories, 1990-2019: a systematic analysis for the Global Burden of Disease Study 2019. *Lancet* 396 (10258), 1204–1222. doi:10.1016/S0140-6736(20)30925-9

Eren, E. D., Guisong, G., Mingming, L., Bingchun, Z., Ke, Y., and Shanshan, C. (2022). A novel chitosan and polydopamine interlinked bioactive coating for metallic biomaterials. *J. Mater Sci. Mater Med.* 33 (10), 65. doi:10.1007/s10856-022-06688-x

Fan, W., Yan, W., Xu, Z., and Ni, H. (2012). Formation mechanism of monodisperse, low molecular weight chitosan nanoparticles by ionic gelation technique. *Colloids Surf. B Biointerfaces* 90, 21–27. doi:10.1016/j.colsurfb.2011.09.042

He, H., Zhou, W., Gao, J., Wang, F., Wang, S., Fang, Y., et al. (2022). Efficient, biosafe and tissue adhesive hemostatic cotton gauze with controlled balance of hydrophilicity and hydrophobicity. *Nat. Commun.* 13 (1), 552. doi:10.1038/s41467-022-28209-8

Hu, S., Li, Z., Shen, D., Zhu, D., Huang, K., Su, T., et al. (2021a). Exosome-eluting stents for vascular healing after ischaemic injury. *Nat. Biomed. Eng.* 5 (10), 1174–1188. doi:10.1038/s41551-021-00705-0

Hu, S., Wang, J., Zhang, Y., Bai, H., Wang, C., Wang, N., et al. (2021b). Three salvianolic acids inhibit 2019-nCoV spike pseudovirus viropexis by binding to both its RBD and receptor ACE2. *J. Med. Virol.* 93 (5), 3143–3151. doi:10.1002/jmv.26874

Inoue, T., Croce, K., Morooka, T., Sakuma, M., Node, K., and Simon, D. I. (2011). Vascular inflammation and repair: implications for re-endothelialization, restenosis, and stent thrombosis. *JACC Cardiovasc Interv.* 4 (10), 1057–1066. doi:10.1016/j.jcin.2011.05.025

Ji, C., Bi, L., Li, J., and Fan, J. (2019). Salvianolic acid B-loaded chitosan/hydroxyapatite scaffolds promotes the repair of segmental bone defect by angiogenesis and osteogenesis. *Int. J. Nanomedicine* 14, 8271–8284. doi:10.2147/IJN.S219105

Jin, D., Hu, J., Xia, D., Liu, A., Kuang, H., Du, J., et al. (2019). Evaluation of a simple off-the-shelf bi-layered vascular scaffold based on poly(L-lactide-co-epsilon-caprolactone)/silk fibroin *in vitro* and *in vivo*. *Int. J. Nanomedicine* 14, 4261–4276. doi:10.2147/IJN.S205569

Joner, M., Finn, A. V., Farb, A., Mont, E. K., Kolodgie, F. D., Ladich, E., et al. (2006). Pathology of drug-eluting stents in humans: delayed healing and late thrombotic risk. *J. Am. Coll. Cardiol.* 48 (1), 193–202. doi:10.1016/j.jacc.2006.03.042

Katary, M. A., Abdelsayed, R., Alhashim, A., Abdelhasib, M., and Elmarakby, A. A. (2019). Salvianolic acid B slows the progression of breast cancer cell growth via enhancement of apoptosis and reduction of oxidative stress, inflammation, and angiogenesis. *Int. J. Mol. Sci.* 20 (22), 5653. doi:10.3390/ijms20225653

Khor, E., and Lim, L. Y. (2003). Implantable applications of chitin and chitosan. *Biomaterials* 24 (13), 2339–2349. doi:10.1016/s0142-9612(03)00026-7

Kim, C. H., Park, S. J., Yang, D. H., and Chun, H. J. (2018a). Chitosan for tissue engineering. *Adv. Exp. Med. Biol.* 1077, 475–485. doi:10.1007/978-981-13-0947-2_25

Kim, R., Lee, S., Lee, C. Y., Yun, H., Lee, H., Lee, M. Y., et al. (2018b). Salvia miltiorrhiza enhances the survival of mesenchymal stem cells under ischemic conditions. *J. Pharm. Pharmacol.* 70 (9), 1228–1241. doi:10.1111/jphp.12950

Kopec, K., Wojasinski, M., and Ciach, T. (2020). Superhydrophilic polyurethane/polydopamine nanofibrous materials enhancing cell adhesion for application in tissue engineering. *Int. J. Mol. Sci.* 21 (18), 6798. doi:10.3390/ijms21186798

Lay, I. S., Chiu, J. H., Shiao, M. S., Lui, W. Y., and Wu, C. W. (2003). Crude extract of Salvia miltiorrhiza and salvianolic acid B enhance *in vitro* angiogenesis in murine SVR endothelial cell line. *Planta Med.* 69 (1), 26–32. doi:10.1055/s-2003-37034

Lee, H., Dellatore, S. M., Miller, W. M., and Messersmith, P. B. (2007). Mussel-inspired surface chemistry for multifunctional coatings. *Science* 318 (5849), 426–430. doi:10.1126/science.1147241

Lee, H. J., Seo, M., and Lee, E. J. (2014). Salvianolic acid B inhibits atherogenesis of vascular cells through induction of Nrf2-dependent heme oxygenase-1. *Curr. Med. Chem.* 21 (26), 3095–3106. doi:10.2174/0929867321666140601195940

Lee, J. H., Kim, E. D., Jun, E. J., Yoo, H. S., and Lee, J. W. (2018). Analysis of trends and prospects regarding stents for human blood vessels. *Biomater. Res.* 22, 8. doi:10.1186/s40824-018-0114-1

Li, J., Zhang, Z., Deng, H., and Zheng, Z. (2021). Cinobufagin-loaded and folic acid-modified polydopamine nanomedicine combined with photothermal therapy for the treatment of lung cancer. *Front. Chem.* 9, 637754. doi:10.3389/fchem.2021.637754

Link, A., Michel, T., Schaller, M., Tronser, T., Krajewski, S., Cattaneo, G., et al. (2020). In vitro investigation of an intracranial flow diverter with a fibrin-based, hemostasis mimicking, nanocoating. *Biomed Mater.* 16 (01), 015026. doi:10.1088/1748-605X/abc8d3

Liu, C., Chen, L., Zhang, K., Li, J., and Guan, S. (2022). Tailoring ZE21B alloy with nature-inspired extracellular matrix secreted by micro-patterned smooth muscle cells and endothelial cells to promote surface biocompatibility. *Int. J. Mol. Sci.* 23 (6), 3180. doi:10.3390/ijms23063180

Liu, J., Wang, J., Xue, Y. F., Chen, T. T., Huang, D. N., Wang, Y. X., et al. (2020). Biodegradable phosphorylcholine copolymer for cardiovascular stent coating. *J. Mater Chem. B* 8 (24), 5361–5368. doi:10.1039/d0tb00813c

Liu, M., Zeng, G., Wang, K., Wan, Q., Tao, L., Zhang, X., et al. (2016). Recent developments in polydopamine: an emerging soft matter for surface modification and biomedical applications. *Nanoscale* 8 (38), 16819–16840. doi:10.1039/c5nr09078d

Liu, X., Feng, Q., Bachhuka, A., and Vasilev, K. (2014). Surface modification by allylamine plasma polymerization promotes osteogenic differentiation of human adipose-derived stem cells. *ACS Appl. Mater Interfaces* 6 (12), 9733–9741. doi:10.1021/am502170s

Lyu, N., Du, Z., Qiu, H., Gao, P., Yao, Q., Xiong, K., et al. (2020). Mimicking the nitric oxide-releasing and glycocalyx functions of endothelium on vascular stent surfaces. *Adv. Sci. (Weinh)* 7 (21), 2002330. doi:10.1002/advs.202002330

Marinas, I. C., Oprea, E., Geana, E. I., Tutunaru, O., Pircalabioru, G. G., Zgura, I., et al. (2020). Valorization of gleditsia triacanthos invasive plant cellulose microfibers and phenolic compounds for obtaining multi-functional wound dressings with antimicrobial and antioxidant properties. *Int. J. Mol. Sci.* 22 (1), 33. doi:10.3390/ijms22010033

Mengatto, L. N., Helbling, I. M., and Luna, J. A. (2012). Recent advances in chitosan films for controlled release of drugs. *Recent Pat. Drug Deliv. Formul.* 6 (2), 156–170. doi:10.2174/187221112800672967

Mrowczynski, R., Jedrzak, A., Szutkowski, K., Grzeskowiak, B. F., Coy, E., Markiewicz, R., et al. (2018). Cyclodextrin-based magnetic nanoparticles for cancer therapy. *Nanomater. (Basel)* 8 (3), 170. doi:10.3390/nano8030170

Pan, C. H., Chen, C. W., Sheu, M. J., and Wu, C. H. (2012). Salvianolic acid B inhibits SDF-1α-stimulated cell proliferation and migration of vascular smooth muscle cells by suppressing CXCR4 receptor. *Vasc. Pharmacol.* 56 (1-2), 98–105. doi:10.1016/j.vph.2011.11.008

Qiu, D., Deng, Y., Wen, Y., Yin, J., Feng, J., Huang, J., et al. (2022). Iron corroded granules inhibiting vascular smooth muscle cell proliferation. *Mater Today Bio* 16, 100420. doi:10.1016/j.mtbio.2022.100420

Ribeiro, N., Albino, M., Ferreira, A., Escrevente, C., Barral, D. C., Pessoa, J. C., et al. (2022). Liposomal formulations of a new zinc(II) complex exhibiting high therapeutic potential in a murine colon cancer model. *Int. J. Mol. Sci.* 23 (12), 6728. doi:10.3390/ijms23126728

Rubic, I., Burchmore, R., Weidt, S., Regnault, C., Kules, J., Baric Rafaj, R., et al. (2022). Multi platforms strategies and metabolomics approaches for the investigation of comprehensive metabolite profile in dogs with babesia canis infection. *Int. J. Mol. Sci.* 23 (3), 1575. doi:10.3390/ijms23031575

Sabate, M. (2022). Sirolimus versus paclitaxel: second round. *JACC Cardiovasc Interv.* 15 (7), 780–782. doi:10.1016/j.jcin.2022.02.007

Saeedi, M., Vahidi, O., Moghbeli, M. R., Ahmadi, S., Asadnia, M., Akhavan, O., et al. (2022). Customizing nano-chitosan for sustainable drug delivery. *J. Control Release* 350, 175–192. doi:10.1016/j.jconrel.2022.07.038

Sangra, M., Estelrich, J., Sabate, R., Espargaro, A., and Busquets, M. A. (2017). Evidence of protein adsorption in pegylated liposomes: influence of liposomal decoration. *Nanomater. (Basel)* 7 (2), 37. doi:10.3390/nano7020037

Tahir, H., Bona-Casas, C., and Hoekstra, A. G. (2013). Modelling the effect of a functional endothelium on the development of in-stent restenosis. *PLoS One* 8 (6), e66138. doi:10.1371/journal.pone.0066138

Tzafriri, A. R., Parikh, S. A., and Edelman, E. R. (2019). Taking paclitaxel coated balloons to a higher level: predicting coating dissolution kinetics, tissue retention and dosing dynamics. *J. Control Release* 310, 94–102. doi:10.1016/j.jconrel.2019.08.019

Venkatesan, J., Bhatnagar, I., and Kim, S. K. (2014). Chitosan-alginate biocomposite containing fucoidan for bone tissue engineering. *Mar. Drugs* 12 (1), 300–316. doi:10.3390/md12010300

Wang, W., and Hu, W. (2018). Salvianolic acid B recovers cognitive deficits and angiogenesis in a cerebral small vessel disease rat model via the STAT3/VEGF signaling pathway. *Mol. Med. Rep.* 17 (2), 10005–10013. doi:10.3892/mmr.2017.8203

Wu, F., Meng, G., He, J., Wu, Y., Wu, F., and Gu, Z. (2014). Antibiotic-loaded chitosan hydrogel with superior dual functions: antibacterial efficacy and osteoblastic cell responses. *ACS Appl. Mater Interfaces* 6 (13), 10005–10013. doi:10.1021/am502537k

Wu, Y. T., Chen, Y. F., Hsieh, Y. J., Jaw, I., Shiao, M. S., and Tsai, T. H. (2006). Bioavailability of salvianolic acid B in conscious and freely moving rats. *Int. J. Pharm.* 326 (1-2), 25–31. doi:10.1016/j.ijpharm.2006.07.003

Xiao, Z., Liu, W., Mu, Y. P., Zhang, H., Wang, X. N., Zhao, C. Q., et al. (2020). Pharmacological effects of salvianolic acid B against oxidative damage. *Front. Pharmacol.* 11, 572373. doi:10.3389/fphar.2020.572373

Zhao, X. S., Zheng, B., Wen, Y., Sun, Y., Wen, J. K., and Zhang, X. H. (2019). Salvianolic acid B inhibits Ang II-induced VSMC proliferation *in vitro* and intimal hyperplasia *in vivo* by downregulating miR-146a expression. *Phytomedicine* 58, 152754. doi:10.1016/j.phymed.2018.11.014

Zhu, H., Kong, L., Zhu, X., Ran, T., and Ji, X. (2022). pH-responsive nanoparticles for delivery of paclitaxel to the injury site for inhibiting vascular restenosis. *Pharmaceutics* 14 (3), 535. doi:10.3390/pharmaceutics14030535

frontiers | Frontiers in Bioengineering and Biotechnology

TYPE Review
PUBLISHED 14 November 2023
DOI 10.3389/fbioe.2023.1320307

Check for updates

OPEN ACCESS

EDITED BY
Mingqiang Li,
Third Affiliated Hospital of Sun Yat-Sen University, China

REVIEWED BY
Chengcheng Yin,
China Medical University, China
Bo Lu,
Wuhan University of Technology, China

*CORRESPONDENCE
Runfa Wu,
zzydf721@163.com
Junchao Wei,
weijunchao@ncu.edu.cn

†These authors have contributed equally to this work and share first authorship

RECEIVED 12 October 2023
ACCEPTED 30 October 2023
PUBLISHED 14 November 2023

CITATION
Wang Z, Wang J, Wu R and Wei J (2023), Construction of functional surfaces for dental implants to enhance osseointegration.
Front. Bioeng. Biotechnol. 11:1320307.
doi: 10.3389/fbioe.2023.1320307

COPYRIGHT
© 2023 Wang, Wang, Wu and Wei. This is an open-access article distributed under the terms of the Creative Commons Attribution License (CC BY). The use, distribution or reproduction in other forums is permitted, provided the original author(s) and the copyright owner(s) are credited and that the original publication in this journal is cited, in accordance with accepted academic practice. No use, distribution or reproduction is permitted which does not comply with these terms.

Construction of functional surfaces for dental implants to enhance osseointegration

Zhenshi Wang[1,2,3†], Jiaolong Wang[1,2,3,4†], Runfa Wu[1,2,3*] and Junchao Wei[1,2,3,4*]

[1]School of Stomatology, Nanchang University, Nanchang, China, [2]Jiangxi Province Key Laboratory of Oral Biomedicine, Nanchang, China, [3]Jiangxi Province Clinical Research Center for Oral Disease, Nanchang, China, [4]College of Chemistry and Chemical Engineering, Nanchang University, Nanchang, China

Dental implants have been extensively used in patients with defects or loss of dentition. However, the loss or failure of dental implants is still a critical problem in clinic. Therefore, many methods have been designed to enhance the osseointegration between the implants and native bone. Herein, the challenge and healing process of dental implant operation will be briefly introduced. Then, various surface modification methods and emerging biomaterials used to tune the properties of dental implants will be summarized comprehensively.

KEYWORDS

dental implants, osseointegration, surface modification, coating, biomimetic, bone regeneration

1 Introduction

Due to the tumor recession, injuries, periodontitis, and the aging of population, the defect or loss of dentition has been a common problem in the world, which has greatly affected the daily life of vast numbers of patients (Gulati et al., 2023). Over the past 50 years, implant dentistry has evolved into a highly reliable choice for replacing lost teeth (Buser et al., 2017). Up to now, implanted teeth have been recognized as an ideal alternative of permanent teeth, so dental implants have aroused great attention worldwide.

Dental implants have obtained favorable clinical results and profoundly altered patients' lives. The global dental market is growing and is expected to be 13.1 billion dollars by 2023 (Alghamdi and Jansen, 2020). Despite dental implants having a 95% estimated 10-year survival (Fischer and Stenberg, 2012), implant failure or loss is still a tough problem. Many studies have demonstrated that bacterial infections, biomechanical mismatch, smoking, aging, and systemic disorders, such as diabetes, osteoporosis, obesity, and the use of drugs, are all factors that can hamper bone regeneration and thus result in the failure of dental implants (Tomasi and Derks, 2022). When the reasons are referred from a more direct or exact point, "failure of osseointegration" is the answer (Alghamdi and Jansen, 2020). It was reported that both the early and late implant loss were related to a failure in osseointegration (Tomasi and Derks, 2022). Thus, optimizing and modifying dental implants to obtain a better osseointegration is still an urgent need.

To provide new ideas for implant modification with better osseointegration, basic concepts of osseointegration and healing processes after implantation are discussed first. Then, current surface modification methods and emerging biomaterials related to biomimetic structures and biological cues to accelerate osseointegration are reviewed comprehensively (Figure 1).

2 Osseointegration and its biological process

Osseointegration is defined as the direct and structural connection between bone and implant without an intermediate layer of connective tissue (Guglielmotti et al., 2019). After being first proposed in the 1960s by Branemark, it has been a revolutionary concept in dental implantology (Brånemark et al., 2001), which is still a hot topic in dental implantology. The osseointegrated dental implants reflect the biological and mechanical fixation of implant fixture into the jaw bone, and the biological fixation is a prerequisite for the long-term success of dental implants.

The process of implant osseointegration is complex and dynamic and takes several weeks of healing. An essential part of osseointegration is the process of bone regeneration, which is regulated by several biological factors (Bosshardt et al., 2017). As reported, there are complex processes underlying bone regeneration, especially the early healing phase and its highly dynamic environment, which impacts the signaling pathways that direct the healing process (Duda et al., 2023). The initial stages of bone healing are characterized by dynamic self-organization of the tissue that governs the healing outcome (Duda et al., 2023). Thus, it is crucial to understand the bone healing process, which may be helpful to understand the critical factors that affect the success of dental implants.

The surface of implants is also a critical factor in affecting the dynamic self-organization of the native bone tissue and their biological responses (Smeets et al., 2016), and thus, it is important to understand the surface properties of dental implants on the results of osseointegration. Since the healing process partially influences bone regeneration and the success of dental implants, the knowledge of the healing process for dental implants may provide us with more endogenous bone regeneration clues and factors to help us to design a better implant surface.

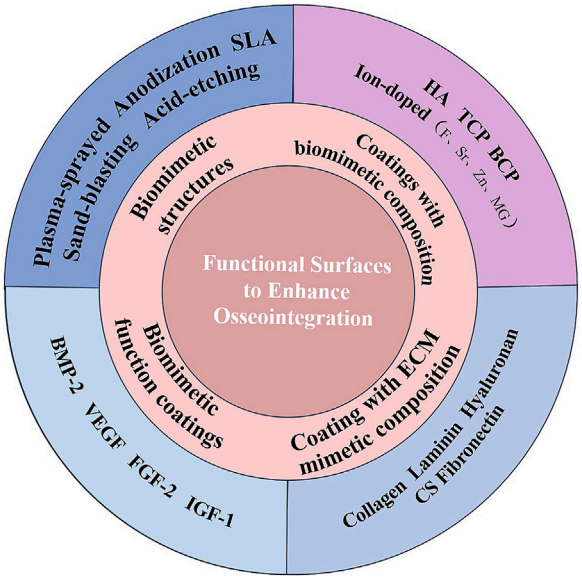

FIGURE 1
Functional surfaces for dental implants to enhance osseointegration.

2.1 Healing process for dental implants

Osseointegration is a time-dependent dynamic process that depends on the biological process of bone healing and the surface properties of dental implants. Generally, when the implant was placed in the bone, several bioresponsive behaviors would take place (Figure 2) (Franz et al., 2011). When the implant is implanted, the contact of implants with blood and tissue fluid will result in the adsorption of proteins on the surface of implants. This layer of proteins determines the activation of the coagulation cascade, complement system, platelets, and immune cells and guides their interplay (Franz et al., 2011). Blood clots form immediately on the surface of dental implants, and platelets are activated to secrete a large number of growth factors for directing preosteoblasts to differentiate into osteoblasts. At this time, the necrotic bone and hematoma are resorbed by osteoclasts and macrophages in granulation tissue, respectively (Chen et al., 2020b). Some special molecules or proteins are adsorbed on the surface of dental implants, which may guide the adhesion of osteoblasts on the surface of dental implants. When osteoblasts are surrounded by their products or matrix, they will be differentiated into osteocytes to promote further bone formation, which means bone is formed on the surface of dental implants. The reaction will continue until the surface of implants is covered by bone (Chen et al., 2020b).

2.2 Challenges for dental implants

An ideal dental implant should have great potential to realize osseointegration. The mechanism of osseointegration is closely related to biomaterials designed to be implanted (Guglielmotti et al., 2019). However, the common biomaterials used in dental implants in clinic such as titanium (Ti) and its alloys, are bioinert and has limited biological activity. From the biological point of view, early and late implant loss is considered a failure to achieve or maintain osseointegration, respectively (Tomasi and Derks, 2022). Therefore, enhancing the bioactivity of dental implants is a vital issue that needed to be addressed. Since the healing process is crucial for bone regeneration, we should consider the healing process to improve osseointegration. The factors that enhance the osseointegration may improve the properties of dental implants. Furthermore, we should also consider the factors that can promote bone healing or bone regeneration (Smeets et al., 2016). Therefore, the challenge for dental implants is how to endow biomaterials designed to be implanted with better bioactivity, fully considering the healing process and bone regeneration.

Many review works have been published about the surface modification of dental implants, most of which are focused on the surface modification methods or surface coating materials (Souza et al., 2019; Inchingolo et al., 2023). Herein, we try to consider the bone healing process and connect the biomimetic idea of bone regeneration to discuss the surface modification of dental implants. We aim to review the functional surface

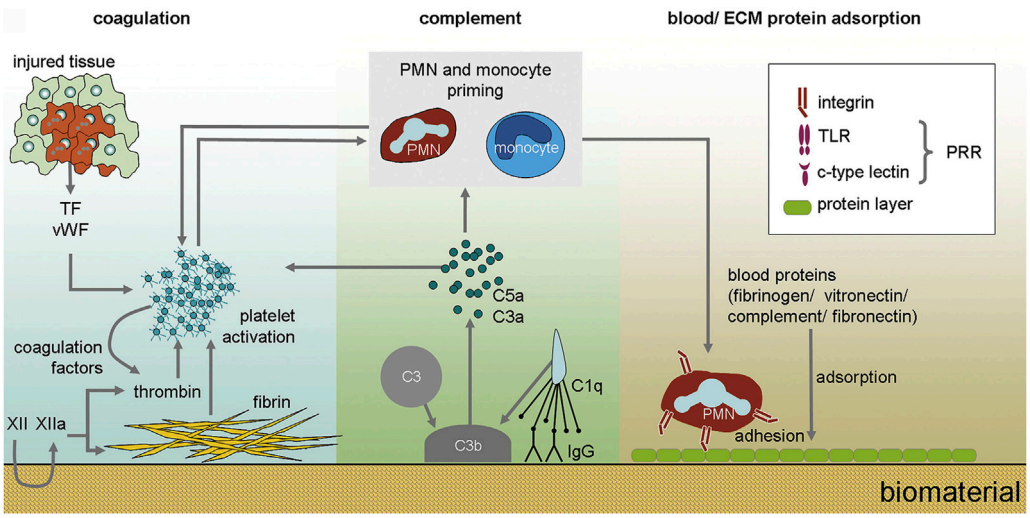

FIGURE 2
The immediate biological processes after implantation of biomaterials. Nanoseconds after the first contact with tissue, proteins from blood and interstitial fluids adsorb to the biomaterial surface. The adsorption of blood proteins determines the activation of coagulation cascade, complement system, platelets and immune cells and guides their interplay (Franz et al., 2011).

modification of dental implants based on the biomimetic concept and provide guidance for optimal osseointegration methods by discussing their biological characteristics.

3 Surface modification of dental implants and biomimetics

Generally, the interactions between the implants and bone first happen on the surface of implants. Thus the surface has great effects on the following healing process of implants, such as protein adsorption, activation of coagulation cascade, complement system, platelets, the subsequent immune responses, osteogenesis, and osteointegration (Franz et al., 2011; Smeets et al., 2016; Chen et al., 2020b). Therefore, it is still necessary to tune the surface properties of dental implants to improve its bioproperties and enhance bone regeneration.

The concept of "osseointegration" is related to bone regeneration, a hot topic in recent years. Therefore, the factors that can promote bone regeneration would be critical for osseointegration. It has been critical to use biomaterials to initiate the regeneration of defected bone. The process of osseointegration is closely associated with biomaterials, which are designed for implantation or incorporation into living organisms with the aim of replacing or regenerating tissues and their functions. It is an ideal strategy for designing implant biomaterials with porous structures, biomimetic composition, and biomimetic functions for bone regeneration (Liu et al., 2016). Since surface topography and compositions can significantly affect bone healing and osseointegration, the surface of dental implants is much important. In this part, we will give a summary of the surface modification of dental implants. We mainly consider the problem from the biomimetic idea, which can mimic the natural healing process of dental implants, and the current surface functionalization or coatings to tune the osseointegration will be summarized in the following part.

3.1 Biomimetic structures of dental implants

The natural bone consists of micro-nano-scale hierarchical structures, and its main components are hydroxyapatite (HA) and collagen (mostly type I) (Figure 3) (Wang et al., 2016). The biomimetic multiscale structures may supply a preferable microenvironment for bone healing and bone regeneration (Liu et al., 2016). Therefore, many bone tissue engineering scaffolds with porous and micro-nano-scale structure have been designed to improve bone regeneration. It is well known that porous structure, biocompatible scaffolds, and special biofunctions are critical in the field of bone tissue engineering. There are some similarities between the scaffolds and dental implants in achieving ideal bone regeneration. Thus, dental implants with biomimetic porous and micro-nano-scale structures may improve osseointegration and reduce the healing time.

When the implant surface is porous, it may mimic the structure of bone. This biomimetic structure is beneficial for the ingrowth of bone and forms interlocks with the new bone, which may greatly improve osseointegration and thus increase the biomechanical stability and resistance fatigue loading of implants (Hasegawa et al., 2020). Besides, it is widely acknowledged that cellular responses and osseointegration to implants vary depending on the surface roughness at micro-, submicro- and nano-scale levels (Hasegawa et al., 2020). For instance, micro-rough structures favor cell attachment, while nano-rough structures encourage gene expression, protein synthesis, and cell differentiation (Gittens et al., 2011; Gittens et al., 2013). A variety of techniques, including plasma-sprayed (Ferraz et al., 2001; Giavaresi et al., 2003), anodization (Sul et al., 2002; Qi et al., 2021), sand-blasting (Gil et al., 2021; Wang et al., 2023), and acid-etching (Park and Davies, 2000; Trisi et al., 2003), have been employed to create biomimetic porous and rough surfaces of dental implants, and the results have demonstrated that implants with biomimetic structures would have better results for successful implant (López-Valverde et al., 2020).

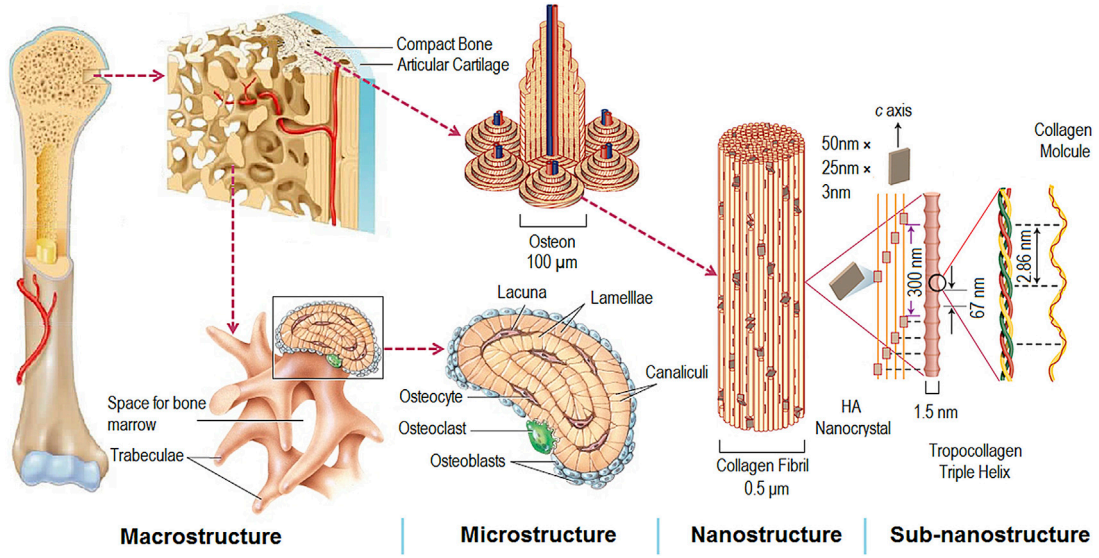

FIGURE 3
Hierarchical and multiscale structure of natural bone (Wang et al., 2016).

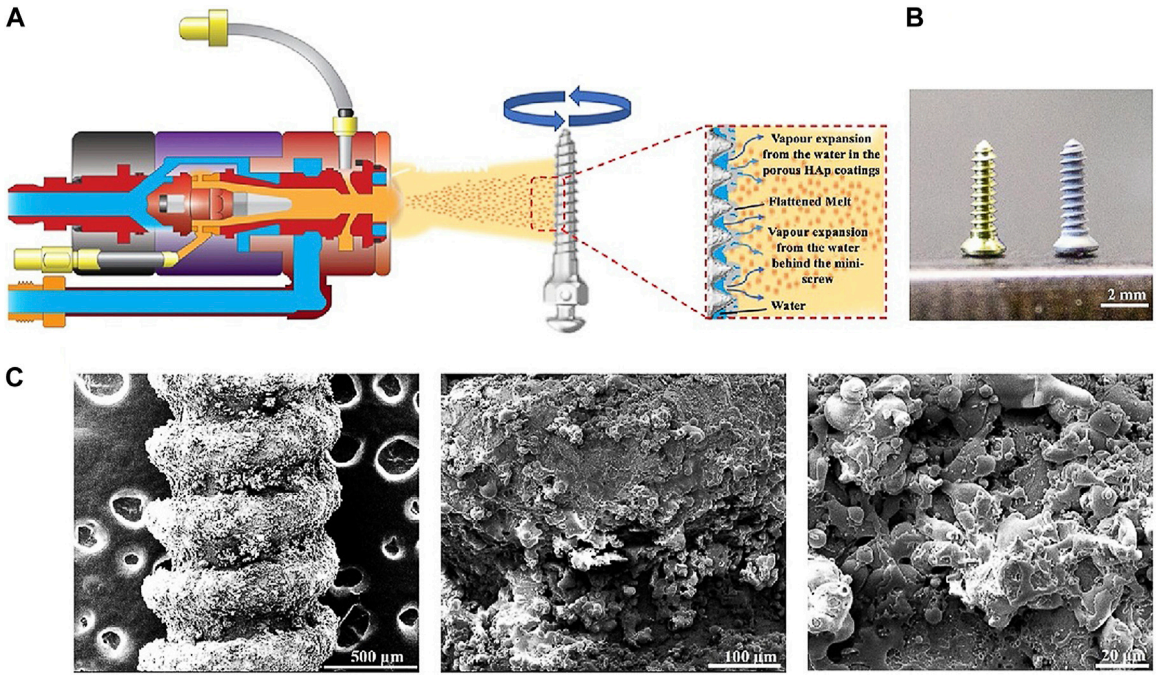

FIGURE 4
Preparation of HA coatings on Ti implants using the vapor-induced pore-forming atmospheric plasma spraying technique (Hou et al., 2023). **(A)** The Ti implant was roughened and then sprayed with a thin layer of HA coatings. **(B)** Left: Ti implants; right: Ti implants with the porous HA coating. **(C)** SEM of HA coatings on implant surfaces at different magnifications (Hou et al., 2023).

Usually, the plasma-sprayed method is used to coat Ti, HA, and zirconia (ZrO_2) onto implant surfaces. This method always creates a surface with micro-scale roughness. For example, plasma-sprayed HA coating shows an average surface roughness of about 1.06 μm (Ferraz et al., 2001; Giavaresi et al., 2003), and plasma-sprayed ZrO_2 coating presents a roughness of about 1.58 μm (Huang et al., 2018b), which are better suitable for osseointegration than uncoated implants. Using the plasma-sprayed method combines with the vapor-induced pore-forming technique, a rough and porous HA coating could be effectively fabricated. The desired thickness of HA

coating is achieved by multiple rapid sprays in pure water (Figure 4) (Hou et al., 2023). The resulting Ti coating via the plasma-sprayed method has an average roughness of around 7 μm, which accelerates the bone/implant interface formation (Le Guéhennec et al., 2007). Another common method to prepare micro- or nano-roughness surfaces is the anodization of Ti (Sul et al., 2002; Qi et al., 2021). Anodization leads to modifications in the microstructure and the crystallinity of the titanium oxide layer (Sul et al., 2002), which strengthens the bone response and generates superior results for biomechanical and histomorphometric tests (Le Guéhennec et al., 2007). The nanostructured implant surfaces via anodization present nanotubes of various sizes (Qi et al., 2021). The nanoscale topography of the Ti surface is altered by various anodization voltages, ranging from 30 nm at 5 V to 80 nm at 20 V (Ma et al., 2014). The prepared Ti surfaces' roughness increased as a result of the increasing anodization voltage. Compared with 80 nm TiO_2 nanotubular and smooth surfaces, 30 nm TiO_2 nanotubular coating exhibits lesser pro-inflammatory properties, more bone formation, and better osseointegration (Ma et al., 2014; Qi et al., 2021). Also, 30 nm TiO_2 surface shows faster collagen synthesis and extracellular matrix (ECM) mineralization in the macrophages' conditioned media (Ma et al., 2018). After implantation *in vivo*, mineralized bone formation is also significantly faster around the 30 nm TiO_2 nanotubular surface implant (Ma et al., 2018).

Besides the common plasma-spraying method, the acid-etching and sand-blasting methods are also widely used and often combined to create the appropriate roughness related to the biological response. The acid-etching method usually produces micro-pit structures, with pit sizes ranging from 0.5 to 2 μm (Park and Davies, 2000; Trisi et al., 2003). Park et al. found that acid-etched surfaces enhanced osseointegration by attaching fibrin and osteoblasts around the implant surface (Park and Davies, 2000; Trisi et al., 2003). Sand-blasting method produces a macro-roughness with very sharp peaks and valleys, and many parameters, including the size and nature of abrasive particles, projection pressure, and the distance from the gun to Ti surfaces, affect the roughness of Ti surfaces (Gil et al., 2021). It is widely recognized that acid treatment alone does not create the proper roughness for osseointegration (Gil et al., 2021). Thus, it is often combined with sand-blasting. Herrero-Climent et al. examined the osseointegration of four Ti implants with surfaces that were either as-machined, acid-etched, sand-blasted, or sand-blasted + acid-etched (Herrero-Climent et al., 2013). The sand-blasted with/without acid-etched Ti implants had a higher roughness and better osseointegration than the other two Ti implants. Besides, the findings showed that, in comparison with the sand-blasted implants, the combination of sand-blasted and acid-etched accelerated lightly bone regeneration at various implantation times (Herrero-Climent et al., 2013). Sand-blasted, large-grit, and acid-etched (SLA) technique has emerged as the most commercially successful Ti-based dental implant, which was introduced in 1997. It is a process that involves blasting with coarse abrasive particles followed by acid-etching (Im et al., 2023). SLA generates a topographical surface that exhibits isotropic characteristics. This topography consists of macro-scale irregularities, as well as interconnected cavities at the micro-scale and submicro-scale levels (Kim et al., 2013). The greater osseointegration is believed to be attributed to several factors, including improved mechanical interlocking with the adjacent bone, increased surface area, surface energy, protein adsorption, and cell adhesion during the initial stages of wound healing (Im et al., 2023). Instead of the conventional dual etching solutions consisting of sulphuric and hydrochloric acids used in SLA, Jae-Seung Im et al. used an eco-friendly hydrogen peroxide (H_2O_2)/sodium bicarbonate ($NaHCO_3$) mixture for etching. Osteoblast adhesion and proliferation were enhanced on the modified SLA surfaces (Im et al., 2023).

While biomimetic structures provide a preferable physical microenvironment, the ability of the sole topography cue to encourage cell attachment and proliferation is constrained in the absence of biological cues like bioactive factors on implants (Li et al., 2021). As a result, the biological modifications on the topological implants have been developed with various osteoinductive biomaterials and bioactive molecules (Agarwal and García, 2015). To date, the composition derived from bone such as HA and collagen, has been immobilized on dental implants for accelerating bone regeneration (Scarano et al., 2019). Besides biomimetic structures, therefore, the surface of dental implants should also mimic the composition of bone or contain osteogenesis-related biofactors to provide sufficient biological cues to promote bone regeneration and osseointegration, and thus biomimetic coatings have been prepared.

3.2 Coatings with biomimetic composition

The natural bone is composed of inorganic and organic composition. The typical components are HA, one kind of calcium phosphate (CaP), and collagen, one kind of ECM proteins, respectively. CaP ceramics, known for their superior osteoinductivity, are able to induce ectopic bone formation in non-osseous sites (Chen et al., 2020a; Wang et al., 2022). Besides, ECM is a dynamic structure that is constantly remodelled to regulate tissue homeostasis, and its components represent promising therapeutic targets (Bonnans et al., 2014). Therefore, coating with the biomimetic bone composition, including CaP and ECM components, should be a promising strategy in the field of surface modification of dental implants to obtain superior osseointegration.

3.2.1 Biomimetic inorganic composition

CaP ceramics, the main inorganic composition of bone, are frequently employed as biomimetic coating materials because of their excellent osteoconductivity and osteoinductivity. A carbonate apatite layer that is chemically and crystallographically identical to the inorganic phase of bone forms on implants as a result of an ion exchange reaction between implants and surrounding body fluids. And this carbonate apatite layer aids the bone healing process (de Jonge et al., 2008). Therefore, CaP coatings are widely used to mimic the bone healing process to construct a new bioactive implant surface to facilitate further bone contact. There are a series of CaP ceramics with various Ca/P ratios. For example, monocalcium phosphate anhydrous ($Ca(H_2PO_4)_2$), dicalcium phosphate anhydrous ($CaHPO_4$), tricalcium phosphate ($Ca_3(PO_4)_2$, TCP), HA ($Ca_{10}(PO_4)_6(OH)_2$), carbonate apatite ($Ca_5(PO_4)_x(CO_3)_y$) present different Ca/P ratio from 0.5 to more than 1.67. These CaP coatings are described to mimic the functions

of natural bone and make it easier to bridge small gaps between implants and surrounding bone, thus improving the osseointegration of dental implants (Hayakawa et al., 2000; de Jonge et al., 2008; Tabrizi et al., 2022).

Among various CaP ceramics, HA, or more specifically carbonate apatite, is by far the most abundant inorganic phase of bone. The adhesion of osteoblasts and the mineralization of new bone can be encouraged by the HA coatings. HA coated dental implants can be prepared via kinds of methods, such as plasma-sprayed (Schopper et al., 2005), spin coating (Tredwin et al., 2013), sol-gel dip-coating (Tredwin et al., 2013; Li et al., 2014), electrophoretic deposition (Iwanami-Kadowaki et al., 2021), electrochemical deposition (Zhao et al., 2013), and atomic layer deposition (Kylmäoja et al., 2022). The only industrial process for fabricating HA coatings on orthopedic and dental implants designed for commercialization is the plasma-sprayed technique (Prezas et al., 2023), which makes implants better than uncoated ones (Schopper et al., 2005). However, the plasma-sprayed coating results in phase and structural inhomogeneity and leads to a reduction in cohesion failure at the coating/implant interface (Cheang and Khor, 1996; Tredwin et al., 2013). Besides, a discrepancy in coefficients of thermal expansion between the metal and HA has an impact on the adhesive bond strength of the HA coating (Ke et al., 2019). By using a gradient HA coating created by the laser designed net shaping and plasma spraying, Ke et al. dramatically increased the adhesive bond strength from 26 ± 2 MPa to 39 ± 4 MPa (Ke et al., 2019). On the contrary, due to low temperature processing, the sol-gel dip coating method presents phase and structural homogeneity (Tredwin et al., 2013). Despite being a straightforward and inexpensive method, dip coating has problems when used for complicated shapes, controlling coating thickness, and obtaining enough adhesive strength (Iwanami-Kadowaki et al., 2021). The application of electrophoretic deposition is hampered by the required multiple steps, high temperature, specialized equipment, and demanding conditions. Further sintering at 600°C or higher and voltages of the order of 20–200 V are used to create HA coatings by electrophoretic deposition (Kim and Ramaswamy, 2009). Besides, highly crystalline HA produced at high temperatures is difficult to degrade, exhibits limited biological activity, and has relatively single structures (Zhao et al., 2020). Currently, researchers have been focused on a bioinspired method to synthesize the HA coating to avoid these limitations (Ma et al., 2023).

The common bioinspired method used in HA-coated implants was the polydopamine (PDA)-assisted method (Ma et al., 2023). It is a simple, mild but effective way to prepare HA-coated by the immersion of PDA-modified Ti into simulated body fluid (SBF). In this process, PDA provides numerous nucleation sites for mineralization and spontaneously reacts with Ca and P ions in SBF, thus leading to HA deposition (Zhe et al., 2016). While HA formed at high temperatures is high crystalline, HA prepared by the PDA-assisted bioinspired method has spherical particle structures and better bioactivity (Xu et al., 2018). Contrary to the aforementioned methods, which frequently resulted in cohesion failure at the coating/implant interface, the PDA-assisted bioinspired method leads to a stable HA coating on implants owing to the superior adhesion properties of PDA (Xu et al., 2018). It is reported that HA coatings remain stable even after strong ultrasonication for 1 h (Xu et al., 2018).

There are many other ions contained in the composition of natural bone, and to mimic the natural composition, various ions such as fluoride (F), strontium (Sr), zinc (Zn), magnesium (Mg) ions have been doped into HA crystals and formed ions doped HA, such as F-HA and Sr-HA have been designed to work as coatings (Bonnelye et al., 2008; Tredwin et al., 2013; Li et al., 2014; Panzavolta et al., 2018). These doped ions are also necessary in the norm physiological system, and thus it is well to design coatings that mimic the composition in the body. The ions can work as they are and show great potential in bone regeneration and thus promote osseointegration. Many studies show that ion-doped HA increased biological efficiency instead of pure HA (Bonnelye et al., 2008; Li et al., 2014). For example, Tredwen et al. compared the potential bond strength and interaction of HA, F-doped HA, and fluarapatite (FA) with Ti, and it was found that increasing F^- substitution significantly increased bond strength (Tredwin et al., 2013). Sr-doped HA coating significantly promotes the proliferation and differentiation of bone mesenchymal stem cells (BMSCs) and osteoblasts when compared with untreated and HA-coated Ti surfaces (Panzavolta et al., 2018). Due to the different radii and properties of the two atoms, the lattice of Sr-doped HA can be distorted, and the biodegradability increases (Li et al., 2007). In addition to the better osseointegration with improved trabecular parameters and higher bone-to-implant contact (BIC) (Zhao et al., 2013), Mg-doped HA coating increases the maximum push-out force and interfacial shear strength compared to HA coatings (Li et al., 2014). To combine the different benefits of various ions, Hou et al. prepared Zn-, Sr- and Mg-multidoped HA (ZnSrMg-HA) porous coatings on implants. ZnSrMg-HA coating showed the most pronounced osteogenesis and concentrated bone growth along implant treads when compared with HA and Zn-doped HA groups (Hou et al., 2023).

Similar to HA, other CaP ceramics such as TCP and biphasic calcium phosphate (BCP) also show superior osteoinductivity and osteoconductivity, and thus, they are widely used as coating materials to modify the surface of dental implants to improve osseointegration (Hayakawa et al., 2000; Tabrizi et al., 2022). It is found that CaP sputter coated implants always show a higher BIC than the non-coated implants *in vivo* (Hayakawa et al., 2000). Besides, BCP coating makes the secondary stability of implants much higher (Tabrizi et al., 2022). Despite the resorption rate of TCP higher than HA, it is still often lower than the rate of new bone formation (Damerau et al., 2022). The ionic substitutions such as silver (Ag), Zn, or copper (Cu) can increase the resorption rate and provide other functional properties to TCP, including antibacterial activity (Fadeeva et al., 2021). From a systematic review in a meta-analysis, there does not seem to be much effect of TCP-coated implants over uncoated implants in the short term, however, there was an increase in differences in BIC for TCP-coated implants over time (Damerau et al., 2022).

In general, the application of biomimetic CaP coatings, especially HA, on Ti implants has proved their effectiveness in promoting osseointegration. The chemical structure, composition, ion doping, and other characteristics of the manufactured CaP coatings vary greatly. Despite the proven efficacy of CaP coatings, the method to fabricate CaP coatings is still a key step for success of dental implants.

3.2.2 ECM biomimetic coatings

During the healing process, osteoblasts adhere to the surface of dental implants, and then proliferation and differentiation happens, which is followed by a series of regeneration process. It is critical to prepare dental implants with a special environment that may be suitable for the growth of osteoblasts and other osteogenic cells. As reported, the behavior of stromal cells and bone healing are affected by the newly forming ECM (Duda et al., 2023). Through ECM, the cell-generated forces are directly transmitted to neighboring cells, and this transmission is highly influenced by ECM composition, which is important in determining the success of bone healing (Duda et al., 2023). That is, ECM has pronounced impacts on guiding bone healing by providing an environment for cellular responses. Thus, a promising method to enhance osseointegration is to coat dental implants with ECM components (Schulz et al., 2014).

Collagen type I (COL1), the main organic composition of natural bone and ECM, is a good choice to act as functional coatings on the surface of dental implants to mimic the natural interface, which promote the adhesion of osteoblasts, and finally improve bone mineralization and osseointegration (Scarano et al., 2019). After coating with COL1, implants present more trabeculae bone in the implant concavities with a small medullary space when compared with the uncoated group (Scarano et al., 2019). The bioactivity, BIC, and bone areas around the implant surfaces are significantly improved, which could be clinically advantageous for shortening the implant healing period (Scarano et al., 2019). COL1 coatings interact with the integrin receptors, and activate the FAK/PI3K/MAPK pathway of BMSCs, thus leading to promotion of cell proliferation and mineralization of the ECM (Hsu et al., 2019). Importantly, Ti implants coated with COL1 are effective in promoting implant osseointegration *in vivo* (Cho et al., 2021), even in compromised bone such as in the osteopenic rat animal models (Sartori et al., 2015). In addition to promoting osteogenesis, COL1 coating can support macrophage timely conversion from the pro-inflammatory to the pro-healing phenotype, and foster a favorable osteoimmune microenvironment (Shao et al., 2022; Zhao et al., 2022). Since HA and COL1 are the most important components of bone, the construction of HA/COL1 coating is a good alternative to mimic the natural bone. Many studies show that HA/COLl or mineralized collagen coating significantly improves the nucleation ability in SBF and bioactivity of implants (Patty et al., 2022), and leads to more rapid osseointegration (Iwanami-Kadowaki et al., 2021).

Generally, two kinds of methods are used to prepare collagen-coated implants, including physical adsorption and chemical covalent bonding methods. The former relies on van der Walls forces, hydrophilicity, and electrostatic forces (Ao et al., 2014). One of the limitations of this technique is that it is unable to handle the fixing and releasing processes of biomolecules on the implant surfaces due to their weak interactions (Lupi et al., 2021). Thus, the originally adsorbed biomolecules could be quickly desorbed from the surface (Lupi et al., 2021; Zhao et al., 2022). The chemical covalent bonding method involves the use of cross-linking agents, such as aminopropylsilane, glutaraldehyde (GA), or carbodiimide (Ao et al., 2014). Besides, gamma-rays (GRs) could also be exploited to cross-link collagen on Ti surfaces, which leads to a similar performance in new bone areas and BIC with GA crosslinked COL1 coating (Cho et al., 2021). The covalently immobilized Ti coating had more collagen than the physically absorptive one, which increases its ability to regulate BMSCs' osteogenic activity (Ao et al., 2014). Silanization is a common way to chemically immobilize collagen onto implants (Lupi et al., 2021), which always changes the distribution and conformation of COL1 on surfaces (Marín-Pareja et al., 2015). After silanization treatment, COL1-coated Ti organizes in globular clusters rather than fibrilllar networks. It results in improved fibroblast adhesion, better cell spreading, and stronger fibronectin fibrillogenesis (Marín-Pareja et al., 2015). In addition to silanization, procyanidin is also employed as a natural cross-linker to immobilize COL1 on implant surfaces (Hsu et al., 2019). Procyanidin, a polyphenolic molecule from natural sources like grapeseed, is less toxic than the widely used cross-linker GA (Han et al., 2003). Previous studies have shown that the abundant hydroxyl groups in procyanidin form hydrogen bonds with COL1 to achieve cross-linking without destroying the collagen structure (He et al., 2011). Besides, genipin obtained from the fruit of Genipa Americana may be an alternative of natural crosslinking agents (Liu et al., 2021). It is worth noting that the PDA-assisted bioinspired method can also be used to covalently immobilize with COL1 on Ti surfaces (Zhao et al., 2022).

Besides, there were many other important organic components of ECM. For example, laminin, hyaluronan, chondroitin sulfate (CS) and fibronectin, are all biocompatible materials and have been used to improve the surface properties of dental implants (Bougas et al., 2012; Yeo et al., 2015; Chang et al., 2016; Aung et al., 2023). It is reported that laminin coatings induce faster osseointegration around Ti implants both *in vitro* and *in vivo* (Bougas et al., 2012; Yeo et al., 2015). Jung-Yoo Choi et al. evaluated the impact of the Ln2-P3 peptide, generated from laminin, on the osseointegration of implants in rabbit models. The BIC and bone area of the Ln2-P3-coated implants were found to be considerably higher when compared with the uncoated implants on Day 9 after implantation (Figure 5) (Choi et al., 2020). Although several studies indicated the potential interest of hyaluronan coating on Ti surfaces, a crossover randomized clinical trial up to 36 months after loading showed that there were no differences in the healing and implant success between the hyaluronan coated and control implants (Lupi et al., 2019).

Rather than a single ECM component coated on implant surfaces, several components used together may exert better osseointegration. For example, higher BIC was observed in the COL1/low sulfated hyaluronan coated Ti implants when compared with commercial pure Ti implants in the early healing period (Schulz et al., 2014). Haiyong Ao et al. developed a novel stable collagen/hyaluronan multilayer covalent-immobilized coating on Ti implants by the combination of LBL and covalent immobilization technique. When compared with collagen/hyaluronan multilayer absorbed Ti coatings, the multilayer covalent-immobilized coating showed favorable stability and better osteogenesis performance both *in vitro* and *in vivo* (Ao et al., 2013; Ao et al., 2018). It has been demonstrated that collagen/CS coatings affect osteoblast adhesion and BMSCs differentiation (Stadlinger et al., 2012). Interestingly, an increased concentration of CS was unable to enhance this impact for the fact that more CS would desorb from the collagen coating correspondingly (Stadlinger et al., 2012). To find out if the

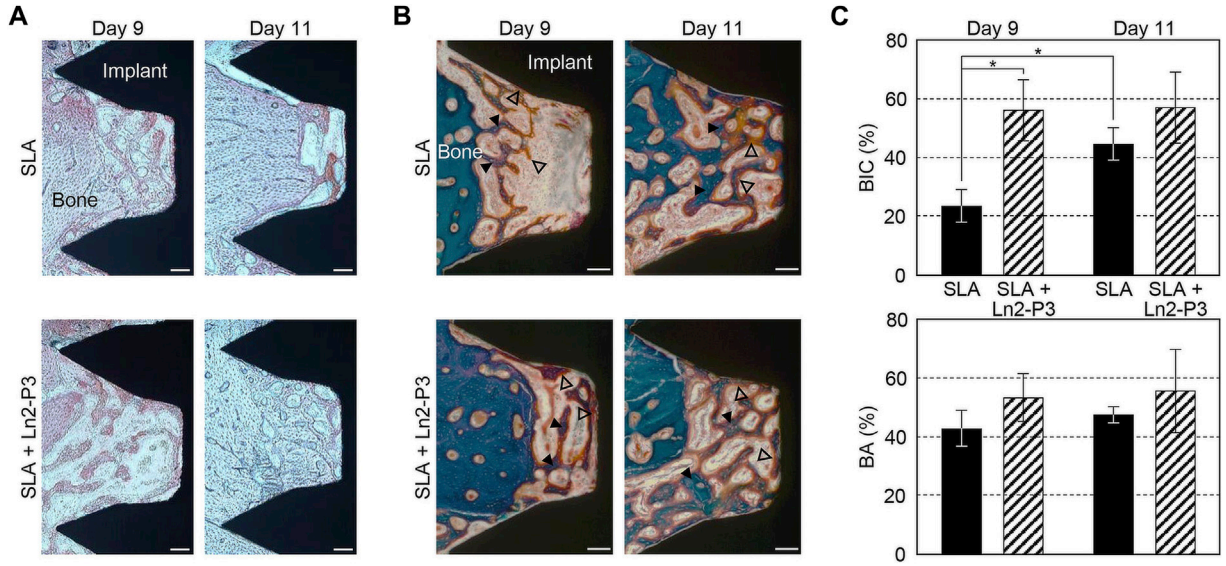

FIGURE 5
Alizarin red staining Images **(A)**, Masson trichrome-stained images **(B)**, BIC (top) and bone area (bottom) ratios **(C)** of the untreated (SLA) and Ln2-P3-treated (SLA + Ln2-P3) implants in the rabbit tibia at 9 and 11 days after insertion (Choi et al., 2020).

collagen-CS coating affected osseointegration, Kellesarian et al. conducted a systematic review and meta-analysis. The collagen-CS coated implants were reported to have superior new bone formation and BIC, and/or bone volume density (Kellesarian et al., 2018). According to the experimental data, osseointegration appeared to be aided by the collagen-CS coating (Kellesarian et al., 2018). Also, the combination of collagen type II and CS could exhibit a positive influence on bone formation after coating on the implant surface (de Barros et al., 2015).

In summary, ECM component coatings exhibit favorable osseointegration, especially when several components were used together. It is worth noting that chemical covalent bonding methods are preferable to physical adsorption methods. ECM biomimetic coating exerts its impact on osseointegration by mimicking the natural interface and providing an environment to influence the response of osteoblasts, thereby its effectiveness is weaker than that of biofunction coatings which directly induce or determine bone regeneration.

3.2.3 Biomimetic function coatings

Although the biomimetic structures or ECM components can promote osseointegration, it is still difficult to mimic the special biofunctions related to the healing process. Since the cell functions and growth factors are essential to bone regeneration, many methods have been employed to prepare the growth factor coated dental implants to mimic the biofunctions and promote bone regeneration. The growth factors can control osteogenesis, ECM formation, and bone regeneration by affecting the recruitment and differentiation of osteoprogenitor cells (Bose et al., 2012). From the point of bone regeneration, although ECM has great potential, the growth factors such as bone morphogenic protein-2 (BMP-2) (Liu et al., 2007; Kim et al., 2015), vascular endothelial growth factor (VEGF) (Leedy et al., 2014; Schliephake et al., 2015), fibroblast growth factor-2 (FGF-2) (Nagayasu-Tanaka et al., 2017; Yasunaga et al., 2022), insulin-like growth factor-1 (IGF-1) (Raju et al., 2023) are also much important in bone tissue regeneration. These growth factors have been recognized as critical factors. Since dental implants are also bone regeneration related, it is a good method to coat the dental implants with these bioactive factors to mimic their special biofunctions.

BMP-2 is a known and effective osteogenic agent and has been approved by the Food and Drug Administration (FDA). Its biological effects are dosage-dependent (Kim et al., 2015). Six types of Ti implants, including uncoated, CaP-coated, BMP-2 adsorbed to uncoated, BMP-2 adsorbed to CaP-coated, BMP-2 incorporated into CaP-coated, and BMP-2 adsorbed to and incorporated into CaP-coated, were implanted in the maxillae of minipigs. After 3 weeks, the groups with no BMP-2 presented the most bone volume and bone coverage. Conversely, implants containing only adsorbed BMP-2 exhibited the lowest bone coverage (Liu et al., 2007). It suggested that osteoconductivity of implants was most severely impaired when BMP-2 was only superficially adsorbed on surfaces, and least so when it was incorporated into a CaP coating (Liu et al., 2007). Hunziker's study also demonstrated that the mode of delivery greatly affected the capacity of BMP-2 to induce and sustain local bone formation. Compared with the adsorbed way, the incorporated way always led to a gradual release and a superior osteogenic response (Hunziker et al., 2012). Rather than direct adsorption of BMP-2, George Calin Dindelegan et al. developed a novel complex coating on Ti implants consisting of a chitosan film engulfing microsphere loaded with BMP-2 (Dindelegan et al., 2021), which could effectively release BMP-2 in a stable and active form that assured short and effective osseointegration (Dindelegan et al., 2021). Chien et al. developed the RGD/HA/BMP-2 coating on Ti implants via the PDA-assisted bioinspired method, and the results indicated that the conjugation of RGD enhanced the adhesion of BMSCs, while the incorporation of HA facilitated cellular osteodifferentiation (Chien

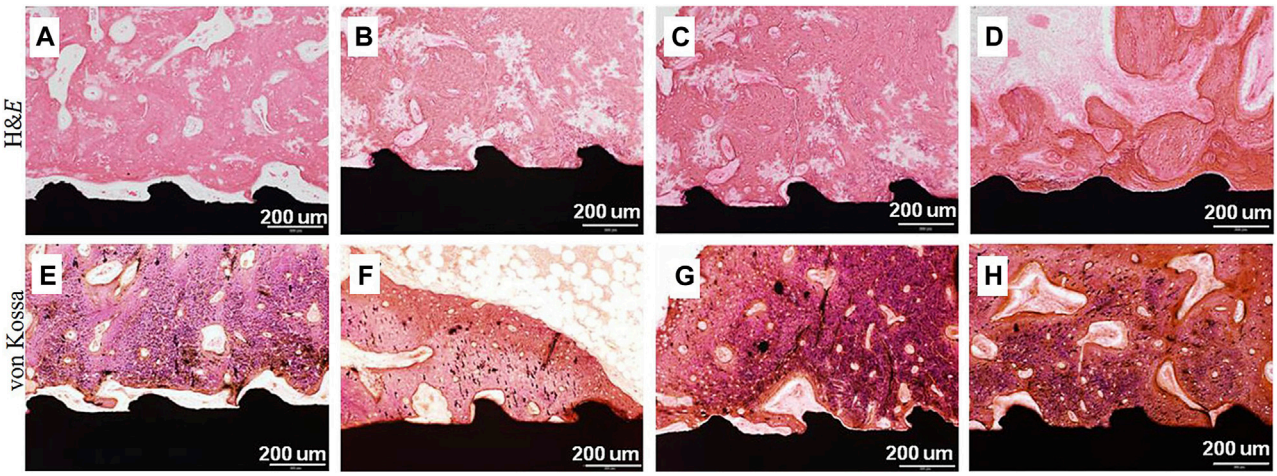

FIGURE 6
H&E and von Kossa stained images on the surrounding tissue around **(A,E)** pristine Ti, **(B,F)** Ti/HA, **(C,G)** Ti/Hep/BMP-2, and **(D,H)** Ti/HA/Hep/BMP-2 samples 4 weeks after implantation (Yang et al., 2015).

and Tsai, 2013), and the immobilization of BMP-2 stimulated osteogenesis of the stem cells. The functionalized coating improved osteogenic differentiation and mineralization (Chien and Tsai, 2013). Yang et al. compared surface-modified Ti samples with HA and heparin (Hep)-BMP-2 complex (Ti/HAp/Hep/BMP-2), Ti/HAp/Hep/BMP-2 samples produced the largest scale of osteons and the maximum number of osteocytes at the interface (Figure 6) (Yang et al., 2015).

VEGF coating on Ti implants has also drawn much attention to improve osseointegration, since vascularization is a crucial prerequisite for bone healing and osseointegration (Leedy et al., 2014; Schliephake et al., 2015). In comparison to uncoated implants, Leedy et al. prepared the VEGF-loaded chitosan coatings on Ti, and found a 2-fold increase in ALP activity and a 10-fold increase in calcium deposition (Leedy et al., 2014). However, around 75% of VEGF was released over the first 12 h, and by day 3, the coatings had released 90%–95% of VEGF. There was a need to reduce the burst release of VEGF and enhance the elution profile (Leedy et al., 2014). DNA oligonucleotide (ODN) strands nano-anchored to Ti surfaces can be used to bind VEGF that has been conjugated to oligonucleotides (Schliephake et al., 2012). After the covalent binding of VEGF on the surface of implants, BIC after 1 month was considerably higher compared to uncoated and ODN strands anchored implants (Schliephake et al., 2015).

Combining BMP-2 and VEGF has been shown to improve bone regeneration and vascularization when compared to using either BMP-2 or VEGF alone (Ramazanoglu et al., 2011). Ramazanoglu et al. studied whether coating with BMP-2 and VEGF affected osseointegration in pigs (Ramazanoglu et al., 2011). There was a notable enhancement in the BV density in the BMP-2 and BMP-2 + VEGF groups at 2 weeks. In contrast, the group treated with BMP + VEGF did not exhibit a statistically significant improvement in BIC at 4 weeks. These suggested that the biomimetic CaP coated implant surfaces along with the addition of BMP and VEGF resulted in increased BV density but not BIC (Ramazanoglu et al., 2011). Interestingly, in the rabbit models after receiving radiotherapy, the combined delivery of BMP-2 and VEGF enhanced bone formation around implants, promoted BIC, and enhanced the stability of implants in irradiated bone (Huang et al., 2018a).

Similar to the coating methods of biomimetic ECM components, covalent binding is better than physical adsorption for fabricating the growth factors functionalized coatings. The burst release of the adsorbed growth factors even impairs the osteoconductivity of implants. Growth factors immobilized on implants pre-coated with CaP are preferable for their effectiveness in inducing bone formation and osseointegration.

4 Conclusion and perspective

Herein, we have summarized the biomimetic approaches to improve osseointegration including the structures and various biomimetic coatings. Regarding the bone healing process, micro-nano-scale and porous structures were preferable. Thus, we have summarized the common techniques to achieve an appropriate structure. Besides, how to mimic the composition of bone and construct the biomimetic function coating were also concluded herein. Also, these modification methods and emerging biomaterials' effects on osseointegration were discussed. The evolution of dental implants has been largely influenced by the integration of new materials and technologies. However, it is still challenging to fabricate uniform biomimetic structures rapidly and on a large scale. With the development of additive manufacturing or three-dimensional (3D) printing technologies, which could provide customized implants, the future of implants should aim to develop surfaces with controlled, refined, and standardized roughness and morphology. Although many traditional or emerging methods were reported very useful on experimental grounds, there were sometimes no significant differences in a systematic review and meta-analysis. Therefore, how to build a multifunctional modified implant surface to meet clinical needs is still on demand. In addition, the immune

microenvironment at the implant-bone interface should be added in the future considering.

Author contributions

ZW: Writing–review and editing, Writing–original draft. JW: Writing–review and editing. RW: Writing–review and editing, Conceptualization, Project administration. JW: Conceptualization, Project administration, Supervision, Writing–review and editing.

Funding

The author(s) declare financial support was received for the research, authorship, and/or publication of this article. This work was supported by the financial support from the National Natural Science Foundation of China (Nos. 52163016 and 82201078), Jiangxi Provincial program for the academic and technological leaders of main subjects (20213BCJL22051), and Jiangxi Provincial Natural Science Foundation (20224BAB216051).

Conflict of interest

The authors declare that the research was conducted in the absence of any commercial or financial relationships that could be construed as a potential conflict of interest.

Publisher's note

All claims expressed in this article are solely those of the authors and do not necessarily represent those of their affiliated organizations, or those of the publisher, the editors and the reviewers. Any product that may be evaluated in this article, or claim that may be made by its manufacturer, is not guaranteed or endorsed by the publisher.

References

Agarwal, R., and García, A. J. (2015). Biomaterial strategies for engineering implants for enhanced osseointegration and bone repair. *Adv. Drug Deliv. Rev.* 94, 53–62. doi:10.1016/j.addr.2015.03.013

Alghamdi, H. S., and Jansen, J. A. (2020). The development and future of dental implants. *Dent. Mater J.* 39, 167–172. doi:10.4012/dmj.2019-140

Ao, H., Xie, Y., Tan, H., Wu, X., Liu, G., Qin, A., et al. (2014). Improved hMSC functions on titanium coatings by type I collagen immobilization. *J. Biomed. Mater Res. A* 102, 204–214. doi:10.1002/jbm.a.34682

Ao, H., Xie, Y., Tan, H., Yang, S., Li, K., Wu, X., et al. (2013). Fabrication and *in vitro* evaluation of stable collagen/hyaluronic acid biomimetic multilayer on titanium coatings. *J. R. Soc. Interface* 10, 20130070. doi:10.1098/rsif.2013.0070

Ao, H., Zong, J., Nie, Y., Wan, Y., and Zheng, X. (2018). An *in vivo* study on the effect of coating stability on osteointegration performance of collagen/hyaluronic acid multilayer modified titanium implants. *Bioact. Mater* 3, 97–101. doi:10.1016/j.bioactmat.2017.07.004

Aung, L. M., Lin, J. C., Salamanca, E., Wu, Y. F., Pan, Y. H., Teng, N. C., et al. (2023). Functionalization of zirconia ceramic with fibronectin proteins enhanced bioactivity and osteogenic response of osteoblast-like cells. *Front. Bioeng. Biotechnol.* 11, 1159639. doi:10.3389/fbioe.2023.1159639

Bonnans, C., Chou, J., and Werb, Z. (2014). Remodelling the extracellular matrix in development and disease. *Nat. Rev. Mol. Cell Biol.* 15, 786–801. doi:10.1038/nrm3904

Bonnelye, E., Chabadel, A., Saltel, F., and Jurdic, P. (2008). Dual effect of strontium ranelate: stimulation of osteoblast differentiation and inhibition of osteoclast formation and resorption *in vitro*. *Bone* 42, 129–138. doi:10.1016/j.bone.2007.08.043

Bose, S., Roy, M., and Bandyopadhyay, A. (2012). Recent advances in bone tissue engineering scaffolds. *Trends Biotechnol.* 30, 546–554. doi:10.1016/j.tibtech.2012.07.005

Bosshardt, D. D., Chappuis, V., and Buser, D. (2017). Osseointegration of titanium, titanium alloy and zirconia dental implants: current knowledge and open questions. *Periodontol* 73, 22–40. doi:10.1111/prd.12179

Bougas, K., Stenport, V. F., Currie, F., and Wennerberg, A. (2012). Laminin coating promotes calcium phosphate precipitation on titanium discs *in vitro*. *J. Oral Maxillofac. Res.* 2, e5. doi:10.5037/jomr.2011.2405

Brånemark, R., Brånemark, P. I., Rydevik, B., and Myers, R. R. (2001). Osseointegration in skeletal reconstruction and rehabilitation: a review. *J. Rehabil. Res. Dev.* 38, 175–181.

Buser, D., Sennerby, L., and De Bruyn, H. (2017). Modern implant dentistry based on osseointegration: 50 years of progress, current trends and open questions. *Periodontol. 2000* 73, 7–21. doi:10.1111/prd.12185

Chang, Y. C., Ho, K. N., Feng, S. W., Huang, H. M., Chang, C. H., Lin, C. T., et al. (2016). Fibronectin-grafted titanium dental implants: an *in vivo* study. *Biomed. Res. Int.* 2016, 1–11. doi:10.1155/2016/2414809

Cheang, P., and Khor, K. A. (1996). Addressing processing problems associated with plasma spraying of hydroxyapatite coatings. *Biomaterials* 17, 537–544. doi:10.1016/0142-9612(96)82729-3

Chen, X., Wang, M., Chen, F., Wang, J., Li, X., Liang, J., et al. (2020a). Correlations between macrophage polarization and osteoinduction of porous calcium phosphate ceramics. *Acta Biomater.* 103, 318–332. doi:10.1016/j.actbio.2019.12.019

Chen, Y. F., Goodheart, C., and Rua, D. (2020b). The body's cellular and molecular response to protein-coated medical device implants: a review focused on fibronectin and BMP proteins. *Int. J. Mol. Sci.* 21, 8853. doi:10.3390/ijms21228853

Chien, C. Y., and Tsai, W. B. (2013). Poly(dopamine)-assisted immobilization of Arg-Gly-Asp peptides, hydroxyapatite, and bone morphogenic protein-2 on titanium to improve the osteogenesis of bone marrow stem cells. *ACS Appl. Mater Interfaces* 5, 6975–6983. doi:10.1021/am401071f

Cho, W. T., Kim, S. Y., Jung, S. I., Kang, S. S., Kim, S. E., Hwang, S. H., et al. (2021). Effects of gamma radiation-induced crosslinking of collagen type I coated dental titanium implants on osseointegration and bone regeneration. *Mater. (Basel)* 14, 3268. doi:10.3390/ma14123268

Choi, J. Y., Kim, S., Jo, S. B., Kang, H. K., Jung, S. Y., Kim, S. W., et al. (2020). A laminin-211-derived bioactive peptide promotes the osseointegration of a sandblasted, large-grit, acid-etched titanium implant. *J. Biomed. Mater Res. A* 108, 1214–1222. doi:10.1002/jbm.a.36895

Damerau, J. M., Bierbaum, S., Wiedemeier, D., Korn, P., Smeets, R., Jenny, G., et al. (2022). A systematic review on the effect of inorganic surface coatings in large animal models and meta-analysis on tricalcium phosphate and hydroxyapatite on periimplant bone formation. *J. Biomed. Mater Res. B Appl. Biomater.* 110, 157–175. doi:10.1002/jbm.b.34899

De Barros, R. R., Novaes, A. B., Jr., Korn, P., Queiroz, A., De Almeida, A. L., Hintze, V., et al. (2015). Bone Formation in a local defect around dental implants coated with extracellular matrix components. *Clin. Implant Dent. Relat. Res.* 17, 742–757. doi:10.1111/cid.12179

De Jonge, L. T., Leeuwenburgh, S. C., Wolke, J. G., and Jansen, J. A. (2008). Organic-inorganic surface modifications for titanium implant surfaces. *Pharm. Res.* 25, 2357–2369. doi:10.1007/s11095-008-9617-0

Dindelegan, G. C., Caziuc, A., Brie, I., Soritau, O., Dindelegan, M. G., Bintintan, V., et al. (2021). Multilayered porous titanium-based 3rd generation biomaterial designed for endosseous implants. *Mater. (Basel)* 14, 1727. doi:10.3390/ma14071727

Duda, G. N., Geissler, S., Checa, S., Tsitsilonis, S., Petersen, A., and Schmidt-Bleek, K. (2023). The decisive early phase of bone regeneration. *Nat. Rev. Rheumatol.* 19, 78–95. doi:10.1038/s41584-022-00887-0

Fadeeva, I. V., Lazoryak, B. I., Davidova, G. A., Murzakhanov, F. F., Gabbasov, B. F., Petrakova, N. V., et al. (2021). Antibacterial and cell-friendly copper-substituted tricalcium phosphate ceramics for biomedical implant applications. *Mater. Sci. Eng. C* 129, 112410. doi:10.1016/j.msec.2021.112410

Ferraz, M. P., Monteiro, F. J., Serro, A. P., Saramago, B., Gibson, I. R., and Santos, J. D. (2001). Effect of chemical composition on hydrophobicity and zeta potential of plasma sprayed HA/CaO-P2O5 glass coatings. *Biomaterials* 22, 3105–3112. doi:10.1016/s0142-9612(01)00059-x

Fischer, K., and Stenberg, T. (2012). Prospective 10-year cohort study based on a randomized controlled trial (RCT) on implant-supported full-arch maxillary prostheses. Part 1: sandblasted and acid-etched implants and mucosal tissue. *Clin. Implant Dent. Relat. Res.* 14, 808–815. doi:10.1111/j.1708-8208.2011.00389.x

Franz, S., Rammelt, S., Scharnweber, D., and Simon, J. C. (2011). Immune responses to implants - a review of the implications for the design of immunomodulatory biomaterials. *Biomaterials* 32, 6692–6709. doi:10.1016/j.biomaterials.2011.05.078

Giavaresi, G., Fini, M., Cigada, A., Chiesa, R., Rondelli, G., Rimondini, L., et al. (2003). Mechanical and histomorphometric evaluations of titanium implants with different surface treatments inserted in sheep cortical bone. *Biomaterials* 24, 1583–1594. doi:10.1016/s0142-9612(02)00548-3

Gil, J., Pérez, R., Herrero-Climent, M., Rizo-Gorrita, M., Torres-Lagares, D., and Gutierrez, J. L. (2021). Benefits of residual aluminum oxide for sand blasting titanium dental implants: osseointegration and bactericidal effects. *Mater. (Basel)* 15, 178. doi:10.3390/ma15010178

Gittens, R. A., Mclachlan, T., Olivares-Navarrete, R., Cai, Y., Berner, S., Tannenbaum, R., et al. (2011). The effects of combined micron-/submicron-scale surface roughness and nanoscale features on cell proliferation and differentiation. *Biomaterials* 32, 3395–3403. doi:10.1016/j.biomaterials.2011.01.029

Gittens, R. A., Olivares-Navarrete, R., Cheng, A., Anderson, D. M., Mclachlan, T., Stephan, I., et al. (2013). The roles of titanium surface micro/nanotopography and wettability on the differential response of human osteoblast lineage cells. *Acta Biomater.* 9, 6268–6277. doi:10.1016/j.actbio.2012.12.002

Guglielmotti, M. B., Olmedo, D. G., and Cabrini, R. L. (2019). Research on implants and osseointegration. *Periodontol. 2000* 79, 178–189. doi:10.1111/prd.12254

Gulati, K., Chopra, D., Kocak-Oztug, N. A., and Verron, E. (2023). Fit and forget: the future of dental implant therapy via nanotechnology. *Adv. Drug Deliv. Rev.* 199, 114900. doi:10.1016/j.addr.2023.114900

Han, B., Jaurequi, J., Tang, B. W., and Nimni, M. E. (2003). Proanthocyanidin: a natural crosslinking reagent for stabilizing collagen matrices. *J. Biomed. Mater Res. A* 65, 118–124. doi:10.1002/jbm.a.10460

Hasegawa, M., Saruta, J., Hirota, M., Taniyama, T., Sugita, Y., Kubo, K., et al. (2020). A newly created meso-micro-and nano-scale rough titanium surface promotes bone-implant integration. *Int. J. Mol. Sci.* 21, 783. doi:10.3390/ijms21030783

Hayakawa, T., Yoshinari, M., Nemoto, K., Wolke, J. G., and Jansen, J. A. (2000). Effect of surface roughness and calcium phosphate coating on the implant/bone response. *Clin. Oral Implants Res.* 11, 296–304. doi:10.1034/j.1600-0501.2000.011004296.x

He, L., Mu, C., Shi, J., Zhang, Q., Shi, B., and Lin, W. (2011). Modification of collagen with a natural cross-linker, procyanidin. *Int. J. Biol. Macromol.* 48, 354–359. doi:10.1016/j.ijbiomac.2010.12.012

Herrero-Climent, M., Lázaro, P., Vicente Rios, J., Lluch, S., Marqués, M., Guillem-Martí, J., et al. (2013). Influence of acid-etching after grit-blasted on osseointegration of titanium dental implants: *in vitro* and *in vivo* studies. *J. Mater Sci. Mater Med.* 24, 2047–2055. doi:10.1007/s10856-013-4935-0

Hou, H. H., Lee, B. S., Liu, Y. C., Wang, Y. P., Kuo, W. T., Chen, I. H., et al. (2023). Vapor-induced pore-forming atmospheric-plasma-sprayed zinc-strontium-and magnesium-doped hydroxyapatite coatings on titanium implants enhance new bone formation-an *in vivo* and *in vitro* investigation. *Int. J. Mol. Sci.* 24, 4933. doi:10.3390/ijms24054933

Hsu, C. M., Sun, Y. S., and Huang, H. H. (2019). Enhanced cell response to zirconia surface immobilized with type I collagen. *J. Dent. Res.* 98, 556–563. doi:10.1177/0022034519828702

Huang, B., Yao, Q., Huang, Y., Zhang, L., Yao, Y., Gong, P., et al. (2018a). Combination use of BMP2 and VEGF165 promotes osseointegration and stability of titanium implants in irradiated bone. *Biomed. Res. Int.* 2018, 1–11. doi:10.1155/2018/8139424

Huang, Z., Wang, Z., Li, C., Yin, K., Hao, D., and Lan, J. (2018b). Application of plasma-sprayed zirconia coating in dental implants: study in implants. *J. Oral Implantol.* 44, 102–109. doi:10.1563/aaid-joi-d-17-00020

Hunziker, E. B., Enggist, L., Küffer, A., Buser, D., and Liu, Y. (2012). Osseointegration: the slow delivery of BMP-2 enhances osteoinductivity. *Bone* 51, 98–106. doi:10.1016/j.bone.2012.04.004

Im, J. S., Choi, H., An, H. W., Kwon, T. Y., and Hong, M. H. (2023). Effects of surface treatment method forming new nano/micro hierarchical structures on attachment and proliferation of osteoblast-like cells. *Mater. (Basel)* 16, 5717. doi:10.3390/ma16165717

Inchingolo, A. M., Malcangi, G., Ferrante, L., Del Vecchio, G., Viapiano, F., Inchingolo, A. D., et al. (2023). Surface coatings of dental implants: a review. *J. Funct. Biomater.* 14, 287. doi:10.3390/jfb14050287

Iwanami-Kadowaki, K., Uchikoshi, T., Uezono, M., Kikuchi, M., and Moriyama, K. (2021). Development of novel bone-like nanocomposite coating of hydroxyapatite/collagen on titanium by modified electrophoretic deposition. *J. Biomed. Mater Res. A* 109, 1905–1911. doi:10.1002/jbm.a.37182

Ke, D., Vu, A. A., Bandyopadhyay, A., and Bose, S. (2019). Compositionally graded doped hydroxyapatite coating on titanium using laser and plasma spray deposition for bone implants. *Acta Biomater.* 84, 414–423. doi:10.1016/j.actbio.2018.11.041

Kellesarian, S. V., Malignaggi, V. R., Kellesarian, T. V., Bashir Ahmed, H., and Javed, F. (2018). Does incorporating collagen and chondroitin sulfate matrix in implant surfaces enhance osseointegration? A systematic review and meta-analysis. *Int. J. Oral Maxillofac. Surg.* 47, 241–251. doi:10.1016/j.ijom.2017.10.010

Kim, B. S., Kim, J. S., Park, Y. M., Choi, B. Y., and Lee, J. (2013). Mg ion implantation on SLA-treated titanium surface and its effects on the behavior of mesenchymal stem cell. *Mater Sci. Eng. C Mater Biol. Appl.* 33, 1554–1560. doi:10.1016/j.msec.2012.12.061

Kim, K. H., and Ramaswamy, N. (2009). Electrochemical surface modification of titanium in dentistry. *Dent. Mater J.* 28, 20–36. doi:10.4012/dmj.28.20

Kim, N. H., Lee, S. H., Ryu, J. J., Choi, K. H., and Huh, J. B. (2015). Effects of rhBMP-2 on sandblasted and acid etched titanium implant surfaces on bone regeneration and osseointegration: spilt-mouth designed pilot study. *Biomed. Res. Int.* 2015, 1–11. doi:10.1155/2015/459393

Kylmäoja, E., Holopainen, J., Abushahba, F., Ritala, M., and Tuukkanen, J. (2022). Osteoblast attachment on titanium coated with hydroxyapatite by atomic layer deposition. *Biomolecules* 12, 654. doi:10.3390/biom12050654

Le Guéhennec, L., Soueidan, A., Layrolle, P., and Amouriq, Y. (2007). Surface treatments of titanium dental implants for rapid osseointegration. *Dent. Mater* 23, 844–854. doi:10.1016/j.dental.2006.06.025

Leedy, M. R., Jennings, J. A., Haggard, W. O., and Bumgardner, J. D. (2014). Effects of VEGF-loaded chitosan coatings. *J. Biomed. Mater Res. A* 102, 752–759. doi:10.1002/jbm.a.34745

Li, G., Zheng, T., Wu, L., Han, Q., Lei, Y., Xue, L., et al. (2021). Bionic microenvironment-inspired synergistic effect of anisotropic micro-nanocomposite topology and biology cues on peripheral nerve regeneration. *Sci. Adv.* 7, eabi5812. doi:10.1126/sciadv.abi5812

Li, X., Li, Y., Liao, Y., Li, J., Zhang, L., and Hu, J. (2014). The effect of magnesium-incorporated hydroxyapatite coating on titanium implant fixation in ovariectomized rats. *Int. J. Oral Maxillofac. Implants* 29, 196–202. doi:10.11607/jomi.2893

Li, Z. Y., Lam, W. M., Yang, C., Xu, B., Ni, G. X., Abbah, S. A., et al. (2007). Chemical composition, crystal size and lattice structural changes after incorporation of strontium into biomimetic apatite. *Biomaterials* 28, 1452–1460. doi:10.1016/j.biomaterials.2006.11.001

Liu, C. F., Chang, K. C., Sun, Y. S., Nguyen, D. T., and Huang, H. H. (2021). Combining sandblasting, alkaline etching, and collagen immobilization to promote cell growth on biomedical titanium implants. *Polym. (Basel)* 13, 2550. doi:10.3390/polym13152550

Liu, Y., Enggist, L., Kuffer, A. F., Buser, D., and Hunziker, E. B. (2007). The influence of BMP-2 and its mode of delivery on the osteoconductivity of implant surfaces during the early phase of osseointegration. *Biomaterials* 28, 2677–2686. doi:10.1016/j.biomaterials.2007.02.003

Liu, Y., Luo, D., and Wang, T. (2016). Hierarchical structures of bone and bioinspired bone tissue engineering. *Small* 12, 4611–4632. doi:10.1002/smll.201600626

López-Valverde, N., Flores-Fraile, J., Ramírez, J. M., Sousa, B. M., Herrero-Hernández, S., and López-Valverde, A. (2020). Bioactive surfaces vs. Conventional surfaces in titanium dental implants: a comparative systematic review. *J. Clin. Med.* 9, 2047. doi:10.3390/jcm9072047

Lupi, S. M., Rodriguez, Y. B. A., Cassinelli, C., Iviglia, G., Tallarico, M., Morra, M., et al. (2019). Covalently-linked hyaluronan versus acid etched titanium dental implants: a crossover rct in humans. *Int. J. Mol. Sci.* 20, 763. doi:10.3390/ijms20030763

Lupi, S. M., Torchia, M., and Rizzo, S. (2021). Biochemical modification of titanium oral implants: evidence from *in vivo* studies. *Mater. (Basel)* 14, 2798. doi:10.3390/ma14112798

Ma, Q. L., Fang, L., Jiang, N., Zhang, L., Wang, Y., Zhang, Y. M., et al. (2018). Bone mesenchymal stem cell secretion of sRANKL/OPG/M-CSF in response to macrophage-mediated inflammatory response influences osteogenesis on nanostructured Ti surfaces. *Biomaterials* 154, 234–247. doi:10.1016/j.biomaterials.2017.11.003

Ma, Q.-L., Zhao, L.-Z., Liu, R.-R., Jin, B.-Q., Song, W., Wang, Y., et al. (2014). Improved implant osseointegration of a nanostructured titanium surface via mediation of macrophage polarization. *Biomaterials* 35, 9853–9867. doi:10.1016/j.biomaterials.2014.08.025

Ma, T., Wang, C. X., Ge, X. Y., and Zhang, Y. (2023). Applications of polydopamine in implant surface modification. *Macromol. Biosci.* 23, e2300067. doi:10.1002/mabi.202300067

Marín-Pareja, N., Cantini, M., González-García, C., Salvagni, E., Salmerón-Sánchez, M., and Ginebra, M. P. (2015). Different organization of type I collagen immobilized on silanized and nonsilanized titanium surfaces affects fibroblast adhesion and fibronectin secretion. *ACS Appl. Mater Interfaces* 7, 20667–20677. doi:10.1021/acsami.5b05420

Nagayasu-Tanaka, T., Nozaki, T., Miki, K., Sawada, K., Kitamura, M., and Murakami, S. (2017). FGF-2 promotes initial osseointegration and enhances stability of implants with low primary stability. *Clin. Oral Implants Res.* 28, 291–297. doi:10.1111/clr.12797

Panzavolta, S., Torricelli, P., Casolari, S., Parrilli, A., Fini, M., and Bigi, A. (2018). Strontium-Substituted hydroxyapatite-gelatin biomimetic scaffolds modulate bone cell response. *Macromol. Biosci.* 18, e1800096. doi:10.1002/mabi.201800096

Park, J. Y., and Davies, J. E. (2000). Red blood cell and platelet interactions with titanium implant surfaces. *Clin. Oral Implants Res.* 11, 530–539. doi:10.1034/j.1600-0501.2000.011006530.x

Patty, D. J., Nugraheni, A. D., Dewi Ana, I., and Yusuf, Y. (2022). Mechanical characteristics and bioactivity of nanocomposite hydroxyapatite/collagen coated titanium for bone tissue engineering. *Bioeng. (Basel)* 9, 784. doi:10.3390/bioengineering9120784

Prezas, P. R., Soares, M. J., Borges, J. P., Silva, J. C., Oliveira, F. J., and Graça, M. P. F. (2023). Bioactivity enhancement of plasma-sprayed hydroxyapatite coatings through non-contact corona electrical charging. *Nanomater. (Basel)* 13, 1058. doi:10.3390/nano13061058

Qi, H., Shi, M., Ni, Y., Mo, W., Zhang, P., Jiang, S., et al. (2021). Size-confined effects of nanostructures on fibronectin-induced macrophage inflammation on titanium implants. *Adv. Healthc. Mater.* 10, 2100994. doi:10.1002/adhm.202100994

Raju, K., Mani, U. M., and Vaidyanathan, A. K. (2023). Evaluating the osteogenic potential of insulin-like growth factor-1 microspheres on osteoblastic activity around dental implants in patients with type 2 diabetes mellitus using bone scintigraphy: a split-mouth randomized controlled trial. *J. Prosthet. Dent.* 129, 561–565. doi:10.1016/j.prosdent.2021.06.016

Ramazanoglu, M., Lutz, R., Ergun, C., Von Wilmowsky, C., Nkenke, E., and Schlegel, K. A. (2011). The effect of combined delivery of recombinant human bone morphogenetic protein-2 and recombinant human vascular endothelial growth factor 165 from biomimetic calcium-phosphate-coated implants on osseointegration. *Clin. Oral Implants Res.* 22, 1433–1439. doi:10.1111/j.1600-0501.2010.02133.x

Sartori, M., Giavaresi, G., Parrilli, A., Ferrari, A., Aldini, N. N., Morra, M., et al. (2015). Collagen type I coating stimulates bone regeneration and osteointegration of titanium implants in the osteopenic rat. *Int. Orthop.* 39, 2041–2052. doi:10.1007/s00264-015-2926-0

Scarano, A., Lorusso, F., Orsini, T., Morra, M., Iviglia, G., and Valbonetti, L. (2019). Biomimetic surfaces coated with covalently immobilized collagen type I: an X-ray photoelectron spectroscopy, atomic force microscopy, micro-CT and histomorphometrical study in rabbits. *Int. J. Mol. Sci.* 20, 724. doi:10.3390/ijms20030724

Schliephake, H., Rublack, J., Förster, A., Schwenzer, B., Reichert, J., and Scharnweber, D. (2015). Functionalization of titanium implants using a modular system for binding and release of VEGF enhances bone-implant contact in a rodent model. *J. Clin. Periodontol.* 42, 302–310. doi:10.1111/jcpe.12370

Schliephake, H., Strecker, N., Förster, A., Schwenzer, B., Reichert, J., and Scharnweber, D. (2012). Angiogenic functionalisation of titanium surfaces using nano-anchored VEGF - an *in vitro* study. *Eur. Cell Mater* 23, 161–169. discussion 169. doi:10.22203/ecm.v023a12

Schopper, C., Moser, D., Goriwoda, W., Ziya-Ghazvini, F., Spassova, E., Lagogiannis, G., et al. (2005). The effect of three different calcium phosphate implant coatings on bone deposition and coating resorption: a long-term histological study in sheep. *Clin. Oral Implants Res.* 16, 357–368. doi:10.1111/j.1600-0501.2004.01080.x

Schulz, M. C., Korn, P., Stadlinger, B., Range, U., Möller, S., Becher, J., et al. (2014). Coating with artificial matrices from collagen and sulfated hyaluronan influences the osseointegration of dental implants. *J. Mater Sci. Mater Med.* 25, 247–258. doi:10.1007/s10856-013-5066-3

Shao, J., Weng, L., Li, J., Lin, H., Wang, H., and Lin, J. (2022). Regulation of macrophage polarization by mineralized collagen coating to accelerate the osteogenic differentiation of mesenchymal stem cells. *ACS Biomater. Sci. Eng.* 8, 610–619. doi:10.1021/acsbiomaterials.1c00834

Smeets, R., Stadlinger, B., Schwarz, F., Beck-Broichsitter, B., Jung, O., Precht, C., et al. (2016). Impact of dental implant surface modifications on osseointegration. *Biomed. Res. Int.* 2016, 1–16. doi:10.1155/2016/6285620

Souza, J. C. M., Sordi, M. B., Kanazawa, M., Ravindran, S., Henriques, B., Silva, F. S., et al. (2019). Nano-scale modification of titanium implant surfaces to enhance osseointegration. *Acta Biomater.* 94, 112–131. doi:10.1016/j.actbio.2019.05.045

Stadlinger, B., Hintze, V., Bierbaum, S., Möller, S., Schulz, M. C., Mai, R., et al. (2012). Biological functionalization of dental implants with collagen and glycosaminoglycans-A comparative study. *J. Biomed. Mater Res. B Appl. Biomater.* 100, 331–341. doi:10.1002/jbm.b.31953

Sul, Y. T., Johansson, C. B., Röser, K., and Albrektsson, T. (2002). Qualitative and quantitative observations of bone tissue reactions to anodised implants. *Biomaterials* 23, 1809–1817. doi:10.1016/s0142-9612(01)00307-6

Tabrizi, R., Sadeghi, H. M., Ghasemi, K., Khayati, A., and Jafarian, M. (2022). Does biphasic calcium phosphate-coated surface increase the secondary stability in dental implants? A split-mouth study. *J. Maxillofac. Oral Surg.* 21, 557–561. doi:10.1007/s12663-020-01448-2

Tomasi, C., and Derks, J. (2022). Etiology, occurrence, and consequences of implant loss. *Periodontol. 2000* 88, 13–35. doi:10.1111/prd.12408

Tredwin, C. J., Georgiou, G., Kim, H.-W., and Knowles, J. C. (2013). Hydroxyapatite, fluor-hydroxyapatite and fluorapatite produced via the sol–gel method: bonding to titanium and scanning electron microscopy. *Dent. Mater.* 29, 521–529. doi:10.1016/j.dental.2013.02.002

Trisi, P., Lazzara, R., Rebaudi, A., Rao, W., Testori, T., and Porter, S. S. (2003). Bone-implant contact on machined and dual acid-etched surfaces after 2 months of healing in the human maxilla. *J. Periodontol.* 74, 945–956. doi:10.1902/jop.2003.74.7.945

Wang, J., Yang, B., Guo, S., Yu, S., and Li, H. (2023). Manufacture of titanium alloy materials with bioactive sandblasted surfaces and evaluation of osseointegration properties. *Front. Bioeng. Biotechnol.* 11, 1251947. doi:10.3389/fbioe.2023.1251947

Wang, J., Zhao, Q., Fu, L., Zheng, S., Wang, C., Han, L., et al. (2022). CD301b+ macrophages mediate angiogenesis of calcium phosphate bioceramics by CaN/NFATc1/VEGF axis. *Bioact. Mater.* 15, 446–455. doi:10.1016/j.bioactmat.2022.02.004

Wang, X., Xu, S., Zhou, S., Xu, W., Leary, M., Choong, P., et al. (2016). Topological design and additive manufacturing of porous metals for bone scaffolds and orthopaedic implants: a review. *Biomaterials* 83, 127–141. doi:10.1016/j.biomaterials.2016.01.012

Xu, Y., Li, H., Wu, J., Yang, Q., Jiang, D., and Qiao, B. (2018). Polydopamine-induced hydroxyapatite coating facilitates hydroxyapatite/polyamide 66 implant osteogenesis: an *in vitro* and *in vivo* evaluation. *Int. J. Nanomedicine* 13, 8179–8193. doi:10.2147/ijn.s181137

Yang, D. H., Lee, D. W., Kwon, Y. D., Kim, H. J., Chun, H. J., Jang, J. W., et al. (2015). Surface modification of titanium with hydroxyapatite-heparin-BMP-2 enhances the efficacy of bone formation and osseointegration *in vitro* and *in vivo*. *J. Tissue Eng. Regen. Med.* 9, 1067–1077. doi:10.1002/term.1973

Yasunaga, M., Kobayashi, F., Sogo, Y., Murotomi, K., Hirose, M., Hara, Y., et al. (2022). The enhancing effects of heparin on the biological activity of FGF-2 in heparin-FGF-2-calcium phosphate composite layers. *Acta Biomater.* 148, 345–354. doi:10.1016/j.actbio.2022.06.013

Yeo, I. S., Min, S. K., Kang, H. K., Kwon, T. K., Jung, S. Y., and Min, B. M. (2015). Identification of a bioactive core sequence from human laminin and its applicability to tissue engineering. *Biomaterials* 73, 96–109. doi:10.1016/j.biomaterials.2015.09.004

Zhao, B., Li, X., Xu, H., Jiang, Y., Wang, D., and Liu, R. (2020). Influence of simvastatin-strontium-hydroxyapatite coated implant formed by micro-arc oxidation and immersion method on osteointegration in osteoporotic rabbits. *Int. J. Nanomedicine* 15, 1797–1807. doi:10.2147/ijn.s244815

Zhao, S. F., Jiang, Q. H., Peel, S., Wang, X. X., and He, F. M. (2013). Effects of magnesium-substituted nanohydroxyapatite coating on implant osseointegration. *Clin. Oral Implants Res.* 24 (Suppl. A100), 34–41. doi:10.1111/j.1600-0501.2011.02362.x

Zhao, Y., Bai, L., Zhang, Y., Yao, R., Sun, Y., Hang, R., et al. (2022). Type I collagen decorated nanoporous network on titanium implant surface promotes osseointegration through mediating immunomodulation, angiogenesis, and osteogenesis. *Biomaterials* 288, 121684. doi:10.1016/j.biomaterials.2022.121684

Zhe, W., Dong, C., Sefei, Y., Dawei, Z., Kui, X., and Xiaogang, L. (2016). Facile incorporation of hydroxyapatite onto an anodized Ti surface via a mussel inspired polydopamine coating. *Appl. Surf. Sci.* 378, 496–503. doi:10.1016/j.apsusc.2016.03.094

frontiers | Frontiers in Bioengineering and Biotechnology

TYPE Review
PUBLISHED 02 February 2024
DOI 10.3389/fbioe.2023.1329959

Check for updates

OPEN ACCESS

EDITED BY
Mingqiang Li,
Third Affiliated Hospital of Sun Yat-sen University, China

REVIEWED BY
Pengfei Wei,
Binzhou Medical University, China
Hong Cheng,
Southern Medical University, China
Zhong Guo,
Beijing Normal University, China

*CORRESPONDENCE
Shaojun Peng,
henry2008_ok@126.com
Yu Liu,
liuyuly1982@163.com

†These authors have contributed equally to this work

RECEIVED 30 October 2023
ACCEPTED 27 November 2023
PUBLISHED 02 February 2024

CITATION
Zhan Y, Dai Y, Ding Z, Lu M, He Z, Chen Z, Liu Y, Li Z, Cheng G, Peng S and Liu Y (2024), Application of stimuli-responsive nanomedicines for the treatment of ischemic stroke.
Front. Bioeng. Biotechnol. 11:1329959.
doi: 10.3389/fbioe.2023.1329959

COPYRIGHT
© 2024 Zhan, Dai, Ding, Lu, He, Chen, Liu, Li, Cheng, Peng and Liu. This is an open-access article distributed under the terms of the Creative Commons Attribution License (CC BY). The use, distribution or reproduction in other forums is permitted, provided the original author(s) and the copyright owner(s) are credited and that the original publication in this journal is cited, in accordance with accepted academic practice. No use, distribution or reproduction is permitted which does not comply with these terms.

Application of stimuli-responsive nanomedicines for the treatment of ischemic stroke

Yongyi Zhan[1†], Yue Dai[1†], Zhejing Ding[1], Mingtian Lu[1], Zehua He[1], Zhengwei Chen[1], Yongkang Liu[1], Zhongliang Li[1], Guangsen Cheng[1], Shaojun Peng[2*] and Yu Liu[1*]

[1]Zhuhai Interventional Medical Center, Cerebrovascular Diseases Department, Zhuhai Clinical Medical College of Jinan University (Zhuhai People's Hospital), Zhuhai, China, [2]Zhuhai Institute of Translational Medicine, Zhuhai Clinical Medical College of Jinan University (Zhuhai People's Hospital), Zhuhai, China

Ischemic stroke (IS) refers to local brain tissue necrosis which is caused by impaired blood supply to the carotid artery or vertebrobasilar artery system. As the second leading cause of death in the world, IS has a high incidence and brings a heavy economic burden to all countries and regions because of its high disability rate. In order to effectively treat IS, a large number of drugs have been designed and developed. However, most drugs with good therapeutic effects confirmed in preclinical experiments have not been successfully applied to clinical treatment due to the low accumulation efficiency of drugs in IS areas after systematic administration. As an emerging strategy for the treatment of IS, stimuli-responsive nanomedicines have made great progress by precisely delivering drugs to the local site of IS. By response to the specific signals, stimuli-responsive nanomedicines change their particle size, shape, surface charge or structural integrity, which enables the enhanced drug delivery and controlled drug release within the IS tissue. This breakthrough approach not only enhances therapeutic efficiency but also mitigates the side effects commonly associated with thrombolytic and neuroprotective drugs. This review aims to comprehensively summarize the recent progress of stimuli-responsive nanomedicines for the treatment of IS. Furthermore, prospect is provided to look forward for the better development of this field.

KEYWORDS

ischemic stroke, stimuli-responsive, nanomedicine, micro-environment, drug delivery

1 Introduction

1.1 What is ischemic stroke?

Ischemic stroke (IS) refers to a medical emergency in which brain cells are damaged or killed due to reduced blood flow to the brain tissue. The reduced blood flow is caused by cerebral artery stenosis, a thrombus in the cerebral artery, or a detached thrombus from other parts of the body. The occurrence of IS involves several risk factors, including hypertension, diabetes, smoking, dyslipidemia, obesity, and hyperhomocystinemia, among others (Gu et al., 2019; Cao et al., 2021; Walter, 2022; Wang et al., 2022). At present, the Trial of Org 10172 in Acute Stroke Treatment (TOAST criteria) is extensively applied in clinical practice. It analyzes the etiology of patients with IS based on the TOAST criteria, which considers large-artery atherosclerosis (LAA), cardioembolism (CE), small-

vessel disease, lacunar (Lac) stroke, cryptogenic (Cry) stroke, and other causes (Arsava et al., 2017; Zhang et al., 2019). Ischemic necrosis of brain tissue in different areas can lead to a variety of symptoms. Common clinical manifestations include sudden unilateral numbness or weakness, slurred speech, visual disturbances, and vertigo.

Statistically, the incidence of stroke has declined in developed countries. However, stroke still remains the second leading cause of death worldwide and the primary cause of acquired disability, imposing a significant economic burden on all countries (Herpich and Rincon, 2020). In recent years, the prevalence of stroke patients has significantly increased. IS accounts for approximately 70%–80% of all stroke cases. While the mortality rate of IS has generally stabilized due to advancements in medical care, it has become as a major cause of death and disability in China (GBD, 2019 Stroke Collaborators, 2019; Wu et al., 2019; Chao et al., 2021; Wang et al., 2022; Tu et al., 2023). Therefore, there is an desperate demand to exploit innovative approaches for treating IS to prolong patient survival and improve their quality of life.

1.2 Pathophysiology of ischemic stroke

In recent years, there has been increasing recognition of the "neurovascular unit (NVU)" concept in the discussion of stroke pathophysiology. The NVU is an integrated functional unit consisting of endothelial cells, perivascular neurons, and astrocytes surrounding blood vessels. It highlights their collective role in cerebral blood flow instead of acting independently as individual units (Tiedt et al., 2022). As a result, IS can lead to a complex pathophysiological response, resulting in neuronal damage. There is currently a consensus on the key mechanisms of ischemic injury. These mechanisms include excitotoxicity, mitochondrial dysfunction, oxidative stress, inflammatory response, disruption of the blood-brain barrier (BBB), and cellular death (George and Steinberg, 2015; Tuo et al., 2022b; Qin et al., 2022). The damage caused by these initial three mechanisms can initiate diverse cell signaling cascades, leading to either programmed or non-programmed cell death in brain cells. The aforementioned complex processes collectively contribute to altering the microenvironment of ischemic tissue. These alterations encompass excessive generation of reactive oxygen species (ROS), energy depletion, imbalances in acid-base levels, aggregation of immune cells, and enhanced production of coagulation factors.

ROS are chemically active oxygen-containing molecules. The primary oxidant forms in ischemic brain tissue are hydrogen peroxide (H_2O_2), superoxide anions ($\cdot O_2^-$), and hydroxyl radicals ($\cdot$OH). After the onset of IS, cerebral blood flow decreases, leading to a reduction in oxygen and glucose supply. Consequently, there is an excessive generation of ROS through various pathways. A major source of ROS in this process is nicotinamide adenine dinucleotide phosphate oxidase 2 (NOX2). Based on the experimental findings of Ye et al. (Yingze et al., 2022), there is a significant increase in the generation of NOX2 and ROS at 3 days post IS, which gradually decreases from 3 to 14 days. Additionally, the ROS resulting from mitochondrial dysfunction can contribute to reperfusion injury and cell death in ischemic conditions.

In hypoxic conditions, the inhibition of mitochondrial oxidative phosphorylation occurs. Cells respond by temporarily switching to anaerobic glycolysis to sustain adenosine triphosphate production. The imbalance between oxidative phosphorylation and anaerobic glycolysis in the ischemic penumbra leads to a decline in extracellular pH.

In ischemic micro-environments, the major contributors to BBB dysfunction are the production of matrix metalloproteinases (MMPs) and myeloperoxidase (MPO), along with cellular abnormalities within the NVU. These disruptions are marked by the degradation of junction proteins and an elevation in permeability (Spitzer et al., 2022). The disruption of BBB function results in the infiltration of prothrombin from the bloodstream into brain tissue. In a study conducted by Tuo et al., 2022a, proteomic analysis was performed on post-ischemic tissues which revealed that prothrombin (stroke/control ratio = 10.88) exhibited the highest upregulation among the proteins analyzed.

1.3 Current treatment

During the acute stage of IS, the primary treatment focuses on achieving vascular recanalization and minimizing brain cell damage. Vascular recanalization therapies include the administration of thrombolytic drugs and endovascular therapy (EVT). The main objective of these therapies is to restore blood flow in ischemic brain tissue. Timely and proactive clinical interventions play a crucial role in improving the prognosis of patients with IS. After a comprehensive evaluation of indications and contraindications, specific individuals may meet the criteria for intravenous thrombolysis and/or EVT. EVT is especially appropriate for patients with large vessel occlusion, as it has been associated with improved functional outcomes. However, it is essential to note that such interventions also have the risk of adverse events, including cerebral hemorrhage. Additionally, many medical institutions that initially admit stroke patients may not have advanced interventional treatment options (Berkhemer et al., 2015; Albers et al., 2018; Yang et al., 2020; Jovin et al., 2022; Yoshimura et al., 2022).

Common thrombolytic drugs include Alteplase (r-tPA), Tenecteplase, among others (Tsivgoulis et al., 2023; Yogendrakumar et al., 2023). r-tPA is currently the only thrombolytic drug approved by the Food and Drug Administration (FDA). Multiple large-scale trials have demonstrated that r-tPA can reduce the risk of long-term disability following IS. However, the utilization rate of intravenous thrombolysis is low, typically ranging from 3.2% to 5.2%, mainly due to strict limitations on the time window, indications, and contraindications. From 2019 to 2020, the overall rate of intravenous thrombolysis for acute IS in stroke center units in China was 5.64% (Ye et al., 2022). Additionally, r-tPA has limited targeting efficiency and reperfusion rates and is associated with a risk of cerebral hemorrhage of approximately 6% (Wang et al., 2022). Thrombolytic drugs can activate fibrinolysis in non-ischemic areas, leading to bleeding complications. As a result, achieving targeted and efficient drug delivery remains a significant challenge in thrombolytic therapy (Herpich and Rincon, 2020; Marko et al., 2022; Walter, 2022; Wang et al., 2022).

Neuroprotective drugs have been used in clinical practice to improve brain tissue tolerance to ischemia and minimize reperfusion injury (Fisher and Savitz, 2022; Parvez et al., 2022; Xiong et al., 2022). Numerous neuroprotective agents that target

TABLE 1 Endogenous and exogenous stimuli-responsive system for drug delivery.

Response	Linker	Nanoparticles	Drug	Model	Year	Reference
ROS						
	Phenylboronic acid pinacol ester	Maleinimide-PEG-DSPE	NR2B9C	MCAO	2018	Lv et al. (Lv et al., 2018)
		C-PEG-LysB polymer	Rapamycin	tMCAO	2019	Lu et al. (Lu et al., 2019)
		β-cyclodextrin	Tempol	MCAO	2021	Yuan et al. (Yuan et al., 2021)
		2-diethylaminoethylen (DEAE)-dextran	18β-glycyrrhetinic acid	Photochemically induced cerebral infarction model	2022	Jin et al. (Jin et al., 2023)
		Cyclic oligosaccharide β-cyclodextrin	DL-3-n-butylphthalide	MCAO	2023	Yang et al. (Yang et al., 2023)
	Oxalate bond	HBA-OC-PEG_{2000}	Rapamycin	MCAO	2021	Luo et al. (Luo et al., 2021)
		SAOR@Cur	Curcumin; Resveratrol; Angelica polysaccharide	tMCAO	2022	Su et al. (Su et al., 2022)
pH						
	Benzamide bond	Polyethylene glycol	uPA	pMCAO	2016	Cui et al. (Cui et al., 2016)
	Imide bond	Oxidized dextran	uPA	_	2018	Li et al. (Li et al., 2019)
		Methoxy poly (ethylene glycol)-block-poly (2-diisopropyl methacrylate)	Succinobucol	tMCAO	2021	He et al. (He et al., 2021)
	The protonation and charge among the polycations	Polyion complex	tPA	MCAO	2019	Mei et al. (Mei et al., 2019)
	PDPA segment	mPEG-b- P (DPA-co-HEMA)-Ce6	Rapamycin	tMCAO	2021	Cheng et al. (Cheng et al., 2021)
	Coulombic force	Hydroxyethyl starch	Smoothened agonist	tMCAO	2021	Yang et al. (Yang et al., 2021)
Enzyme						
$sPLA_2$	sn-2 ester bond	PMP-inspired nanovesicle	Streptokinase	Carotid artery thrombosis model in mice	2017	Christa L. Pawlowski et al. (Pawlowski et al., 2017)
Thrombin	NH2onorleucineoTPRSFLoCo SH	Block copolymer	Glyburide	MCAO	2018	Guo et al. (Guo et al., 2018)
	Thrombin-cleavable peptide with a sequence of LTPRGWRLGGC	Acetal-modified dextran polymer	r-tPA; ZL006e	MCAO	2019	Xu et al. (Xu et al., 2019)
	Thrombin-responsive peptide (GGLVPRGFGG, pep)	MnO_2 nanoplatform	uPA	$FeCl_3$-induced carotid thrombosis model	2021	Zhang et al. (Zhang et al., 2021)
Matrix metalloproteinase	The MMP-cleavable peptides and MMP-inactive peptides	Polyelectrolyte complex NPs	Stromal derived factor-1α; Basic fibroblast growth factor	Photothrombotic ischemic stroke	2018	Jian et al. (Jian et al., 2018)
Light						
	Au	Janus polymeric motors	Heparin	_	2018	Shao et al. (Shao et al., 2018)
	DPPT-BTTPE	Photothermal-activatable liposome	tPA	Photothrombotic ischemia model	2021	Cai et al. (Cai et al., 2022)

(Continued on following page)

TABLE 1 (*Continued*) Endogenous and exogenous stimuli-responsive system for drug delivery.

Response	Linker	Nanoparticles	Drug	Model	Year	Reference
	Thermosensitive phospholipid (DPPC)	Ultrasmall gold nanorods	uPA	_	2021	Ahmed Refaat et al. (Refaat et al., 2021)
	Platelet membrane vesicle (PM)	Melanin nanoparticle	tPA	Rat carotid artery thrombosis model	2021	Yu et al. (Yu et al., 2022c)
Magnetic field						
	γ-Fe_2O_3	γ-Fe_2O_3 magnetic nanoparticle	L-arginine	Mouse model of cerebral, cortical ischemic stroke	2020	Li et al. (Li et al., 2020)
	IONP	Magnetic nanovesicles using IONP-harbored MSC	_	tMCAO	2020	Han Young Kim et al. (Kim et al., 2020)
	γ-phase iron oxide nanoring	Ferrimagnetic vortex-domain iron oxide nanoring (FVIO)	MSC	MCAO	2022	Liu et al. (Liu et al., 2022a)
Ultrasound						
	Mechanical vibration of the gel shell	Hollow nanogels	uPA	MCAO	2017	Teng et al. (Teng et al., 2018)
	_	Sub-micrometric $CaCO_3$ –templated polymer capsules	r-tPA	_	2019	Clara Correa-Paz et al. (Correa-Paz et al., 2019)
	Sonosensitizer protoporphyrin IX (PPIX)	Platelet hybrid microglia platform	Interleukin-4 (IL-4)	MCAO	2020	Li et al. (Li et al., 2021b)

*NPs, Nanoparticles; MCAO, Middle cerebral artery occlusion; tMCAO, Transient middle cerebral artery occlusion; pMCAO, Permanent middle cerebral artery occlusion; uPA, Urokinase-type plasminogen activator; t-PA, Tissue plasminogen activator; r-tPA/rtPA, Recombinant tissue plasminogen activator; sPLA2:Secreted phospholipase A2; PMP, Platelet microparticle; IONP, iron oxide nanoparticle; MSC, Mesenchymal stem cell.

various mechanisms, particularly those that combat oxidative and nitrosative stress, have been discovered. Bisufenton and uric acid function as oxygen free radical scavengers, while Edaravone acts as an antioxidant. These compounds have shown considerable therapeutic potential in preclinical trials for IS. However, the lack of established strategies hampers the translation of promising neuroprotective agents from preclinical efficacy to effective stroke treatments (Chamorro et al., 2016). A multi-center randomized controlled trial demonstrated the efficacy of Nerinetide, a neuroprotective agent, in preclinical stroke models of ischemia-reperfusion. However, in clinical trials, Nerinetide did not significantly improve favorable clinical outcomes after endovascular embolectomy compared to the placebo group (Hill et al., 2020). Numerous neuroprotective agents have the potential to mitigate ischemia/reperfusion (I/R) injury. However, these drugs are frequently limited by their short half-lives, restricted BBB penetration, and ineffective targeting efficiency. Traditional antithrombotic and neuroprotective drug therapies are limited by safety concerns and inadequate targeting capabilities. Therefore, there is an urgent demand to address the clinical gaps in the treatment of IS.

1.4 Nanomedicine therapy

Nanomedicines represent a groundbreaking approach in the prevention, diagnosis, and treatment of various diseases. Due to their size-dependent characteristics and increased surface area, nanomedicines exhibit remarkable capabilities in the field of drug delivery. Nanomedicines accomplish targeted delivery to precise tissues or cells by fine-tuning their size, shape, and surface properties, which allows for the increased drug concentration at specific sites. Moreover, nanomedicines possess distinctive optical and magnetic properties, rendering them well-suited for diagnostic imaging and therapeutic interventions (Liu et al., 2022b; Parvez et al., 2022; Zhuang et al., 2022; Khizar et al., 2023).

Up to now, various nanomedicines have been applied in the treatment of IS, as shown in Table 1. According to Table 1, nanomedicines which are used for drug delivery to IS can be broadly classified into four categories: organic, inorganic, biomimetic, and composite nanomedicines. Organic nanomedicines, composed of organic molecules, offer various advantages including exceptional biocompatibility, high bioavailability, and easy fabrication. Furthermore, they usually do not generate toxic byproducts during degradation within the body. Inorganic nanomedicines exhibit greater stability, unique optical and magnetic properties, and a higher surface area to volume ratio compared to organic nanomedicines. However, their synthesis process typically requires sophisticated and precise conditions and methods. Biomimetic nanomedicines are designed and manufactured by imitating the structures, functions, and mechanisms found in biological systems. They can enhance drug stability, solubility, and absorption by modifying their physical and chemical characteristics, enabling targeted delivery and precise release of medications. Nevertheless, it is crucial to emphasize that safety remains a

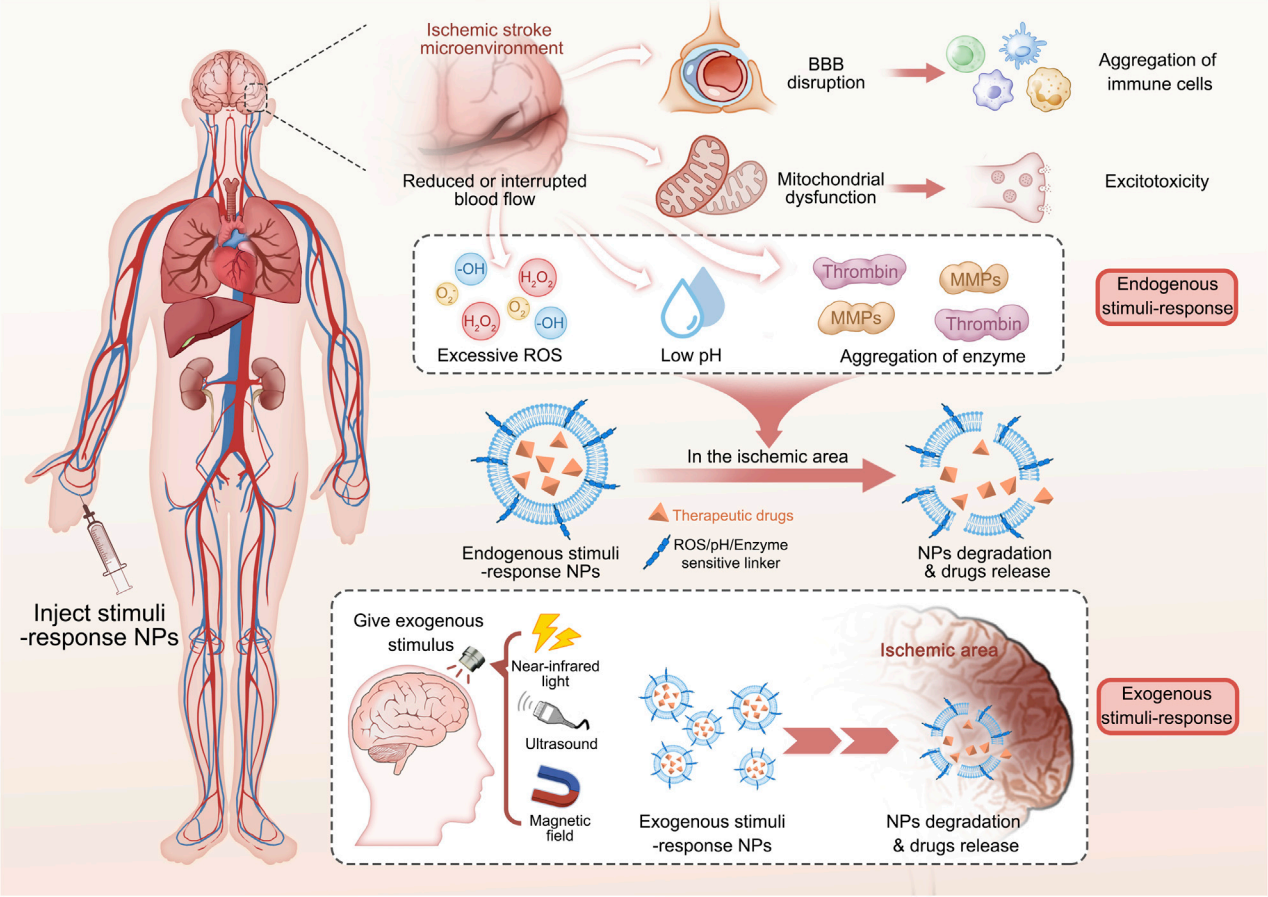

SCHEME 1
Endogenous and exogenous stimuli-responsive nanomedicines for the treatment of ischemic stroke.

top priority when using biomimetic nanomedicines for drug delivery purposes. Composite nanomedicines can combine the advantages of organic materials and inorganic materials. A commonly encountered composite nanomedicine is the metal-organic frameworks (MOFs), comprising of a crystalline structure formed by metal ions and organic ligands. MOFs display a porous structure and a significant surface area-to-volume ratio, facilitating enhanced drug loading. Their porous structure and surface modifications offer a high degree of flexibility, enabling effective targeted drug delivery and controlled release (Alkaff et al., 2020; Zenych et al., 2020; Ma et al., 2021; Yu et al., 2022b; Lin et al., 2022; Cheng et al., 2023; Ruscu et al., 2023).

In the treatment of IS, nanomedicines can be used to achieve controlled drug release, which is essential for maximizing therapeutic efficacy and ensuring *in vivo* safety. By carefully selecting appropriate nanomedicines and precisely manipulating their structures and properties, various methods can be utilized to achieve desired outcomes in drug release. In recent years, extensive research has shown that stimuli-responsive nanomedicines have the potential to greatly enhance therapeutic outcomes. These nanomedicines are designed to release payloads in response to either endogenous or exogenous stimuli. Endogenous stimuli-responsive nanomedicines achieve targeted drug release based on the pathophysiological conditions of ischemic brain tissue. These conditions include activated thrombin, excessive generation of ROS, and decreased pH levels in the ischemic tissues. By concentrating drug levels at the site of IS, this approach enhances treatment efficacy while minimizing adverse effects. Exogenous stimuli-responsive strategies use external stimuli such as magnetic fields, light, and ultrasound to precisely control the accumulation of nanomedicines in ischemic brain tissue. The targeted approach facilitates efficient drug delivery to the affected area, leading to controlled release, improved drug bioavailability, lower dosage and dosing frequency, effective therapeutic outcomes, and reduced drug-related side effects (Hassanpour et al., 2020; Li et al., 2021a). This review summarizes the recent research progress of nanomedicines in the field of IS therapy and analyzes their functional mechanisms (Scheme 1).

2 Endogenous stimuli-responsive nanomedicines

2.1 ROS stimuli-responsive nanomedicines

Specific pathophysiological changes occur in the IS microenvironment, and multiple mechanisms can induce ROS production or worsen oxidative stress injury. You et al., 2023

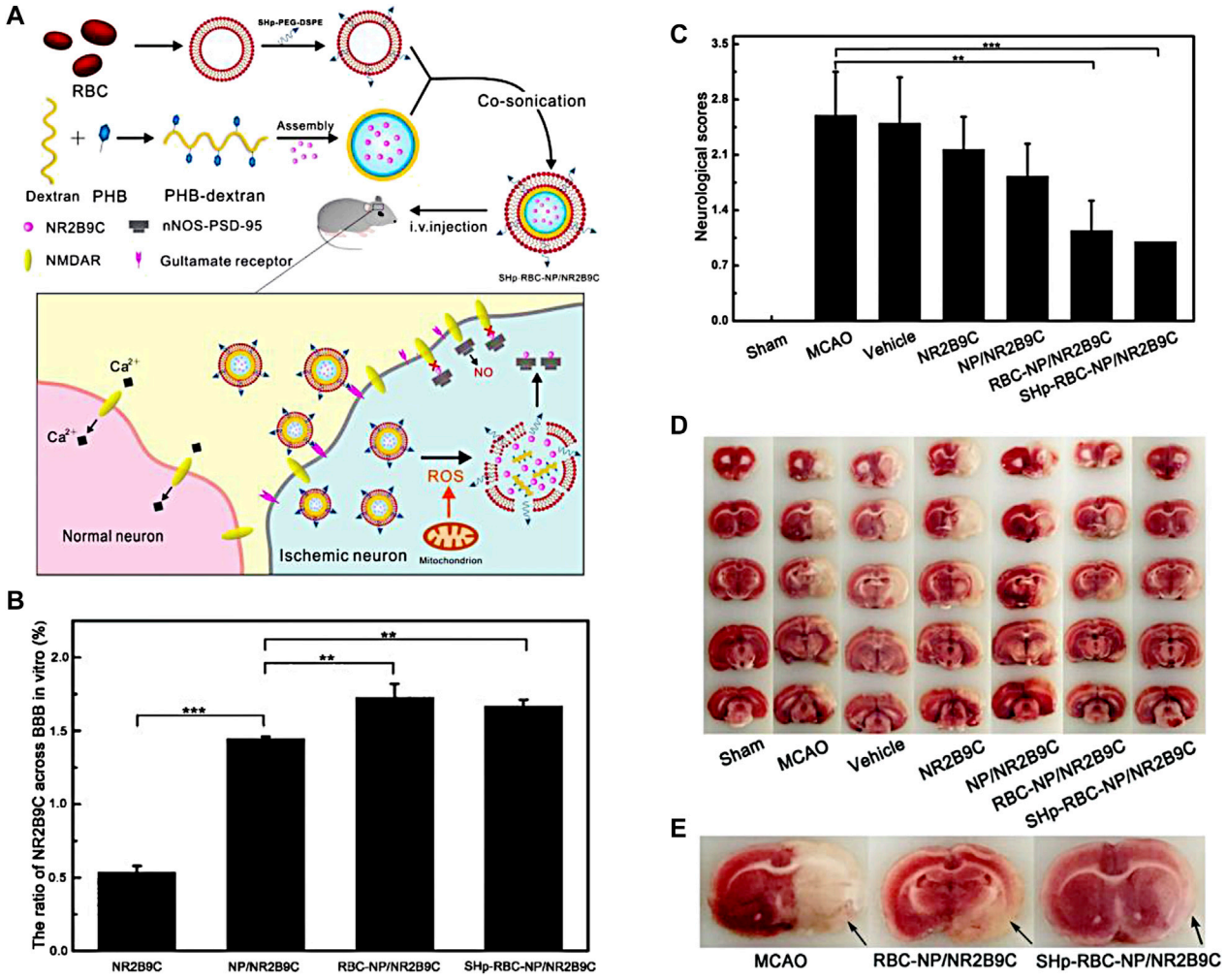

FIGURE 1
The fabrication of SHp-RBC-NP/NR2B9C and the results of animal experiments. **(A)** The fabrication of the nanomedicine. **(B)** The ratio of NR2B9C encapsulated in different samples transported to pass through BBB. **(C)** Neuroscores of rats after cerebral ischemia. **(D)** Representative slices of brain tissue from each experimental group. **(E)** Representative tissue slices demonstrating that the ROS-responsive nanomedicine greatly reduces the infarct volume. Reproduced with permission from ref (Lv et al., 2018). Copyright 2018, American Chemical Society.

confirmed that the cellular ROS levels of experimental group increased rapidly to 1.8 times than that of the control group *in vitro* experiments using an oxygen-glucose deprivation model. Furthermore, an excessive generation of ROS following reperfusion therapy has the potential to induce reperfusion injury, thereby contributing to an unfavorable prognosis. Therefore, clearing ROS effectively and limiting oxidative stress are crucial in preventing extensive cytotoxicity caused by ischemia or reperfusion injury. Considering this pathophysiological mechanism, researchers have developed ROS-responsive nanomedicines consisting of ROS-responsive moiety, which can be broadly classified into four types: boric acid, carbonyl, sulfur or selenium, and proline oligomers (Saravanakumar et al., 2017; Liu et al., 2020; Zhao et al., 2020; Wang et al., 2021).

Phenylboronic acid and its derivatives are primarily utilized as ROS-responsive groups for constructing targeted drug delivery systems in the treatment of IS. For instance, Lv et al., 2018 have developed a ROS-responsive nanomedicine containing with phenylboronic acid for IS treatment, as shown in Figure 1A. This nanomedicine utilizes the over-expressed ROS in the ischemic tissue as an intelligent "drug release switch," which incorporates a ROS bio-reactive polymer named as glucan-conjugated phenylborate and utilizes borate-modified glucan polymer vesicles to load the neuroprotector NR2B9C. The surface of the vesicles is then encapsulated with red blood cell membranes (RBC) and modified with the stroke homing peptide (SHp). This nanomedicine could reduce the clearance by the reticuloendothelial system through the signaling molecule CD47 on the RBC, which extends its blood circulation and enables high-effective delivery to the ischemic injury area with the assistance of the SHp. Upon ROS stimulation, the phenylborate in the backbone of nanomedicines undergoes fast oxidation to form phenol and boric acid, resulting in the breakage of chemical bonds. As a result, the neuroprotector NR2B9C can be rapidly released into the IS tissue to facilitate neuronal repair (Figures 1B, C). *In vivo* experiments revealed that

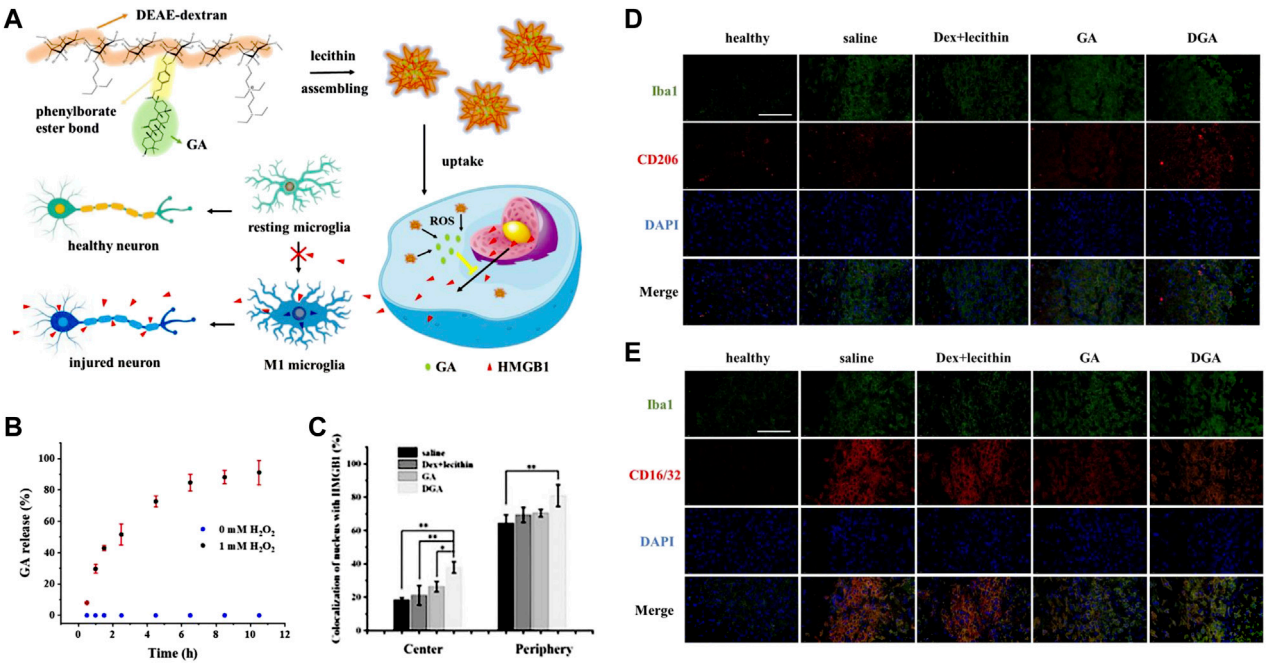

FIGURE 2
ROS-responsive DGA micelles for the treatment of IS. **(A)** The fabrication of DGA and its functional mechanisms. **(B)**The release behavior of GA in high-level of H_2O_2. **(C)** The quantitative nuclear localization percentages of HMGB1 measured in the central region of brain tissue injury. **(D)** Immunofluorescence staining on BV2 cells at the periphery of the injury site. CD206 was stained in red while Iba1 was stained in green. **(E)** Immunofluorescence staining was performed on BV2 cells at the periphery of the injury site. CD16/32 was stained in red. Reproduced with permission from ref (Jin et al., 2023).

the group treated with the designed nanomedicine exhibited a significant decrease in cerebral infarction area and improved neurological deficits after ischemia-reperfusion (Figures 1D,E).

Enhanced mammalian target of rapamycin (mTOR) activity occurs during IS, and the signaling pathway contributes to ischemia-reperfusion injury. Inhibiting this pathway can exert a neuroprotective effect. Therefore, Lu et al., 2019 designed a polymeric micelle system called CPLB/RAPA which is utilized phenylborate as the ROS-responsive group. A fibrin-binding peptide called CREKA was conjugated to the micelle as a targeted group. Rapamycin (RAPA), an mTOR inhibitor, was loaded within the nanoparticles (NPs). In ischemic tissues, high-level of ROS facilitated the degradation of LysB, leading to the rapid release of rapamycin in local IS tissue. Therefore, CPLB/RAPA exhibits a direct neuroprotective effect by clearing ROS and the released rapamycin significantly inhibits the mTOR signaling pathway, which induces microglia polarization, protects the BBB, improves microvascular perfusion, and reduces brain tissue damage.

In addition, Jin et al., 2023 recently fabricated ROS-responsive 18β-glycyrrhetinic acid (GA) conjugated diethylaminoethylen (DEAE)-dextran nanomedicines (DGA) by incorporating phenylborate into polymer backbones (Figure 2A). Phenylborate serves as the linkage between GA and glucan, which can be broken down by H_2O_2 in the oxidative stress environment of the IS. Consequently, GA can be released specifically in the focal area (Figure 2B). After stroke, high mobility group box 1 (HMGB1) exacerbates brain cell injury by participating in the neuroinflammatory cascade and promoting microglia polarization to the M1 phenotype. GA which is derived from glycyrrhizic acid significantly inhibits HMGB1 expression and phosphorylation (Figure 2C). Experiments have demonstrated that DGA effectively reduces brain tissue damage and provides protection to the ischemic penumbra (Figures 2D,E).

In a recent study conducted by Luo et al., 2021, a ROS-responsive amphiphilic copolymer named HBA-OC-PEG2000 (HOP) was developed, which was synthesized by chemically polymerizing hydroxybenzaldehyde (HBA) with oxalyl chloride (OC) and polyethylene glycol 2000 (PEG 2000). Rapa, as an effective drug for I/R injury, was loaded into HOP and subsequently encapsulated with a biomimetic cell membrane. This process led to the formation of RAPA@BMHOP, which is a promising approach. In the ischemic microenvironment, the OC in the NPs undergo rapid cleavage, leading to the fast release of RAPA. Owing to the anti-inflammatory, antioxidant, and neuroprotective effects, the accumulation of RAPA in IS tissue contributes to the relieving of the damage caused by ischemia and enhanced functional recovery following stroke. Additionally, Su et al., 2022 developed a type of nanomedicine named as MSAOR@Cur, which employed carbonyl groups as the ROS-responsive group and encapsulated with macrophage membrane to enhance the delivery efficiency. Notably, MSAOR@Cur exhibited a remarkable enhancement in post-stroke neurological function scores, thus offering a novel strategy for the neuroprotective treatment of stroke. You et al., 2023 developed ROS-responsive micelles loaded with luteolin and conducted *in vivo* experiments using the MCAO rat model. Under the high-level of ROS generated in the ischemic microenvironment,

10.3389/fbioe.2023.1329959

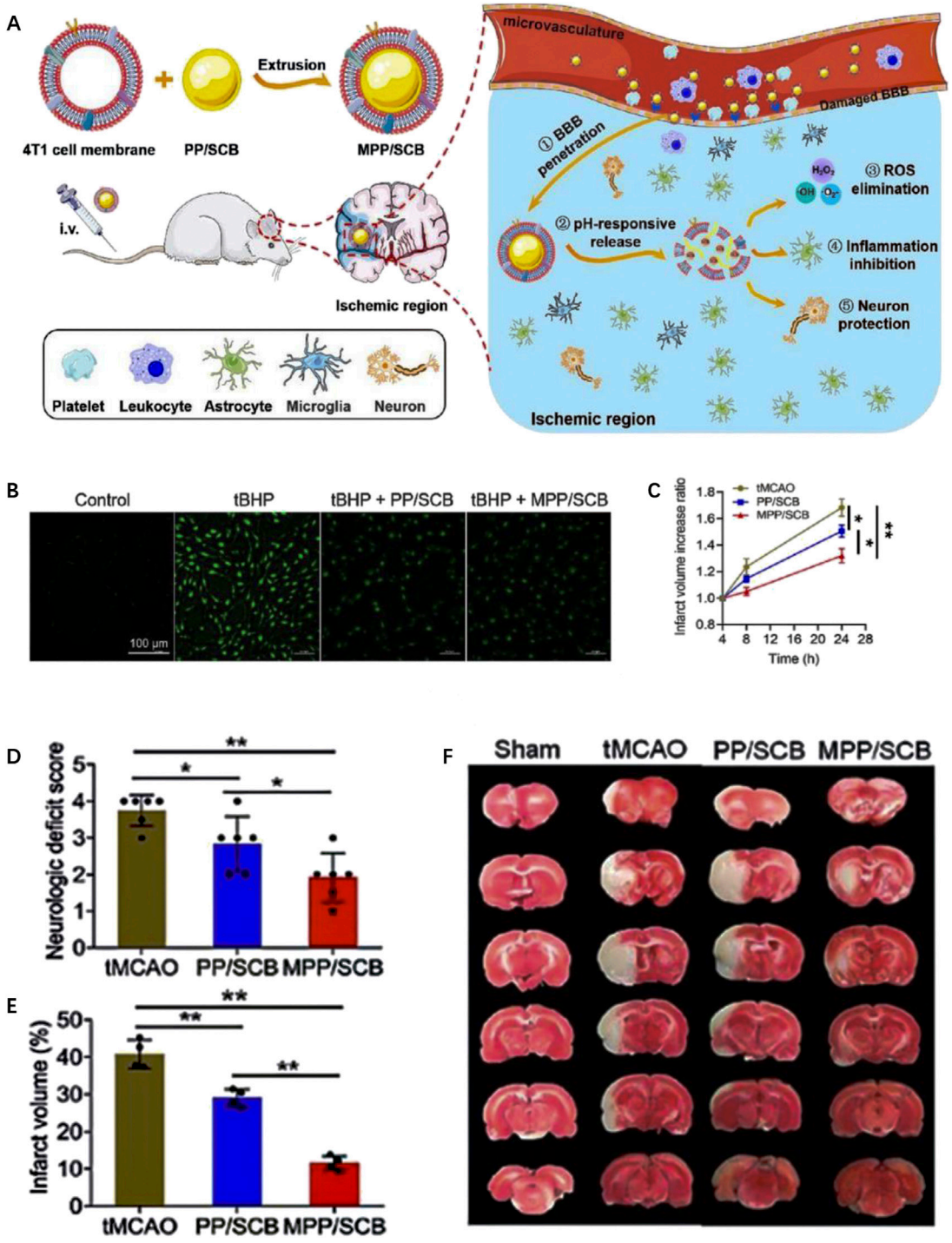

FIGURE 3
The preparation and therapeutic effect of pH-responsive MPP/SCB nanomedicine. **(A)** Scheme of the preparation and functional mechanism of MPP/SCB nanomedicine. **(B)** ROS-eliminating effects of each sample revealed by fluorescent image. **(C)** The increased ratio of brain infarct volume of tMCAO rats treated with different samples. **(D)** Neurological deficit scores of the tMCAO rats after different treatments. **(E)** Typical TTC staining images of the brain slices in sham-operated rats and tMCAO rats after different treatments. **(F)** Quantitative results of cerebral infarct volume after the treatments by different samples. Reproduced with permission from ref (He et al., 2021).

the thioketal bond of the polymer is cleaved, leading to the disintegration of the micelles. The release of luteolin from the micelles provides neuroprotective effects, leading to the superior treatment of IS.

In general, there is now much successful research for designing and synthesizing nanomedicines that can respond to high-level of ROS in the ischemic environment. The application of ROS-responsive nanomedicines for targeted delivery and controlled

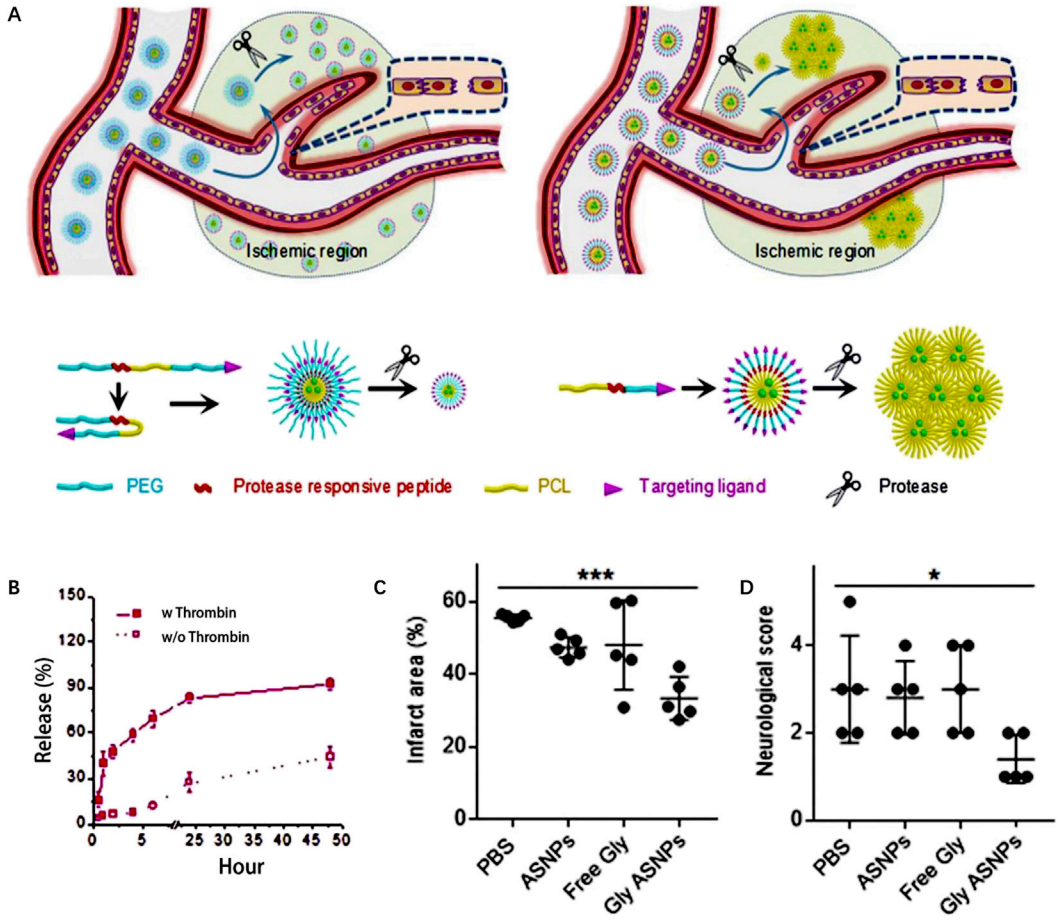

FIGURE 4
Enzyme-responsive polymeric micelles for enhanced anti-IS therapy. **(A)** The fabrication and functional mechanism of enzyme-responsive nanomedicines for anti-IS therapy. **(B)** Drug release profile with and without thrombin (100 nm). **(C)** The infarct area of MCAO mice after different treatment on postoperative day 3. **(D)** The neurological functional scores of MCAO mice after different treatment on postoperative day 3. Reproduced with permission from ref (Guo et al., 2018).

release of therapeutic drugs is a promising research field in the treatment of IS. However, large-scale clinical trials are still needed to further confirm their safety and efficacy. The results of these trials will determine whether ROS-responsive nanomedicines can become a clinically applicable treatment option. Therefore, continuous investment and effort are required in the research and development of this field to ultimately provide a safe and effective treatment for IS.

2.2 pH stimuli-responsive nanomedicines

After IS, the brain tissue experiences metabolic acidosis due to anaerobic glycolysis, ion imbalances and other factors. In a study conducted by Ilya V Kelmanson et al., 2021, it was found that the pH value in the core area dropped by approximately 0.5 units after the occurrence of an IS, ranging from 7.25 to 6.7. Furthermore, this decrease in pH level persisted for an extended period of time. The decreased pH level can activate cytokine receptors and inflammatory pathways, which further exacerbate brain tissue damage (Zhang et al., 2017). Recent studies suggest that pH can serve as a metabolic marker for distinguishing the ischemic core and penumbra following an IS. Nanotechnology offers promising prospects for utilizing pH-responsive NPs in delivering drugs to ischemic brain tissue (Harston et al., 2015; Leigh et al., 2018; Cheung et al., 2021). pH-responsive properties are typically attained through the utilization of chemical bonds that are stable at physiological pH value while susceptible to breakage at low pH values.

By utilizing benzamide bonds as pH-responsive sites, Cui *et al.* (Cui et al., 2016) developed a type of pH-responsive nanomedicine which is composed of polyethylene glycol and urokinase (PEG-UKs). It was observed that urokinase is released from PEG-UKs in acidic ischemic tissue due to the breakage of benzamide bonds in IS local environment. It is important to note that their findings do not assess the long-term efficacy of drug administration beyond the time window studied. However, they suggest that PEG-UKs have the potential to alleviate ischemic injury, although the precise underlying mechanism requires further elucidation. In a another study, Li et al., 2019 developed an RGD peptide-modified uPA-Oxd conjugate using imide bonds as the pH-responsive groups. In the

acidic environment of ischemic brain tissue, the hydrolysis of imide bonds facilitates the fast release of uPA from the nanomedicine, thereby improving efficacy in thrombolytic treatment while reducing the risk of bleeding. In a related study conducted by He et al., 2021, pH-sensitive imines are incorporated into succinylbutylbutylene (SCB) glycol polymer and is camouflaged with the 4T1 cell membrane, resulting in the formation of a biomimetic nanomedicine (MPP/SCB) (Figure 3A). 4T1 cell membrane on the surface of MPP/SCB effectively facilitates the nanomedicine to across the BBB. ROS could be eliminated by the nanomedicine as shown in fluorescence imaging (Figure 3B). Of note, imine bonds are cracked in the acidic environment of IS tissue, leading to the rapid release of SCB. *In vivo* experiments demonstrated that MPP/SCB exhibits potent antioxidant and anti-inflammatory properties, which significantly optimizes the therapeutic outcomes of IS (Figures 3C–F).

In addition to the pH-triggered bond breakage, protonation behavior was also employed to fabricate pH-responsive nanomedicines in IS treatment. For instance, Cheng et al., 2021 developed pH-sensitive amphiphilic block copolymers with PDPA fragments. In the IS acidic environment, the hydrophobic PDPA fragments undergo a transition to hydrophilicity, leading to the expansion of the nanomedicines and subsequent rapid release of the loaded drugs. Furthermore, Yang et al., 2021 have developed pH-responsive dual-targeted NPs conjugated with an integrin ligand. Subsequently, they combined the negatively charged nanocarrier with a positively charged smoothened agonist (SAG) via pH-dependent electrostatic adsorption. *In vitro* experiments demonstrated that the release rate of SAG from NPs increases with decreasing pH, which can be attributed to the reduction in negative charge within the acidic environment of ischemic brain tissue. In a particular study by Zhang et al., 2022b, betulinic acid (BA) was selected as an antioxidant for promoting neuroprotection following a stroke. To ensure swift drug release under acidic conditions, they modified the carboxyl group at the edge of the BA ring to an amino terminal group through chemical conversion, resulting in the formation of betulamin (BAM). The results suggest that the acid responsiveness of the BAM is facilitated by the amino protonation process, which disrupts the nanoparticle structure, leading to the rapid drug release.

2.3 Enzyme-responsive nanomedicines

Following the occurrence of IS, various enzymes play a role in the pathophysiological processes, including thrombin and MMPs. Tuo et al., 2022a utilized lipid metabolomics, proteomics, and immunohistochemistry techniques to investigate this phenomenon. Through their research, they identified thrombin and its downstream product ACSL4, which is involved in arachidonic acid metabolism, as key proteins in the ferroptosis-induced cell death pathway during I/R. Moreover, the researchers analyzed serum samples collected from IS patients and compared them to a healthy control group. Surprisingly, proteomic analysis revealed no significant increase in thrombin levels within the serum of IS patients. This suggests that the observed substantial increase in thrombin within ischemic brain tissue is primarily produced in the brain itself rather than originating from the serum.

Christa L. Pawlowski et al., 2017 develop platelet-inspired NPs (PMINs) which are designed to release thrombolytic agents in response to the clot-relevant enzyme phospholipase-A2 (sPLA2). sPLA2 is produced by activating platelets and inflammatory cells in ischemic tissue, which could cleave the sn-2 ester bonds in distearyl phosphatidyl choline (DSPC). The cleavage destabilizes the lipid bilayer of the vesicle, resulting in the release of the encapsulated streptokinase (SK) contained within PMINs. *In vitro* experiments demonstrated the significant membrane degradation effect of sPLA2 on PMINs. The percentage of SK released by PMINs exposed to sPLA2 within the first 2 h was approximately four times higher than that of unexposed enzymes. Furthermore, *in vivo* experiments demonstrated that SK-loaded PMINs could effectively achieve thrombolysis while reducing off-target side effects on systemic hemostasis. Guo et al., 2018 developed a ligand-conjugated polymeric nanomedicines for the enhanced treatment of IS (Figure 4A). The nanomedicines were fabricated with polyethylene (PEG), poly (ε-caprolactone) (PCL), enzyme-cleavable peptides and ligands AMD3100 (CXCR4 antagonists). The peptides in the micelles were cleaved by high-level of thrombin in the ischemic environment, leading to the disruption of the micelle structure and enhances drug release to brain tissue (Figure 4B). *In vivo* results demonstrated that enzyme-responsive micelles achieved effective anti-IS therapy by enhancing local drug concentrations in IS tissue (Figures 4C,D). Moreover (Xu et al., 2019), developed a thrombin-responsive platelet biomimetic nanomedicine (named as tP-NP-rtPA/ZL006e). This nanomedicine is composed of a thrombin-cleavable peptide which is conjugated to a core of dextran derivative polymer and is coated with platelet membranes (Figure 5A). In the presence of thrombin, glyburide is accelerated released owing to the breakage of peptide in the nanomedicine (Figure 5B). *In vitro* experiments shows that the nanomedicine demonstrates enhanced uptake by BCEC cells with thrombin (Figure 5C). *In vivo* experiments revealed that tP-NP-rtPA/ZL006e significantly improved the anti-ischemic stroke treatment effect in the model of MCAO rats (Figures 5D, E).

Except for thrombin, MMPs also represent crucial enzyme targets for IS drug delivery. For instance, Jian et al., 2018 developed a nanohybrid hydrogel using hyaluronic acid (HA) hydrogel matrices which are incorporated with stromal derived factor-1α (SDF-1α) and basic fibroblast growth factor (bFGF). The hydrogel enables controlled release of nerve growth factor in IS, due to the high-level of MMP in ischemic brain tissue, which effectively cleaves the HA. In addition, Zhang et al., 2021 made modifications to the surface of MnO_2 NPs by incorporating fucoidan (Fuco), a naturally occurring water-soluble polysaccharide, which is conjugated with a thrombin-reactive peptide (GGLVPRGFGG, pep). Additionally, urokinase-type plasminogen activators (uPA) were used as the therapeutic drug to create an enzyme-responsive nanomedicine for anti-IS therapy. Both *in vitro* and *in vivo* experiments confirmed the efficacy of the fabricated nanomedicine in achieving precise thrombolysis and remodeling of the neuroinflammatory microenvironment associated with stroke. What's more (Wang et al., 2023), developed a peptide-based template PNzyme/MnO_2 nano enzyme which utilizes the T7 sequence (HAIYPRH) and stroke homing sequence

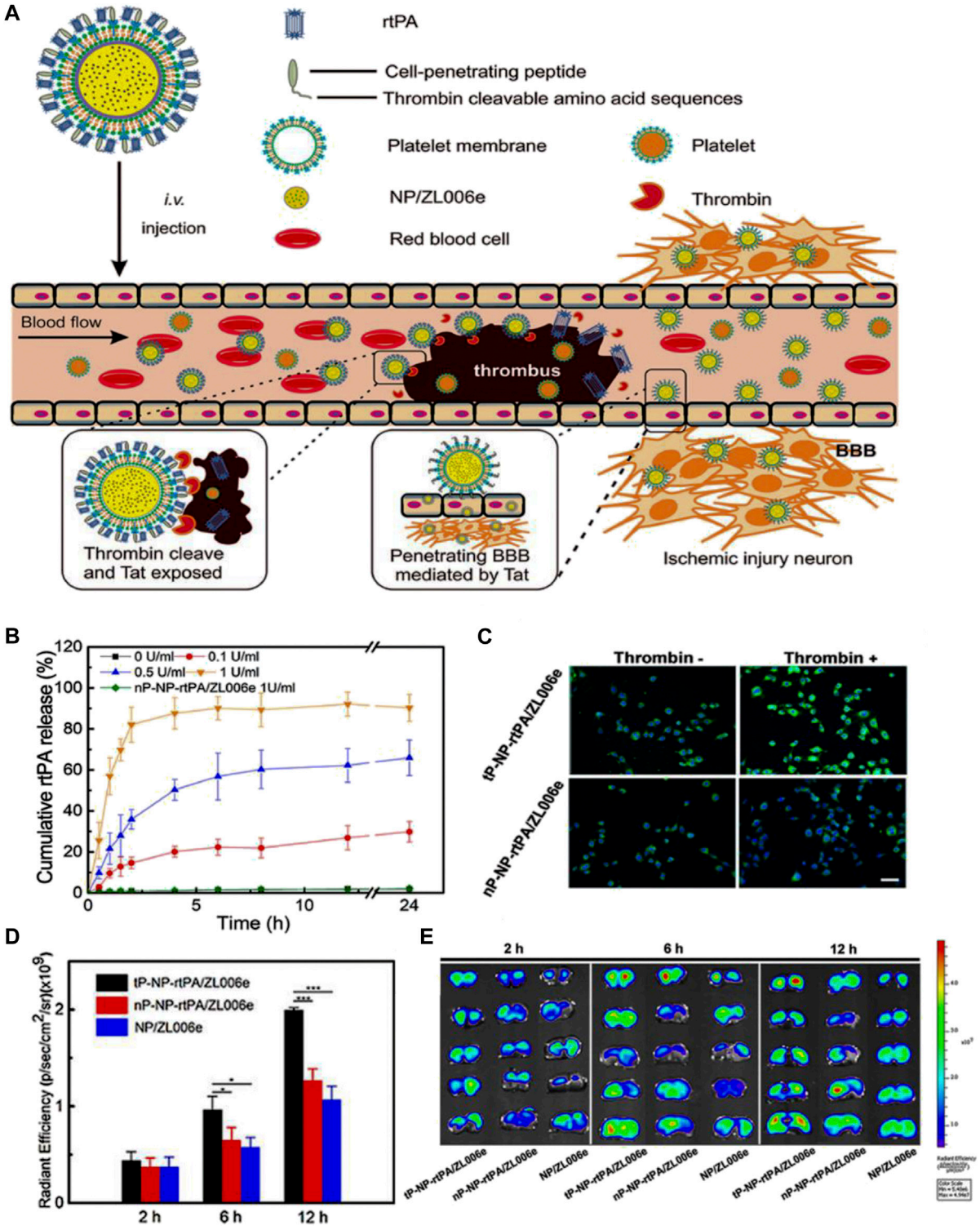

FIGURE 5
Enzyme-responsive biomimic nanomedicine for enhanced anti-IS therapy. **(A)** The fabrication and functional mechanism of enzyme-responsive biomimic nanomedicine for anti-IS therapy. **(B)** The release profile of rtPA from the nanomedicine in different level of thrombin. **(C)** The uptake behavior of the nanomedicine by BCEC cells with or without thrombin. **(D)** Fluorescence quantification of brain sections of different groups after systematic injection. **(E)** Fluorescence microscopy images of brain sections after systematic injection. Reproduced with permission from ref (Xu et al., 2019).

(CLEVSRKNC) to facilitate crossing of the BBB and accumulation in ischemic tissue. Upon recognition and cleavage by thrombin, the nanomedicine releases a thrombolytic peptide, initiating the process of thrombolysis. Moreover (Yu et al., 2022a), utilized a polyphenolic complex called tannin (TA) to establish non-covalent interactions between uPA, thrombin-cleavable peptides, and mesoporous silica

10.3389/fbioe.2023.1329959

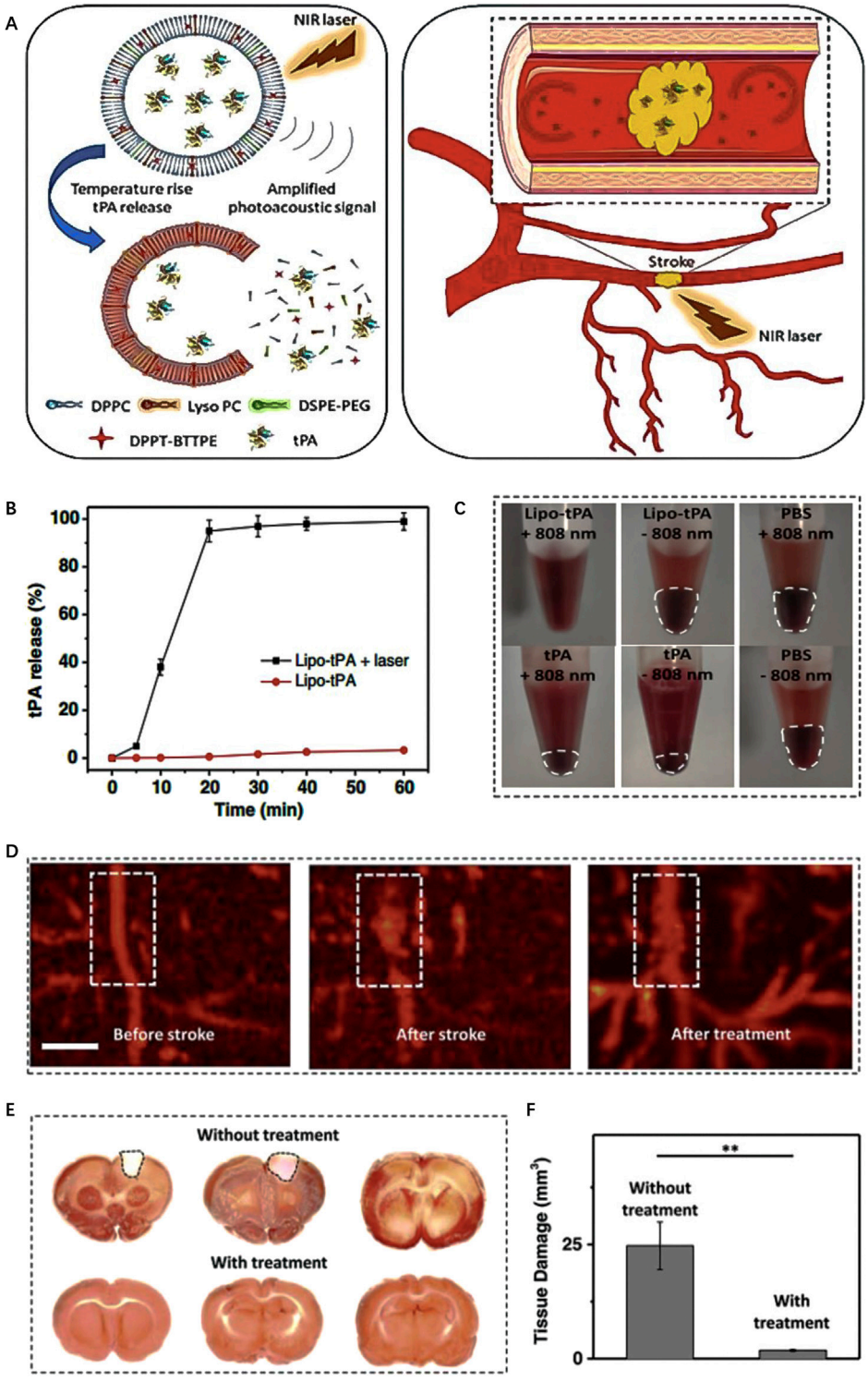

FIGURE 6
Enzyme-responsive biomimic nanomedicine for enhanced anti-IS therapy. **(A)** The fabrication and functional mechanism of enzyme-responsive biomimic nanomedicine for anti-IS therapy. **(B)** The release profile of rtPA from the nanomedicine in different level of thrombin. **(C)** The uptake behavior of the nanomedicine by BCEC cells with or without thrombin. **(D)** Fluorescence quantification of brain sections of different groups after systematic injection. **(E)** Fluorescence microscopy images of brain sections after systematic injection. Reproduced with permission from ref (Xu et al., 2019).

templates. This approach allowed for the construction of a thrombin responsive nanodrug delivery system (NDDS) known as MS@uPA/PEP/TA NPs. By employing TA as a connecting agent, the uPA and thrombin-cleavable peptides were efficiently linked to the mesoporous silica templates. This design enables the NDDS to respond to thrombin in a controlled manner. The resulting MS@

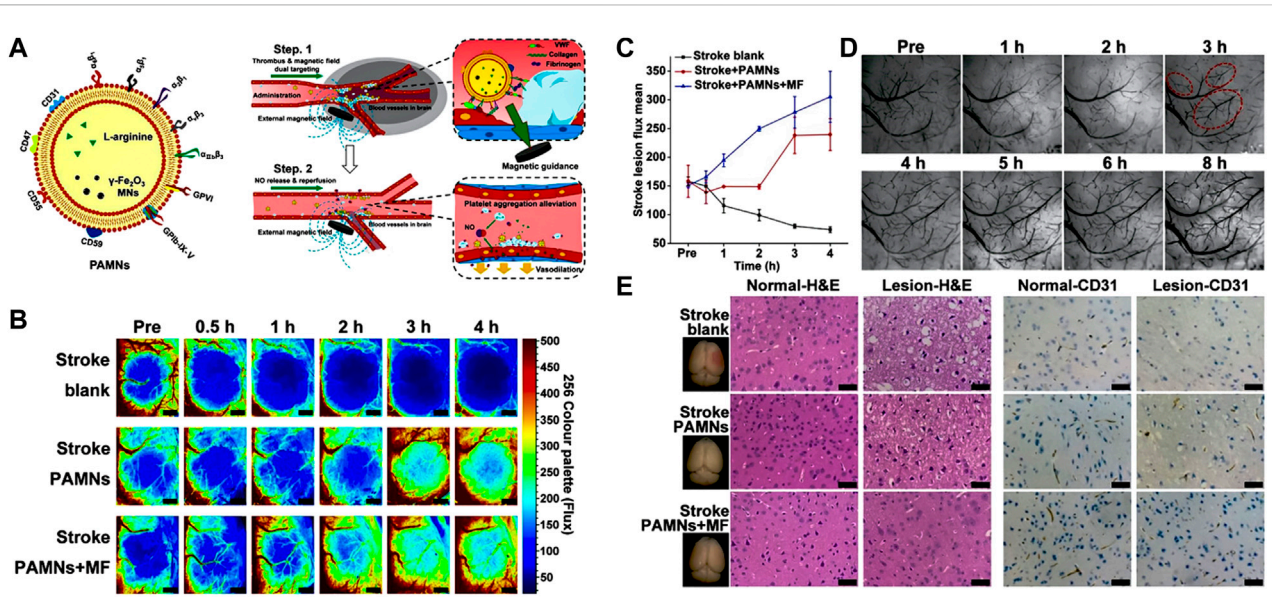

FIGURE 7
Magnetic stimuli-responsive platelet membrane biomimetic nanomedicine for anti-IS therapy. **(A)** The targeting mechanism of the designed nanomedicine *in vivo*. **(B)** The blood flow is observed by color-coded laser speckle images after different treatments. **(C)** Quantitative analysis of blood flow in ischemic lesions. **(D)** Bright field images of the stroke vascular vessel network. **(E)** H&E staining and CD31 staining for normal brain (left) tissue and ischemic lesion (right) tissue. Reproduced with permission from ref (Li et al., 2020).

uPA/PEP/TA NPs hold promise for precise drug delivery and targeted therapy in the context of stroke treatment (Wu et al., 2023). designed the MMP-responsive NDDS using the sequence -GPLGIAGQ-as a cleavable peptide. Mesoporous polydopamine NPs were used as carriers and conjugated with RAP-12, a brain-targeting peptide on the surface. It was found that the NDDS could successfully deliver the neuroprotective agent, 9-aminominocycline, into the ischemic brain region. Importantly, the NDDS achieved triggered drug release by responding to the excessive level of MMP-2, which leaded to the enhanced therapeutic outcome.

3 Exogenous stimuli-responsive nanomedicine

Exogenous nanomedicines usually rely on the unique properties of metal inorganic NPs, such as magnetic and optical features, to respond to externally applied stimuli, including near-infrared light (NIR), magnetic fields, ultrasound, and so on. External stimulus response has the advantages of spatiotemporal control, precision, and convenience. The exogenous stimuli could facilitate targeted drug delivery and controlled release in IS local tissue, thereby resulting in improved efficacy of anti-IS treatment (Rahoui et al., 2017; Zhao et al., 2019).

3.1 Light stimuli-responsive nanomedicine

Recently, photothermal effect has been found to exert excellent anti-thrombotic effect in anti-IS therapy. Upon NIR irradiation, heat is generated locally in IS tissue, which could effectively disrupt the non-covalent interaction of fibrin, leading to the dissolution of blood clots (Cook and Decuzzi, 2021). Numerous studies have suggested the therapeutic potential of photothermal induced thrombolysis in the treatment of thrombotic diseases. In addition to the thrombolytic properties, researchers have also proposed that NIR radiation may have a neuroprotective effect in animal models of ischemia (Gerace et al., 2021). Commonly utilized NPs in the field include a variety of metal inorganic nanomaterials like gold nanorods, as well as organic nanomaterials such as liposomes and micelles. In the realm of light triggered NDDS, several methods have been employed to control drug release. These include: 1) Inducing a temperature increase through light irradiation, which in turn triggers the cleavage of covalent bonds to facilitate drug release. 2) Exploiting light irradiation-induced structural changes in NPs.

For instance, Shao et al., 2018 developed a type of light-responsive nanomotors, which harness the conversion of NIR light energy into mechanical kinetic energy, thereby generating autonomous motion. The researchers utilized chitosan (CHI) and heparin (Hep) to construct Janus capsules via layer-by-layer self-organization techniques. These capsules were then cloaked with RBC to enhance biocompatibility and partially coated with a layer of gold (Au) to confer NIR responsiveness. The asymmetrical Au coating of nanomotor leads to the generation of a temperature gradient when exposed to NIR laser irradiation. As a result, the nanomotor exhibit movement through an autophoretic effect, wherein the “on/off” switch is controlled by NIR stimulation. *In vitro* experiments demonstrate that nanomotor exhibits controllable motor performance under NIR irradiation and can effectively ablate thrombi through photothermal therapy. Besides, Cai et al., 2022 devised a photothermally activated liposome encapsulating tPA (Figure 6A). The liposome is composed with DPPT-BTTPE,

which is an organic molecule with a propeller structure that exhibits proper absorption within the NIR range. The DPPT-BTTPE molecule serves dual roles: amplifying the photoacoustic signal and regulating the localized temperature rise that occurs due to the photothermal effect. This control ensures that the temperature remains within an optimal range, thus preventing tPA inactivation and potential tissue damage caused by excessive heating. Under NIR irradiation, the lipid bilayer of the liposome experiences heating and expansion, leading to the release of tPA (Figures 6B,C). Consequently, this system enables the controlled delivery of thrombolytic drugs specifically within the ischemic brain tissue, promoting effective thrombolysis, and minimizing the risk of thermal-related complications (Figures 6D–F).

Furthermore, Ahmed Refaat et al., 2021 developed a novel NIR-responsive liposomes consisting of gold nanorods (AuNRs), thermosensitive phospholipid (DPPC) and non-ionic surfactant (Brij58). When exposed to NIR light, the local temperature increases and the presence of Brij58 enables the disruption of the liposome membrane through the formation of stable nanopores, facilitating the efficient release of the encapsulated drug. In addition, Yu et al., 2022c devised a biomimetic nanovesicle termed tPA/MNP@PM (tMP), which is consisting of melanin NPs with high photothermal conversion efficiency, tPA and platelet membrane vesicles. Due to the thrombus-targeting and adhesive properties of platelet membrane, the nanovesicles exhibit effective localization at thrombus sites. Additionally, the NIR-mediated photothermal effect of tMP facilitates nanovesicle rupture, leading to precise release of tPA within the thrombus. Both *in vivo* and *in vitro* experiments have confirmed the therapeutic efficacy for IS. The study demonstrates the potential of biomimetic nanovesicles as a promising approach for targeted thrombus treatment, leveraging the benefits of thrombus specificity and controlled drug release under NIR-mediated photothermal effect.

3.2 Magnetic stimuli-responsive nanomedicine

Magnetic NPs offer significant potential as a platform for precise nanomedicine delivery, as they can be controlled and guided under external magnetic fields. To improve the stability and biocompatibility, magnetic NPs are usually coated with biocompatible polymers or encapsulated within lipid NPs. For instance, Hu et al., 2018 incorporated tPA into porous magnetic iron oxide microrods (tPA-MRs) for targeted thrombolytic therapy in IS. The magnetic properties of the NPs can be tailored based on the direction of the applied magnetic field. In a similar vein, Alba Grayston et al., 2022 functionalized poly (D-L-lactic acid-co-glycolic acid) (PLGA) with superparamagnetic iron oxide. The obtained NPs enabled magnetically targeted delivery of drugs to the IS local tissue. It is worth noting that Li et al., 2020 developed a type of platelet membrane biomimetic nanomedicine which is loaded with L-arginine and γ-Fe_2O_3 magnetic NPs (PAMNs) (Figure 7A). The magnetization of PAMNs was measured using a vibrating sample magnetometer (VSM), demonstrating excellent water solubility and superparamagnetic characteristics. The platelet membrane on PAMNs facilitated the effective across over BBB, due to its thrombus targeting ability. Under the stimulation by magnetic field, PAMNs could improve the blood flow effectively by the controlled release of L-arginine which generated NO in IS tissue to realize the significant vasodilatation (Figures 7B–D). *In vivo* experiments validated that magnetic stimuli-responsive platelet membrane nanomedicine could effectively relieve the stroke symptom, as shown in Figure 7E.

Han Young Kim et al., 2020 developed magnetic nanovesicles (MNV) using iron oxide nanoparticle-harbored mesenchymal stem cells (MSC-IONP). The superparamagnetic nature of IONP allows them to be guided to ischemic areas in the brain under an applied magnetic field. The *in vitro* and *in vivo* experiments revealed that the utilization of a magnetic field resulted in a substantial increase in the accumulation of MNV in the cerebral ischemic tissue of a rat stroke model. The accumulation of MNV was observed to be approximately 5.1 times higher compared to the group that did not receive the magnetic field application. MNV treatment exerted its therapeutic effects through three pathways, including stimulating angiogenesis, preventing apoptosis, and promoting the differentiation of macrophages from an M1 to an M2 phenotype. In another study, Liu et al., 2022a utilized γ-Phase ferrimagnetic vortex-domain iron oxide nanorings (γ-FVIOs) for labeling mesenchymal stem cells (MSCs) for field-mediated targeted delivery (Figures 8A,B). Under magnetic field, the nanomedicine showed enhanced intracellular uptake by MSCs (Figures 8C,D). Furthermore, the superparamagnetic properties of γ-FVIOs enabled sensitive and sustained *in vivo* magnetic resonance imaging (MRI) tracking (Figures 8E,F). Both *in vitro* and *in vivo* experiments demonstrated the enhanced magnetic mobility of MSCs, enabling their rapid delivery to ischemic brain tissue for enhanced anti-IS therapy (Figures 8G,H). These studies highlight the potential of superparamagnetic NPs in facilitating targeted delivery of therapeutic agents to ischemic brain tissue, offering promising strategies for stroke treatment.

3.3 Ultrasound stimuli-responsive nanomedicine

Ultrasound possesses several advantages such as non-invasiveness, safety, ease of operation and excellent tissue penetration. Consequently, ultrasound-responsive nanomedicines have been widely used for targeted drug delivery. Ultrasound-responsive drug delivery primarily exploits the acoustic effects of ultrasound, which encompass mechanical and thermal effects. The mechanical effect involves the disruption of nanomedicine structures through acoustic radiation and cavitation effects to facilitate drug release. The thermal effect entails the conversion of ultrasound energy into heat, thereby raising the temperature within the target region, which causes structural changes in the nanomedicine to trigger drug release and increases vascular permeability to enhance drug accumulation (Zhao et al., 2013; Athanassiadis et al., 2022; Zhang et al., 2022a; Fan et al., 2022).

For example, Teng et al., 2018 synthesized uPA-loaded hollow nanogels (nUKs) comprised of glycol chitosan (GC) and benzaldehyde-capped polyethylene oxide. The experiments

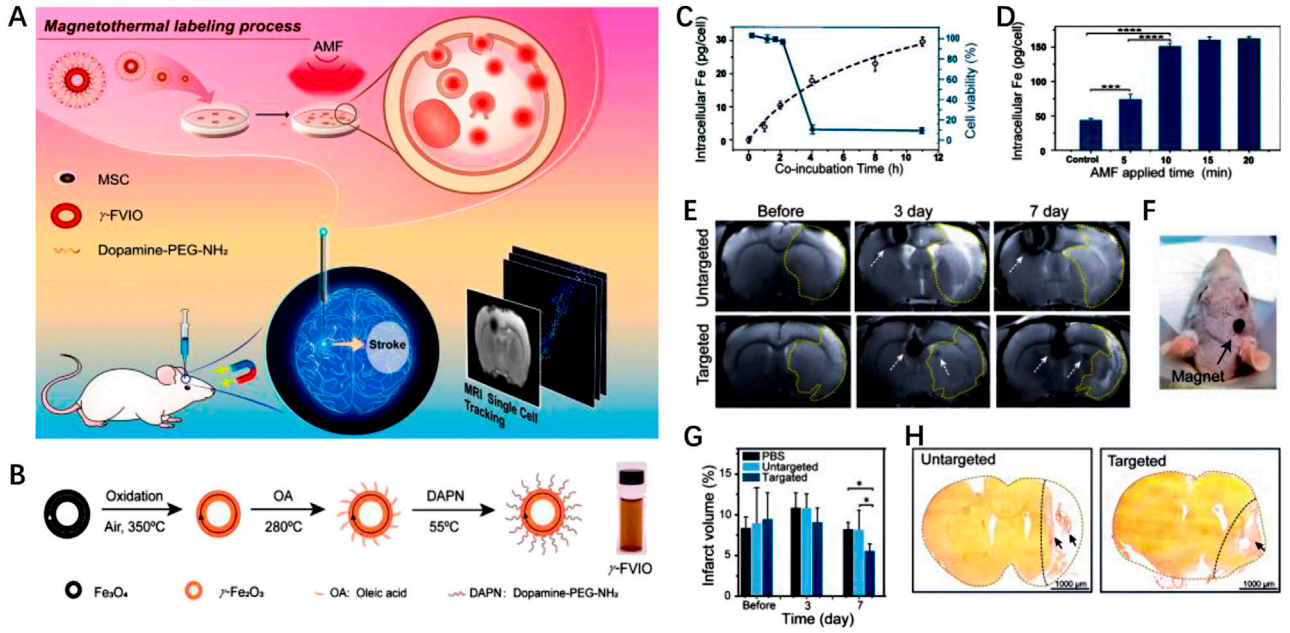

FIGURE 8
Magnetic stimuli-responsive mesenchymal stem cells-based nanomedicine for anti-IS therapy. **(A)** Scheme of the designed nanomedicine for MRI-guided imaging and therapy. **(B)** The fabrication process of γ-FVIO. **(C)** Intracellular uptake and cell viability of γ-FVIOs in different conditions. **(D)** Intracellular Fe content of MSCs at different time. **(E)** MRI imaging of cerebral infarct rats before and after treatment. **(F)** Photograph of magnetic targeting in rat brain. **(G)** The infarct volume of rats at different times. **(H)** The brain tissues rats with different treatments. Reproduced with permission from ref (Liu et al., 2022a).

revealed that nUKs exhibited a responsive behavior to 2 MHz ultrasound. When exposed to ultrasonic energy, the cross-linked polymer matrix of nUKs underwent vibration, enabling the effective release of encapsulated uPA. To evaluate the therapeutic potential of nUKs in IS treatment, the researchers employed an IS rat mode, which demonstrated that nUKs, triggered by mechanical stress under ultrasound mediation, enhanced thrombolytic efficacy without increasing the risk of bleeding. Using the layer-by-layer method, Clara Correa-Paz et al., 2019 engineered nanocapsules (NCs) referred to as sub-micrometric $CaCO_3$-templated polymer capsules with a diameter of approximately 600 nm, which were utilized to encapsulate r-tPA. *In vitro* experiments demonstrated that ultrasound-mediated delivery of r-tPA promotes thrombus decomposition. *In vivo* experiments revealed that a significant extension in the half-life of r-tPA when it is encapsulated within ultrasound-responsive NCs, suggesting enhanced thrombolytic efficacy under ultrasound stimulation. During an IS event, microglia usually exhibit two phenotypes known as M1 and M2. M1 microglia upregulate pro-inflammatory cytokines, exacerbating neuroinflammation, while M2 microglia play an anti-inflammatory role. In this context, Li et al., 2021b encapsulated interleukin-4 (IL-4) within the PPIX (sonosensitizer approved by FDA)-loaded liposomes to create an ultrasound-responsive nanomedicine. To enhance IS targeting ability, liposomes were coated with platelet membrane. Upon ultrasound irradiation, PPIX generates ROS, triggering peroxidation of the lipid bilayers, which facilitates the rapid release of IL-4. The localized accumulation of IL-4 in IS tissue induces the polarization of microglia towards the M2 phenotype, which ultimately serves a therapeutic role in neuroprotection. *In vivo* experiments performed on mouse with MCAO demonstrated that ultrasound-triggered liposomes showed significant protective effects on cerebral ischemic tissue after stroke.

4 Summary and prospect

Nanotechnology is currently utilized in various ways in the field of IS, including nanotechnology-assisted imaging diagnostics, targeted delivery of thrombolytic drugs to blood clots, and controlled drug release. Restoring blood flow and providing neuroprotection to ischemic brain tissue are crucial therapeutic strategies for IS. Administering effective neuroprotective treatment in a timely manner following a stroke or ischemic reperfusion injury can significantly enhance patients' subsequent recovery and quality of life. However, the BBB poses a challenge to delivering neuroprotective agents to ischemic brain tissue at effective concentrations due to the short half-life and low bioavailability of drugs. Consequently, drug delivery methods for IS are gaining increasing attention in recent years.

Compared to traditional drug delivery methods, stimuli-responsive nanomedicines demonstrate higher efficiency in targeted delivery and better control over drug release, which enables more effective treatment while reducing the occurrence of adverse reactions such as cerebral hemorrhage. Stimuli-responsive nanomedicines generally involve endogenous stimuli response (ROS, enzymes, pH), exogenous stimuli response (light, magnetic field, ultrasound), and dual stimuli response. Many researchers have successfully designed and prepared nanocarriers with stimuli-responsive characteristics, including organic

nanocarriers, inorganic nanocarriers, biomimetic nanocarriers, and composite nanocarriers. Organic nanomaterials are easily obtained, exhibit high biocompatibility, and are biodegradable *in vivo*. However, they have drawbacks such as poor stability and low encapsulation efficiency, which pose challenges for their practical clinical application in medicine. Biomimetic nanomaterials derived from red blood cells, immune cells, mesenchymal cells, and platelets demonstrate high biocompatibility, extended circulation time in the body, and enhanced efficiency in targeted delivery. Nevertheless, challenges in biomimetic nanocarrier research include low specificity in drug release and difficulty in large-scale production. Inorganic NPs possess photonic and magnetic responsiveness, making them more suitable for constructing exogenous stimuli-responsive nanomedicines. However, their potential toxicity and limited biocompatibility hinder the development prospects of inorganic nanomaterials. Studies have suggested that inorganic NPs can accumulate in neural tissue, but the potential long-term neurodegenerative effects remain unclear. In recent years, the combining of organic and inorganic NPs to form composite NPs has received significant attention from research teams due to their high biocompatibility, strong targeting ability, and low biological toxicity. This approach enables improved targeted drug delivery and specific drug release.

In spite of the great progress, there are still noticeable disparities between preclinical research and clinical applications in this field. The preparation of stimuli-responsive nanomedicines highlights their ability to target ischemic brain tissue, minimizing the impact on healthy tissue. However, the current assessment of safety and biocompatibility for stimuli-responsive nanomedicines is insufficient. Most studies provide data related to assessing drug toxicity to cells and tissues in animal models, but there is still a lack of research on stability, tissue compatibility, and immune response. In addition to short-term safety and biocompatibility assessments, more studies are necessary to evaluate the long-term safety of stimuli-responsive nanomedicines. These studies may include long-term animal experiments and clinical trials.

Furthermore, the complex pathophysiological processes involved in IS contribute to the apparent disparity between preclinical studies and clinical applications of stimuli-responsive nanomedicine delivery for IS treatment. This disparity arises from the necessity of conducting safety and biocompatibility assessments, optimizing the selection of drugs and carriers, and considering the intricacy and cost associated with large-scale clinical trials. In summary, long-term efforts are still needed to promote better development of stimuli-responsive nanomedicines in the field of anti-IS therapy.

Author contributions

YZ: Writing–original draft. YD: Writing–original draft. ZD: Writing–original draft. ML: Writing–original draft. ZH: Writing–original draft. ZC: Writing–original draft. YoL: Writing–original draft. ZL: Writing–original draft. GC: Writing–review and editing. SP: Writing–review and editing, Funding acquisition, Investigation, Supervision. YuL: Writing–review and editing, Investigation, Supervision.

Funding

The author(s) declare financial support was received for the research, authorship, and/or publication of this article. This work is financially supported by the National Natural Science Foundation of China (Grant No. 8217070298), Guangdong Basic and Applied Basic Research Foundation (2021A1515220011, 2022A1515010335).

Conflict of interest

The authors declare that the research was conducted in the absence of any commercial or financial relationships that could be construed as a potential conflict of interest.

Publisher's note

All claims expressed in this article are solely those of the authors and do not necessarily represent those of their affiliated organizations, or those of the publisher, the editors and the reviewers. Any product that may be evaluated in this article, or claim that may be made by its manufacturer, is not guaranteed or endorsed by the publisher.

References

Albers, G. W., Marks, M. P., Kemp, S., Christensen, S., Tsai, J. P., Ortega-Gutierrez, S., et al. (2018). Thrombectomy for stroke at 6 to 16 hours with selection by perfusion imaging. *N. Engl. J. Med.* 378 (8), 708–718. doi:10.1056/NEJMoa1713973

Alkaff, S. A., Radhakrishnan, K., Nedumaran, A. M., Liao, P., and Czarny, B. (2020). Nanocarriers for stroke therapy: advances and obstacles in translating animal studies. *Int. J. Nanomedicine* 15, 445–464. doi:10.2147/ijn.S231853

Arsava, E. M., Helenius, J., Avery, R., Sorgun, M. H., Kim, G. M., Pontes-Neto, O. M., et al. (2017). Assessment of the predictive validity of etiologic stroke classification. *JAMA Neurol.* 74 (4), 419–426. doi:10.1001/jamaneurol.2016.5815

Athanassiadis, A. G., Ma, Z., Moreno-Gomez, N., Melde, K., Choi, E., Goyal, R., et al. (2022). Ultrasound-responsive systems as components for smart materials. *Chem. Rev.* 122 (5), 5165–5208. doi:10.1021/acs.chemrev.1c00622

Berkhemer, O. A., Fransen, P. S., Beumer, D., van den Berg, L. A., Lingsma, H. F., Yoo, A. J., et al. (2015). A randomized trial of intraarterial treatment for acute ischemic stroke. *N. Engl. J. Med.* 372 (1), 11–20. doi:10.1056/NEJMoa1411587

Cai, X., Bandla, A., Wang, C., Liu, Y.-H., Chuan, C. K., Xu, Y., et al. (2022). Photothermal-activatable liposome carrying tissue plasminogen activator for photoacoustic image-guided ischemic stroke treatment. *Small Struct.* 3 (2), 2100118. doi:10.1002/sstr.202100118

Cao, Z., Li, S., Yang, H., Xu, C., Zhang, Y., Yang, X., et al. (2021). Associations of behaviors, biological phenotypes and cardiovascular health with risks of stroke and stroke subtypes: a prospective cohort study. *EClinicalMedicine* 33, 100791. doi:10.1016/j.eclinm.2021.100791

Chamorro, Á., Dirnagl, U., Urra, X., and Planas, A. M. (2016). Neuroprotection in acute stroke: targeting excitotoxicity, oxidative and nitrosative stress, and inflammation. *Lancet Neurol.* 15 (8), 869–881. doi:10.1016/s1474-4422(16)00114-9

Chao, B. H., Tu, W. J., and Wang, L. D. (2021). Initial establishment of a stroke management model in China: 10 years (2011-2020) of stroke prevention project committee, national health commission. *Chin. Med. J. Engl.* 134 (20), 2418–2420. doi:10.1097/cm9.0000000000001856

Cheng, X., Xie, Q., and Sun, Y. (2023). Advances in nanomaterial-based targeted drug delivery systems. *Front. Bioeng. Biotechnol.* 11, 1177151. doi:10.3389/fbioe.2023.1177151

Cheng, Y., Cheng, A., Jia, Y., Yang, L., Ning, Y., Xu, L., et al. (2021). pH-responsive multifunctional theranostic rapamycin-loaded nanoparticles for imaging and treatment

of acute ischemic stroke. *ACS Appl. Mater Interfaces* 13 (48), 56909–56922. doi:10.1021/acsami.1c16530

Cheung, J., Doerr, M., Hu, R., and Sun, P. Z. (2021). Refined ischemic penumbra imaging with tissue pH and diffusion kurtosis magnetic resonance imaging. *Transl. Stroke Res.* 12 (5), 742–753. doi:10.1007/s12975-020-00868-z

Cook, A. B., and Decuzzi, P. (2021). Harnessing endogenous stimuli for responsive materials in theranostics. *ACS Nano* 15 (2), 2068–2098. doi:10.1021/acsnano.0c09115

Correa-Paz, C., Navarro Poupard, M. F., Polo, E., Rodríguez-Pérez, M., Taboada, P., Iglesias-Rey, R., et al. (2019). *In vivo* ultrasound-activated delivery of recombinant tissue plasminogen activator from the cavity of sub-micrometric capsules. *J. Control Release* 308, 162–171. doi:10.1016/j.jconrel.2019.07.017

Cui, W., Liu, R., Jin, H., Lv, P., Sun, Y., Men, X., et al. (2016). pH gradient difference around ischemic brain tissue can serve as a trigger for delivering polyethylene glycol-conjugated urokinase nanogels. *J. Control Release* 225, 53–63. doi:10.1016/j.jconrel.2016.01.028

Fan, C. H., Ho, Y. J., Lin, C. W., Wu, N., Chiang, P. H., and Yeh, C. K. (2022). State-of-the-art of ultrasound-triggered drug delivery from ultrasound-responsive drug carriers. *Expert Opin. Drug Deliv.* 19 (8), 997–1009. doi:10.1080/17425247.2022.2110585

Fisher, M., and Savitz, S. I. (2022). Pharmacological brain cytoprotection in acute ischaemic stroke - renewed hope in the reperfusion era. *Nat. Rev. Neurol.* 18 (4), 193–202. doi:10.1038/s41582-021-00605-6

GBD 2019 Stroke Collaborators (2019). Global, regional, and national burden of stroke and its risk factors, 1990-2019: a systematic analysis for the Global Burden of Disease Study 2019. *Lancet Neurol.* 20 (10), 795–820. doi:10.1016/s1474-4422(21)00252-0

George, P. M., and Steinberg, G. K. (2015). Novel stroke therapeutics: unraveling stroke pathophysiology and its impact on clinical treatments. *Neuron* 87 (2), 297–309. doi:10.1016/j.neuron.2015.05.041

Gerace, E., Cialdai, F., Sereni, E., Lana, D., Nosi, D., Giovannini, M. G., et al. (2021). NIR laser photobiomodulation induces neuroprotection in an *in vitro* model of cerebral hypoxia/ischemia. *Mol. Neurobiol.* 58 (10), 5383–5395. doi:10.1007/s12035-021-02496-6

Grayston, A., Zhang, Y., Garcia-Gabilondo, M., Arrúe, M., Martin, A., Kopcansky, P., et al. (2022). Endovascular administration of magnetized nanocarriers targeting brain delivery after stroke. *J. Cereb. Blood Flow. Metab.* 42 (2), 237–252. doi:10.1177/0271678x211028816

Gu, X., Li, Y., Chen, S., Yang, X., Liu, F., Li, Y., et al. (2019). Association of lipids with ischemic and hemorrhagic stroke: a prospective cohort study among 267 500 Chinese. *Stroke* 50 (12), 3376–3384. doi:10.1161/strokeaha.119.026402

Guo, X., Deng, G., Liu, J., Zou, P., Du, F., Liu, F., et al. (2018). Thrombin-responsive, brain-targeting nanoparticles for improved stroke therapy. *ACS Nano* 12 (8), 8723–8732. doi:10.1021/acsnano.8b04787

Harston, G. W., Tee, Y. K., Blockley, N., Okell, T. W., Thandeswaran, S., Shaya, G., et al. (2015). Identifying the ischaemic penumbra using pH-weighted magnetic resonance imaging. *Brain* 138 (Pt 1), 36–42. doi:10.1093/brain/awu374

Hassanpour, S., Kim, H. J., Saadati, A., Tebon, P., Xue, C., van den Dolder, F. W., et al. (2020). Thrombolytic agents: nanocarriers in controlled release. *Small* 16 (40), e2001647. doi:10.1002/smll.202001647

He, W., Mei, Q., Li, J., Zhai, Y., Chen, Y., Wang, R., et al. (2021). Preferential targeting cerebral ischemic lesions with cancer cell-inspired nanovehicle for ischemic stroke treatment. *Nano Lett.* 21 (7), 3033–3043. doi:10.1021/acs.nanolett.1c00231

Herpich, F., and Rincon, F. (2020). Management of acute ischemic stroke. *Crit. Care Med.* 48 (11), 1654–1663. doi:10.1097/ccm.0000000000004597

Hill, M. D., Goyal, M., Menon, B. K., Nogueira, R. G., McTaggart, R. A., Demchuk, A. M., et al. (2020). Efficacy and safety of nerinetide for the treatment of acute ischaemic stroke (ESCAPE-NA1): a multicentre, double-blind, randomised controlled trial. *Lancet* 395 (10227), 878–887. doi:10.1016/s0140-6736(20)30258-0

Hu, J., Huang, S., Zhu, L., Huang, W., Zhao, Y., Jin, K., et al. (2018). Tissue plasminogen activator-porous magnetic microrods for targeted thrombolytic therapy after ischemic stroke. *ACS Appl. Mater Interfaces* 10 (39), 32988–32997. doi:10.1021/acsami.8b09423

Jian, W. H., Wang, H. C., Kuan, C. H., Chen, M. H., Wu, H. C., Sun, J. S., et al. (2018). Glycosaminoglycan-based hybrid hydrogel encapsulated with polyelectrolyte complex nanoparticles for endogenous stem cell regulation in central nervous system regeneration. *Biomaterials* 174, 17–30. doi:10.1016/j.biomaterials.2018.05.009

Jin, L., Zhu, Z., Hong, L., Qian, Z., Wang, F., and Mao, Z. (2023). ROS-responsive 18β-glycyrrhetic acid-conjugated polymeric nanoparticles mediate neuroprotection in ischemic stroke through HMGB1 inhibition and microglia polarization regulation. *Bioact. Mater* 19, 38–49. doi:10.1016/j.bioactmat.2022.03.040

Jovin, T. G., Li, C., Wu, L., Wu, C., Chen, J., Jiang, C., et al. (2022). Trial of thrombectomy 6 to 24 hours after stroke due to basilar-artery occlusion. *N. Engl. J. Med.* 387 (15), 1373–1384. doi:10.1056/NEJMoa2207576

Kelmanson, I. V., Shokhina, A. G., Kotova, D. A., Pochechuev, M. S., Ivanova, A. D., Kostyuk, A. I., et al. (2021). *In vivo* dynamics of acidosis and oxidative stress in the acute phase of an ischemic stroke in a rodent model. *Redox Biol.* 48, 102178. doi:10.1016/j.redox.2021.102178

Khizar, S., Alrushaid, N., Alam Khan, F., Zine, N., Jaffrezic-Renault, N., Errachid, A., et al. (2023). Nanocarriers based novel and effective drug delivery system. *Int. J. Pharm.* 632, 122570. doi:10.1016/j.ijpharm.2022.122570

Kim, H. Y., Kim, T. J., Kang, L., Kim, Y. J., Kang, M. K., Kim, J., et al. (2020). Mesenchymal stem cell-derived magnetic extracellular nanovesicles for targeting and treatment of ischemic stroke. *Biomaterials* 243, 119942. doi:10.1016/j.biomaterials.2020.119942

Leigh, R., Knutsson, L., Zhou, J., and van Zijl, P. C. (2018). Imaging the physiological evolution of the ischemic penumbra in acute ischemic stroke. *J. Cereb. Blood Flow. Metab.* 38 (9), 1500–1516. doi:10.1177/0271678x17700913

Li, B., Chen, R., Zhang, Y., Zhao, L., Liang, H., Yan, Y., et al. (2019). RGD modified protein-polymer conjugates for pH-triggered targeted thrombolysis. *ACS Appl. Bio Mater* 2 (1), 437–446. doi:10.1021/acsabm.8b00644

Li, C., Sun, T., and Jiang, C. (2021a). Recent advances in nanomedicines for the treatment of ischemic stroke. *Acta Pharm. Sin. B* 11 (7), 1767–1788. doi:10.1016/j.apsb.2020.11.019

Li, M., Li, J., Chen, J., Liu, Y., Cheng, X., Yang, F., et al. (2020). Platelet membrane biomimetic magnetic nanocarriers for targeted delivery and *in situ* generation of nitric oxide in early ischemic stroke. *ACS Nano* 14 (2), 2024–2035. doi:10.1021/acsnano.9b08587

Li, Y., Teng, X., Yang, C., Wang, Y., Wang, L., Dai, Y., et al. (2021b). Ultrasound controlled anti-inflammatory polarization of platelet decorated microglia for targeted ischemic stroke therapy. *Angew. Chem. Int. Ed. Engl.* 60 (10), 5083–5090. doi:10.1002/anie.202010391

Lin, X., Li, N., and Tang, H. (2022). Recent advances in nanomaterials for diagnosis, treatments, and neurorestoration in ischemic stroke. *Front. Cell Neurosci.* 16, 885190. doi:10.3389/fncel.2022.885190

Liu, B., Wu, R., Gong, S., Xiao, H., and Thayumanavan, S. (2020). *In situ* formation of polymeric nanoassemblies using an efficient reversible click reaction. *Angew. Chem. Int. Ed. Engl.* 59 (35), 15135–15140. doi:10.1002/anie.202004017

Liu, H., Sun, R., Wang, L., Chen, X., Li, G., Cheng, Y., et al. (2022a). Biocompatible iron oxide nanoring-labeled mesenchymal stem cells: an innovative magnetothermal approach for cell tracking and targeted stroke therapy. *ACS Nano* 16 (11), 18806–18821. doi:10.1021/acsnano.2c07581

Liu, M., Yang, M., Wan, X., Tang, Z., Jiang, L., and Wang, S. (2022b). From nanoscopic to macroscopic materials by stimuli-responsive nanoparticle aggregation. *Adv. Mater* 35, e2208995. doi:10.1002/adma.202208995

Lu, Y., Li, C., Chen, Q., Liu, P., Guo, Q., Zhang, Y., et al. (2019). Microthrombus-targeting micelles for neurovascular remodeling and enhanced microcirculatory perfusion in acute ischemic stroke. *Adv. Mater* 31 (21), e1808361. doi:10.1002/adma.201808361

Luo, L., Zang, G., Liu, B., Qin, X., Zhang, Y., Chen, Y., et al. (2021). Bioengineering CXCR4-overexpressing cell membrane functionalized ROS-responsive nanotherapeutics for targeting cerebral ischemia-reperfusion injury. *Theranostics* 11 (16), 8043–8056. doi:10.7150/thno.60785

Lv, W., Xu, J., Wang, X., Li, X., Xu, Q., and Xin, H. (2018). Bioengineered boronic ester modified dextran polymer nanoparticles as reactive oxygen species responsive nanocarrier for ischemic stroke treatment. *ACS Nano* 12 (6), 5417–5426. doi:10.1021/acsnano.8b00477

Ma, H., Jiang, Z., Xu, J., Liu, J., and Guo, Z. N. (2021). Targeted nano-delivery strategies for facilitating thrombolysis treatment in ischemic stroke. *Drug Deliv.* 28 (1), 357–371. doi:10.1080/10717544.2021.1879315

Marko, M., Miksova, D., Ebner, J., Lang, M., Serles, W., Sommer, P., et al. (2022). Temporal trends of functional outcome in patients with acute ischemic stroke treated with intravenous thrombolysis. *Stroke* 53 (11), 3329–3337. doi:10.1161/strokeaha.121.038400

Mei, T., Kim, A., Vong, L. B., Marushima, A., Puentes, S., Matsumaru, Y., et al. (2019). Encapsulation of tissue plasminogen activator in pH-sensitive self-assembled antioxidant nanoparticles for ischemic stroke treatment - synergistic effect of thrombolysis and antioxidant. *Biomaterials* 215, 119209. doi:10.1016/j.biomaterials.2019.05.020

Parvez, S., Kaushik, M., Ali, M., Alam, M. M., Ali, J., Tabassum, H., et al. (2022). Dodging blood brain barrier with "nano" warriors: novel strategy against ischemic stroke. *Theranostics* 12 (2), 689–719. doi:10.7150/thno.64806

Pawlowski, C. L., Li, W., Sun, M., Ravichandran, K., Hickman, D., Kos, C., et al. (2017). Platelet microparticle-inspired clot-responsive nanomedicine for targeted fibrinolysis. *Biomaterials* 128, 94–108. doi:10.1016/j.biomaterials.2017.03.012

Qin, C., Yang, S., Chu, Y. H., Zhang, H., Pang, X. W., Chen, L., et al. (2022). Signaling pathways involved in ischemic stroke: molecular mechanisms and therapeutic interventions. *Signal Transduct. Target Ther.* 7 (1), 215. doi:10.1038/s41392-022-01064-1

Rahoui, N., Jiang, B., Taloub, N., and Huang, Y. D. (2017). Spatio-temporal control strategy of drug delivery systems based nano structures. *J. Control Release* 255, 176–201. doi:10.1016/j.jconrel.2017.04.003

Refaat, A., Del Rosal, B., Palasubramaniam, J., Pietersz, G., Wang, X., Moulton, S. E., et al. (2021). Near-infrared light-responsive liposomes for protein delivery: towards

bleeding-free photothermally-assisted thrombolysis. *J. Control Release* 337, 212–223. doi:10.1016/j.jconrel.2021.07.024

Ruscu, M., Cercel, A., Kilic, E., Catalin, B., Gresita, A., Hermann, D. M., et al. (2023). Nanodrugs for the treatment of ischemic stroke: a systematic review. *Int. J. Mol. Sci.* 24 (13), 10802. doi:10.3390/ijms241310802

Saravanakumar, G., Kim, J., and Kim, W. J. (2017). Reactive-oxygen-species-responsive drug delivery systems: promises and challenges. *Adv. Sci. (Weinh)* 4 (1), 1600124. doi:10.1002/advs.201600124

Shao, J., Abdelghani, M., Shen, G., Cao, S., Williams, D. S., and van Hest, J. C. M. (2018). Erythrocyte membrane modified Janus polymeric motors for thrombus therapy. *ACS Nano* 12 (5), 4877–4885. doi:10.1021/acsnano.8b01772

Spitzer, D., Guérit, S., Puetz, T., Khel, M. I., Armbrust, M., Dunst, M., et al. (2022). Profiling the neurovascular unit unveils detrimental effects of osteopontin on the blood-brain barrier in acute ischemic stroke. *Acta Neuropathol.* 144 (2), 305–337. doi:10.1007/s00401-022-02452-1

Su, Y., Guo, C., Chen, Q., Guo, H., Wang, J., Kaihang, M., et al. (2022). Novel multifunctional bionanoparticles modified with sialic acid for stroke treatment. *Int. J. Biol. Macromol.* 214, 278–289. doi:10.1016/j.ijbiomac.2022.06.102

Teng, Y., Jin, H., Nan, D., Li, M., Fan, C., Liu, Y., et al. (2018). *In vivo* evaluation of urokinase-loaded hollow nanogels for sonothrombolysis on suture embolization-induced acute ischemic stroke rat model. *Bioact. Mater* 3 (1), 102–109. doi:10.1016/j.bioactmat.2017.08.001

Tiedt, S., Buchan, A. M., Dichgans, M., Lizasoain, I., Moro, M. A., and Lo, E. H. (2022). The neurovascular unit and systemic biology in stroke - implications for translation and treatment. *Nat. Rev. Neurol.* 18 (10), 597–612. doi:10.1038/s41582-022-00703-z

Tsivgoulis, G., Katsanos, A. H., Sandset, E. C., Turc, G., Nguyen, T. N., Bivard, A., et al. (2023). Thrombolysis for acute ischaemic stroke: current status and future perspectives. *Lancet Neurol.* 22, 418–429. doi:10.1016/s1474-4422(22)00519-1

Tu, W. J., Zhao, Z., Yin, P., Cao, L., Zeng, J., Chen, H., et al. (2023). Estimated burden of stroke in China in 2020. *JAMA Netw. Open* 6 (3), e231455. doi:10.1001/jamanetworkopen.2023.1455

Tuo, Q. Z., Liu, Y., Xiang, Z., Yan, H. F., Zou, T., Shu, Y., et al. (2022a). Thrombin induces ACSL4-dependent ferroptosis during cerebral ischemia/reperfusion. *Signal Transduct. Target Ther.* 7 (1), 59. doi:10.1038/s41392-022-00917-z

Tuo, Q. Z., Zhang, S. T., and Lei, P. (2022b). Mechanisms of neuronal cell death in ischemic stroke and their therapeutic implications. *Med. Res. Rev.* 42 (1), 259–305. doi:10.1002/med.21817

Walter, K. (2022). What is acute ischemic stroke? *Jama* 327 (9), 885. doi:10.1001/jama.2022.1420

Wang, P., Gong, Q., Hu, J., Li, X., and Zhang, X. (2021). Reactive oxygen species (ROS)-Responsive prodrugs, probes, and theranostic prodrugs: applications in the ROS-related diseases. *J. Med. Chem.* 64 (1), 298–325. doi:10.1021/acs.jmedchem.0c01704

Wang, Y. J., Li, Z. X., Gu, H. Q., Zhai, Y., Zhou, Q., Jiang, Y., et al. (2022). China stroke statistics: an update on the 2019 report from the national center for healthcare quality management in neurological diseases, China national clinical research center for neurological diseases, the Chinese stroke association, national center for chronic and non-communicable disease control and prevention, Chinese center for disease control and prevention and institute for global neuroscience and stroke collaborations. *Stroke Vasc. Neurol.* 7 (5), 415–450. doi:10.1136/svn-2021-001374

Wang, Z., Zhao, Y., Hou, Y., Tang, G., Zhang, R., Yang, Y., et al. (2023). A thrombin-activated peptide-templated nanozyme for remedying ischemic stroke via thrombolytic and neuroprotective actions. *Adv. Mater*, e2210144. doi:10.1002/adma.202210144

Wu, D., Zhou, J., Zheng, Y., Zheng, Y., Zhang, Q., Zhou, Z., et al. (2023). Pathogenesis-adaptive polydopamine nanosystem for sequential therapy of ischemic stroke. *Nat. Commun.* 14 (1), 7147. doi:10.1038/s41467-023-43070-z

Wu, S., Wu, B., Liu, M., Chen, Z., Wang, W., Anderson, C. S., et al. (2019). Stroke in China: advances and challenges in epidemiology, prevention, and management. *Lancet Neurol.* 18 (4), 394–405. doi:10.1016/s1474-4422(18)30500-3

Xiong, Y., Wakhloo, A. K., and Fisher, M. (2022). Advances in acute ischemic stroke therapy. *Circ. Res.* 130 (8), 1230–1251. doi:10.1161/circresaha.121.319948

Xu, J., Wang, X., Yin, H., Cao, X., Hu, Q., Lv, W., et al. (2019). Sequentially site-specific delivery of thrombolytics and neuroprotectant for enhanced treatment of ischemic stroke. *ACS Nano* 13 (8), 8577–8588. doi:10.1021/acsnano.9b01798

Yang, H., Luo, Y., Hu, H., Yang, S., Li, Y., Jin, H., et al. (2021). pH-sensitive, cerebral vasculature-targeting hydroxyethyl starch functionalized nanoparticles for improved angiogenesis and neurological function recovery in ischemic stroke. *Adv. Healthc. Mater* 10 (12), e2100028. doi:10.1002/adhm.202100028

Yang, P., Zhang, Y., Zhang, L., Zhang, Y., Treurniet, K. M., Chen, W., et al. (2020). Endovascular thrombectomy with or without intravenous Alteplase in acute stroke. *N. Engl. J. Med.* 382 (21), 1981–1993. doi:10.1056/NEJMoa2001123

Yang, Q., Pu, W., Hu, K., Hu, Y., Feng, Z., Cai, J., et al. (2023). Reactive oxygen species-responsive transformable and triple-targeting butylphthalide nanotherapy for precision treatment of ischemic stroke by normalizing the pathological microenvironment. *ACS Nano* 17 (5), 4813–4833. doi:10.1021/acsnano.2c11363

Ye, Q., Zhai, F., Chao, B., Cao, L., Xu, Y., Zhang, P., et al. (2022). Rates of intravenous thrombolysis and endovascular therapy for acute ischaemic stroke in China between 2019 and 2020. *Lancet Reg. Health West Pac* 21, 100406. doi:10.1016/j.lanwpc.2022.100406

Yingze, Y., Zhihong, J., Tong, J., Yina, L., Zhi, Z., Xu, Z., et al. (2022). NOX2-mediated reactive oxygen species are double-edged swords in focal cerebral ischemia in mice. *J. Neuroinflammation* 19 (1), 184. doi:10.1186/s12974-022-02551-6

Yogendrakumar, V., Beharry, J., Churilov, L., Alidin, K., Ugalde, M., Pesavento, L., et al. (2023). Tenecteplase improves reperfusion across time in large vessel stroke. *Ann. Neurol.* 93 (3), 489–499. doi:10.1002/ana.26547

Yoshimura, S., Sakai, N., Yamagami, H., Uchida, K., Beppu, M., Toyoda, K., et al. (2022). Endovascular therapy for acute stroke with a large ischemic region. *N. Engl. J. Med.* 386 (14), 1303–1313. doi:10.1056/NEJMoa2118191

You, Y., Liu, Y., Ma, C., Xu, J., Xie, L., Tong, S., et al. (2023). Surface-tethered ROS-responsive micelle backpacks for boosting mesenchymal stem cell vitality and modulating inflammation in ischemic stroke treatment. *J. Control Release* 362, 210–224. doi:10.1016/j.jconrel.2023.08.039

Yu, H., Palazzolo, J. S., Zhou, J., Hu, Y., Niego, B., Pan, S., et al. (2022a). Bioresponsive polyphenol-based nanoparticles as thrombolytic drug carriers. *ACS Appl. Mater Interfaces* 14 (3), 3740–3751. doi:10.1021/acsami.1c19820

Yu, Q., Jian, Z., Yang, D., and Zhu, T. (2022b). Perspective insights into hydrogels and nanomaterials for ischemic stroke. *Front. Cell Neurosci.* 16, 1058753. doi:10.3389/fncel.2022.1058753

Yu, W., Yin, N., Yang, Y., Xuan, C., Liu, X., Liu, W., et al. (2022c). Rescuing ischemic stroke by biomimetic nanovesicles through accelerated thrombolysis and sequential ischemia-reperfusion protection. *Acta Biomater.* 140, 625–640. doi:10.1016/j.actbio.2021.12.009

Yuan, J., Li, L., Yang, Q., Ran, H., Wang, J., Hu, K., et al. (2021). Targeted treatment of ischemic stroke by bioactive nanoparticle-derived reactive oxygen species responsive and inflammation-resolving nanotherapies. *ACS Nano* 15 (10), 16076–16094. doi:10.1021/acsnano.1c04753

Zenych, A., Fournier, L., and Chauvierre, C. (2020). Nanomedicine progress in thrombolytic therapy. *Biomaterials* 258, 120297. doi:10.1016/j.biomaterials.2020.120297

Zhang, H., Li, Z., Dai, Y., Guo, E., Zhang, C., and Wang, Y. (2019). Ischaemic stroke etiological classification system: the agreement analysis of CISS, SPARKLE and TOAST. *Stroke Vasc. Neurol.* 4 (3), 123–128. doi:10.1136/svn-2018-000226

Zhang, H., Qu, H., He, Q., Gao, L., Zhang, H., Wang, Y., et al. (2021). Thrombus-targeted nanoparticles for thrombin-triggered thrombolysis and local inflammatory microenvironment regulation. *J. Control Release* 339, 195–207. doi:10.1016/j.jconrel.2021.06.043

Zhang, J., Li, X., Kwansa, H., Kim, Y. T., Yi, L., Hong, G., et al. (2017). Augmentation of poly(ADP-ribose) polymerase-dependent neuronal cell death by acidosis. *J. Cereb. Blood Flow. Metab.* 37 (6), 1982–1993. doi:10.1177/0271678x16658491

Zhang, L., Lin, Z., Zeng, L., Zhang, F., Sun, L., Sun, S., et al. (2022a). Ultrasound-induced biophysical effects in controlled drug delivery. *Sci. China Life Sci.* 65 (5), 896–908. doi:10.1007/s11427-021-1971-x

Zhang, S., Peng, B., Chen, Z., Yu, J., Deng, G., Bao, Y., et al. (2022b). Brain-targeting, acid-responsive antioxidant nanoparticles for stroke treatment and drug delivery. *Bioact. Mater* 16, 57–65. doi:10.1016/j.bioactmat.2022.02.033

Zhao, W., Zhao, Y., Wang, Q., Liu, T., Sun, J., and Zhang, R. (2019). Remote light-responsive nanocarriers for controlled drug delivery: advances and perspectives. *Small* 15 (45), e1903060. doi:10.1002/smll.201903060

Zhao, Y., Xie, R., Yodsanit, N., Ye, M., Wang, Y., and Gong, S. (2020). Biomimetic fibrin-targeted and H(2)O(2)-responsive nanocarriers for thrombus therapy. *Nano Today* 35, 100986. doi:10.1016/j.nantod.2020.100986

Zhao, Y. Z., Du, L. N., Lu, C. T., Jin, Y. G., and Ge, S. P. (2013). Potential and problems in ultrasound-responsive drug delivery systems. *Int. J. Nanomedicine* 8, 1621–1633. doi:10.2147/ijn.S43589

Zhuang, J., Zhang, X., Liu, Q., Zhu, M., and Huang, X. (2022). Targeted delivery of nanomedicines for promoting vascular regeneration in ischemic diseases. *Theranostics* 12 (14), 6223–6241. doi:10.7150/thno.73421

Frontiers in
Bioengineering and Biotechnology

Accelerates the development of therapies, devices, and technologies to improve our lives

A multidisciplinary journal that accelerates the development of biological therapies, devices, processes and technologies to improve our lives by bridging the gap between discoveries and their application.

Discover the latest Research Topics

See more →

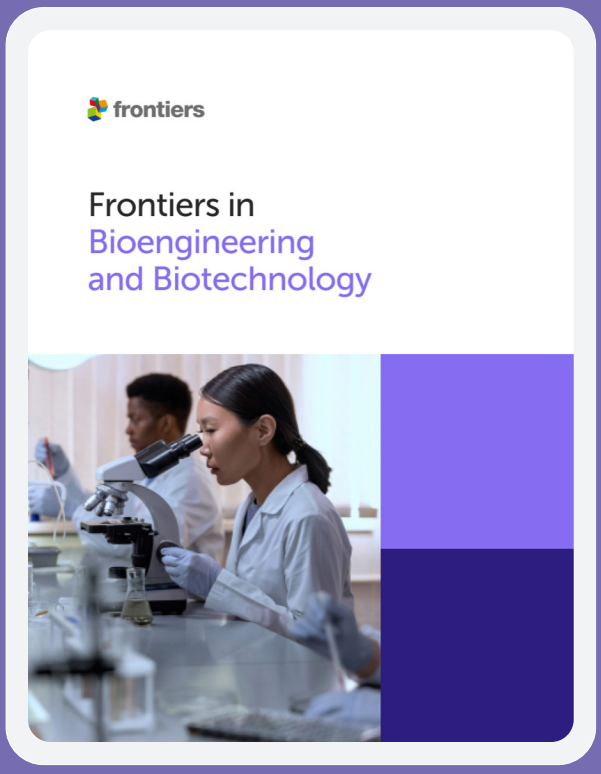

Frontiers

Avenue du Tribunal-Fédéral 34
1005 Lausanne, Switzerland
frontiersin.org

Contact us

+41 (0)21 510 17 00
frontiersin.org/about/contact